Challenges and Advances
in Computational Chemistry and Physics 16
Series Editor: Jerzy Leszczynski

Jorge M. Seminario *Editor*

Design and Applications of Nanomaterials for Sensors

Springer

Challenges and Advances in Computational Chemistry and Physics

Volume 16

Editor
Jerzy Leszczynski
Jackson State University, Jackson, Mississippi, USA

This book series provides reviews on the most recent developments in computational chemistry and physics. It covers both the method developments and their applications. Each volume consists of chapters devoted to the one research area. The series highlights the most notable advances in applications of the computational methods. The volumes include nanotechnology, material sciences, molecular biology, structures and bonding in molecular complexes, and atmospheric chemistry. The authors are recruited from among the most prominent researchers in their research areas. As computational chemistry and physics is one of the most rapidly advancing scientific areas such timely overviews are desired by chemists, physicists, molecular biologists and material scientists. The books are intended for graduate students and researchers.

More information about this series at http://www.springer.com/series/6918

Jorge M. Seminario
Editor

Design and Applications of Nanomaterials for Sensors

Springer

Editor
Jorge M. Seminario
Department of Chemical Engineering
3122 TAMU
Texas A&M University
College Station
Texas
USA

ISBN 978-94-017-8847-2 ISBN 978-94-017-8848-9 (e-Book)
DOI 10.1007/978-94-017-8848-9
Springer Dordrecht Heidelberg London New York

Library of Congress Control Number: 2014940055

© Springer Science+Business Media Dordrecht 2014
This work is subject to copyright. All rights are reserved by the Publisher, whether the whole or part of the material is concerned, specifically the rights of translation, reprinting, reuse of illustrations, recitation, broadcasting, reproduction on microfilms or in any other physical way, and transmission or information storage and retrieval, electronic adaptation, computer software, or by similar or dissimilar methodology now known or hereafter developed. Exempted from this legal reservation are brief excerpts in connection with reviews or scholarly analysis or material supplied specifically for the purpose of being entered and executed on a computer system, for exclusive use by the purchaser of the work. Duplication of this publication or parts thereof is permitted only under the provisions of the Copyright Law of the Publisher's location, in its current version, and permission for use must always be obtained from Springer. Permissions for use may be obtained through RightsLink at the Copyright Clearance Center. Violations are liable to prosecution under the respective Copyright Law.
The use of general descriptive names, registered names, trademarks, service marks, etc. in this publication does not imply, even in the absence of a specific statement, that such names are exempt from the relevant protective laws and regulations and therefore free for general use.
While the advice and information in this book are believed to be true and accurate at the date of publication, neither the authors nor the editors nor the publisher can accept any legal responsibility for any errors or omissions that may be made. The publisher makes no warranty, express or implied, with respect to the material contained herein.

Printed on acid-free paper

Springer is part of Springer Science+Business Media (www.springer.com)

Contents

1 A Quantum Chemistry Approach for the Design and Analysis of Nanosensors for Fissile Materials 1
Narendra Kumar and Jorge M. Seminario

2 Distinct Diameter Dependence of Redox Property for Armchair, Zigzag Single-walled, and Double-walled Carbon Nanotubes 31
Wenming Sun, Yuxiang Bu and Yixuan Wang

3 Design and Applications of Nanomaterial-Based and Biomolecule-Based Nanodevices and Nanosensors 61
Ke Xu, Mohsen Purahmad, Kimber Brenneman, Xenia Meshik, Sidra Farid, Shripriya Poduri, Preeti Pratap, Justin Abell, Yiping Zhao, Barbara Nichols, Eugene Zakar, Michael Stroscio and Mitra Dutta

4 Gas Sensing and Thermal Transport Through Carbon-Nanotube-Based Nanodevices 99
Y. Pouillon, A. Pérez Paz, J. Mäklin, N. Halonen, Y. Leroy, D. Mowbray, J.M. García Lastra, G. Tóth, K. Kordás, Z. Kónya, Á. Kukovecz and A. Rubio

5 Challenges Associated to the Multi-Scale Modeling of Fuel Electro-Oxidation for Fuel Cell Applications 137
King-Ki Fung, Purnima Kharidehal and Daniela S. Mainardi

6 Molecular Dynamics Studies of Graphite Exfoliation Using Supercritical CO_2 171
Jose L. Gomez-Ballesteros, Alejandro Callejas-Tovar, Luiz A. F. Coelho and Perla B. Balbuena

7 Functionalized Graphene and Cobalt Phthalocyanine Based Materials with Potential Use for Electrical Conduction 185
Gloria I. Cárdenas-Jirón, Paola León-Plata and Jorge M. Seminario

8 Computational Nanochemistry Report of the Molecular Structure, Properties and Chemical Reactivity of Pheophorbide A 217
Daniel Glossman-Mitnik

9 The Local Ionization Energy as a Guide to Site Reactivities on Graphenes 249
Jane S. Murray, Zenaida Peralta-Inga Shields and Peter Politzer

10 Moiré Patterns Observed in Bi Layer Graphene Irradiated with High Energetic Protons 271
D. H. Galvan, A. Posada Amarillas, S. Mejía, C. Wing and M. José-Yacamán

11 Theoretical Study of bi Layer Graphene used as Gas Detector 281
Diana Barraza-Jimenez, M. A. Flores-Hidalgo and D. H. Galvan

Index 289

Contributors

Justin Abell Nanoscale Science and Engineering Center, Department of Biological and Agricultural Engineering, The University of Georgia, Athens, GA, USA

A. Posada Amarillas Departamento de Investigación en Física, Universidad de Sonora, Hermosillo, SON, México

Perla B. Balbuena Department of Chemical Engineering, Texas A&M University, College Station, USA

Diana Barraza-Jimenez Centro de Investigación en Alimentación y Desarrollo, A. C. Unidad Delicias, Delicias, Chih, México

Kimber Brenneman Bioengineering Department, University of Illinois at Chicago, Chicago, IL, USA

Alejandro Callejas-Tovar Department of Chemical Engineering, Texas A&M University, College Station, USA

Gloria I. Cárdenas-Jirón Laboratorio de Química Teórica, Facultad de Química y Biología,, Universidad de Santiago de Chile, Santiago, Chile

Luiz A. F. Coelho Materials Science and Engineering Department, Santa Catarina State University, Florianópolis, Brazil

Mitra Dutta Electrical and Computer Engineering Department, University of Illinois at Chicago (UIC), Chicago, IL, USA

Physics Department, University of Illinois at Chicago, Chicago, 851 S. Morgan Street IL, USA

Sidra Farid Electrical and Computer Engineering Department, University of Illinois at Chicago (UIC), Chicago, IL, USA

M. A. Flores-Hidalgo Centro de Investigación en Materiales Avanzados, Chihuahua, Chih, México

King-Ki Fung Chemical Engineering Program, Institute for Micromanufacturing, Louisiana Tech University, Ruston, LA, USA

D. H. Galvan Centro de Nanociencias y Nanotecnología—Universidad Nacional Autónoma de México, Ensenada, BC, México

Department of Chemical Engineering and International Center for Nanotechnology & Advanced Materials, University of Texas at Austin, Austin, TX, USA

San Ysidro, CA, USA

J. M. Garcaí Lastra Nano-Bio Spectroscopy group and ETSF Scientific Development, Universidad del Paíis Vasco, Centro de Física de Materiales CSIC-UPV/EHU-MPC and DIPC, San Sebastián, Spain

Daniel Glossman-Mitnik Departamento de Simulación Computacional y Modelado Molecular, Laboratorio Virtual NANOCOSMOS, Centro de Investigación en Materiales AvanzadosCIMAV, Chihuahua, Mexico

Jose L. Gomez-Ballesteros Department of Chemical Engineering, Texas A&M University, College Station, USA

N. Halonen Microelectronics and Materials Physics Laboratories, and EMPART Research Group of Infotech Oulu, University of Oulu, Oulu, Finland

M. José-Yacamán Department of Chemical Engineering and International Center for Nanotechnology & Advanced Materials, University of Texas at Austin, Austin, TX, USA

Purnima Kharidehal Chemical Engineering Program, Institute for Micromanufacturing, Louisiana Tech University, Ruston, LA, USA

Z. Kònya MTA-SZTE "Lendulet" Porous Nanocomposites Research Group, Department of Applied andEnvironmental Chemistry, University of Szeged, Szeged, Hungary

K. Kordás Microelectronics and Materials Physics Laboratories, and EMPART Research Group of Infotech Oulu, University of Oulu, Oulu, Finland

Á Kukovecz MTA-SZTE "Lendulet" Porous Nanocomposites Research Group, Department of Applied andEnvironmental Chemistry, University of Szeged, Szeged, Hungary

Narendra Kumar Department of Chemical Engineering, Texas A&M University, College Station, USA

Paola León-Plata Department of Chemical Engineering, Texas A&M University, Texas, USA

Y. Leroy MTA-SZTE "Lendulet" Porous Nanocomposites Research Group, Department of Applied andEnvironmental Chemistry, University of Szeged, Szeged, Hungary

Daniela S. Mainardi Chemical Engineering Program, Institute for Micromanufacturing, Louisiana Tech University, Ruston, LA, USA

S. Mejía Facultad de Ciencias Físico-Matemáticas, Universidad Autónoma de Nuevo León, San Nicolas de los Garza, México

Xenia Meshik Bioengineering Department, University of Illinois at Chicago, Chicago, IL, USA

D. Mowbray Nano-Bio Spectroscopy group and ETSF Scientific Development, Universidad del Paíis Vasco, Centro de Física de Materiales CSIC-UPV/EHU-MPC and DIPC, San Sebastián, Spain

Jane S. Murray CleveTheoComp, Cleveland, OH, USA

Department of Chemistry, University of New Orleans, New Orleans, LA, USA

J. Mèklin Microelectronics and Materials Physics Laboratories, and EMPART Research Group of Infotech Oulu, University of Oulu, Oulu, Finland

Barbara Nichols SEDD Directorate, US Army Research Laboratory, Adelphi, MD, USA

Shripriya Poduri Electrical and Computer Engineering Department, University of Illinois at Chicago (UIC), Chicago, IL, USA

Peter Politzer CleveTheoComp, Cleveland, OH, USA

Department of Chemistry, University of New Orleans, New Orleans, LA, USA

Y. Pouillon Nano-Bio Spectroscopy group and ETSF Scientific Development, Universidad del Paíis Vasco, Centro de Física de Materiales CSIC-UPV/EHU-MPC and DIPC, San Sebastián, Spain

Preeti Pratap Bioengineering Department, University of Illinois at Chicago, Chicago, IL, USA

A. P′rez Paz Nano-Bio Spectroscopy group and ETSF Scientific Development, Universidad del Paíis Vasco, Centro de Física de Materiales CSIC-UPV/EHU-MPC and DIPC, San Sebastián, Spain

Mohsen Purahmad Electrical and Computer Engineering Department, University of Illinois at Chicago (UIC), Chicago, IL, USA

A. Rubio Nano-Bio Spectroscopy group and ETSF Scientific Development, Universidad del Paíis Vasco, Centro de Física de Materiales CSIC-UPV/EHU-MPC and DIPC, San Sebastián, Spain

Jorge M. Seminario Department of Chemical Engineering, Texas A&M University, College Station, USA

Department of Materials Science and Engineering, Texas A&M University, College Station, USA

Department of Electrical and Computer Engineering, Texas A&M University, College Station, USA

Zenaida Peralta-Inga Shields CleveTheoComp, Cleveland, OH, USA

Michael Stroscio Electrical and Computer Engineering Department, University of Illinois at Chicago (UIC), Chicago, IL, USA

Bioengineering Department, University of Illinois at Chicago, Chicago, IL, USA

Physics Department, University of Illinois at Chicago, Chicago, 851 S. Morgan Street IL, USA

Wenming Sun The Center for Modeling & Simulation Chemistry, Institute of Theoretical Chemistry, Shandong University, Jinan, P.R. China

G. Tòth Microelectronics and Materials Physics Laboratories, and EMPART Research Group of Infotech Oulu, University of Oulu, Oulu, Finland

Yixuan Wang Department of Natural Science, Albany State University, Albany, GA, USA

C. Wing Instituto Nacional de Energía Nuclear, Ocoyoacac, Estado de México, México

Ke Xu Electrical and Computer Engineering Department, University of Illinois at Chicago (UIC), Chicago, IL, USA

Eugene Zakar SEDD Directorate, US Army Research Laboratory, Adelphi, MD, USA

Yiping Zhao Nanoscale Science and Engineering Center, Department of Physics and Astronomy, The University of Georgia, Athens, GA, USA

Chapter 1
A Quantum Chemistry Approach for the Design and Analysis of Nanosensors for Fissile Materials

Narendra Kumar and Jorge M. Seminario

Abstract The contamination of groundwater due to accidental leakage of radioactive wastes pose a grave danger to the environment and human life and hence trace characterization of these radioactive materials is of paramount importance in nuclear forensics and reprocessing. In this work, we examine the applicability of graphene-based nanosensor for detection of radionuclides based on *ab initio* density functional theory and Greens function theory. The presence of foreign moiety near graphene or graphene oxide causes an amplification of observable quantities in the whole molecule as successfully observed in the past with chemical and biological agents (Rangel and Seminario, J Chem Phys 132(125102):1–4, 2010). Changes in the molecular electrostatic potential due to presence of radionuclides near graphene or GO can be transduced and amplified into current-voltage characteristics at nanoscale which can enable us to detect trace amounts of these radionuclides.

1.1 Introduction

Today's world is galloping at a rapid pace towards nuclear energy as largest, economical and emission-free source of energy. But the potential hazards and unforeseen disasters (recent accident in Fukushima, Japan) have always played on the minds of think tanks and researchers globally. The presence of uranium and plutonium complexes in contaminated soil and water around nuclear processing facilities especially after a nuclear accident would provide us with critical information to guide a proper and timely response. As a consequence, design and fabrication of electronic molecular devices as sensors for radionuclides using theoretical and

J. M. Seminario (✉) · N. Kumar
Department of Chemical Engineering, Texas A&M University,
College Station, TX 77843, USA
e-mail: seminario@tamu.edu

J. M. Seminario
Department of Materials Science and Engineering, Texas A&M University,
College Station, TX 77843, USA

Department of Electrical and Computer Engineering, Texas A&M University,
3122 TAMU, College Station, TX 77843, USA

J. M. Seminario (ed.), *Design and Applications of Nanomaterials for Sensors*,
Challenges and Advances in Computational Chemistry and Physics 16,
DOI 10.1007/978-94-017-8848-9_1, © Springer Science+Business Media Dordrecht 2014

experimental studies has gained paramount importance in the nuclear community. We review in this chapter our *ab initio* density functional theory calculations of U and Pu complexes with graphene and graphene oxide in order to examine the applicability of a graphene-based fissile sensor. Changes in the molecular electrostatic potential due to presence of a foreign moiety near graphene or GO can be transduced and amplified into current-voltage characteristics at nanoscale. By comparing the change in current due to presence of U or Pu complexes near a graphene and graphene oxide, we should be able to detect trace amounts of these radionuclides. The plasmonic features of nanosized graphene sheets (or graphene oxides) are strongly coupled to their electrical, magnetic, vibronic, and optical characteristics, and are significantly affected by presence of other molecules(such as nuclear agents) that may attach to its surface. Theoretical simulations in the past have shown the possible application of graphene-based devices to identify single molecules with high selectivity [1].Recently, graphene oxide (GO) is shown experimentally to be more effective in removal of radionuclides compared to traditional bentonite clays and activated carbon [2]. It was reported that flakes of graphene oxide (GO) when added to water containing U/Pu along with Ca and Na, caused radionuclides to condense into clumps.

In order to design a fissile nanosensor, the first step is to identify the major radionuclides and their form present in soils and groundwater around contaminated sites and production facilities and obtain their optimized structure. Based on earlier works uranium and plutonium are known to be major constituents dissolved in nuclear waste water in the form of chlorides, nitrates, carbonates and sulfates [3–5]. Uranium in aqueous solution is predominantly present in the form of UO_2^{2+} complexes while plutonium exhibits four different oxidation states, III, IV, V and VI; the last two as the dioxo-species PuO_2^{+} and PuO_2^{2+} [6]. A lot of research has been done to study the chemistry of UO_2^{2+} and PuO_2^{2+} ions and their complexes in aqueous solution using *ab initio* calculations [4, 7–11]. The ground state of the plutonyl ion (PuO_2^{2+}) has been determined as ^3H_g while that of uranyl (UO_2^{2+}) is found to be $^1\Sigma_g^{+}$ [12]. The actinyls UO_2^{2+}, PuO_2^{2+} and NpO_{2+} form pentagonal bipyramidal complexes with the surrounding water molecules [7], with five water molecules strongly bound in equatorial plane. A six-coordination complex is also reported to be equally favorable for UO_2^{2+} in aqueous solution based on solvation free energy [9]. When counter-ions (CO_3^{2-}, OH^- and NO_{3-}) are present, one or two water molecules in the first shell are replaced by the counter-ions preserving five-fold symmetry. The structure and stability of nitrate and sulfate complexes of uranyl and plutonyl have been also reported in literature [4]. In addition, electronic and spectroscopic properties for silicate, phosphate, and arsenate complexes of uranyl complexes $H_2UO_2SiO_4(H_2O)_3$, $HUO_2PO_4(H_2O)_3$, and $HUO_2AsO_4(H_2O)_3$ and carbonate complexes for plutonyl of the types PuO_2CO_3 and the hydrated forms, $PuO_2CO_3(H_2O)_n$ (n = 1, 2) have been studied in great detail [10, 11].

DFT has been heavily used to study the structural properties of these complexes as can be seen from literature. The aquo and nitrate complexes of PuO_2^{2+} and Pu^{4+} in addition to the aquo-chloro complexes of PuO_2^{2+} have been reported using DFT and scalar relativistic effective core potentials (RECP)in vacuum as well as with

polarizable continuum solvation model [13]. The solvation of Pu^{3+} ion in water was also investigated using relativistic DFT [5].The actinides (U^{3+}, Pu^{3+} and Pu^{4+}) show a higher coordination number of 9–10 with water molecules [14, 15].The maximal number of chloride ions in the first coordination sphere of Pu(III) and Pu(IV) ions is found to be eight using DFT calculations [16].

1.2 Theory of Electron Transport Through a Molecule

For a molecular system of N-electrons and M-nuclei, the time-independent Schrödinger equation for a non-relativistic system is

$$\hat{\mathrm{H}}(\{R_i\};\{r_i\})\Psi(\{r_i\}) = E(\{R_i\})\Psi(\{r_i\}) \tag{1.1}$$

where $\hat{\mathrm{H}}$ is the total energy operator defined as

$$\hat{\mathrm{H}} = -\sum_{i=1}^{N}\frac{\hbar^2}{2m}\nabla_i^2 - \sum_{A=1}^{M}\frac{\hbar^2}{2m}\nabla_A^2 - \sum_{i=1}^{N}\sum_{A=1}^{M}\frac{Z_A e^2}{r_{iA}} + \sum_{A=1}^{M}\sum_{B>A}^{M}\frac{Z_A Z_B e^2}{R_{AB}} + \sum_{i=1}^{N}\sum_{j>i}^{N}\frac{e^2}{r_{ij}} \tag{1.2}$$

and $\Psi(\{r_i\}) = \Psi(\vec{r}_1, \vec{r}_2, \vec{r}_3 \ldots\ldots, \vec{r}_N)$ is in 3N-dimensional space assuming spin is implicitly included.

The above equation can be solved analytically for hydrogen-like atoms or ions having single electron and the solution is found to be of the form

$$\Psi_{nlm}(\vec{r}) = \Psi_{nlm}(r,\theta,\varphi) = R_{nl}(r)Y_l^m(\theta,\varphi) \tag{1.3}$$

For a system of two or more electrons, no analytical solution can be obtained in closed form as in the case of hydrogen. Using the Born-Oppenheimer approximation of decoupling the electronic and nuclear motion due to huge mass of nuclei compared to that of electron, one can partition the wavefunction into electronic and nuclear components.

$$\hat{\mathrm{H}} = \hat{\mathrm{H}}_{elec} + \hat{\mathrm{H}}_{nuc} \tag{1.4}$$

where

$$\hat{\mathrm{H}}_{elec} = -\sum_{i=1}^{N}\frac{\hbar^2}{2m}\nabla_i^2 - \sum_{i=1}^{N}\sum_{A=1}^{M}\frac{Z_A e^2}{r_{iA}} + \sum_{i=1}^{N}\sum_{j>i}^{N}\frac{e^2}{r_{ij}} \tag{1.5}$$

or,

$$\hat{\mathrm{H}} = \hat{T} + \hat{V}_{ext} + \hat{V}_{ee} \tag{1.6}$$

where

$$\hat{T} = -\sum_{i=1}^{N} \frac{\hbar^2}{2m} \nabla_i^2 = \text{kinetic energy of electrons}$$

$$\hat{V}_{ext} = -\sum_{i=1}^{N} \sum_{A=1}^{M} \frac{Z_A e^2}{r_{iA}} = \text{nuclei-electron interaction energy}$$

$$\hat{V}_{ee} = \sum_{i=1}^{N} \sum_{j>i}^{N} \frac{e^2}{r_{ij}} = \text{electron-electron interaction energy}$$

Variational principle: According to this principle, any trial wavefunction for the ground state always yields an upper bound to the exact energy E,

$$E \leq \left\langle \Psi^t \left| \hat{\mathrm{H}} \right| \Psi^t \right\rangle \tag{1.7}$$

and

$$\Psi^t = \sum_i C_i u_i \tag{1.8}$$

This allows us to choose a basis-set of functions $\{u_i\}$ such that a linear combination of them will tend to exact energy. Thus the problem reduces to finding the coefficients of linear combination which minimizes Eq. (1.7).

1.2.1 Standard Ab-Initio Methods

Mean field approximation: Wavefunction is a product of single-electron wavefunctions and there is no correlation between motions of two electrons. In other words, each single electron sees a smeared out cloud of other electrons and moves in an average potential due to other electrons present.

$$\Psi(\{r_i\}) = \phi_1(\vec{r}_1)\phi_2(\vec{r}_2)\phi_3(\vec{r}_3)\ldots\ldots\phi_N(\vec{r}_N) \tag{1.9}$$

This reduces the 3N-dimensional problem to N 3-dimensional problem. For each electron, we can then write, [17]

$$\left[-\frac{\hbar^2}{2m}\nabla^2 - \sum_{A=1}^{M} \frac{Z_A e^2}{r_{iA}} + \sum_{i \neq j}^{N} e^2 \int \frac{|\phi_j(r_j)|^2}{r_{ij}} d^3 r_j \right] \phi_i(\vec{r}_i) = E' \phi_i(\vec{r}_i) \tag{1.10}$$

The above set of equations is called Hartree equation. However, as per Pauli's exclusion principle, an orbital can have only two electrons of opposite spin and electrons are indistinguishable. This principle puts a restriction on the wavefunction that

it has to be anti-symmetric with respect to the exchange of electrons and therefore, it has to be in the form of a Slater determinant,

$$\Psi(\vec{r}_1,\vec{r}_2,\vec{r}_3\ldots\ldots,\vec{r}_N)=\frac{1}{\sqrt{N!}}\begin{bmatrix}\phi_1\left((\vec{r}_1)\right) & \cdots & \phi_N\left((\vec{r}_1)\right)\\ \vdots & \ddots & \vdots\\ \phi_1\left((\vec{r}_N)\right) & \cdots & \phi_N\left((\vec{r}_N)\right)\end{bmatrix} \tag{1.11}$$

Substituting the above wavefunction in Eq. 1.5, results in the Hartree-Fock equations [17]

$$\begin{aligned}&\left[-\frac{\hbar^2}{2m}\nabla^2-\sum_{A=1}^{M}\frac{Z_A e^2}{r_{iA}}\right]\phi_i(\vec{r}_i)\\&+\sum_{j=1}^{N}e^2\int\frac{|\phi_j\left(r_j\right)|^2\ \phi_i\ (r_i\ )}{r_{ij}s}d^3r_j+\sum_{j=1}^{N}e^2\int\frac{\phi_j^*\left(r_j\right)\phi_i\left(r_j\right)\phi_j\left(r_i\right)}{r_{ij}}d^3r_j\\&=E'\phi_i\left(\vec{r}_i\right)\end{aligned} \tag{1.12}$$

The second integral is the exchange energy which arises due to indistinguishability of electrons. Both Hartree and Hartree-Fock equations are iterative in nature. To solve the wavefunction for one electron, we need wavefunction of other electrons in the system i.e. they are self-consistent in nature and the procedure is called SCF.

Density Functional Theory (DFT) solves the Schrödinger equation through an exact procedure that bypasses the calculation of the wavefunction [18]. DFT method uses the electron density instead of wavefunction to obtain the energy eigenvalues and is based on the Hohenberg-Kohn theorems (1964).

Theorem 1: Ground state wavefunction $\Psi_o(\vec{r}_1,\vec{r}_2,\vec{r}_3\ldots\ldots,\vec{r}_N)$ is a functional of ground state electron density $\rho_o(\vec{r})$ where

$$\rho_o(\vec{r})=N\int d^3\vec{r}_2 d^3\vec{r}_3\ldots d^3\vec{r}_N\left|\Psi_o(\vec{r}_1,\vec{r}_2,\vec{r}_3\ldots\ldots,\vec{r}_N)\right|^2 \tag{1.13}$$

In matrix form, $\rho_o(\vec{r})=N\left\langle\Psi|\delta(\vec{r}-\vec{r}_i)|\Psi\right\rangle$

Theorem 2: Ground state energy is also a functional of electron density,

$$E=E_v[\rho] \tag{1.14}$$

Using variational principle, we can then write $E_v[\rho^t]\geq E$

The electronic part of Schrodinger equation for ground state can then be written as

$$E[\rho] = \hat{T}[\rho] + \hat{V}_{ext}[\rho] + \hat{V}_{ee}[\rho] \tag{1.15}$$

The classical electron-electron repulsion $(\hat{V}_H)$ can be extracted out of $\hat{V}_{ee}[\rho]$ and the remainder is called exchange-correlation energy (E_{XC}).

$$\hat{V}_{ee}[\rho] = \hat{V}_H[\rho] + E_{XC}[\rho] \tag{1.16}$$

This results in the Kohn-Sham equations (1965) as shown, [17]

$$\left[-\frac{\hbar^2}{2m}\nabla^2 + V_{ext}(r) + V_H(r) + V_{XC}(r)\right]\phi_i(\vec{r}) = \varepsilon_i\phi_i(\vec{r}) \tag{1.17}$$

with $\rho_o(\vec{r}) = N\sum_{i=1}^{N} |\phi_i|^2$.

The idea is to use a set of molecular orbitals with a sole purpose of representing the electron density of non-interacting electrons that have the same density as the real system.

Basis-sets: A basis-set is a set of vectors (generally non-orthogonal one-particle functions) which span a space used to build molecular orbitals (MO). These MOs are linear combinations of atomic orbitals (LCAO); thus the MOs are also one-particle functions. From Schrödinger equation,

$$\hat{\mathrm{H}}\Phi = E\Phi$$

and $\Phi = \sum_m \phi_m u_m$ where ϕ_m are the coefficients and $\{u_m\}$ are the basis functions. Substituting in above equation yields:

$$\hat{\mathrm{H}}\sum_m \phi_m u_m = E\sum_m \phi_m u_m \tag{1.18}$$

Multiplying by u_n^* on both sides and integrating over $\vec{r}$ gives:

$$\sum_m H_{nm}\,\phi_m = E\sum_m S_{nm}\,\phi_m \tag{1.19}$$

$$H_{nm} = \int d\vec{r}\,u_n^*(\vec{r})\hat{\mathrm{H}}u_m(\vec{r}); S_{nm} = \int d\vec{r}\,u_n^*(\vec{r})u_m(\vec{r}) \tag{1.20}$$

In matrix form, this can be written as:

$$[H]\{\Phi\} = E[S]\{\Phi\} \tag{1.21}$$

[H] is the Hamiltonian matrix and [S] is the overlap matrix. If the basis functions $\{u_m\}$ are orthonormal, then [S] becomes an identity matrix.

There are different types of basis-sets available. The smallest basis-set is called minimal basis set where each AO is represented by only one basis function called Slater type orbital (STO).

$$\phi_{abc}^{STO}(x,y,z) = Nx^a y^b z^c e^{-\zeta r} \tag{1.22}$$

Atomic orbitals (AOs) in most quantum mechanics programs are represented by atom-centered Gaussians or Gaussian type orbitals (GTOs)because of the simplicity to solve the four-center integrals compared to the direct use of hydrogenic functions or even Slater type orbitals.

$$\phi_{abc}^{GTO}(x,y,z) = Nx^a y^b z^c e^{-\zeta r^2} \tag{1.23}$$

For example, one STO is constructed with three Gaussian functions, also called primitives, in the STO-3G basis set. Well, the nomenclature relates to the fit the three Gaussians to get the Slater orbital. Then we have double-zeta and triple-zeta basis sets where each valence AO is represented by two and three basis functions respectively and the core electrons mostly by just one. Typical of this type are the common split-valence basis sets. A double split-valence basis set (also named double-ζ) is represented as *c*-*mn*G (also referred to as Pople basis-sets [19]) where *c* is the number of primitive (Gaussian) functions to represent the core orbitals and the valence orbitals are split in two groups: one with *m* primitives representing the inner valence and another with *n* Gaussians for the outer valence orbitals (for example, the 6–31G). These rules were followed at the earlier days of quantum chemistry but several deviations were made in order to provide the best basis sets, especially when second row or higher atoms are involved. For instance, the triple-ζ basis set 6–311G for silicon does not follow exactly such distribution of Gaussian primitives. Often polarization functions (denoted by *) and diffuse functions (denoted by+) are added to these basis-sets to make them more flexible and therefore to obtain more accurate results.

1.2.2 Electron Transport Through Single Molecule

To account for semi-infinite metallic contacts attached to the molecule, Schrödinger equation is modified as

$$E[I]\Psi = [H]\Psi + [\Sigma]\Psi + \{s\} \tag{1.24}$$

where $\sum$ and $\{s\}$ represent outflow and inflow of electrons from contacts respectively [20, 21]. The wavefunction Ψ for the modified Schrödinger equation can be written as

$$\Psi = G^R\{s\} \tag{1.25}$$

where G^R is called the retarded Greens function for the molecule including the effect of contacts and is defined as

$$G^R = [EI - \Sigma - H]^{-1} \tag{1.26}$$

In this approach, sometimes called non-equilibrium Green function, [20, 21] the Green function G for the whole system in matrix form has infinite dimensions but can be partitioned into a set of finite matrices, [22]

$$G(E) = \begin{bmatrix} g_1^{-1} & -\tau_1 & 0 \\ -\tau_1^{\dagger} & E1 - H_C & -\tau_2^{\dagger} \\ 0 & -\tau_2 & g_2^{-1} \end{bmatrix}^{-1} = \begin{bmatrix} G_1 & G_{1M} & G_{12} \\ G_{M1} & G_M & G_{M2} \\ G_{21} & G_{2M} & G_2 \end{bmatrix} \tag{1.27}$$

The submatrices G and g in above matrix represent Green functions when interactions among subsystems are included or excluded, respectively. H_C is the Hamiltonian of the isolated molecule and E is the electron energy. G_M is the retarded Green function G^R in above equation. The self-energy term Σ accounting for the interaction between the molecule and the contacts are calculated as

$$\Sigma = \Sigma_1 + \Sigma_2 \tag{1.28}$$

where $\Sigma = \tau_i^{\dagger} g_i \tau_i$.

The Hamiltonian matrix H_C used for molecular description is obtained using DFT calculations where few metallic atoms are added to each end of the molecule of interest. This helps us to describe molecular electronic structure as well as the coupling between the molecule and the contacts more accurately. From the matrix form of the Schrodinger Equation,

$$[H_{KS}]\Psi = \varepsilon[S]\Psi$$

and making

$$H \rightarrow [S]^{-1}[H_{KS}]$$

The calculated Kohn-Sham Hamiltonian in the atomic basis set can be partitioned in submatrices, where the subscripts 1 and *2* refer to the contacts and *M* to the molecule [22].

$$[H_{KS}] = \begin{bmatrix} H_{11} & H_{1M} & H_{12} \\ H_{M1} & H_{MM} & H_{M2} \\ H_{21} & H_{2M} & H_{22} \end{bmatrix} \tag{1.29}$$

The overlap matrix [*S*] can also be partitioned in similar fashion. The Hamiltonian and the overlap matrices for the extended molecule are recalculated at each bias field in order to account for the reorganization of the molecular electronic structure due to the external field as well as charge transfer between molecule and contacts. H_{MM} is assigned to H_C and H_{iM} and H_{Mi} are assigned to τ_i and $\tau_i^{\dagger}$ respectively. This simplifies the expressions for calculating self-energy terms as

$$\sum_i = H_{Mi} g_i H_{iM} \tag{1.30}$$

The Green function for nano-contacts (clusters of *n* Au atoms), g_i, can be approximated as a diagonal matrix $n \times n$ with each element being a diagonal matrix proportional to their local, *s*, *p*, and d_{t2e} and d_{eg} density of states over all atoms representing the nano-contacts.

$$g_i(E) = \begin{pmatrix} g_i^1 & \cdots & 0 \\ \vdots & \ddots & \vdots \\ 0 & \cdots & g_i^n \end{pmatrix} \tag{1.31}$$

The DOS and its *s*, *p* and *d* contributions for the gold clusters are obtained from the electronic structure of optimized geometry and its converged electronic structure. Thus, the Green function for each atom of the metallic contact is given by [22]

$$g_i^k(E) = \begin{bmatrix} D_i s^k(E) & 0 & 0 & 0 \\ 0 & D_i p^k(E) & 0 & 0 \\ 0 & 0 & D_i d_{t_{2g}}^k(E) & 0 \\ 0 & 0 & 0 & D_i d_{e_g}^k(E) \end{bmatrix} \tag{1.32}$$

The rate at which electrons are released from the contacts is given by Γ where Σ is the self-energy matrix and $\Sigma^{\dagger}$ is its adjoint.

$$\Gamma = i[\Sigma - \Sigma^{\dagger}] \tag{1.33}$$

where

$$G^A = [G^R]^{\dagger} \tag{1.34}$$

The current flowing through the molecule depends on number of electrons flowing through the channel given by [20]

$$N = Trace(\{\Psi\}\{\Psi\}^{\dagger}) = \frac{Trace[G^n]}{2\pi} \tag{1.35}$$

where

$$G^n = G^R \Sigma^{in} G^A \tag{1.36}$$

and

$$\Sigma^{in} = \Gamma_1 f_1 + \Gamma_2 f_2 \tag{1.37}$$

The spectral function A of the system contact-molecule-contact is given by

$$A = G^R \Gamma G^A \tag{1.38}$$

The trace of matrix A gives the density of state (DOS). The current through a terminal 'p' is given by

$$I_p = \frac{q}{h} Trace\left[\Gamma_p A f_p - \Gamma_p G^n\right] \tag{1.39}$$

This further can be modified for current from contact 1 to

$$I_1(E) = \frac{q}{h} Trace\left[\Gamma_1 G^R \Gamma_2 G^A\right](f_1(E) - f_2(E)) \tag{1.40}$$

The terms $f_1(E)$ and $f_2(E)$ are the Fermi functions for the two contacts. Hence, conductance of the junction can be calculated as

$$G(E) = \frac{q^2}{h} T(E) \tag{1.41}$$

where $\bar{T}(E)$ is called the Transmission function and it is defined as

$$T(E) = Trace\left[\Gamma_1 G^R \Gamma_2 G^A\right] \tag{1.42}$$

The total current is obtained by integrating Eq. (1.37) over energy states,

$$I(V) = \frac{2e}{h} \int_{-\infty}^{+\infty} dE T(E,V)\left[f_1(E,V_1) - f_2(E,V_2)\right] \tag{1.43}$$

The applied voltage shifts the Fermi level in the metal contacts by E_{f1} and E_{f2} up and down and the chemical potential of the molecule (μ) (shifts in between which defines the limits for electron transport [22, 23].

$$E_{f1} = \mu - \frac{1}{2} eV \tag{1.44}$$

and

$$E_{f2} = \mu + \frac{1}{2} eV \tag{1.45}$$

1.3 Methodology

The Hamiltonian and overlap matrices required in above formulation are obtained from optimized molecular structures of interest using density functional theory [24, 25] with the hybrid functional B3PW91. This functional utilizes Becke exchange [26] with some component of Hartree-Fock [27–29] and the correlation functional of Perdew-Wang [30–34], and has been used successfully in a variety of applications involving molecular electronics devices [35, 36]. The basis-set used for DFT calculations are Stuttgart effective core potential and associated basis set (ECP60MWB_SEG)for plutonium and uranium [37, 38] and the LANL2DZ basis set and effective core potentials for gold atoms [39, 41]. For other atoms present in the system, 6–31G(d) basis set is used [42]. The ECP parameters for Au have been derived from atomic wavefunctions obtained in relativistic Hartree-Fock calculations [39–41] and hence include some relativistic effects while the ECP parameters for U and Pu are based on a quasi-relativistic level of theory [37, 38]. The Stuttgart small-core scalar relativistic effective core potential (also referred as RECP) has been used widely to study structure of plutonium complexes and have shown good agreement with experimental results. Successful comparison with experiment for Pu were reported (experimental values inside parentheses) for the ionization potentials 5.69–5.74 eV (6.03 eV); [37, 38] and for geometry of several plutonium complexes, e.g., $PuO_2(H_2O)_5^{2+}$: Pu–O = 1.72 Å (1.74 Å) and $Pu–O_w$ = 2.44 Å (2.41 Å); $PuO_2(NO_3)_2(H_2O)_2$: Pu–O = 1.74 Å (1.73 Å), $Pu–O_w$ = 2.53 Å (2.43 Å), and $Pu–O_N$ = 2.46 Å (2.50 Å); $PuO_2(Cl)_2(H_2O)_3$: Pu–O = 1.73 Å (1.75 Å), $Pu–O_w$ = 2.53 Å (2.49 Å), and Pu–Cl = 2.67 Å (2.70 Å); $Pu(H_2O)_8^{4+}$: $Pu–O_w$ = 2.39 Å (2.39 Å) [13]. Stuttgart ECP as implemented in Gaussian 09 has also been used to study hydration and oxidation study of plutonyl ion in gas phase [43].

All of the DFT calculations are performed with the program GAUSSIAN-09 [44].The convergence threshold for self-consistent cycle (SCF) to obtain the wavefunction is set as 10^{-6} for density matrix and 10^{-8} for root-meansquare and maximum density matrix error respectively. Geometry optimizations are carried out with the Berny method [45, 46] and checked to be local minima using frequency calculations. The optimization step is followed by single point energy calculations at each bias voltage to account for charge transfer between molecule and the contact atoms as well as the reorganization of electronic structure of the molecule. The Hamiltonian and the overlap matrices are extracted for each applied voltage to obtain current−voltage curves for the molecule using our own GENIP [22, 47, 48] program. The effect of the neighbor contact atoms to the molecule is directly considered in the discrete ab initio calculations by using an extended molecule which consists of single gold atom directly bonded to the molecule at both ends (Au–M–Au). These two gold atoms are then further connected to a continuous electronic state of gold clusters connected to an external potential difference. This approach is based on the assumption that the source of electrons is provided by the DOS of the contacts and not by the individual gold atom whose presence is to produce an adequate geometry and retain the chemistry of interface in the neighborhood of the carbon attached to

the gold contact. Thus we are assuming in these calculations that the pathway of electrons is through this minimum junction setting. The same setting, for the sake of comparison, is used for all cases where we are analyzing the I-V characteristics. In case of larger sensors, we would expect larger number of gold atoms attached to graphene sheets yielding larger currents. Although the scalability might not be linear, we choose the minimum size point contact for the molecule-electrode interface to design smallest possible sensor. The GENIP program uses Hamiltonian and overlap matrices obtained from density functional and applies Green's functions theories for calculating the current-voltage relationship as described in detail in Sect. 2. The GENIP program has been used successfully for small molecules like thioalkanes [48].

1.4 Results and Discussion

The first ionization potential of plutonium using B3PW91/ECP60MWB_SEG is estimated as 5.72 eV (expt. value 6.03 eV); [49] however, it falls nicely in the range 5.69–5.74 eV obtained with the same basis-set but with state-averaged CASSCF with subsequent multi-reference averaged coupled-pair functional calculations [37, 38] thus validating our chosen level of theory and basis-set. Furthermore, in order to confirm that the chosen level of theory correctly identifies lowest energy spin-state, two or more spin states are considered for each of the bare ions, Pu^{4+}, PuO_2^{+}, PuO_2^{2+} studied here (Table 1.1). The lowest spin-state of the Pu^{4+} is found to be quintet, PuO_2^{+} quartet, PuO_2^{2+} triplet and UO_2^{2+} singlet, similar to those reported in previous work [12].

The lowest-energy spin-state for successive hydrates of the bare ions AnO_2^{z+} (z = 1,2) An being U, Np or Pu, are found to be same as that of bare ion as reported in literature [43]. We also used several multiplicities for other complexes in order to confirm that addition of other components does not alter the lowest spin state of bare ion (Table 1.2). In all cases, it is found that the lowest energy spin state of the complex is the same as that of the corresponding bare ion.

Once ground state multiplicities are confirmed, geometry of some common U and Pu complexes present in nuclear waste water were optimized, the results of which are shown in Fig. 1.1 and 1.2 followed by frequency calculations. All the geometries are fully optimized at B3PW91//ECP60MWB_SEG/6–31G(d) level of theory. The bond lengths, energy and Mulliken charges for several U and Pu complexes are listed in Table 1.3 and 1.4.

When these uranyl or plutonyl complexes interact with a graphene molecule (Fig. 1.3), the Pu–O and U–O bond lengths increase, thus indicating weakening of these bonds due to interactions of the actinide ions with graphene. Table 1.5 lists the bond distances of some U/Pu complexes for comparison purposes.

Table 1.1 Properties of several spin states of Pu^{4+}, PuO_2^{2+}, and PuO_2^{1+} ions. (Adapted from Kumar and Seminario [50])

Complex	m	Pu–O	q(Pu)	q(O)	Energy[a]
Pu^{4+}	1		4		−551.04015
Pu^{4+}	3		4		−551.14892
Pu^{4+}	5		4		−551.19622
Pu^{4+}	7		4		−550.63525
Pu^{4+}	9		4		−550.07474
PuO_2^{2+}	1	1.654	2.15	−0.08	−703.61595
PuO_2^{2+}	3	1.656	2.15	−0.08	−703.65683
PuO_2^{2+}	5	1.711	2.19	−0.09	−703.63662
PuO_2^{1+}	2	1.690	1.56	−0.28	−704.21144
PuO_2^{1+}	4	1.707	1.59	−0.29	−704.28787
PuO_2^{1+}	6	1.761	1.64	−0.32	−704.20830

[a] Energy are reported in hartrees

1.4.1 Molecular Electrostatic Potential

The graphene plasmons (π-electrons) are highly sensitive and significantly affected by the electrostatic field of a single molecule adsorbed on its surface. Indeed, a change in the molecular electrostatic potential(MEP) of graphene can be observed when interacting with the Pu and U complexes. The molecular electrostatic potential (MEP) of graphene and some U/Pu complexes obtained from DFT calculations are plotted on their electron density as shown in Fig. 1.4. The figure also reflects changes in MEP of graphene when U/Pu complexes are adsorbed on its surface which can be used as a signature for detection of these radionuclides. The magnitude of the potentials is shown by the solid surface colors. Blue is the most positive potential and red is the most negative. All complexes are shown at the same color scale (bottom of Fig. 1.4). However, a potential challenge for the detection is that some waters are closer to graphene than are Pu or U, indicating the need for graphene functionalization to enhance sensitivity. All calculations have been done at B3PW91 level using Stuttgart ECP for U and Pu and the 6–31G(d) for other atoms.

GO contains random arrangement of functional groups and large structural disorder in the carbon skeleton as a result of partial oxidation. Common functional groups reported on oxidation of graphene are –COOH, –OH, –C=O at edges and C–O–C and –OH on the basal plane [51–54]. We studied the interaction of plutonium complex with graphene oxide (GO) using several functional groups as mentioned earlier. In this study, we present results for (i) a graphene oxide with two –OH and one –O– functional groups present or type I (Fig. 1.5a), (ii) a graphene oxide containing a carbonyl functional group or type II (Fig. 1.5b), and (iii) a graphene oxide with a –COOH group (type III). The introduction of –CO group on graphene oxide surface leads to breaking of few bonds and hence those C atoms are saturated with H atoms to satisfy the valence of carbon atoms. The hydrated form of plutonium nitrate was chosen for study due to the fact that nitrates form very strong

Table 1.2 Calculated properties of several plutonium complexes: q=complex net charge, m=multiplicity, Pu–O distance, Pu–O_w distance, q(A)=partial charge in atom A, and total energy. (Adapted from Kumar and Seminario [50])

Complex	q	m	Pu–O	Pu–O_w	q(Pu)	q(O)	q(O_w)	q(H_w)	Energy
$PuO_2^{2+}(H_2O)_5$	2	1	1.695	2.438	1.59	−0.26	−0.83	0.51	−1085.95722
$PuO_2^{2+}(H_2O)_5$	2	3	1.698	2.441	1.59	−0.27	−0.83	0.51	−1085.99667
$PuO_2(NO_3)_2(H_2O)_2$	0	1	1.712	2.520	1.41	−0.33	−0.79	0.47	−1417.77320
$PuO_2(NO_3)_2(H_2O)_2$	0	3	1.716	2.510	1.42	−0.34	−0.80	0.48	−1417.81304
cis-$PuO_2(Cl)_2(H_2O)_2$	0	1	1.72	2.492	0.94	−0.34	−0.79	0.49	−1777.69323
cis-$PuO_2(Cl)_2(H_2O)_2$	0	3	1.72	2.488	0.96	−0.34	−0.79	0.49	−1777.72976
trans-$PuO_2(Cl)_2(H_2O)_2$	0	1	1.72	2.465	1.02	−0.34	−0.79	0.48	−1777.69659
trans-$PuO_2(Cl)_2(H_2O)_2$	0	3	1.72	2.464	1.03	−0.34	−0.79	0.48	−1777.73405
cis-$PuO_2(Cl)_2(H_2O)_3$	0	1	1.72	2.587	0.95	−0.34	−0.80	0.47	−1854.09703
cis-$PuO_2(Cl)_2(H_2O)_3$	0	3	1.72	2.582	0.97	−0.34	−0.80	0.47	−1854.13428
trans-$PuO_2(Cl)_2(H_2O)_3$	0	1	1.71	2.523	1.03	−0.33	−0.79	0.47	−1854.10337
trans-$PuO_2(Cl)_2(H_2O)_3$	0	3	1.72	2.523	1.04	−0.33	−0.79	0.47	−1854.14221

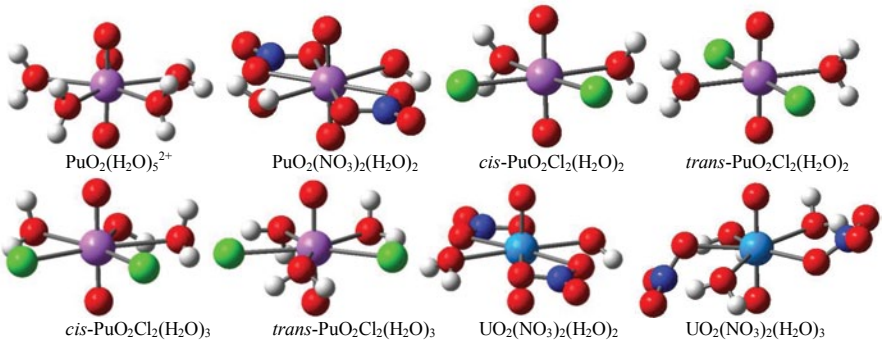


Fig. 1.1 Optimized structures of common PuO_2^{2+} and UO_2^{2+} moieties in nuclear waste water

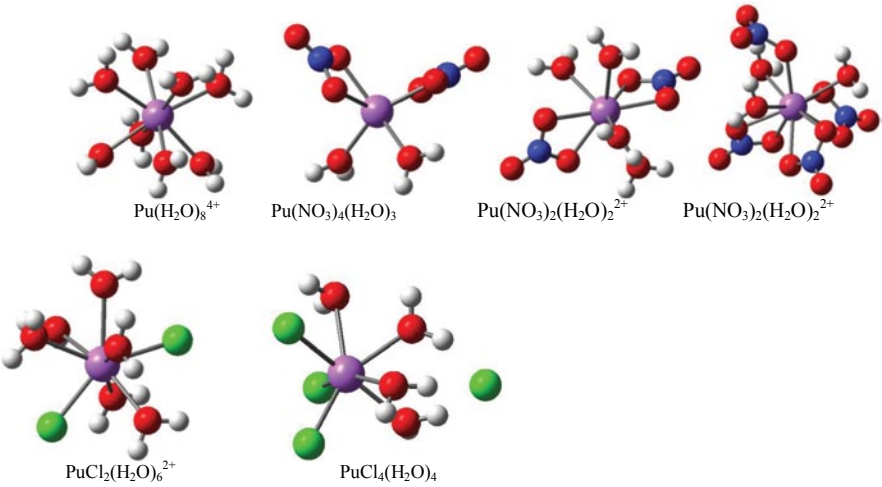


Fig. 1.2 Optimized structures of common Pu(IV) complexes present in nuclear waste water

bonds with Pu(IV) ion and hence a real comparison can be made with respect to its interaction with graphene oxide. In case of type I graphene oxide (Fig. 1.5a), water molecules still remain closest to the GO nanosheet as observed for interaction of plutonium complex with just graphene nanosheet. The molecular orbitals HOMO and LUMO, mainly responsible for electron transport remain unaffected by presence of Pu (IV) complex thus indicating weak interaction between –OH/ –O– and Pu (IV) complex. However, when GO with carbonyl group (type II) was tested, we observed rearrangement of nitrates around Pu(IV) ion in order to accommodate carbonyl group (Fig. 1.5b). –CO group is known to form strong co-ordination complexes with d-block elements. The molecular electrostatic potential when plotted on electron density also shows strong changes as can be seen in Fig. 1.4c.

Table 1.3 Calculated bond distance, atomic Mulliken charges, and energies of AnO_2^{z+} (z = 1, 2; An = U, Pu) complexes. (Adapted from Kumar and Seminario [50])

Complex	q	m	An–O	An–O_w	q(An)	q(O)	q(O_w)	q(H_w)	Energy
PuO_2^{2+}	2	3	1.656		2.15	−0.08	NA	NA	−703.65683
$PuO_2(H_2O)_2^{2+}$	2	3	1.696	2.373	1.66	−0.25	−0.83	0.52	−1009.57653
$PuO_2(H_2O)_5^{2+}$	2	3	1.698	2.441	1.59	−0.27	−0.83	0.51	−1085.99667
$PuO_2(H_2O)_6^{2+}$	2	3	1.701	2.432[a]	1.56	−0.28	−0.83	0.51	−1162.42399
$PuO_2(NO_3)_2(H_2O)_2$	0	3	1.716	2.510	1.42	−0.34	−0.80	0.48	−1417.81304
PuO_2^{1+}	1	4	1.707		1.59	−0.29			−704.28787
$PuO_2(H_2O)^{1+}$	1	4	1.719	2.403	1.48	−0.33	−0.83	0.51	−780.73266
$PuO_2(H_2O)_2^{1+}$	1	4	1.731	2.452	1.41	−0.36	−0.83	0.50	−857.16925
$PuO_2(H_2O)_3^{1+}$	1	4	1.743	2.456	1.32	−0.39	−0.82	0.49	−933.60248
$PuO_2(H_2O)_4^{1+}$	1	4	1.752	2.498	1.27	−0.41	−0.82	0.48	−1010.01966
$PuO_2(H_2O)_5^{1+}$	1	4	1.757	2.568	1.17	−0.42	−0.82	0.47	−1086.42230
cis-$PuO_2(Cl)_2(H_2O)_2$	0	3	1.72	2.488	0.96	−0.34	−0.79	0.49	−1777.72976
trans-$PuO_2(Cl)_2(H_2O)_2$	0	3	1.72	2.464	1.03	−0.34	−0.79	0.48	−1777.73405
cis-$PuO_2(Cl)_2(H_2O)_3$	0	3	1.72	2.582	0.97	−0.34	−0.80	0.47	−1854.13428
trans-$PuO_2(Cl)_2(H_2O)_3$	0	3	1.72	2.523	1.04	−0.33	−0.79	0.47	−1854.14221
$UO_2(NO_3)_2(H_2O)_2$	0	1	1.755	2.527	1.66	−0.39	−0.81	0.48	−1340.93304
$UO_2(NO_3)_2(H_2O)_3$	0	1	1.755	2.526	1.54	−0.39	−0.82	0.48	−1417.32142

[a] PuO_2^{2+} can accommodate only 5 water molecules in first shell, the sixth water molecule starts forming second shell (at 4.133 Å) around the PuO_2^{2+} ion

Table 1.4 Calculated bond distance and atomic Mulliken charges of common Pu(IV)complexes. (Adapted from Kumar and Seminario [50])

Complex	q	m	Pu–O_w	Pu–X (X = Cl/O_N)	q(Pu)	q(X)	q(O_w)	q(H_w)	Energy
$Pu(H_2O)_8^{4+}$	4	5	2.41	NA	2.09	NA	−0.85	0.54	−1163.68949
$Pu(NO_3)_2(H_2O)_2^{2+}$	2	5	2.394	2.246	1.96	−0.42	−0.85	0.53	−1266.71432
				3.906		−0.17			
$Pu(NO_3)_2(H_2O)_4^{2+}$	2	5	2.420	2.316	1.87	−0.45	−0.84	0.52	−1419.61169
				3.970		−0.23			
$Pu(NO_3)_4(H_2O)_3$	0	5	2.510	NA	1.73	−0.44	−0.82	0.48	−1904.26732
$PuCl_2(H_2O)_6^{2+}$	2	5	2.467	2.512	1.18	−0.16	−0.83	0.51	−1932.38799
$PuCl_4(H_2O)_4$	0	5	2.545	2.391,	1.01	−0.28,	−0.82	0.47	−2700.52621
			4.216	2.575		−0.60			

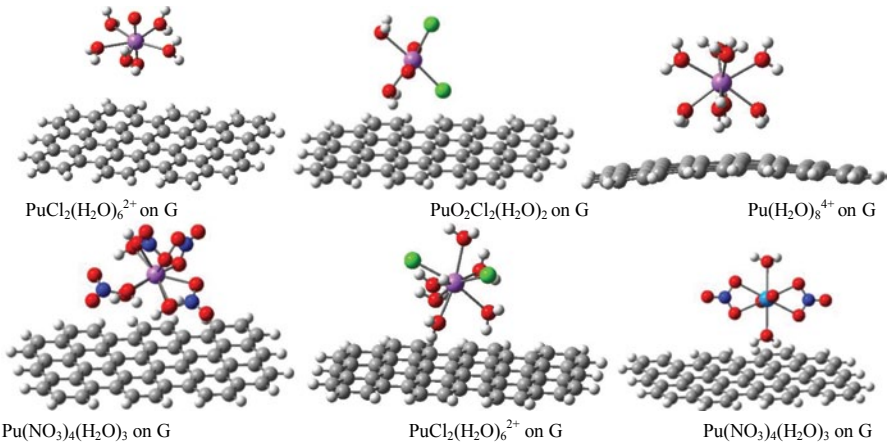


Fig. 1.3 Optimized geometries of some common U and Pu moieties adsorbed on a graphene (G) molecule

The change in current-voltage characteristics of the molecular junction is coupled to the change in molecular orbitals involved in electron transport at low bias voltages. A high conductance is obtained if the molecular orbital (MO) covers the entire molecule (delocalized) as there are high probabilities of electron transport at energies similar to the one of the MO. On the contrary, if the MOs are localized in certain region, this gives rise to high impedance. The MOs in the vicinity of highest occupied molecular orbital (HOMO) and lowest unoccupied molecular orbital (LUMO) for graphene/graphene oxide nanosheets with and without $Pu(NO_3)_4(H_2O)_3$ complex adsorbed on its surface are presented in Fig. 1.6a–f.The approaching plutonium nitrate complex causes localization of HOMO and LUMO indicating strong interaction (Fig. 1.6), and thus significantly reduces the current as will be discussed in later sections.

1.4.2 I-V Characteristics

The current-voltage characteristics are obtained through Au-molecule-Au junctions using GENIP program. As explained earlier, the geometries of the molecular junctions Au-molecule-Au are first fully optimized using the Gaussian program and their Hamiltonians and overlap matrices are evaluated in presence of the applied external fields. The DOS of the bulk gold contacts is calculated using the Crystal-06 program [55] using periodic boundary conditions.

The current-voltage curves for above three junctions (Fig. 1.7a–c) are presented below in Fig. 1.8. As indicated earlier, graphene needs to be functionalized to act as an effective sensor for detection of fissile materials such as uranium and plutonium complexes. The covalent functionalization can have significant effect on electronic properties. The conductance of graphene –O– group causes transformation of sp^2

Table 1.5 Calculated bond distances, atomic Mulliken charges, and energies of Pu complexes adsorbed on Graphene. (Adapted from Kumar and Seminario [50])

Complex	Pu–O	Pu–O_w	Pu–X X=Cl, O_N	q(Pu)	q(O)	q(X)	q(O_w)	q(H_w)	Energy
$PuO_2(H_2O)_5^{2+}$	1.757	2.564		1.16	−0.42	NA	−0.81	0.48	−3155.46987
cis-$PuO_2Cl_2(H_2O)_2$	1.739	2.543	2.632	0.96	−0.38	−0.44	−0.79	0.48	−3847.03326
$Pu(H_2O)_8^{4+}$		2.513		1.59			−0.86	0.49	−3233.42383
$Pu(NO_3)_2(H_2O)_2^{2+}$		2.458	2.358	1.59		−0.48	−0.86	0.49	−3336.23895
			3.999			−0.30			
$Pu(NO_3)_2(H_2O)_4^{2+}$		2.512	2.427	1.50		−0.49	−0.84	0.49	−3489.08394
			4.071			−0.33			
$Pu(NO_3)_4(H_2O)_3$		2.526	2.874	1.65		−0.45	−0.83	0.48	−3973.56671
			3.323						
$PuCl_2(H_2O)_6^{2+}$		2.551	2.672	0.93		−0.43	−0.83	0.49	−4001.83962

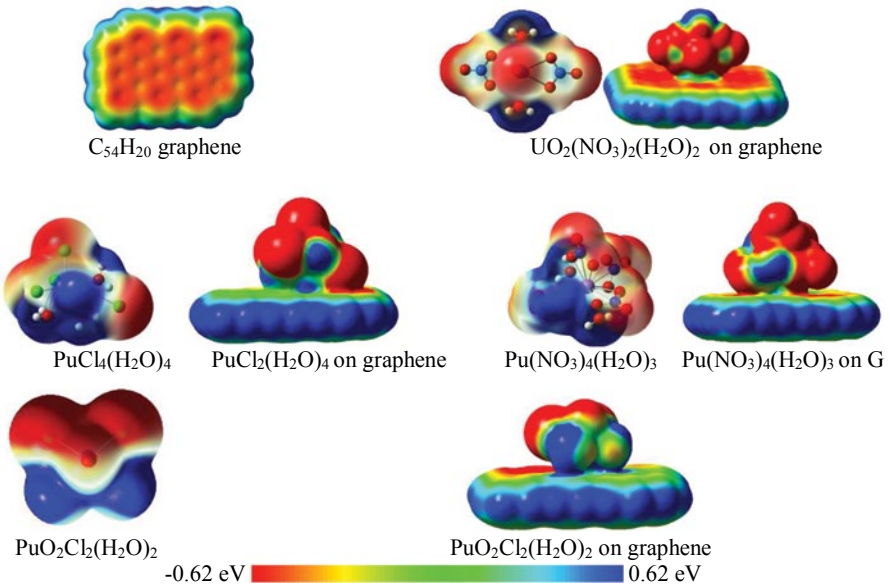


Fig. 1.4 MEPs of U and Pu complexes adsorbed on grapheme. (Adapted from Kumar and Seminario [50])

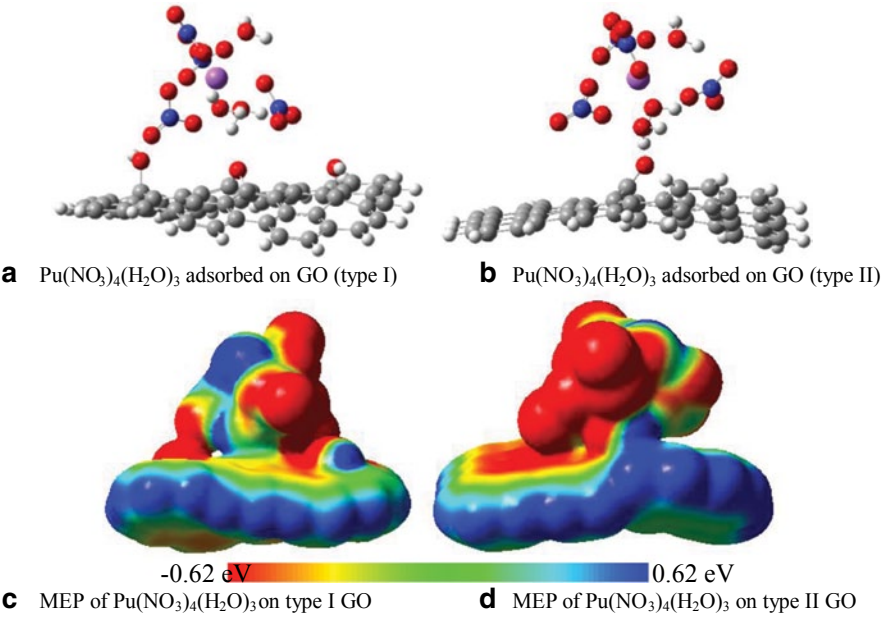


Fig. 1.5 Optimized geometry of nitrato-aquo-complex of Pu (IV) adsorbed on GO (type I) and GO (type II) and their corresponding molecular electrostatic potential (MEP). **a** $Pu(NO_3)_4(H_2O)_3$ adsorbed on GO (type I). **b** $Pu(NO_3)_4(H_2O)_3$ adsorbed on GO (type II). **c** MEP of $Pu(NO_3)_4(H_2O)_3$ on type I GO. **d** MEP of $Pu(NO_3)_4(H_2O)_3$ on type II GO. (Adapted from Kumar and Seminario [50])

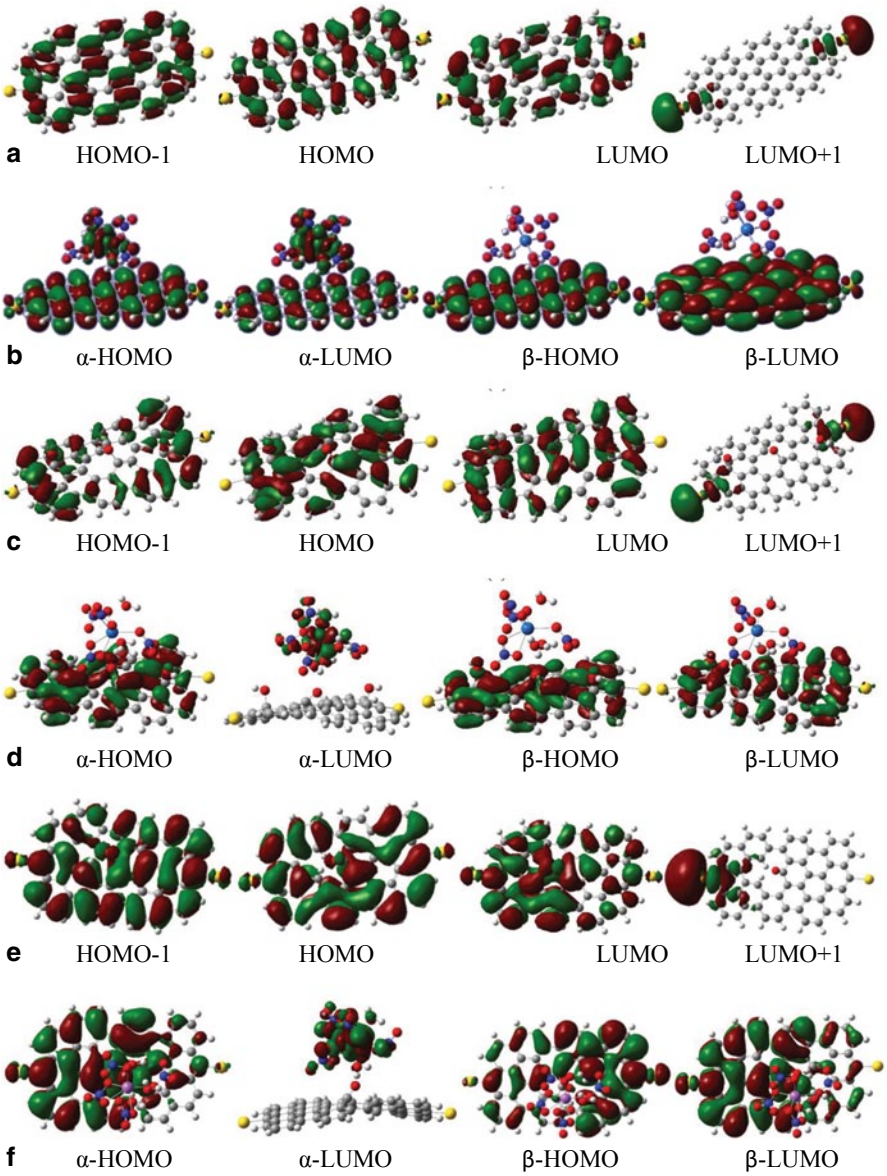


Fig. 1.6 Molecular orbital diagrams of (**a**) graphene nanosheet, (**b**) $Pu(NO_3)_4(H_2O)_3$ adsorbed on graphene, (**c**) graphene oxide GO (type I), (**d**) $Pu(NO_3)_4(H_2O)_3$ adsorbed on GO (type I), (**e**) graphene oxide GO (type II), (**f**) $Pu(NO_3)_4(H_2O)_3$ adsorbed on GO (type II). (Adapted from Kumar and Seminario [50])

hybridized C atoms to sp^3 hybridization. This causes conductance to reduce from 0.67 μAV^{-1} (for graphene) to 0.035 μAV^{-1}. The conductance decreases exponentially with further addition of –O– group. However, addition of –CO group preserves

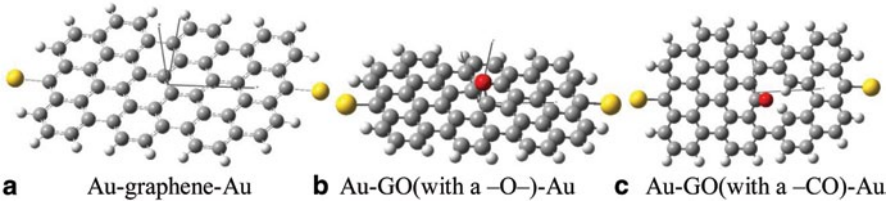


Fig. 1.7 Optimized structures of graphene/graphene oxide junctions to be used as sensing molecule. **a** Au-graphene-Au. **b** Au-GO(with a –O–)-Au. **c** Au-GO(with a –CO)-Au

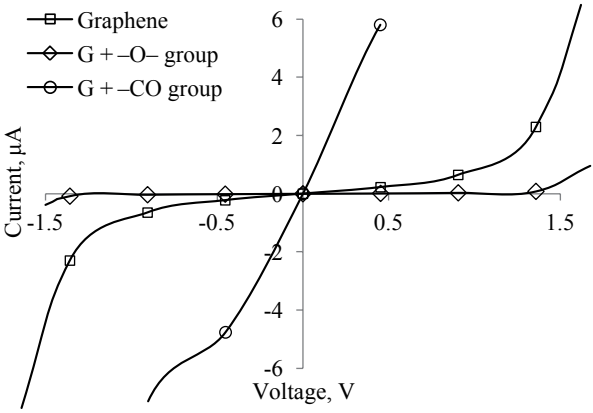


Fig. 1.8 Current-voltage curves for graphene/graphene oxide junctions

sp^3 hybridization of C atoms and conductance in this case is found to increase from 0.67 to 9.5 μAV^{-1}.

The conductance obtained depends mainly on the energies of the orbitals in the neighborhood of the frontier molecular orbitals HOMO and LUMO) of the molecular junction as well as on the Fermi level of the gold electrodes and their coupling to the graphene complex. The density of states (DOS) plots for three cases shown in Fig. 1.9a–c are obtained using GaussSum program [56]. The HOMO-LUMO gap appears to be widened by adding –O– group while it is significantly reduced when –CO group is present which explains the trend observed in conductance values.

We also tried to compare our calculated results to those obtained using experiments. We find similar trend as reported in literature for electrical conductivities comparing graphene and graphene oxide [57]. The minimum sheet resistance for graphene is reported as 6.45 kΩ/sq using experiments [58]. "Based on lateral dimensions and calculated current-voltage characteristics, the sheet resistance is found to be ~1150 kΩ/sq for our case, which is consistent with the fact that resistance increases with decrease in number of channels for electron transport and we consider a single point of contact; thus comparing to experiment, a 200 points-contact or ~60 nm electrode would yield the same resistance sheet" [50].

The optimized geometries of the molecular junctions Au—graphene+U/Pu-Au used to generate current-voltage curves are presented below in Fig. 1.10. All the

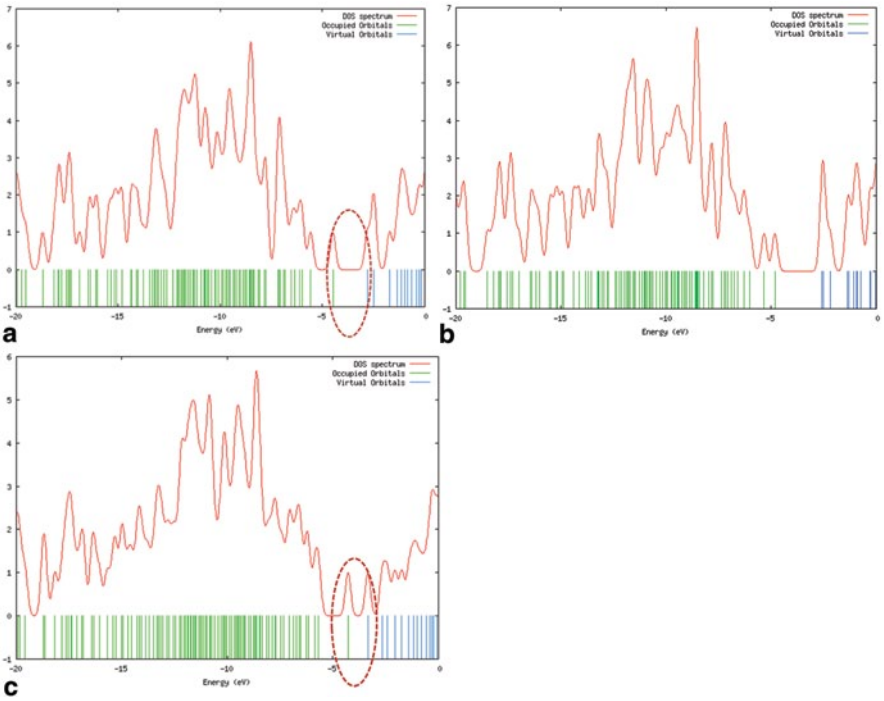


Fig. 1.9 Density of states plot for (**a**) DOS of Au-graphene-Au, (**b**) Au-GO (with a –O–)-Au, and (**c**) Au-GO(with a –CO)-Au

geometries were optimized at B3PW91 level using ECP60MWB_SEG/6–31G(d) basis-sets. Following optimization, single point calculations were performed at each bias voltage to extract Hamiltonian and overlap matrices.

The resulting current-voltage characteristics are shown in Fig. 1.11. As indicated earlier, since we did not observe appreciable change in pi-pi orbitals on graphene surface in the presence of Pu^{4+} complex, the same is reflected in the I-V characteristics with and without plutonium complex adsorbed on a graphene sheet (Fig. 1.11a) or GO of type I (Fig. 1.11b). However, a significant reduction in current values is observed in the presence of plutonium complex for type II GO (Fig. 1.11c). The change in average conductance in the linear region is presented in Table 1.6.

The current-voltage for uranium nitrate complex with graphene and graphene oxide are also calculated using similar principles and are shown in Fig. 1.12. As in the case of $Pu(NO_3)_4(H_2O)_3$complex, GO with –CO group (type II) appears as more effective sensing material than graphene for UO_2^{2+} complexes as well. The average conductance of graphene in linear region of I-V curve changes marginally from 0.67 to 0.59 μAV^{-1} on exposure to $UO_2(NO_3)_2(H_2O)_2$ complex. But in case of GO (type II), the average conductance changes significantly from 9.5 to 6.3 μAV^{-1} on exposure to UO_2^{2+} complex.

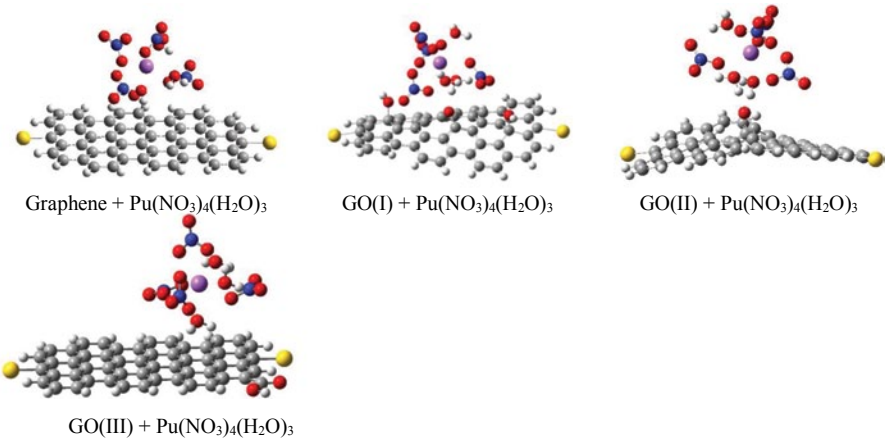


Fig. 1.10 Au-molecule-Au junctions used for generation of I-V characteristics

Above results shows GO with –CO group as the most promising sensing material for detection of radionuclides.

1.5 Summary and Conclusions

In summary, we obtained current-voltage curves using a combination of Greens function and DFT to test the applicability of graphene-based nanosensor for detection of radionuclides in nuclear waste water. Graphene nanosheets need to be functionalized to act as an effective sensor for U/Pu complexes as indicated by MEPs calculated from ab-initio DFT calculations. Since graphene oxide (GO) has a higher affinity for U and Pu complexes [2], we used three types of GO: (a) GO with two –OH and one –O– functional groups present (type I), (b) GO containing a carbonyl functional group (type II): and (c) GO containing –COOH group (type III) to study their interactions with plutonium complexes. Our calculations show significant reduction in current values for GO containing –CO functional group as compared to a graphene sheet or type I GO with –O– functional group in the presence of Pu complex. The plutonium nitrate complex causes localization of HOMO and LUMO which results in significant reduction in current values.

Future work has to focus on the selectivity of these towards lanthanides and actinides in particular U/Pu when other ions are present. Commonly found ions present in waste water include Fe(III), Na^+, Ca^{2+}, Mg^{2+}, Cl^- and NO_3^- etc. We also need to increase the selectivity of graphene-based sensor by using functional groups. Also, molecular dynamics simulations can be used to examine the metal environments and interface phenomena. Quantum chemistry calculations can determine initial geometries and the potential of all of the relevant species in the system. Then, the MD simulations can be done emulating experimental parameters.

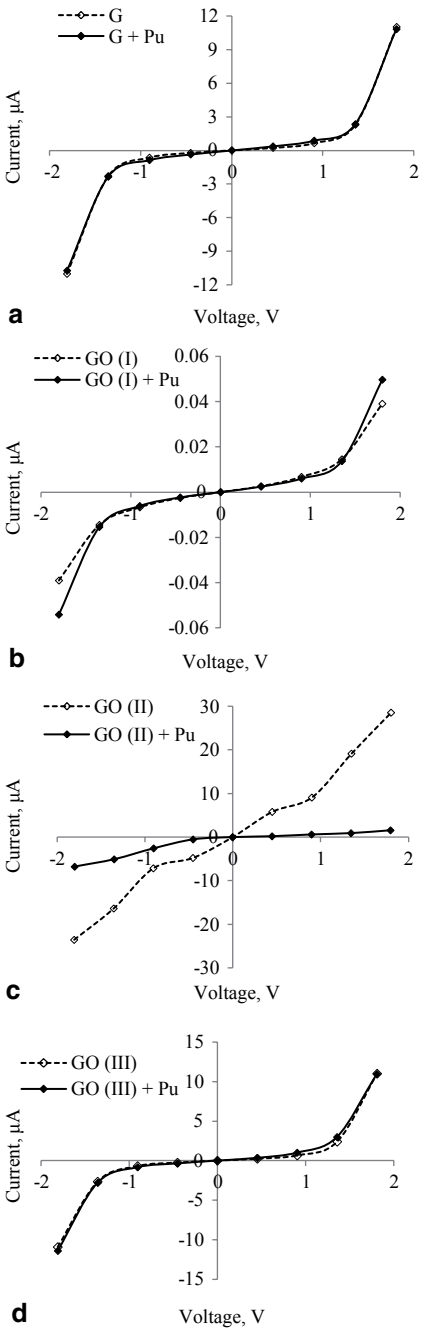


Fig. 1.11 Current-Voltage characteristics of Pu(IV) complex adsorbed on Graphene/Graphene Oxide: (**a**) $Pu(NO_3)_4(H_2O)_3$ on graphene, (**b**) $Pu(NO_3)_4(H_2O)_3$ on GO (type I), (**c**) $Pu(NO_3)_4(H_2O)_3$ on GO (type II), and (**d**) $Pu(NO_3)_4(H_2O)_3$ on GO (type III). Figure 1.11a–c adapted from Kumar and Seminario [50]

Table 1.6 Average conductance of graphene/graphene oxide before and after exposure to $Pu(NO_3)_4(H_2O)_3$ complex

Sensing molecule	Avg. conductance before exposure (μAV^{-1})	Avg. conductance after exposure (μAV^{-1})
Graphene	0.67	0.93
GO (type I)	0.007	0.006
GO (type II)	9.5	1.6
GO (type III)	0.70	0.97

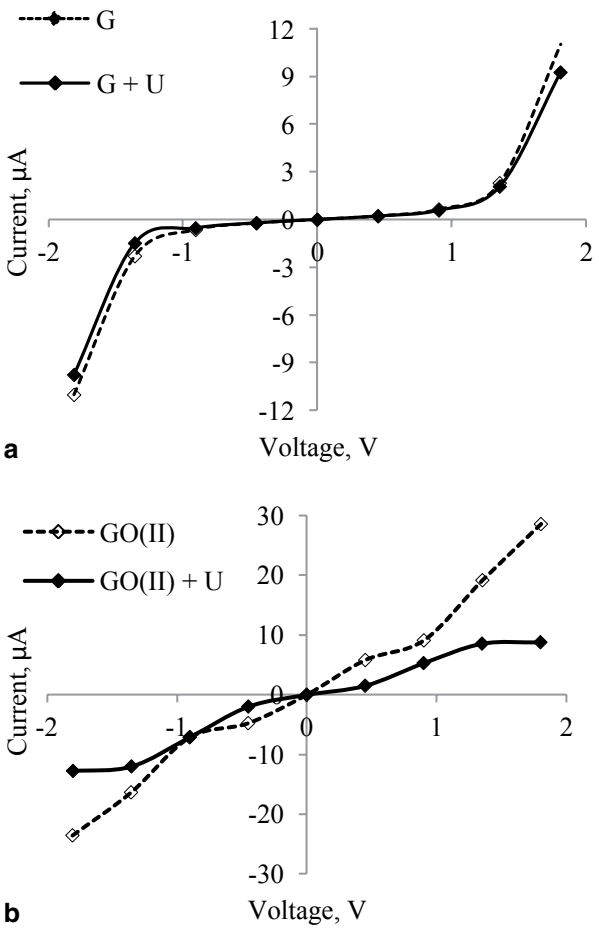


Fig. 1.12 Current-Voltage characteristics of UO_2^{2+} complex adsorbed on Graphene/Graphene Oxide: (**a**) $UO_2(NO_3)_2(H_2O)_2$ on graphene, and (**b**) $UO_2(NO_3)_2(H_2O)_2$ on GO (type II)

References

1. Rangel NL, Seminario JM (2010) Vibronics and plasmonics based graphene sensors. J Chem Phys 132(125102):1–4
2. Romanchuk AY, Slesarev AS, Kalmykov SN, Kosynkin DV, Tour JM (2013) Graphene oxide for effective radionuclide removal. Phys Chem Chem Phys 15(7):2321–2327

3. Greathouse JA, O'Brien RJ, Bemis G, Pabalan RT (2002) Molecular dynamics study of aqueous uranyl interactions with quartz (010). J Phys Chem B 106(7):1646–1655
4. Craw JS, Vincent MA, Hillier IH, Wallwork AL (1995) Ab initio quantum chemical calculations on uranyl UO22+, plutonyl PuO22+, and Their nitrates and sulfates. J Phys Chem 99(25):10181–10185
5. Blaudeau J-P, Zygmunt SA, Curtiss LA, Reed DT, Bursten BE (1999) Relativistic density functional investigation of Pu(H2O)n3+ clusters. Chem Phys Lett 310(3–4):347–354
6. Choppin GR, Morgenstern A (2001) Distribution and movement of environmental plutonium. In: Radioactivity in the environment, vol 1. Elsevier, pp 91–105
7. Spencer S, Gagliardi L, Handy NC, Ioannou AG, Skylaris C-K, Willetts A, Simper AM (1999) Hydration of UO22+ and PuO22+. J Phys Chem A 103(12):1831–1837
8. Majumdar D, Balasubramanian K (2004) Theoretical studies on the nature of uranyl–silicate, uranyl–phosphate and uranyl–arsenate interactions in the model H2UO2SiO4.3H2O, HUO2PO4.3H2O, and HUO2AsO4.3H2O molecules. Chem Phys Lett 397(1–3):26–33
9. Cao Z, Balasubramanian K (2005) Theoretical studies of $UO_2(H_2O)_n^{2+}$,$NpO_2(H_2O)_n^{+}$, and $PuO_2(H_2O)_n^{2+}$ complexes (n = 4–6) in aqueous solution and gas phase. J Chem Phys 123(11):12
10. Chaudhuri D, Balasubramanian K (2004) Electronic structure and spectra of plutonyl complexes and their hydrated forms: PuO_2CO_3 and $PuO_2CO_3.nH_2O$ (n = 1,2). Chem Phys Lett 399(1–3):67–72
11. Balasubramanian K, Chaudhuri D (2008) Computational modeling of environmental plutonyl mono-, di- and tricarbonate complexes with Ca counterions: structures and spectra:, $PuO_2(CO_3)_2Ca$, and $PuO_2(CO_3)_3Ca_3$. Chem Phys Lett 450(4–6):196–202
12. Ismail N, Heully J-L, Saue T, Daudey J-P, Marsden CJ (1999) Theoretical studies of the actinides: method calibration for the UO_2^{2+} and PuO_2^{2+} ions. Chem Phys Lett 300(3–4):296–302
13. Odoh SO, Schreckenbach G (2011) Theoretical study of the structural properties of plutonium(IV) and (VI) complexes. J Phys Chem A 115(48):14110–14119
14. Duvail M, Martelli F, Vitorge P, Spezia R (2011) Polarizable interaction potential for molecular dynamics simulations of actinoids(III) in liquid water. J Chem Phys 135(4):044503–044510
15. Marjolin A, Gourlaouen C, Clavaguéra C, Ren P, Wu J, Gresh N, Dognon J-P, Piquemal J-P (2012) Toward accurate solvation dynamics of lanthanides and actinides in water using polarizable force fields: from gas-phase energetics to hydration free energies. Theor Chem Acc 131(4):1–14
16. Buz'ko V, Chuiko G, Kushkhov K (2012) DFT study of the structure and stability of Pu(III) and Pu(IV) chloro complexes. Russ J Inorg Chem 57(1):62–67
17. Strachan A (2011) Tutorial 1: atomistic material science—ab initio simulations of materials
18. Seminario JM (1995) An introduction to density functional theory in chemistry. In: Seminario JM, Politzer P (eds) Theoretical and computational chemistry, vol 2. Elsevier, pp 1–27
19. Ditchfield R, Hehre WJ, Pople JA (1971) Self-consistent molecular-orbital methods. IX. An extended gaussian-type basis for molecular-orbital studies of organic molecules. J Chem Phys 54(2):724–728
20. Datta S (1997) Electronic transport in mesoscopic systems. Cambridge University Press, Cambridge
21. Datta S (2012) Lessons from nanoelectronics: a new perspective on transport. World Scientific Publishing Co., Singapore
22. Derosa PA, Seminario JM (2000) Electron transport through single molecules: scattering treatment using density functional and green function theories. J Phys Chem B 105(2):471–481
23. Tian W, Datta S, Hong S, Reifenberger R, Henderson JI, Kubiak CP (1998) Conductance spectra of molecular wires. J Chem Phys 109:2874
24. Hohenberg P, Kohn W (1964) Inhomogeneous electron gas. Phys Rev B 136:864–871
25. Kohn W, Sham LJ (1965) Self-consistent equations including exchange and correlation effects. Phys Rev A 140:1133–1138

26. Becke AD (1993) Density-functional thermochemistry. III. The role of exact exchange. J Chem Phys 98(7):5648–5652
27. Roothaan CCJ (1951) New developments in molecular orbital theory. Rev Mod Phys 23(2):69–89
28. Pople JA, Nesbet RK (1954) Self-consistent orbitals for radicals. J Chem Phys 22(3):571–572
29. McWeeny R, Diercksen G (1968) Self-consistent perturbation theory. II. Extension to open shells. J Chem Phys 49(11):4852–4856
30. Perdew JP, Chevary JA, Vosko SH, Jackson KA, Pederson MR, Singh DJ, Fiolhais C (1993) Erratum: atoms, molecules, solids, and surfaces—applications of the generalized gradient approximation for exchange and correlation. Phys Rev B 48(7):4978–4978
31. Perdew JP, Chevary JA, Vosko SH, Jackson KA, Pederson MR, Singh DJ, Fiolhais C (1992) Atoms, molecules, solids, and surfaces: applications of the generalized gradient approximation for exchange and correlation. Phys Rev B 46(11):6671–6687
32. Perdew JP, Burke K, Wang Y (1996) Generalized gradient approximation for the exchange-correlation hole of a many-electron system. Phys Rev B 54(23):16533–16539
33. Perdew JP (1991) Unified theory of exchange and correlation beyond the Local density approximation. In: Ziesche P, Eschrig H (eds) Electronic structure of solids. Akademie Verlag, Berlin, pp 11–20
34. Burke K, Perdew JP, Wang Y (1998) In: Dobson JF, Vignale G, Das MP (eds) Electronic density functional theory: recent progress and new directions. Plenum Press, New York
35. Seminario JM, Araujo RA, Yan L (2004) Negative differential resistance in metallic and semiconducting clusters. J Phys Chem B 108(22):6915–6918
36. Seminario JM, Derosa PA, Cordova LE, Bozard BH (2004) A molecular device operating at terahertz frequencies. IEEE Trans Nanotechnol 3(1):215–218
37. Cao X, Dolg M, Stoll H (2003) Valence basis sets for relativistic energy-consistent small-core actinide pseudopotentials. J Chem Phys 118(2):487–496
38. Cao X, Dolg M (2004) Segmented contraction scheme for small-core actinide pseudopotential basis sets. J Mol Struct (Theochem) 673(1–3):203–209
39. Hay PJ, Wadt WR (1985) Ab initio effective core potentials for molecular calculations—potentials for the transition-metal atoms Sc to Hg. J Chem Phys 82(1):270–283
40. Hay PJ, Wadt WR (1985) Ab initio effective core potentials for molecular calculations—potentials for K to Au including the outermost core orbitals. J Chem Phys 82(1):299–310
41. Wadt WR, Hay PJ (1985) Ab initio effective core potentials for molecular calculations—potentials for main group elements Na to Bi. J Chem Phys 82(1):284–298
42. Hehre WJ, Ditchfield R, Pople JA (1972) Self-consistent moleculer-orbital methods. XII. Further extensions of Gaussian-type basis sets for use in molecular-orbital studies of organic-molecules. J Chem Phys 56(5):2257
43. Rios D, Michelini MC, Lucena AF, Marçalo J, Bray TH, Gibson JK (2012) Gas-phase uranyl, neptunyl, and plutonyl: hydration and oxidation studied by experiment and theory. Inorg Chem 51(12):6603–6614
44. Frisch MJ, Trucks GW, Schlegel HB, Scuseria GE, Robb MA, Cheeseman JR, Scalmani G, Barone V, Mennucci B, Petersson GA, Nakatsuji H, Caricato M, Li X, Hratchian HP, Izmaylov AF, Bloino J, Zheng G, Sonnenberg JL, Hada M, Ehara M, Toyota K, Fukuda R, Hasegawa J, Ishida M, Nakajima T, Honda Y, Kitao O, Nakai H, Vreven T, Montgomery JA Jr, Peralta JE, Ogliaro F, Bearpark M, Heyd JJ, Brothers E, Kudin KN, Staroverov VN, Kobayashi R, Normand J, Raghavachari K, Rendell A, Burant JC, Iyengar SS, Tomasi J, Cossi M, Rega N, Millam NJ, Klene M, Knox JE, Cross JB, Bakken V, Adamo C, Jaramillo J, Gomperts R, Stratmann RE, Yazyev O, Austin AJ, Cammi R, Pomelli C, Ochterski JW, Martin RL, Morokuma K, Zakrzewski VG, Voth GA, Salvador P, Dannenberg JJ, Dapprich S, Daniels AD, Farkas Ö, Foresman JB, Ortiz JV, Cioslowski J, Fox DJ (2009) Gaussian 09, Revision B.01, Gaussian, Inc
45. Peng C, Ayala PY, Schlegel HB, Frisch MJ (1996) Using redundant internal coordinates to optimize equilibrium geometries and transition states. J Comput Chem 17(1):49–56

46. Li X, Frisch MJ (2006) Energy-represented DIIS within a hybrid geometry optimization method. J Chem Theory Comput 2(3):835–839
47. Seminario JM, Zacarias AG, Derosa PA (2002) Analysis of a dinitro-based molecular device. J Chem Phys 116(4):1671–1683
48. Seminario JM, Yan L (2005) Ab initio analysis of electron currents in thioalkanes. Int J Quantum Chem 102(5):711–723
49. Blaise J, Wyart JF (1992) Energy levels and atomic spectra of actinides, international tables of selected constants, vol 20. CNRS, Paris
50. Kumar N, Seminario JM (2013) Design of nanosensors for fissile materials in nuclear waste water. J Phys Chem C 117(45):24033–24041
51. Sheka EF, Popova NA (2013) Molecular theory of graphene oxide. Phys Chem Chem Phys 15(32):13304–13322
52. Lahaye RJWE, Jeong HK, Park CY, Lee YH (2009) Density functional theory study of graphite oxide for different oxidation levels. Phys Rev B 79(12):125435
53. Hernández Rosas JJ, Ramírez Gutiérrez RE, Escobedo-Morales A, Chigo Anota E (2011) First principles calculations of the electronic and chemical properties of graphene, graphane, and graphene oxide. J Mol Model 17(5):1133–1139
54. Dreyer DR, Park S, Bielawski CW, Ruoff RS (2010) The chemistry of graphene oxide. Chem Soc Rev 39(1):228–240
55. Dovesi R, Saunders VR, Roetti C, Orlando R, Zicovich-Wilson CM, Pascale F, Civalleri B, Doll K, Harrison NM, Bush IJ, DArco P, Llunell M (2006) CRYSTAL06. User's manual. University of Torino, Torino
56. O'Boyle NM, Tenderholt AL, Langner KM (2008) cclib: a library for package-independent computational chemistry algorithms. J Comput Chem 29(5):839–845
57. Punckt C, Muckel F, Wolff S, Aksay IA, Chavarin CA, Bacher G, Mertin W (2013) The effect of degree of reduction on the electrical properties of functionalized graphene sheets. Appl Phys Lett 102(2):023114–5
58. Geim AK, Novoselov KS (2007) The rise of graphene. Nat Mater 6(3):183–191

Chapter 2
Distinct Diameter Dependence of Redox Property for Armchair, Zigzag Single-walled, and Double-walled Carbon Nanotubes

Wenming Sun, Yuxiang Bu and Yixuan Wang

Abstract Multiscale density functional theories (DFTB, PBE, and M06-2X) were used to investigate redox properties, such as ionization potentials (IP), electron affinities (EA), electronegativities (χ), and Fermi levels (E_f) for infinite armchair single-walled carbon nanotubes (SWNT) (n,n) (n = 3 − 16), zigzag SWNT (n,0) (n = 5 − 16), as well as double-walled carbon nanotubes (DWNT) (n,n)@(n + 5, n + 5) (n = 3, 5 and 6). These properties show strong and different diameter dependence. With increasing diameter, IPs of armchair SWNTs (n,n) decrease monotonically, while EAs increase monotonically. Although IPs of zigzag SWNTs (n,0) also generally decrease, there is an increase occurring just after (3k, 0) (k = 2, 3, 4, and 5) and shows a group behavior, in which every three neighbourhood (3k, 0), (3k − 1, 0) and (3k − 2, 0) form a group. However, opposite to the armchair SWNTs, the EAs of zigzag SWNTs decrease rapidly with increasing diameter till (11,0) and then gently increase. EAs of the zigzag SWNTs also exhibit a group behavior, yet are not synchronous with IPs. With increasing diameter, the IPs and EAs of both the armchair and zigzag SWNTs approach to approximately 4.7 and 3.9 eV. For the armchair SWNTs electronegativity (χ) and Fermi level ($-E_f$) change very slightly with diameter, while for the zigzag they decrease rapidly till (9,0) and then gently oscillate to the similar levels to those of the armchair. The IPs and EAs for (n,n) @ (n + 5, n + 5) DWNTs have the same trend as armchair SWNTs. It was also found that these DWNTs characterize better redox properties than their constituents. These interesting findings are important for redox chemistry based on CNTs and may offer a new strategy for separation of CNTs. The biomedical implication of SWNT, C_{60} and $Li@C_{60}$ was also discussed. Similar to $Li@C_{60}$, the binding and HOMO analysis shows that SWNT may also be able to well protect DNA bases from radiation.

Submitted to the book "Design and Applications of Nanomaterials for Devices and Sensors" edited by J. Seminario, 2013

Y. Bu (✉) · W. Sun
The Center for Modeling & Simulation Chemistry, Institute of Theoretical Chemistry, Shandong University, Jinan 250100, P.R. China
e-mail: byx@sdu.edu.cn

Y. Wang
Department of Natural Science, Albany State University, Albany GA 31705, USA
e-mail: Yixuan.Wang@asurams.edu

J. M. Seminario (ed.), *Design and Applications of Nanomaterials for Sensors*, Challenges and Advances in Computational Chemistry and Physics 16,
DOI 10.1007/978-94-017-8848-9_2, © Springer Science+Business Media Dordrecht 2014

2.1 Introduction

Since their discovery in 1991, [1] carbon nanotubes (CNTs) have attracted considerable interests in the field of nanotechnology due to their unique properties. Their high electrical conductivity and strength have made them promising materials for new applications such as field emitters [2] and scanning probes [3]. Single-walled carbon nanotubes (SWNTs) are π-bond aromatic molecules that can be either semiconducting or metallic, depending on the helical angle and diameter [4]. Original simple considerations based on band structure of graphite lead to a conclusion that SWNT (n,m) is metallic for $n=m$, has a narrow band gap for $n-m=3k$ (integer k), and is a moderate-gap semiconductor otherwise [5]. The "$n-m=3k$" rule was refined later by both theoretical and experimental studies [6].

CNTs are expected to be one of promising materials of the next-generation electronic devices, and they have already manifested their advantage as an efficient electron source through their excellent field-emission properties. Electrodes made from sheets of SWNTs have been demonstrated to actuate electromechanically in an electrochemical cell [7]. The redox chemistry of noncovalently functionalized SWNTs has received intensive attention [8]. For example, dispersion with polymers and surfactants such as proteins, DNA and sodium dodecyl sulfates (SDS) results in excellent SWNTs aqueous suspensions for redox chemistry studies [9]. Experimentalists have shown that SWNTs could be oxidized by strong oxidants such as $KMnO_4$, and fully reduced by reductants such as $NaBH_4$ [8]. Extensive literatures exist on the subjects such as electronic structures, CNTs with defects, deformation and extra charges [8, 9e, 10]. Their electronic structures in the external electrical fields have also been theoretically discussed [10]. The properties of oxidative state of CNTs could affect the separation and enrichment process [11]. Recently theoretical calculations also showed that the injected charge could enhance the binding interaction between molecular hydrogen and fullerenes and CNTs [12]. Guo et al. reported that the electron injection was more effective in decreasing the energy barrier for the chemisorption of hydrogen molecules on armchair CNTs, while the hole injection was more effective for zigzag CNTs [13]. Luo et al. determined that fullerenes and CNTs have positive EAs, which was claimed to be related to the aggregation property of these carbon materials [14]. The electron affinity (EA) is defined as the total energy difference between the neutral and the negatively charged system, and the positive EA therefore implies that the neutral system has tendency to gain an electron and get reduced. Balbuena et al. reported the effect of nanotube length on the aromaticity of SWNTs [15].

SWNTs are also interesting to bioelectrochemistry. It is demonstrated that SWNTs could construct the nanostructured biointerfaces [16], enhance the electrochemistry reactivity and the electron transfer (ET) rates of biomolecules [17], considerably accumulate biomolecules[18], and assuage surface fouling effects [19]. SWNTs have also potential to prevent DNA from oxidation [20]. Due to the extensive applications mentioned above, the detailed understanding of the redox properties of the CNTs is very essential. However, the ionization potentials (IPs) and electron

affinities (EAs), two important indexes for field-emission and redox properties, seem to have been less examined. Herein, we report a comprehensive investigation of the size-dependences of IPs, EAs, and Mulliken electronegativity for three kinds of CNTs, armchair SWNT (n,n), zigzag SWNT (n,0) and DWNT (n,n) @ (n+5, n+5) on the basis of density functional theory analysis and calculation.

Electronic structures and activity distributions for H-passivated SWCNTs are not well defined, e.g., the ground state, and the variation of frontier molecular orbital with the size of the cluster. Besides the discussion of redox properties for the H-passivated SWCNTs, the electronic structures and frontier molecular orbitals were also discussed in the present chapter.

To provide biomedical implication of carbon nanotubes, ionization potentials of DNA bases (nucleic acid bases, NAB) with different DFT methods were provided at the end for a direct comparison with SWNTs, and the noncovalent interaction between a SWNT with guanine was visualized with reduced density gradient method [21]. As a comparison the interaction among C_{60}, Li@C_{60} and NAB were also briefly reviewed.

2.2 Models and Methods

Generalized gradient approximation (GGA) type of density functional theory, Perdew and Wang's scheme (PW91) [22] with a double numerical plus polarization function (DNP), implemented in DMol^3 of Material Studio 4.4 suite of program [23], was used to fully optimize the armchair and zigzag SWNT systems under periodic condition and calculate relevant properties. In order to ensure that the CNTs do not interact with their periodic images, supercell parameters, a and b (the sizes in the direction perpendicular to the nanotube axis) were defined by $a=b=$D+25 Å, as a function of the nanotube diameter D (D denotes the diameter of outer tube in the DWNTs). The parameter c (the size of the supercell along the nanotube axis) for armchair and zigzag SWNTs is 9.84 and 17.04 Å, respectively. The investigated SWNTs range from $n=3$ to 16 for (n,n) armchair and from 5 to 16 for (n,0) zigzag. The spin polarization scheme was applied to deal with open-shell systems. A 1*1*12 Monkhorst-Pack k-point grid was used in the sampling of Brillouin zone, while 1*1*49 k-point was used in the calculation of band gaps and Fermi energies. In the optimizations, the energy gradients and atomic displacements converged to within $1*10^{-5}$ Hartree/Bohr and $2*10^{-3}$ angstrom, respectively. The values of global orbital cutoff were set at 3.9 and 3.7 Å for anion systems and neutral systems, respectively. The same calculation method and parameters were applied to the DWNT systems. Due to the large system, only 1*1*8 k-point setting is used in the optimization.

For an isolated system, the ionization potential is usually defined as IP$=E(N-1)-E(N)$, while the electron affinity is EA$=E(N)-E(N+1)$, where $E(N)$, $E(N+1)$, $E(N-1)$ are the total ground-state energies in the neutral (N), single negatively charged $(N+1)$, and single positively charged $(N-1)$ configurations,

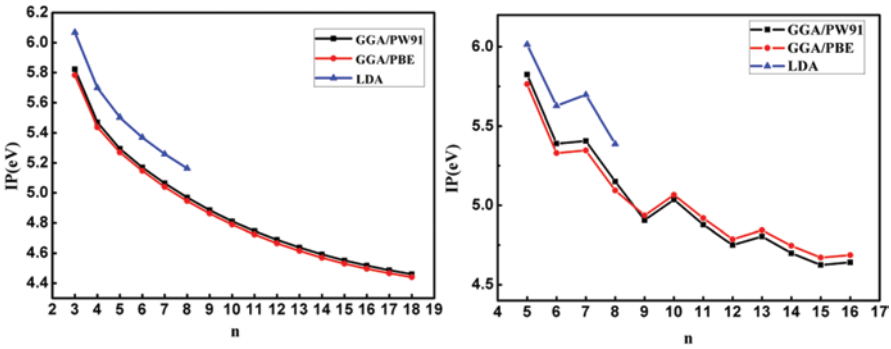


Fig. 2.1 Adiabatic ionization potential aIP of armchair (n,n) SWNTs (*left*) and zigzag (n,0) SWCNTs (*right*) as a function of *n* with different DFT methods

respectively. The definitions are also frequently employed to periodic systems [24]. For a periodic system, the electron affinity is estimated as $EA = E_{vac} - E_{LUMO}$ and the ionization potential as $IP = E_{vac} - E_{HOMO}$ (the vacuum energy E_{vac} is defined as the electrostatic potential energy in the vacuum, far away from the system) [25], and $WF = E_{vac} - (E_{LUMO} + E_{HOMO})/2$. Using all electron static and time-dependent DFT calculation, Zhou et al. reported that the IP decreases with the length of finite length (5,5) SWNT overall, exhibiting a periodicity [26]. The WFs of metallic and semiconducting SWNT's vs the inverse tube diameter $1/D$ vary in different ways, decrease in the former yet increase in the latter (WF was approximated as the negative Fermi energy $-E_F$, $Evac \sim 0$) [27].

The GGA method of Perdew, Burke and Enzerhof's scheme [28] (PBE) and local density approximation (LDA) method were also used to calculate IP and EA values (as shown in Fig. 2.1), and a good agreement with those from PW91 was observed, validating the applied GFT method in the present work. LDA predicts higher IP than the GGA methods for both armchair and zigzag SWNTs.

To validate the calculation procedure, careful examinations for the employed scheme and parameters, such as the grid size for k-sampling, were also carried out and the results were shown in Fig. 2.2. For zigzag SWNTs, the adiabatic IP and EA with 1*1*8 and 1*1*12 *k*-point samplings are too close to be distinguished; for the armchair ones the results with the two large k-point samplings are rather close to each other. However, the results for all of cases with 1*1*2 k-point are indeed far from those with the two large k-point samplings. Thus, 1*1*12 Monkhorst-Pack k-point grid was used in the sampling of Brillouin zone.

As shown in Table 2.1, although Fermi levels (E_f) with 1*1*12 and 1*1*49 k-points are almost the same, energy gaps (E_g) with 1*1*49 k-points are considerably improved especially for the armchair SWNTs. Thus the band gap needs much larger k-points to deal with than the Fermi level.

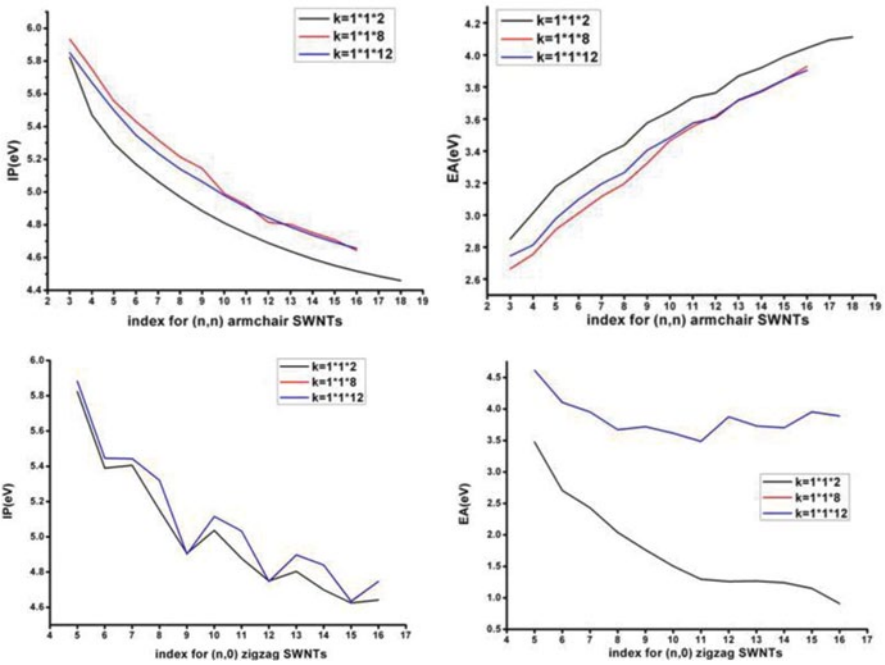


Fig. 2.2 Adiabatic ionization potential (aIP) and adiabatic electron affinity (aEA) of armchair (n,n) SWCNTs (*top*) and zigzag (n,0) SWCNTs (*bottom*) as a function of n with different k-point settings. For zigzag SWNTs, the 1*1*8 and 1*1*12 k-point settings are too close to be distinguished. Clearly, the 1*1*2 is an ill-defined quantity

2.3 Results and Discussions

2.3.1 IP and EA of Armchair SWNT

The IP and EA estimated by the energy difference for armchair (n,n) SWNTs were collected in Table 2.2, and plotted against n in Fig. 2.3, respectively. Figure 2.3 shows that the adiabatic IPs for armchair (n,n) SWNTs decrease monotonically and smoothly with increasing SWNT diameters, whereas the adiabatic EAs monotonically increase. For the first few SWNTs from $n=3$ to 9 IPs drop rapidly by approximately 0.79 eV, and then IPs decrease gradually by only 0.33 eV from (10,10) to (16,16). The adiabatic EA has a similar change pattern with SWNTs to the IPs, e.g., EA increases from 2.75 for (3,3) to 3.40 eV for (9,9), and then is just increased by 0.42 eV from $n=10$ to 16. To the best of our knowledge, there are only few reports on IP and EA values of CNTs. In a similar periodic PBE type of DFT calculation to this work [24], the reported IPs for (5,5) SWNTs (60 atoms/cell) is 5.91 eV, which is in an excellent agreement with our result with the same model [5.98 eV for (5,5)−(60 atoms/cell)]. The work function (WF, $\sim -E_F$) has the same increase

Table 2.1 Calculated Fermi energy (E_f) and band gap E_g for (n,n) and (n,0) SWNTs at different k-point settings

(n,n)	k=1*1*12		k=1*1*49		(n,0)	k=1*1*12		k=1*1*49	
	E_f	E_g	E_f	E_g		E_f	E_g	E_f	E_g
n=3	−4.386	0.21	−4.391	0	n=5	−5.242	0.18	−5.242	0.17
4	−4.407	0.21	−4.414	0.02	6	−4.839	0	−4.839	0
5	−4.435	0.12	−4.432	0.05	7	−4.877	0.22	−4.875	0.21
6	−4.452	0.04	−4.452	0.06	8	−4.706	0.63	−4.707	0.62
7	−4.463	0.13	−4.464	0.03	9	−4.436	0.21	−4.436	0.13
8	−4.469	0.15	−4.469	0.05	10	−4.494	0.76	−4.494	0.73
9	−4.471	0.18	−4.472	0.06	11	−4.427	0.96	−4.427	0.95
10	−4.476	0.21	−4.476	0.03	12	−4.46	0.18	−4.46	0.08
11	−4.478	0.22	−4.472	0	13	−4.49	0.62	−4.49	0.59
12	−4.482	0.24	−4.484	0.03	14	−4.459	0.76	−4.459	0.74
13	−4.483	0.25	−4.483	0.01	15	−4.474	0.18	−4.473	0.06
14	−4.485	0.26	−4.484	0.02	16	−4.488	0.53	−4.488	0.5
15	−4.485	0.27	−4.488	0.03					
16	−4.487	0.27	−4.486	0.03					

Table 2.2 Calculated geometrical and electronic parameters for armchair SWCNT

(n,n)	D(Å)[f]	aIP[b]	vIP[c]	λ_h[d]	aEA[b]	vEA[c]	λ_e[e]	E_f	E_g
n=3	4.07	5.85	5.86	0.01	2.75	2.74	0.01	−4.391	0
4	5.42	5.67	5.67	0	2.81	2.81	0	−4.414	0.02
5	6.78	5.50	5.50	0	2.98	2.98	0	−4.432	0.05
6	8.14	5.35	5.36	0.01	3.10	3.09	0.01	−4.452	0.06
7	9.49	5.24	5.25	0.01	3.20	3.18	0.02	−4.464	0.03
8	10.85	5.14	5.14	0	3.27	3.26	0.01	−4.469	0.05
9	12.20	5.06	5.06	0	3.40	3.40	0	−4.472	0.06
10	13.56	4.98	4.98	0	3.48	3.48	0	−4.476	0.03
11	14.92	4.91	4.91	0	3.57	3.57	0	−4.472	0
12	16.27	4.84	4.84	0	3.61	3.61	0	−4.484	0.03
13	17.63	4.79	4.79	0	3.72	3.72	0	−4.483	0.01
14	18.98	4.74	4.74	0	3.77	3.77	0	−4.484	0.02
15	20.34	4.69	4.69	0	3.85	3.83	0.02	−4.488	0.03
16	21.70	4.66	4.66	0	3.90	3.90	0	−4.486	0.03

Fermi energy (E_f) and band gap (E_g)
[a] all energies are in eV
[b] adiabatic ionization potential (electron affinity)
[c] vertical ionization potential (electron affinity)
[d] hole reorganization energy
[e] electron reorganization energy
[f] diameter

trend as that for the metallic SWNTs [27]. The WF of 4.435 eV for the infinite (5,5) agrees very well with that of 4.37 eV predicted with all-electron method, and higher than that from plane-wave result of 4.28 eV [25].

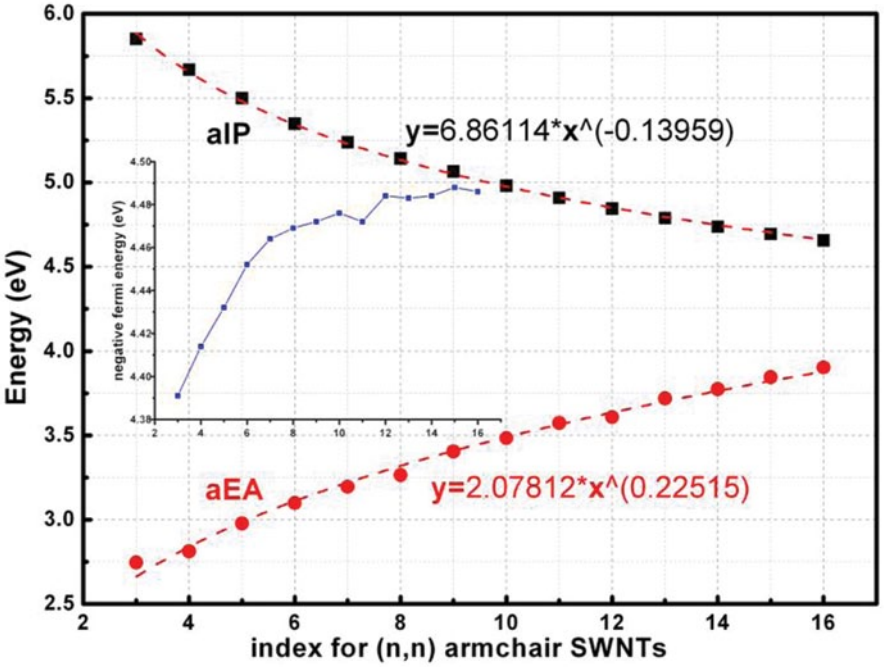


Fig. 2.3 Adiabatic ionization potentials (aIPs) and electron affinities (aEAs) of armchair SWNTs as a function of n, calculated with IP=$E(N-1)-E(N)$, and EA=$E(N)-E(N+1)$, The insert plot refers to the variation of negative Fermi energy (WF)

The difference between adiabatic IPs (EAs) and vertical IPs (EAs) are nonsignificant (as shown in Table 2.2), indicating that the hole reorganization energies ($\boldsymbol{\lambda}_h$, the difference between the vertical IP and the adiabatic IP) and the electron reorganization energies ($\boldsymbol{\lambda}_e$, the difference between the adiabatic EA and the vertical EA) for (n,n) SWNT are quite small. Generally, $\boldsymbol{\lambda}_e$ for an individual armchair SWNT is slightly larger than or equal to $\boldsymbol{\lambda}_h$. This means that armchair SWNTs are more sensitive to an electron injection as compared with a hole injection.

The above results show that the thinner armchair SWNTs possess higher IP and lower EA, while the thicker ones possess lower IP and higher EA. Thus, the armchair SWNTs with small diameter do not tend to characterize either as an oxidant or a reductant, while the large diameter armchair SWNTs may be active as an oxidant as well as a reductant simultaneously. Regarding the application in redox chemistry, the (n,n) SWNTs with large diameter prefer to be both reduced and oxidized.

However, according to Fig. 2.4 both IP~$-E_{HOMO}$ and EA~$-E_{LUMO}$ show opposite trends to those shown in Fig. 2.3 although WFs remain the same trend. In the scheme of DMol[3], the frontier molecular orbitals are predicted with only Gamma point, implying that the HOMO and LUMO actually refer to those for the truncated SWNT rather than periodic one. This is also the reason why the HOMO-LUMO gap is so significant, yet the band gaps for k=1*1*49 in Table 2.1 approach to zero. It is most likely that the IP and EA in Fig. 2.4 from the E_{HOMO} and E_{LUMO} represent

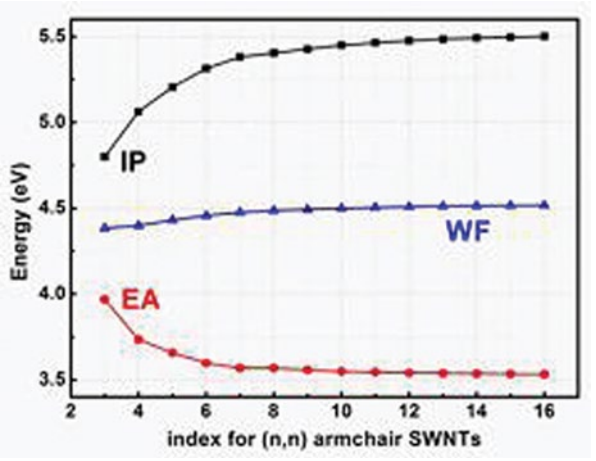


Fig. 2.4 Adiabatic ionization potentials (aIPs) and electron affinities (aEAs) of armchair SWNTs as a function of n, calculated with $EA = E_{vac} - E_{LUMO}$, $IP = E_{vac} - E_{HOMO}$, $WF = E_{vac} - (E_{LUMO} + E_{HOMO})/2$ (E_{vac} is approximated as zero)

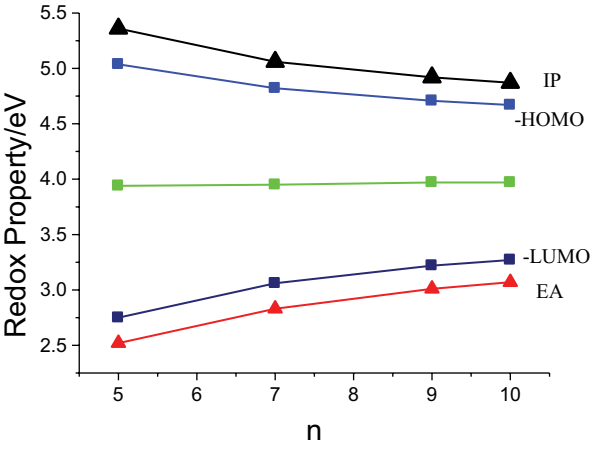


Fig. 2.5 Adiabatic ionization potentials ($IP = E(N-1) - E(N)$, *black triangle*), electron affinities ($EA = E(N) - E(N+1)$, *red triangle*), $-E_{HOMO}$, $-E_{LUMO}$, and Mulliken electronegativity χ (*green*) for H-passviated armchair (n,n) SWNTs (~22.2 Å in length) as a function of n

those of finite length SWNT without H-passivated. In addition, to solve convergence problem the occupation numbers are calculated by setting the occupation keyword at "thermal smearing" in DMol^3 package, which uses a finite-temperature Fermi function to provide fractional occupation numbers [29]. Therefore, HOMO and LUMO were not well defined as well.

For a few H-passivated armchair SWNTs ($n = 5$, 7, 9 and 10) with approximated length of 22.2 Å (optimized with a hybrid GGA, M06-2X/6-31G*, implemented in Gaussian09 version B [30]) corresponding to 10 repeating units, IP, EA, -HOMO, and -LUMO are also evaluated, shown in Fig. 2.5. Similar to Fig. 2.3, the IP shows a decrease trend with the diameter, and the EA tends to increase with the diameter. These trends also agree with the variations of IP and EA with the length of H-passivated (5,5) SWNT [25]. In addition, $-E_{HOMO}$ and $-E_{LUMO}$ exhibit the same trends as IP and EA, respectively. The adiabatic IPs are approximately 0.2–0.3 eV higher than

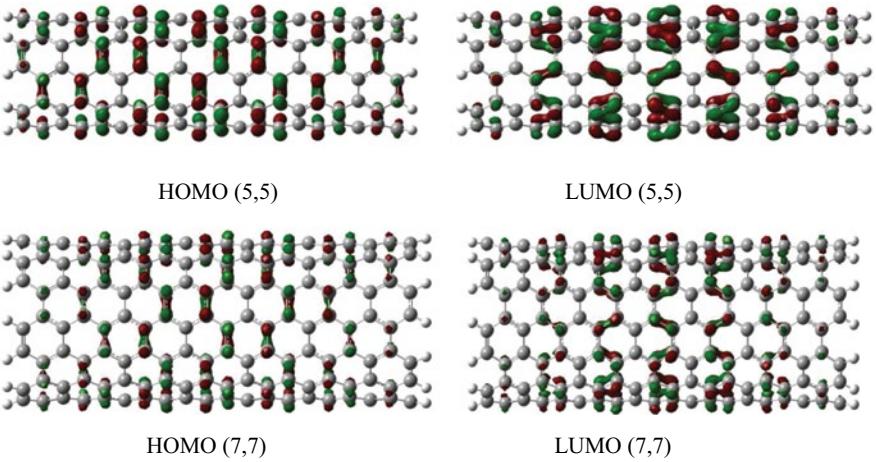


Fig. 2.6 The frontier orbitals for the H-passivated ~22 Å long armchair SWNT. (isovalue = 0.02 au)

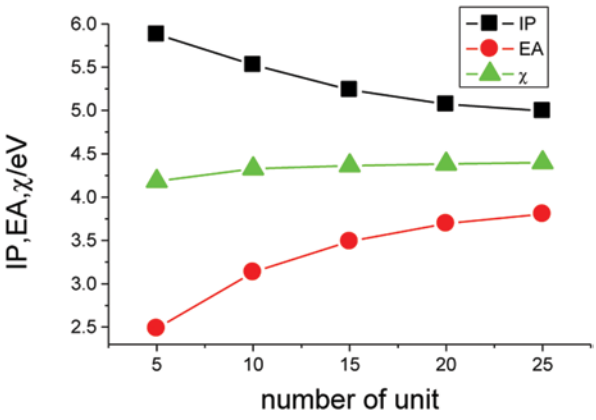


Fig. 2.7 IP, EA and Mulliken electronegativity variation for H-passivated (5,5) SWNT ($C_{100}H_{20}$–$C_{500}H_{20}$) predicted with DFTB method

$-\boldsymbol{E}_{\mathbf{HOMO}}$, while the EAs are lower than $-\boldsymbol{E}_{\mathbf{LUMO}}$. The Mulliken electronegativity, the average of IP and EA only shows slightly increase with thickness of the SWNT.

To discuss the reaction activity of the H-passivated SWNT, the HOMO and LUMO for (5,5) and (7,7) are shown in Fig. 2.6. For both SWNTs the LUMOs dominantly spread over the inside carbons rather than the end carbons, while the carbons on the ends contribute a little to the HOMOs. The SWNT clusters in the length of 20 Å may be proper to simulate their chemical activity.

For the larger H-passivated armchair SWNTs (20 units, ~43 Å) the IP and EA were also estimated with DFTBA method that is a density-functional based tight-binding semi-empirical calculation, a method that is parametrized via the results of DFT calculations [31]. To validate the DFTB method, it was applied to H-passivated (5,5) SWNT for 5–25 units (C_{100}–$C5_{00}H_{20}$). Compared with those for $C_{200}H_{20}$ from M06-2X/6-31G* in Fig. 2.5, the IP and EA shown in Fig. 2.7 are higher by

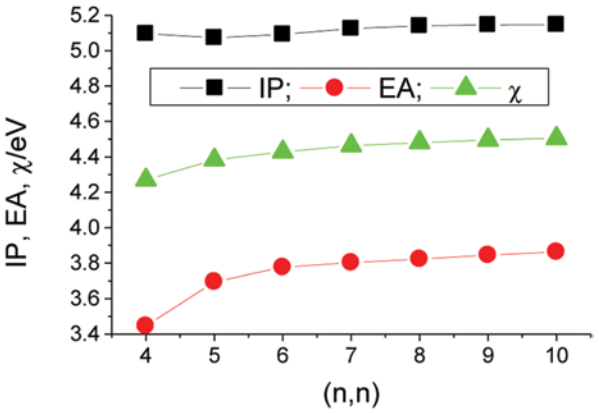


Fig. 2.8 IP, EA and Mulliken electronegativity variation for 20 units H-passivated (n,n) SWNT (~43 Å) predicted with DFTB method

0.17 and 0.61 eV, respectively. However, the general variation trend agree with that from Buonocore et al. [25].

The DFTB was then used to investigate the IP and EA for the H-passivated (n,n) SWNT (20 units, ~43 Å). The structures were fully optimized, and adiabatic IP and EA were then calculated. However, although EAs increase with the diameter of SWNTs as predicted with M06-2X for the short SWNTs (~22 Å in length), the adiabatic IPs in Fig. 2.8 do not significantly change. On the basis of the geometries from the DFTB method, the IPs and EAs will be estimated with more accurate DFT method, like GGA. It was worth to mention that the triplet states for the H-passivated (n,n) SWNT (n=4,5, and 6; 20 units) have higher energy than the singlet state with the DFTB method, implying that the ground state for H-passivated (n,n) SWNT is singlet state.

2.3.2 IPs and EAs of Zigzag SWNTs

The zigzag (n,0) tubes are predicted at the Hückel theory to be metallic or nearly metallic when n is a multiple of 3, and semiconductors for the rest. Adiabatic IPs and EAs for zigzag (n,0) SWNTs were shown in Fig. 2.9. It can be seen that similar to the cases of armchair SWNTs the adiabatic IPs for (n,0) SWNTs also generally decrease with diameter, but obviously there are a few local increases occurring just after n=3k, exhibiting a steplike pattern. This can be attributed to the well-known fact that (3k, 0) SWNTs behave like metals usually having low IPs. Figure 2.9 shows that the IP of (9,0) is smaller than those of (7,0) and (8,0) SWNTs, i.e., (9,0) SWNT can easily donate an electron as compared with (7,0) and (8,0) SWNTs, which agrees with the conclusion in a recent report [32]. Table 2.3 indicates that the applied PW91 does predict rather small band gaps for (3k, 0) zigzag, 0.0, 0.13, 0.08, and 0.06 eV for k=2-5, which are comparable to those from the hybrid DFT B3LYP [33]. It is interesting to note that the above step like feature of IPs is periodic, or exhibits a group behavior. Such a group behavior is somehow characterized by the IPs for SWNTs with n=3k (k=2-6) as compared with their neighbors, (n−1, 0) and

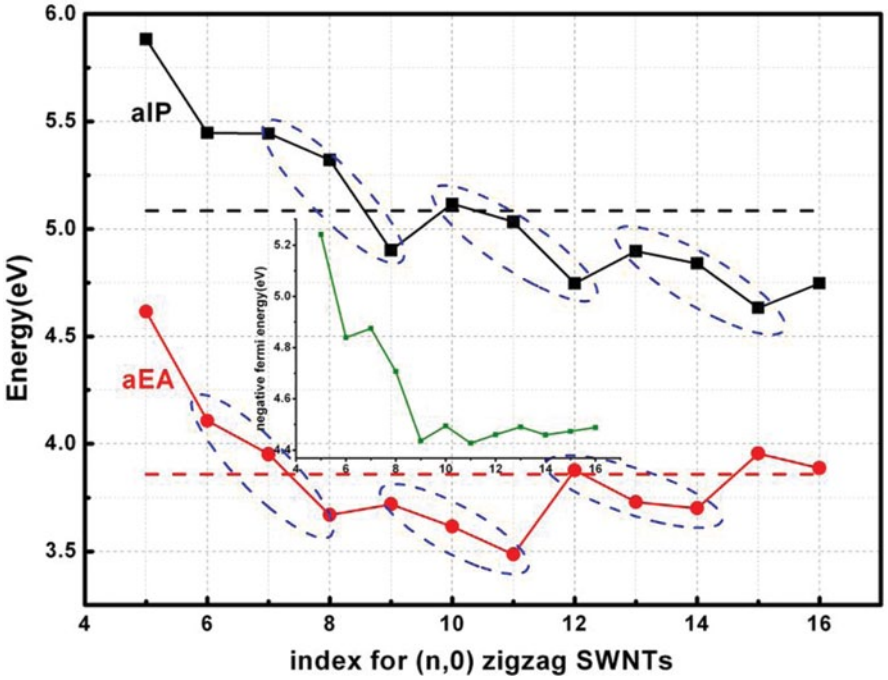


Fig. 2.9 Adiabatic IPs and EA as a function of index for zigzag (n,0) SWNTs. The insert graph is the variation of negative Fermi energy. The *black* and *red* dash lines denote the average IP and EA of these SWNTs, respectively

Table 2.3 Adiabatic IP, EA, Mulliken electronegativity $\chi=(IP+EA)/2$, $-E_{HOMO}$, and $-E_{LUMO}$ (eV) predicted with M06-2X/6-31G* for 22.2 Å long H-passivated armchair (n,n) SWNTs

n		IP	EA	χ	$-E_{HOMO}$	$-E_{LUMO}$
5	$C_{200}H_{20}$	5.36	2.52	3.94	5.04	2.75
7	$C_{280}H_{28}$	5.06	2.83	3.95	4.82	3.06
9	$C_{360}H_{36}$	4.92	3.01	3.97	4.71	3.22
10	$C_{400}H_{40}$	4.87	3.07	3.97	4.67	3.27

(n−2, 0) SWNTs with a metallic and two semiconducting tubes in a group. A similar group behavior was also shown in the change of energy gaps [34], the formation energy of 5-7-7-5 defects [35], single vacancy for (n,0) SWNTs [35b], and adsorption energy of a single H atom on (n,0) SWNT surface [36]. Sun et al. suggested that the bonding characteristics of the orbitals in these group behaviors correspond to the difference of energy level around k point in the Brillouin zone [37]. In spite of the distinct physical properties, the previously examined properties exhibit similar periodic features to the present IPs. Thus, the observed family behavior either in the energy gaps, defective cases or adsorption energies is essentially associated with the intrinsic geometrical property of the (n,0) zigzag SWNTs (Table 2.4).

Table 2.4 Calculated geometrical and electronic parameters for zigzag SWCNT

(n,0)	D(Å)	HOMO[a]	LUMO	Gap	aIP[b]	vIP[c]	λ_h[d]	aEA[b]	vEA[c]	λ_e[e]	E_f	E_g
$n=5$	3.91	−5.327	−5.081	0.246	5.88	5.92	0.04	4.62	4.56	0.06	−5.242	0.17
6	4.7	−4.601	−4.583	0.018	5.45	5.45	0	4.11	4.10	0.01	−4.839	0
7	5.48	−4.971	−4.769	0.202	5.44	5.45	0.01	3.95	3.94	0.01	−4.875	0.21
8	6.26	−5.016	−4.398	0.618	5.32	5.33	0.01	3.67	3.66	0.01	−4.707	0.62
9	7.05	−4.51	−4.379	0.131	4.90	4.90	0	3.72	3.71	0.01	−4.436	0.13
10	7.83	−4.855	−4.125	0.73	5.12	5.12	0	3.62	3.60	0.02	−4.494	0.73
11	8.61	−4.901	−3.952	0.949	5.03	5.04	0.01	3.49	3.49	0	−4.427	0.95
12	9.39	−4.502	−4.425	0.077	4.75	4.75	0	3.88	3.88	0	−4.46	0.08
13	10.18	−4.782	−4.191	0.591	4.90	4.90	0	3.73	3.72	0.01	−4.49	0.59
14	10.96	−4.829	−4.087	0.742	4.84	4.84	0	3.70	3.70	0	−4.459	0.74
15	11.74	−4.503	−4.448	0.055	4.63	4.63	0	3.96	3.94	0.02	−4.473	0.06
16	12.53	−4.734	−4.235	0.499	4.75	4.75	0	3.89	3.88	0.01	−4.488	0.5

Fermi energy (E_f) and band gap E_g

[a] all energies are in eV

[b] adiabatic ionization potential (electron affinity)

[c] vertical ionization potential (electron affinity)

[d] hole reorganization energy

[e] electron reorganization energy

[f] diameter

Opposite to the armchair SWNTs, the adiabatic EAs of the zigzag SWNTs decrease rapidly with increasing diameter till (11,0) and then gently increase. Similar to IPs, the EAs of zigzag SWNTs also exhibit the group behavior; however, in these groups (3k,0) SWNTs, such as (6,0), (9,0), (12,0) and (15,0) have higher EA than their neighbors. Thus, (3k,0) zigzag SWNTs could also be characterized as better oxidants compared with their neighboring (3k − 1,0) and (3k + 1,0) tubes. It should be noted that the group behaviors for the IPs and EAs of (n,0) SWNT are not synchronous. For example, (7,0), (8,0) and (9,0) compose a monotonically decreasing IPs group, whereas (6,0), (7,0) and (8,0) compose a monotonically decreasing EAs group. The negative Fermi level (or the approximated WF) decreases with the diameter of zigzag SWNT, which also agree with that for the semiconducting SWNTs [27]. For the infinite (7,0) nanotube the current WF of 4.875 eV again is rather close to predicted by all-electron (4.82 eV) and (4.75 eV) [25].

In order to further analyze redox property for zigzag SWNTs, individual IP and EA were compared with the averaged IP and EA over the investigated SWNTs, *AVG*(IP) and *AVG*(EA), respectively. If the relative IP (ΔIP = IP − *AVG*(IP)) is negative, this SWNT will be a good electron donator in the entire region; whereas if the relative EA (ΔEA) is positive, this SWNT will be a good electron acceptor. A combination of the performance of ΔIP and ΔEA will be used to characterize the redox property of SWNTs. The electron donator/acceptor map is shown in Fig. 2.10. Because of positive ΔEA and negative ΔIP, the large diameter zigzag SWNTs, (12,0), (15,0), (16,0) could be characterized as relatively good reductants as well as good oxidants. The small diameter zigzag SWNTs, such as (5,0), (6,0), and (7,0),

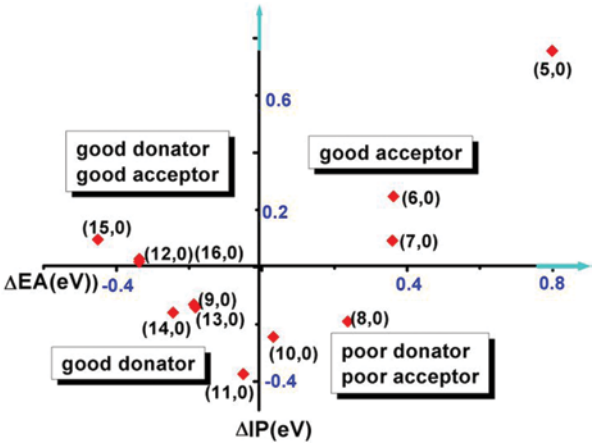


Fig. 2.10 The electron donator/acceptor map of zigzag SWNTs. ΔIP and ΔEA were defined as the difference between the individual one and the average IP and EA for the investigated zigzag SWNTs

exhibit positive ΔIP and ΔEA. Accordingly, they could only be characterized good oxidants, yet poor reductants. Finally, (8,0) and (10,0) zigzag are poor reductants and oxidants.

According to the above analysis, it is most likely that three factors determine the redox properties of these two types of SWNTS: diameter, electronic property and chirality. If a SWNT possesses both large diameter and metallic behavior, because of low IP and high EA it could act as a good reductant and good oxidant, no matter whether armchair or zigzag. The small diameter armchair SWNTs, such as (3,3), (4,4) and (5,5) may be difficult to be reduced and oxidized because of high IP and low EA. The small diameter zigzag SWNTs, such as (5,0), (6,0) and (7,0), could act as a good oxidant, yet a poor reductant. These conclusions are very important to the potential application of SWNTs in bio-electrochemistry field. It could be predicted that large diameter (n,n) and (3k,0) tubes are suitable for the redox chemistry of noncovalently functionalized SWNTs. This difference among these tubes may also offer a new strategy for separating SWNTs.

To directly compare their convergence, the evolutions of adiabatic IP and EA for the armchair and zigzag SWNTs as a function of diameters are summarized in Fig. 2.11. From this figure, it could be seen that the IP curve for the armchair SWNTs has already rather flat and tends to converge to approximately 4.6 eV, very similar to that of graphite [38], while the EA curve has a slightly bigger slope (0.055 vs −0.041). In spite of oscillation of IP/EA for the zigzag SWNTs, the IPs and EAs for a few large zigzags have already been similar to those of the armchair (16,16), IP and EA being approximately 4.6 and 3.9 eV, respectively. It could be anticipated that with increasing diameter, the IP for that armchair and zigzag SWNTs converge together to that of graphene, so does the EA.

Figure 2.11 also shows for the given diameter SWNTs, the zigzag has lower IP and higher EA than the armchair. However, as mentioned above the IPs and EAs for the both SWNTs have tendency to converge to those of graphene. The WFs for the armchair and zigzag SWNTs were directly compared in Fig. 2.12. The WF of (n,n)

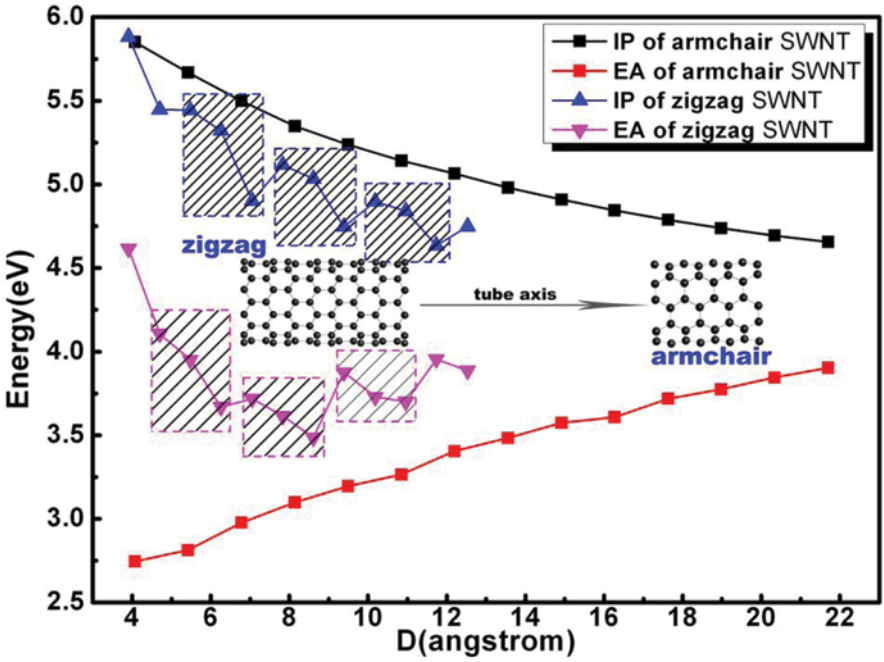


Fig. 2.11 The evolution of IP and EA for armchair and zigzag SWNT as a function tube diameter (D). The shadow rectangle regions denote triple groups

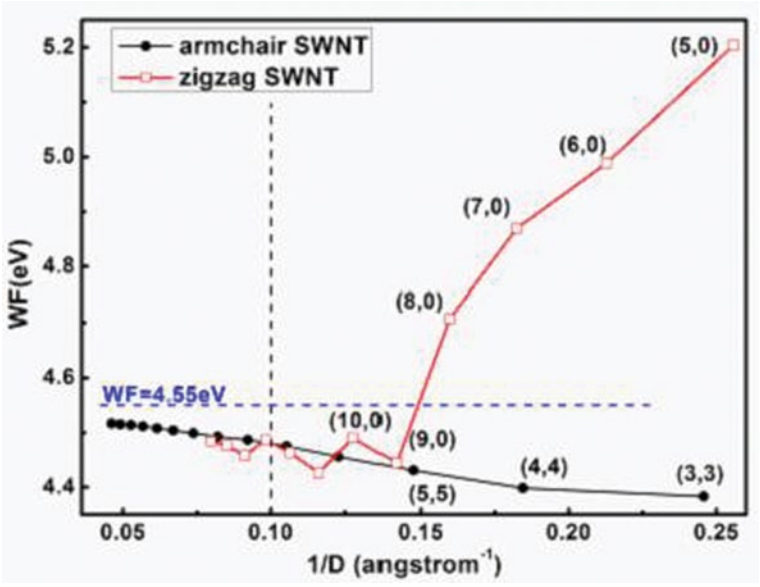


Fig. 2.12 Work functions (eV) of armchair and zigzag SWNTs as a function of the inverse tube diamaters 1/D ($Å^{-1}$)

Table 2.5 The singlet-triplet energy gaps ($\Delta E/eV = E_{singlet} - E_{triplet}$) for H-passivated (n,0) SWNT

(n,0)	(5,0)	(6,0)	(7,0)	(8,0)	(9,0)	(10,0)	(11,0)
5-unints with M06-2X/6-31G*	−0.18	0.02	−0.31	1.67	1.73	0.84	1.40
20-units with DFTB	0.12	0.68	0.48	0.03	–	0.05	0.44

SWNTs verse 1/D exhibits a good linear correlation including a few thick metallic zigzag ones such as (12,0) and (15,0).

2.3.3 IP, EA, and electronic states for H-passivated (n,0) zigzag SWNT

Although the ground state for the H-passivated (n,n) SWNT is singlet, the H-passivated (n,0) SWNT is different. The singlet-triplet energy gaps were summarized in Table 2.4. It shows that for the 5-units (n,0) cluster (~21.3 Å in length) the singlet state for (5,0) and (7,0) is ground state, yet the triplet is ground state for the other (n,0). For the 20-units H-passivated (n,0) (~85.1 Å in length) the DFTB predicts that the triplet state is ground state for all the cases (Table 2.5).

To discuss the density dependence on the size of H-passivated (n,0) SWNT, the HOMOs of 5-units (5,0), (6,0), (7,0), (8,0), and (10,0) are shown in Fig. 2.13. For the thin SWNTs, the HOMOs primarily locate over the central carbons and there is little distribution on the end carbons, especially for the (5,0). However, as the diameter increases the HOMO dominantly localizes over the end carbons. The similar scenario exists in the LUMOs (not shown). This result indicates that the 5-units (n,0) H-passivated SWNTs are not able to describe the activity behavior of the SWNT, and larger models are required. Therefore, care should be taken as cluster model of (n,0) SWNT is chosen.

For the 30-units H-passivated (n,0) SWNTs, the adiabatic IP, EA and absolute electronegativity were estimated with DFTB method. It is acknowledged that the DFTB cannot provide so accurate energy as DFT methods (Fig. 2.14); however, the variation trends with the diameter are comparable to those in Fig. 2.9.

2.3.4 DOS Difference Between Armchair and Zigzag SWNTs

To understand the effect of electron or hole injection on the electronic structure, density of state (DOS) diagrams of (5,5), (6,6), (8,0), (9,0), and (10,0) were plotted in Fig. 2.15. The electronic structures near the Fermi level for some cases are significantly affected by electron and hole injections. For all SWNTs, as compared with neutral systems Fig. 2.15 shows that both the −1 and +1 charged ones undergo shifts toward the valence band to different extent, and the shifts for the −1 charged (blue) are much more significant than +1 charged ones (red). The shifts between the neutral and the +1 charged in zigzag SWNTs (n,0)

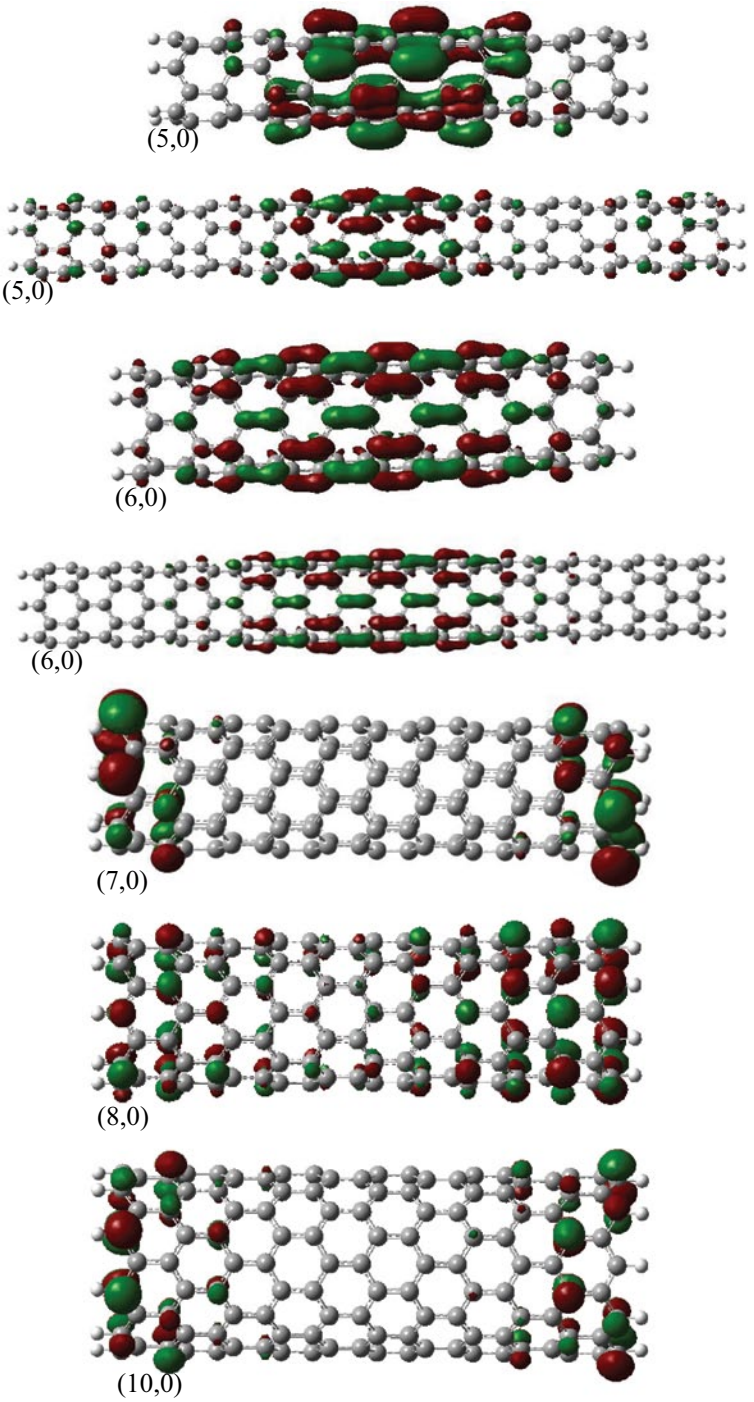


Fig. 2.13 The HOMOs for the 5-units H-passivated (n,0) SWNTs (~21.3 Å in length). The HOMOs in *red* box refer to 10-units (5,0) and (6,0) SWNTs (42.4 Å in length)

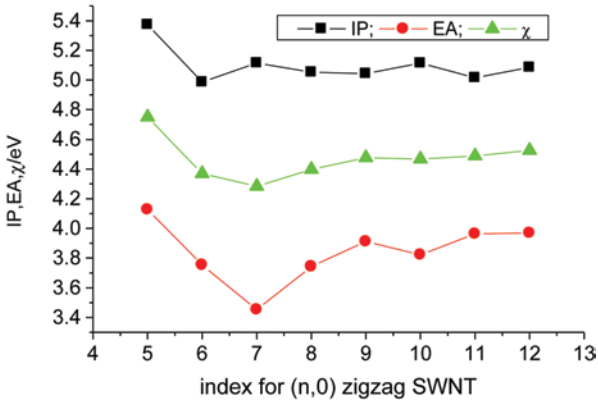


Fig. 2.14 Adiabatic IP, EA and Mulliken electronegativity variation for 30 units H-passivated (n,0) SWNT (~127.8 Å) predicted with DFTB method

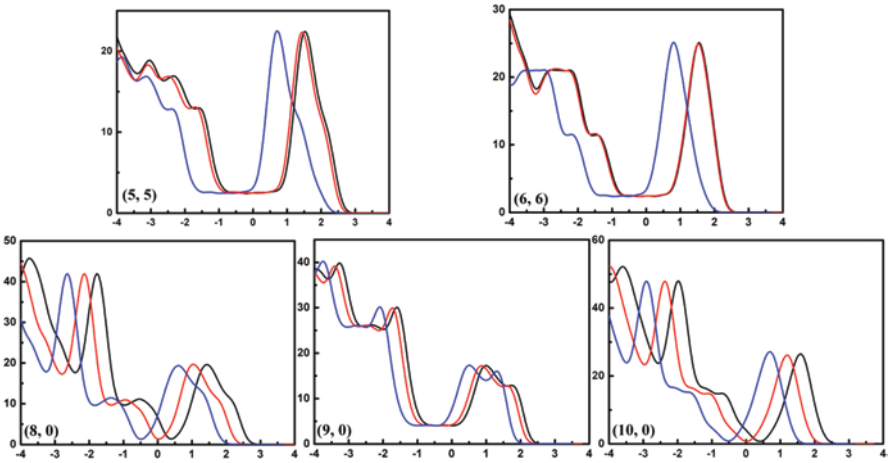


Fig. 2.15 Density of states (DOS) for (5,5), (6,6) armchair SWNTs and (8,0), (9,0) and (10,0) zigzag SWNTs. The DOS of neutral, + 1 and − 1 charged systems are represented by *black*, *red* and *blue* lines. The horizontal and vertical axis represents energy (given in eV) and DOS, respectively

(the latter three in the panel of Fig. 2.15) are much more considerable than those in armchair ones (the former two in Fig. 2.15), where the DOS shifts due to hole injection is rather minor. The different DOS shifts for + 1 charged armchair and zigzag SWNTs also agree well with the above different patterns between vertical and adiabatic IPs. It can be concluded that both armchair and zigzag SWNTs are very sensitive to an electron injection, yet zigzag SWNTs are more sensitive to a hole injection than armchair ones. This conclusion is in a good agreement with Guo's report about charge effect on hydrogen molecule chemisorption on SWNTs [13].

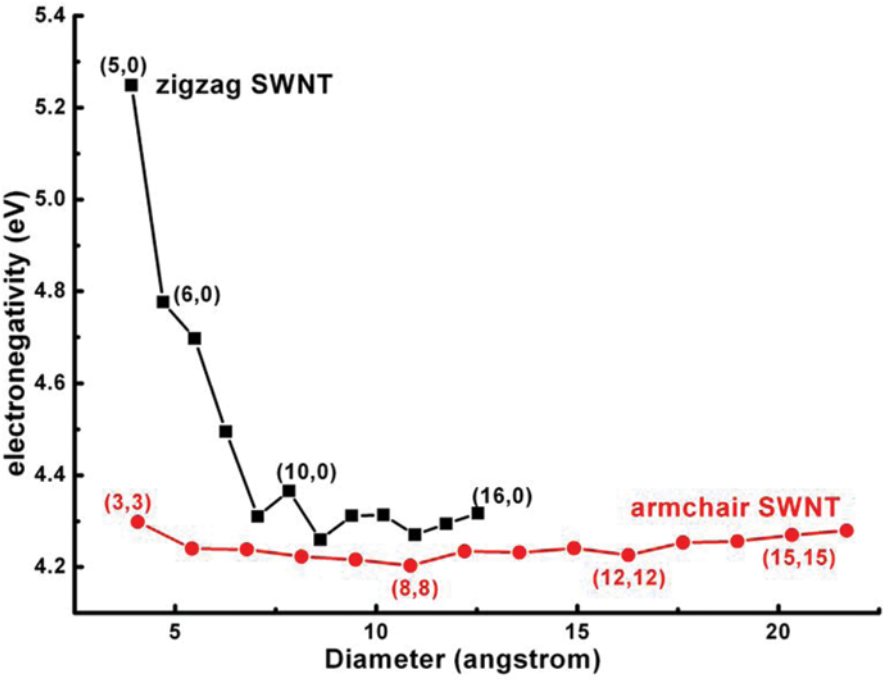


Fig. 2.16 Mulliken electronegativity, (IP+EA)/2, of armchair and zigzag SWNTs as a function of diamaters

2.3.5 Mulliken Electronegativity of SWNTs

To generally discuss the ability to gain electrons for SWNTs, an empirical measure, Mulliken electronegativity (χ) was plotted in Fig. 2.16 as a function of diameters. χ was defined as the average of IP and EA. According to Fig. 2.16, χ of the armchair and zigzag SWNTs also have quite different evolutions. For the investigated armchair SWNTs the electronegativities are almost a constant within 4.2–4.3 eV. It slightly decreases from 4.30 eV for (3,3) to 4.20 eV for (8,8), and then increase to 4.23 eV for (9,9). Thereafter, it remains a constant of 4.23–4.24 eV till (12,12), and finally slightly increases to 4.28 eV for (16,16). However, similarly to the distinct IP and EA change patterns χ of the zigzag SWNTs vary quite differently from those of the armchair. In spite of similar diameters, (5,0) has a much higher χ than (3,3) by approximately 1.0 eV (5.25 vs 4.30 eV). χ of the zigzag SWNTs rapidly drops to 4.31 eV for (9,0), and then fluctuates around 4.3 eV. It is interesting to note that χ for thick zigzag beyond 8 Å approaches to that for that armchair. Once again, the variation of χ indicates that large diameter SWNTs exhibit similar redox property, while the small ones with diameter of less than approximately 1 nm may quite differ from each other.

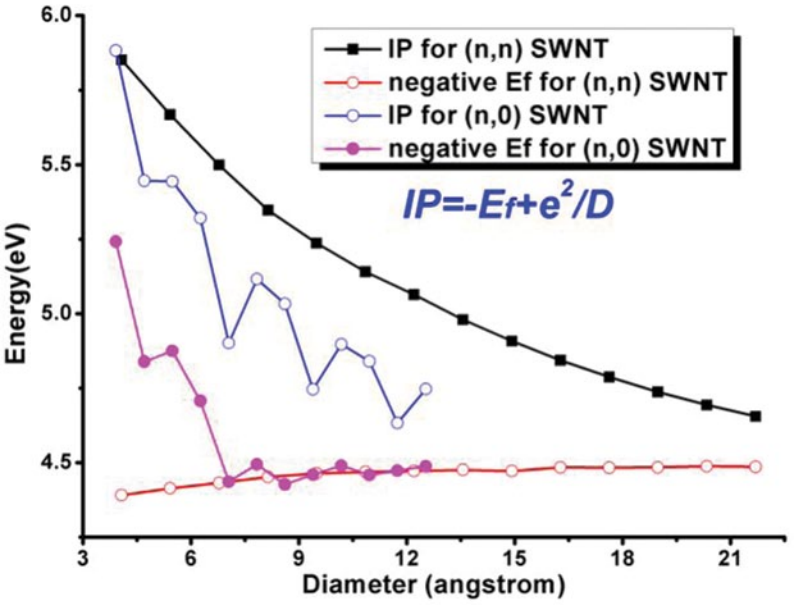


Fig. 2.17 The correlation between IP and Fermi level for the armchair and zigzag SWNTs

2.3.6 Correlation between IP/EA and Fermi level

Figure 2.17 shows that the Fermi energies of the armchair SWNTs only slightly decrease from −4.39 for (3,3) to −4.49 eV for (16,16) SWNT. For the zigzag SWNTs the Fermi energies, however, significantly increase from −5.24 eV for (5,0) to −4.44 eV for (9,0) SWNT, and then converge to a similar level to the armchair of approximately −4.5 eV. The distinct Fermi energy trends for the armchair and zigzag SWNTs may determine their redox property variation. The IP variation for the armchair could be understood with an empirical rule for cluster models [39], IP$=-E_f+e^2/D$, where D is the diameter of cluster. Because of rather small variation of E_f for the investigated armchair SWNTs, the IP trend was mainly determined by the quantum size effect term (e^2/D), smoothly decreasing IP with increasing diameters. As for the zigzag SWNTs, the IPs seems to be determined by $-E_f$ for small diameter SWNTs till (9,0), which is revealed by a good correspondence between IP and E_f.

In line with the empirical equation for EA, EA$=-E_f-e^2/D$, Fig. 2.18 indicates that EAs for both the armchair and zigzag SWNTs are less than their corresponding $-E_f$ curves. The smooth increase of EAs with diameters for the armchair SWNTs can be mainly attributed to quantum size effect term because of an almost constant E_f. For the small diameter zigzag, both the EAs and $-E_f$ decrease concurrently with diameters. In spite of a group behavior, similar to the armchair SWNTs the general increase of EAs for the zigzag SWNTs beyond (11,0) may also be due to the gentle increase of $-E_f$ and the decrease of quantum size effect term ($-e^2/D$).

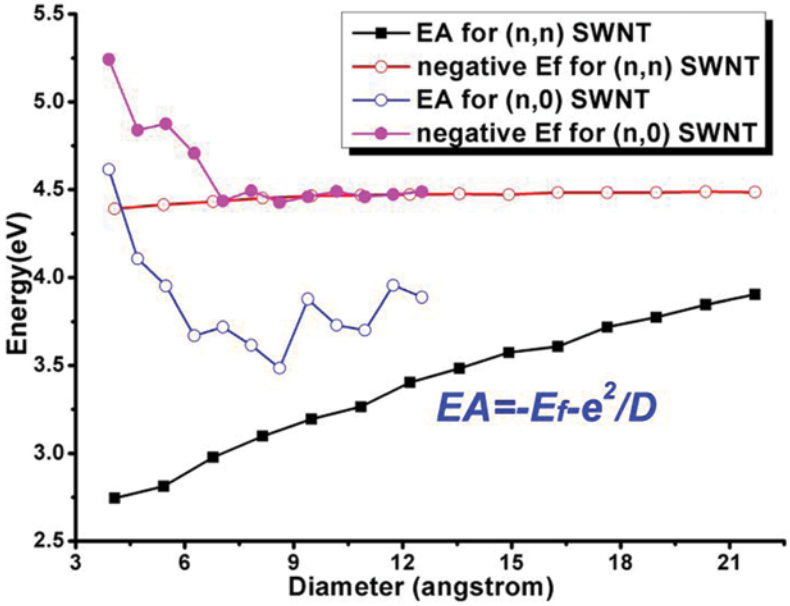


Fig. 2.18 The correlation between IP and Fermi level for the armchair and zigzag SWNTs

In the DMol^3 scheme, although energy calculations can be carried out for periodic models with k-points, orbitals cannot be calculated other than Gamma point. Thus, the orbitals actually refer to the clusters and may not be accurate for infinite systems. Because of much a bigger Gamma point than the (n,n) SWNTs (parameter c: 17.04 vs 9.84 Å), the orbitals for the (n,0) may be qualitatively reliable. As shown by Fig. 2.19, the band gaps and HOMO-LUMO gaps are nearly the same except for (5,0) SWNT. The corresponding changes of energy gap generally follow the Hückel theory. HOMO-LUMO gaps and band gaps oscillate and are rather small for metallic SWNTs, 0.131/0.13 eV for (9,0), 0.077/0.08 eV for (12,0), and 0.055/0.06 eV for (15,0). The present band gaps for the (3k,0) armchair SWNTs are slightly higher than those from either the experimental [0.080 ± 0.005 eV for (9,0), 0.042 ± 0.004 eV for (12,0), and 0.029 ± 0.004 eV for (15,0)] [40] or the recently reported using B3LYP method [0.079 eV for (9,0), 0.041 eV for (12,0), and 0.036 eV for (15,0)] [33]. A detailed comparison is also shown in Table 2.6. It should be noted that the trend of band gaps of the three (3k,0) SWNTs is in a good agreement with the values of B3LYP and the experiment. As shown in Fig. 2.20, these gaps scale as an almost linear plot of $1/D^2$. Zigzag SWNTs with $n < 8$ do not well follow the oscillation due to their small diameters and significant σ-π mixing [41]. The calculated band gap for (6,0) is zero. Here, the calculated band gap for (5,0) is 0.17 eV that is not following the B3LYP method [33]. This result shows that PW91/DNP still has some flaws in the calculations of accurate band gaps for SWNTs.

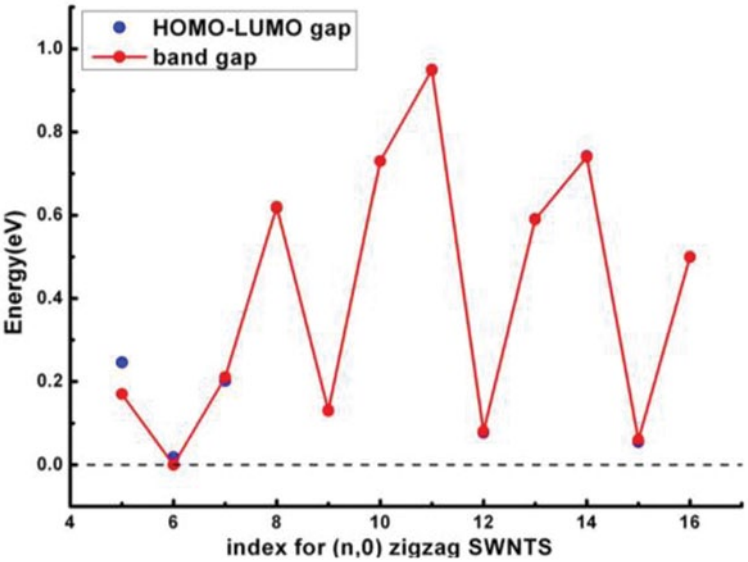


Fig. 2.19 HOMO-LUMO energy gap/band gap as functions of index for the zigzag SWNTs. Some *blue* and *red* points are too close to be distinguished

Table 2.6 Band gaps (*Eg*) of (3k,0) zigzag SWNTs for PW91, B3LYP, PBE and LDA compared to experiment

(n,0)	PW91 *Eg*(eV)	B3LYP *Eg*(eV)[a]	Experimental *Eg*(eV)[a]	PBE *Eg*(eV)[a]	LDA *Eg*(eV)[a]
$n=6$	0.00	0.00			
9	0.13	0.079	0.080 ± 0.005	0.003	0.024
12	0.08	0.041	0.042 ± 0.004	0.006	0.002
15	0.06	0.036	0.029 ± 0.004	0.00	0.00

[a] Reference [33]

2.3.7 IPs and EAs for DWNT

We also calculated the IPs and EAs for three types of DWNT, which were (3,3)@(8,8), (5,5) @ (10,10) and (6,6) @ (11,11). The distance between the outer and inner layer of the three DWNTs is 3.39 Å, a typical value for DWNTs [4]. Figure 2.21 clearly shows that the aIPs and aEAs of these three (armchair @ armchair) DWNTs have the similar variation to the armchair SWNTs, i.e., IP decrease while EA increase with diameters. It should be noted that the IP of DWNT is lower than its constituents, and EA is higher than its constituents. The results reveal that DWNTs possess better redox properties compared with its constituents.

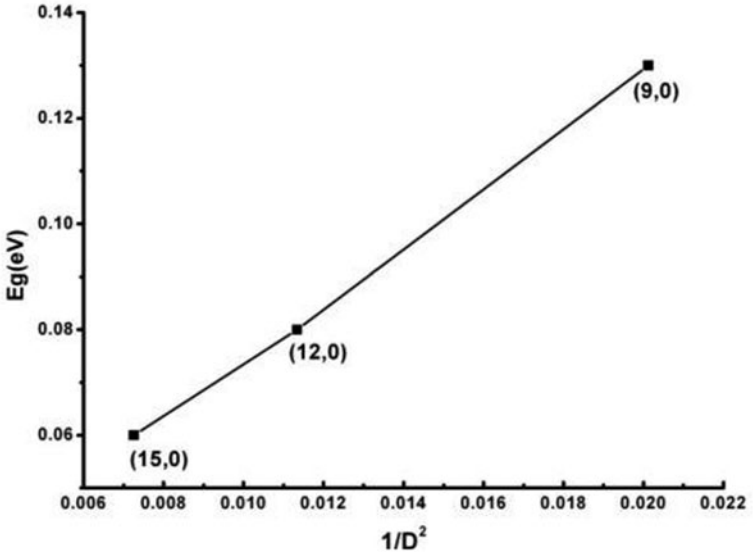


Fig. 2.20 The correlation of *Eg* and $1/D^2$ for some (3k,0) zigzag SWNTs

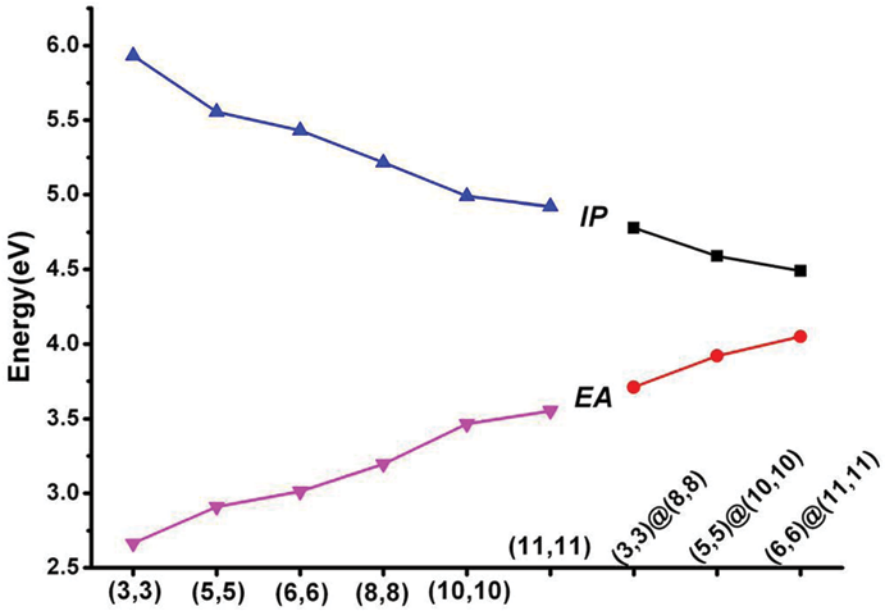


Fig. 2.21 aIPs and aEAs for the different DWNTs and their constituents

Table 2.7 The first adiabatic and vertical ionization potentials (aIP and vIP/eV) for nucleic acid bases, C_{60}, Li@C_{60} and SWNT at various theoretical levels. (Reprinted with permission from [43b])

	Thymine	Cytosine	Adenine	Guanine	C_{60}	Li@C_{60}	SWNT
aIP, M052x/cc-pVDZ	8.73	8.59	8.02	7.56	8.04		
aIP, M062x/cc-pVDZ	8.71	8.58	8.02	7.56	7.96		
aIP, M062x/6-311++G**	8.97	8.90	8.31	7.87	8.03	5.98	
aIP, PBE-D/cc-pVDZ	8.34	8.14	7.68	7.23	7.25		
vIP, PBE-D/cc-pVDZ	8.47	8.29	7.89	7.54	7.31		
aIP, MPWB1K/cc-pVDZ	8.62	8.38	7.88	7.38	7.68		
aIP, Exp.[a, b]	8.87/8.80	8.68/8.45	8.26/7.80	7.77/7.85			4–6
IP, Experimental range[c]					7.54–8.1		

[a] Photoionization mass spectroscopy in the gas phase [44]
[b] Photoelectron spectra [45]
[c] Ionization energy determinations for C_{60} at chemistry web book of NIST

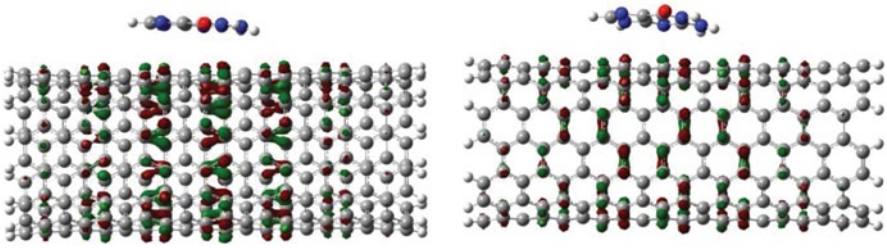


Fig. 2.22 HOMO (*left*) and LUMO (*right*) of the complex of guanine and (7,7) SWNT. (isovalue = 0.02 au) The frontier MOs only delocalize over the SWNT, indicating that SWNT may prevent DNA from radiation

2.3.8 *Biomedical Implication of the Interaction of DNA Bases with SWNT, and C_{60} Derivatives*

According to the above discussion, although the IPs of SWNT vary with the thickness and electronic structure they are in the range of 4–6 eV, much lower than those of C_{60}, Li@C_{60}, as well as DNA bases shown in Table 2.7. Because of lower IP, it is apparent that SWNTs are able to protect DNA bases from radiation damage, and perform better than C_{60} and Li@C_{60} in this aspect. Taking guanine (G) as an example of DNA bases that has the lowest IP among the four DNA bases, the interaction between a H-passivated (7,7) SWNT (22.2 Å in length) and G was investigated with the M06-2X/6-31G*, a hybrid meta-GGA DFT method, [42] which was demonstrated to relatively accurately account for non-covalent interaction among DNA bases with C_{60} and derivatives [43]. The SWNT binds to guanine through π-π stacking, showing an almost parallel configuration in Fig. 2.22. The

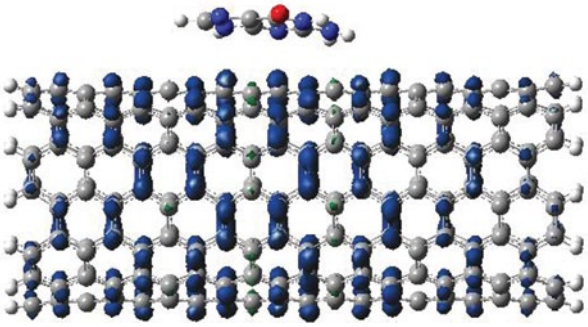


Fig. 2.23 Spin density for the cation of the complex (7,7)-guanine with M06-2X method (isovalue = 0.004)

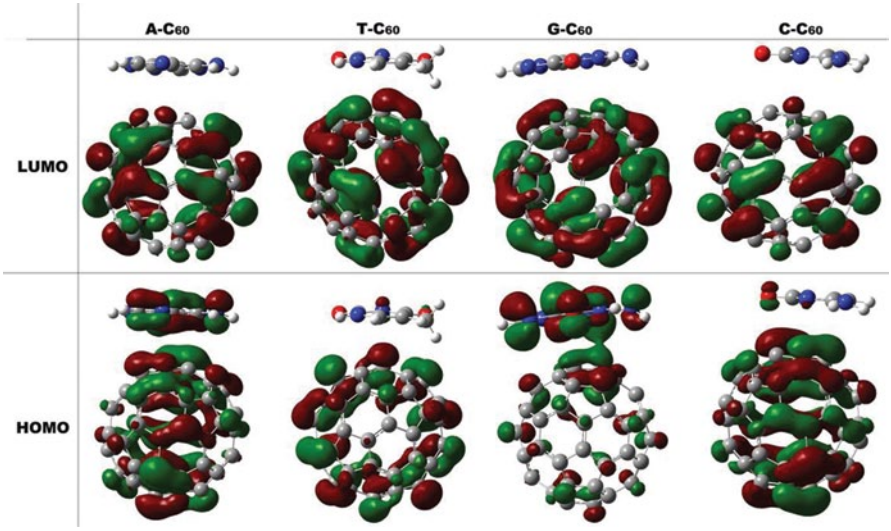


Fig. 2.24 Plots of the frontier orbitals of the DNA bases and C_{60} complexes. The isovalue is 0.02 au Reprinted with permission from [43b] American Chemical Society

binding energy, −13.3 kcal/mol at M06-2x/6-31G* level, indicates that their interaction is also stronger than G with C_{60} or Li@C_{60}, the respective binding energies of −7.55 kcal/mol and −11.73 kcal/mol (M06-2x/6-311++G**) [43].

As shown in Fig. 2.22, the HOMO and LUMO for the complex of guanine and (7,7) SWNT are solely made of the SWNT. In spite of rather strong interaction, their MO orbital interaction is quite weak and the binding dominantly arises from dispersion and partial electrostatic attraction. The HOMO also implies that an electron will be ejected from the SWNT rather than G upon radiation, which can be verified by the spin density of the cation of the complex (7,7)+G, where the spin density solely distribute over the SWNT.

The interaction of G with SWNT is rather different than those of DNA bases with C_{60} [43b, 46]. Figure 2.24 illustrates the HOMO and LUMO of the complexes of DNA bases with C_{60} predicted with M06-2X method [43b]. LUMO of all these complexes

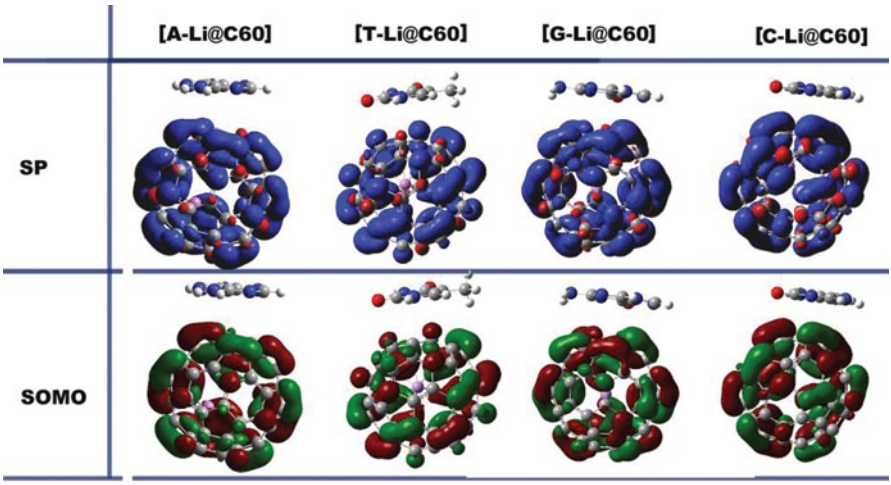


Fig. 2.25 Plots of the SOMO and spin density (SP) of the neutral complexes, NAB-Li@C_{60}. The isovalue of SOMO and SP are 0.02 and 0.0004 au, respectively. ([43a])

localizes on C_{60}. Orbital energies for the HOMO of the six individual molecules are as follows: SWNT (−0.16 ~ −0.17 au) > G(−0.208 au) > A(−0.218) > C_{60} (−0.220) > C (−0.227) > T(−0.240). As shown by the molecular orbitals in Fig. 2.23, HOMOs from the DNA bases and C_{60} make different contributions to the HOMO of complexes. For G–C_{60} and A–C_{60}, the HOMO levels of the complexes are close to the HOMO of DNA bases, while the HOMO levels of complexes C–C_{60} and T–C_{60} are close to the HOMO level of C_{60}. According to Fig. 2.24, HOMOs delocalize over both guanine/adenine moiety and C_{60} for G/A–C_{60} complexes, while they almost localize on C_{60} in T/C–C_{60} complexes. Accordingly, the presence of C_{60} molecule may well protect thymine and cytosine from radiation damage. However, whether fullerene could protect guanine and adenine from radiation damage needs to be further investigated [43b].

As a typical metallofullerene, Li@C_{60} has been synthesized and characterized experimentally in several studies [47], and theoretical calculations on these systems have also been carried out [48]. According to Table 2.6, its ionization potential is considerably decreased as compared with C_{60}, yet slightly higher than SWNT. G-Li@C_{60} complex is the strongest binding (E_b: −8.27 kcal/mol), followed by C-Li@C_{60} (−7.36 kcal/mol) and A-Li@C_{60} (−6.95 kcal/mol), and T-Li@C_{60} complex is the weakest binding (−6.62 kcal/mol). The binding between NABs and Li@C_{60} is generally stronger by 0.7–1.6 kcal/mol than that between the corresponding base with intrinsic C_{60}, which may be due to higher electrostatic interaction between the charged C_{60} and NAB. The M06-2x predicted binding sequence for NABs-Li@C_{60} is also different from the trend of interaction between NABs and C_{60}: G–C_{60} (−6.80 kcal/mol) > A–C_{60}(−6.24) > C–C_{60}(−5.64) > T–C_{60} (−5.29) [43b]. To gain further insight into the influence of the non-covalent interaction on the electronic structure of NABs-Li@C_{60}, singly occupied molecular orbital (SOMO) plots of the complexes were given in Fig. 2.25. For all these complexes, the SOMOs dominantly

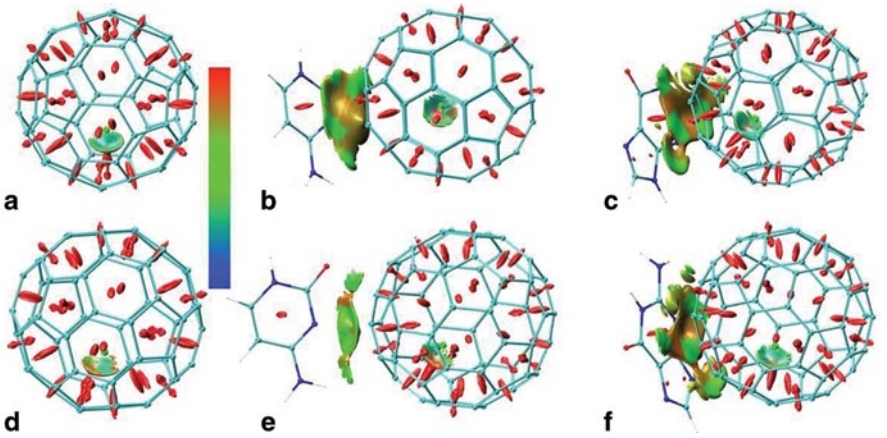


Fig. 2.26 Gradient isosurfaces (s = 0.5 au) for neutral and cationic Li@C_{60} (**a**, **d**), C-Li@C_{60} (**b**, **e**), and G-Li@C_{60} (**e**, **f**) complexes. The surfaces are colored on a *blue-green-red*(BGR) scale according to values of sign(λ_2)ρ, ranging from −0.04 to 0.02 au. *Blue* indicates strong attractive interactions, and *red* indicates strong nonbonded overlap. The functions such as RDG and sign(λ_2)ρ were calculated with Multiwfn software [49]. The gradient isosurface was plotted with VMD [50]. [43a]

localize on the surface of C_{60}, indicating that it is most likely the ionization process would occur in the metallofullerene due to its low ionization potential. Similar to SWNT, this implies that the Li@C_{60} is able to well protect NABs from radiation.

From Yang's approach, the sign of reduced density gradient λ_2 can be used to distinguish bonded ($\lambda_2 < 0$) from nonbonded ($\lambda_2 > 0$) interactions. The gradient isosurfaces are colored according to the corresponding values of sign(λ_2)ρ, which is found to be a good indicator of interaction strength. Large negative values of sign(λ_2)ρ are indicative of attractive interactions (such as dipole-dipole or hydrogen bonding); while if sign(λ_2)ρ is large and positive, the interaction is nonbonding [21]. Values near zero indicate very weak, van der Waals interactions. The gradient isosurfaces provide a rich visualization of noncovalent interaction as broad regions of real space, rather than simple pairwise contacts between atoms. We first consider the neutral and cationic Li@C_{60} molecule. As shown in Fig. 2.26, there are areas of nonbonded overlap located at the center of the hexagonal and pentagonal rings. Meanwhile, there is another lower density surface between Li and cage. Comparing *a* and *d* in Fig. 2.26, it could be detected that there are more orange splashes in *d*, where the stronger repulsion is expected. The stronger repulsion also agrees with the judgment based on charge population. As for the NAB-Li@C_{60} systems (b–c, and e–f), there are lower density surfaces between the overlapping portions of NAB and cage, where either π-π stacking or σ-π is expected. It should be noted that graph e has the largest percent of blue region, indicating the largest noncovalent interaction among the four complexes. This trend also agrees with the above binding energies. Figure 2.26 shows that the sign(λ_2)ρ can be employed to visualize noncovalent interaction between DNA bases and carbon nano-materials.

2.4 Conclusions

In summary, we have investigated ionization potentials (IPs), electron affinities (EAs), electronegativities (χ) and Fermi levels (E_f) for infinite length armchair single-walled carbon nanotubes (SWNT) (n,n) (n=3–16), zigzag SWNT (n,0) (n=5–16), as well as double-walled carbon nanotubes (DWNT) (n,n)@(n+5, n+5) (n=3, 5 and 6). These properties show a strong and different diameter dependence. (a) IPs of the armchair SWNTs decrease monotonously, while the EAs increase monotonously; (b) IPs of zigzag SWNTs generally decrease, and show a "family behavior", where every three neighbourhood form a triplets family. The IPs which dispersed in these triplets decreases monotonously as the diameters increase. Opposite to the armchair SWNTs, the EAs of zigzag SWNTs decrease rapidly with increasing diameter till (11,0) and then gently increase. (c) For the armchair SWNTs electronegativity (χ) and Fermi level ($-E_f$) change very slightly with diameters, while for the zigzag they decrease rapidly till (9,0) and then gently oscillate to the similar levels to those of the armchair. (d) The (n,n) @ (n+5, n+5) DWNTs have the same evolution as the armchair SWNTs. DWNTs characterize better redox properties than their constituents. Furthermore our calculations indicated that there are three factors to determine the redox properties of the two types of SWNTS: diameter, electronic property and chirality. These findings are very important in redox chemistry based on NTs and would offer a new strategy for separating NTs.

Although the IPs of SWNT vary with the thickness and electronic structure they are in the range of 4–6 eV, much lower than those of C_{60}, Li@C_{60}, as well as DNA bases. Together with the low IP, the dominant localization of HOMO on SWNT moiety of the complexes G-SWNT indicates that an electron would be ejected from SWNT upon radiation, and similar to Li@C_{60} the SWNT is therefore able to protect DNA bases from radiation. Finally, Yang's reduced density gradient approach clearly shows that the weak and strong noncovalent interaction regions in the complexes, NABs-Li@C_{60} and (NABs-Li@C_{60})$^+$. The method will be extended to visualize the noncovalent interactions for other bio-nano systems.

Acknowledgement This work at Shandong University (Sun and Bu) is supported by NSFC (20633060, 20973101, 21373123), the Independent Innovation Foundation of Shandong University (2009JC020), and NCET. The project described here was also supported by the National Institute of General Medical of the National Institute of Health (SC3GM082324) (Wang at Albany State University).

References

1. Iijima S (1991) Helical microtubules of graphitic carbon. Nature 354(6348):56–58
2. (a) deJN, Lamy Y, Schoots K, Oosterkamp TH (2002) High brightness electron beam from a multi-walled carbon nanotube. Nature 420(6914):393–395; (b) de Heer WA, Châtelain A, Ugarte D (1995) A carbon nanotube field-emission electron source. Science 270(5239):1179–1180
3. Hansma PK, Cleveland JP, Radmacher M, Walters DA, Hillner PE, Bezanilla M, Fritz M, Vie D, Hansma HG, Prater CB, Massie J, Fukunaga L, Gurley J, Elings V (1994) Tapping mode atomic force microscopy in liquids. Appl Phys Lett 64(13):1738–1740

4. Ajayan PM (1999) Nanotubes from carbon. Chem Rev 99(7):1787–1800
5. Wallace PR (1947) The band theory of graphite. Phys Rev 71:622 (Copyright (C) 2009 The American Physical Society).
6. (a) Saito R, Fujita M, Dresselhaus G, Dresselhaus MS (1992) Electronic structure of graphene tubules based on C60. Phys Rev B 46(3):1804; (b) O'Connell, MJ, Bachilo SM, Huffman CB, Moore VC, Strano MS, Haroz EH, Rialon KL, Boul PJ, Noon WH, Kittrell C, Ma J, Hauge RH, Weisman RB, Smalley RE (2002) Band gap fluorescence from individual single-walled carbon nanotubes. Science 297(5581):593–596
7. Baughman RH, Cui C, Zakhidov AA, Iqbal Z, Barisci JN, Spinks GM, Wallace GG, Mazzoldi A, De Rossi D, Rinzler AG, Jaschinski O, Roth S, Kertesz M (1999) Carbon nanotube actuators. Science 284(5418):1340–1344
8. Zheng M, Diner BA (2004) Solution redox chemistry of carbon nanotubes. J Amer Chem Soc 126(47):15490–15494
9. (a) Kam NWS, Dai HJ (2005) Carbon nanotubes as intracellular protein transporters: generality and biological functionality. J Amer Chem Soc 127:6021–6026; (b) Kam NWS, Liu ZA, Dai HJ (2006) Carbon nanotubes as intracellular transporters for proteins and DNA: an investigation of the uptake mechanism and pathway. Angew Chem Int Ed 45:577–581; (c) Kam NWS, O'Connell M, Wisdom JA, Dai HJ (2005) Carbon nanotubes as multifunctional biological transporters and near-infrared agents for selective cancer cell destruction. Proc Natl Acad Sci USA 102(33):11600–11605; (d) Lin Y, Allard LF, Sun YP (2004) Protein-affinity of single-walled carbon nanotubes in water. J Phys Chem B 108(12):3760–3764; (e) Xu Y, Pehrsson PE, Chen L, Zhao W (2008) Controllable redox reaction of chemically purified dna-single walled carbon nanotube hybrids with hydrogen peroxide. J Amer Chem Soc 130(31):10054–10055
10. Kim C, Choi YS, Lee SM, Park JT, Kim B, Lee YH (2002) The effect of gas adsorption on the field emission mechanism of carbon nanotubes. J Amer Chem Soc 124:9906–9911
11. Lu J, Lai L, Luo G, Zhou J, Qin R, Wang D, Wang L, Mei WN, Li G, Gao Z, Nagase S, Yutaka M, Akasaka T, Yu D (2007) Why semiconducting single-walled carbon nanotubes are separated from their metallic counterparts. Small 3(9):1566–1576
12. Yoon M, Yang S, Wang E, Zhang Z (2007) Charged fullerenes as high-capacity hydrogen storage media. Nano Lett 7(9):2578–2583
13. Zhou B, Guo W, Tang C (2008) Chemisorption of hydrogen molecules on carbon nanotubes: charging effect from first-principles calculations. Nanotech 19(7):75707
14. Luo J, Peng LM, Xue ZQ, Wu JL (2002) Density-functional-theory calculations of charged single-walled carbon nanotubes. Phys Rev B 66(11):115415
15. Zhao J, Balbuena PB (2008) Effect of nanotube length on the aromaticity of single-wall carbon nanotubes. J Phys Chem C 112:3482–3488
16. Chen D, Wang G, Li J (2006) Interfacial bioelectrochemistry: fabrication, properties and applications of functional nanostructured biointerfaces. J Phys Chem C 111(6):2351–2367
17. (a) Gooding JJ, Wibowo R, Liu J, Yang W, Losic D, Orbons S, Mearns FJ, Shapter JG, Hibbert DB (2003) Protein electrochemistry using aligned carbon nanotube arrays. Journal of the American Chemical Society 125(30):9006–9007; (b) Yu X, Chattopadhyay D, Galeska I, Papadimitrakopoulos F, Rusling JF (2003) Peroxidase activity of enzymes bound to the ends of single-wall carbon nanotube forest electrodes. Electrochem Commun 5(5):408–411
18. (a) Wang J, Kawde A-N, Musameh M (2003) Carbon-nanotube-modified glassy carbon electrodes for amplified label-free electrochemical detection of DNA hybridization. Analyst 128:5; (b) Wang Y, Bu Y (2007) Noncovalent interactions between cytosine and SWCNT: curvature dependence of complexes via $\pi \cdot \pi$ stacking and cooperative $CH \cdot \pi/NH \cdot \pi$. J Phys Chem B 111(23):6520–6526; (c) Wang Y (2008) Theoretical evidence for the stronger ability of thymine to disperse SWCNT than cytosine and adenine: self-stacking of DNA bases vs their cross-stacking with SWCNT. J Phys Chem C 112(37):14297–14305; (d) Sun W, Bu Y, Wang Y (2008) Interaction between glycine/glycine radicals and intrinsic/boron-doped (8,0) single-walled carbon nanotubes: a density functional theory study. J Phys Chem B 112(48):15442–15449; (e) Wang Y, Ai H (2009) Theoretical insights into the interaction mechanism between proteins and SWCNTs: adsorptions of tripeptides GXG on SWCNTs. J Phys Chem B 113(28):9620–9627

19. Musameh M, Wang J, Merkoci A, Lin Y (2002) Low-potential stable NADH detection at carbon-nanotube-modified glassy carbon electrodes. Electrochem Commun 4(10):743–746
20. Petersen EJ, Tu X, Dizdaroglu M, Zheng M, Nelson BC (2013) Protective roles of single-wall carbon nanotubes in ultrasonication-induced DNA base damage. Small 9:205–208
21. Johnson ER, Keinan S, Mori-SaÌnchez P, Contreras-GarciÌa J, Cohen AJ, Yang W (2010) Revealing noncovalent interactions. J Am Chem Soc 132(18):6498–6506
22. Perdew JP, Wang Y (1992) Accurate and simple analytic representation of the electron-gas correlation energy. Phys Rev B 45(23):13244
23. (a) Delley B (2000) An all-electron numerical method for solving the local density functional for polyatomic molecules. J Chem Phys 92(1):508–517; (b) Delley B (2000) From molecules to solids with the DMol[sup 3] approach. J Chem Phys 113(18):7756–7764
24. Lim SH, Li R, Ji W, Lin J (2007) Effects of nitrogenation on single-walled carbon nanotubes within density functional theory. Phys Rev B 76(19):195406
25. Buonocore F, Trani F, Ninno D, Matteo AD, Cantele G, Iadonisi G (2008) Ab initio calculations of electron affinity and ionization potential of carbon nanotubes. Nanotechnology 19:25711
26. Zhou Z, Steigerwald M, Hybertsen M, Brus L, Friesner RA (2004) Electronic structure of tubular aromatic molecules derived from the metallic (5,5) armchair single wall carbon nanotube. J Am Chem Soc 126(11):3597–3607
27. Zhao J, Han J, Lu JP (2002) Work functions of pristine and alkali-metal intercalated carbon nanotubes and bundles. Phys Rev B 65:193401
28. Perdew JP, Burke K, Ernzerhof M (1996) Generalized gradient approximation made simple. Phys Rev Lett 77(18):3865
29. Weinert M, Davenport JW (1992) Fractional occupations and density-functional energies and forces. Phys Rev B 45:13709
30. Frisch MJ, Trucks GW, Schlegel HB et al (2009) Gaussian 09, Revision A.02,. Gaussian, Inc., Wallingford CT 2009, Gaussian 09, Revision B.01
31. Zheng G, Witek H, Bobadova-Parvanova P, Irle S, Musaev DG, Prabhakar R, Morokuma K, Lundberg M, Elstner M, Kohler C, Frauenheim T (2007) Parameter calibration of transition-metal elements for the spin-polarized self-consistent-charge density-functional tight-binding (DFTB) method: Sc, Ti, Fe, Co and Ni. J Chem Theory Comput 3:1349–1367
32. Wang H, Ceulemans A (2009) Physisorption of adenine DNA nucleosides on zigzag and armchair single-walled carbon nanotubes: a first-principles study. Phys Rev B 79:195419
33. Matsuda Y, Tahir-Kheli J, Goddard WA I (2010) Definitive band gaps for single-wall carbon nanotubes. J Phys Chem Lett 1:2946–2950
34. Bulusheva LG, Okotrub AV, Romanov DA, Tomanek D (1998) Electronic structure of (n,0) zigzag carbon nanotubes; cluster and crystal approach. J Phys Chem A 102(6):975–981
35. (a) Pan BC, Yang WS, Yang J (2000) Formation energies of topological defects in carbon nanotubes. Phys Rev B 62:12652 (Copyright (C) 2009 The American Physical Society); (b) Lu AJ, Pan BC (2004) Nature of single vacancy in achiral carbon nanotubes. Phys Rev Lett 92(10):105504
36. Nikitin A, Zhang Z, Nilsson A (2009) Energetics of C–H bonds formed at single-walled carbon nanotubes. Nano Lett 9(4):1301–1306
37. (a) Sun G, Kurti J, Kertesz M, Baughman RH (2003) Dimensional changes as a function of charge injection in single-walled carbon nanotubes. J Amer Chem Soc 124(50):15076–15080; (b) Sun G, Kurti J, Kertesz M, Baughman RH (2003) Variations of the geometries and band gaps of single-walled carbon nanotubes and the effect of charge injection. J Phys Chem B 107(29):6924–6931
38. Endo M (2003) Graphite intercalation compounds and applications. Oxford University Press.
39. Brus LE (1983) A simple model for the ionization potential, electron affinity, and aqueous redox potentials of small semiconductor crystallites. J Chem Phys 79
40. Ouyang M, Huang J-L, Cheung CL, Lieber CM (2001) Energy gaps in “Metallic” single-walled carbon nanotubes. Science 292(5517):702–705

41. Blase X, Benedict LX, Shirley EL, Louie SG (1994) Hybridization effects and metallicity in small radius carbon nanotubes. Phys Rev Lett 72:1878 (Copyright (C) 2009 The American Physical Society)
42. Zhao Y, Schultz NE, Truhlar DG (2006) Design of density functionals by combining the method of constraint satisfaction with parametrization for thermochemistry, thermochemical kinetics, and noncovalent interactions. J Chem Theory Comput 2(2):364–382
43. (a) Sun W, Bu Y, Wang Y (2012) Interaction and protection mechanism between Li@C60 and nucleic acid bases (NABs): performance of PM6-DH2 on noncovalent interaction of NABs-Li@C60. J Comput Chem 33(5):490–501; (b) Sun W, Bu Y, Wang Y (2011) On the binding strength sequence for nucleic acid bases and C60 with density functional and dispersion-corrected density functional theories: whether C60 could protect nucleic acid bases from radiation-induced damage. J Phys Chem C 115(8):3220–3228
44. Orlov VM, Smirnov AN, Varshavsky YM (1976) Ionization potentials and electron-donor ability of nucleic acid babes and their analogues. Tetra Lett 17(48):4377–4378
45. Lias SG, Bartmess JE, Liebman JF, Holmes JL, Levin RD, Mallard WG (1988) Gas-phase ion and neutral thermochemistry. J Phys Chem Ref Data 17(supplement 1)
46. Shukla MK, Dubey M, Zakar E, Namburu R, Leszczynski J (2010) Interaction of nucleic acid bases and Watson-Crick base pairs with fullerene: computational study. Chem Phys Lett 493:130–134
47. (a) Belash IT, Bronnikov AD, Zharikov OV, Palnichenko AV (1990) Effect of the metal concentration on the superconducting properties of lithium-, sodium- and potassium-containing graphite intercalation compounds. Synthetic Metals 36(3):283–302; (b) Guha S, Nakamoto K (2005) Electronic structures and spectral properties of endohedral fullerenes. Coordination Chem Rev 249(9–10):1111–1132; (c) Bethune DS, Johnson RD, Salem JR, de Vries MS, Yannoni CS (1993) Atoms in carbon cages: the structure and properties of endohedral fullerenes. Nature 366(6451):123–128
48. (a) Broclawik E, Eilmes A (1998) Density functional study of endohedral complexes M@C_{60} (M = Li, Na, K, Be, Mg, Ca, La, B, Al): electronic properties, ionization potentials, and electron affinities. J Chem Phys 108(9):3498–3503; (b) Chang CM, Jalbout AF (2009) Adsorption of Polar Molecules on Rb/Sr@C_{60}. A theoretical analysis. J Comput Theor Nanosci 6(7):1487–1490; (c) Dunlap BI, Ballester JL, Schmidt PP (1992) Interactions between fullerene (C60) and endohedral alkali atoms. J Phys Chem 96(24):9781–9787
49. Lu T (2010) Multiwfn: a multifunctional wavefunction analyzer. Version 1.5 http://Multiwfn.codeplex.com
50. Humphrey W, Dalke A, Schulten K (1996) VMD: visual molecular dynamics. J Mol Graph 14(1):33–38

Chapter 3
Design and Applications of Nanomaterial-Based and Biomolecule-Based Nanodevices and Nanosensors

Ke Xu, Mohsen Purahmad, Kimber Brenneman, Xenia Meshik, Sidra Farid, Shripriya Poduri, Preeti Pratap, Justin Abell, Yiping Zhao, Barbara Nichols, Eugene Zakar, Michael Stroscio and Mitra Dutta

Abstract This review will highlight recent research underlying the design of novel nanodevices and nanosensors that incorporate graphene, nanodots, nanowires, and biomolecules including DNA aptamers and peptides. The emphasis is on models and theory that guide the design of these nanodevices and nanosensors. In selected cases, research designed to test the usefulness of these designs is highlighted in this chapter.

3.1 Introduction

The design considerations and applications of nanomaterial-based and biomolecule-based nanodevices and nanosensors vary greatly from one specific nanosystem to another. Herein, a selection of such nanodevices and nanosensors are highlighted

M. Stroscio (✉) · K. Xu · M. Purahmad · S. Farid · S. Poduri · M. Dutta
Electrical and Computer Engineering Department, University of Illinois at Chicago (UIC), 851 S. Morgan Street, Chicago IL 60607, USA
e-mail: stroscio@uic.edu; m.stroscio@frontier.com

K. Brenneman · X. Meshik · P. Pratap · M. Stroscio
Bioengineering Department, University of Illinois at Chicago, 851 S. Morgan St., Chicago IL, USA

J. Abell
Nanoscale Science and Engineering Center, Department of Biological and Agricultural Engineering, The University of Georgia, Athens GA, USA

Y. Zhao
Nanoscale Science and Engineering Center, Department of Physics and Astronomy, The University of Georgia, Athens, GA, USA

B. Nichols · E. Zakar
SEDD Directorate, US Army Research Laboratory, Adelphi, MD, USA

M. Stroscio · M. Dutta
Physics Department, University of Illinois at Chicago, 851 S. Morgan Street, Chicago, IL, USA

J. M. Seminario (ed.), *Design and Applications of Nanomaterials for Sensors,* Challenges and Advances in Computational Chemistry and Physics 16,
DOI 10.1007/978-94-017-8848-9_3, © Springer Science+Business Media Dordrecht 2014

and a combination of theoretical considerations and empirical observations are invoked to guide the design on a case-by-case basis. Among the nanosystems considered are: biomolecule-based sensors with active biomolecule elements anchored on graphene-like surfaces; nanowires with strong piezoelectric interactions in the presence of depletion regions; systems with quantum-dots in contact with semiconductor substrates; nanowire polarizers; indirect bandgap semiconductors bound to DNA as a means of realizing light-induced cleaving of DNA; and nanosencors incorporating surface-enhanced Raman scattering. In each case specific design considerations and background materials are discussed.

3.2 Design of Aptamer-Based Sensors with Graphene and Carbon Nanotube Substrates

Herein, the design of aptamer-based sensors with graphene and carbon nanotube substrates is surveyed. In order to design such devices, it is necessary to consider the underlying mechanisms and principles by which these aptamer-based sensors function. Aptamers are short strands of specific oligonucleic acid sequences containing about 30–80 oligonucleotides. Aptamers can recognize specific ligands or analytes and bind to various target molecules ranging from small ions to large proteins with high selectivity and affinity. In 1990 within a short period of time, three groups independently developed in vitro selection and amplification technique for the isolation of specific nucleic acid sequences able to bind to target molecules with high affinity and specificity [1–3]. Both RNA and DNA aptamers are found and selected by a process called SELEX (Selection Evolution of Ligands by Exponential Enrichment) from vast populations of random sequences. Aptamers are sometimes called synthetic antibodies because they have similar properties in a number of applications.

Biosensors are integrated devices capable of detecting the presence of a target by using a particular recognition element and then providing quantitative or semi-quantitative analytical information. Biosensors detect the target analyte by monitoring the mass, optical or electronic signal changes induced by the interaction between the recognition element and the target analyte. When the recognition component of the biosensor is an aptamer it is also called an aptasensor [4]. Aptamer-based biosensors can takes advantage of the high affinity and tunable properties of aptamers. Comparing with antibodies, aptamers have a wide range of advantages such as smaller size, ability to be labeled without affecting affinity, ability to bind with drugs and toxic substance, etc.

3.2.1 Considerations Underlying the Design of Optical Aptamer-Based Biosensor

Fluorescent detection is the most used technique in aptamer-based bio-recognition of optical bioassays. Aptamers can be easily labeled with fluorescent dyes and func-

tionalized with different fluorophores as well as quenchers. Fluorescent detection also has the advantage of inherent capability for real-time detection.

One of the first examples of an optical aptamer-based sensor was discovered by Kleinjung et al. [5] for the detection of L-adenosine. They immobilized a biotinylated RNA aptamer on streptavidin-derivatized optical fibers. The approach made evaluation of the association and dissociation kinetic possible and showed the capability of aptamers for the sub-micron detection of specific analytes. Several other approaches have been developed for converting aptamers into fluorescent signaling probes. A frequently adopted method is aptamer-based molecular beacons. A molecular beacon is a nucleic acids probe that is able to undergo spontaneous conformational change when encountering their complementary nucleic acid targets and translate the conformational change into a change in fluorescent properties. An aptamer-based molecular beacon is a modified version of traditional molecular beacon and usually called aptabeacon [6]. It places an aptamer sequence in a molecular beacon-like hairpin structure, and terminated the ends with a fluorophore and a quencher, respectively. Theoretically, any known aptamer can be engineered into a molecular aptamer beacon by adding a small nucleotide sequence to its 5′-end as well as a small sequence added to its 3′-end [6]. A fluorophore can then be covalently added to the 5′-end, and a quencher can be attached to the 3′-end. In the absence of target ligand, the beacon will form into a stem structure, resulting in the fluorophore and quencher to be close to each other. This time there will be no fluorescence signal because the fluorophore is quenched by energy transfer to the quencher. When the ligand is present, the aptamer will bind to the target ligand and forming a probe. The binding of target is stronger and more stable than the stem and thus it can disrupt the stem, open the structure, separate quencher from the fluorophore and leading to fluorescence signals that is able to be measured quantitively or semi-quantitively [7].

3.2.2 Electrochemical Aptamer-Based Biosensor

Typical electrochemical aptamer-based biosensors operate by reacting the aptamer with an analyte of interest and producing an electrical signal proportional to the analyte concentration. The electrochemical aptamer-based biosensors can be divided into three major types based on the assay format and the method of detection. The first type is sandwich and competition-type assays, in which an electrode-bound aptamer is used to bring a complex composed of the target and some redox-active analytes to the electrode. The second type involves the use of electrochemical impedance spectroscopy to detect targets adsorbed onto an aptamer-terminated electrode surface. And the third type utilizes electrochemistry to monitor binding-related conformational changes in an electrode-bound aptamer.

In a typical beacon format, Xiao et al. [8] reported detection based on a 3-D conformational change with thrombin binding where the aptamer undergoes a structural rearrangement. The conformational change allows thrombin detection with a beacon that does not require a stem-loop. Thrombin is a proteolytic enzyme which

facilitates blood clotting by converting fibrinogen into fibrin, which is also used as a tumor marker in the diagnosis of pulmonary metastasis. The aptamer molecular beacon was constructed [8] by attaching a methylene blue molecule to one end of the aptamer and a thiol group to the other end. The thiol group is used as a linker for its immobilization on a gold electrode surface. Before interaction with thrombin, the aptamer was elastically able to interact with the electrode surface and transferring electrons. However, after interaction occurred, a longer electron-tunneling distance was created, and thus decreasing the signal. A similar aptamer molecular beacon approach was used by the team for the electrochemical detection of platelet-derived growth factor in picomolar levels, and demonstrated this aptamer-based biosensor directly in blood serum [9].

A difficulty with sandwich assays was later removed by Radi et al. [10], who developed "signal-on" architecture rather than the "signal-off" architecture, in which the binding of the target analyte resulted in a decrease in the signal. In this case, the aptamer molecular beacon had a ferrocene label and a shorter spacer. Detection was carried out using cyclic voltammetry, DPV and impedance measurements. In the absence of thrombin the ferrocene label is far from the electrode surface and would not provide any electron transfer to the surface. When thrombin is present, G-quadruplex would form leading to the ferrocene label close enough to the electrode and allowing effective electron transfer as well as signal generation. With the use of DPV a detection limit of 0.5 nM was achieved with a linear range of 5–35 nM. Xiao et al. [11] made similar efforts to modify their previous structure and fabricate "signal-on" electrochemical aptamer sensor. They introduced double-stranded DNA consisted of a short DNA sequence tagged with methylene blue (MB) that can hybridize with an aptamer, and a sequence complementary to it which contained the anti-thrombin aptamer sequence. The duplex of DNA maintained the redox label at "standing" position with a distance from the electrode surface. When thrombin is introduced to the complex, the complementary sequence would displaced and the MB tagged single stranded DNA would approaches the electrode surface and producing electric current due to improvement of electron transfer.

3.2.3 Graphene and Graphene-Based FET Structure

Graphene is a two-dimensional network of single layer sp^2-bonded carbon atoms arranged on a honeycomb lattice. The name graphene is sometimes used to describe multiple layer graphite. Multilayer graphite can have up to ten layers and still be called graphene. It should be noted that the variation in properties of graphene is quite significant when going from one layer to several layers. Ten layers is the limit where graphene becomes graphite, which is stack of graphene sheets bounded by weak van der Waals forces.

The atomic structure of graphene gives rise to exceptional electrical, optical, mechanical and thermal properties [12]. The most interesting electrical properties of graphene are high electron mobility [13] and ballistic transport of charge carriers

[14]. The high mobility is caused primarily by the absence of backscattering due to the pseudo spin nature of the charge carries in graphene similar to the case of the carbon nanotube (CNT) [15]. Weak electron-phonon coupling, high sound velocity, and the near defect-free lattice also contribute to the high mobility and high current density sustainability of graphene. Graphene can sustain high current density up to 5×10^8 A/cm^2, or about 1 uA per atomic row of carbon atoms [16]. Ballistic transport over sub-micron scales is usually associated with high mobility and the quantization of conductance in narrow channels [14]. Also, graphene technology can be easily integrated into the existing planar processing infrastructure, grown on numerous substrates such as silicon dioxide, and processed by conventional semiconductor methods. Due to graphene's unique electronic properties, ultrafast electronic devices with operating frequencies up to THz are expected.

These properties of graphene come from its special bank structure. Graphene is a zero-bandgap semiconductor. In other words, it's both a semiconductor and a semi-metal. Theoretically, Wallace [17] first studied the band structure of graphene and demonstrated its unusual semi-metallic behavior. The lack of a bandgap in intrinsic graphene is a major engineering issue. The zero-bandgap means that graphene is difficult to be switched off (from conductive state to non-conductive state). Graphene nanoribbons or bilayer graphene are good alternatives to circumvent this problem, both of them can have a band gap and being tuned to meet the requirements of a solid state switch. Nevertheless, the zero-bandgap of large area graphene is not an issue in radio frequency (RF) applications.

Applications of graphene include many fields such as graphene thin film electrodes, using graphene as sensing material, graphene-based nanocomposites and graphene-based field-effect transistor (GFET) [18, 19]. A field-effect transistor (FET) is an electronic device normally with three terminals. The conductivity between two of the terminals known as source and drain can be controlled by the electric field created by the third terminal known as gate. Gate voltage can be tuned to modulate the free carrier density in the channel between source and drain, leading to a current change in the channel controlled directly by gate voltage. This shift of current can be used as a switch which indicates an "On" state when the current is in high value and an "Off" state when very low current is in the channel. The semiconductor industry is considering GFET as a possible alternative to replace the silicon field-effect transistor [20]. Carbon nanotubes offer similar electronic properties as graphene and had been considered as a replacement for silicon for years. But the fact that graphene has planar geometry and thus can be processed with more conventional complementary metal oxide semiconductor (CMOS) technology gives it a significant advantage over CNTs. The structure of a GFET is identical to a silicon FET.

Figure 3.1 shows a typical current (I_{SD})/voltage (V_{SD}) characteristics of chemically converted graphene devices. Single layer and bilayer graphene were grown in collaboration with Army Research Laboratory using low pressure chemical vapor deposition (LPCVD) and transferred to Si/SiO_2 substrate. The thickness of graphene was later confirmed with Raman spectroscopy to be consisting of 94% bilayer and 6% single layer graphene. The FET structure is fabricated with chromium

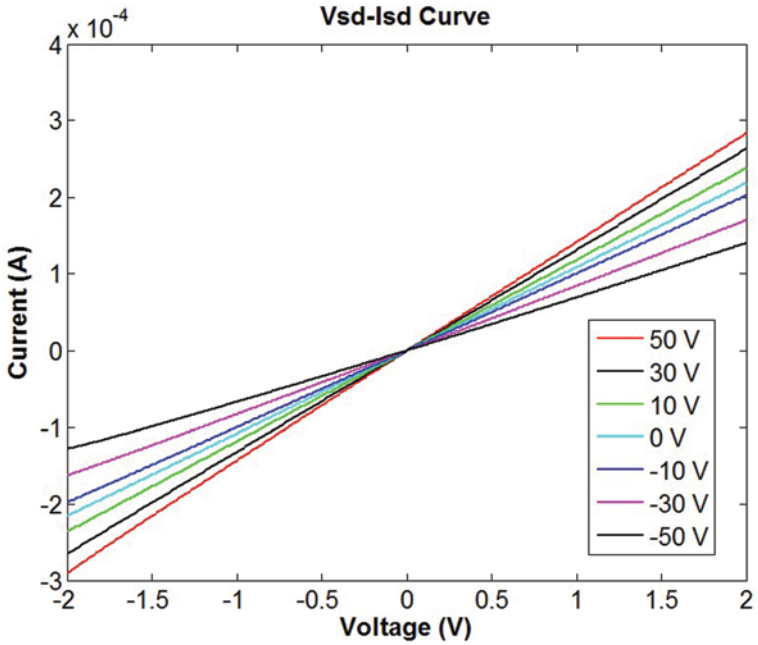


Fig. 3.1 Current voltage characteristic of a graphene-based FET structure

and gold as source and drain electrodes. Current between source and drain can be effectively modulated by gate voltage. When the gate voltage varied from 50 to −50 V, the conductance of the device increased, indicating a p-type semiconductor under ambient conditions.

3.2.4 Aptamer-Based Sensors with Graphene and CNT Substrates

Since the first biosensor with Si nanowire was reported in 2001 [21] and the development of the chemical sensor using carbon nanotubes in 2000 [22], massive research efforts have been initiated in developing nanowire-based or nanotube-based sensors. In the case of carbon nanotubes, all constituent atoms are at the surface and any small change on the surface can lead to a large change in electrical current, which made possible of developing sensors with exceptional sensitivity.

So et al. fabricated a single-walled carbon nanotube (SWNT) field-effect transistor to monitor the binding processes between aptamer and protein [23]. SWNTs behave as p-type semiconductors in ambient atmosphere. The merit of using aptamers in FET-based sensor lies in their small size. Debye length is defined as the typical distance required for screening the surplus charge by the mobile electric

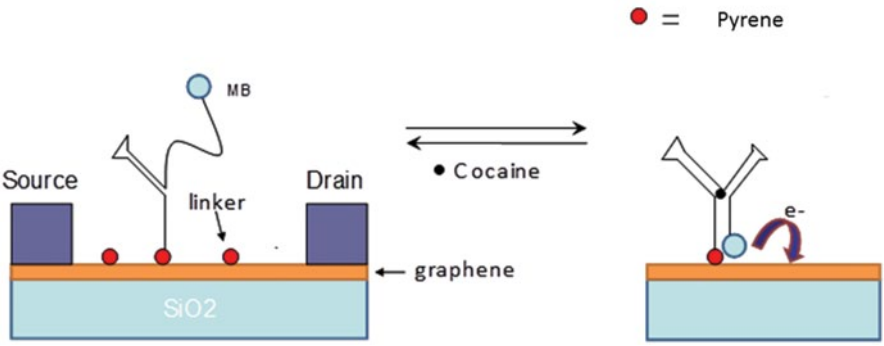


Fig. 3.2 Device schematic of a aptamer-based biosensor with graphene-based FET structure

carrier present in a nanostructure. The size of antibodies is about 10 nm, which is much larger than the Debye length or electrical double layer that is about 3 nm in 10 mM ionic concentration. As a result, the recognition of protein-protein binding process might occur outside the electrical Debye length and left very weak potential changes to be observed on the gate. Aptamers, on the other hand, have an average of 2 nm for 30 bases, which is within the Debye length and can enable the perturbation of gate potential by proteins that link to aptamers. SWNTs were deposited between source and drain electrodes, and anti-thrombin aptamers were attached on the CNTs. The binding of thrombin to the aptamer altered conductance between source and drain, thus enabling detection of the protein.

The applications of SWNTs, however, are often plagued with several problems. For example, it is difficult to separate metallic nanotubes from semiconducting nanotubes. Also, when only a few SWNTs are used, it is challenging to manipulate them for device fabrication because they are too small to interface with large-sized biomolecules. Graphene, with similar properties as SWNT but comes in a flat structure, has many advantage in fabricating sensors.

Figure 3.2 is an example of aptamer-based sensor with graphene FET structure using cocaine as a target. The aptamer is terminated with methylene-blue (MB) which functions as an electron donor. 1-pyrenebutanoic acid, succinimidyl ester (merchandise name: P130) as the red dot in the figure is used as linker molecule to noncovalently bind the aptamer to the graphene surface by the pyrene group in the linker. Due to the overlapping of π-bonds between aromatic side chains, the pyrene group which is highly aromatic in nature could interact strongly with the basal plane of graphite via π-stacking. The cocaine aptamer is about 2-nm in length with 30 bases, which is less than the Debye length. When the target molecule is present, the aptamer will undergo a conformation change and lead to a closer distance between the MB and the graphene surface. When the MB approaches the surface, it can provide excess electrons and cause a shift in the I-V characteristics of the graphene-FET. It is known that electrical contacts to a graphene surface typically exhibit high

resistance. This is possibly due to the weak electron conduction on the interface. The electronic structure and the weak van der Waals binding can cause relatively small matrix elements for electrons to cross the interface. When conduct the device characteristic calculations using a p-type MOSFET model, after the formation of inversion layer the net charge carrier density will reduce due to the external excess charge. We can assume,

$$Q(Net) = Q_p - Q_{ext}, \tag{3.1}$$

where Q_p is the inversion charge and Q_{ext} is the extra electron charge provided by methylene blue. At equilibrium, the inversion layer charge in MOS-C will balances the charge added to the gate when V_G exceeds V_T. Therefore,

$$Q_p = -Q_{gate} \cong -C_o \Delta V_G = -C_o (V_G - V_T). \tag{3.2}$$

The external charge Q_{ext} depends on the concentration of cocaine. More cocaine molecules near the structure will cause more aptamers to make the conformational change, leading to additional electron charge at the surface. Since the current flow in the conducting channel is almost exclusively in one direction (taken to be y direction), and since the diffusion current is usually negligible compared with more numerous carriers at a certain point, the equation can be simplified to

$$J_p = q\mu_p p\varepsilon = -q\mu_p p \frac{d\phi}{d\mathrm{y}}. \tag{3.3}$$

where μ_p is the mobility of holes. The effective mobility may be defined as

$$\overline{\mu_p} = -\frac{q}{Q_{N(y)}} \int_0^{x_c(y)} \mu_p(x,y) p(x,y) dx. \tag{3.4}$$

Integrating I_D over the length of channel gives

$$\int_0^L I_D \, dy = I_D L = -Z \int_0^{-V_D} \overline{\mu_p} Q_p \, d\phi \tag{3.5}$$

$$I_D = -\frac{Z\overline{\mu_p}}{L} \int_0^{-V_D} Q_p \, d\phi. \tag{3.6}$$

where Q_p is the positive charge/cm^2 in the channel. In this model, due to the existence of excess electron charges provided by methylene blue,

$$Q_p(Net) = -C_0 (V_G - V_T - \phi) - Q_{ext}, \tag{3.7}$$

where Q_{ext} is the trapped external charge from MB. From the two equations above, we obtain the $I_D - V_D$ relation as

$$I_D = \frac{Z\overline{\mu_p}C_0}{L}\left[(V_G - V_T)V_D - \frac{V_{D^2}}{2}\right] - \frac{Z\overline{\mu_p}V_D}{L}Q_{ext}. \tag{3.8}$$

Similar structure had also demonstrated by Huang et al. [24] who used large-sized CVD grown graphene films to configure field-effect transistors for real-time biomolecular sensing. Glucose or glutamate molecules were detected by the conductance change of the graphene transistor as the molecules are oxidized by the specific redox enzyme (glucose oxidase or glutamic dehydrogenase) which functions as mediator to attach to the graphene surface. These results from current aptamer-based biosensors with graphene-based structure show exceptional electronic response and the ability to support cell adhesion and growth, which postulates the promising potentials of graphene in nanoelectronic biosensing as well as applications in interfacing with living cells and detecting dynamic bimolecular analytes.

3.3 Design Concepts of Nanoscale Piezoelectric Structures

Recent advancements in portable and lightweight mobile devices, has led to needing alternate power sources instead of conventional batteries. Batteries are not feasible in many applications because of their lifetime, weight, size, safety and for use in remote locations. There are emerging applications such as biomedical drug-delivery implants, implantable medical electronic devices and wireless micro-sensor networks, where conventional batteries are impractical because of the difficulty in replacing the batteries [25–28]. Several energy sources such as solar, thermal and mechanical energy can be used as sources of energy in self-powered devices. However, using the mechanical energy has garnered significant attention in self-powered devices, as such a source is commonly available in small-scale systems. Taking the forms of irregular air flow/vibration, ultrasonic waves, body movement, and hydraulic pressure, mechanical energy is pervasive and accessible from the surrounding environment. From this point of view piezoelectric elements are among the best candidates due to their unique properties such high energy densities and integration potential which make them promising for the design of self-powered small-scale devices [28, 29]. The schematic diagram of a vibration energy harvesting system is shown in Fig. 3.3. The conversion of mechanical energy to electrical energy has been well demonstrated using piezoelectric cantilever-based microelectromechanical (MEMS) devices working at their resonating mode [30]. However, the large unit size, large triggering force and specific high resonance frequency of the traditional cantilever-based energy harvester limit their applicability and adaptability in nanoscale devices and systems. In this domain, one dimensional (1D) nanostructures

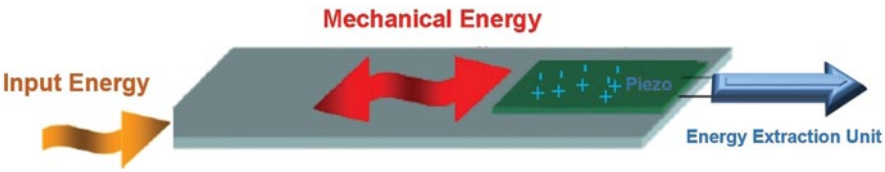


Fig. 3.3 Schematic diagram of a vibration energy harvesting system

have attracted much attention in the fabrication of nanogenerators. Recently, it has been demonstrated that nanogenerators (NGs) based on piezoelectric nanowires (NWs) have the potential to harvest mechanical energy [29]. The first nanoscale energy harvester based on ZnO NWs was introduced by Wang et al. [31]. Among the piezoelectric nanostructures such as lead zirconate titanate (PZT) NWs and Polyvinylidene fluoride (PVDF) nanofibers, the piezoelectric semiconductor nanowires such as ZnO NWs and GaN NWs have been the focus of considerable research.

Because piezoelectric semiconductors can be used to convert mechanical energy to electrical energy and also since they are semiconductors, they can be used as a junction device for performing diode and transistor-type functions. These properties make them strong candidates for use in electromechanically coupled sensors and transducers [31, 32]. However, due to the presence of free carriers in semiconductor piezoelectric materials the physics behind the semiconductor nanogenerators such as ZnO NWs is not well known [33]. Hence, the application of piezoelectric semiconductor nanowires (NWs) requires a good understanding of their electrical and piezoelectric properties. Herein, one of the main concepts for design of ZnO NWs-based nanogenerators (NGs) is addressed.

3.3.1 Fundamentals of Piezoelectricity

The origin of piezoelectricity effect is the displacements of ions in the crystal by an induced strain. This effect is seen for crystal structures with no center of symmetry. Since compound semiconductors such as ZnO usually belong to non-centrosymmetric crystal groups, they are piezoelectric materials. The crystal symmetry of ZnO is responsible for the different components of the internal polarization, spontaneous polarization and piezoelectric polarization. The charge produced by the piezoelectric effect is a bound charge (polarization or dielectric displacement) and the piezoelectric strain equations can be described as follows [33, 34].

$$\begin{aligned} T &= -e.E + c^E : S \\ D &= \varepsilon^S .E + e : S \end{aligned} \tag{3.9}$$

where T is the stress, c is the elastic stiffness constant, e is the polarization constant, E is the electric field, D is the electric displacement, S is the strain and, and ε is the electric permittivity. However, the above equations are valid in the case of an ideal

insulator, in which the density of free carriers is zero or negligible. In this case, the generation of the piezoelectric charge might be considered equivalent to the generation of an electrical field or a potential. Therefore, in the case of a piezoelectric semiconductor, such as ZnO NWs, the piezoelectric constitutive equations cannot be applied directly due to the presence of free carriers [33]. In the non-depleted region of a piezoelectric semiconductor the free carries migrate to the region where piezoelectric polarization appears to maintain the quasi-neutrality. The migration time of free carries is on the order of the dielectric relaxation time. However, in the depletion region of a semiconductor, where the density of free carriers is negligible, the piezoelectric charges may be added to the ionized impurities (donors or acceptors) [35].

3.3.2 *Piezoelectricity Effect in 1D Piezoelectric Semiconductor Nanostructures*

In case of 1D nanostructures such as ZnO NWs where the ratio of surface to volume is high, the surface the adsorbed species such as O_2 molecules undergo chemisorption on the surface of the NW by capturing a free electron from the n-type ZnO result in a surface depletion region [36]. In Fig. 3.4, the schematic representation of a single nanowire and its band bending is depicted, the radius of non-depleted region is r_{elec} and the depletion region width is d. As discussed above, in the depleted region of a piezoelectric semiconductor, the generation of the piezoelectric charge might be considered equivalent to the generation of an electrical field or a potential. Hence, in the surface depletion region of a ZnO NW where the density of free carriers is negligible, the piezoelectric strain equations can be applied. In a detailed study [37], by considering a non-depleted region and a surface depleted region in a ZnO NWs and solving the Poisson equation in radial coordinate system, the effect of induced piezoelectric charges on the surface potential of ZnO NWs have been investigated. The surface depletion width (d) in 1D structure shown in Fig. 3.2 can be described as given [37]:

$$d = r_{phys} - \sqrt{r^2{}_{phys} - \frac{2r_{phys}q^2 D_{it}\psi_0}{\rho\left(1+\frac{r_{phys}q^2 D_{it}}{2\varepsilon_s}\right)}} \tag{3.10}$$

where D_{it} is the interface state density and

$$\rho(r) = q\left[N_v \exp\left(\frac{-E_g}{2KT}\right)\exp\left(\frac{-q}{KT}\psi_r\right) - N_c \exp\left(\frac{-E_g}{2KT}\right)\exp\left(\frac{q}{KT}\psi_r\right) + N_D - N_A\right]$$

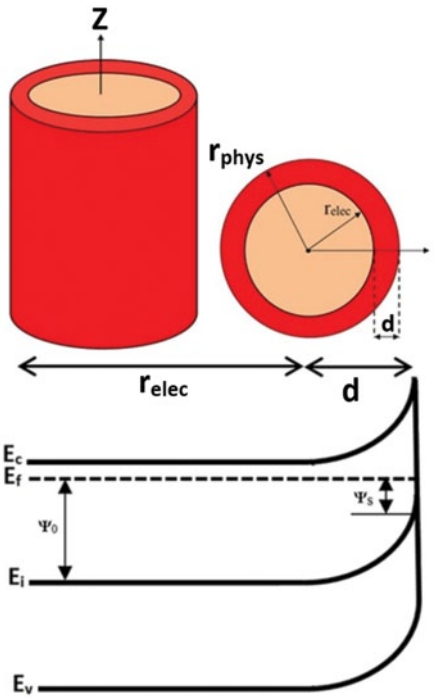


Fig. 3.4 Schematic representation of the nanowire and its band bending

By solving the Poisson equation in a radial coordinate system, the electrostatic potential in surface depleted region can be expressed as shown below [37]:

$$\begin{aligned}
&\psi(r) = \psi_o && 0 \le r \le r_{relec} \\
&\psi(r) = \psi_o - \frac{eN_D}{4\varepsilon}(r^2 - (r_{Phys} - d)^2) \\
&\quad + \frac{eN_D}{2\varepsilon}(r_{Phys} - d)^2 \left(Ln\left(\frac{r}{r_{Phys} - d} \right) \right) && r_{elec} \le r \le r_{phys}
\end{aligned} \tag{3.11}$$

Considering a uniform plane wave propagating with an arbitrary angle in the XZ plane of a wurtzite crystal the radial piezoelectrically induced polarization component can be expressed as follows [38]:

$$\begin{aligned}
p_r = &(e'_{x1}\cos^3\Phi + e'_{x2}\cos\Phi\sin^2\Phi + e'_{y6}\sin\Phi\sin 2\Phi)\frac{\partial u_r}{\partial r} \\
&+ (e'_{x1}\cos\Phi\sin^2\Phi + e'_{x2}\cos^3\Phi - e'_{y6}\sin\Phi\sin 2\Phi)
\end{aligned} \tag{3.12}$$

$$\times\left(\frac{u_r}{r}+\frac{1}{r}\frac{\partial u_r}{\partial \Phi}\right)+e'_{x3}\cos\Phi\frac{\partial u_z}{\partial z}+(e'_{y4}\sin\Phi\cos\Phi-e'_{x5}\cos\Phi\sin\Phi)\left(\frac{\partial u_\Phi}{\partial z}+\frac{1}{r}\frac{\partial u_z}{\partial \Phi}\right)$$
$$+(e'_{y4}\sin^2\Phi+e'_{x5}\cos^2\Phi)\times\left(\frac{\partial u_r}{\partial z}+\frac{\partial u_z}{\partial r}\right)+\left(-e'_{x1}\cos\Phi\frac{\sin 2\Phi}{2}\right.$$
$$\left.+e'_{x2}\cos\Phi\frac{\sin 2\Phi}{2}+e'_{y6}\sin\Phi\cos 2\Phi\right)\times\left(\frac{1}{r}\frac{\partial u_r}{\partial \Phi}+\frac{\partial u_\Phi}{\partial r}-\frac{u_\Phi}{r}\right)$$

where u is the displacement and the piezoelectric stress tensor $\overline{e'}$ is [38],

$$\overline{e'}=\begin{pmatrix} e'_{x1} & e'_{x2} & e'_{x3} & 0 & e'_{x5} & 0 \\ 0 & 0 & 0 & e'_{y4} & 0 & e'_{y6} \\ e'_{z1} & e'_{z2} & e'_{z3} & 0 & e'_{z5} & 0 \end{pmatrix}$$

Since the internal electric field in the surface depletion region of NWs has a radial direction, the radial piezoelectric polarization component (P_r) may result in an increase or decrease of the internal electric field strength. This effect can be modeled by considering an equivalent density of piezoelectric charges as given [37]:

$$N_{PE}=-\frac{1}{q}\left[(e'_{x1}\cos^3\Phi+e'_{x2}\cos\Phi\sin^2\Phi+e'_{y6}\sin\Phi\sin 2\Phi)\frac{\partial^2 u_r}{\partial r^2}\right. \quad (3.13)$$
$$+(e'_{x1}\cos\Phi\sin^2\Phi+e'_{x2}\cos^3\Phi-e'_{y6}\sin\Phi\sin 2\Phi)$$
$$\times\left(-\frac{u_r}{r^2}+\frac{\partial u_r}{\partial r}\frac{1}{r}-\frac{1}{r^2}\frac{\partial u_r}{\partial \Phi}+\frac{1}{r}\frac{\partial^2 u_r}{\partial \Phi\partial r}\right)+e'_{x3}\cos\Phi\frac{\partial^2 u_z}{\partial z\partial r}$$
$$+\left(e'_{y4}\sin\Phi\cos\Phi-e'_{x5}\cos\Phi\sin\Phi\right)\left(\frac{\partial^2 u_\Phi}{\partial z\partial r}-\frac{1}{r^2}\frac{\partial u_z}{\partial \Phi}+\frac{1}{r}\frac{\partial^2 u_z}{\partial \Phi\partial r}\right)$$
$$+\left(e'_{y4}\sin^2\Phi+e'_{x5}\cos^2\Phi\right)\times\left(\frac{\partial^2 u_r}{\partial z\partial r}+\frac{\partial^2 u_z}{\partial r^2}\right)+\left(-e'_{x1}\cos\Phi\frac{\sin 2\Phi}{2}\right.$$
$$\left.+e'_{x2}\cos\Phi\frac{\sin 2\Phi}{2}+e'_{y6}\sin\Phi\cos 2\Phi\right)$$
$$\left.\times\left(-\frac{1}{r^2}\frac{\partial u_r}{\partial \Phi}+\frac{1}{r}\frac{\partial^2 u_r}{\partial \Phi\partial r}+\frac{\partial^2 u_\Phi}{\partial r^2}+\frac{u_\Phi}{r^2}-\frac{\partial u_\Phi}{\partial r}\frac{1}{r}\right)\right]$$

Considering this equivalent charge density which will be added to the ionized impurities (donor or acceptor), the effect of piezoelectric charges in the surface depletion region of a ZnO NW can be illustrated in Fig. 3.5 which presents the surface potential of ZnO NW with a radius 60 nm in the presence of different induced piezoelectric charge densities [37].

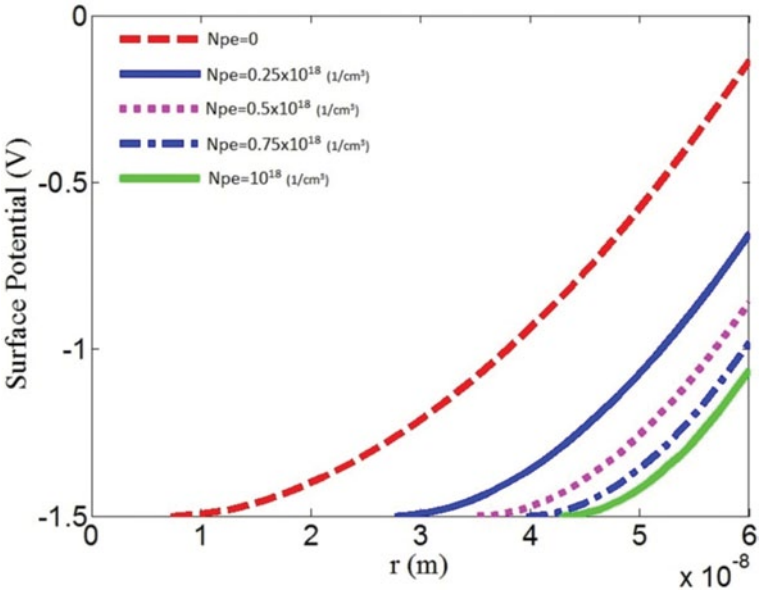


Fig. 3.5 The potential electric distribution in a ZnO NW with radius 60 nm in presence of different piezoelectric charge densities

The effect of induced piezoelectric charges on the surface potential of NWs with different radius is also depicted in Fig. 3.6. As shown the effect of piezoelectric charges on the surface potential of NWs with a smaller radius is stronger. The simulation results indicate using NWs with a small radius may increase the efficacy of NGs [37].

3.4 Design Considerations for Systems with Quantum Dots on Semiconductor Surfaces: Influence, Characterization and Applications

In many nanodevices, quantum dots (QDs) are in close proximity to semiconductor surfaces. As a means of designing such devices, the properties of these quantum-dot–semiconductor structures must be taken into account. Herein, these systems are characterized as an input to the design of nanodevices based on these systems.

Quantum dots (QDs) are nanocrystalline semiconductor materials whose size varies on the order of a few nanometers to a few hundred nanometers. They constitute a class of material having properties between the bulk and the molecular forms of matter (quantum dots) [39] These QDs exhibits discrete size dependent energy levels where electrons are confined with respect to motion in all three dimensions. By tuning the size and the composition of the QDs, light wavelengths from the

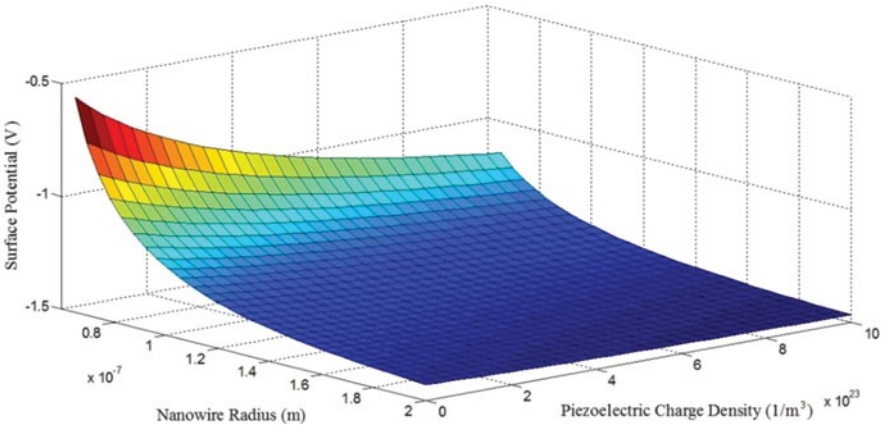


Fig. 3.6 The surface potential of a ZnO NWs with different radii as a function of of piezoelectric charges

ultraviolet to the infrared range can be achieved [40]. The wavelength of emission bands is dependent on the particle size, temperature and its distribution [41]. Because of their unique optical and physical properties, they have variety of applications in, semiconductor lasers [42–44], biomedical imaging [45, 46], optoelectronic devices [47, 48], photovoltaic and solarcells [49].

3.4.1 Core Shell Quantum Dots

Compared to plain core quantum dots (QDs), core/shell QDs offer an enhanced stability and tunability of the optical and electronic properties [50]. These core/shell quantum dots consisting of one material buried in another material with a larger band gap have received much attention due to their ability to improve the photoluminescence quantum yields by passivating surface nonradiative recombination sites [51]. The purpose of the shell material is to passivate surface trap sites and to energetically confine the electron and hole. Compared to the organically passivated dots, these coreshell structures poses higher tolerance to processing conditions that are required for integrating into solid state structures and thus more useful for optoelectronic devices [51]. Some of the examples of core-shell quantum dot structures reported earlier includes CdSe/ZnS [52], ZnSe/CdSe [53], PbSe/CdSe [41], CdS/CdSe [54], ZnS/CdS [55].

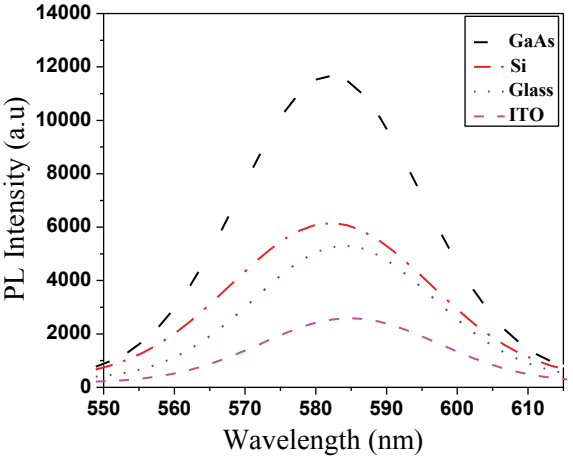


Fig. 3.7 Photoluminescence spectra of CdSe/ZnS quantum dots on GaAs, Si, Glass and ITO substrates

3.4.2 Quantum Dots on Semiconductor Surfaces

Due to the high surface to volume ratio, energy relaxation and recombination dynamics in QDs strongly depend on surface passivation conditions [56]. Not much of the work has been done to investigate the effects of quantum dots on surfaces of different substrates. Also the study of heterojunctions formed between the deposited material and substrate is highly motivated due to their applications in varied fields for example InAs QDs grown on Si substrate with good luminescence will benefit the integration of Si electronics with high-speed, low-power optoelectronic functions and permits the fabrication of large-scale optoelectronic integrated circuits [57].

In case of CdSe/ZnS core/shell QDs the fast initial relaxation dynamics has been usually explained in terms of carrier trapping at the interface (or surface related) defect states. However the origin of these states is not understood yet. Thus the optical as well as the interface state study in CdSe/ZnS core-shell QDs needs to be done and is under investigation.

a- Luminescence properties of Quantum Dots and Zinc Oxide nanowires on Surfaces of Different Substrates For getting an insight on the behavior of QDs deposited on semiconductor surfaces, CdSe/ZnS core/shell QDs is deposited on the surfaces of different substrates such as Gallium Arsenide (GaAs), Silicon (Si), glass and Indium tin oxide (ITO). In order to explore the effects of substrates on the optical properties of these quantum dots, photoluminescence (PL) measurements using a continuous wave He-Cd laser having an excitation wavelength of 325 nm. The room temperature PL spectra of CdSe/ZnS quantum deposited on the GaAs, Si, Glass and ITO coated glass are shown in Fig. 3.7. As it is seen for all the samples, the PL spectra have a peak value at a wavelength of about 582 nm with different PL intensities. Quantum dots deposited on the GaAs have the highest PL intensity and quantum dots on the ITO coated glass shows the lowest intensity [58].

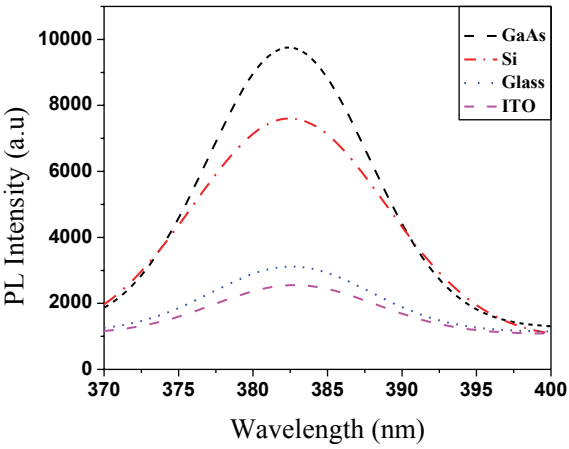


Fig. 3.8 Photoluminescence spectra of ZnO nanowires on different substrate

For more investigation the experiment was repeated by replacing the CdSe/ZnS quantum dots with the as grown ZnO NWs. ZnO nanowires were grown by the vapor liquid solid (VLS) method inside a horizontal quartz tube at atmospheric pressure at a growth temperature of 900–910 °C with a constant flow (350 sccm) of Ar for 30–50 min with a source consisting of zinc oxide powder mixed with graphite in a weight ratio of 1:1 with Au deposited as a catalyst. After the growth process, ZnO NWs were drop casted on the same substrates that were used for analyzing quantum dots surface properties that are GaAs, Si, ITO and glass. Figure 3.8 represent the PL spectra of ZnO NWs on GaAs, Si, ITO and glass.

The experimental results indicates that the PL intensities order for ZnO NWs deposited on substrates are similar to the PL intensities order for CdSe/ZnS quantum dots on the same substrates. This results shows that the degree of PL intensities of both samples, deposited with quantum dots and NWs, is dependent on the type of substrate being used and not on the material being deposited on them [58].

b- Heterojunction effects It has also been shown that the PL intensities order variations are not a function of the contact formed between the deposited material and the substrates. This was investigated by doing analysis at the junctions of the ZnO and ITO, GaAs and glass substrates and drawing energy band profiles for each material as shown in Fig. 3.9.

The comparison of energy barriers at the interface of junctions shows that the energy barrier seen by electrons at the interface of ITO and ZnO is minimum showing a negative energy barrier value, while the energy barrier between glass and ZnO is the highest, which is in contradictory with the experimental results. The heterojunction analysis indicates that the observed PL intensities differences is not a function of the contact formed between the deposited material and the substrates and electron transferring from substrate to the conduction band of ZnO NW cannot be responsible for the observed PL intensity difference.

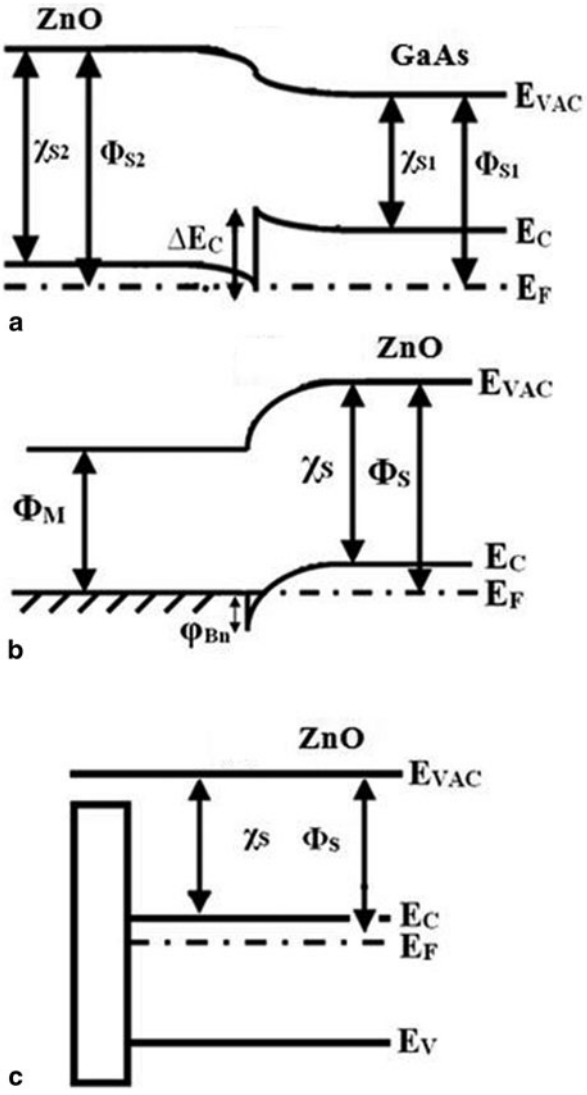


Fig. 3.9 (**a**) Energy band diagram of ZnO-GaAs heterojunction, where φ_{s1} and χ_{s1} be the work function and electron affinity of GaAs and φ_{s2} and χ_{s2} be the work function and electron affinity of ZnO respectively. (**b**) Energy band diagram of ZnO-ITO heterojunction, where χ_s is the electron affinity of ZnO; φ_s be the work function of ZnO and φ_m-work function of ITO. (**c**) Energy band diagram of ZnO-glass heterojunction, where φ_s and χ_s be the work function and electron affinity of ZnO respectively

3.4.3 Biological Applications of Quantum Dots as Mode for Designing Devices

Microcrystalline and nanostructured semiconductors are promising materials for different technological and biological applications such as quantum dots that are rapidly being applied to many emerging and existing technologies. These applications arise from their unique properties, such as tunable emission spectra, high brightness, simultaneous detection of multiple signals and long-term stability. Also the

crystalline quantum dots are useful in biomedical applications because they glow brightly in different colors (depending upon their atomic structure and size) and offer valuable applications in image-guided surgery and light-activated therapies, as well as highly sensitive diagnostic tests. Compared to core type quantum dots, the core-shell type nanoparticles are more desirable for biological applications as the core being passivated by the shell that improves fluorescent properties and prevents leaching [40]. Not only in the bioimaging, these quantum dots are also used in the in solar cell construction, LEDs, and even quantum computing. Some of the major biological applications of these quantum dots are discussed in the following section.

a- Cancer Diagnostic and Therapeutic Applications Bioconjugated QDs can be used to identify potential molecular biomarkers for cancer diagnosis, treatment and prognosis. They may allow the surgeon to map sentinel lymph nodes and perform a complete surgical resection. Their unique optical properties make them ideal donors of fluorescence resonance energy transfer (FRET) and photodynamic therapy studies. Multifunctional QDs have become effective materials for synchronous cancer diagnosis, targeting and treatment [40, 59, 60]. Serum assay is most commonly used for detection of prostate cancer besides other detection probes like protein, specific DNA, mRNA sequences [61] but cancer diagnostic from serum samples only can only be possible through specific biomarker probes for which quantum dots not only serves as biosensitive probes but also used for the detection of thousands of molecules simultaneously [62].

b- Fluorescence probes for cellular proteins Quantum dots have been readily adopted by the bioscience community as fluorescence probes for biomolecular applications because of their unique optical properties, broad absorption, narrow emission spectra, high quantum yields and photostability [63, 64]. These QDs can be used as fluorescence probes for labeling cellular proteins where preservation of enzyme activity is desirable [65]. QDs that were coated with Streptavidin were used to label individual isolated biotinylated F-actin fibers. However, compared with Alexa488 (an organic fluorophore), a smaller proportion of labeled filaments were motile and intracellular labeling of these filaments has also been shown to be possible [66]. QDs have also been used to label mortalin, and p-glycoprotein, molecules that are important in tumor cells [67, 68]. Labeling with QDs was much more photostable than with organic dyes, with a 420-fold increase over the organic fluorophore. Also the photostability and advantageous signal-to-noise ratio achievable with QDs proves that they could be ideal probes for single molecule tracking studies [69].

c- Multiplexed biological detection and imaging Colloidal QDs possess excellent fluorescence properties including high emission quantum yields at room temperature and tunable emission wavelength [70]. Bioconjugated QDs have been used in DNA hybridization [71], immunoassay [72], receptor-mediated endocytosis [71], and time-gated fluorescence imaging of tissue sections [73]. Nanocrystals are also emerging as a new class of fluorescent labels for in vivo cellular imaging. An important advantage is that the extremely high photostability of QDs allows real-time

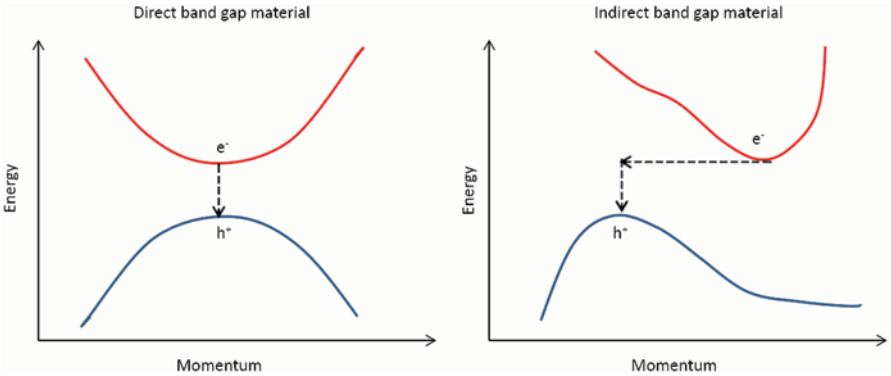


Fig. 3.10 Relative energies and momenta of valence (*blue*) and conduction (*red*) bands in direct band gap (*left*) and indirect band gap (*right*) materials

monitoring or tracking of intracellular processes over long periods of time. Another advantage is the ability to use multicolor nanocrystals to simultaneously image multiple targets inside living cells or on the cell surface. Furthermore, with an inert layer of surface coating, the nanocrystals are believed to be less toxic than organic dyes. Also conjugated luminescent QDs is used to transfer an iron transport protein antibodies that recognize cancer biomarkers, and folic acid (a small vitamin molecule recognized by many cancer cells). In each case, it was found that receptor-mediated endocytosis occurred and the nanocrystals were transported into the cell [74].

3.5 Nanodevices for DNA Cleaving

Herein, design considerations are presented that enable the fabrication of nanodevices that undergo photo-production of electron/hole pairs in indirect bandgap semiconductors; as will be discussed the holes produced in this process can be filled by electrons from an electron-rich DNA molecule bound to the indirect bandgap semiconductor. The physics underlying the design of these nanodevices for cleaving DNA sheds light in important design consideration for the nanodevices.

In semiconductors, recombination can occur if both energy and momentum are conserved.

After the generation of an electron/hole pair, recombination can occur if both energy and momentum are conserved as illustrated in Fig. 3.10. This is easily achieved in a direct band gap material because the electrons and holes possess the same momentum, and the energy difference resulting from the recombination is released in the form of a photon. In an indirect band gap material, however, the electron and hole momenta differ, making it necessary for the electron to participate in a momentum-chasnging process before recombining. Because recombination is less favorable in indirect band gap materials, they are often used to generate current flow.

TiO_2 has an indirect band gap of 3.2 eV [75]. When exposed to light of energy greater than the band gap, electon/hole pairs are formed, which then have the

potential to oxidize surrounding species. If the oxidation potential of the TIO_2/dopamine is more positive than the redox properties of the attached DNA, which is generally the case, the holes are transferred to the DNA from TiO_2 [75, 76]; dopamine is used as a surfactant since it has energy level that facilitate charge transfer as discussed in Ref. 76. This charge transfer was determined to occur via multi-step hopping, where a charge is propelled from one base to the next via thermal fluctuations [77, 78]. Accumulation of holes in one location can results in DNA cleavage. Out of the four DNA nucleosides, guanosine has redox potential most conducive to hole transfer, and, consequently, it was found that guanine (G) undergoes hydroxylation in DNA-TiO_2 complexes after exposure to light [79]. Kanvah et al. studied the cleavage of DNA bound to anthraquinone derivative (AQ) photosynthesizer, which functions similarly to TiO_2 in that it modifies DNA bases to their radical cation form upon exposure to light. It was confirmed that the reaction most frequently occurs at guanine, resulting in its conversion to 8-oxo-7,8-dihydroguanine. In addition, adjacent guanines have a lower relative potential energy than isolated guanines. This means that holes are more likely to accumulate in and cleave at regions of DNA with several adjacent guanines. A correlation also exists between the likelihood of cleavage and distance from the particle where the electron/hole pairs are generated. GG sites closest to AQ react and cleave at a much higher rate than those further away. The hopping model of charge transfer attributes this phenomenon to the rate constant for reversible hopping (k_{hop}) and the rate constant for irreversible trapping (k_{trap}). When $k_{hop} > k_{trap}$, all trapping sites in the sequence have an equal probability of reaction. When $k_{hop} < k_{trap}$, the reaction is more likely to occur closer to the site of initial oxidation. The surrounding bases also influence the reactivity of guanines; it has been shown that adjacent cytoxine (C), thymine (T) and, in the case of RNA, uracil (U), all decrease the reactivity of G [78].

Using this information, one can create a nanocomposite for cleaving DNA [80, 81]. In Paunesku et al., TiO_2 particles 4.5 nm in diameter were created by first synthesizing TiO_2 colloids via dropwise addition of titanium(IV) tetrachloride to cooled water. Oxygen was removed by bubbling with nitrogen, and the particles were suspended in glycidyl isopropyl ether. This provides a coating for TiO_2 and prevents unwanted reactions between hydroxyl groups on the TiO_2 with phosphodiester groups on the DNA oligonucleotides. The nucleotides were synthesized with a carboxyl group on the 5′ end, which was then used to bind to an amine group on a dopamine molecule. When exposed to TiO_2, the dopamine replaces glycidyl isopropyl ether coating the TiO_2 particles, resulting in the binding of TiO_2 to DNA via dopamine. The ratios used were such that there were approximately 50 DNA molecules per TiO_2 particles. The oligonucleotides were then hybridized to complimentary strands to obtain double stranded DNA bound to TIO_2. Vasudev et al. confirmed that binding in achieved by performing Raman spectroscopy measurements on the resulting compounds. The spectra contained characteristic DNA peaks in the 800–1,500 cm^{-1} range, as well as a TiO_2 peak around 190 cm^{-1} ([82], Fig. 3.11).

Paunesku et al. demonstrated that these nanocomposites can be used to cleave DNA at the guanine sites. Gel electrophoresis analysis of the nanocomposites after 0, 8 and 10 min of UV light exposure indicated a higher percentage of cleaved DNA for longer exposure times [80]. UV light also causes cleavage at G-rich sites

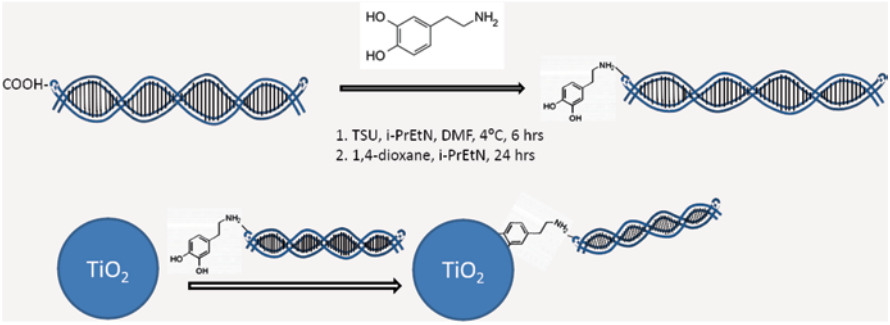


Fig. 3.11 Synthesis of DNA-dopamine-TIO_2 nanocomposites. Diagram not to scale

in TiO_2-DNA composites with three DNA strands that form a T-shaped three-way junction [83, 84].

3.6 SERS Nanosensors

Surface-enhanced Raman spectroscopy can be used to determine the biological composition of a sample by detecting the unique vibrational signature of specific molecules. In order to obtain these vibrational signatures, a nanosensor needs to be designed [85].

An example of a nanosensor is Apt-$\alpha_V\beta_3$ adsorbed to a silver nanorod (AgNR) SERS substrate [86]. Apt-$\alpha_V\beta_3$ is a 85-base long RNA molecule generated for binding to a cellular membrane protein called $\alpha_V\beta_3$ integrin. This integrin normally interacts with the RGDV peptide, a process which is amplified in cancerous cells. By binding to this integrin, Apt-$\alpha_V\beta_3$ blocks the binding site, possibly hindering cancer progression [87]. Obtaining the Raman spectrum of this potentially useful molecule would help in its further studies.

Apt-$\alpha_V\beta_3$ (exact 5′ to 3′ sequence: GGGAGACAAGAAUAAACGCUCAAUUCAACGCUGUGAAGGGCUUAUACGAGCGGAUUACCCUUCGACAGGAGGCUCACAAACAGGC) with an amine modifier at the 5′ end was suspended in water and placed on a patterned multiwall AgNR SERS chip [88] in nitrogen for 24 h. The substrate was then washed, removing the access RNA and leaving only the RNA adsorbed to the nanorods. The SER spectrum obtained with a 514 nm laser contained peaks consistent with previously-published spectra of DNA and RNA bases [85, 89–91]. In addition, the substrate enhanced the signal by as much as 58 times compared to standard microRaman [86], demonstrating the effectiveness of the AgNR substrate in nanosensor design.

3.7 Design of Nanowire Polarizers

Recent progress in the synthesis of semiconductor nanowires has enabled the testing of quantum confinement effects and developing nanodevices based on these materials. However, isolating and manipulating the free-standing tangled nanowires still remains a challenges. Great interest has been shown in research focused on growing nanowires on a substrate in a controlled fashion, so that little or no post-processing device applications. The polarization anisotropy can be explained in terms of the large dielectric difference between these freestanding nanowires and surrounding environment. This property of polarization anisotropy is considered here as it relates to polarization sensitive nanoscale photodetectors that can be useful in integrated photonic circuits, optical switches and interconnects, near-field imaging, and high resolution detectors [92].

Before considering the theory underlying the design of such nanowire polarizers, it is instructive to consider relevant details of the fabrication process. In order to achieve free standing nanowires, large periodic arrays of semiconductor nanoporous structure needs to be fabricated that will allow (i) the size and composition to be varied, (ii) flexibility to use a variety of substrate materials, and (iii) compatibility with various fabrication processes. Porous alumina templates have the best attributes for growing uniform pores of nanowires or nanotubes due to their high aspect ratio. They are durable and can withstand high temperatures (up to 800 or 1,000 °C) [94, 97]. The length and diameter of the pores can also be controlled by changing the experimental conditions [93–97].

Advantages of using an insulating alumina matrix is that it allows us to (i) easy to perform annealing treatments without losing nanocrystallinity, and (ii) study a single nanoscale heterojunction inside the pores. With such a template we have (i) uniform regular distribution of nanopores of the order of a few nanometers, (ii) arrangement of vertically directed pores with high aspect ratio, (iii) ability to control diameter of cells and pores by changing electrolyte composition and electrochemical processing parameters, and (iv) high reproducibility of the film structure.

Confinement of materials like CdS nanowires inside these templates have a unique advantage of increased band gap energy due to quantum confinement. Thus making nano-structured CdS a better window material than bulk CdS [98]. Hence, the alumina matrix is the best template for growing free standing nanowires and the alumina template can be dissolved leaving behind only the nanowires.

3.7.1 Theoretical Model

The polarization anisotropy in PL measurements between the free standing nanowires and its surrounding environment can be modeled by treating the nanowire as an infinite dielectric cylinder in a vacuum, since the wavelength of the exciting light is much greater than the wire diameter. When the incident field is polarized parallel to the cylinder, the electric field inside the cylinder is not reduced. But when polarized perpendicular to the cylinder, the electric field amplitude is attenuated according to

$$E_i = \frac{2\varepsilon_0}{\varepsilon + \varepsilon_0} E_e \tag{3.14}$$

where E_i is the electric field inside the cylinder, E_e the excitation field, and ε_0 is the dielectric constant of the cylinder (vacuum) (100) and ε is the dielectric constant of the surrounding material. For $\varepsilon > \varepsilon_0$, the probability of optical transitions in a nanowire depend on light polarization, acquiring maximal values for light with polarization parallel to the nanowire axis whereas illuminating with unpolarized light creates a high frequency electric field in the nanowire in the direction of polarization parallel to the nanowire axis. These polarizations exhibit a strong dependence on the absorption coefficient, *k*, both inter- and intraband, on the light polarization for a system of parallel wires. The ratio of absorption coefficient, *k*, for the two light polarizations is given by the Eq. (3.15)

$$\frac{k \parallel}{k \perp} = \left(\frac{\varepsilon + \varepsilon_0}{2\,\varepsilon_0} \right)^2 \tag{3.15}$$

This absorption coefficient, k, ratio is more than 30 for free standing nanowires having air with $\varepsilon_0 = 1$ otherwise, it is 4.7 for nanowires in an Al_2O_3 matrix which has $\varepsilon_0 = 3$ [100]. Due to the dielectric constant difference between the nanowires and their surrounding, huge polarization anisotropy is manifested in photoluminescence (PL) measurements. The PL spectra [101] can be recorded from a number of individual wires as a function of excitation or emission polarization [1]. On average, the excitation and emission polarization ratio is given by equation:

$$\rho = \frac{I \parallel - I \perp}{I \parallel + I \perp} \tag{3.16}$$

with the intensities parallel $(I_\parallel)$ and perpendicular $(I_\perp)$ to the wire being measurable with PL measurements at different angles of orientation.

Polarization anisotropy in quantum wires is caused by the mixing of valence bands due to quantum confinement. This quantum mechanical effect results in smaller polarization ratios ($\rho < 0.60$) which are reported [102–104]. The large polarization response is due primarily to the large dielectric contrast between the nanowire and its air or vacuum surroundings. With the increasing excitation power density, the photoconductance (PC) of nanowires is increased in a reproducible and reversible manner with respect to the excitation power. The photoconductive response results from direct carrier collection at the nanowire–metal contact interface versus population of surface traps. The photoconductivity anisotropy ratio is given by the following equation:

$$G = \frac{G_\parallel - G_\perp}{G_\parallel + G_\perp} \tag{3.17}$$

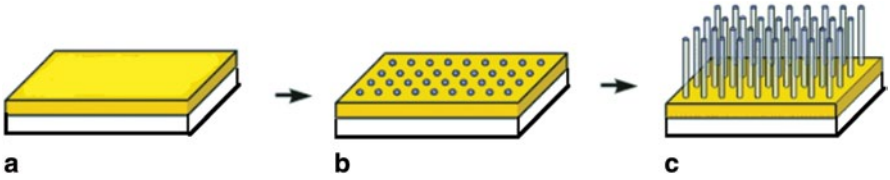


Fig. 3.12 Flowchart for the fabrication of CdS nanowires **a** 200 nm of Aluminum layer (*yellow*) deposited on ITO coated glass substrate. **b** After anodization of Al layer leading to formation of nanopores of 40–100 nm. **c** CdS nanowire array after the DC electrodeposition growth

where $G_{\parallel}$ and $G_{\perp}$ are the conductances with parallel and perpendicular excitations respectively. To summarize the nanowire is modeled as an infinite dielectric cylinder in a vacuum with the light polarizations causing the electric fields. The electric field intensities calculated from Maxwell's equations imply that the field is strongly attenuated inside the nanowire for the perpendicular polarization, $E_{\perp}$ whereas the field inside the nanowire is unaffected for the parallel polarization, $E_{\parallel}$.

3.7.2 Implementation of Design Concepts

Nanopores were produced in Anodized Aluminium Oxide (AAO) nanoporous template layer coated on ITO-coated (indium tin oxide-coated) glass using a two step anodization process in 0.3 M oxalic acid solution. The procedure for fabricating anodized aluminum oxide consists of an electro chemical cell with the aluminum substrate as anode, platinum plate (1″ × 1″) as cathode at 5 °C. The anodized substrate is then rinsed with DI water and dried in nitrogen. The grown AAO layer has pores of 40–60 nm but it also grows with a barrier layer of oxide at the interface of the Al and Al_2O_3 which can be removed by dipping the substrate in 50 % phosphoric acid (H_3PO_4) for 2–4 min.However, due to poor adhesivity of Al layer to the ITO/glass substrate, a thin layer of titanium (Ti) or titanium dioxide (TiO_2) is deposited prior to anodization. CdS nanowires are grown by DC electrodeposition. The electrolyte for CdS deposition is 0.055 M $CdCl_2$ and 0.19 M elemental sulfur, dissolved in 50 ml dimethyl sulfoxide (DMSO) at 120 °C with a constant current density supply of 7.5 mA cm^{-2} for 7 s. The estimated growth rate was 30 nm s^{-1}. The flowchart for the electrodeposition is given below in Fig. 3.12:

The bottleneck lies in growing the cadmium sulphide (CdS) nanowires in a reproducible fashion. The non uniform thickness of the aluminum oxide barrier layer leads to these problems which include: template cracking at the electrolyte/air interface during anodization, low filling ratio of nanorods/nanowires, and large variance in the length of nanorods/nanowires [105].

After the growth of CdS nanowires, the alumina matrix is usually dissolved in 1 M sodium hydroxide solution leaving behind the free standing nanowires.

For these designs, the PL and PC polarization anisotropy is expected to be nearly wavelength-independent for energies larger than the nanowire band gap. For these designs it is possible to realize devices that simultaneously measure intensity and polarization and use them as optical photodetectors [106–108]. The ability

synthesize nanowires out of any group IV, III–V, or II–VI semiconductor material like InP, CdS, GaN, etc. facilitates the creation of a wide range of detectors and high-resolution detector arrays for different spectral regimes.

3.7.3 Sensing Elements on Graphene-Based and Carbon-Nanotube-Based Substrates

The design of biosensors with molecular sensing elements on graphene-based and carbon-nanotube-based substrates is sensitive to the nature of the bond between the molecular sensing element and the substrate. In particular, it is important that the binding be accomplished in a manner so as to leave the transport properties of the carbon-based substrate unaffected. Non-covalent functionalization may be accomplished effectively, as it does not create atomic scale defects, which are disruptive. Herein, the functionalization of carbon nanotubes and graphene using peptides is considered in the context of designing these nanobiosensors.

3.7.4 Peptides that Bind to Graphene

Kim et al. [109] presented findings on the preferential binding of peptides to the graphene edges and planes. The peptides EPLQLKM and HSSYWYAFNNKT have been found to preferentially bind to graphene edges and surfaces, respectively. This critically helps in defining the electronic and mechanical properties of graphene and is attributed to the π- π interactions. EPLQLKM interacts with the positively-charged hydrogen-terminated edge of the graphene through the negatively-charged glutamate residue, E, while the graphene plane binding peptide does so through π-π stacking [110] of the aromatic rings of the H-Y-W-Y-F residue [111].

Lu et al. [112] have used pyrene moiety (1-pyrenebutyric acid) attached to N-terminus of peptides to bind to graphene oxide layer to monitor protein-peptide interactions. Peptides used are pyrene-GGGRKRIHIGPGPAFYTT and pyrene-GGGNSWGCAFRQVC. Pyrene-based fluorophores re-emit light upon excitation and the number of times a specific event occurs per photon adsorbed is very high, hence making it a good choice for an optical contrast agent in molecular beacons [113, 114]. Also, pyrene reacts noncovalently with carbon nanotubes and graphene due to π bonds present [115]. Due to the proximity of graphene oxide layer to pyrene, the fluorescence of pyrene is quenched but owing to the adhesive properties of pyrene [112], when the peptide binds to the protein, there is competition between pyrene and target-protein for the graphene oxide layer, leading to desorption and dequenching of pyrene, which aids in detecting target protein.

Self-assembling peptide sequences are made use of by So et al. [116] to bind to graphene surfaces. Among the biocombinatorially selected sequences, one of the peptides—IMVTESSDYSSY, designated as wild type is used. Using AFM, the capability of the peptide to form highly ordered structures over graphite was

determined and a high level of symmetric formation observed. This is likely due to the molecular recognition of the hexagonal structure of the graphite. A very high correlation was observed between the sequence of the peptide and the formation of the self-assembled structures. Also, the process of formation of a peptide over graphene involves a transition between the amorphous state to an orderly state and further analysis has shown that the aromatic, hydrophilic and hydrophobic domains of a peptide correspond to the binding ability, diffusion and the self-assembly of the peptides [116].

Katoch et al. [117] have made use of the peptide GAMHLPWHMGTL, previously known to bind to graphene [118] to observe its structure on binding. It has been observed that the peptide formed a helical structure on binding with the graphene surface and the structure was much different than that of an α-helical structure. Further, Raman spectra were analyzed to determine if incubation of the peptide had any effect on the binding but no significant difference was observed. Also, it has been shown that tryptophan is an essential amino acid required for binding to graphene [117].

3.7.5 Peptides that Bind to Carbon Nanotubes

Wang et al. [119] have used phage display technique [119] to determine one of the possible sequences of peptide that can be used to bind to carbon nanotubes. In this method, the bacteriophage is infused exteriorly with different peptide sequences and suspended in a detergent solution, in the presence of nanotubes. This mixture is then incubated for about an hour at room temperature which was then followed by centrifugation. This resulted in the elution of bound phage particles. The binding was stronger when the number of plaque forming units (PFU), a measure of binding phage concentration, was higher. To further establish the binding, phage clones were loaded onto microspheres and incubates with SWNTs. The specific peptide sequences were determined by using a single crystal graphite and one such sequence is WPHHPHAAHTIR. Also, the middle region of the peptide sequence seem to be reacting more with the nano tube than the ends and W and H seem to play an important role in stronger binding [119].

Dieckmann et al. [120] has developed reversible cyclic peptides, based on the cyclic peptides synthesized by Ghadiri and co-workers [13]. These RCPs have alternating L and D chiralities, have the ability to adopt a planar formation due to all the side chains pointing radially outward, leaving the middle open, where the SWNT is infused. The presence of open cysteine bonds instead of being introduced into the backbone, makes it easier to synthesize as well as helps in closing of the peptide, by wrapping itself around the carbon nano tube of appropriate diameter. This also prevents aggregation of CNTs in solution due to hydrophobicity [120].

Wang et al. [122] used fluorescent-labeled p21WAF-1 (cyclin-dependent kinase inhibitor 1) derived CBM peptide probe, FITC-HAKRRLIF to bind to graphene oxide, synthesized by a modified Hummers method [123] and carbon nanotubes. The

interaction between the phenylalanine residue present at the end of the peptide and the α-bond shows binding between the amino acid residues and graphene, further demonstrated by the steady increasing curve of graphene in the Stern-Volmer plot [124]. This setup is used to detect Cyclin A_2, an important indicator of early-stage cancer by the process of quenching of the peptide by Graphene oxide and detection is possible at the nano scale, 10 fold better than SWNTs and 1200 fold better than the Tb^{3+} chelating macrocycle [122].

Pantarotto et al. [125] makes use of peptides binding to CNTs to devise vaccines. Fragment condensation or chemical ligation is employed in this process. While the former method involves coupling of peptide fragments and has the disadvantages of racemization and the presence of excess concentration of the coupling fragment, the latter operates through a chemoselective reaction of deprotected peptides to give rise to a unique reaction product that binds to the CNT. A pentapeptide is used in fragment condensation while a peptide isolated from a Foot and Mouth disease virus is used in chemical ligation. As confirmed by ELISA and surface plasmon resonance test, the FMDV peptide retained its antigenic properties. Characterization of the peptide bound was performed by TEM and NMR spectroscopy. Thus, this paper discusses that the peptide isolated from the FMDV virus induces an immune response that can be made use of by making vaccines [125].

Huan et al. [126] make use of a Multi Walled Carbon Nanotube with a sensing layer of polyalinine, a polymer with high electrical conductivity, to bind to a peptide sequence of HKHAHNYRLPASGGKK, a peptide sensitive to Antharax protective antigen (PA) [127]. Detection was possible at concentrations as low as 0.4 pM. The polyalanine was formed on glassy carbon electrode using cyclic voltammetry while the MWCNT is modified to have a COCl group by suspending in HNO_3 and $SOCl_2$. This COCl group helps in binding with the peptide by forming a CON bond, releasing HCl. Square wave voltammograms (SWVs) of peptide immobilized MWCNT-PANI with different concentrations of PA ranging from 20–100 pM were collected. The sensitivity, correlation coefficient, sensing area and limit of detection were measured for every different concentration using regression analysis, selectivity was measured by observing the SWVs of a mixture of Bovine Serum Albumin (BSA) and PA and the longevity of the sensor was measured over a span of 6 days, with a signal drop of 60 % on the sixth day. High sensitivity and electrochemical signal of this sensor shows good promise in devising similar sensors for a wide range of diseases by using peptides that bind to disease-specific markers.

Mirzaei et al. [128] demonstrated that peptides that bind to carbon nanotubes have specific configurations and preferences, based on various parameters obtained from Density Functional Theory (DFT) calculations. Different models of (5,0) zigzag CNTs functionalized with a $(Me)_2CONH$ peptide through the tip or sidewall were assessed. The most favorable structure, determined from binding energy values was observed when the nitrogen of the peptide group attached to the tip of the CNT while the bonding environment of the carbonyl carbon was kept unaltered. Another parameter, the quadrupole coupling constant (C_Q), was evaluated at the

oxygen and nitrogen sites of the peptide bond and significant decrease in their values was observed when compared with their original values which possibly suggests that electrons are shared between these atoms and the CNTs, critical for the bridging property of the peptide with other molecules.

3.8 Design Considerations for SERS-based Nanosensors for Biomolecules

The use of surface-enhanced Raman scattering (SERS) in the design of nanosensors present unique features in terms of designing the nanosensors for optimum performance. Herein, the basic properties of such SERS-based nanosensors are considered as the basis for optimizing the design of these nanosensors.

Surface-enhanced Raman scattering (SERS) is a phenomenon used to enhance the signal produced by Raman scattering. Raman spectroscopy is a useful tool for sensor development with potential for remote sensing. Raman spectra provide information on the vibrational modes or phonons, between and within molecules. Therefore, you can produce a unique spectral fingerprint for single molecules. SERS is accomplished through the use of substrates with nanometer scale geometries made of metals with many free electrons, such as silver, gold, or copper. Silver is the best choice for frequencies in the visible range and has the lowest damping rate when compared to Au, Cu, and Al [129]. These metals produce surface plasmons, which are oscillating electrons, when excited with a laser. The predominant theory on why SERS causes large enhancements of Raman signals is mainly explained by the electromagnetic properties of nanostructures [130]. The strong localized surface plasmons produced on the surface of the metal by laser excitation enhance the Raman scattering of the molecule near the metal surface. This enhancement is important because Raman cross sections are between 10^{-31} and 10^{-29} cm^2/molecule, compared to fluorescence cross sections which are up to 10^{-16} cm^2/molecule. Furthermore, the Raman signal is proportional to the Raman cross section, the excitation laser intensity, and the number of molecules in the field of detection. Therefore, by enhancing the signal via SERS, fewer molecules are required for a sufficient signal to be produced.

From Pre-lim: Progress in the use of SERS is illustrated by the fabrication of SERS substrates using silver [131–133]. Moreover, SERS has been considered as a possible basis for chemical and biological nanosensors [134]. Furthermore, the fundamental role played by plasmons in the SERS process has been considered by a number of authors including Ref. [135]. Techniques for enhancing Raman signals through substrate fabrication include: (a) nanosphere lithography to produce a silver film over nanospheres (AgFON)(Van Duyne ref and milana's paper) [136], (b) silver nanorod (AgNR) arrays fabricated with the Oblique Angle Deposition (OAD) technique at University of Georgia—Athens [131] and used to detect trace levels of viruses by Shanmukh et al. 2006 [137], (c) optical antennas

[138], (d) metal doped sol-gels [139], and (e) gold core with silver shell nanoparticles [140, 141].

AgNR arrays produce enhancement factors of 10^8 without the formation of "hot-spots" [131] Chen et al. showed how an array of silver nanoparticles or AgFON, has much greater enhancement where defects occur in the array (10^8 compared with 10^4), but these spaces only account for 0.3 % of the excited area [136]. The more homogenous surface of the AgNR substrate in terms of enhancement, allows for a more reproducible substrate to be fabricated. Oblique angle deposition is a physical method using a modified E-beam evaporation system. The substrate was created by first applying a titanium adhesion layer, followed by a 200 nm Ag-film base layer onto a glass slide. In order to form silver nanorods, the substrate was positioned such that it formed an oblique angle (4°) relative to the incident vapor. This caused the surface normal of the substrate to be almost parallel with the incident vapor direction. While in this arrangement 2,000 nm of Ag was deposited to produce the nanorod array. This process allows for the length and diameter of the nanorods to be controlled, which in turn means the aspect ratio of the nanorods is controlled. A higher aspect ratio will produce a stronger enhancement effect [131, 142]. The enhancement factor is also influenced by the lateral arrangement of the nanorods. The more overlap there was between nanorods, the greater the SERS signal [131, 142, 143]. This distance dependent effect, due to the coupling of surface plasmons between nearest-neighbor nanorods, has also been shown with Ag nanoparticles by Schatz et al. [144].

Brenneman et al. used the AgNR array substrates for the detection of single stranded DNA sequences with a Renishaw microRaman system with an Ar^+-ion laser (514.5 nm wavelength) [145]. Figure 3.13 shows the spectrum obtained for a sequence of 15 thymine bases. A solution of the DNA was applied to the substrate and allowed to incubate overnight to allow adsorption of the target to the nanorods. The substrate was then rinsed with Milli-Q water to leave only a monolayer for analysis. This spectrum illustrates modes that are characteristic of thymine oligonucelotides, including multiple ring breathing modes at 610, 788, 1,007, and 1,230 cm^{-1} [146]. The sharp peak at 1,293 cm^{-1} was attributed to ring distortion and anti-symmetric bending of N3-H and C6-H [147]. A vibration form the sugar-phosphate backbone was also identified at 1,184 cm^{-1}. In addition to the detection of thymine, the vibrational modes also provide information regarding the adsorption of the molecule to the substrate. The presence of a line for stretching of the single bond C2-O (1,331 cm^{-1}) coupled with the absence of a line for the double bond C2=O indicates that thymine is adsorbing to the nanorods through that atom.

A second sequence, known as the thrombin binding aptamer (TBA), was also evaluated using the AgNR SERS substrate. The TBA contains thymine and guanine bases and the SERS fingerprint is below in Fig. 3.14. There are several peaks attributed to guanine that are not scene in the poly-thymine spectrum. The TBA sample has a sharp peak at 805 cm^{-1}, which has been shown to be a SERS mode for guanine [89]. The SERS spectra collected for these two different sequences using AgNR arrays demonstrate how a spectral fingerprint can be used to distinguish between samples. It could also identify or detect targets with known SERS signatures.

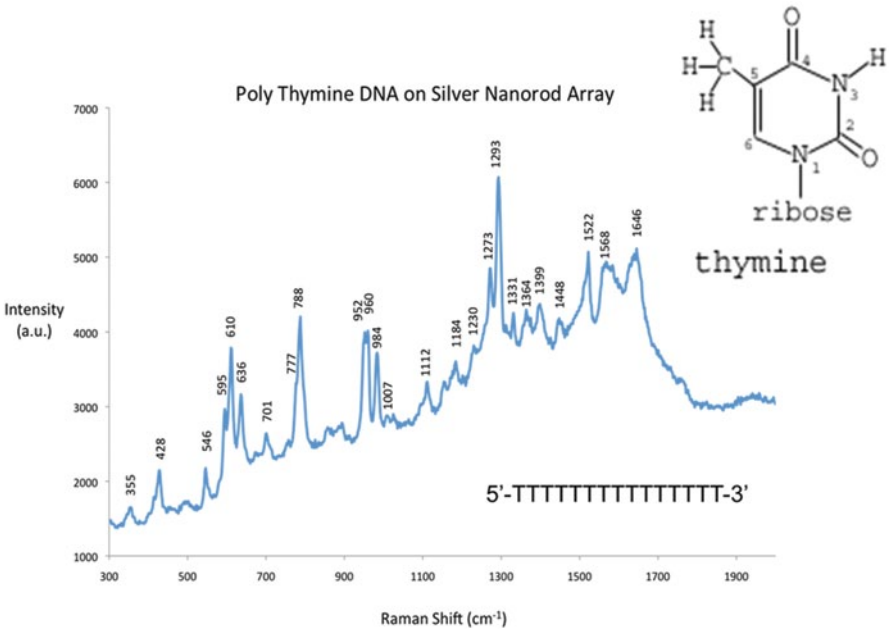


Fig. 3.13 SERS spectrum of single stranded poly-thymine oligonucleotides on AgNR array. *Upper left* is thymine and the ribose sugar and phosphate group, which comprise the DNA backbone

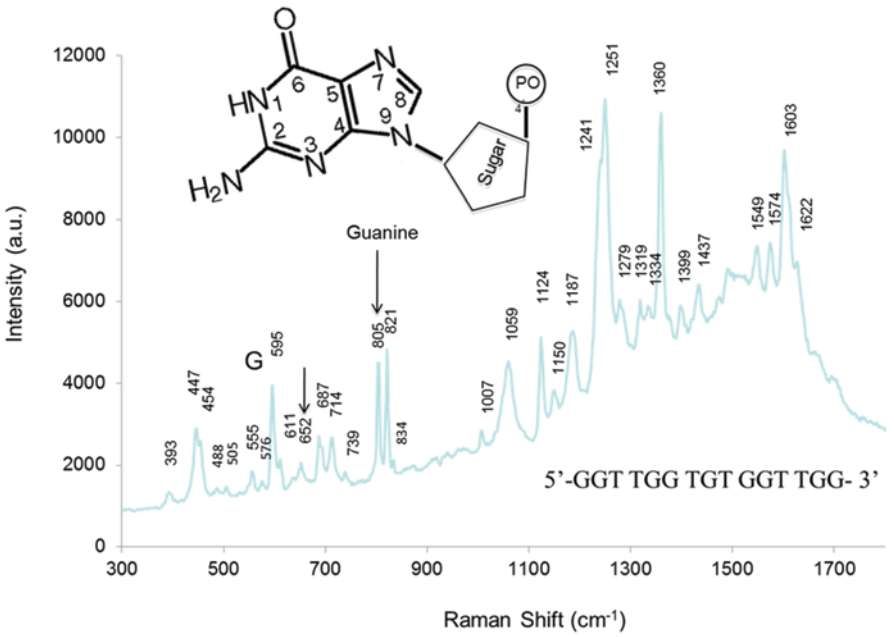


Fig. 3.14 SERS spectrum of DNA sequence TBA. *Upper left* is the base guanine. *Arrows* indicate peaks associated with the base guanine

Biosensing can be accomplished using Raman spectroscopy through the use of SERS substrates like the AgNR arrays fabricated with the oblique angle deposition technique discussed above. Moreover, it can be done using very low sample concentrations, which is useful in biomedical applications where samples can be expensive as well as in detecting harmful toxins.

References

1. Robertson DL, Joyce GF (1990) Nature 344:467–468
2. Tuerk C, Lold G (1990) Science 249:505–510
3. Ellington AD, Szostak JW (1990) Nature 346:818–822
4. O'Sullivan CK (2002) Anal Bioanal Chem 372:44–48
5. Kleinjung F, Klussmann S, Erdmann VA, Scheller FW, Furste JP, Bier FF (1998) Anal Chem 70:328–331
6. Yamamoto R, Baba T, Kumar PK (2000) Genes Cells 5:389–396
7. Fang X, Sen A, Vicens M, Tan W (2003) ChemBioChem 4:829–834
8. Xiao Y, Lubin A, Heeger A, Plaxco K (2005) Angew Chem Int Ed Engl 44:5456–5459
9. Lai R, Plaxco K, Hegger A (2007) Anal Chem 79:229–233
10. Radi AE, Acero Sánchez JL, Baldrich E, O'Sullivan CK (2006) J Am Chem Soc 128:117–124
11. Xiao Y, Piorek BD, Plaxco KW, Heeger AJ (2005) J Am Chem Soc 127:17990–17991
12. Geim AK, Novoselov KS (2007) Nat Mater 6:183–191
13. Chen JH, Jang C, Xiao S, Ishigami M, Fuhrer MS (2008) Nat Nano 3:206–209
14. Peres NMR, Castro Neto AH, Guinea F (2006) Phys Rev B 73:195411
15. Ando T, Nakanishi T, Saito R (1998) J Phy Soc Jap 67:2857–2862
16. Standley B, Bao W, Zhang H, Bruck J, Lau CN, Bockrath M (2008) Nano Lett 8:3345–3349
17. Wallace PR (1947) Phys Rev 71:622
18. Xu K, Erricolo D, Dutta M, Stroscio M (2012) Superlattice Microstruct 51:606–612
19. Xu K, Qian J, Shukla P, Dutta M, Stroscio MA (2012) 15th International Workshop on Computational Electronics(IWCE). doi:10.1109/IWCE.2012.6242868
20. Bourianoff G, Brillouet M, Cavin RK, Hiramoto T, Hutchby JA, Ionescu AM, Uchida K (2010) IEEE Proc 98:1986–92
21. Cui Y, Wei Q, Park H, Lieber CM (2001) Science 293:1289–1292
22. Kong J, Franklin NR, Zhou C, Chapline MG, Peng S, Cho K, Dai H (2000) Science 287:622–625
23. So HM, Won K, Kim YH, Kim BK, Ryu BH, Na PS, Kim H, Lee JO (2005) J Am Chem Soc 127:11906
24. Huang Y, Dong X, Shi Y, Li CM, Li L, Chen P (2010) Nanoscale 2:1485–1488
25. La Van DA, McGuire T, Langer R (2003) Small-scale systems for in vivo drug delivery. Nat Biotechnol 21(10):1184–1191
26. Calhoun B, Daly D, Verma N, Finchelstein D, Wentzloff D, Wang A, Cho S-H, Chandrakasan A (2005) Design considerations for ultra-low energy wireless microsensor nodes. IEEE Trans Comput 54(6):727–740
27. Flatscher M, Dielacher M, Herndl T, Lentsch T, Matischek R, Prainsack J, Pribyl W, Theuss H, Weber W (2010) A bulk acoustic wave (BAW) based transceiver for an in-tire-pressure monitoring sensor node. IEEE J Solid-State Circuits 45(1):167–177
28. Guyomar D, Lallart M (2011) Recent progress in piezoelectric conversion and energy harvesting using nonlinear electronic interfaces and issues in small scale implementation. Micromachines 2:274–294
29. Zhu G, Yang R, Wang S, Lin Wang Z (2010) Flexible high-output nanogenerator based on lateral ZnO nanowire array. J Nano Lett 10:3151–3155

30. Aktakka EE, Peterson RL, Khalil Najafi (2011) A self-supplied inertial piezoelectric energy harvester with power-management IC. ISSCC
31. Wang ZL, Song J (2006) Piezoelectric nanogenerators based on zinc oxide nanowire arrays. Science 312(5771):242–246
32. Hickernell FS (2005) The piezoelectric semiconductor and acoustoelectronic device development in the sixties. IEEE Trans Ultrason Ferroelectr Freq Control 52:737–745
33. Alexe M, Senz S, Schubert MA, Hesse D, Gosele U (2008) Energy harvesting using nanowires? Adv Mater 20:4021–4026
34. Auld BA (1973) Acoustic fields and waves in solids. Wiley, New York
35. Withers RS (1984) Electron devices on piezoelectric semiconductors: a device model. IEEE Trans Sonic Ultrason 31:117–123
36. Li M, Xing G, Foong Nien Ah Qune L, Xing G, Wu T, Hon Alfred Huan C, Zhang X, Sum TC (2012) Tailoring the charge carrier dynamic in ZnO nanowires: the role of surface hole/electron traps. Phys Chem Chem Phys 14:3075–3082
37. Purahmad M, Stroscio MA, Dutta M (2013) A theoretical study on the effect of piezoelectric charges on the surface potential and surface depletion region of ZnO nanowires. IOP J Semicond Sci Technol 18(1):015019 (6 pp)
38. Sen B, Stroscio M, Dutta M (2011) Piezoelectricity in wurtzite polar semiconductor nanowires: a theoretical study. J App Phys 110:024506
39. Brus L (1991) Quantum crystallites and nonlinear optics. Appl Phys A 53:465–474
40. Wang J, Han S, Ke D, Wang R (2012) Semiconductor quantum dots surface modification for potential cancer diagnostic and therapeutic applications. J Nanomater 2012(129041):1–8
41. Reiss P, Protie`re M, Li L (2009) Core/shell semiconductor nanocrystals. Wiley-inter Sci 2:154–168
42. Dutta M, Stroscio MA (2000) Advances in semiconductor lasers and applications to optoelectronics. World Sci 16:235–240
43. Koroknay E, Schulz W-M, Eichfelder M, Roßbach R, Jetter M, Michler P (2010) InP quantum dots for applications in laser devices and future solid-state quantum gates. J Phys 245:012077
44. Stroscio MA, Dutta M (2004) Biological nanostructures and applications of nanostructures in biology. Bioelectr Eng 2
45. Alexson D et al (2005) Semiconductor nanostructures in biological applications. J Phys: Condens Matter 17:26
46. Lembrikov BI, Ben-Ezra Y (2005) Quantum dot-in-a-well laser applications in analog optical links. IEEE ICTON, pp 1–4
47. Wang KL, Cha D, Liu J, Chen C (2007) Ge/Si self-assembled quantum dots and their optoelectronic device applications. Proc IEEE 95(9):1866
48. Stokes EB, Stiff-Roberts AD, Dameron CT (2006) Quantum dots in semiconductor optoelectronic devices. Electrochem Soc Interface 15:23–27
49. Ren S, Chang L, Lim S, Zhao J, Smith M, Zhao N, Bulovic V, Bawendi M, Gradecak S (2011) Inorganic–organic hybrid solar cell: bridging quantum dots to conjugated polymer nanowires. Nano Lett 11(9):3998–4002
50. De Geyter B et al (2012) Broadband and picosecond intraband absorption in lead-based colloidal quantum dots. ACS NANO 5(1):6067–6074
51. Dabbousi BO, Rodriguez-Viejo J, Mikulec FV, Heine JR, Mattoussi H, Ober R, Jensen KF, Bawendi MG (1997) (CdSe)ZnS core-shell quantum dots: synthesis and characterization of a size series of highly luminescent nanocrystallites. J Phys Chem B 101(46):9463–9475
52. Pechstedt K et al (2010) Photoluminescence of colloidal CdSe/ZnS quantum dots: the critical effect of water molecules. J Phys Chem C 114:12069–12077
53. Zhong S et al (2005) High quality violet to red emitting ZnSe/CdSe core shell nanocrystal. Chem Mater 17(16):4038–4042
54. Pan Z, Zhang H, Cheng K, Hou Y, Hua J, Zhong X (2012) Highly efficient inverted type-I CdS/CdSe core/shell structure QD-sensitized solar cells. ACS Nano 6(5):3982–3991
55. Steckel JS et al (2004) Blue luminescence from (CdS)ZnS Core–shell nanocrystals. Angew Chem Int Ed 43:2154–2158

56. Torchynska TV, Douda J, Sierra RP (2009) Photoluminescence of core-shell CdSe/ZnS quantum dots of different sizes. Phys Status Solidi C 6(S1):S143–S145
57. Li L, Zhang F, Guimard D, Nishioka M, Arakawa Y (2010) 1.3 μm InAs quantum dots grown on silicon substrate. ASOT Conference publication, pp 99–102
58. Farid S, Purahmad M, Stroscio MA, Dutta M (2012) Computational analysis on the emission of ZnO Nanowires and coreshell CdSe/ZnS quantum dots deposited on different substrates. International Workshop on Computational Electronics (IWCE), pp 1–3
59. Luo G, Long J, Zhang B, Liu C, Ji S, Xu J, Yu X, Ni Q (2012) Quantum dots in cancer therapy. 9(1):47–58
60. Zhang H, Yee D, Wang C (2008) Quantum dots for cancer diagnosis and therapy: biological and clinical perspectives. Nanomedicine (Lond) 3(1):83–91
61. Hernández J, Thompson IM (2004) Prostate-specific antigen: a review of the validation of the most commonly used cancer biomarker. Cancer 101(5):894–904
62. Smith AM et al (2006) Multicolor quantum dots for molecular diagnostic of cancer. Expert Rev Mol Diagn 6(2):231–244
63. Medintz IL, Uyeda HT, Goldman ER, Mattoussi H (2005) Quantum dot bioconjugates for imaging, labelling and sensing. Nature Mater 4(6):435–446
64. Dyadyusha L, Yin H, Jaiswal S, Brown T, Baumberg JJ, Booy FP, Melvin T (2005) Quenching of CdSe quantum dot emission, a new approach for biosensing. Chem Commun 25:3201–3203
65. Mansson A, Sundberg M, Balaz M, Bunk R, Nicholls IA, Omling P, Tagerud S, Montelius L (2004) In vitro sliding of actin filaments labelled with single quantum dots. Biochem Biophys Res Commun 314:529–534
66. Wu X, Liu H, Liu J, Haley KN, Treadway JA, Larson JP, Ge N, Peale F, Bruchez MP (2003) Immunofluorescent labeling of cancer marker Her2 and other cellular targets with semiconductor quantum dots. Nat Biotechnol 21:41–46
67. Kaul Z, Yaguchi T, Kaul SC, Hirano T, Wadhwa R, Taira K (2003) Mortalin imaging in normal and cancer cells with quantum dot immuno-conjugates. Cell Res 13:503–507
68. Sukhanova A, Devey J, Venteo L, Kaplan H, Artemyev M, Oleinikov V, Klinov D, Pluot M, Cohen JHM, Nabiev I (2004) Biocompatible fluorescent nanocrystals for immunolabeling of membrane proteins and cells. Anal Biochem 324:60–67
69. Jamieson T, Bakhshi R, Petrova D, Pocock R, Imani M, Seifalian AM (2007) Biological applications of quantum dots. Biomaterials 28:4717–4732
70. Wang YC, Yuan CT, Kuo MY, Wu MC, Jau Tang et al (2012) Enhancement of the Purcell effect for colloidal CdSe/ZnS quantum dots coupled to silver nanowires by a metallic tip. Appl Phys Lett 100:253110
71. Mitchell GP, Mirkin CA, Letsinger RL (1999) Programmed assembly of DNA functionalized quantum dots. J Am Chem Soc 121:8122–8123
72. Chan WC, Nie S (1998) Quantum dot bioconjugates for ultrasensitive nonisotopic detection. Science 281:2016–2018
73. Dahan M, Laurence T, Pinaud F, Chemla DS, Alivisatos AP, Sauer M, Weiss S (2001) Time-gated biological imaging by use of colloidal quantum dots. Opt Lett 26:825–827
74. Chan WCW et al (2002) Luminescent quantum dots for multiplexed biological detection and imaging. Curr Opin Biotechnol 13:40–46
75. Rajh T et al (2004) Charge Transfer across the Nanocrystal-DNA Interface: probing DNA recognition. Nano Lett 4:1017–1023
76. Rajh T, Dimitrijevic NM, Elhofyand A, Rozhkova E (2010) Chapter 4. Biofunctionalized TiO2-based nanocomposites. Handbook of nanophysics. CRC Press, Hoboken, pp 4-1–4–28
77. Lewis FD et al (2008) Getting to guanine: mechanism and dynamic of charge separation and charge recombination in DNA revisited. Photochem Photobiol Sci 7(5):534–539
78. Kanvah S et al (2010) Oxidation of DNA: damage to nucleobases. Acc Chem Res 43(2):280–287
79. Warner WG, Yin JJ, Wei RR (1997) Oxidative damage to nucleic acids photosensitized by titanium dioxide. Free Radic Biol Med 23:851

80. Paunesku T et al (2003) Biology of TiO2-oligonucleotide nanocomposites. Nat Mater 2(5):343–346
81. Enders PJ, Paunesku T, Vogt S, Meade TJ, Woloschak GE (2007) DNA-TiO2 nanoconjugates Labeled with magnetic resonance contrast agents. J Am Chem Soc 129(51):15760–15761
82. Vasudev M et al (2008) Optoelectronic signatures of biomolecules including hybrid nanostructure-DNA ensembles. IEEE Sensors J 8(6):743–749
83. Ramadurai D et al (2007) Interactions of THz vibrational modes with charge carriers in DNA: Polaron-Phonon interactions. Int J High Speed Electron Syst 17(2):293–309
84. Ramadurai D et al (2008) Environmental effects influencing the vibrational modes of DNA: nanostructures couples to biomolecules. Int J High Speed Electron Syst 18(1):47–61
85. Stroscio MA, Dutta M (2001) Phonons in nanostructures. Cambridge University Press, Cambridge
86. Meshik X, Brenneman K, Xu K, Ranginwala S, Abell J, Zhao Y, Dutta M, Stroscio M (2012) Surface-enhanced raman spectroscopy signatures of an RNA molecule: an aptamer that binds to αVβ3 integrin. AIP Conf Proc 1506:49–52
87. Mi J, Zhang Z, Giangrande PH, McNamara JO II, Nimjee SM, Sarraf-Yazdi S, Sullenger BA, Clary BM (2005) Targeted inhibition of αVβ3integrin with an RNA aptamer inpairs endothelial cell growth and survival. Biochem Biophys Res Commun 228:956–963
88. Chaney SB, Shanmukh S, Dluhy RA, Zhao Y-P (2005) Aligned silver nanorod arrays produce high sensitivity surface-enhanced raman spectroscopy substrates. Appl Phys Lett 87:031908
89. Otto C, Van Den Tweel TJJ, de Mul FFM, Greve J (1986) Surface-enhanced Raman spectroscopy of DNA bases. J Raman Spec 17:289–298
90. Biese B, McNaughton D (2002) Surface-enhanced Raman spectroscopic study of uracil. The influence of the surface substrate, surface potential, and pH. J Phys Chem B 106:1461–1470
91. Vasudev M, Wu T-C, Bitwas S, Dutta M, Stroscio MA, Guthrie S, Reed M, Burris KP, Stewart CN Jr (2001) Optoelectronic signatures of DNA-based hybrid nanostructures. IEEE Trans Nanotechnol 10:35–43
92. Wang J, Gudiksen MS, Duan X, Cui Y, Lieber CM (2001) Science 293:1455
93. Kong KJ, Franklin N, Zhou C, Chapline M, Peng S, Cho K, Dai H (2000) Science 287:622
94. Sarkar J, Khan GG, Basumallick A (2007) Bull Mater Sci 30(3):271–290
95. Kumar C (ed) (2007) Nanomaterials for biosensors. Wiley-VCH, Weinheim
96. Friedman AL, Menon L (2007) J Elec Soc 154(4):E68–E70
97. Menon L (2003) Synthesis of quantum wires using porous alumina. In: Bandyopadhyay S, Nalwa H (eds) Quantum Dots and Quantum Wires, American Scientific Publishers, pp 142–191: ISBN: 1-58883-013-6
98. Alivisatos AP (1996) J Phys Chem 100:13226–13239
99. Landau LD, Lifshitz EM, Pitaevskii LP (1984) Electrodynamics of continuous media. Pergamon, Oxford, pp 34Ð42
100. Ruda HE, Shik A (2005) Physical Rev B 72:115308
101. Empedocles SA, Norris DJ, Bawendi MG (1996) Phys Rev Lett 77:3873
102. Vouilloz F et al (1998) Phys Rev B 57:12378
103. Akiyama H, Someya T, Sakaki H (1996) Phys Rev B 53:R4229
104. Ils P et al (1995) Phys Rev B 51:4272
105. Liu P, Singh VP, Jarro CA, Rajaputra S (2011) IOP Sci Nanotechnol 22:145304 (9 pp)
106. Duan X, Huang Y, Cui Y, Wang J, Lieber CM (2001) Nature 409:66
107. Huang Y, Duan X, Wei Q, Lieber CM (2001) Science 291:630
108. Cui Y, Lieber CM (2001) Science 291:851
109. Kim SN, Kuang Z, Slocik JM, Jones SE, Cui Y, Farmer BL, McAlpine MC, Naik RR (2011) Preferential binding of peptides to graphene edges and planes. J Am Chem Soc 133(37):14480–14483
110. Tomaisio SM, Walsh TR (2009) Modeling the binding affinity of peptides for graphitic surfaces; influences of aromatic content and interfacial shape. J Phys Chem C 113:8778–8785

111. Kuang Z, Kim SN, Crookes-Goodson WJ, Farmer BL, Naik RR (2010) Biomimetic chemosensor: designing peptide recognition elements for surface functionalization of carbon nanotube field effect transistors. ACS Nano 4(1):452–458
112. Lu CH, Li J, Zhang XL, Zheng AX, Yang HH, Chen X, Chen GN (2011) General approach for monitoring peptide-protein interactions based on graphene-peptide complex. Anal Chem 83:7276–7282
113. Oh KJ, Cash KJ, Plaxco KW (2006) Excimer-based peptide beacons: a convenient experimental approach for monitoring polypeptide-protein and polypeptide-oligonucleotide interactions. J Am Chem Soc 128(143):14018–14019
114. Geim AK (2009) Graphene: status and prospects. Science 324:1530–1534
115. Xu Y, Bai H, Lu G, Li C, Shi G (2008) Flexible graphene films via the filtration of water-soluble noncovalent functionalized graphene sheets. J Am Chem Soc 130(18):5856–5857
116. So CR, Hayamizu Y, Yazici H, Gresswell C, Khatayevich D, Tamerler C, Sarikaya M (2012) Controlling self-assembly of engineered peptides on graphite by rational mutation. ACS Nano 6(2):1648–1656
117. Katoch J, Kim SN, Kuang Z, Farmer BL, Naik RR, Tatulian SA, Ishigami M (2012) Structure of a peptide adsorbed on graphene and graphite. Nano Lett 12:2342–2346
118. Cui Y, Kim SN, Jones SE, Wissler LL, Naik RR, McAlpine MC (2010) Chemical functionalization of graphene enabled by phage displayed peptides. Nano Lett 10(11):4559–4565
119. Wang S, Humphreys ES, Chung SY, Delduco DF, Lustig SR, Wang H, Parker KN, Rizzo NW, Subramoney S, Chiang YM, Jagota A (2003) Peptides with selective affinity for carbon nanotubes. Nature 2:196–200
120. Acevedo AO, Xie H, Zorbas V, Sampson WM, Dalton AB, Baughman RH, Draper RK, Musselman IH, Dieckmann GR (2005) Diameter-selective solubilization of single-walled carbon nanotubes by reversible cyclic peptides. J Am Chem Soc 127:9512–9517
121. Lopez SF, Kim HS, Choi EC, Delgado M, Granja JR, Khasanov A, Kraehenbuehl K, Long G, Weinberger DA, Wilcoxen KM (2011) Antibacterial agents based on the cyclic D, L-peptide architecture. Nature 412:425–455
122. Wang X, Wang C, Qu K, Song Y, Ren J, Miyoshi D, Sugimoto N, Qu X (2010) Ultrasensitive and selective detection of prognostic indicator in early-stage cancer using graphene oxide and nanotubes. Adv Funct Mater 20:3967–3971
123. Song Y, Qu K, Zhao C, Ren J, Qu X (2010) Graphene oxide: intrinsic peroxidase catalytic activity and its application to glucose detection. Adv Mater 22:2206–2210
124. Rajesh C, Majumder C, Mizuseki H, Kawazoe Y (2009) A theoretical study on the interaction of aromatic amino acids with graphene and single walled carbon nanotube. J Chem Phys 130:124911
125. Pantarotto D, Partidos CD, Graff R, Hoebeke J, Briand JP, Prato M, Bianco A (2003) Synthesis, structural characterization, and immunological properties of carbon nanotubes functionalized with peptides. J Am Chem Soc 125:6160–6164
126. Huan TN, Ganesh T, Han SH, Yoon MY, Chung H (2011) sensitive detection of an antharax biomarker using a glassy carbon electrode with consecutively immobilized layer of polyalinine/carbon nanotube/peptide. Biosens Bioelectron 26:4227–4230
127. Huan TN, Ha VTT, Hung LQ, Yoon MY, Han SH, Chung H (2009) Square wave voltammetric detection of antharax utilizing a peptide for selective recognition of a protein biomarker. Biosens Bioelectron 25(2):469–474
128. Mirzaei M, Meskinfam M, Yousefi M (2012) Covalent hybridizations of carbon nanotubes through peptide linkages: a density functional approach. Comput Theoretical Chem 981:47–51
129. West PR, Ishii S, Naik GV et al (2010) Searching for better plasmonic materials. Laser Photonics Rev 4(6):795–808
130. Moskovits M (2005) Surface-enhanced Raman spectroscopy: a brief retrospective. J Raman Spectrosc 36(6–7):485–496
131. Chaney SB, Shanmukh S, Dluhy RA et al (2005) Aligned silver nanorod arrays produce high sensitivity surface-enhanced Raman spectroscopy substrates. App Phys Lett 87(3):3

132. Willets KA, Van Duyne RP (2007) Localized surface plasmon resonance spectroscopy and sensing. Annual review of physical chemistry. Annual Reviews, Palo Alto, pp 267–297
133. Shafer-Peltier KE, Haynes CL, Glucksberg MR et al (2003) Toward a glucose biosensor based on surface-enhanced Raman scattering. J Am Chem Soc 125(2):588–593
134. Yonzon CR, Stuart DA, Zhang XY et al (15 September 2005) Towards advanced chemical and biological nanosensors—an overview. Talanta 67(3):438–448
135. Yonzon CR, Jeoungf E, Zou SL et al (2004) A comparative analysis of localized and propagating surface plasmon resonance sensors: the binding of concanavalin a to a monosaccharide functionalized self-assembled monolayer. J Am Chem Soc 126(39):12669–12676
136. Chien F-C, Huang WY, Shiu J-Y et al (2009) Revealing the spatial distribution of the site enhancement for the surface enhanced Raman scattering on the regular nanoparticle arrays. Opt Express 17(16):13974–13981
137. Shanmukh S, Jones L, Driskell J et al (2006) Rapid and sensitive detection of respiratory virus molecular signatures using a silver nanorod array SERS substrate. Nano Lett 6(11):2630–2636
138. Li J, Fattal D, Li Z (2009) Plasmonic optical antennas on dielectric gratings with high field enhancement for surface enhanced Raman spectroscopy. Appl Phys Lett 94(26):263114
139. Lee YH, Dai S, Young JP (1997) Silver-doped sol-gel films as the substrate for surface-enhanced Raman scattering. J Raman Spectrosc 28(8):635–639
140. Huang Y, Yang Y, Chen Z et al (2008) Fabricating Au-Ag core-shell composite films for surface-enhanced Raman scattering. J Mater Sci 43(15):5390–5393
141. Kahraman M, Aydin O, Culha M (2009) Oligonucleotide-mediated Au-Ag core-shell nanoparticles. Plasmonics 4(4):293–301
142. Yang Y, Xiong LM, Shi JL et al (2006) Aligned silver nanorod arrays for surface-enhanced Raman scattering. Nanotechnology 17(10):2670–2674
143. Liu YJ, Zhang ZY, Dluhy RA et al (2010) The SERS response of semiordered Ag nanorod arrays fabricated by template oblique angle deposition. J Raman Spectrosc 41(10):1112–1118
144. Zhao LL, Kelly KL, Schatz GC (2003) The extinction spectra of silver nanoparticle arrays: influence of array structure on plasmon resonance wavelength and width. J Phy Chem B 107(30):7343–7350
145. Brenneman KL, Meshik X, Xu et al (2012) Surface-enhanced Raman spectroscopy study of single stranded DNA sequences on silver nanorod array, PHONONS 2012, AIP Conf. Proc. 1506, pp 53–56; doi: 10.1063/1.4772525
146. Shang Z-G, Ting DN, Wong YT et al (2007) A study of DFT and surface enhanced Raman scattering in silver colloids for thymine. J Mol Struct 826(1):64–67
147. Shang Z, Gao Y, Jia T et al (2009) Vibrational modes study of thymine on the surface of copper electrode using SERS-measurement and the DFT method. J Mol Struct 930(1–3):60–64

Chapter 4
Gas Sensing and Thermal Transport Through Carbon-Nanotube-Based Nanodevices

Y. Pouillon, A. Pérez Paz, J. Mäklin, N. Halonen, Y. Leroy, D. Mowbray, J.M. García Lastra, G. Tóth, K. Kordás, Z. Kónya, Á. Kukovecz and A. Rubio

Abstract Designing nanoscale devices, such as gas sensors and thermal dissipators, is challenging at multiple levels. Exploring their properties through combined experimental and theoretical collaborations is a valuable approach that expands the understanding of their peculiarities and allows for the optimization of the design process. In order to select the most relevant functional molecules for carbon-based gas sensors, and provide the best sensitivity and selectivity possible, we study the electronic transport properties of functionalized carbon nanotubes (CNTs), both through experiments and theoretical calculations. The measurements are carried out both in argon and synthetic air, using CO, NO, and H_2S as test cases, with carboxyl-functionalized CNTs. The calculations, performed in the framework of density functional theory, consider both metallic and semi-conducting prototype CNTs, with respective chiralities (6,6) and (7,0), exploring a broader range of functional molecules and gases. The behavior of individual carboxyl-functionalized CNTs deduced from the multiscale results consistently reflect what happens at a larger scale and provides useful insights regarding the experimental results. CNTs

Y. Pouillon (✉) · A. Pérez Paz · D. Mowbray · J. M. García Lastra · A. Rubio
Nano-Bio Spectroscopy group and ETSF Scientific Development, Universidad del País Vasco, Centro de Física de Materiales CSIC-UPV/EHU-MPC and DIPC, Av.de Tolosa 72, San Sebastián 20018, Spain
e-mail: yann.pouillon@ehu.es

A. Rubio
e-mail: angel.rubio@ehu.es

J. Mäklin · N. Halonen · G. Tóth · K. Kordás
Microelectronics and Materials Physics Laboratories, and EMPART Research Group of Infotech Oulu, University of Oulu, P.O. Box, Oulu 90014, Finland

Y. Leroy
Laboratoire ICube-DESSP/MaCÉPV, Télécom Physique Strasbourg, 300 Bd Sébastien Brant, 67400 Illkirch-Graffenstaden, France

Y. Leroy · Z. Kónya · Á. Kukovecz
MTA-SZTE "Lendulet" Porous Nanocomposites Research Group, Department of Applied and Environmental Chemistry, University of Szeged, Rerrich Bela ter 1., Szeged 6720, Hungary

Z. Kònya
MTA-SZTE Reaction Kinetics and Surface Chemistry Research Group, Department of Applied and Environmental Chemistry, University of Szeged, Rerrich Bela ter 1., Szeged 6720, Hungary

J. M. Seminario (ed.), *Design and Applications of Nanomaterials for Sensors,* Challenges and Advances in Computational Chemistry and Physics 16,
DOI 10.1007/978-94-017-8848-9_4, © Springer Science+Business Media Dordrecht 2014

are excellent thermal conductors as well and show much promise as heat dissipators in microelectronics. However, in practice, thermal properties of CNTs are affected due to the unavoidable presence of defects and interface with the environment. We investigated these limitations using a multiscale approach. Using molecular dynamics simulations, here we investigate the heat flow across the interface of a (10,10) CNT with various substances, including air and water. We also analyzed computationally the impact of CNT defects on its thermal transport properties using *first principles* calculations.

4.1 Introduction

When designing nanoscale devices, a common experimental strategy is to follow empirical approaches and educated guesses to obtain desired properties. Although generally successful, this methodology is not satisfactory because it does not bring any valuable contribution to the understanding in the corresponding fields of research. Although more complex and slower to set-up, combining simultaneously experimental and theoretical studies allows for a comprehensive exploration of the various parameters that may influence the devices and their working conditions, as well as for a systematic screening of their possible functional components. In this case, it is possible to optimize the design, broaden the working conditions of the devices and identify more precisely their limitations. In addition, these two strategies are not mutually exclusive and may take place one after the other.

Carbon-based gas sensors and heat conductors are typical examples of such nanoscale devices. Two very promising base components are carbon nanotubes (CNTs) and graphene ribbons, which both exhibit novel and extremely interesting electronic and thermal properties. Since at least one of their dimensions is generally between 1 and 50 nm, understanding these properties requires an accurate accounting for quantum effects. At the same time, they represent a challenge for current quantum mechanics-based theories, since at least one of their other dimensions is of macroscopic scale, generally of the order of 1 μm. Graphene is known to present less defects and produce less noise than CNTs when used for gas detection [1], however defects might be desirable in some cases, e.g. to attach functional molecules to a CNT in order to tune its selectivity. Regarding thermal conduction, both CNTs and graphene are known to exhibit ballistic transport at room temperature, which may improve significantly the dissipation of heat in integrated circuits over the usual diffusive mechanism [2]. In addition, vast explorations are still needed to clearly identify which applications these two materials are best suited for and which kinds of devices will be more easily produced at an industrial scale. In the following, we present our collaborative work on CNT-based gas sensing and thermal transport.

Gas sensing through miniaturized devices has a lot of potential applications in various areas, ranging from industrial processes to environmental issues. As such, it attracts a lot of attention [3]. Since carbon-nanotube-based sensors offer a promising path for ppm and sub-ppm gas detection, a lot of efforts are currently undertaken to better understand their structural and electronic properties [4]. With the use of CNTs, various challenges arise at different levels. First, the properties of one CNT

can be significantly affected by the presence of defects, deformations, adsorbed molecules, and dopants [5–7]. Then, when two CNTs are in contact, their respective chiralities and relative positions may strongly influence the overall properties of the device [8], in particular when networks of random CNTs are involved [9, 10]. And finally, the quality of the contacts between CNTs and electrodes strongly influence the operating conditions of the sensor on a larger scale [11].

The quality and interest of a sensor are determined by four key concepts: (i) sensitivity, measured here by the effect a specified quantity of a gas has on the conductivity of the system, (ii) selectivity, i.e. the obtention of a response for a reduced set of gases, ideally one at a time, (iii) sensing dynamics, accounting for the necessary time to obtain a response from the device as well as the frequency at which it has to be reset or recalibrated, (iv) cost effectiveness, i.e. achievement of manufacturing scalability [12, 13]. Finding an improved set of parameters is the result of a delicate compromise, as improving one aspect might often degrade the others. Among the possible solutions explored so far, the use of sensors based on random networks of functionalized CNTs, as well as the providing of different functionalizations on the same chip, have proven promising ways of building devices suitable for both laboratory investigations and manufacturing [14].

Semi-conducting nanotubes are known to be very sensitive but poorly selective to the presence of gases, while metallic nanotubes have a very low overall sensitivity [15]. By functionalizing appropriately the semi-conducting CNTs, it should be possible to modulate their sensitivities in a non-destructive manner and at the same time improve their selectivity [16–18]. Ultimately, all factors potentially affecting the stability of the response, e.g. oxygen, water vapor, or the presence of contaminants in the nanotubes, have to be explored as systematically as possible, in order to get closer and closer to real working conditions, both in simulations and experiments [19].

Besides gas sensing, the peculiar properties of CNTs make them suitable for numerous other potential applications. One of them is heat dissipation, a critical issue to address to e.g. further increase the transistor density in microprocessors. In this case, the key parameter is thermal conductivity, which is the property that measures the rate at which energy is transferred from two regions of a material that are kept at different temperatures. Electrons and phonons are responsible in transferring energy in a metal and insulator, respectively. At high temperatures, *umklapp* phonon-phonon scattering events provide the dominant mechanism for the increase of thermal resistance in non-metals, while electron-phonon interactions are responsible for the decrease in thermal conductivity in metals. In non-ideal materials, scattering with defects and/or boundaries provide further mechanisms for the reduction of thermal conductivity.

For small temperature gradients, that is, in the realm of linear response theory, the heat flux vector $\mathbf{J}_Q$ in a bulk material is linearly proportional to the spatial temperature gradient ∇T via Fourier's law, $\mathbf{J}_Q = -\kappa \nabla T$, where κ is the thermal conductivity coefficient, which has SI units of [J/(s·m·K)]. In an isotropic medium, such as a liquid, $\mathbf{J}_Q$ and ∇T are collinear and therefore κ reduces to a scalar. In general, however, the thermal conductivity coefficient will be a tensor, in particular for highly anisotropic materials such as CNTs.

The interfacial thermal resistance, also known as Kapitza resistance R_K, represents the barrier to heat flow that causes an abrupt temperature discontinuity ∇T across interfaces according to the relationship $J_Q = -G\ \nabla T$ (valid in the linear re-

gime) where J_Q is the heat flux across the interface [20]. The interfacial conductance G is defined as the inverse of the thermal resistance; that is, $G = 1/R_K$. Interfacial thermal conductance measures the efficiency by which heat carriers (electron, phonons) flow from one material to another. Generally, similar insulator materials facilitate a very efficient phonon transmission between them. More specifically, a good overlap or match between the thermal vibration spectra is required to minimize the Kapitza resistance at the interface of two materials.

Heat has deleterious effects on micro-electronics by rendering these components unreliable and often causing them a premature failure. Therefore, research into novel materials with enhanced thermal capabilities is highly desirable for industrial and economic reasons. Perfect CNTs are expected to be ballistic thermal conductors, and for this reason, in principle CNTs would be ideal candidates for dissipating heat produced in chips or processors. The heat dissipation by CNT can be modeled in three steps:

1. The CNTs receive heat directly from the chip through a metallic interface to which is anchored.
2. Then, heat is transported along the CNT. This process is extremely efficient on ideal CNTs but in practice is limited by the presence of defects. These naturally-occurring defects have negative effects on the thermal conductance of CNTs.
3. Finally, heat is dissipated to the ambient from the CNTs. This interface CNT/environment limits considerably the efficiency of the cooling.

The third section of this chapter deals with the computational study of heat dissipation at the CNT/air and CNT/water interfaces using classical molecular dynamics (MD) simulations. The effect of the gas pressure and the coupling between CNT and water on the interfacial thermal resistance is reported herein.

There are several methods to compute the thermal properties of a material. In general, all these approaches often require a large cell along the heat transport direction to avoid the lost of long-wavelength phonons, which contribute significantly to the thermal properties. Mathematically, the phonon relaxation time in MD calculations can be decomposed in two contributions: (i) phonon scattering due to *umklapp* processes and point defects in the bulk; and (ii) phonon scattering with the boundaries and heat sink/source in the computational cell.

The first method for computing thermal conductivity coefficient κ is based on the application of Green-Kubo (GK) relations to equilibrium molecular dynamics (MD). [21, 22] In this method, the thermal conductivity coefficient κ is proportional to the time integral of the heat flux autocorrelation function. The advantage of the GK method is that it allows us to compute the full thermal conductivity tensor from a single albeit long MD simulation and often it does not require very large computational cells. The main disadvantage of this method, however, is that it converges very slowly in time.

The second general method is based on non-equilibrium molecular dynamics (NEMD). One of the best NEMD methods is the algorithm proposed by Florian Müller-Plathe, [23] which can be used to compute the thermal conductivity of a condensed phase material. In this approach, the velocities of two particles in different regions of the system are swapped at regular times so as to induce a hopefully linear

temperature gradient, from which the thermal conductivity can be extracted directly from Fourier's law. The main disadvantage of the method is that it requires particularly large computational cells to converge the thermal conductivity coefficient.

We must mention that the calculated and experimentally measured values for the thermal conductivity coefficient κ in CNTs are greatly scattered in the literature. The disagreement between reported calculations are due inconsistencies in simulation protocols used, poor sampling, or a combination of thereof. The disagreement between theory and experiment is due in part to ill-defined quantities such as the superficial area and the intrinsic slow convergence of quantities involved. In this work, however, we pursue a simple and direct strategy to characterize thermal transport in CNT/air and CNT/water interfaces, by which we apply directly temperature gradients across the interface and we observe the response of the system in time. In the following, we summarize our findings.

This chapter is organized as follows: Sect. 4.2 is dedicated to the gas sensor; in Sect. 4.2.1, we first describe the experimental setup as well as the computational details of our *ab initio* calculations, before explaining our use of transmission integrals as indicators of the individual sensing characteristics, and finish with the ballistic model we use to evaluate Fermi energy shifts; in Sect. 4.2.2, we discuss the experimental, *ab initio*, and ballistic results. Section 4.3 is about the thermal properties of nanotubes; in Sect. 4.3.1, we describe the computational details; in Sect. 4.3.2, we discuss the dynamical properties of the CNT/air system, as well as the results of non-equilibrium molecular dynamics simulations of the CNT/air and CNT/water systems.

4.2 Carbon Nanotube-Based Gas Sensor

Gas sensing through nanoscale devices is multiply challenging: the measured signals are very small and noisy, the fabrication of the devices implies a high level of integration, and the modelling of the process requires the inclusion of quantum effects associated to a multiscale approach. Meeting these challenges involves the efficient use and extension of cutting-edge methodological and technological approaches, in a multidisciplinary framework.

4.2.1 Methods

In the present collaboration, we focus on comparing the computational results with the experimental ones, in order to assess the overall consistency between both levels. Our purpose is to design a generic strategy for combined experiments and calculations, in order to speed-up the selection of relevant functional molecules providing a good compromise between sensitivity, selectivity, and resilience, for the detection of gases. Our calculations include the determination of ground-state and quantum-transport properties of the core ingredients of the sensors, together with their validation through confrontation with the experimental results.

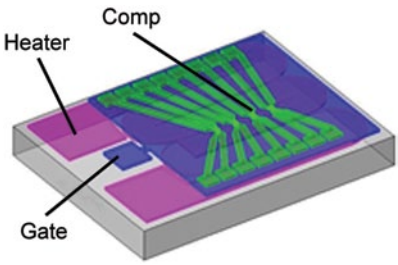


Fig. 4.1 Sensor chip used in measurements, featuring a series of inkjet-printed CNT networks of different sizes, a gate with variable voltage for the measurements, and a heater to desorb gases between measurements

4.2.1.1 Experimental Setup

The gas measurements are performed with nitrogen monoxide (NO), carbon monoxide (CO), hydrogen (H_2), hydrogen sulfide (H_2S) and ammonia (NH_3), using synthetic air (dry mix of N_2 and O_2, SA in the following) as a buffer gas at 150° C. Oxygen (O_2) is measured in an argon (Ar) buffer at 150° C. In addition, three of the gas analytes (NH_3, H_2S and NO) are tested at 30° C in a SA buffer. The chamber used for the measurements is around 200 ml in volume and the gas flow is 0.5 l/min during the tests.

The sensor device is shown in Fig. 4.1 and fully described in [24]. It is made by inkjet-printing carboxyl-functionalized SWCNTs on Si-chips between Pt electrodes on a 200 nm-thick thermal SiO_2. By printing a small amount of SWCNTs on the chip, a gate-tunable semiconducting channel is formed, having p-type gate response between the electrodes [25–27]. The electrical conductance of the channel in the sensors is ≈0.5 µS with a relatively small gate effect (≈30 %) when varying the gate voltage from -5 V to +5 V. As the typical resistance of the devices may vary a lot, we have selected both highly-resistive (in the MΩ range) and weakly-resistive (in the kΩ range) sensors. The whole measurement system is PC-controlled in a LabVIEW environment.

The sensors were measured by monitoring the source-drain (S-D) current with a constant source-drain bias of 1 V. The effect of the gate voltage on the variation of sensor response was tested by measuring the same gas pulse with three different gate voltage values (-5 V, 0 V and +5 V). It is worth noting that at a temperature of 150° C the gate-effect is negligible, mostly due to an enhanced Schottky emission at the interfaces of semiconducting and metallic nanotubes [26–29]. This enhancement of Schottky emission is also seen as a lower resistance of the sample at 150° C than at room temperature. Each gas pulse is preceded, and followed, by at least 10 min of exposure to only the SA (or Ar).

4.2.1.2 Theoretical Modeling

At the theoretical level, CNT-based systems require a multiscale description. Simulating a complete 400 nm-long junction with atomic-scale details is indeed way above the current limits of our most sophisticated models. In these conditions, the

calculations provide complementary information with respect to the experimental results, in order to facilitate the understanding of the phenomena involved in the measurements. They also bring useful support in speeding-up the process of identifying relevant functional molecules for a selective detection of gases. Since for systems such as CNTs we have to account for quantum effects, we have chosen to first model the individual sensing units with as much accuracy as possible. Since they are abundant in the experimental devices, we have chosen the (6,6) and (7,0) CNTs as model systems for metallic and semi-conducting CNTs, respectively. We also want to be systematic, which is why we have developed a general strategy to give a consistent access to the conductivities of the systems and their other parameters. When needed, tight-binding models can easily be parametrized after the atomic-scale results, in order to access larger scales.

In order to progressively build accurate models of the gas sensor, we start with an *ab initio* description of the structural and transport properties of a functionalized CNT. The results then allow us to tune semi-empirical models and treat a bigger part of the sensor when necessary. The typical length-scale of experimental interest is of the order of 50 nm, which means around 5000 atoms for a nanotube. This is actually tractable provided that multiscale simulations are performed, because we will not be able to take efficiently into account the many functional molecules attached to those portions of tubes with our most accurate models. Before considering a larger part of the sensor, the first step is to explore the contributions the individual CNTs can bring by themselves to the sensor response and how far they can account for the experimental results. This is what we focus on in this second section of the present chapter.

4.2.1.3 *Ab initio* Calculations

We first focus on very small portions of nanotubes (typically 5 nm) and describe them in a fully *ab initio* framework. The purpose of this first step is to build a comprehensive database describing what happens in the immediate surroundings of a functional molecule when a molecule of gas approaches, as well as the local influence of its presence on the electrical conductance of the CNT. These results can be used later to parametrize tight-binding models, in order to be able to encompass several dozens of functional molecules at once [30]. Though less accurate, such models should provide a useful insight on the dynamics of the detection, since we are able to expose the functional molecules to a mixture of gases at various concentrations. The system sizes that can be reached at this level comprise several thousands of atoms, and thus carbon nanotubes of around 20–50 nm in length.

The following discussion will focus on the most detailed calculations we have carried out. The geometries are optimized within the framework of Density Functional Theory (DFT), using the Atomic Simulation Environment (ASE) [31] piloting the SIESTA code [32]. We use a double-zeta polarized basis for the wavefunctions, the PBE approximation for exchange-correlation, and a periodic simulation cell along the nanotube axis. The quantum transport calculations are performed within the Non-Equilibrium Green's Function (NEGF) formalism [33, 34], using

the Wannier function-based technique [35] specifically implemented in ASE [31]. Comparisons and tests are also conducted using Abinit [36].

Experimentally, by applying a bias voltage, it is indeed possible to explore the transport properties around the Fermi level of the system, with a typical range of 1 or 2 eV. By applying a gate voltage, the Fermi level can be shifted, thus further tuning the transport properties of the sensor. We have thus chosen to focus our attention on the $[-1.5,+1.5]$ eV energy interval, even if the calculations give us access to a much broader energy range. In order to provide an instant and synthetic access to our results, we have devised a strategy to determine the qualitative effect the presence of a gas will have on the transport properties of the functionalized CNTs. In order to stay as consistent as possible between experiments and calculations, we have based our analysis exclusively on the transmission, which is the only quantity directly linked to the experimental measurements. Our guideline has been that the stronger a molecule binds to the CNTs, the higher is the effect on the CNTs' transport properties: strongly bound molecules indeed tend to close or open a full conduction channel. We have thus organized our calculations in 3 steps:

1. determine the transmission $\mathfrak{T}_0^0$ for a selected (n,m) CNT, bare;
2. determine the transmission $\mathfrak{T}_f^0$ for the selected CNT, functionalized with a selected group *f*;
3. determine the transmission $\mathfrak{T}_f^g$ for the selected CNT, functionalized with *f*, and with a molecule of a selected gas *g* at a close distance (typically 2 Å) from the functional group.

Our objective is to provide an easy-to-read and direct indicator, which means a number in the present case. To extract such a number, we first integrate the difference of the transmissions $\mathfrak{T}_f^0$ and $\mathfrak{T}_0^0$ over the energy interval of interest $[E_1, E_2]$. At this stage, we obtain the overall perturbation of the electrical conductance due to the presence of the functional molecule:

$$\alpha_f^0 = \int_{E_1}^{E_2} dE \left[\mathfrak{T}_f^0(E) - \mathfrak{T}_0^0(E) \right] \tag{4.1}$$

By integrating the difference of the transmissions $\mathfrak{T}_f^g$ and $\mathfrak{T}_f^0$ over the same energy interval, as well as isolating the positive and negative parts, we obtain a reliable indicator of the sensitivity of the functional group to a gas:

$$\alpha_f^g = \int_{E_1}^{E_2} dE \left[\mathfrak{T}_f^g(E) - \mathfrak{T}_f^0(E) \right] \tag{4.2}$$

For metallic nanotubes we could even define a relative value and give results in percents. The only problem with this approach is that it would not hold anymore for semi-conducting tubes because the transmission in the bare CNT drops to zero around the Fermi level.

Calculating these integrals is in some sense a way of summarizing the exploration of the sensitivity by applying different bias and/or gate voltages. Despite their qualitative character, they provide a compact, simple and direct view of the most

interesting molecule/gas combinations. It is also much more reliable than the DOS, which is known to reflect the transport properties very poorly, when not wrongly, when extracted from Kohn-Sham orbitals obtained with LDA-based approximations [37–39]. Another great advantage is that we are able to provide an immediately usable summary of the information to the experimentalists in the format of tables: by a simple look at these, one gets instantly an idea about the possible additional sensitivity and selectivity brought by the functional molecules, and which ones among them are the best candidates for sensor applications. As a bonus, high values pinpoint gas molecules that might poison and/or damage the sensor because of their strong binding to the CNTs. In addition, our post-processing tools display separately the positive and negative parts of these integrals, in case the whole integral would occur to be near zero because of compensations, and thus automatically highlight the systems for which a detailed analysis is immediately necessary. Since such cases have been rare among all the systems considered here, and for sake of simplicity, we will only present the whole integrals in the following.

4.2.1.4 Ballistic Model

In order to provide the experimentalists with relevant device parameters, we evaluate Fermi energy shifts in the case of a (n,0) semi-conducting CNT by calculating band structures with the MOSCNT software package [40–42]. As it is not possible to simulate a CNT-based field-effect nanotransistor (CNTFET) with a 200 nm-thick oxide layer and a channel length of 400 nm, we have looked for an equivalent and accessible electrostatic structure. An illustration of the simulated CNTFET device is given in Fig. 4.2. The agreement between both equivalent structures has to be found for the reference oxide layer before introducing the CNT, since this is precisely where the CNT will find itself. It corresponds to finding an identical potential profile on the oxide surface ($z = 0$ nm, $0 < x < 400$ nm), where the CNT will be located.

Figure 4.3 shows the electrostatic potential distribution obtained for the initial device (Fig. 4.3a) and compares it to that of a device with a 50 nm-long channel and 22.5 nm-thick oxide layer (Fig. 4.3b), for drain-source and gate voltages corresponding to experimental conditions ($V_{ds} = 1$ V, $V_g = 0$ V). This reshaping of the device provides an equivalent distribution of the potential on the oxide surface ($z = 0$ nm), as shown in Fig. 4.4, where the two surface potentials have been compared for gate voltages spanning the experimental range going from -5 V to 5 V. The potential is plotted there as a function of the relative position x / L in the channel, L being the total length of the considered channel. The plots are superimposed for the whole range of gate voltages.

The 50 nm channel length is sufficiently large to have the potential in the middle of the CNT free from constraints coming from the source and drain electrodes. The behaviour of a longer CNT will thus be similar, with a ballistic behaviour in the central area, correlated with the existence of a plateau on the band diagrams.

These band diagrams are shown on Fig. 4.5 for a 110 nm-long (7,0) CNT, considered as a channel for a transistor with an oxide layer of 22.5 nm, for the three experimentally used gate voltages. As shown, the effective channel has a length of 50 nm.

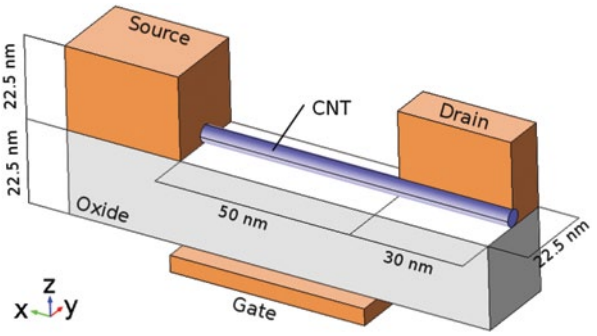


Fig. 4.2 Representation of the simulated CNTFET. A single (n,0) semi-conducting CNT is used as the channel of the transistor

The plots have been generated considering both electrons and holes as carriers, and using the full NEGF settings of the MOSCNT package: NEGF transport is used rather than semiclassical ballistic transport; the recursive Green's function method is preferred here to solve the NEGF problem, as the CNT is quite long. The package

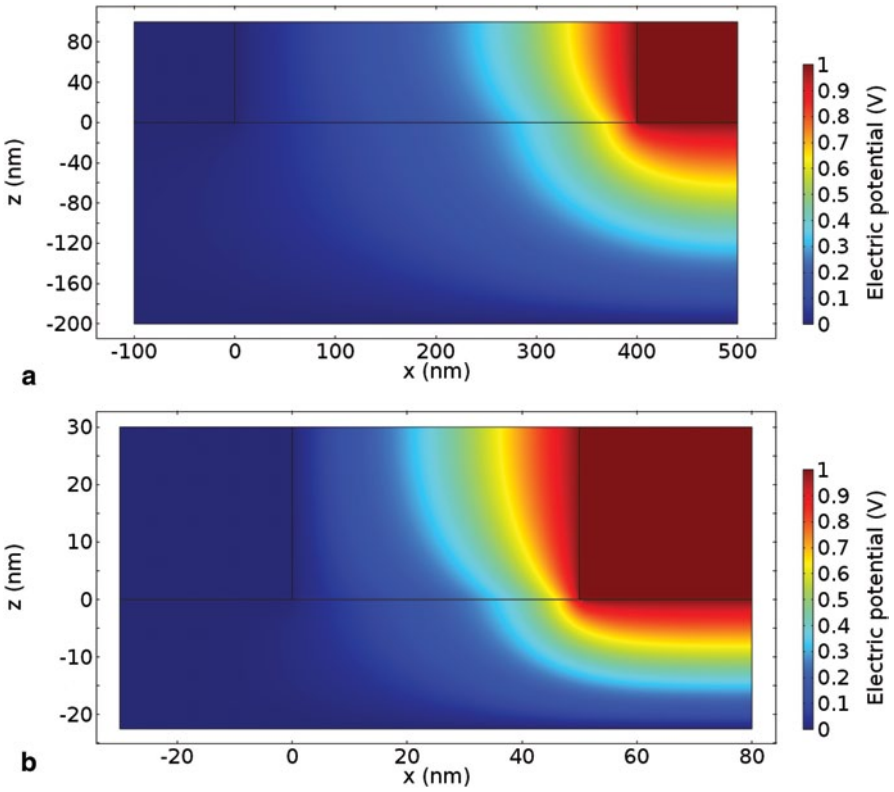


Fig. 4.3 Potential profiles for the drain-source voltage fixed to $V_{ds} = 1$ V and the gate voltage $V_g = 0$ V. **a** the real 400 nm-long / 200 nm-thick device. **b** the equivalent 50 nm-long / 22.5 nm-thick device. An agreement is looked for in the oxide only

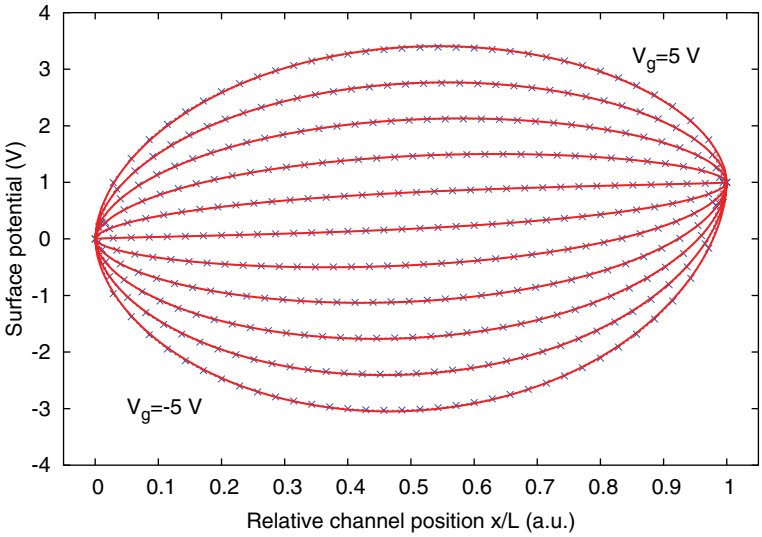


Fig. 4.4 Surface potentials ($z = 0$ nm) between the source and drain electrodes of the two equivalent devices, for various gate voltages V_g between -5 V and +5 V (*bottom to top*). The potentials are plotted as functions of the relative position (x/L) in the channel. The source-drain voltage is again fixed at $V_{ds} = 1$ V. Real 400 nm-long/200 nm-thick devise (*solid red lines*), equivalent 50 nm-long/22.5 nm-thick device (*dotted blue lines with cross*)

does not take into account the electron-electron (hole-hole) interactions, or electron-hole interactions. To be able to compute a Fermi energy shift, band diagrams are computed for $V_{ds} = 0$ V (*dotted curves*) and $V_{ds} = 1$V (*solid curves*), the latter corresponding to the experimental configuration and the former used as reference.

The pseudo-Fermi level E_F is plotted with symbols in each diagram (*line with open symbols* and *line with closed symbols* respectively for $V_{ds} = 0$ V and $V_{ds} = 1$V). It corresponds to the electrochemical potential which makes the link between the density of carriers and the electrostatic potential within the CNT by means of the CNT carrier statistics. As expected, E_F goes below the valence band for negative gate bias, confirming that conduction occurs thus through the holes, whereas it goes above the conduction band for positive gate bias where electrons are transported. Simulations with other CNT chiralities show similar behaviours (not shown).

4.2.2 Results and Discussion

Figures 4.6 to 4.8 show a summary of the dynamical sensor responses, measured at different temperatures under the conditions discussed in Sect. 4.2.1. The sensor responses were measured by monitoring source-drain (S-D) current while applying a constant source-drain bias voltage of 1.0 V. The sensor resistance was calculated as:

$$R_{\text{sensor}} = \frac{U_{\text{bias}}}{I_{\text{meas}}} \tag{4.3}$$

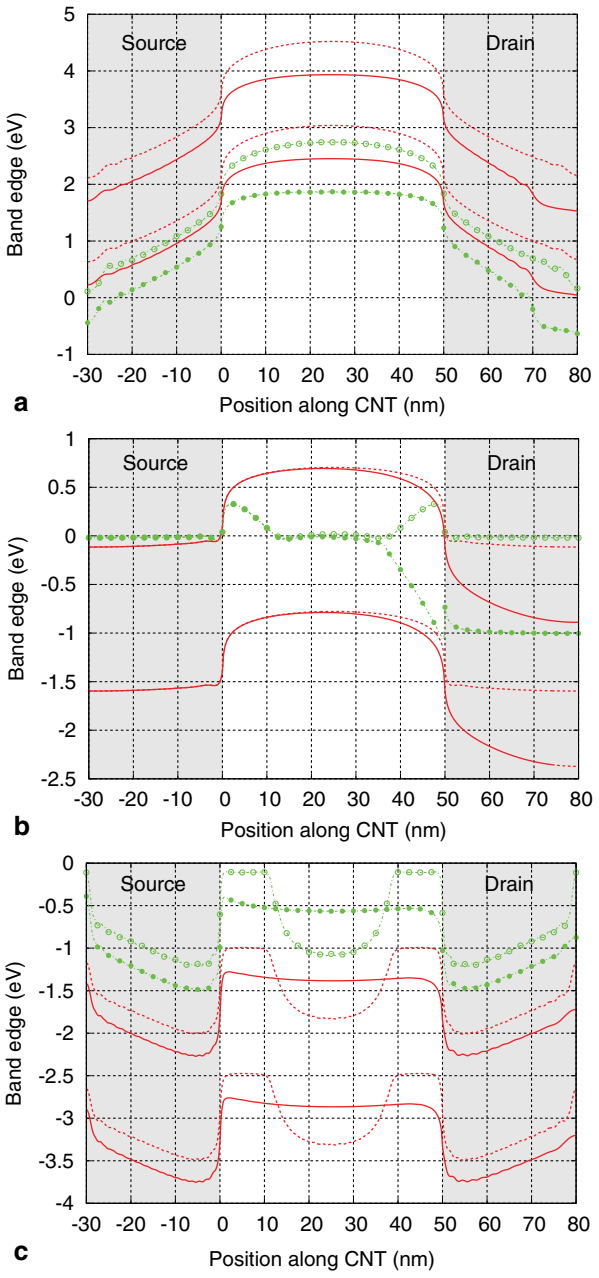


Fig. 4.5 Band diagrams of the equivalent device, with both electrons and holes taking into account. The conduction and valance bands are given for $V_{ds} = 1\,V$ (*solid red lines*) and $V_{ds} = 0\,V$ (*dotted red lines*) together with their corresponding pseudo-Fermi levels (in *line with open symbols* and *line with closed symbols* respectively). **a** $V_g = -5\,V$. **a** $V_g = 0\,V$. **a** $V_g = 5\,V$

where R_{sensor} is sensor resistance, U_{bias} is the used S-D bias of 1.0 V and I_{meas} is the measured current. The tested gas profiles were pre-mixed in a PC-controlled gas blender before introducing them into the measurement chamber, meaning a homogenous gas injection into chamber. Here with 5 min gas pulse we mean that the sensors were exposed to tested gas (concentration) for 5 min.

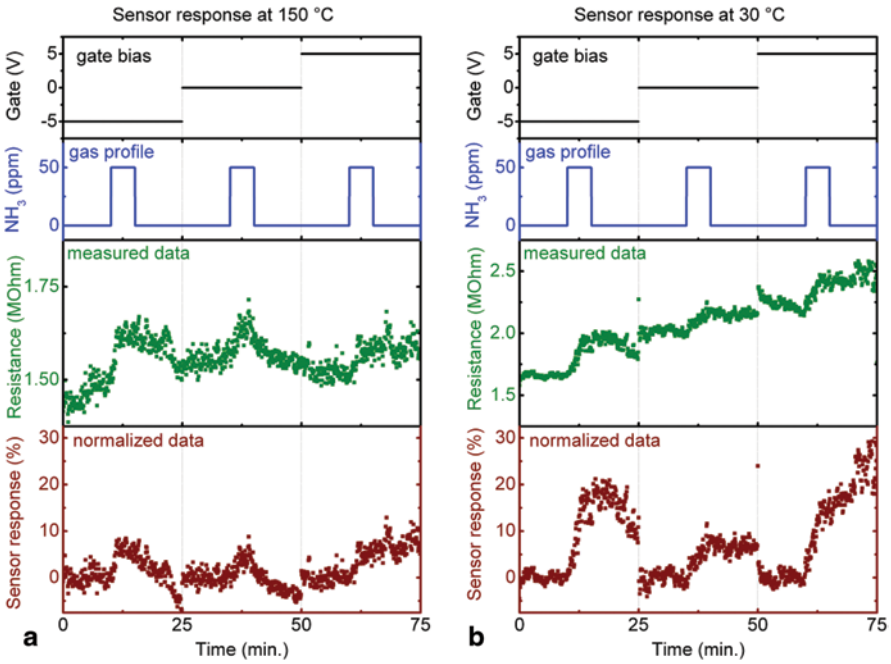


Fig. 4.6 Sensor responses for 50 ppm of NH_3. **a** at 150° C. **b** at 30° C. Gate voltage is changed step-wise at 25, 50 and 75 mn from -5 V to 0 V to +5 V, respectively. At both temperatures, the first pulse causes the largest relative response due to a cleaner sensor surface. Only small differences are seen with different gate voltages. The response at higher temperature is remarkably lower than at room temperature and sensor recovery is naturally better at higher temperature. Note, that at 30° C, the resistance value changes while the gate voltage varies

The graphs are organized vertically in four axes, showing applied gate voltage, gas profile, raw measurement data (resistance) and relative sensor response (SR). The horizontal axis is divided in three segments to clarify measurements performed with different gate voltage values. The relative sensor responses are calculated as:

$$SR = \frac{R_{\text{analyte}} - R_0}{R_0} \tag{4.4}$$

where SR is the relative sensor response, R_{analyte} is the resistance during a gas pulse and R_0 is the reference resistance, which is the linear fit of the resistance taken within the 10 min before the gas is introduced into the chamber (being individual for every gate voltage value and gas pulse).

In the measurements with NH_3 (50 ppm) and NO (50 ppm), Figs. 4.6 and 4.7 respectively, the changes in resistance (conductivity) are significant and realizable for practical gas sensing applications. Especially with NH_3, the tested gas concentration is very low. With both gases, the temperature plays a key role for gas detection.

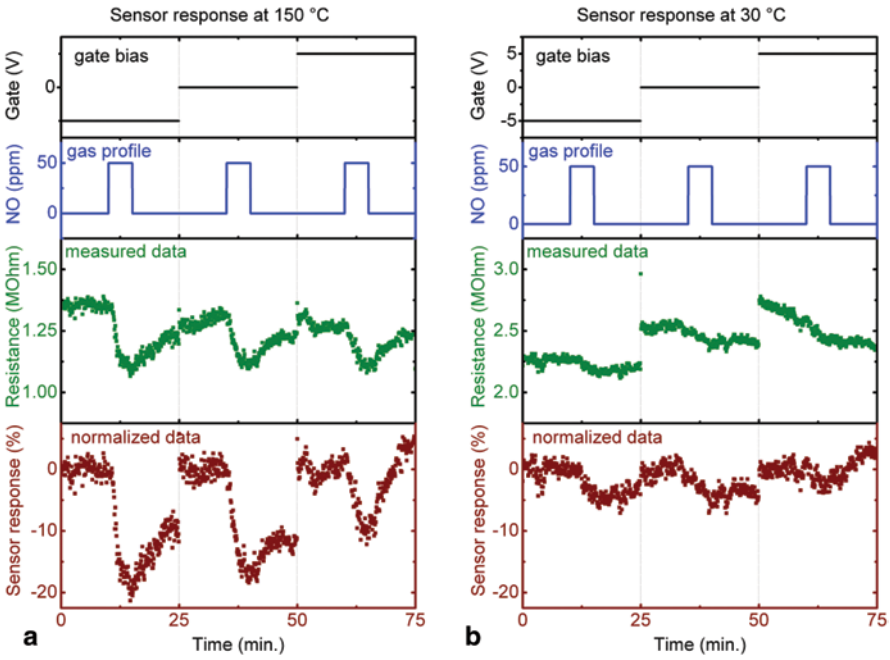


Fig. 4.7 Sensor responses for 50 ppm of NO. **a** at 150° C. **b** at 30° C. Sensor recovery is again better at higher temperature. At 150° C, only small differences in sensitivity are observed with a different gate bias. At 30° C, the sensor starts to drift at the end of measurement causing the last relative response to be very small

With NH_3, better detection (bigger sensor response) was obtained at 30° C while for NO; the sensitivity is increased at higher temperature. We expected to have different sensor responses with varying gate bias for our sensors. For NH_3 detection, changing gate bias did not have significant effect on sensors responses, even though with zero gate bias the sensor response was the smallest. For NO detection, small differences in sensitivities were observed with highest sensor response with negative gate bias and the smallest with positive gate bias. In all measurements the sensor drift was relative small except in NH_3 measurement at 30° C.

In the sensor memory studies shown on Fig. 4.8 (applying different analytes sequentially on same sensor) it was shown that for detecting NH_3, the previous measurements conducted with the sensor does not have an influence on the sensor response, i.e. sensor response is almost identical for the first NH_3 pulse no matter what have been the previous measured gas. Of course, for second NH_3 pulse, the imperfect sensor recovery resulted in lower responses. In case of sensing NO, the preceding NH_3 measurement decreases the sensitivity but the sensor recovery remains fast. As a whole, the repeatability of the sensor is high.

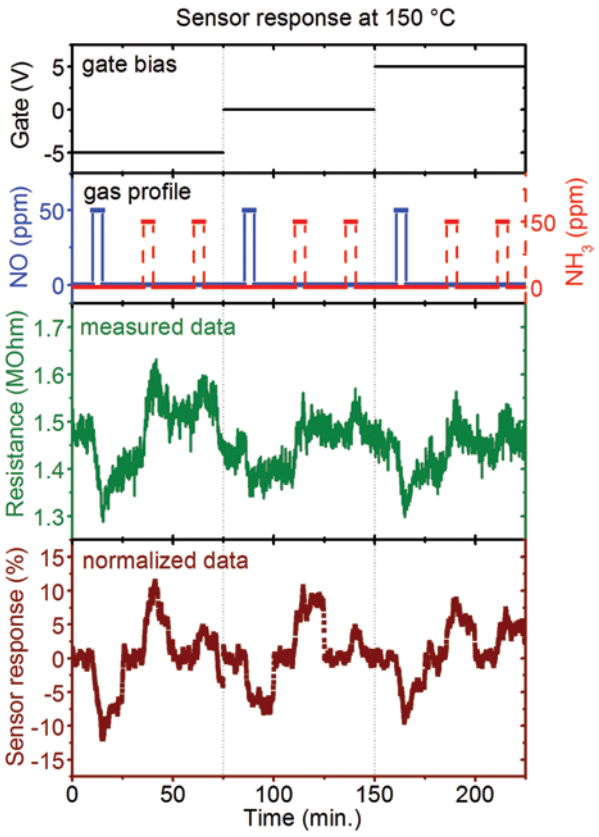


Fig. 4.8 Sensor responses for mixed 50 ppm pulses of NO and NH_3 at 150° C. Each pulse of NO (solid line) is followed by 2 pulses of NH_3 (*dashed line*)

4.2.2.1 Measurements of CO, H_2S, H_2 and O_2

Negligible detection is obtained with the CO (50 ppm), H_2S (100 ppm), H_2 (50 ppm) and O_2 (1 %) analytes at 150° C (results not shown here). For this temperature, the sensors showed a small response for H_2S at the very first gas pulse but the sensitivity became negligible afterwards. The reason for this phenomenon remains unclear, however it has been shown that H_2S can undergo oxidation in air and on activated carbon surfaces [43, 44], resulting in the formation of elemental sulphur. Moreover, in the presence of catalysts and water, SO_2 and H_2SO_4 might form on the surface of the sensor, thus poisoning it [45, 46].

4.2.2.2 Measurements of NH_3

When exposing the sensor to 5-minute-long 50 ppm NH_3 pulses (with a 20 minute recovery at 150° C between pulses), the channel resistance increases by 12 % during the first pulse (Fig. 4.6a), followed by a 8 % change during the second and 10 %

in the third pulse. At 30° C the change in channel resistance is bigger, being 20 % for the first pulse and 10 % for the second (Fig. 4.6b). The third pulse is causing the biggest relative sensor response, being 20 % during the pulse and even more after it. The difference between the first and second pulses indicates non-complete recovery of the sensor after the first gas pulse. Nevertheless, the first and the third gas pulses give almost identical responses at both temperatures and the second pulse the lowest response. As a whole, there are no significant differences in sensitivity with the three different gate voltage values, even though a 0 V gate bias corresponds to the smallest sensor responses.

4.2.2.3 Measurements of NO

Measuring the sensing device response using 50 ppm pulses of NO at 150° C, we observe a lowering of the resistance value of 20 % during the first pulse, of 17 % during the second, and 10 % during the third pulse (Fig. 4.7a). At 30° C, the resistance decreases by 7, 7 and 5 %, respectively (Fig. 4.7b).

4.2.2.4 Measurements with Sequential NO and NH_3 Pulses

In order to study the effect of different analytes measured sequentially on the same sensor (sometimes referred to as sensor memory), one pulse of 50 ppm of NO and two pulses of 50 ppm of NH_3 are introduced after each other into the chamber at 150° C. The insertion of three gas pulses are repeated with three different gate voltages (-5 V, 0 V and +5 V). After each 5-minute-long pulse, a 20-minute recovery time is applied. Because of the noisy measured signal and the opposite sensor responses with the two tested gas analytes, the relative sensor response curve is plotted using a 6-point running average to smooth the curve. All the relative responses are calculated using the preceding 10 mn time period with only carrier gas (synthetic air) in the chamber (Fig. 4.8).

At -5 V gate bias, the introduced NO gas decreases the resistance by 12 % (smaller than measured previously showing 20 % drop). The first NH_3 pulse increases resistance with 13 %, which is almost identical to the previously measured value (without preceding NO pulse). At 0 V gate bias, the sensor response for NO is -7 %, which is less than the previously measured value without NH_3 pulses. On the other hand, the first NH_3 pulse is giving the same response (10 %) as in the earlier experiment without NO. Moreover, the second pulse is similar as with a -5 V gate bias; in absolute, it is similar to the first pulse, but relatively smaller. At +5 V gate bias, sensor response for NO is -10 %, which is again smaller than that measured without NH_3. On the other hand, it is higher than with 0 V gate. At least in this case, varying the gate voltage has a contribution in the sensor sensitivity towards NO because when NH_3 was not involved, the sensitivity was equal with 0 V and +5 V gate biases. For NH_3 the situation is similar as with previous gate voltages (-5 V and 0 V); the first pulse is giving similar response as when NO is not involved and the response for the second pulse is smaller.

As a whole, this measurement reveals that the sensor response is similar to the first NH_3 pulse, no matter what is measured before. In other words, there is no sensor memory when measuring NH_3, i.e. the sensor sensitivity and repeatability towards NH_3 are maintained during repeated measurements with different gas analytes. On the other hand, when measuring NH_3, the sensor needs either higher temperature or longer recovery time at 150° C for a more complete desorption of gas molecules from the sensor surface. In the case of NO, sensor recovery is faster than with NH_3 but the sensitivity is decreased.

The results are in qualitative agreement with other works published in the literature on CNT-based gas sensors. Overall, oxidizing analytes or those undergoing oxidation in air during the measurement feature an increased electrical conductance of the channel, while the reducing moieties decrease the latter [47–59]. The absolute value of the sensor response shows considerable dependence on the sensor itself. Devices made of individual semiconducting nanotubes clearly outperform those made of films of tangled networks and show significant molecular gating effect [47]. In the case of nanotube networks or bundles, the sensor response is typically higher for the less conductive sensing layers [54, 55].

4.2.2.5 Simulation Results

The transport calculations give us direct access to the transmission $\mathfrak{T}(E)$ as a function of energy within the CNTs, which describes the conduction channels and their modifications, both due to the functionalization and to the presence of gases. The electrical conductance can be obtained by multiplying the transmission by the quantum of electrical conductance ($G_0 = 2e^2 / h$) [60].

Figure 4.9 shows the calculated transmissions obtained for metallic CNTs and semi-conducting CNTs. In the case of metallic CNTs (Fig. 4.9b), a gas is detected only when it chemisorbs on the nanotube, which results in the loss of one conduction channel at around a specific energy close to the Fermi level. Analyzing the response of a semi-conducting CNT is a much more complex task, as all molecules tend to bind stronger to it. However, the influence of the gas on the electrical conductance always shows up in a region below the Fermi energy (Fig. 4.9d), the position and extent of which depend on both the functional molecule and the gas involved. This means that, by properly tuning the bias and gate voltages, both the sensitivity and selectivity of the sensor could be optimized to specific gases.

While analysing transmission plots brings a lot of insight for each considered functional molecule, its practical interest quickly decreases when the number of possible configurations is large. In order to provide a global and synthetic view, we go back to a basic statement: the stronger a molecule binds, the larger it will open or close conduction channels in the CNT. We assume that the effect on the electrical transport properties of the CNTs can be expressed as a monotonic function of the binding energy of the functional molecules with the CNTs. The characteristics of this function will not be explored here, since SIESTA suffers from Basis Set Superposition Error (BSSE) [61] and achieves poor accuracy regarding binding energies. Instead we follow a statistical approach, in order to determine thresholds of interest

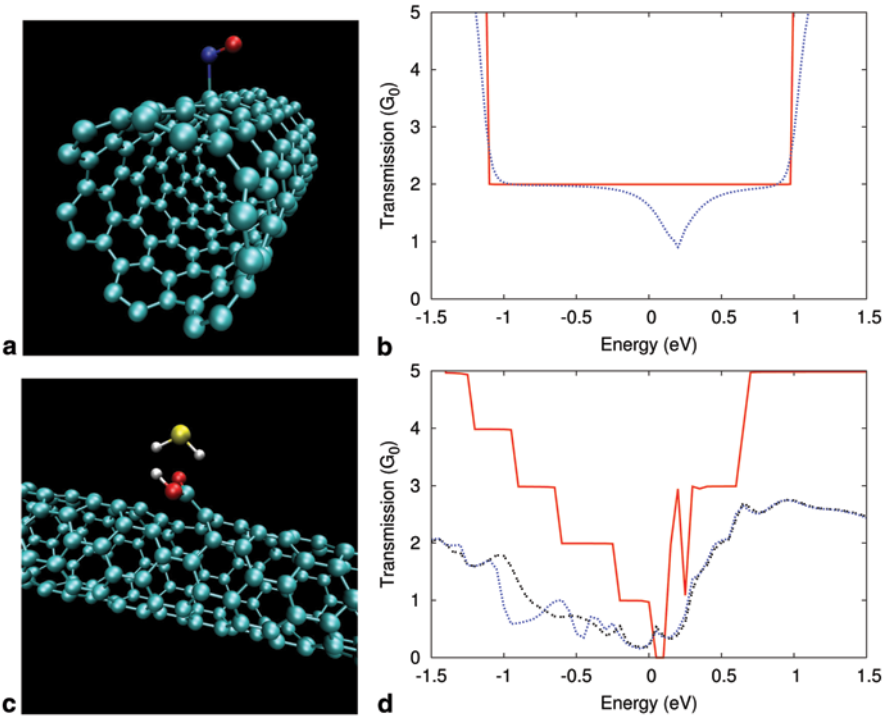


Fig. 4.9 Equilibrium geometries and transmission coefficients (in units of conductance) of simulated CNT. **a** equilibrium geometry of a perfect (6,6) metallic CNT exposed to NO. **b** corresponding transmission coefficients obtained for the perfect metallic CNT in vacuum (*solid red line*) and for the metallic CNT exposed to NO (*dotted blue line*). **c** equilibrium geometry of a 1-vacancy (7,0) semi-conducting CNT functionalized with COOH exposed to H_2S. **d** corresponding transmission coefficients obtained for the perfect semi-conducting CNT in vacuum (*solid red line*), for the functionalized CNT in vacuum (*dashed black line*) and for the functionalized CNT exposed to H_2S (*dotted blue line*)

for the transmission integral α_f^g from Eq. 4.2 corresponding to inert, physisorbing, and chemisorbing molecules. Figure 4.10 shows the value ranges of the transmission integrals for the 260 systems we have performed calculations on. Both semi-conducting and metallic CNTs display very similar behaviors, which is why we have grouped them together. Three regimes can be distinguished in Fig. 4.10a: inert and physisorbed molecules produce values of α below 0.20, strongly physisorbed ones range between 0.20 and 0.80, and chemisorbed ones reach above 1.00. In order to separate noise from physisorption, Fig. 4.10b focuses on the 0.00–0.20 range. By individually matching molecules and transmission plots with the histograms, we have determined that physisorbed molecules typically peak out in the 0.09–0.15 range. Thus, in practice, we consider that the use of transmission integrals provides good hints about successful detections when the empirically-determined condition is fulfilled:

$$0.10 < \alpha_f^g < 1.00 \tag{4.5}$$

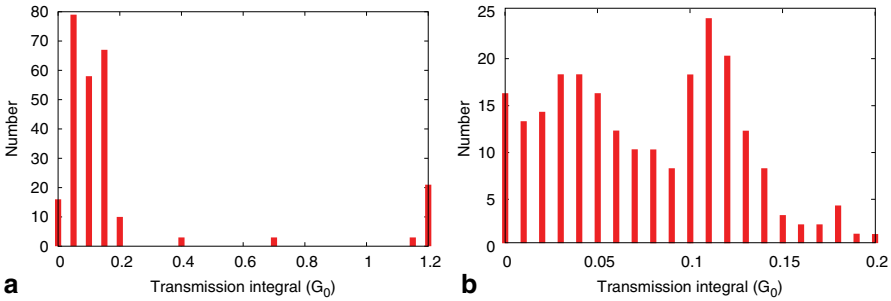


Fig. 4.10 Histograms of the values spanned by transmission integrals α_f^g over the 260 systems simulated. **a** full range. **b** low-value range. Each system corresponds to a CNT type/functional molecule/gas combination. Correlating the values of α_f^g and the binding of the functional molecules makes it possible to make categories and define intervals of interest for physisorption, chemisorption, and passivation

otherwise the difference between the curves is either not significant enough to obtain a reliable one-to-one correspondence between α_f^g and the curves themselves, or reflecting a too strong binding to achieve detection (passivation of the CNTs) and properly desorb the molecules. But as this simple technique tends to underestimate the real difference between the compared data sets (because of the positive and negative areas in the integrals), the fulfilling of condition (4.5) is already the sign of a good sensitivity. Moreover, since it is computationally cheap, this analysis can be repeated at will to validate the introduction of new systems into the database and/or the modification of computational parameters (e.g. basis sets and exchange-correlation functionals).

Tables 4.1 and 4.2 show the transmission integrals α_f^g for metallic CNTs and semi-conducting CNTs for two sets of molecules and gases, both for perfect and defected CNTs. Our results are fully consistent with experiments. As expected, the metallic tubes display a low sensitivity but have a good selectivity. Functionalizing them might slightly increase their sensitivity, but significantly degrades their selectivity. On the contrary, and not surprisingly, the semi-conducting tubes display a much higher sensitivity but a very poor selectivity. Functionalization decreases the sensitivity significantly, while opening the way to improving the selectivity. By exploring further functionalizations, it might indeed be possible to find the best compromises for a specific set of gases.

4.2.2.6 Fermi Energy Shifts

Figure 4.11 shows both the calculated drain-source current as a function of the gate voltage $I_{ds}(V_g)$ (Fig. 4.11a), as well as the Fermi energy shifts that can be deduced in the same conditions (Fig. 4.11b). The same results are obtained when including 4 subbands in the model instead of the 2 subbands taken into account here. The Fermi energy shifts are calculated by making the difference between the pseudo-Fermi level E_F obtained at any V_{ds} and V_{g}, and that provided by $V_{\mathrm{ds}} = V_{\mathrm{g}} = 0V$ (see Fig. 4.5).

Table 4.1 Theoretical evaluation of the sensitivity of metallic carbon nanotubes to different gases. The first column indicates the kind of CNT defect considered — "ideal" standing for no defect and "vacancy" corresponding to an axisymmetric vacancy, as well as the functional molecule under focus. The transmission integrals for selected gases are reported in the other columns. Values fulfilling condition 4.5 are highlighted in bold

Defect/Function	CH_4	CO	CO_2	H_2O	H_2S	NH_3	NO	NO_2
Ideal/none	0.00	0.00	0.00	−0.02	−0.03	−0.07	*−0.41*	*−0.67*
Ideal/NH_2	0.02	0.01	0.00	0.02	0.06	0.05	−0.02	0.03
Ideal/OH	0.02	0.01	0.03	0.06	0.03	*0.14*	0.06	*0.17*
Vacancy/none	0.02	−0.01	0.07	0.06	0.10	–	*−0.18*	0.08
Vacancy/CF_3	−0.01	−0.01	0.01	–	0.00	0.04	−0.00	0.00
Vacancy/COOH	*0.12*	0.10	*0.13*	*0.12*	0.10	*0.12*	*0.11*	*0.11*

Table 4.2 Theoretical evaluation of the sensitivities of semi-conducting carbon nanotubes to different gases. The first column indicates the kind of defect considered — "ideal" standing for no defect and "vacancy" corresponding to an axisymmetric vacancy, as well as the functional molecule under focus. The transmission integrals for selected gases are reported in the other columns. Values fulfilling condition 4.5 are highlighted in bold

Defect/Function	CO	H_2O	H_2S	N_2	NO	NO_2	O_2	SO_2	SO_3
Ideal/none	*−1.09*	*−1.16*	*−1.18*	*−1.15*	*−1.14*	*−1.21*	*−1.18*	*−1.16*	*−1.19*
Ideal/NH_2	−0.02	−0.01	−0.01	−0.00	−0.00	0.05	−0.00	0.02	0.05
Vacancy/COOH	−0.02	−0.05	*−0.14*	0.02	−0.06	*−0.12*	−0.05	−0.05	0.03

They aim at providing further practical information to the experimentalists. By combining these results with the locations of the maximum deviations on the transmission curves caused by the presence of a gas, we can extract ranges of interest for gate voltages. For instance, on Fig. 4.9, one can see that for the functionalized (7,0) CNT, the maximum deviations between the transmission curves with H_2S (blue dashed curve) and those without H_2S (black dotted curve) is obtained at E_m = -0.95 eV. Detection could thus be improved by shifting the Fermi level towards lower energies, in order to align this maximum with the middle of the detection window. From Fig. 4.11b, we can extract the gate voltages that will maximize the detection for this specific case: they will be located around 2 V. Thanks to this insight, and as soon as the modeled CNTs match the experimental setup, the experimentalists will be able to focus on specific intervals instead of having to sweep a broad range of gate voltages.

4.3 Thermal Transport in Carbon Nanotubes

As stated in the introduction, CNTs are excellent thermal conductors but, in practice, thermal properties are lost due to the presence defects and interfaces. In this section of the chapter, we address computationally the impact of defects and interfaces on thermal properties of CNTs [62]. To this end, we investigate the heat flow

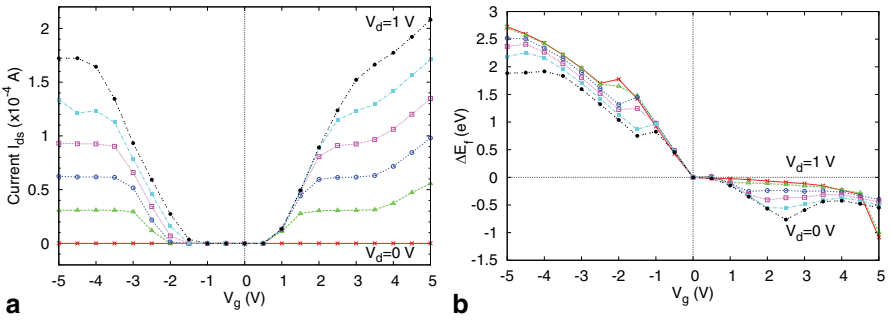


Fig. 4.11 **a** Source-drain current I_{ds} as a fuction of the gate voltage V_g for source-drain voltages V_{ds} ranging from 0 to 1 V. **b** Shifts of the pseudo Fermi energy level induced by the gate voltage of the device in the same condition as in **a** (*see text*)

at the CNT/air and CNT/water interfaces via non-equilibrium classical molecular dynamics (MD) simulations. In addition, we complete the description with an estimation of the impact of defects on CNT's thermal conductance using *First Principles* calculations.

4.3.1 Computational Details

We describe now the computational details of our classical MD simulations of a (10,10) CNT immersed in either air or water. The *First Principles* calculations on the defected CNTs are also described.

4.3.1.1 Air/CNT System

Classical MD simulations were performed using the large-scale atomic/molecular massively parallel simulator (LAMMPS) molecular dynamics code (version December 2011) from Sandia National Laboratories (Albuquerque, New Mexico) [63]. All MD simulations considered a single 40 nm long (10,10) CNT (6520 carbon atoms) immersed in a bath of air molecules (see setup depicted in Fig. 4.12) maintained at 1 atm or 10 atm to investigate the effect of pressure. The ratio of N_2/O_2 number of molecules was the one corresponding to normal air (0.78/0.22). In total, we used 1600 air molecules (1248 nitrogen and 352 oxygen molecules) for the 1 atm case and 10 times more for the 10 atm system. The system was placed in a cubic box of volume 400 $Å^3$. An ideal armchair (10,10) CNT has 40 carbon atoms per unit cell, a diameter of 13.562 Å, and translation period of length 2.461 Å. Thus, our system contains 163 unit cells along the nanotube axis, which is sufficient to minimize finite size effects on thermal transport properties. Periodic boundary conditions (PBCs) were imposed in all directions so that the CNT is essentially infinite in the axial z direction. The PBC eliminates the effects of phonon-boundary scattering.

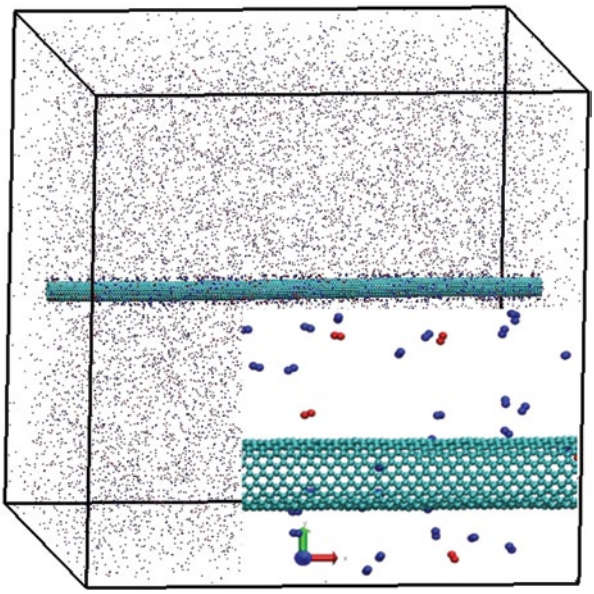


Fig. 4.12 Snapshot of an equilibrated 400 Å long (10,10) carbon nanotube with 16,000 air molecules at 10 atm. The figure shows a cylindric halo of air molecules around the nanotube. A close-up view is shown down to the right. Nitrogen (oxygen) atoms are depicted as blue (red) dots, while the nanotube is the horizontal cylindrical structure of cyan color

The x and y dimensions of the simulation cell were large enough so as to minimize the interaction of the CNT with its own periodic images in the lateral perpendicular directions.

The Adaptive Intermolecular Reactive Empirical Bond Order (AIREBO) [64] potential model was employed to approximate the bonded as well as the non-bonded Lennard-Jones dispersion-repulsion interactions in the CNT. The AIREBO force field is an improvement of the well-known Brenner potential. [65, 66]

The air molecules were considered explicitly as diatomic molecules. The covalent bond in nitrogen and oxygen molecules was described by a Morse-type potential:

$$V(r) = D\left[1 - \exp(-\alpha(r - r_{\text{eq}}))\right]^2, \tag{4.6}$$

with dissociation energy $D = 9.7597$ (5.1147) eV, equilibrium internuclear distance $r_{\text{eq}} = 1.098$ (1.207) Å, and $\alpha = 2.642$ (2.680) Å^{-1} for nitrogen (oxygen) molecule. The actual experimental molecular parameters are very close; namely, $D = 9.8$ (5.1) eV and $r_{\text{eq}} = 1.09$ (1.21) Å for nitrogen (oxygen) molecule.

The several intermolecular interactions were modeled with the usual 6–12 Lennard-Jones (LJ) potential:

$$V(r) = 4\varepsilon\left[\left(\frac{\sigma}{r}\right)^{12} - \left(\frac{\sigma}{r}\right)^{6}\right]. \tag{4.7}$$

The LJ parameters were taken from [67] and are collected in Table 4.3. The LJ cutoff radius was set to 14 Å in all our CNT/air MD simulations. Clearly, our modeling of

Table 4.3 Lennard-Jones parameters for the different intermolecular pair interactions in the CNT/air system

Intermolecular Pair	ϵ (eV)	σ (Å)
C-N	0.004 3666	3.54
C-O	0.004 8480	3.42
N-N	0.007 8877	3.68
O-O	0.009 7393	3.43
O-N	0.008 7636	3.56

the interaction between the CNT and air molecules is too simplified because it neglects, among other aspects, the different adsorption topologies (air molecule over C-C bond, atop a C atom, or at the center of an hexagon). Nonetheless, we remark that no consensus has been yet achieved on the adsorption energetics of these molecules on CNT [68]. For example, Arora and Sandler [69] used the LJ parameters $\varepsilon_{C\text{-}N} = 0.002\,8782$ eV, $\varepsilon_{C\text{-}O} = 0.003\,2401$ eV, $\sigma_{C\text{-}N} = 3.36$ Å and $\sigma_{C\text{-}O} = 3.19$ Å, which were obtained previously by Bojan and Steele [70] by fitting low coverage adsorption data of nitrogen and oxygen molecules on planar graphite sheets. Arab and coworkers [71] reported slightly different values for the modeling of the interaction between air molecules and CNT, namely, $\varepsilon_{C\text{-}N} = 0.002\,63$ eV, $\varepsilon_{C\text{-}O} = 0.003\,10$ eV, $\sigma_{C\text{-}N} = 3.44$ Å and $\sigma_{C\text{-}O} = 3.23$ Å.

Typically, our MD simulations usually start off with an energy minimization of the system to eliminate steric clashes. The system was then equilibrated at constant temperature (T = 300 K) and pressure (P = 1 atm and 10 atm were used here) for over 0.5 ns in the isotropic NPT ensemble. We employed the Nosé-Hoover thermostat and an isotropic barostat, with a coupling time constants of 10 and 100 fs, respectively. It was necessary to couple each subsystem (air and CNT) to a different thermostat to avoid non-equilibrium situations such as the coexistence of temperature gradients across the system.

After the NPT equilibration, the cell contracted slightly to the final volume of 395.048 Å^3 for the system at 10 atm and 395.106 Å^3 for 1 atm case. Next, the system was further relaxed in the NVT ensemble at 300 K for over 2 ns. This protocol ensured that the system was free of internal stresses and relaxed to their corresponding thermodynamic state. All MD simulations used a time step of 0.4 fs, which ensured a very stable time propagation of the system. To further check the stability of the MD simulations, a subsequent equilibration in the NVE (constant energy) ensemble was carried out to monitor the total energy and other thermodynamic variables (pressure, temperature) of the system. No drifts were observed during these NVE calculations as shown in Fig. 4.13.

4.3.1.2 Water/CNT System

All MD simulations of the water/CNT interface were also performed with the LAMMPS code [63]. For consistency with previous calculations on the CNTs, the carbon atoms were described using the AIREBO potential [64–66]. The SPC/Fw force field [72] was adopted in all simulations to model bulk liquid water in contact

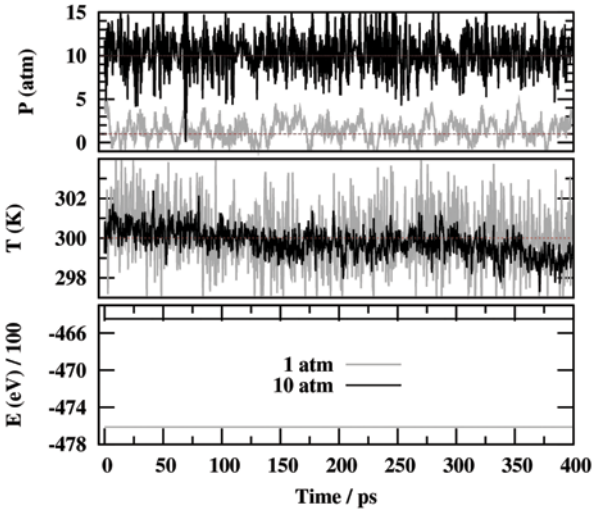


Fig. 4.13 Typical time evolution of the pressure (in atm), temperature (in Kelvin), and total energy (in eV) from our NVE/MD simulations of the 1 atm (*grey*) and 10 atm (*black*) equilibrated systems. All thermodynamic quantities remained stable (no drifts) during molecular dynamics simulations indicating that the systems are well equilibrated

with a (10,10) CNT. This flexible model is based on the well-known rigid simple point charge (SPC) model but reproduces better the liquid properties of bulk water. The SPC/Fw force field parameters are collected in Table 4.4.

The interaction between water molecules and the CNT was approximated via a simple Lennard-Jones 6–12 potential. The LJ parameters were taken from the graphite/water force field as reported in [70]. Due to the large variability in water/CNT Lennard-Jones parameters reported in the literature, here we investigated how a scaling of these parameters affects the interfacial heat transfer between water and the CNT. Namely, the functional form adopted is the following:

$$\begin{aligned} V(r;\lambda) &= 4\varepsilon_{\mathrm{OC}}(\lambda)\left[\left(\frac{\sigma_{\mathrm{OC}}(\lambda)}{r}\right)^{12} - \left(\frac{\sigma_{\mathrm{OC}}(\lambda)}{r}\right)^{6}\right] \\ &= 4\varepsilon_{\mathrm{OC}}\left[\left(\frac{\sigma_{\mathrm{OC}}}{r}\right)^{12} - \lambda\left(\frac{\sigma_{\mathrm{OC}}}{r}\right)^{6}\right] \end{aligned} \tag{4.8}$$

where $\sigma_{\mathrm{OC}}(\lambda) = \sigma_{\mathrm{OC}}/\lambda^{1/6}$ and $\varepsilon_{\mathrm{OC}}(\lambda) = \lambda^2\varepsilon_{\mathrm{OC}}$ are the scaled version of the original Lennard-Jones parameters. In this approach, values of λ greater (less) than 1 increase (diminish) linearly the relative importance of the attractive over the repulsive part, whereas a value of $\lambda = 1$ reverts to the original force field parameters [70]. In our calculations, we considered the values of 1.0 and 1.2 for λ. The resulting water/CNT Lennard-Jones parameters are collected in Table 4.5.

All Lennard-Jones interactions between different species were truncated at 12 Å, while the electrostatics due to water molecules was handled by the P^3M scheme [73] with a 12 Å cutoff in the short-range part. Separated thermostats were attached to

Table 4.4 The SPC/Fw force field parameters introduced in [72]. The functional form $K(d-d_{eq})^2$ was adopted for harmonic stretching (similarly for bending) interactions

d_{OH} (Å)	K_{OH} (kcal mol^{-1} Å^{-2})	θ_{HOH} (deg)	K_{HOH} (kcal mol^{-1} rad^{-2})	σ_{OO} (Å)	ε_{OO} (kcal mol^{-1})	q_H (e)	q_O (e)
1.012	529.581	113.24	37.95	3.165 492	0.155 4253	0.41	−0.82

Table 4.5 The SPC/Fw water-carbon nanotube force field parameters as a function of parameter λ [72]

λ	σ_{OC} (Å)	ε_{OC} (kcal . mol^{-1})
1.0	3.1900	0.074 928 2982
1.2	3.0945	0.107 896 7495

the water molecules and nanotube subsystems to facilitate the temperature equilibration. The whole system was equilibrated at 300 K and 1 atm. A conservative time step of 0.2 fs was adopted in all MD simulations.

The molecular dynamics (MD) simulations started with the equilibration of a cubic box of volume 97.61 Å^3 of 30,916 SPC/Fw water molecules at 300 K and 1 atm. The average density from our isobaric-isothermal (NPT) MD simulations was 1.008 g cm^{-1}, which is in good agreement with the reported value (1.012±0.016 g cm^{-1}) [72]. After several nanoseconds of equilibration, we took the final configuration and drilled a cylindrical cavity to insert a (10,10) CNT such that all water molecules are exterior to the latter. The final system contained 29,097 water molecules around a CNT of 1,640 carbon atoms (41 unit cells) oriented along the periodic *z* direction. Equilibration was assessed by visual inspection of the time evolution of several thermodynamic quantities during MD simulations in the microcanonical (NVE) ensemble. No drifts were observed in the calculated quantities as shown in Fig. 4.14.

4.3.1.3 CNT with Defects

Pristine carbon nanotubes (CNTs) are predicted to be excellent thermal conductors. However, this ideal picture is limited by the presence of defects [48]. These defects, which are always present in realistic CNTs have deleterious effects on the overall thermal conductance of CNT. It is possibly to study the impact of these defects in the CNT's thermal conductance through *First Principles* calculations. This can be done in two steps: (i) First, the formation energy of the different defects is calculated through Density Functional Theory (DFT). This allows us to know their relative abundance. (ii) Later on, the phonon scattering due to the defects is calculated combining Non-Equilibrium Green's Function (NEGF) formalism with Brenner potential, using a Divide and Conquer strategy [74]. We remark that more sophisticated approaches, which include the effect of anharmonicity and phonon-phonon interactions, can be applied to study the thermal conductivity [75]. However, those are computationally heavier and, in practice, unaffordable for the system sizes considered here.

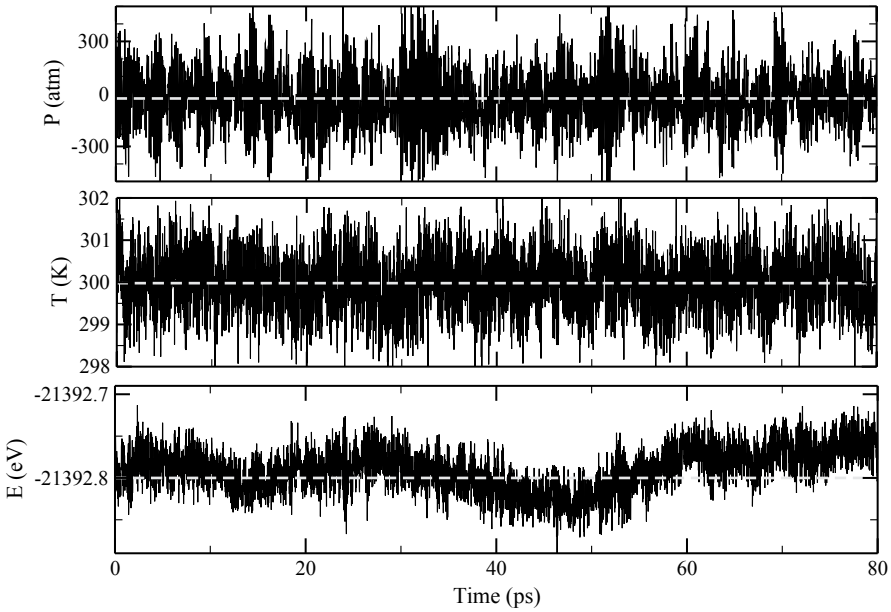


Fig. 4.14 Instantaneous values of the temperature, internal pressure, and total energy during constant energy (NVE ensemble) molecular dynamics simulations of the SPC/Fw water-nanotube system. No drifts are observed and the thermodynamic properties remained stable and fluctuating around target values during the simulation

4.3.2 Results and Discussion

4.3.2.1 The CNT/Air Interface

A snapshot of a typical configuration of the CNT/air system is given in Fig. 4.12. Equilibrated snapshots were taken for subsequent production runs to characterize the static and dynamic properties of the system. Visual inspection of equilibrated configurations (for a snapshot, see Fig. 4.12) reveals the presence of a concentric halo of air molecules around the CNT. First, we characterize the strength of the coupling between the CNT and air molecules via an analysis of the vibrational density of states. Later, non-equilibrium molecular dynamics (NEMD) simulations are presented to study the transport of heat due to artificial gradients imposed to the system.

4.3.2.2 Dynamical Properties of the CNT/Air System

The vibrational density of states (VDOS) was computed to measure the degree of coupling between the CNT and air molecules and is shown in Fig. 4.15. In general,

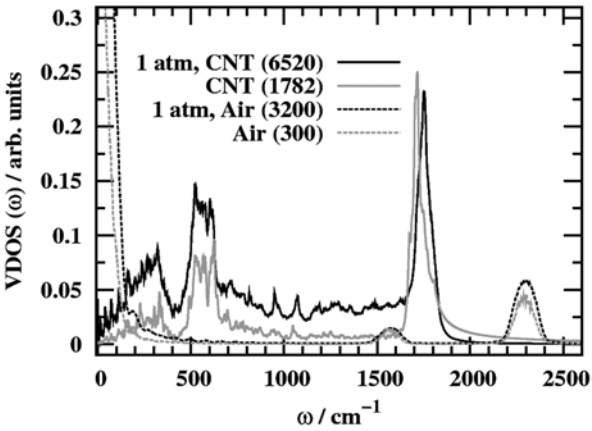


Fig. 4.15 Vibrational density of states (VDOS) of a 400 Å long (10,10) CNT and 1600 air molecules at 1 atm. In grey, it is shown the VDOS of a smaller system, a 100 Å long (10,10) CNT immersed in 150 air molecules. In both cases, only oxygen molecules show significant coupling at high frequencies with the vibrations of the CNT, which occurs in the spectral region of about 1600 cm^{-1}. The number of atoms is indicated in parentheses

a large overlap between vibrational modes is associated with a more efficient heat transfer between them, while a mismatch in vibrational modes usually implies the converse. The vibrational density of states (VDOS) or power spectrum was computed from the Fourier transform,

$$\mathrm{VDOS}(\omega) = \int \exp(-\mathrm{i}\omega t)\, \mathrm{C_{vv}}(t)\, dt, \tag{4.9}$$

of the normalized velocity autocorrelation function:

$$\mathrm{C}_{vv}(t) = (1/\mathrm{N}) \sum_{i=1}^{\mathrm{N}} \langle \mathbf{v}_i(0) \cdot \mathbf{v}_i(t) \rangle / \langle \mathbf{v}_i(0) \cdot \mathbf{v}_i(0) \rangle, \tag{4.10}$$

where N is the number of atoms. Due to the large volume of data generated only the system at 1 atm was analyzed. Figure 4.15 also shows the VDOS of a smaller system (a 100 Å long (10,10) CNT immersed in 150 air molecules) and confirms that the conclusions remain the same. From Fig. 4.15, both nitrogen and oxygen are expected to couple with the acoustic modes of the CNT. At high frequencies, however, oxygen gas couples to the so-called *G mode* of the CNT (1600 cm^{-1}) better than nitrogen molecules, whose stretching vibrations fall outside the spectral range of CNT. The calculated fundamental stretching frequencies of isolated nitrogen and oxygen molecules are 2238.16 and 1504.37 cm^{-1}, respectively, which agree well with the experimental values of 2358 (1580) cm^{-1} for nitrogen (oxygen).

4.3.2.3 Non-Equilibrium Molecular Dynamics Simulations of the CNT/Air System

After equilibration, thermal transport properties were computed by introducing an artificial temperature gradient across the system. To this end, we have performed

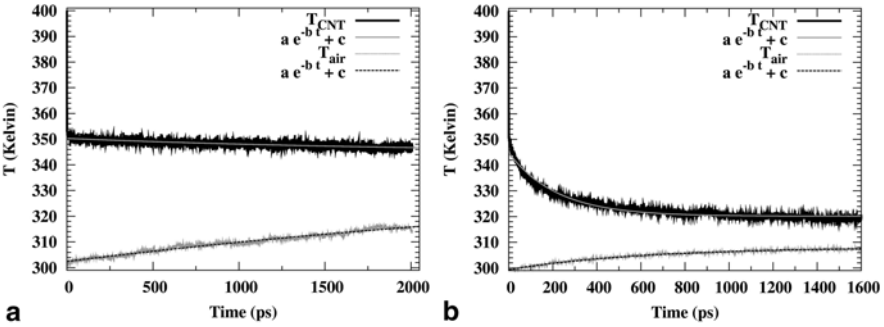


Fig. 4.16 Time evolution of the temperature of a 400 Å long (10,10) CNT (initially heated at 400 K) and air system (initially at 300 K) at different total pressures. **a** at 1 atm. **b** at 10 atm. The curves are the average over 10 independent MD trajectories. Fits to the Newton cooling-heating law Eq. 4.11 are shown by the grey solid and black dashed lines

temperature jump MD simulations in which we suddenly raised the temperature of the CNT in an otherwise equilibrated system. Then, we followed the time evolution of each subsystem temperature in the microcanonical (NVE) ensemble. More specifically, the method consists of imposing a sudden rescaling of the velocities of carbon atom in the CNT to match the preset temperature (400 K). Then, we allow the system to thermally relax at constant energy and volume conditions (NVE ensemble). We monitor the temporal temperature profile of the air molecules and CNT to understand the time evolution of the heat transfer. This setup actually resembles the experimental conditions, where the heat is dissipated from a source to the environment.

Figure 4.16 shows the temperature decay of an initially heated CNT at 400 K embedded in a bath of air molecules at 300 K at 1 atm (Fig. 4.16a) and 10 atm (Fig. 4.16b). The displayed curves are the average over 10 independent MD trajectories that started from totally uncorrelated and equilibrated configurations. The total simulation time was 1.6 ns for the 10 atm system (Fig. 4.16b) to reach steady state and up to 2 ns for the 1 atm case (Fig. 4.16a).

From Fig. 4.16, it is clear that larger pressures favor faster cooling of the initially heated CNT. This result is not surprising since the impingement rate r of an ideal gas on a surface is linearly proportional to the pressure P according to the expression $r = \mathrm{P} / \sqrt{2\pi m k_\mathrm{B} \mathrm{T}}$, where m is the mass of the gas molecule and k_B is the Boltzmann constant.

To be more quantitative, the time evolution of the temperature of each subsystems was fitted to a Newton-like cooling-heating law equation,

$$\mathrm{T}(t)=\mathrm{T}_\infty+(\mathrm{T}_0-\mathrm{T}_\infty)\exp(-t/\tau), \tag{4.11}$$

where T_∞ is the steady-state temperature (once all transients die off), T_0 is the initial temperature, and τ is a relaxation time constant. Thus, a larger relaxation time

Table 4.6 Fitting parameters according to Newton's cooling law Eq. 4.11 for the time evolution of the temperature shown in Fig. 4.16

Subsystem	Pressure	$(T_0 - T_\infty)$ (K)	T_∞ (K)	τ^{-1} (1/ps)
CNT	10 atm	24.615	320.142	0.004 535
CNT	1 atm	5.695	344.608	0.000 495
AIR	10 atm	−8.724	308.054	0.001 654
AIR	1 atm	−35.493	337.924	0.000 236

τ implies a slower decay to the final temperature T_∞. The fitted parameters are collected in Table 4.6. The inverse time constant can be expressed mathematically as

$$\frac{1}{\tau} = \frac{Ah}{mC_P}, \tag{4.12}$$

where A is the superficial area of contact, C_P is the specific heat at constant pressure, m is the mass of the nanotube, h is the coefficient of heat transfer between the CNT and the air (power per unit of area and temperature difference). The ratio,

$$\tau^{-1}(10\text{atm}) / \tau^{-1}(1\text{atm}) = h(10\text{atm}) / h(1\text{atm}) \approx 9.15, \tag{4.13}$$

allows us to cancel several unknowns and affords a quantitative measure of the difference in efficiency with respect to air pressure. Thus, it is estimated that at 10 atm, the heat transfer between the nanotube and the air is about 9 times more efficient than at 1 atm, in agreement with the ideal gas law prediction.

4.3.2.4 Non-Equilibrium Molecular Dynamics Simulations of the CNT/Water System

A snapshot of a typical equilibrated CNT/water configuration for the scale parameter of the used Lennard-Jones functional of Eq. 4.8 taken to $\lambda = 1.0$ is shown in Fig. 4.17. Similar MD calculations were repeated for $\lambda = 1.2$ to gauge the impact of the water/CNT force field parameters in the interfacial heat transfer. These simulations proceed similarly as in the CNT/air case. We performed temperature jump MD simulations in which the temperature of the CNT was suddenly raised to 400 K in an otherwise equilibrated system at 300 K and 1 atm. The temperature jump of the CNT was achieved by a simple rescaling of the carbon velocities to match the target value (400 K) at the beginning of the non-equilibrium NVE/MD simulation. We monitored the cooling of the nanotube as time progresses during this simulation. An average over five independent trajectories is shown in Fig. 4.18a–b for values of $\lambda = 1.0$ and 1.2, respectively. As expected, the presence of a condensed phase as water provides a more efficient way of cooling than the previously studied case of air. In the latter case, the CNT did not cool down to ambient temperature even after 1.6 ns, whereas for the case of water the relaxation

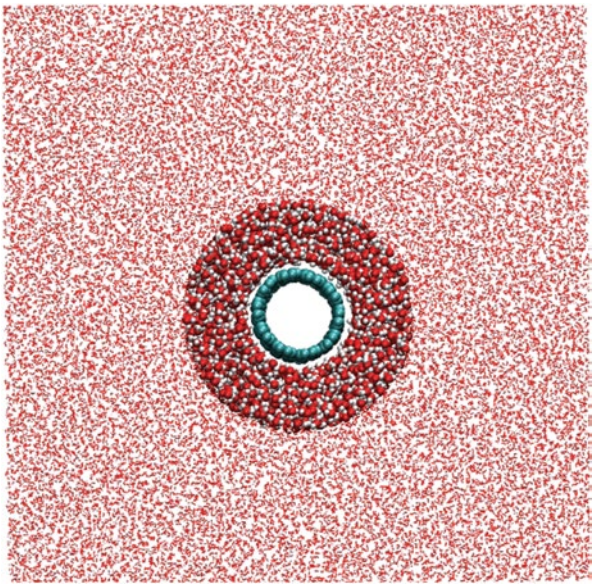


Fig. 4.17 Snapshot of a typical equilibrated configuration of the SPC/Fw water/CNT system. Oxygen (*hydrogen*) atoms are depicted as red (*white*) spheres, while carbon atoms are the cyan spheres. View along the nanotube axis. A cylindrical shell of water molecules around the nanotube was colored as CPK for clarity

just took about 200 ps. Figure 4.18 clearly shows that a greater water/CNT coupling leads to a better heat transfer. The water bath hardly changed its temperature due to the large heat capacity of water and the presence of large number of these molecules.

We fitted the temperature decay of the nanotube according to the Newtons cooling law Eq. 4.11. The fitted parameters are displayed in Table 4.7.

As explained before, a large value of the parameter τ^{-1} is related to a more efficient heat transfer. The table shows that a larger coupling between CNT/water results in a more effective heat transfer. Taking the ratio between τ^{-1} values yields a quantitative measure of the difference in heat transfer between the two MD simulations. The cooling of the CNT in water with λ value of 1.2 takes place about 1.42 times faster than with $\lambda = 1.0$. Finally, we note that the fitted parameters for τ^{-1} (Table 4.7) are much greater than the ones corresponding to the CNT/air interface (Table 4.6). This results underlines the superior efficiency of water as a cooling agent over the air when dissipating heat from CNTs.

4.3.2.5 Impact of CNT Defects on Thermal Transport

As mentioned before, real CNTs have defects which limit the intrinsic thermal conductivity of these nanostructures. To investigate how defects affect the thermal properties of CNTs, first, we calculated their formation energy in pristine CNTs to estimate probability of ocurrance; and then we estimate computationally the reduction in thermal conductance due to defects.

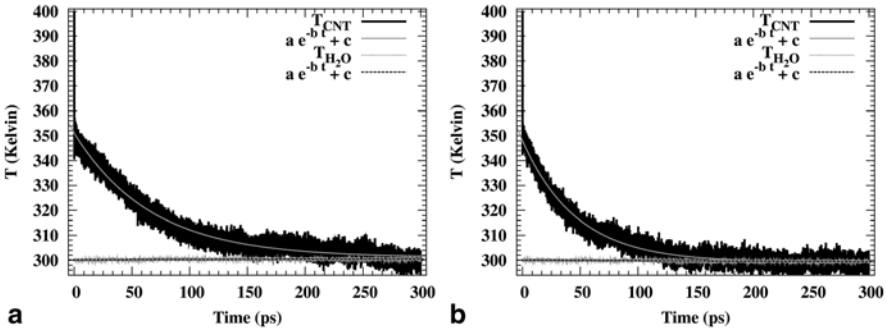


Fig. 4.18 Time evolution of the temperature of carbon nanotube (CNT in legend) and water bath in a non-equilibrium NVE/MD simulations. The curves are the average over five independent trajectories. The plot also shows the fitted curve according to the Newton's cooling law (see text). **a** the value of coupling CNT/water parameter was $\lambda = 1.0$. **b** coupling CNT/water parameter was $\lambda = 1.2$

Table 4.7 Fitted parameters for different values of the parameter λ of the temperature decay shown in Fig. 4.18 of the (10,10) carbon nanotube surrounded by SPC/Fw water molecules according to Newton's cooling law of Eq. 4.11

λ	$(T_0 - T_\infty)$ (K)	τ^{-1} (ps^{-1})	T_∞ (K)
1.0	49.899	0.015 0851	301.134
1.2	48.712	0.021 4132	299.248

In our DFT analysis of the formation energies of defects in CNTs we considered three of the most common defects in CNTs, which have been extensively studied in the literature [76–82]: (i) Stone-Wales (SW), (ii) Mono-vacancies (MV), and (iii) Di-vacancies (DV). In all cases, the defects can be oriented in two possible configurations (parallel and perpendicular to the CNTs axis, see Fig. 4.19). Moreover, an additional type of di-vacancy structure, with a bigger reconstruction, is also studied (see also Fig. 4.19).

It is surprising that the DVs are more stable than MVs (see Fig. 4.20). However, in DVs, all the C atoms are three-fold coordinated, whereas in mono-vacancies, one of the C atoms is two-fold coordinated, making the structures rather unstable. It is observed a general trend: The formation energies increase upon the size of the CNT increase. This is due to the curvature effects (more important in small radii CNTs), that stabilize the defects. In the case of the zigzag CNTs, this is not strictly true and an oscillatory behavior can be observed. This is because not all the CNTs are metallic—only the (3*p*,0) are—whereas all the armchair ones are. All these findings are in good agreement with previous works in the literature [18, 76–78, 80–82].

The main conclusion of this part is that the di-vacancies and Stone-Wales are the most stable defects on CNTs. However, all the studied defects have small enough formation energy so that all could be created during the growing process of CNT, that usually takes place at high temperatures. Regarding the scattering that these defects produce in the phonon transport in CNTs, firstly we calculate the thermal

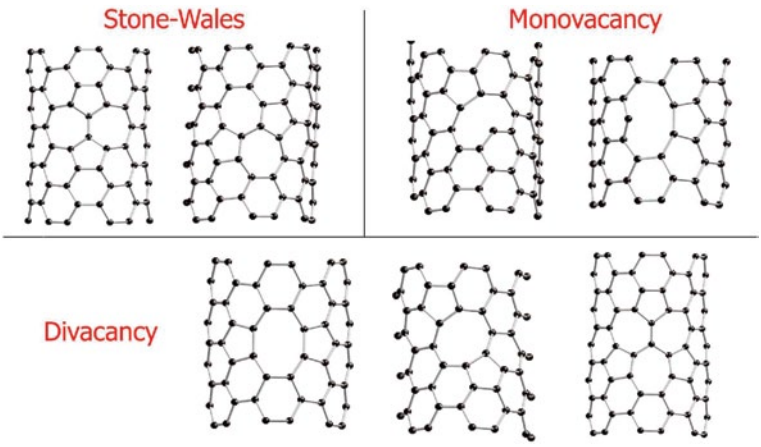


Fig. 4.19 The seven different defects studied in this chapter (in armchair CNTs). Bottom-Right: The 5-7-5-7-5-7 more reconstructed divacancy

conductance of the pristine CNTs at room temperature (see Fig. 4.21a). As salient features, we find that the conductance does not depend on the chirality of the CNTs and scales linearly with its diameter (i.e. the thermal conductance is an intrinsic property of CNTs and is proportional to the number of C atoms of the CNT). When a defect is introduced in the CNT, a scattering process occurs and the thermal conductance is reduced by a factor F with respect to the pristine CNT. The results for the zigzag CNTs are shown in Fig. 4.21b (similar trends are obtained for armchair CNTs). Obviously the impact of a defect decreases as the radius of the CNT increases. This is because phonons can find alternative pathways to propagate easier in wider CNTs rather than in narrower ones. The impact of all investigated defects on CNT's thermal conductance is very similar, with the exception of the reconstructed di-vacancy, which reduces the conductance 20–30 %. We remark that for the (7,0) CNT with a Stone-Wales defect, our reduction factor (0.81) agrees quite well with a previous NEGF calculation (0.82) [83].

Finally, with all these data, we can use the Divide and Conquer strategy to investigate how the thermal conductivity decays with the concentration of impurities. Figure 4.22 shows the results for SWs and DVs in a zigzag (7,0) nanotube as an example. The results are very similar for other defects and CNTs.

4.4 Concluding remarks

In summary, we have presented a fundamental exploration of the properties of CNT-based gas sensors and thermal conductors, both at the experimental and theoretical levels. We have provided a methodology to perform a computational screening of functionalized CNTs for gas sensing and described the interfacial thermal dynamics of CNTs in contact with air or water.

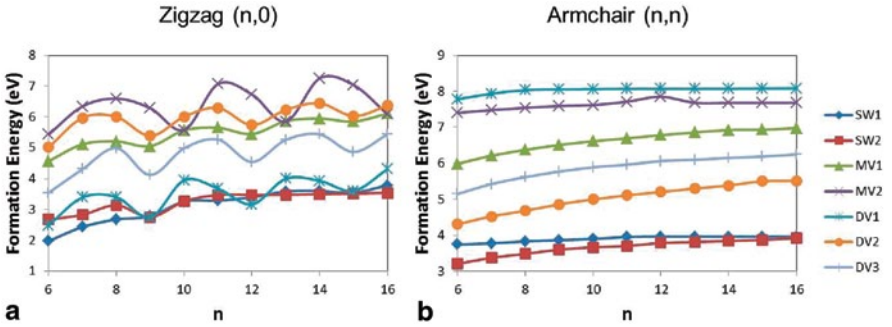


Fig. 4.20 Formation energies for different types of defects. **a** in zigzag CNTs. **b** in armchair CNTs

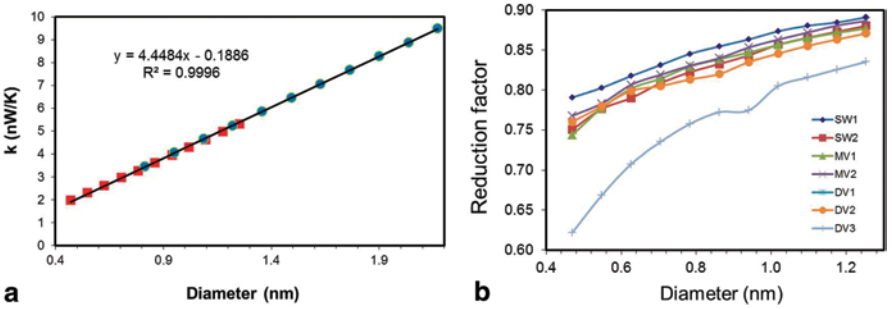


Fig. 4.21 **a** Thermal conductance of CNTs *vs.* their diameter. The data for armchair (*blue circles*) and zigzag (*red squares*) CNTs are shown all together since the conductance does not depend on the chirality. **b** Reduction factors F for the different defects in zigzag CNT as a function of their radius

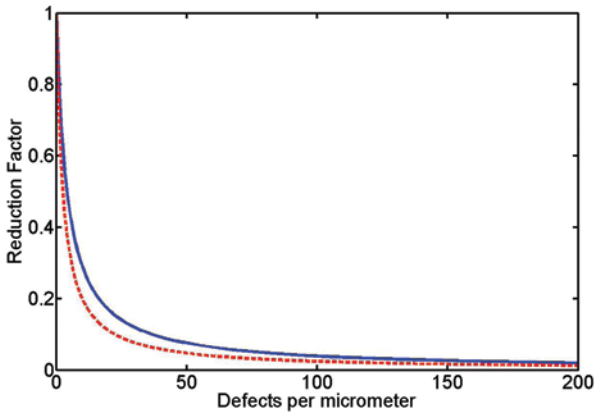


Fig. 4.22 Reduction factor by a SW (*solid line*) and DV (*dashed line*) defects in a zigzag (7,0) CNT *vs.* the concentration of defects

Regarding gas sensing, we can conclude that, at the experimental level, the sensitivities of the sensors for the investigated analytes are limited in terms of absolute change of channel resistivity and gate effect. The following conditions are essential to achieve improved sensor performance:

1. CNT films show non-linear behaviors, i.e. are diluted networks. Positive gate is applied, i.e. a larger Schottky barrier is seen by the carriers to inject from the semiconducting nanotubes to the metallic ones. This is confirmed by the theoretical results, which additionally point to reduced intervals of gate voltages.
2. Low channel bias is applied, since only a small fraction of the carriers can pass the barrier and any local modulation of the field (gas absorption on the CNTs nearby the junctions) can induce large relative changes in the channel current.
3. Increasing the temperature of the sensor with an integrated heater. Actually, a small increase (up to +50° C) may be needed to improve significantly the sensitivity (in the case of NO).
4. The role of the buffer gas is crucial as it might react with the analyte. NO in an Ar buffer induced insignificant change of any sensor parameter, while in a synthetic air buffer NO oxidizes to NO_2, bringing the detection limit lower than 1 ppm.

The main challenge is to find molecules that do not passivate the CNTs, and this is where calculations can bring significant contributions. From the theoretical point of view, the combination of DFT and NEGF formalisms allow for a qualitatively correct description of the intrinsic transport properties of the CNT-based sensors. To be fully quantitative, one has to span a representative sample of the various configurations encountered in real systems, including varying CNT chiralities, defect densities, rate of functionalization, and the surrounding environment of each CNT. In any case, the calculations have to take the techniques used to produce the sensor into account. In order to efficiently speed-up the selection of functional molecules, the theoretical and experimental works have to be performed in tight collaboration, since the calculation results have to reflect the experimental choices, in addition to be accurate. With the advent of higher computing power and the currently progressing integration of the available software, it will be possible to address this kind of devices more and more accurately and get much closer to the experimental conditions. In the near future, the theoretical study of multiple nanotubes at once in contact with a mix of gases will become accessible at the quantum level, while a better and faster processing of the signal will occur at the experimental level.

CNTs are known to be excellent thermal conductors and represent, therefore, ideal candidates for micro-electronics cooling. In general, the presence of an interface results in a degradation of the thermal transfer properties of CNT. Extensive classical molecular dynamics simulations have been carried out to understand the interfacial transfer of heat between a CNT and the air. To this end, we investigated computationally a 400 Å long (10,10) CNT immersed in a large bath of explicit air molecules. We monitored the time evolution of the temperature of each subsystem under non-equilibrium conditions. The unit cell was filled with varying amounts of air molecules (a total of 1600 and up to 16000 air molecules were used) to elucidate the effect of pressure on the heat transfer across the interface. We have demonstrat-

ed that higher air pressures lead to more efficient heat dissipation from the CNT. From the analysis of the vibrational density of states, we conjecture that oxygen molecules may be more effective in such dissipation process as they exhibit strong overlap with the vibrations of the nanotube (*G-band mode*). Finally, from temperature-jump molecular dynamics simulations, we estimate that the system at 10 atm is about 9 times more efficient at dissipating heat than the system at 1 atm, which is consistent with the ideal gas behavior. The relation between efficiency and pressure was found to be approximately linear within the investigated pressures. As for the CNT/water interface, our molecular dynamics simulations confirm that water is a more efficient cooling agent than air. The cooling efficiency in presence of water is significantly greater than in presence of air, easily by one order of magnitude. We have shown that larger Lennard-Jones coupling between water and CNT subsystems favors a more efficient heat dissipation of the CNT to the water. In summary, our molecular dynamics simulations have convincingly shown the role of gas pressure on heat dissipation from CNT and the effect of the coupling between CNT and water on the overall thermal transport properties.

The current work has focused on the atomic scale, in order to examine the very mechanisms of the physical and chemical processes involved in gas detection and heat transfer. The comparison of the experimental and theoretical results show that the individual contributions of the basic components—in this case the CNTs—play an essential role in the qualitative understanding of these processes, and account for a significant part of the quantitative results. They constitute a solid base for the elaboration of larger-scale models, which will bring forward this understanding to other important aspects of the devices: collective outcome when having CNT networks, contacts with electrodes, mixing of CNT chiralities and diameters, et c. In the near future, by growing sufficiently comprehensive databases, it might be possible to evidence general trends that will make it easier to manufacture, among other things, nanoscale CNT-based sensors and cooling systems. In parallel, the currently ongoing progress in understanding the properties of graphene might as well bring a growing body of very useful information.

Acknowledgement We are grateful to Profs. S. Roth and V. Skakalova for very interesting discussions and helpful insights. The SGI/IZO-SGIker UPV/EHU (Arina cluster), supported by the Development and Innovation - Fondo Social Europeo, MCyT and Basque Government, is gratefully acknowledged for generous allocation of computational resources and high-quality user support, as well as the Red Española de Supercomputación. Y.P. and J.M.G.L. would like to thank the group of K. Thygesen for providing computational resources and assistance in running the transport code of ASE. We acknowledge financial support from the European Union through the FP7 project: "Thermal management with carbon nanotube architectures" (THEMA-CNT, contract number 228539), the European Research Council Advanced Grant DYNamo (ERC-2010-AdG - 267374) and European Commission projects CRONOS (Grant number 280879-2 CRONOS CP-FP7) and POCAONTAS (FP7-PEOPLE-2012-ITN.Project number 316633). We also received financial support from the Spanish Grants FIS2011-65702-C02-01 and PIB2010US-00652, as well as from the Ikerbasque foundation. Y.P. and A.R. acknowledge funding by the Spanish MEC (FIS2007-65702-C02-01), "Grupos Consolidados UPV/EHU del Gobierno Vasco" (IT-319-07 & IT578-13). Y.P. also acknowledges a contract funded by MICINN (PTA2008-0982-I) and ETORTEK-inanoGUNE (2009–2011).

References

1. Ao Z, Jiang Q, Li S (2012) Al-doped graphene for ultrasensitive gas detection. Momentum Press, Highland Park. doi:10.5643/9781606503140
2. Muñoz E, Lu J, Yakobson BI (2010) Nano Lett 10(5):1652. doi:10.1021/nl904206d
3. Qiu X (2011) Gas sensors: developments, efficacy and safety. Safety and risk in society series. Nova Science Pub Incorporated
4. Fam D, Palaniappan A, Tok A, Liedberg B, Moochhala S (2011) Sens Actuators B Chem 157(1):1. doi:10.1016/j.snb.2011.03.040
5. Charlier JC (2002) Acc Chem Res 35(12):1063. doi:10.1021/ar010166k
6. Ayala P, Miyata Y, De Blauwe K, Shiozawa H, Feng Y, Yanagi K, Kramberger C, Silva SRP, Follath R, Kataura H, Pichler T (2009) Phys Rev B 80:205427. doi:10.1103/PhysRevB.80.205427
7. Ayala P, Arenal R, Rümmeli M, Rubio A, Pichler T (2010) Carbon 48(3):575. doi:10.1016/j.carbon.2009.10.009
8. Yao Z, Postma HWC, Balents L, C. Dekker (1999) Nature 402(6759):273. doi:10.1038/46241
9. Hu L, Hecht DS, Grner G (2004) Nano Lett 4(12):2513. doi:10.1021/nl048435y
10. Lin X, Rümmeli MH, Gemming T, Pichler T, Valentin D, Ruani G, Taliani C (2007) Carbon 45(1):196. doi:10.1016/j.carbon.2006.06.022
11. Chen Z, Appenzeller J, Knoch J, Lin Y, Avouris P (2005) Nano Lett 5(7):1497. doi:10.1021/nl0508624
12. Simon I, Bârsan N, Bauer M, Weimar U (2001) Sens Actuators B Chem 73(1):1. doi:10.1016/S0925-4005(00)00639-0
13. Sinha N, Ma J, Yeow JT (2006) J Nanosci Nanotechnol 6(3):573. doi:10.1166/jnn.2006.121
14. Marulanda JM (ed) (2010) Carbon nanotubes. InTech, Rijeka. doi:10.5772/3451
15. Maeng S (2011) Single-walled carbon nanotube network gas sensor. InTech, Rijeka. doi:10.5772/17884
16. Mowbray DJ, Morgan C, Thygesen KS (2009) Phys Rev B 79:195431. doi:10.1103/PhysRevB.79.195431
17. Rouxinol FP, Gelamo RV, Moshkalev SA (2010) Gas sensors based on decorated carbon nanotubes. InTech, Rijeka
18. García-Lastra JM, Mowbray DJ, Thygesen KS, Rubio A, Jacobsen KW (2010) Phys Rev B 81:245429. doi:10.1103/PhysRevB.81.245429
19. Mowbray DJ, García-Lastra JM, Thygesen KS, Rubio A, Jacobsen KW (2010) Phys Status Solidi (b) 247(11–12):2678. doi:10.1002/pssb.201000171
20. Pollack GL (1969) Rev Mod Phys 41:48
21. Green MS (1954) J Chem Phy 22(3):398
22. Kubo R, Yokota M, Nakajima S (1957) J Phy Soc Japan 12(11):1203. doi:10.1143/JPSJ.12.1203
23. Müller-Plathe F (1997) J Chem Phy 106(14):6082. doi:10.1063/1.473271
24. Kukovecz A, Molnár D, Kordás K, Gingl Z, Moilanen H, Mingesz R, Kónya Z, Mäklin J, Halonen N, Tóth G, Haspel H, Heszler P, Mohl M, Spi A, Roth S, Vajtai R, Ajayan PM, Pouillon Y, Rubio A, Kiricsi I (2010) Phys Status Solidi (c) 7(3–4):1217. doi:10.1002/pssc.200982973
25. Beecher P, Servati P, Rozhin A, Colli A, Scardaci V, Pisana S, Hasan T, Flewitt AJ, Robertson J, Hsieh GW, Li FM, Nathan A, Ferrari AC, Milne WI (2007) J Appl Phys 102:043710
26. Mustonen T, Mäklin J, Kordás K, Halonen N, Tóth G, Saukko S, Vähäkangas J, Jantunen H, Kar S, Ajayan PM, Vajtai R, Helisto P, Seppa H, Moilanen H (2008) Phys Rev B 77:125430
27. Gracia-Espino E, Sala G, Pino F, Halonen N, Luomahaara J, Mäklin J, Tóth G, Kordás K, Jantunen H, Terrones M, Helist P, Seppä H, Ajayan P, Vajtai R (2010) ACS Nano 4:3318
28. Mott N (1979) Electronic processes in non-crystalline materials, 2nd ed
29. Skákalová V, Kaiser AB, Woo YS, Roth S (2006) Phys Rev 74:085403. doi:10.1103/PhysRevB.74.085403

30. García-Lastra JM, Thygesen KS, Strange M, Rubio A (2008) Phys Rev Lett 101:236806. doi:10.1103/PhysRevLett.101.236806
31. Bahn S, Jacobsen K (2002) Com Sci Eng 4(3):56. doi:10.1109/5992.998641
32. Soler JM, Artacho E, Gale JD, García A, Junquera J, Ordejón P, Sánchez-Portal D (2002) J Phy Conden Matter 14(11):2745
33. Hall H (1975) Phys A Math Gen 8(2)
34. Wagner M (1991) Phys Rev B 44(12):6104. doi:10.1103/PhysRevB.44.6104
35. Thygesen K, Jacobsen K (2005) Chem Phys 319(1–3):111. doi:10.1016/j.chemphys.2005.05.032
36. Gonze X, Amadon B, Anglade PM, Beuken JM, Bottin F, Boulanger P, Bruneval F, Caliste D, Caracas R, Côté M, Deutsch T, Genovese L, Ghosez P, Giantomassi M, Goedecker S, Hamann D, Hermet P, Jollet F, Jomard G, Leroux S, Mancini M, Mazevet S, Oliveira M, Onida G, Pouillon Y, Rangel T, Rignanese GM, Sangalli D, Shaltaf R, Torrent M, Verstraete M, Zerah G, Zwanziger J (2009) Compu Phys Commun 180(12):2582. doi:10.1016/j.cpc.2009.07.007
37. Toher C, Filippetti A, Sanvito S, Burke K (2005) Phys Rev Lett 95:146402. doi:10.1103/PhysRevLett.95.146402
38. Indlekofer KM, Knoch J (2005) Appenzeller Phys Rev B 72:125308. doi:10.1103/PhysRevB.72.125308
39. Varga K, Pantelides ST (2007) Phys Rev Lett 98:076804. doi:10.1103/PhysRevLett.98.076804
40. Guo J, Datta S, Lundstrom M, Brink M, McEuen P, Javey A, Dai H, Kim H, McIntyre P (2002) Electron devices meeting. IEDM '02. international. pp. 711–714. doi:10.1109/IEDM.2002.1175937
41. Guo J, Datta S, Lundstrom M, Anantam MP (2004) Int J Multiscale Comput Eng 2(2):257. doi:10.1615/IntJMultCompEng.v2.i2.60
42. Koswatta SO, Lundstrom MS, Anantram MP, Nikonov DE (2005) Appl Phys Lett 87(25):253107. doi:10.1063/1.2146065
43. Shinkarev V, Glushenkov A, Kuvshinov D, Kuvshinov G (2010) Carbon 48(7)
44. Cariaso O, Walker Jr P (1975) Carbon 13(3):233
45. Yan R, Liang D, Tsen L, Tay J (2002) Environ Sci Technol 36(20):4460
46. Xiao Y, Wang S, Wu D, Yuan Q (2008) Separ Purif Technol 59(3):326
47. Kong J, Franklin NR, Zhou C, Chapline MG, Peng S, Cho K, Dai H (2000) Science 287:622
48. Collins PG, Bradley K, Ishigami M, Zettl A (2000) Science 287:1801
49. Li J, Lu Y, Ye Q, Cinke M, Han J, Meyyappan M (2003) Nano Lett 3:929
50. Bekyarova E, Davis M, Burch T, Itkis ME, Zhao B, Sunshine S, Haddon RC (2004) J Phys Chem B 108:19717
51. Sayago I, Terradob E, Lafuente E, Horrillo M, Maser W, Benito A, Navarro R, Urriolabeitia E, Martinez M, Gutierrez J (2005) Synth Metals 148:15
52. Parikh K, Cattanach K, Rao R, Suh DS, Wu A, Manohar SK (2006) Sens Actuators B 113:55
53. Mäklin J, Mustonen T, Kordás K, Saukko S, Tóth G, Vähäkangas J (2007) Phys Stat Sol (b) 244:4298
54. Mäklin J, Mustonen T, Halonen N, Tóth G, Kordás K, Vähäkangas J, Moilanen H, Kukovecz A, Kónya Z, Haspel H, Gingl Z, Heszler P, Vajtai R, Ajayan PM (2008) Phys Stat Sol (b) 245(10):2335. doi:10.1002/pssb.200879580
55. Wongwiriyapan W, Honda SI, Konishi H, Mizuta T, Ikuno T, Ito T, Maekawa T, Suzuki K, Ishikawa H, Oura K, Katayama M (2005) Jpn J Appl Phys 44(L):482
56. Nguyen HQ, Huh JS (2006) Sens Actuators B 117:426
57. Lee JH, Kim J, Seo HW, Song JW, Lee ES, Won M, Han CS (2008) Sens Actuators B 129:628
58. Lucci M, Regoliosi P, Reale A, Carlo AD, Orlanducci S, Tamburri E, Terranova M, Lugli P, Natale CD, DAmico A, Paolesse R (2005) Sens Actuators B 181:111
59. Lucci M, Reale A, Carlo AD, Orlanducci S, Tamburri E, Terranova M, Davoli I, Natale CD, DAmico A, Paolesse R (2006) Sens Actuators B 118:226
60. van Wees BJ, van Houten H, Beenakker CWJ, Williamson JG, Kouwenhoven LP, van der Marel D, Foxon CT (1988) Phys Rev Lett 60:848. doi:10.1103/PhysRevLett.60.848

61. Salvador P, Paizs B, Duran M, Suhai S (2001) J Comput Chem 22(7):765. doi:10.1002/jcc.1042
62 Pérez Paz A, García-Lastra JM, Markussen T, Thygesen KS, Rubio A (2013) *Carbon nanotubes as heat dissipaters in microelectronics*. The European Physical Journal B, 86(5) 234: *1–14*. DOI:10.1140/epjb/e2013-40113-5
63. Plimpton S (1995) Comp J Phys 117:1
64. Brenner DW, Shenderova OA, Harrison JA, Stuart SJ, Ni B, Sinnott SB (2002) J Phys Condens Matter 14(4):783
65. Brenner DW (1990) Phys Rev B 42:9458. doi:10.1103/PhysRevB.42.9458
66. Stuart SJ, Tutein AB, Harrison JA (2000) J Chem Phy 112(14):6472. doi:10.1063/1.481208
67. Cervellera VR, Albertí M, Huarte-Larrañaga F (2008) Int J Quantum Chem 108(10):1714. doi:10.1002/qua.21590
68. Giannozzi P, Car R, Scoles G (2003) J Chem Phy 118(3):1003. doi:10.1063/1.1536636
69. Arora G, Sandler SI (2006) J Chem Phy 124(8):084702. doi:10.1063/1.2166373
70. Bojan MJ, Vernov AV, Steele WA (1992) Langmuir 8(3):901. doi:10.1021/la00039a027
71. Arab M, Picaud F, Devel M, Ramseyer C, Girardet C (2004) Phys Rev B 69:165401. doi:10.1103/PhysRevB.69.165401
72. Wu Y, Tepper HL, Voth GA (2006) J Chem Phy 124(2):024503. doi:10.1063/1.2136877
73. Hockney JWERW (1988) Particle-particle-particle-mesh (P3M) algorithms. Computer simulation using particles. CRC Press
74. Markussen T, Rurali R, Brandbyge M, Jauho AP (2006) Phys Rev B 74:245313
75. Mingo N (2006) Phys Rev B 74:125402. doi:10.1103/PhysRevB.74.125402
76. Berber S, Oshiyama A (2008) Phys Rev B 77:165405. doi:10.1103/PhysRevB.77.165405
77. Berber S, Oshiyama A (2006) Phy B Condens Matter 376–377:272
78. Krasheninnikov A, Lehtinen P, Foster A, Nieminen R (2006) Chemi Phy Lett 418(1–3):132
79. García-Lastra JM, Mowbray DJ, Thygesen KS, Rubio A, Jacobsen KW (2010) Phys Rev B 81:245429. doi:10.1103/PhysRevB.81.245429
80. Lu AJ, Pan BC (2004) Phys Rev Lett 92:105504. doi:10.1103/PhysRevLett.92.105504
81. Amorim RG, Fazzio A, Antonelli A, Novaes FD, Silvada AJR (2007) Nano Lett 7(8):2459
82. Kotakoski J, Krasheninnikov AV, Nordlund K (2006) Phys. Rev. B 74:245420. doi:10.1103/PhysRevB.74.245420
83. Mingo N, Stewart DA, Broido DA, Srivastava D (2008) Phys Rev B 77:033418

Chapter 5
Challenges Associated to the Multi-Scale Modeling of Fuel Electro-Oxidation for Fuel Cell Applications

King-Ki Fung, Purnima Kharidehal and Daniela S. Mainardi

Abstract The high-cost of materials and efficiency limitations of chemical fuel cells is a topic of primary concern. Industries are currently focusing on proton-exchange membrane (PEM) fuel cells engineering and design for improved performance, durability, and reduced cost. This situation has led to an urgent need for understanding, predicting, and optimizing the various transport and electrochemical processes that occur in PEM fuel cells, where modeling plays a key role. Challenges associated to a multi-scale modeling approach to model fuel electro-oxidation in PEM and bio fuel cells are discussed here. A combination of tools involving Density Functional Theory, Transition State Theory, Molecular Mechanics and Kinetic Monte Carlo are combined in order to model fuel electro-oxidation. Information regarding energy barriers and pre-exponential factors needed to determine reaction rates are obtained from Density Functional Theory and Transition State Theory respectively. These microscopic reaction rates are then provided as inputs in a Kinetic Monte Carlo approach, and the fuel oxidation process is modeled on a 2-D reactive surface representing the catalyst.

5.1 Introduction

Securing a permanent form of energy is a global concern, as current energy requirements depend on a finite supply of fossil fuels; which cannot sustain the rapidly increasing energy needs indefinitely. Additionally, combustion engines have brought about environmental harm that is just now being realized. In response to these issues, a necessity for a clean and renewable energy source is desired.

In the past decade, solar energy, geothermal energy, wind energy, and fusion power technologies have been explored as alternative energy supplies. Among these, fuel cells have been nominated as a solution to this crisis. Fuel cells take advantage of combustion engines continuous operation as long as fuel is supplied, and batteries' ability to convert chemical energy into electrical energy; however,

D. S. Mainardi (✉) · K.-K. Fung · P. Kharidehal
Chemical Engineering Program, Institute for Micromanufacturing, Louisiana Tech University, 911 Hergot Ave., Ruston, LA 71272, USA
e-mail: mainardi@latech.edu

J. M. Seminario (ed.), *Design and Applications of Nanomaterials for Sensors,* Challenges and Advances in Computational Chemistry and Physics 16,
DOI 10.1007/978-94-017-8848-9_5, © Springer Science+Business Media Dordrecht 2014

they lack the energy output of traditional combustion engines. In order to compete with combustion engines, numerous obstacles need to be overcome before fuel cells can be fully commercialized at a reasonable cost. Fuel cells, moreover, are plagued with sluggish oxidation and reduction reactions at the electrodes, fuel crossover, low proton conductivity, and dehydration of the nafion membrane which drastically reduces the efficiency of the fuel cells. Additionally, the overall cost of fuel cells, a major portion due to the platinum catalyst used, hinders mass production [1–3].

There are various types of fuel cells, but the proton exchange membrane (PEM) fuel cell is the one that will be considered in this chapter. A PEM fuel cell is composed of three sequential segments (anode, electrolyte, and cathode) which convert chemical energy into electrical energy. The fuel, a hydrogen source, passes through the anode. At the anode, the fuel is broken down into H^+ and electrons in the presence of a catalyst; typically platinum on a carbon black support. The PEM prevents the electrons from passing through, but allows the protons to travel to the cathode; hereby, forcing electrons to travel through an electrical circuit and generate energy on their way to the cathode. At the cathode, the electrons, protons, and oxygen react to form water according to the following chemical reaction:

$$\frac{1}{2}O_2 + 2e^- + 2H^+ \leftrightarrow H_2O$$

Although pure hydrogen gas is highly desired as fuel to avoid catalyst poisoning with carbon monoxide, it is not readily available and typically undergoes a reforming step. Hydrogen reformation, sometimes referred to as "steam reforming", typically begins with a hydrocarbon and is an endothermic process; heat is supplied to carry out the reaction as shown below:

$$C_xH_y + xH_2O \rightarrow \left(x + \frac{y}{2}\right)H_2 + xCO$$

The heat required for hydrogen reforming may be provided in part by the fuel cell itself or by burning the fuel itself; which has been shown to reduce the efficiency of the fuel cell. Furthermore, CO generation from hydrogen reforming can poison the platinum catalyst. It is possible to further convert CO to CO_2 with a water-gas shift reaction as shown below:

$$CO + H_2O \leftrightarrow CO_2 + H_2$$

However, higher temperatures tend to favor the production of CO. Therefore, the gas must be cooled and processed through a series of reactors. Even after this process, the amount of CO is in the range of 2500–5000 ppm, which exceeds the allowed limit of CO for PEM fuel cells by a factor of 100. Therefore, additional processes such as methanation, use of a selective oxidation reactor, or the use of palladium/platinum membranes are necessary.

It is possible to store hydrogen to avoid the issue of production of hydrogen on a "as needed" basis. Storing hydrogen also provides the advantage of simplicity in

Table 5.1 Energy density comparison for methanol and hydrogen

Storage method	Net energy density (kWh/kg)
H_2 in composite cylinders	0.20
H_2 in metal hydride cylinders	0.22
Methanol in plastic tanks	5.26

fuel cell design, has an indefinite storage time, and zero purity limits. However, hydrogen has one of the lowest energy density, which implies that a great amount of pressure is necessary to store a large mass of hydrogen. Furthermore, hydrogen is difficult to liquefy and, in its liquid state, it still has a low density. Despite these difficulties, hydrogen can be compressed in gas cylinders, stored as a cryogenic liquid, and even stored in carbon nanofibers. Storage of hydrogen ultimately leads to considerations of safety due to hydrogen's unique gas elements. Hydrogen has been shown to have a leak rate 2.8 times faster than methane and 3.3 times faster than air. Additionally, hydrogen is a highly volatile and flammable gas which can detonate in certain mixtures of hydrogen and air.

The use of hydrogen sources as fuels for fuel cell applications is therefore a natural choice and compromise in terms of damage (poisoning) of the chemical catalyst being used. The overall fuel cell efficiency is partially determined by the catalyst. When pure hydrogen is not used, catalysts active sites are plagued with CO poisoning which drastically reduces their efficiency.

Alcohols, such as methanol, have been proposed due to a higher net energy density when compared to hydrogen, as shown in Table 5.1. Furthermore, there is no need for a reforming step and it is quick to refill. Additionally, methanol is easily produced due to highly efficient production process developed for industrial uses, at approximately 20 million tons per year.

While direct alcohol fuel cells (DAFCs) makes up for some of the shortcomings of typical hydrogen-fed PEM fuel cells, DAFCs are hindered by their own limitations. The main issue involves the slow reaction that take place at the anode, as shown below

$$CH_3OH + H_2O \rightarrow 6H^+ + 6e^- + CO_2$$

The use of an alcohol as fuel in fuel cells is particularly attractive due to the high amount of electrons generated. However, the reaction at the anode is not a simple reaction, but a complex process that takes place in multiple steps with a variety of pathways which can be visualized in Fig. 5.1.

In the methanol oxidation mechanism shown in Fig. 5.1, hydrogen removal and a proton-electron pair generation is carried out in which the end product will always include the production of carbon dioxide and 6 proton-electron pairs, regardless of the pathway taken. The only stable compounds are methanol, formaldehyde (CH_2O), formic acid (COOH), and carbon dioxide, therefore, it is considered the main pathway.

The second main limitation that DAFCs have, lies in fuel crossover across the PEM, where water is an essential component that plays an important role in the pro-

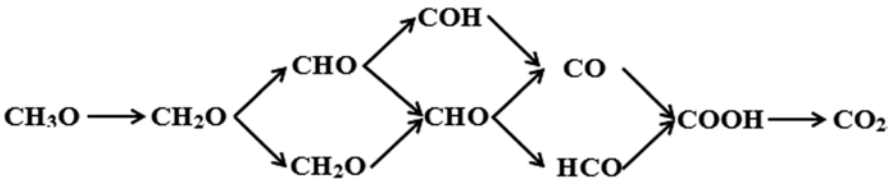


Fig. 5.1 Methanol oxidation mechanism

ton transfer. Although fuel crossover occurs normally in all fuel cells, it is particularly more severe in DAFCs due to alcohol's affinity for mixing with water. Once the alcohol reaches the cathode, it will react readily at the cathode creating a mixed potential. The reactions that take place at the cathode do not generate current, and, thereby, cause the wasting of fuel.

A common approach to alleviate the issues of commercialization is the addition of other metals to pure platinum to be used as catalysts. By creating a binary/ternary catalyst, researchers are able to promote ethanol oxidation, lower cost, and decrease catalyst poisoning. Recently the Department of Energy has invested $ 75 million into fuel cell research and development in 2012 in hopes of reaching the 2015 targets [4]. By 2015 and for transportation applications, PEM fuels cells are expected to have a peak performance of 60 %, a power density of 650 W/L, a specific power of 650 W/kg, and a cost of $ 30/kW among other targets [4].

5.1.1 Types of Catalysts for Fuel Cell Applications

5.1.1.1 Chemical Catalysts

Most PEM fuel cells use platinum as catalyst, which is expensive, limited in availability, and easily poisoned by carbon monoxide (CO), a by-product of many hydrogen production reactions in the fuel cell anode chamber [5, 6]. In PEM fuel cells, the type of fuel used dictates the appropriate type of catalyst needed. Within this context, tolerance to CO is an important issue. It has been shown that the PEM fuel cell performance drops significantly with a CO concentration of only several parts per million, due to the strong chemisorption force of CO onto the catalyst [7]. Numerous studies have been aimed toward reducing the amount of platinum required in current fuel cells [5, 8–13]. For catalyst materials, tertiary platinum/ruthenium-based alloys seem to offer the best performance when CO poisoning is of concern [5, 12, 14]. In an attempt to keep reducing the amount of platinum used, small atomic clusters of platinum deposited on carbon supports [9, 15]and platinum-based bimetallic catalysts [8, 12–14] were proposed, but metal-metal and metal-adsorbate interactions [16] were observed to affect their reactivity [11, 17–19]. In spite of environmental, social, and political concerns surrounding the use of platinum and other more rare and valuable metals in fuel cells, the use of platinum-based alloys has been the focus of study in the last decades.

For ethanol, a promising fuel, oxidation, platinum works well in cleaving the C-C bond of ethanol at low potentials, but at higher potentials (0.6 V vs RHE) the formation of carbon monoxide blocks platinum active sites [20]. This has lead researchers to focus on catalyst that have reaction rates at lower potentials. Platinum is also an expensive metal and therefore leads to high costs of fuel cells. To alleviate this problem, researchers are looking at new catalyst that have higher resistance to poisoning and lower cost. The development of a catalyst that can completely oxidize ethanol begins with additions to the traditional catalyst, platinum. Typically a single additive (Ru, Re, Pb, Sn, etc) is applied to promote complete ethanol oxidation. In this chapter, the use of a ternary Pt-Ru-Sn catalyst for ethanol oxidation is discussed with the objective to outperform binary catalysts. Once a catalyst capable of complete oxidation of ethanol is discovered, ethanol-fed fuel cells will become one step closer to commercialization due to an increase energy output. This will allow sustaining energy demands, while keeping the environment clean.

5.1.1.2 Biological Catalysts

With increasing challenges in creating alternative fuels, reducing harmful by-products in manufacturing, preventing pollution, and dealing with the causes of global warming, highly active and efficient catalysts are essential to meet these challenges [21]. Biocatalysts such as enzymes have gained much inspiration, as they are sustainable, accelerate reactions enormously (with turnover frequencies of a few to thousands per second), and are endowed with high stereo-, regio- and chemoselectivity [22, 23].

Since the 1960s, with advancements in technology and science, enzymes have been used as catalysts for biofuel cells applications. In 1964, the first enzyme-based biofuel cell was reported; which used glucose as the fuel, and glucose oxidase (GOx) as the anode catalyst [24]. Since then different enzymes have been used as catalysts for various special applications such as implantable devices, sensors, drug delivery, micro-chips, and portable power supplies, instead of considering biofuel cells as a general device for power generation [25]. For instance, to monitor some specific pollutants, enzymes such as horse radish peroxidase (HRP), and acetylcholinesterase have been used on environmental sensors [26, 27], and a biofuel cell using sugar as the fuel and enzymes as catalysts was developed by Sony to power a Walkman® [28].

Alcohol dehydrogenases (ADH) produced by several aerobic bacteria and containing pyrroloquinoline quinone (PQQ) as the prosthetic group have achieved significant consideration as bio-electrocatalysts.

When pyrroloquinoline quinone(PQQ)-containing enzymes are used as anode catalysts in fuel cells, they transfer electrons from the substrate (fuel) to an electron acceptor other than oxygen, and additionally, can transfer electrons directly to the electrode surface; making it an efficient electrocatalyst [29]. Also, in PQQ-containing enzymes, the cofactor (PQQ) is bound to the enzyme and avoids the addition or generation of a separate cofactor, like NAD or FAD, hence has gained much more importance as biofuel cell catalysts and has been used as potential objects

for biosensors for the past 15 years [29]. For example, electrochemical glucose test strips that use gene engineered apo-PQQ-dependent glucose dehydrogenase (PQQ-GDH) have been employed successfully. But it was found that the PQQ cofactor bonds very weakly and that these were single-use test strips. Later using redox mediators, which help transfer the electrons from the enzyme active region to the electrode, have increased the efficiency of such systems [29, 30]. Also Lapėnaitė et al. showed that PQQ-dependent glucose dehydrogenase can be employed in the design of enzymatic biosensors that can be used for detection of heavy metals such as Cd^{2+} and Pb^{2+} ions in concentration range of 15×10^{-5} mol/l [31].

One such, PQQ dependent enzyme is Methanol Dehydrogenase (MDH) which contains a calcium ion in its active site and has been developed by Zhang et al. as an anode catalyst for methanol-fed bio-catalytic fuel cell [32]. This methanol-fed-biocatalytic fuel cell uses bacterial MDH enzyme immobilized on *N,N,N',N'*-tetramethyl-*p*-phenylenediamine (TMPD)-functionalized carbon paste electrode as the anode catalyst, and produces a continuous power output of 0.25 mW/cm^2 for 30 days of continuous operation [32]. It is believed that the TMPD mediator, responsible for electron transfer resulting from the fuel oxidation by the enzyme to the electrode, is the major factor limiting the power output that deteriorates the fuel cell performance (expected (theoretical) output is 100 mW/cm^2 [33]). Particularly, the oligomerization (the forming of polymers by the combination of relatively few monomers) of the mediator molecules seems to be increased when stimulating the fuel cell operating conditions by subjecting the mediator to repeated charge-discharge cycles. This oligomerization causes the fuel cell performance to be deteriorated due to reduced electron transfer from the enzyme to the electrode. Moreover, another cause for this bio-fuel cell limited performance is associated to the formation of formaldehyde (formic acid) as result of methanol (fuel) oxidation by MDH [32]. The continuous accumulation of such a strong acid in the bio-fuel cell may slowly reduce the activity of the enzyme, thus limiting the overall power output [32].

By overcoming power output limitations, enzymatic fuel cells might offer potentially attractive power sources for some consumer electronic devices. Hence in this chapter, a clear understanding of the reactivity of MDH enzymes at molecular level is presented to unravel the secret of its catalytic activity towards methanol electro-oxidation.

5.1.2 Need for Modeling Work

The most focused target in the commercialization of PEM fuel cells at large scales is the cost of the fuel cell. Currently, the cost of a fuel cell is approximately $ 73/kW where the platinum catalyst makes up 47 % of the fuel cell cost. This has lead research to expand into catalyst design and engineering; which requires a more in-depth understanding of the occurring processes. Identification, understanding, prediction, control and optimization of various transport and electrochemical processes are possible by computational modeling.

Molecular modeling and simulation techniques have been proven to be powerful tools to understand chemical and biochemical reactions as catalysis involves processes of disparate length and time scales [34, 35]. Even though experimental techniques such as X-ray crystallography, Nuclear Magnetic Resonance, and other spectroscopic methods provide explicit information about catalyst structure, details about the catalytic mechanisms are not sufficient enough to clearly understand the reactivity of the catalysts [36]. Insights into these mechanisms have potential applications in the design of new catalysts. And in these developments, computational modeling has an important role to play as it can provide information about the unstable species such as transition states and reaction intermediates that cannot be studied directly by experiments in complex systems [34–36].

5.2 Multi-Scale Approach to Understand Catalysis

In order to study catalytic processes, a multi-scale modeling approach has proven to be an effective tool integrating various techniques spanning from atomistic to macroscopic simulations (Fig. 5.2) [37]. A combination of various computational tools is usually required in order to effectively model an entire system, which can be treated as a cascade of individual subsystems. Classification of these subsystems is based on their different body interactions which depend on magnitudes of time and length [38].

Quantum mechanical (QM) methods such as *ab initio*, semiempirical, and density functional theory (DFT) [39] are used to study the structural and energetic information in molecular systems containing less than hundreds of atoms which belong to the microscopic regime (picometers to angstrom length scale). These atomistic simulations provide parameters for larger time and length scales. DFT methods have become a powerful tool in calculating not only structural and energetic molecular information but also other quantities, such as the activation energies of chemical and biological reactions. DFT is computationally cheaper than correlated *ab* initio methods, such as configuration interaction and Møller–Plesset perturbation theory, which reduces the many-body electron problem treated by the wave function to a single electron problem dealt with the electron density instead [40].

In general, QM methods are useful in modeling smaller site-specific systems, like reactions at a small region within an enzyme active site (limited to a few hundreds of atoms). Molecular mechanics (MM) and molecular dynamics (MD) are used for larger systems (containing thousands of atoms), and these techniques rely on the parameterization of bonding and nonbonding interactions via force fields [41]. These methods are operative over wide length- and time-scale ranges, while still dealing with individual atoms. Classical MD simulations have been employed in the literature for determining enzyme mechanisms, and understanding the role of the enzyme active site residues that are of fundamental importance for a better description of catalytic mechanisms.

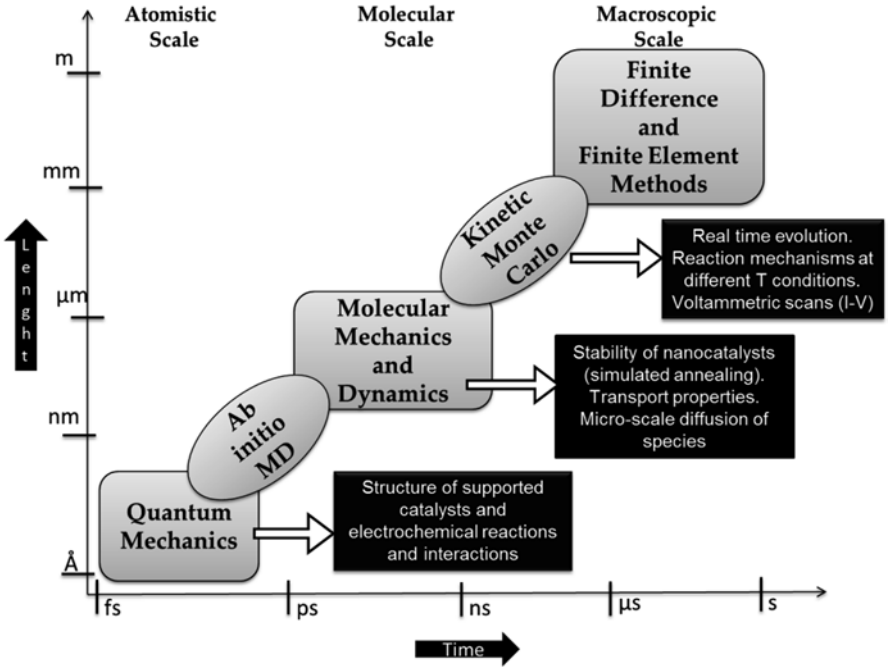


Fig. 5.2 Flowchart showing the multi-scale approach needed to study catalytic processes

A high resolution X-ray crystal structure of the enzyme in the presence of substrate can be used as the starting coordinates for exploration of structure and enzyme mechanisms. DFT-based MD simulations are similar to classical force-field based MD, with the main difference being that the atomic forces are derived by solving DFT equations rather than from empirical potentials of inter-atomic interactions. These DFT-MD simulations perform much better than MD but at the cost of more computational effort.

Finite element analysis, finite difference methods, and Monte Carlo methods are used to model systems in the macroscopic spatial regime (millimeters to meters length scale) [42]. In particular, the kinetic Monte Carlo (kMC) methods are designed to deal with a large range of scales, and require parameters that can be obtained from experiments or simulations from smaller scales. In a typical kMC simulation, the short time dynamics and the interactions between species are represented by discrete hops from one position to another based on random probabilities. These simulations are usually conducted on a grid that acts as a platform for the species to interact, and these interactions are dependent on a set of predefined rules and the initial and final atomic configurations [43].

kMC methods yield time evolution of individual reaction rates (difficult to determine experimentally); which compete with each other as a function of external variables such as pressure and temperature. The rates are specified as probabilities and

the time evolution of surface configuration is given by a Master Equation [44] (5.1), which is derived from first principles, as Monte Carlo is a probabilistic approach.

$$\frac{dP(c,t)}{dt} = \sum_{c' \neq c} \left[P(c',t) r_{c',c} - P(c,t) r_{cc'} \right] \tag{5.1}$$

In Eq. (5.1), $P(c, t)$ is the probability of finding the system in configuration c, at time t, and $r_{cc'}$ is the microscopic rate of the reaction that transfer c into c'. There are methods which are used internally by the Carlos kMC program to solve this equation: First-Reaction Method (FRM), Variable Step Size Method (VSSM), Random Selection Method (RSM) [44]. The First-Reaction Method (FRM) [44] is used in the kMC calculations presented in this chapter, which is appropriate for cases where reaction constants vary with time. According to this method, when the system is in a given configuration c, the set of all possible reactions is determined, and a time of occurrence $t_{c'c}$ is generated for each reaction i compatible with configuration c, according to Eq. (5.2) [45].

$$\exp\left[-\int_{t}^{t_{c'c}} r^{i}_{c'c}(t') \cdot dt \right] = \delta \tag{5.2}$$

In Eq. (5.2), $r^{i}_{c'c}$ is the time dependent rate of reaction i, and δ is a random number selected uniformly in the (0,1) interval. Then, the reaction with the smallest time is selected, the configuration is changed accordingly, and the time is incremented to t. Finally, the set of possible reactions is generated according to the new configuration c', and the procedure is repeated. The microscopic rate r_i are related to macroscopic parameters as stated by Eq. (5.3) [45],

$$r_i = v_i \exp\left[-\frac{E_{ai}}{RT} \right] \tag{5.3}$$

where v_i is the prefactor, and E_{ai} is the activation energy of a reaction i. In the case of electrochemical reactions, it is necessary to introduce the potential dependence of the reaction rate. In the presence of an overpotential V (defined as the difference between the actual and the equilibrium potential), the microscopic rate of a reaction r_i [46] is given by Eq. (5.4).

$$r_i = v_i^0 \exp\left(-\frac{\left(E_{a_i} + a e_o V \right)}{K_B T} \right) \tag{5.4}$$

where, e_0 is the charge of an electron, V is the overpotential and α is the transfer coefficient (α = 0.5 if the reaction consumes electrons, and α = −0.5 if it produces them) [46]. By taking the difference between the rates of reactions (reactions/unit

cell/sec in the kMC output) for the reactions that produce electrons and those that consume electrons, the net electrode currents can be calculated. From these the polarization curves (also known as I-V curves) can be obtained for the fuel cell investigations.

In this chapter, a combination of tools involving Density Functional Theory (DFT), Transition State Theory (TST), and Molecular Mechanics (MM) were combined in a Kinetic Monte Carlo (kMC) approach. Information regarding microscopic energy barriers and pre-exponential factors needed to determine reaction rates involved in each step of the reaction mechanisms was obtained from DFT and TST respectively. This microscopic reaction rates were then provided as inputs in the kMC program, and the oxidation process was modeled on a 2-D reactive surface representing the catalyst. A grid representing possible reactions sites was mapped onto the projected catalyst image in a 2-D surface for a random substrate approach onto the reactive surface. kMC simulations predicted then information on the macroscopic rates for oxidation processes.

To achieve these goals, the first challenge was to obtain an appropriate quantum chemical model of the chemical or biological catalyst to investigate the oxidation mechanisms. The second challenge was to model the oxidation processes using a kMC approach on a 2-D reactive surface to predict the macroscopic rates of the reaction which in turn will provide information on the polarization curves (I-V curves) in fuel cell anodic chambers. In this chapter, these challenges are described in detail.

5.3 Challenges Modeling Chemical Catalysts

In order to meet the DOE's technical targets for 2015, ethanol is chosen as the fuel. Ethanol is an ideal fuel choice due to its high energy density at 26.8 MJ/kg and ease of production via biomass [47]. However, ethanol is difficult to oxidize and requires the use of a catalyst. An ideal catalyst should be inexpensive, exhibit a high tolerance for CO, and facilitate chemical reactions. The most common approach to avoid CO poisoning is alloying with another metal to form a binary or ternary catalyst. Additionally, alloying has been shown to increase the power density and reduce the cost of PEM fuel cells in general.

In one study conducted by Vigier et al., three metals (Ru, Mo, and Sn) were paired with platinum to improve the ethanol oxidation rate. Among these metals, Sn had the most promising results with an atomic Pt:Sn ratio of 90:10 [20]. Vigier et al. concluded that these results are due to the product distribution which was an increase in acetic acid, and decrease in acetaldehyde and carbon monoxide. Tin is said to favor the dissociative adsorption of ethanol and lead to the weakening of the Pt-CO bond. It should also be noted that CO_2 formation occurs at a lower potential and is oxidation of CO to CO_2 is easier due to the presence of tin [48].

In another study by Datta, the effects of ruthenium and platinum are explored at different atomic compositions. Datta found that ruthenium's purpose is to provide oxygen for CO oxidation to CO_2 through a bifunctional mechanism, thus increas-

ing Pt tolerance to CO [49]. In this mechanism, Ru acts as a decomposer of water and absorbs OH [49]. This allows Ru to supply oxygen species to the absorbed CO, which is attached to platinum, and promotes ethanol oxidation by fostering the CO to CO_2 conversion and decreasing the poisoning of the catalyst's active sites. Ru itself is inactive to ethanol oxidation [49]. In a study conducted by Riberio, the synergetic effect in promoting ethanol oxidation by the addition of Sn and W to Pt has been demonstrated [50].

5.3.1 Case Study of Ethanol Oxidation Across Pt/Ru/Sn Catalyst

Direct ethanol fuel cells (DEFCs) are currently being researched because ethanol has a higher energy density output (twice the energy density of hydrogen) and is easily transported [51]. The overall reaction in a DEFC is separated into the half reaction at the electrodes and follows the same principles as Fig. 5.1. Ethanol oxidation occurs at the anode:

$$CH_3CH_2OH + 3H_2O \rightarrow 12H^+ + 12e^- + 2CO_2 \tag{5.5}$$

and reduction at the cathode:

$$O_2 + 4H^+ + 4e^- \rightarrow 2H_2O \tag{5.6}$$

This gives the overall reaction in a DEFC:

$$CH_3CH_2OH + 3O_2 \rightarrow 3H_2O + 2CO_2 \tag{5.7}$$

For ethanol oxidation, platinum works well in cleaving the C–C bond of ethanol at low potentials, but at higher potentials (0.6 V vs RHE) the formation of carbon monoxide blocks platinum's active sites [48]. This has led some researchers to discover new catalyst that will facilitate the oxidation of ethanol.

In a study of various binary catalyst, platinum-ruthenium (Pt/Ru) showed cell performance (in the presence of 100 ppm CO) equivalent to a pure platinum catalyst (in the presence of pure hydrogen) [52]. This phenomenon is attributed to Ru's ability to decompose water and adsorb OH molecule [53]. Therefore, CO molecules bound to Pt sites can be readily oxidized to CO_2 due to the adsorb OH molecule on neighboring Ru sites. Further alloying with tungsten (Pt/Ru/W) led to even higher cell performance compared to Pt/Ru[52]. Therefore, a ternary catalyst with constructive effects of Sn and Ru should perform similar or better than a pure platinum catalyst. Furthermore, the cost of the catalyst will be reduced when Pt ($ 5000 per 100 g) is alloyed with Ru ($ 650 per 100 g) and Sn ($ 1.80 per 100 g).

5.3.1.1 Ethanol Oxidation Across Pt/Ru/Sn: Challenge #1—Modeling Catalyst Structure

There are three known methods for studying catalyst systems: cluster, embedded-cluster, and periodic methods. The cluster method uses a fixed amount of atoms to model the active site with the assumption that chemisorption and reactivity occur locally. However, this method does not accurately represent the electronic system due to its' small size. The embedded-cluster method involves using the cluster representing the catalyst, and embedding the cluster into an external electronic environment to correctly model the electronic system. This is performed by applying an empirical force field to simulate the external environment. The only issue with this method is accurately representing the external environment with the force field at the interface of the cluster and external model. In this approach, the cluster is modeled with DFT and the outer shell with molecular mechanics. The periodic method allows us to simulate the electronic structure and external field effects as an infinite-slab. This approach takes a unit cell, which defines the system, and is then repeated in two dimensions, which generates an infinite slab.

The work presented in this chapter focuses on the DFT algorithms that are available in the DMOL3 module of the Material Studio software by Accelrys, Inc. Due to its' unique approach to electrostatics, DMOL3 is capable of performing quick structure optimization calculations by utilizing delocalized internal coordinates.

Exact internal/atomic coordinates for a Pt/Ru/Sn based catalyst are unknown. Therefore assumptions are made to determine the catalyst surface: (1) Oxidation occurs on the (111) and (100) plane, (2) The atomic ratio of Pt/Ru/Sn is 2:2:1 as a given stoichiometry to test.

The best oxidation rates typically take place on the (111) and (100) plane of pure platinum because decomposition of ethanol is structure sensitive [54]. Thus we have decided to utilize the same two planes for the ternary Pt_2Ru_2Sn catalyst of this work. The (111) and (100) planes of a FCC cube (typical of a platinum or platinum based alloy) is taken as the surface of choice with an initial guess of the atomic positions as shown in Fig. 5.3 [55].

The (100) plane configuration can have a total of five distinct configurations, taking into account symmetry, as shown in Fig. 5.4a. Similarly, the (111) plane configuration can have a total of 15 distinct configurations, taking into account symmetry, as shown in Fig. 5.4b. Ground state conformations of these 20 configurations are obtained using the DMOL3 module at a generalized gradient approximation PBE/DNP theory level.

After the completion of the geometry optimization process, three types of structures were observed: 3-D cluster configurations, (100) plane configurations, and (111) plane configurations. For industrial applications three dimensional structures are usually used to model catalyst [56]. However, in our work there were only three cases where the final optimized structures were in 3-D form as shown in Fig. 5.5. These clusters were less stable than the most favored planar configuration in each case. Hence, 3-D clusters models were not considered to represent the catalyst.

The most stable planar conformation corresponding to the (100) and (111) planes were configurations 3 and 4 respectively (Figs. 5.4a and b). During the geometry

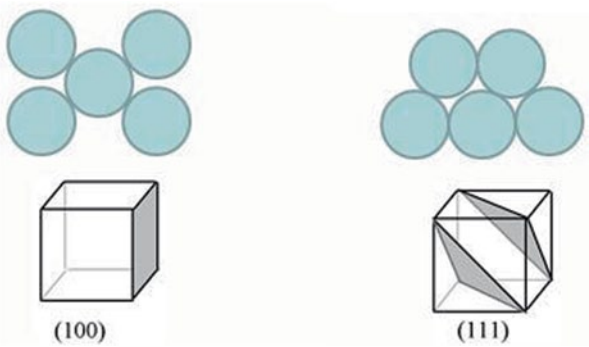


Fig. 5.3 Possible atomic positions for the atoms forming the Pt_2Ru_2Sn cluster model following the (100) and (111) arrangements. Minimum cluster size contains five atoms

optimization process, an interesting observation made is that configuration 3 of the (100) arrangement evolved into configurations 5 of the (111) arrangement (Fig. 5.6).

Another observation made during this simulation is the difficulty in the bonding of ruthenium and platinum. It can be seen through Fig. 5.6 *B–E* that ruthenium is trying to maintain a constant bond with one or the other platinum, but the addition of tin causes interference. Other researchers have also noticed that the range of

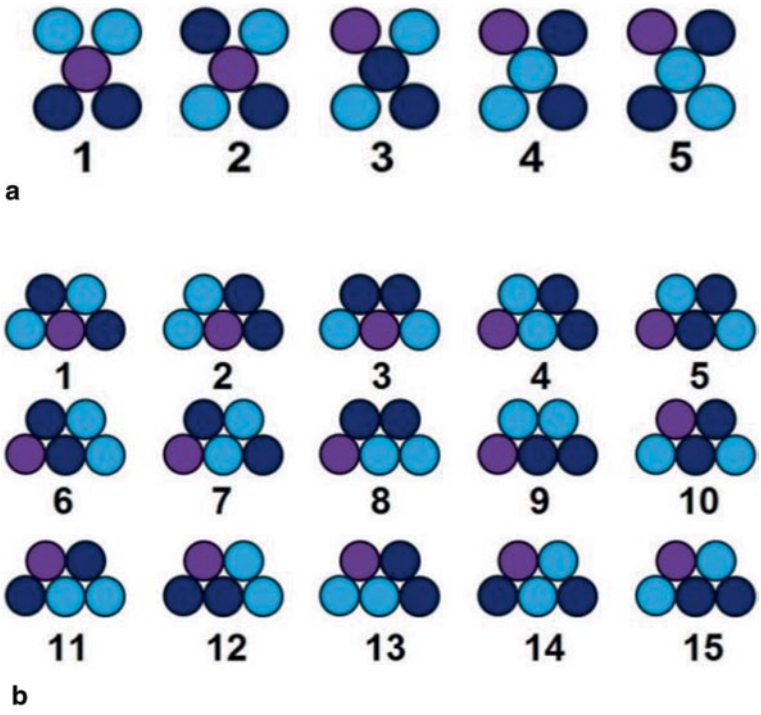


Fig. 5.4 **a** Five distinct configurations for the (1 0 0) plane. **b** Fifteen distinct configurations for the (111) plane. *Indigo circle* Ru, *blue circle* Pt, *purple circle* Sn

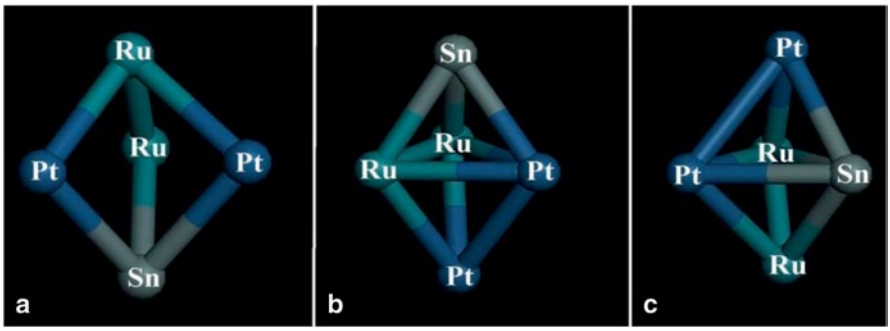


Fig. 5.5 Final optimized three dimensional structures from (1 0 0) plane from configuration 3(*A*), 4(*B*), and 5(*C*) of Fig. 5.4

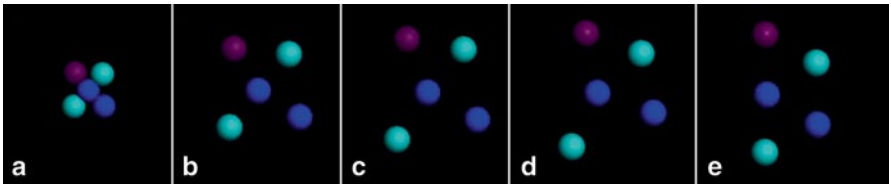


Fig. 5.6 Schematic of the optimization process of configuration 3 of the (100) arrangement evolving to configuration 5 of the (111) plane

alloying ruthenium to platinum decreases when the addition of a third particle is made [57]. For the third particle, there are three possibilities: fully alloyed, partially alloyed and no alloy with platinum [52]. It can be seen in Fig. 5.6 that tin is only partially alloyed with platinum. The general rule is that addition of a third metal will lead to a lower chance of alloying with platinum [55]. In this case, Sn is only partially bonded to Pt.

The adsorption energy of ethanol to each (100) and (111) configurations is next investigated (Table 5.2). Since configuration 4 of the (111) plane showed the strongest adsorption energy, it is chosen as the catalyst model for Pt_2Ru_2Sn.

5.3.2 Ethanol Oxidation Across Pt/Ru/Sn: Challenge #2: Ethanol Mechanism

Ethanol oxidation is a multistep and multi-selective process. Because of this, there have been a number of proposed mechanisms for ethanol oxidation. Most of these analyze the energy it takes to decompose ethanol by breaking down single bonds in a series of steps to form known species [58]. A similar approach is taken in this work where the amount of energy (the activation energy) to break each bond is calculated. The lowest activation energy will suggest the most favorable path, and the highest activation energy is considered difficult to achieve [59].

Table 5.2 Adsorption energy of configurations with similar high energy in the (111) and (100) plane according to Fig. 5.4

Structure in (111)	4	8	9	10	11	12	15
Adsorption energy (kcal/mol)	−3.955	−3.949	−3.821	−3.887	−3.809	−3.870	−3.860
Structure in (100)	*2*	*3*					
Adsorption energy (kcal/mol)	−3.756	−3.873					

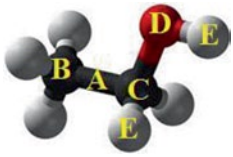


Fig. 5.7 Possibilities of ethanol decomposition: *A* Carbon–Carbon bond. *B* β dehydrogenation. *C* α dehydrogenation. *D* Hydroxyl dehydrogenation. *E* Acetaldehyde formation (α and hydroxyl dehydrogenation)

Using the ethanol oxidation mechanism reported on pure platinum as a reference, there are a total of four steps for the decomposition of ethanol [20]. In the first step, there are a total of five possibilities as shown in Fig. 5.7.

The first possibility involves decomposition of ethanol via the carbon–carbon bond (*A*). This is typically the most difficult bond to cleave for ethanol oxidation and occurs much later in the process. The other possibilities involve dehydrogenation of any of the β-hydrogen (*B*), α-hydrogen (*C*), hydroxyl group (*D*), or a combination of α-hydrogen and hydroxyl hydrogen to form acetaldehyde(*E*).

The initial configuration (ethanol), the reactant, the five possibilities, and the intermediates/products, are geometry optimized in Material Studio's DMOL3 module [60]. Once the known reactants and intermediates/products are optimized, a transition state calculation is performed. In order to confirm the transition state, a vibrational analysis is performed to determine a single negative frequency which is then optimized to ensure it is the true transition state. By locating the transition state, the activation energy can be calculated for each step as shown in Figs. 5.8, 5.9, and 5.10.

By following this process, it is possible to map out the following ethanol mechanism; which is proposed to happen on Pt_2Ru_2Sn catalysts:

$$H_2O+CH_3CH_2OH \rightarrow CH_3CHO+2H^+ +2e^- +H_2O$$
$$H_2O+CH_3CHO \rightarrow CH_3CO+H^+ +e^- +H_2O$$
$$H_2O+CH_3CO \rightarrow CH_3COOH+H^+ +e^-$$
$$CH_3COOH \rightarrow CH_3 +CO_2 +H^+ +e^-$$
$$CH_3 +H^+ +e^- \rightarrow CH_4$$

which gives the overall chemical reaction as (Fig. 5.11):

$$H_2O+CH_3CH_2OH \rightarrow CH_4 +CO_2 +4H^+ +4e^-$$

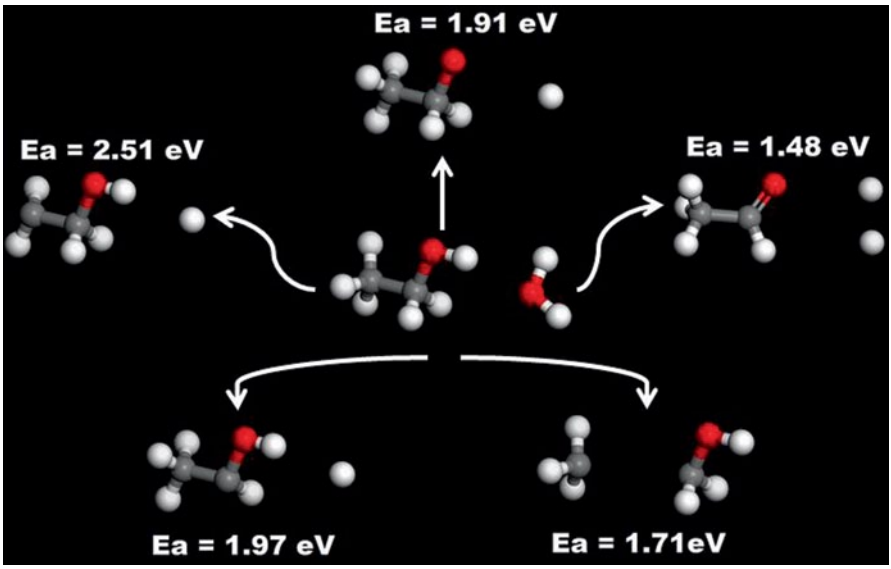


Fig. 5.8 Activation energy for step one of ethanol oxidation

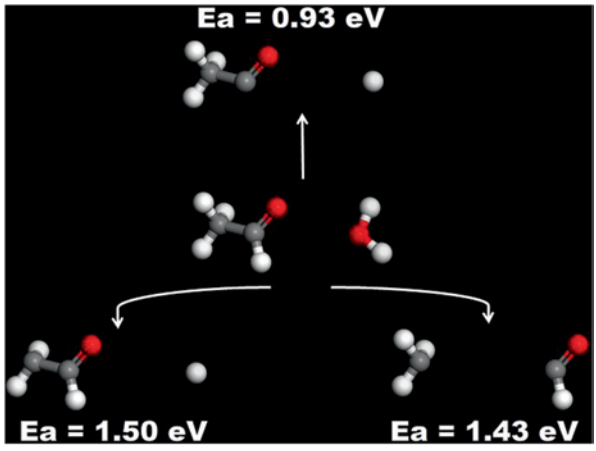


Fig. 5.9 Activation energy for step two of ethanol oxidation

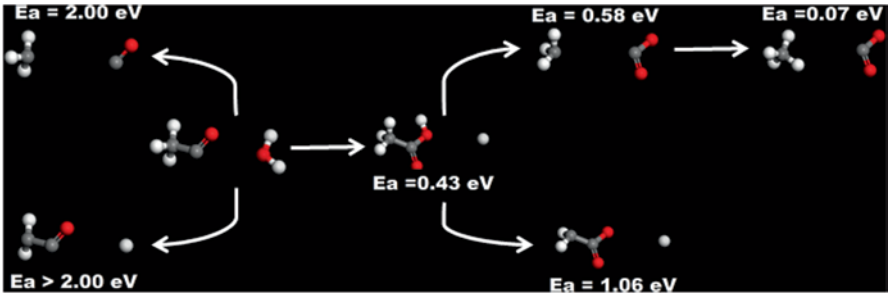


Fig. 5.10 Activation energy for step three and four of ethanol oxidation

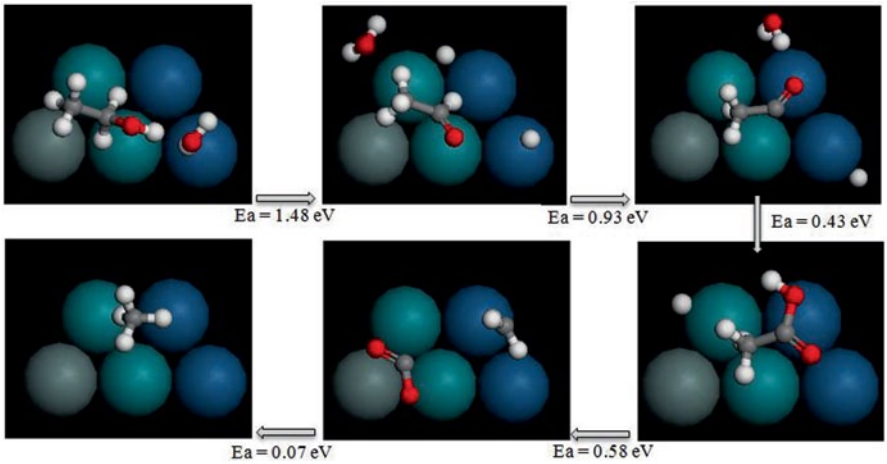


Fig. 5.11 Ethanol mechanism with activation energy for each step

5.3.3 Ethanol Oxidation Across Pt/Ru/Sn: Challenge #3: Kinetic Monte Carlo Model

For this work, Carlos 4.1, developed by John Lukkien and A. P. J Jansen, is used to explore the kinetics of the system. The following assumptions are made to describe and simplify the model.

1. There are no interaction effects between intermediates (blocking/electronic effects)
2. Molecules do not diffuse from one site to another
3. Intermediate molecules do not desorb (only adsorption of ethanol and desorption of CH_4 and CO_2 are considered)
4. Ethanol adsorption and CO_2/CH_4 desorption are independent of overpotential and time

Table 5.3 Binding frequency of 100 molecules

Binding frequency of 100 molecules (%)				
Binding site	Ethanol	Acetaldehyde	Acetyl	Absorbed acetate
Molecules bonded	55	49	52	62
Sn-Ru	12.0	7.0	6.0	3.0
Ru-Ru	7.0	7.0	4.0	10.0
Ru-Pt	24.0	32.0	33.0	26.0
Pt-Pt	2.0	5.0	2.0	4.0
Sn-Ru-Ru	0.0	2.0	0.0	3.0
Ru-Ru-Pt	16.0	7.0	19.0	8.0
Pt-Ru-Pt	11.0	3.0	4.0	13.0
Sn	2.0	3.0	2.0	0.0
Pt	13.0	17.0	15.0	21.0
Ru	13.0	17.0	15.0	13.0

Table 5.4 Binding energies of active site

Binding energies (eV)				
Binding site	Ethanol	Acetaldehyde	Acetyl	Acetate
Sn-Ru	32.0	0.68	0.45	0.11
Ru-Ru	6.54	0.71	0.91	0.25
Ru-Pt	42.9	0.75	1.07	0.42
Pt-Pt	6.79	0.70	0.58	0.31
Sn-Ru-Ru	9.50	0.70	0.53	0.23
Ru-Ru-Pt	5.33	0.71	0.75	0.32
Pt-Ru-Pt	32.0	0.71	0.64	0.36
Sn	11.3	0.67	0.68	0.16
Pt	6.82	0.69	1.02	0.39
Ru	12.6	0.68	1.27	0.28

In order to begin simulations with Carlos 4.1, a crystal lattice and rate constants need to be defined. A 32×32 crystal lattice of actives sites is constructed to perform KMC simulations. In order to develop the crystal lattice we first determine adsorption sites of ethanol and intermediates on configuration 4 of the (1 1 1) plane. Using Adsorption Locator, configuration 4 has a total of 3 top sites, 4 bridge sites, and 3 hollow sites. However, a majority of adsorption for ethanol and intermediates have shown to favor the Pt/Ru bridge site as can be seen in Table 5.3. This is due to the availability of the Pt/Ru bridge site when compares to the other active sites.

A majority of adsorption for ethanol and intermediates was shown to favor the Pt-Ru bridge site as can be seen in Table 5.3. The favoring of the Pt-Ru bridge site was determined by calculating the binding energy of each absorbent to each active site as shown in Table 5.4.

Two observations can be drawn from Table 5.4. The first was that ethanol binds strongly compared to the other species considered in the proposed mechanism. Additionally, a proportional relationship between binding frequency and binding energy may not exist. While Pt-Ru binding energies are typically stronger, there are

Table 5.5 Rate constants used for KMC simulations

	Step 1	Step 2	Step 3	Step 4
ΔG (kcal/mol)	23.1	21.5	9.92	13.4
Rate constant (s^{-1})	2.60E−2	4.69E−1	4.33 E6	2.90E4

cases where the binding energy is similar to the other active sites, such as in the case of acetaldehyde binding, or the Pt-Ru binding energy is not the strongest, such as in the case of acetyl binding. Therefore, there are other factors (such as blocking effects, periodic conditions, theory level) besides binding energy that determines the most active site. Since the KMC simulations showed the Pt-Ru bridge site bonding occurs most frequently, the Pt-Ru bridge site of the catalyst was taken as its active site.

With known activation energies for each step, the rate of reaction under the effect of a voltage can be calculated using Eq. (5.4) which is used as inputs for the kMC simulations (Table 5.5). The simulations begin with a clean catalyst surface and the simulation time is counted using Monte Carlo steps. With each step, the probability for ethanol/intermediate adsorption is calculated.

Once the intermediate is reacted to the final product, CH_4 and CO_2 are desorbed until a preset amount of time has passed. This allows the generation of a concentration profile as shown in Figs. 5.10 and 5.12.

Figure 5.10 shows that the concentration reached steady state in approximately 10s for all species. However, there was no acetyl or acetic acid shown. Acetyl and acetic acid concentration was not shown because they are converted to the next series of species quickly due to their lower energy barrier. Once the simulation has completed, the current can be calculated as the difference of electron producing rates and electron consuming rates. In order to generate the polarization curve, the current is expressed in units of mA/cm^2. The current must be calculated as shown below:

$$i = e_o \sum_{n=1}^{\infty} r_n$$

where i is the current, e_o is the charge of an electron ($e_o = 1.60217646 \times 10^{-19}$°C), and r are the rates of the reactions that generate or consume electrons. For this work, this can be rewritten as

$$i = e_o \cdot (2r_1 + r_2 + r_3 + r_4 - r_5)$$

The reaction rate for the first step, ethanol conversion to acetaldehyde, has a stoichiometric coefficient of 2 due to the generation of 2 electrons. The sign change for the fifth step, r_5, is due to the consumption of an electron during that reaction.

The surface area of the catalyst was calculated starting with an average particle size for Pt_2Ru_2Sn, which was 6.4 nm in diameter [61]. Since a square crystal lattice of 32×32 was considered in this study, the area can be expressed as $(6.4\ \text{nm} \times 32)^2 = 41{,}943\ \text{nm}^2$. Since there were 4 bridge sites, 3 hollow, and 3 top

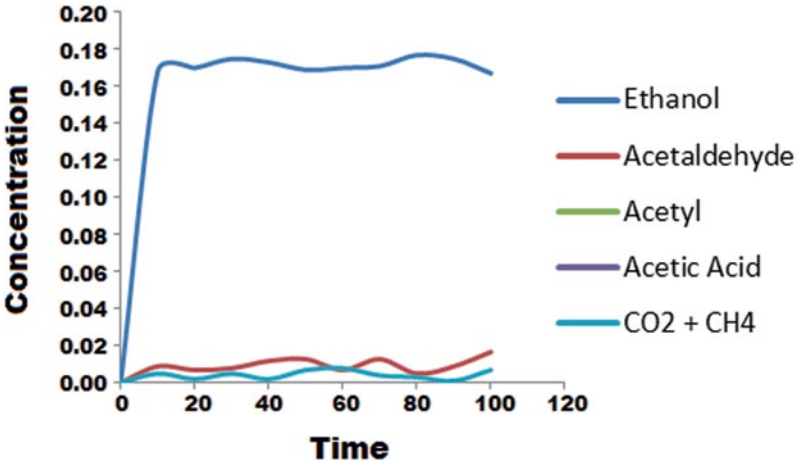


Fig. 5.12 kMC generated concentration profile for ethanol oxidation

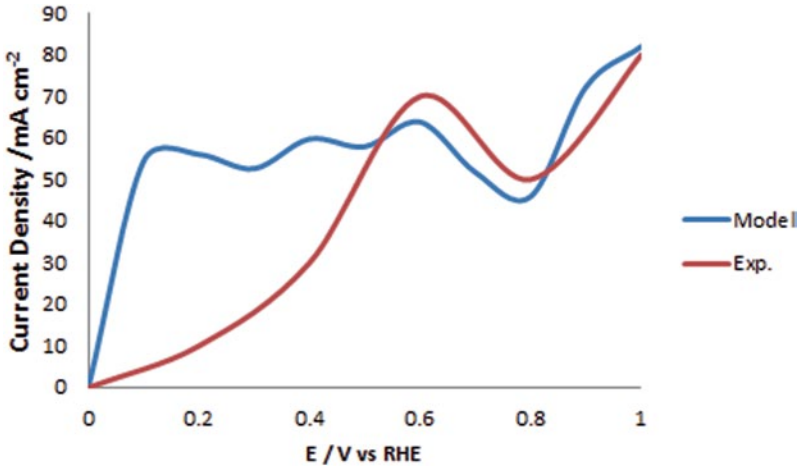


Fig. 5.13 Polarization curve from KMC simulations

sites, the total number of sites in the lattice were $(4+3+3)\times 32\times 32=10{,}240$ sites. The area for a single site can then be expressed as the area of the lattice (41,943 nm^2) divided the number of sites (10,240), which gives a catalytic area of 4.096 nm^2. By knowing the area of an active site, it is then possible to generate a polarization curve that can be compared with experimental results as shown in Fig. 5.13. The polarization curve was generated using a sweeping rate of 10 mV/sec.

Figure 5.13 shows that the calculated I-V curve has an immediate spike to approximately 55 mA/cm^2 from 0.0 V to 0.1 V and fluctuates until 0.8 V. In this range,

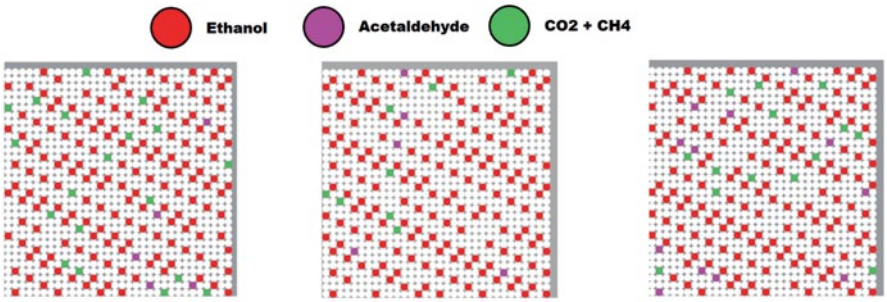


Fig. 5.14 Catalyst surface during ethanol oxidation simulations

the current density is relatively constant because the ethanol molecules have taken up the active sites and the high activation energy required to breaking ethanol into acetaldehyde leaves ethanol on the active sites (Fig. 5.14).

It has been shown that dissociative adsorption of water occurs in the 0.6–0.8 V range and acetic acid is produced as a result. However, in the modeling investigations, dissociative adsorption of water was accounted for in the activation energy calculations. Therefore, it is observed that the voltage began to play a more dominant role in the rate equation around 0.8 V. The overall trend in the calculated I-V curve is the same trend observed by Chu et al. who performed ethanol oxidation across PtRuSn catalyst using 2M Ethanol at 32 °C as shown in red in Fig. 5.13.

While the trends follow the experimental values, the calculated polarization curve did not accurately predict the experimental results up to 0.5 eV. This inaccuracy was attributed to the complexity of kinetics and the assumptions used in this simulation work. In these studies, a single pathway for the ethanol oxidation mechanism has been determined. However, there are always competing and parallel reactions taking place and the possibility of reactions that only occur at the lower potential range, 0–0.5 eV, which were not taken into account in the model presented here. This could lead to the over prediction observed up to 0.5 eV.

The assumptions made for the model may also be the reason for the over prediction of the calculated polarization curve up to 0.5 eV. In this model, zero diffusion effects have been assumed; although there has been research shown that the most active site for binding and the most active site for reacting take place on different active sites [62]. Furthermore, the model did not take into account the interactions between intermediates and the effects of site blocking. These effects are known to either promote or prevent the adsorption of intermediates onto the catalyst. The last assumption that may lead to the discrepancies seen in the modeled and experimental polarization curves is the use of only the most active binding site. From Table 5.3, it can be seen that there are other sites with similar binding frequencies, such as Acetate's binding on both the Pt-Ru bridge site and Pt top site. The model results may vary with the incorporation of additional binding sites.

5.4 Challenges Modeling Biological Catalysts

5.4.1 Case Study of Methanol Oxidation by Methanol Dehydrogenase Enzyme

A prototype bio-fuel cell was built by immobilizing MDH on N, N,N',N'-tetramethyl-p-phenylenediamine (TMPD)-functionalized carbon paste electrode and used as the anodic catalyst that produced a continuous power output of 0.25 mW/cm^2 for 30 days [32]. It is believed that the major factor that effects this fuel cell performance by limiting the power output (expected (theoretical) output is 100 mW/cm^2) is the TMPD mediator, which is responsible for electron transfer resulting to the electrode from the fuel oxidation by the enzyme. Studies on methanol oxidation by ion–modified MDH have shown that the activation energy for the reaction is altered [32].

Enzymatic fuel cells using MDH might offer potentially attractive power sources for some small electronic devices. Thus, for its better usefulness, it is important to increase the stability/activity of this enzyme; hence, understanding the mechanism behind enzyme catalysis becomes significant. With the emergence of powerful and effective computational chemistry tools such as density functional theory and other multi-scale approaches over the past two decades, functioning of enzymes has been unfolded substantially. And such multiscale studies can help design bio-inspired synthetic catalysts.

5.4.1.1 Challenge 1: Active Site Model Size

Typically, enzymes contain thousands of atoms and studying the reactivity of enzymes using small quantum chemical clusters of hundreds of atoms is one of major issue in modeling enzymes [17, 63–66]. It is considered that the catalysis occurs at the reactive cleft known as the active site of the enzyme. In order to represent this reactive portion of the enzyme, a proper model of the active site has to be designed first [17, 63–66]. Normally, these models start from a crystal structure of the enzyme, available from the Protein Data Base (PDB) and most computational studies are based on these structures. As a large number of calculations are involved in studying the reaction pathways, it is extremely important to keep the size of the quantum chemical model as small as possible. Also, it is crucial to choose the model in such a way that, it accurately represents the chemistry taking place at the active site and no essential groups are left out [17, 63–66].

With the aim to reduce the size of the model, cluster approach for modeling enzymes has been employed effectively, where the residues of the active site are truncated in such a way that their side chains or important backbones are included in the model. Both the protonated and unprotonated states of amino acids should be considered in calculations depending on their role in the catalytic mechanism [17, 63–66]. Additionally, based on available structures of enzyme-substrate complexes,

several possible binding modes have to be considered. In metalloenzymes, a large part of the catalysis is influenced by the electronic structure of the metal ion and its immediate environment. To represent the correct model of a metal active site, the coordination shell of the metal ion should be included appropriately. In most instances, the first coordination shell of the metal with a solvation environment is adequate enough; but in circumstances where some second shell residues are known to effect the reactions, they are included explicitly [66–68].

For the model to be a good representation of the enzyme and act like the actual system, two approximations are used, namely the polarizable continuum model and a coordinate-locking scheme as discussed in earlier chapters. From systematic cluster size investigations by Himo et al., it is clearly understood that, as the model size increases the solvation effects are reduced and a more realistic system is possible. This implies more advanced applications will be feasible [17, 63, 64, 66, 68]. In these lines, cluster model studies have been conducted and presented in this chapter to represent the quantum chemical model for MDH [69, 70].

The active site of MDH contains a Pyrroloquinoline Quinone (PQQ) cofactor, a divalent calcium cation, a catalytic base ASP-303, twelve other amino acids, and water molecules. It has been found that the Ca^{2+} ion in the active site of MDH is bonded to the nitrogen atom molecule (N6), the C5 quinone oxygen (O5), the oxygen of the carboxylate (O10) of the PQQ, the oxygen atoms (O12 and O13) from the carboxylate of Glu-177, and the oxygen atoms O11 and O14 of Asn-261 and Asp-303, respectively (Fig. 5.15) [71]. Results from X-ray studies, distances from the Ca^{2+} ion to the N6, O5, and O10 atoms of PQQ are in the 2.32–2.47, 2.25–2.77, and 2.30–2.44 Å range, respectively. Ca^{2+} ion in the active site holds the PQQ in place and also acts as a Lewis acid during the oxidation mechanism. From previous studies, it was observed that the energy barrier for the oxidation of methanol was influenced by the atomic size of the metal ion in the active site of MDH [71–73].

Different active site models were considered with relevant amino acids to shed light on which amino acid acts as the most active catalytic base for the methanol oxidation to proceed. From our methanol binding energy calculations, it was reported that Asp303 plays a key role and representative MDH model should contain this amino acid [69]. Also, it was concluded that additional amino acids and water molecules in the active site model need to be included for studying the oxidation mechanism by MDH. Accordingly, the best active site model for MDH was determined as PQQ + Ion + Asp-303 + Glu-177 + Asn-261 + 3 nearby water molecules, to provide accurate information about the reaction mechanisms [69, 70]. Although, this active site model is sufficient enough to study the enzyme kinetics at the microscopic level, to model enzyme kinetics using a kinetic Monte Carlo approach, at the macroscopic level, larger active site model need to be considered. Thus, an active site model containing all the 13 amino acids and nearby water molecules is considered in the DFT based MD simulations to validate the already proposed oxidation mechanisms.

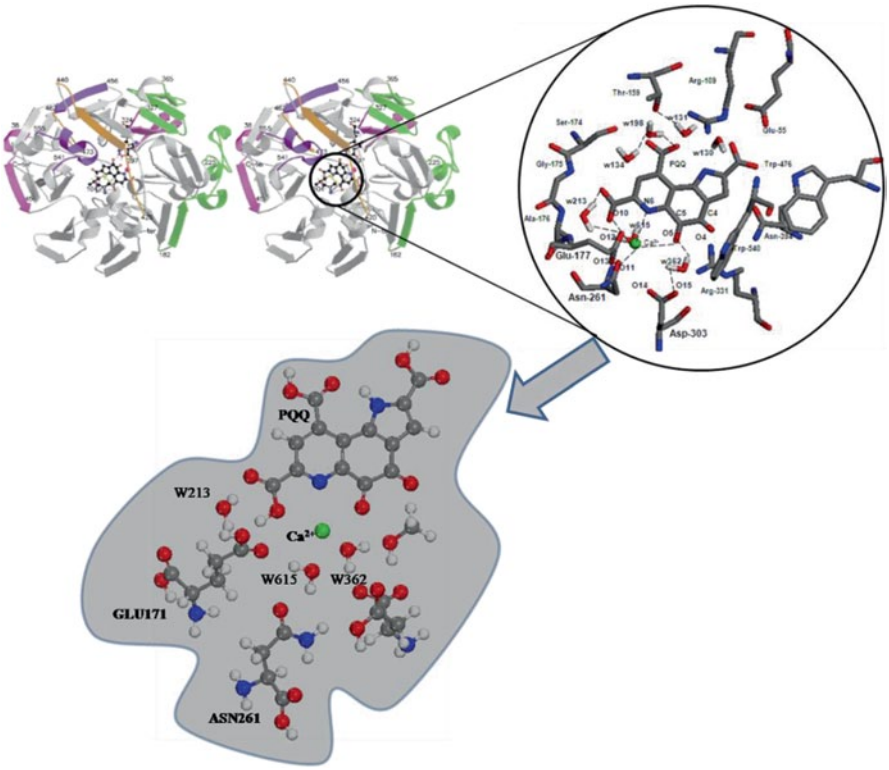


Fig. 5.15 Active site model by identifying important groups from MDH active site

5.4.1.2 Challenge 2: Methanol Oxidation Mechanism—Macroscopic Reaction Rates

The next challenge is to obtain the macroscopic rates for the methanol electro-oxidation mechanism, for which the activation barriers for the reactions need to be obtained first. In the literature, two mechanisms for the oxidation of methanol by the naturally occurring Ca^{2+}-containing MDH have been commonly proposed: the three step addition-elimination (A–E) mechanism and the four step Hydride transfer (H–T) mechanism [72]. The rate determining step for methanol oxidation is known to be the formation of formaldehyde. No agreement has been reached in the literature regarding which mechanism (A–E or H–T) actually operates in nature; however the Hydride Transfer (H-T) mechanism seems to be the preferred one from recent studies. Hence, in this study the Hydride transfer mechanism is considered.

The four-step H-T mechanism (Fig. 5.16) shows the simultaneous transfer of two protons (H16 and H17) from methanol to the active site base (H16) and to the carbon C5 of PQQ (H17), leading to the formation of formaldehyde in the very first step of the mechanism. Thus, the presence of the catalytic base Asp-303 at the MDH

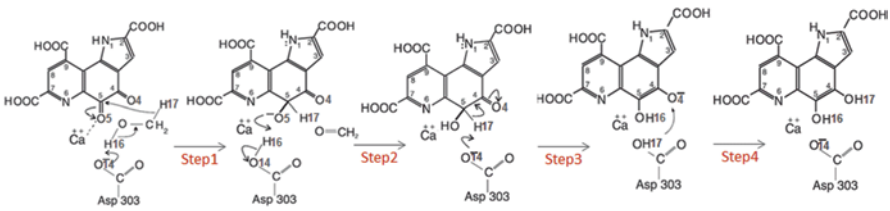


Fig. 5.16 Proposed hydride transfer methanol oxidation mechanisms by Ca^{2+}-containing methanol dehydrogenase enzymes [72]

active site is believed to initiate the oxidation reaction [72, 73]. In the second step, H16 is transferred from the active base to the oxygen O5 of PQQ. The third step involves the transfer of H17 from C5 of PQQ to the active site base, and finally in the last step, H17 is transferred from the active site base to the oxygen atom O4 of PQQ [72, 73].

In order to investigate the H-T methanol oxidation mechanism, the MDH active site model consists of the PQQ molecule, divalent ion, aspartic acid, glutamic acid, asparagine and three water molecules (Fig. 5.15). According to the Himo et al. approach, unprotonated (charged) amino acids can be modeled by their corresponding protonated (neutral) amino acids. This was implemented and tested by Himo et al. and well justified by the fact that proteins and enzymes have low dielectric constants ($\varepsilon \sim 4$), indicating that charge separation, if present, should be very small [17]. These authors have shown that, by using these charge-neutral models, accurate enzymatic reaction energies and barriers were yielded. Thus, in our model we used the "Charge-neutral models" for amino acids.

The reactant, intermediates and product for the four steps of the mechanism were optimized using the DMOL^3 module of the Materials Studio® software by Accelrys, Inc. [60]. It is a quantum mechanical package that models the electronic structure and energetics of molecules, solids and surfaces using Generalized Gradient Approximation (GGA) functionals within the Density Functional Theory formalism [60]. The Becke–Lee–Yang–Parr (BLYP) [74, 75] exchange correlation functional and the double numerical with polarization (DNP) basis set, the best set available in DMOL^3, [60] were used for performing the optimization calculations. The DNP basis set considers a polarization *d* function on heavy atoms and a polarization *p* function on hydrogen atoms. It can be compared to split-valence double zeta 6-31G** basis set in size, but is more accurate than the Gaussian basis sets of the same size. The errors are expected to be in the second decimal for calculated bond lengths (Å) and in the order of 2–5 (kcal/mol) in energies when BLYP/DNP theory level is used; which has been proven to be acceptable for the study of Ca^{2+}- and Ba^{2+} -MDH [69, 76].

Quantum chemical models of enzyme active sites are used to study the enzyme H–T reaction mechanism (Fig. 5.16). Accordingly for treating the neglected enzyme environment, a homogeneous polarizable medium with some assumed dielectric constant is used, and density functional theory calculations are then performed to obtain reaction energy barriers. A homogeneous polarizable medium was

considered with a continuum solvation model known as COSMO (conductor-like screening model) as implemented in the DMOL^3 module, to estimate solvation effects of the rest of the enzyme that are not included in the model. This model works in such a way that the solute molecule forms a cavity within the dielectric continuum of permittivity that represents the solvent [60]. To model the protein surroundings, the standard value for the dielectric constant ε was chosen to be 4 and so that the final energy includes the DMOL^3/COSMO electrostatic energy, the geometry optimizations were performed in the presence of this solvation model. To confirm that the stationary points on the potential energy surface of the systems are in fact local minima (all real frequencies) or transition states (only one imaginary frequency), the harmonic vibrational frequency calculations were performed [60].

5.4.1.3 Challenge 3: Kinetic Monte Carlo Modeling

The kMC program, Carlos 4.1, developed by John Lukkien and A. P. J Jansen is used in this work. To explore the kinetics and construction of the lattice representing the enzyme active site, it is important to discuss the assumptions and boundary conditions of the systems, since the reaction mechanics are relative to these aspects. The assumptions made to describe the model and to reduce complexity are noted as follows [45]:

1. On the surface of the lattice, the substrate molecules follow a random walk.
2. The individual substrate molecules do not interact with each other.
3. There are no interactions between the substrate molecules and the obstacles.
4. The substrate molecules move towards the active site by the shortest available distance following the random walk motion.
5. The excluded volume condition is maintained i.e. at any instant of time one lattice site cannot be occupied by more than one molecule of the same or different species.

A simple Michaelis-Menten equilibrium enzyme kinetics equation is considered [77]:

$$E + S \rightarrow ES \rightarrow E + P \tag{5.8}$$

where E denotes the enzyme, S denotes the substrate (methanol), ES is the intermediate complex (enzyme–substrate), and P is the product (formaldehyde).

It is considered that the reaction is diffusion limited, thus, the formation of an intermediate ES is not taken into account and the substrate is almost instantaneously converted to product at the active site (A). Therefore, Eq. (5.1) reduces to a simpler reaction between the active site (A) and the substrate (S) molecule [45].

$$A + S \xrightarrow{k_{(t)}} A + P \tag{5.9}$$

A 64×64 lattice with cyclic boundary conditions was used to carry out the simulations. To construct the 2-D lattice, a coarse graining method where the molecules

Table 5.6 Rate constants used in the kMC MDH-assisted methanol oxidation mechanism study

	Step 1	Step2	Step3	Step4
ΔG (kcal/mol)	19.7	16.2	15.3	12
Rate constant, r (sec−1)	2.25E−02	8.27E+00	3.78E+01	9.92E+03

are represented as beads was considered, where, the center of masses for all the amino acids in MDH were obtained and plotted with the active site amino acids as the center. To model enzymatic reactions, the distribution of the substrate and obstacles (amino acids that are not part of the active site) is an important aspect to consider. Hence, random sampling methods to distribute the species on the lattice have been used for enzyme kinetics modeling and they have showed that the enzyme kinetics was influenced by aspects like obstacle density. Thus, according to the approach described by Dandala et al., a biased approach is used in sampling the lattice and to investigate its effect on the kinetics of methanol oxidation by MDH [45].

The rate constants of H-T process are given as input at the start of each simulation and these are calculated from the activation energies obtained through the DFT calculations [70, 78]. The free energy reaction barriers for the rate limiting step of the H-T mechanism (Step1) were used for this case study (Table 5.6).

At the start of each simulation, the obstacle and substrate concentrations are specified and the simulation time is counted in Monte Carlo steps. The simulation is initiated with the substrate molecules (*red*) diffusing (making a random walk) towards the active site amino acids (*green*) which are distributed at the center of the lattice with the obstacles scattered (*black*) on it (Fig. 5.17). And when the substrate molecules come in contact with any one of the active site amino acids, a product (*blue*) is formed which also diffuses on the lattice. Apart from gaining insight about the catalytic reactions taking place inside the enzyme, useful information, such as the concentration profiles of substrate and product with respect to Monte Carlo time, obstacle density, reaction rate constants and the positions of obstacles on the lattice can be obtained using this model [45].

Enzyme kinetics is typically governed by the rate of formation of product or the disappearance of a reactant. In the event that either the reactant or product is electroactive i.e. can either produce or consume electrons during the catalytic mechanism; the progress of the reaction can be monitored using amperometry. And this concept of the bio-electrochemical reactions taking place on the surface of an electrode can be used for the generation of current for bio-sensors/fuel cell devices. Enzyme oxidation process produces electrons which are transferred to the anode, where they proceed through an electrical circuit before reaching the cathode. Hence, by the catalytic activity of the enzyme, current now flows over a potential difference and power is generated directly from the fuel [79].

Likewise, according to Zhang et al., the energy generation in the MDH catalyzed biofuel cell follows a five step process. In the first step, electrons are released by the process of oxidation of methanol (substrate) by the enzyme (reaction taking place at the active site of the enzyme) and this step is considered potentially limiting. The second step involves the transfer of the electrons from the reduced enzyme to the

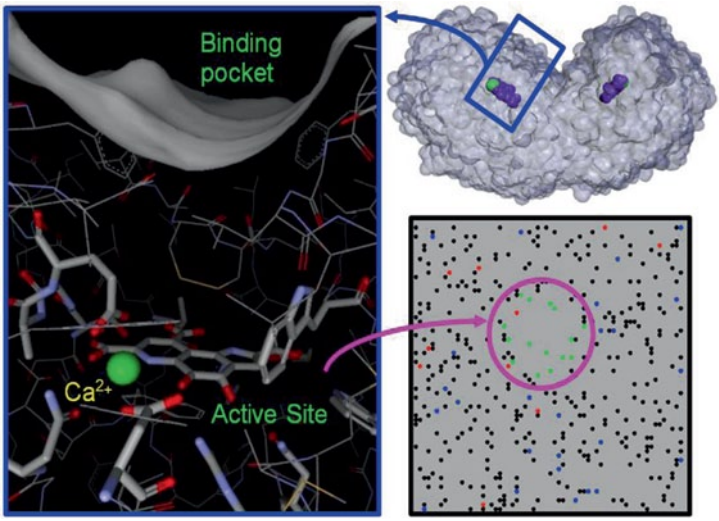


Fig. 5.17 Ca^{2+}-containing MDH (*top-right*) and view of its binding pocket and active site (*left*) [45]. Projection of active site components (*green*) and other residues (*black*) according to their center of masses (and plotted as *dots*), onto a 2-D lattice representing the biocatalytic surface (*right*). Red and blue dots represent substrate (methanol) and product (formaldehyde) molecules

mediator (TMPD). The next steps (Step 3 and 4) involve the transfer of the electrons from the oxidized mediator to the cathode through an external circuit when a load is applied and this cycle of electron transfer continues. In the final step, a cathodic reaction with potassium permanganate occurs [32].

Since the first step is considered the potentially limiting step, it is important to understand thoroughly the oxidation mechanism of methanol and the enzyme kinetics behind it. In order to understand the MDH enzyme kinetics, the rate of consumption of substrate (methanol) and rate of formation of product (formaldehyde) were obtained as shown in Fig. 5.18. It was observed that methanol concentration is reduced and formaldehyde concentration increased.

Further, the current at the electrode can be obtained using the equation below

$$\text{Current} = \Sigma\left(e^{-}\text{production rates}\right) - \Sigma\left(e^{-}\text{consumption rates}\right) \tag{5.10}$$

In order to investigate the electrochemistry associated with MDH kinetics, the four step H-T mechanism can be considered as follows

$$\mathbf{S + PQQ + ASP^{-} \rightarrow P + PQQH^{+} + ASPH^{+} + 2e^{-}}$$
$$\mathbf{ASPH^{+} + PQQH^{+} + e^{-} \rightarrow PQQ^{*}H_{2} + ASP^{-}}$$
$$\mathbf{PQQ^{*}H_{2} + ASP^{-} + e^{-} \rightarrow PQQ*H^{+} + ASPH^{+} + e^{-}}$$
$$\mathbf{ASPH^{+} + PQQH^{+} + e^{-} \rightarrow PQQH_{2} + ASP^{-} + e^{-}}$$

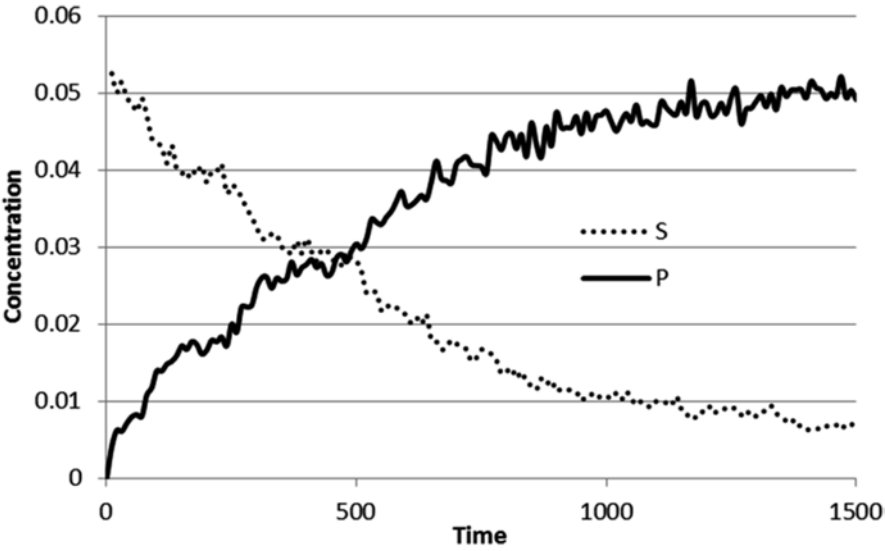


Fig. 5.18 Concentration profiles of substrate and product molecules formed for MDH active site models with respect to time

Thus, in this case current, $i = e_0(2r_2 - r_3 + r_4 + r_5)$, where e_0 is the charge of an electron, are used to evaluate the polarization curves. The rates for the mechanism steps are obtained by the kMC program using the Eq. (5.10) and these outputs will provide current. Hence, these will provide information on the performance of the bio-fuel cell using MDH as an electrode.

5.5 Conclusions

Currently, discovering a permanent form of energy is a growing concern for mankind. The world relies on a finite supply of fossil fuels to fuel everyday needs, which cannot sustain the world's population indefinitely. Furthermore, traditional combustion engines utilized to break down fossil fuels into energy have been shown to be inefficient. These issues have brought about a necessity for clean and renewable energy. Numerous power technologies have been explored and among them fuel cells have been nominated as a potential solution for this crisis. Fuels cells have the ability to convert chemical energy to electrical at higher efficiency compared to combustion engines at the cost of a lack of energy output.

Numerous obstacles will need to be cleared before commercialization of fuel cells become viable such as sluggish reaction rate, expensive catalyst, and energy output. In this chapter, these challenges are presented and exampled with two case studies dealing with the modeling of chemical and biological catalysts for fuel oxidation in PEM fuel cells. In the case of chemical catalysts, the oxidation of ethanol

across a ternary catalyst composed of platinum (Pt), ruthenium (Ru), and tin (Sn) is presented. As the corresponding crystal structure is unknown, a feasible substrate model for Pt_2Ru_2Sn catalyst has been created, and a reaction network for ethanol oxidation based on transition state and free energy barrier calculations proposed. Furthermore, kinetic motel carlo (kMC) simulations were performed utilizing the energy barrier calculations for real time data across a ternary catalyst.

The ethanol oxidation mechanism on Pt_2Ru_2Sn was shown to be a four step process, which differs from the one observed on pure platinum by an additional step. The rate limiting step is determined to be the first step, ethanol conversion to acetaldehyde, due to a high energy barrier of 1.48 eV. Furthermore, the production of CO is a possible side reaction, which occurs in the first step of this mechanism that has a low energy barrier, 0.07 eV, compared to the oxidation of CO to CO_2 at 2.84 eV. The calculated energy barriers for each steps are used to generate rates of reaction to be used in Carlos 4.1 Kinetic Monte Carlos simulation to produce a polarization curve which have been shown to match the trends of experimental results fairly.

In the case of biological catalysts, enzymes have been considered as molecular electrocatalysts due to their extraordinary characteristics. However, enzymatic fuel cells have been reported to have power output and stability limitations; which are restricting the use of this kind of fuel cell to small electronic devices. Methanol dehydrogenase (MDH) is one such enzyme, which oxidizes methanol and other primary alcohols to their corresponding aldehydes.

From the proposed mechanisms for methanol oxidation by MDH in the literature, the Hydride Transfer mechanism seems, to the best of our knowledge, to be the preferred one under normal conditions. Density Functional Theory (DFT) calculations at BLYP/DNP theory level are performed using the $DMOL^3$ module of the Materials Studio software to evaluate ground state structures and investigate the reaction pathways. Further, polarization curves corresponding to the electrochemical methanol oxidation in bio fuel cell anodic chambers when MDH enzymes are used as the anode catalysts are obtained using kinetic Monte Carlo approach. Microscopic reaction rates, obtained from free energy barriers evaluated using DFT and transition state theory are provided as inputs in a kinetic Monte Carlo approach to model the oxidation process at macroscopic level. These simulations give a better understanding of the catalytic methanol oxidation mechanism by MDH, helping evaluate the enzyme catalysis.

References

1. Aaron D, Yiacoumi S, Tsouris C (2008) Effects of proton-exchange membrane fuel-cell operating conditions on charge transfer resistances measured by electrochemical impedance spectroscopy. Sep Sci Technol 43(9–10):2307–2320
2. Larminie J, Dicks A (2003) Fuel cell systems explained. Wiley, Chichester
3. Sahu AK et al (2009) Nafion and modified-Nafion membranes for polymer electrolyte fuel cells: an overview. Bull Mater Sci 32(3):285–294

4. DOE announces up to $ 74 million for fuel cell research and development. Department of Energy, Editor. 2010, GPO, Washington. http://energy.gov/articles/doe-announces-74-million-fuelcell-research-and-development.
5. Markovic NM, Ross PN Jr (2002) Surface science studies of model fuel cell electrocatalysts. Surf Sci Rep 45:117–229
6. Cleghorn SJC, Ren X, Springer TE, Wilson MS, Zawodzinski C, Zawodzinski TA, Gottesfeld S (1997) PEM fuel cells for transportation and stationary power generation applications. Int J Hydrog Energy 22:1137–1144
7. Iwase M, Kawatsu S (1995) Optimized CO tolerant electrocatalysts for polymer electrolyte fuel cells. In: Proceedings of the first International Symposium on proton conducting membrane fuel cells
8. Beard BC, Ross PN (1990) The structure and activity of Ptâ€ co alloys as oxygen reduction electrocatalysts. J Electrochem Soc 137(11):3368–3374
9. Bockris JOM, Khan SUM (1993) Surface electrochemistry: a molecular level approach. Plenum Press, New York
10. Ghosh M et al (1995) The refined structure of the quinoprotein methanol dehydrogenase from *Methylobacterium extorquens* at 1.94 Å. Structure (London) 3:1771–1787
11. Fernandez GM, Anderson JA (1996) Alloy formation and stability in Pd-Cu bimetallic catalysts. J Phys Chem 100:16247–16254
12. Toda T et al (1999) Enhancement of the electroreduction of oxygen on Pt alloys with Fe, Ni, and Co. J Electrochem Soc 146(10):3750–3756
13. Toda T, Igarashi H, Watanabe M (1999) Enhancement of the electrocatalytic O2 reduction on Pt-Fe alloys. J Electroanal Chem 460(1):258–262
14. Neergat M, Shukla AK, Gandhi KS (2001) Platinum-based alloys as oxygen reduction catalysts for solid polymer electrolyte direct methanol fuel cells. J Appl Electrochem 31(4):373–378
15. Huang SP, Mainardi DS, Balbuena PB (2003) Structure and dynamics of graphite-supported bimetallic nanoclusters. J Surf Sci 545:163–179
16. Markovic NM et al (1999) Oxygen reduction reaction on Pt(111): effects of bromide. J Electroanal Chem 467(1–2):157–163
17. Himo F (2002) Catalytic mechanism of benzylsuccinate synthase, a theoretical study. J Phys Chem B 106(31):7688
18. Combe N, Jensen P, Pimpinelli A (2000) Changing shapes in the nanoworld. Phys Rev Lett 85(1):110–113
19. Heinebrodt M et al (1999) Bonding character of bimetallic clusters Au[sub n]X[sub m] (X = Al, In, Cs). J Chem Phys 110(20):9915–9921
20. Vigier F et al (2006) Electrocatalysis for the direct alcohol fuel cell. Top Catal 40(1–4):111–121
21. Kannan AM, Renugopalakrishnan V, Filipek S, Li P, Audette GF, Munukutla L (2009) Bio-batteries and bio-fuel cells: leveraging on electronic charge transfer proteins. J Nanosci Nanotechnol 3:1665–1678
22. Hibbert EG et al (2005) Directed evolution of biocatalytic processes. Biomol Eng 22(1–3):11–19
23. Hollmann F et al (2011) Enzyme-mediated oxidations for the chemist. Green Chem 13(2):226–265
24. Yahiro AT, Lee SM, Kimble DO (1964) Bioelectrochemistry: I. Enzyme utilizing bio-fuel cell studies. Biochim Biophys Acta (BBA)—specialized section on biophysical subjects 88(2):375–383
25. Kim J, Ping Wang HJ (2006) Challenges in biocatalysis for enzyme-based biofuel cells. Biotechnol Adv 24:296–308
26. Liu L et al (2008) A novel inhibition biosensor constructed by layer-by-layer technique based on biospecific affinity for the determination of sulfide. Sens Actuators B: Chem 129(1):218–224

27. Suwansa-ard S et al (2005) Semi disposable reactor biosensors for detecting carbamate pesticides in water. Biosens Bioelectron 21(3):445–454
28. Sakai H et al (2009) A high-power glucose/oxygen biofuel cell operating under quiescent conditions. Energy Environ Sci 2(1):133–138
29. Laurinavicius V et al (2002) Bioelectrochemical application of some PQQ-dependent enzymes. Bioelectrochemistry 55:29–32
30. Duine JA (1999) The PQQ story (Review). J Biosci Bioeng 88:231–236
31. Lapėnaitė I, Kurtinaitienė B, Pliuškys L, Laurinavičius V, Bachmatova I, Marcinkevičienė L, Ramanavičius A (2003) Application of PQQ-GDH based polymeric layers in design of biosensors for detection of heavy metals. Mater Sci (MEDŽIAGOTYRA) 9(4):431–435
32. Zhang XC, Ranta A, Halme A (2006) Direct methanol biocatalytic fuel cell—considerations of restraints on electron transfer. Biosens Bioelectron 21:2052–2057
33. Zhang XC, Ranta A, Halme A (2003) Effect of different catalytic oxidants on the performance of a biocatalytic methanol fuel cell. In: Proceedings 204th meeting of the electrochemical society
34. Tozzini V (2010) Multiscale modeling of proteins. Acc Chem Res 43:220–230
35. Dalby PA (2007) Engineering enzymes for biocatalysis. Recent Pat Biotechnol 1:1–9
36. Parks JM, Imhof P, Smith JC (2010) Understanding enzyme catalysis using computer simulation. Encyclopedia of catalysis 2nd edition. Wiley
37. Lyubartsev A, Tu Y, Laaksonen A (2009) Hierarchical multiscale modelling scheme from first principles to mesoscale. J Comput Theor Nanosci 6:1–9
38. Medina GM, Rey RM (2009) Molecular and multiscale modeling: review on the theories and applications in chemical engineering. CT&F—Ciencia, Tecnologíay Futuro 3(5):205–224
39. Car R (2002) Introduction to density-functional theory and ab-initio molecular dynamics. Quant Struct-Activity Relatsh 21(2):97–104
40. Marques MAL, Gross EKU (2004) Time-dependent density functional theory. Annu Rev Phys Chem 55(1):427–455
41. Ponder JW, Case DA (2003) Force fields for protein simulations. Adv Protein Chem 66:27–85
42. Nieminen RM (2002) From atomistic simulation towards multiscale modelling of materials. J Phys Condens Matter 14:2859–2876
43. Lukkien JJ et al (1998) Efficient Monte Carlo methods for the simulation of catalytic surface reactions. Phys Rev E 58(2):2598–2610
44. Nieminen RM, Jansen APJ (1997) Monte Carlo simulations of surface reactions. Appl Catal A:General 160:99–123
45. Dandala NKR, Jansen APJ, Mainardi DS (2010) A multi-scale modeling approach for studying MDH-catalyzed methanol oxidation. In: Derosa P, Cagin T (eds) Multiscale modeling: from atoms to devices. CRC Press, Florida, pp 91–112
46. Hills CW et al (1999) Carbon support effects on bimetallic Pt-Ru nanoparticles formed from molecular precursors. Langmuir 15(3):690–800
47. Thomas G (2000) Overview of storage development. D.o. Energy, San Ramon
48. Vigier F et al (2004) Development of anode catalysts for a direct ethanol fuel cell. J Appl Electrochem 34(4):439–446
49. Datta J et al (2009) A comprehensive study on the effect of Ru addition to Pt electrodes for direct ethanol fuel cell. Bull Mater Sci 32(6):643–652
50. Ribeiro J et al (2008) Effect of W on PtSn/C catalysts for ethanol electrooxidation. J Appl Electrochem 38(5):653–662
51. Demirbas A (2008) Direct use of methanol in fuel cells. Energy Sour Part A Recovery Util Environ Eff 30(6):529–535
52. Mehta V, Cooper JS (2003) Review and analysis of PEM fuel cell design and manufacturing. J Power Sour 114(1):32–53
53. Gurau B et al (1998) Structural and electrochemical characterization of binary, ternary, and quaternary platinum alloy catalysts for methanol electro-oxidation 1. J Phys Chem B 102(49):9997–10003

54. Ferrin P et al (2009) Modeling ethanol decomposition on transition metals: a combined application of scaling and Brønsted–Evans–Polanyi relations. J Am Chem Soc 131(16):5809–5815
55. Antolini E (2007) Platinum-based ternary catalysts for low temperature fuel cells: part I. Preparation methods and structural characteristics. Appl Catal B Environ 74(3–4):324–336
56. Westmoreland PR et al (2002) Applying molecular and materials modeling. Kluwer Academic Publishers, Boston
57. Jusys Z et al (2002) Activity of PtRuMeOx (Me = W, Mo or V) catalysts towards methanol oxidation and their characterization. J Power Sour 105(2):297–304
58. Marinov NM (1999) A detailed chemical kinetic model for high temperature ethanol oxidation. Shock 3:2
59. Wang HF, Liu ZP (2008) Comprehensive mechanism and structure-sensitivity of ethanol oxidation on platinum: new transition-state searching method for resolving the complex reaction network. J Am Chem Soc 130(33):10996
60. Accelrys Inc (2003) DMOL3 user guide 2003. San Diego
61. Yang LX et al (2004) A comparative study of PtRu and PtRuSn thermally formed on titanium mesh for methanol electro-oxidation. J Power Sour 137(2):257–263
62. Bruce DA (2013) Catalysis: making the leap to tomorrow's fuels. In: LA-SiGMA. Ruston
63. Himo F (2006) Quantum chemical modeling of enzyme active sites and reaction mechanisms. Theor Chem Acc 116:232–240
64. Siegbahn PE, Himo F (2011) The quantum chemical cluster approach for modeling enzyme reactions. WIREs Comput Mol Sci 1:323–336
65. Siegbahn PEM, Himo F (2009) Recent developments of the quantum chemical cluster approach for modeling enzyme reactions. J Biol Inorg Chem 14:643–651
66. Shi-Lu C, Wei-Hai F, Himo F (2008) Technical aspects of quantum chemical modeling of enzymatic reactions: the case of phosphotriesterase. Theor Chem Acc 120:515–522
67. Noodleman L et al (2004) Quantum chemical studies of intermediates and reaction pathways in selected enzymes and catalytic synthetic systems. Chem Rev 104:459–508
68. Lovell T et al (2003) Density functional methods applied to metalloenzymes. Coordination Chem Rev 238–239: 211–232
69. Idupulapati NB, Mainardi DS (2009) Coordination and binding of ions in Ca^{2+}- and Ba^{2+}-containing methanol dehydrogenase and interactions with methanol. J Mol Struct: THEOCHEM 901(1–3):72
70. Idupulapati NB, Mainardi DS (2010) Methanol electro-oxidation by methanol dehydrogenase enzymatic catalysts: a computational study. In: Balbuena PB, Subramanian VR (eds) Theory and experiment in electrocatalysis. Springer, New York, pp 243–274
71. Williams PA et al (2005) The atomic resolution structure of methanol dehydrogenase from *Methylobacterium extorquens*. Acta Cryst Sect D D61:75–79
72. Anthony C, Williams P (2003) The structure and mechanism of methanol dehydrogenase. Biochim Biophys Acta 1647:18–23
73. Anthony C (2000) Methanol dehydrogenase, a PQQ-containing quinoprotein dehydrogenase. In: Holzenburg A, Scrutton NS (eds) Subcellular biochemistry. Kluwer Academic, New York, pp 73–118
74. Becke AD (1988) Density-functional thermochemistry III. The role of exact exchange. J Chem Phys 88:2547
75. Lee C, Yang W, Parr R (1998) Accurate and simple analytic representation of the electron-gas correlation energy. Phys Rev B 37:786
76. Idupulapati NB, Mainardi DS (2008) A DMOL3 study of the methanol addition-elimination oxidation mechanism by methanol dehydrogenase enzyme. Mol Sim 34:1057–1064
77. Cornish-Bowden A (2004) Fundamentals of enzyme kinetics. Portland Press, London
78. Idupulapati NB, Mainardi DS (2010) Quantum chemical modeling of methanol oxidation mechanisms by methanol dehydrogenase enzyme: effect of substitution of calcium by barium in the active site. J Phys Chem A 114(4):1887
79. Sarmaa AK, Vatsyayan P, Goswami P, Minteer SD (2009) Recent advances in material science for developing enzyme electrodes. Biosens Bioelectron 24:2313–2322

Chapter 6
Molecular Dynamics Studies of Graphite Exfoliation Using Supercritical CO_2

Jose L. Gomez-Ballesteros, Alejandro Callejas-Tovar, Luiz A. F. Coelho and Perla B. Balbuena

Abstract Molecular dynamics simulations are used to investigate the microscopic mechanisms of graphite exfoliation using CO_2 at supercritical conditions. Two approaches are used: simulations in the canonical ensemble are done by keeping the atoms in the graphite structure fixed but increasing the interlayer separations above their normal value. This procedure allows us to determine the interlayer separation at which the CO_2 molecules may be able to intercalate graphite at near and supercritical pressures and temperatures, and to evaluate self-diffusion coefficients at those conditions. In the second approach, the isothermal-isobaric ensemble is utilized allowing graphite to relax, to observe how the exfoliation process may take place at the various pressures and temperatures near and above the CO_2 critical point. Analyses of the simulation trajectories reveal that the exfoliation process takes place at increasing rates as the pressure increases at constant temperature, with intercalation of CO_2 molecules causing bending and then separation of graphene layers.

6.1 Introduction

Nanostructured materials are composed of ultra-small elements that are self-assembled during synthesis or are the result of a controlled synthesis (metamaterials) [1, 2]. The first group (uncontrolled synthesis) constitutes the majority of the nanomaterials currently integrating devices [1]; the second group is a goal which could provide numerous advantages in fields as diverse and equally influential for society as medicine, energy, and education [3, 4]. Current engineering design approaches tend to follow one of the possible built-knowledge tactics for evolving the design toward refined materials: (a) Understanding the behavior of new materials synthe-

P. B. Balbuena (✉) · J. L. Gomez-Ballesteros · A. Callejas-Tovar
Department of Chemical Engineering, Texas A&M University,
College Station TX 77843, USA
e-mail: balbuena@tamu.edu

L. A. F. Coelho
Materials Science and Engineering Department, Santa Catarina State University,
Florianópolis, Brazil

J. M. Seminario (ed.), *Design and Applications of Nanomaterials for Sensors,*
Challenges and Advances in Computational Chemistry and Physics 16,
DOI 10.1007/978-94-017-8848-9_6, © Springer Science+Business Media Dordrecht 2014

sized via trial and error procedures; (b) Understanding the behavior of model experimental systems that are created simplifying the physical reality; (c) Use of theoretical and simulation approaches. The three approaches are not incompatible; thus the optimal situation should consider design based on all these elements. However, both the advent of nanotechnology and the extraordinary advances in hardware and software place us in an advantageous position to strongly focus and advance the third line of approaching the design problem [5]. For this, we need to make a clear characterization of the system (s) of interest using the best theoretical/computational methods available and developing new ones.

In this work, we focus on one of the most novel and promising nanomaterials: graphene. After the discovery of carbon nanotubes by Iijima [6, 7] a huge amount of experimental and theoretical works have been developed aiming to find diverse applications for these and other carbon-based nanomaterials [8–12]. More recently, graphene was isolated by a very simple and somehow unusual method: micromechanical cleavage or Scotch tape method [13–16].Because of its outstanding mechanical, thermal, optical and electronic properties [17], graphene is among the set of recently discovered materials that are expected to hugely impact diverse fields of science and engineering such as nanoelectronics, sensors, hydrogen and energy storage [17], water desalination [18], catalysis [19], composite materials [20] and biomedicine [21]. Considerable high carrier mobility, quantum hall effect at room temperature and the detection of a single molecule adsorption event for the first time are some of the observations that have triggered substantial efforts to implement graphene in different kinds of devices to make the most of it, and at the same time to find methods to produce high-quality monolayers of graphene [17, 19].

Graphene can be obtained by chemical or physical methods or a combination of both. Thus, currently graphene nanosheets are obtained either by chemical synthesis or by physical separation of the individual layers present in graphite [17]. The first approach comprises bottom-up methods to grow graphene from organic precursors and substrate-based growth using chemical vapor deposition methods. On the other hand, separation of the graphene layers by overcoming van der Waals interactions between layers in graphite has been achieved by purely physical (mechanical) exfoliation, by chemical methods: chemical and electrochemical exfoliation, and by combination of physical and chemical techniques such as ultrasonic treatment in organic solvents [19]. Some of the disadvantages of these techniques are low throughput and yield in the mechanical methods, modification of the crystal lattice, and limitations in size and uniformity in the chemical approaches [17, 19]. Efficient procedures to produce graphene ought to incorporate an appropriate balance between speed of production, preservation of graphene quality, low cost and reduced environmental impact.

A viable alternative is the use of supercritical fluids to intercalate and exfoliate the tightly-stacked graphene layers in graphite. The main advantage of the use of fluids above their critical temperature and pressure is the displaying of both gaseous and liquid properties, their ability to permeate materials as a gas due to a high diffusivity, low viscosity, and zero surface tension, together with their ability to easily

dissolve other materials as a liquid. Particularly, supercritical CO_2 is in addition a nontoxic, nonflammable, eco-friendly solvent and has been shown to be relatively easy to attain at its critical conditions ($T_c = 304.2$ K and $P_c = 7.38$ MPa) [22]. As for graphite, the separation distance between layers is approximately 3.35 Å, but can be expanded by rotation and twisting of the layers [22]. Furthermore, some features of carbon dioxide such as its polarizability, high kinetic energy, and molecular size being smaller than the interlayer distance (0.33 nm, vertically), make it suitable to achieve separation of graphene sheets [22].

The procedure consists basically in the immersion of the graphitic material in the supercritical CO_2, followed by depressurization, allowing CO_2 to expand inside graphite, and evaporation leaving no solvent residues. The addition of co-solvents is also used to enhance the solvation and stabilization processes, avoiding aggregation of the exfoliated graphene nanosheets through van der Waals interactions [22].

Recently, Pu et al. [23] were able to obtain a yield as high as ~30 to 40 wt.% using a similar method and dispersing the exfoliated graphene in a solution of sodium dodecyl sulfate (SDS). Li et al. [8] added pyrene derivatives to assist the exfoliation with supercritical CO_2, a few layers of high quality and noncovalent functionalized graphene were obtained. In other studies, the supercritical density, which depends on the supercritical conditions (T_c, P_c), was found to be an important factor that affects the size and stability of the flakes obtained [22]. Low supercritical density was associated with larger size and lower stability, whereas smaller size and higher stability was observed at high supercritical density [24].

The purpose of our study is to gain further insights into the microscopic mechanisms behind the exfoliation process using supercritical CO_2, through the analysis of transport and structural properties at various pressures and temperatures in the neighborhood of the critical point using classical molecular dynamics (MD) simulations, and to provide some useful information that may allow the design of experiments maximizing yield and quality of the graphene sheets obtained through this method. To this end, we perform MD simulations using two different protocols. First, we utilize the canonical NVT ensemble [25] to examine the behavior of CO_2 molecules at near critical densities and temperatures when the fluid is confined within graphite layers at various separations larger than the normal interlayer distance of 3.35 Å. These enlarged separations are assumed to occur when the high pressure fluid intercalates the graphite layers. In these simulations the graphite geometry is kept fixed at the experimental geometries. Diffusion coefficients are calculated for the confined fluid at various T and P conditions as well as in different confinement regimes. Second, we use the isothermal-isobaric NPT ensemble [25] to evaluate the evolution of the system at fixed temperature and pressure. In this set of simulations, the graphite structure is represented by the Tersoff force field [26, 27] and is allowed to relax during the entire simulation. In this way, we can observe the insertion of the fluid molecules into the graphite interlayers and the changes in the overall structure, as well as the exfoliation of graphene sheets as a function of pressure and temperature. Transport properties and radial distribution functions allow quantification of the phenomena.

Table 6.1 LJ potential parameters for carbon–carbon (in Graphite and CO_2) and oxygen–oxygen (in CO_2) interactions

Pair interaction	E_{ij}/κ (K)	σ_{ij} (Å)
$C–C_{graphite}$ [32]	28	3.40
$O–O_{CO2}$ [29]	79	2.80
$C–C_{CO2}$ [29]	27	3.05

6.2 Computational Details

6.2.1 MD Simulations in the NVT Ensemble

Graphite is modeled as a 4-layer slab with interlayer separations of 4, 5, and 6 Å in different simulations. Bulk conditions are obtained by using periodic boundary conditions in the three spatial directions to reproduce solid graphite.Each layer is fixed and the CO_2 molecules are distributed in the space between layers. The dimensions of each graphene layer are 24.6×24.6 Å and the number of CO_2 molecules for each simulation is set to reproduce the CO_2 density at the conditions corresponding to temperatures and pressures ranging in $0.95\ T_c < T < 1.05\ T_c$ and $0.95\ P_c < P < 1.05\ P_c$ with increments of 0.05. The experimental critical temperature of CO_2 is 304.13 K, and its critical pressure is 7.38 MPa; the CO_2 density is obtained from the Span and Wagner equation of state [28].

The TraPPE force field [29] represents the CO_2 molecule as a three-site rigid body with partial charges of +0.70 and −0.35 for C and O atoms respectively. The calculated CO_2 critical properties for the TraPPE model [30] are 7.2 MPa and 309.1 K respectively that are in relatively good agreement with the experimental values (7.38 MPa and 304.13 K). In the NVT simulations, C-C interactions in graphite are described by a Lennard-Jones (LJ) potential. Long-range coulombic interactions between the CO_2 molecules are considered using the Ewald sum method [31]. The accuracy of the method is verified comparing the coulombic energy and the coulombic virial. The short-range interactions are represented through LJ potentials using the parameters reported in Table 6.1 for the like pairs and the Lorentz–Berthelot mixing rules for the unlike pairs.

DLPOLY 2.20 simulation package [33] is used to carry out the MD simulations in the canonical NVT ensemble. The temperature is kept constant using the Berendsen thermostat [34] with a relaxation constant of 0.4 ps. The systems are first equilibrated during 1,000 ps with a time step of 1 fs and production times of 10,000 ps. In order to estimate the equilibrium separation between layers in presence of CO_2 at different P and T conditions, MD simulations were also performed using Materials Studio 5.5 [35] using the Dreiding force field [36] and allowing the atoms in the graphene layers to relax around their optimized positions. From these simulations, we observed that the equilibrium separation for the studied range of CO_2 densities is between 3.5 to 6 Å. Thus NVT simulations at fixed interlayer separations were performed at 4, 5, and 6 Å.

Using the saved time trajectories of the equilibrated system, the molecular diffusion is analyzed through the time evolution of the mean square displacement

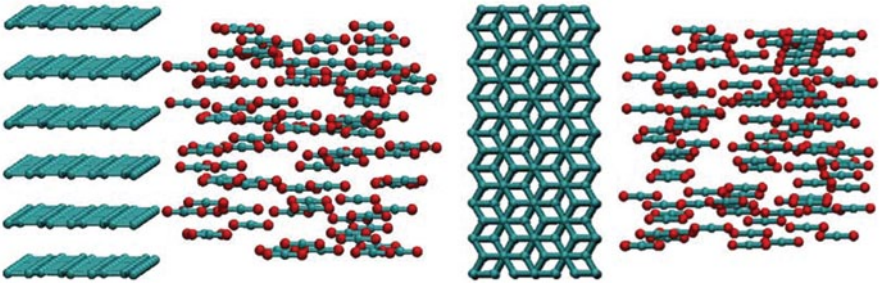


Fig. 6.1 Top and side views of the initial configuration of the system with six graphene layers and the CO_2 molecules used to simulate CO_2 interactions with graphite in the NPT ensemble. The initial distance between layers is 3.35 Å. Periodic boundary conditions are used in the 3 spatial directions

(MSD), a measure of the mobility of the molecules, which is defined by the Einstein relation [25]:

$$MSD(t) = \left\langle \left| \underline{r}_i(t) - \underline{r}_i(t_0) \right|^2 \right\rangle_{t_0} \tag{6.1}$$

where r_i is the position vector of a given molecule i at time t, and t_0 is the initial time, and the ensemble average is obtained through computations at many different initial times. For sufficiently long time intervals the MSD is related to the diffusion coefficient according to:

$$D = \frac{1}{\delta} \lim_{t \to \infty} \frac{\left\langle \left| \underline{r}_i(t) - \underline{r}_i(t_0) \right|^2 \right\rangle}{t} \tag{6.2}$$

where δ depends on the space dimensionality.

6.2.2 MD Simulations in the NPT Ensemble

MD simulations of 120 ps are performed in the NPT ensemble on a system consisting of six graphene layers adjacent to 100 CO_2 molecules. The total length of the simulations was shorter than in the NVT case because a much smaller time step (0.1 fs) was required for the reactive Tersoff potential. In any case, as shown in the next section, the most important features of the system evolution are well captured. Figure 6.1 shows the initial configuration. The isothermal-isobaric ensemble (NPT) is kept at the given P and T conditions with the Nosé-Hoover thermostat [37]. As in the NVT simulations, the pressure and temperature are varied in the range of 0.95 to 1.05 of the experimental critical conditions with increments of 0.05. Each simulation starts with the same initial configuration, using the Tersoff potential

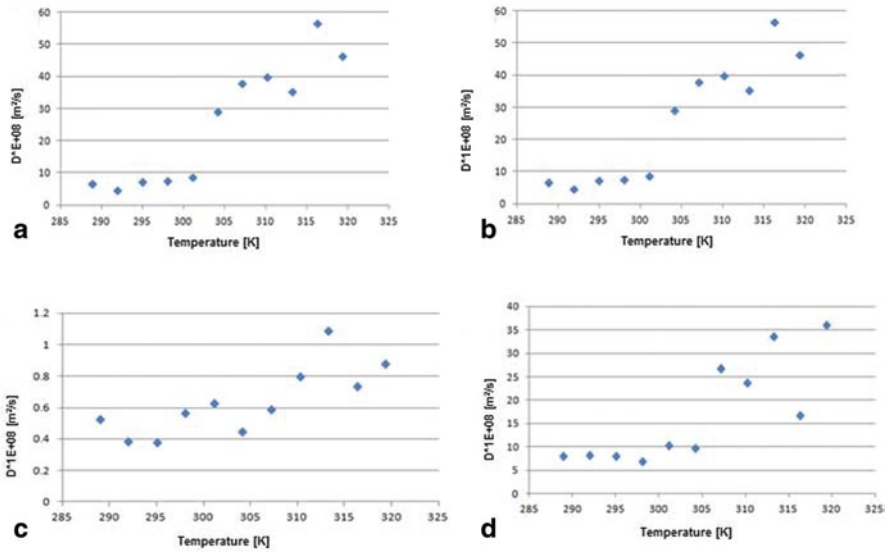


Fig. 6.2 Diffusion coefficient of CO_2 in the xy plane direction versus temperature at constant values of pressure: 0.95 P_c **a** and **b**, and 1.05 P_c **c** and **d**. Separation distances between graphene layers are 5 Å for the cases **a** and **c**, and 6 Å for **b** and **d**

[26, 27] for the graphite layers, and the TraPPE force field for the CO_2 molecules, and LJ interactions as shown in Table 6.1 are used between CO_2 and the graphene layers.

6.3 Results and Discussion

6.3.1 Diffusion Coefficients from NVT Simulations

At an interlayer separation of 4 Å the calculated diffusivities showed no physical meaning since the values were extremely small and in some cases became negative due to the fact that the molecules are in an extremely confined environment with a scarce mobility. Instead, Fig. 6.2 displays results of diffusion coefficients at a pressure slightly below the critical (7.01 MPa) and for various values of temperature in the neighborhood of the critical for interlayer separations of 5 and 6 Å. The self-diffusion coefficients calculated in the 3 spatial directions and in the xy plane only revealed that the only significant contribution to CO_2 diffusion confined between graphite layers comes from molecular motion in the x and y directions, whereas the contribution from the z direction is almost negligible. When the separation between graphite layers is fixed at 5 Å, the diffusion coefficient does not follow a clear pattern as a function of temperature, although a slight increasing tendency is observed. Fluctuations are larger in the close neighborhood of the critical temperature.

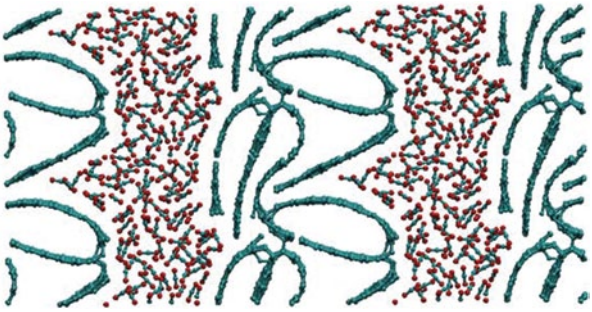


Fig. 6.3 Periodic graphite–CO_2 system after a NPT simulation at $T_c = 304.15K$ and $P_c = 7.38$ MPa. The graphite layers start to bend and the interlayer distance is still approximately 3.35 Å. Snapshot taken approximately at 5 ps

When the interlayer separation is fixed at 6 Å, the diffusion coefficient is about constant at temperatures below the critical and then increases significantly. For the cases with a separation of 6 Å, the diffusivities range between 4-74 E-08 m^2/s in the XY direction and 0.25-1.2 E-08 m^2/s between with separations of 5 Å; which are in good agreement with theoretical values reported in the literature [38] of 0.2-1.4 E-08 m^2/s for CO_2 diffusion in C slit pores at 298K, pressure between 1.0 E-03 and 2.0 MPa and separations around 7 Å.

From the behavior observed for the diffusion coefficients in Fig. 6.2, it can be inferred that supercritical temperatures may favor much higher fluid motion which may lead to pushing apart the graphene sheets.

6.3.2 Results from NPT Simulations

Since in the NVT simulations we are fixing the interlayer separations, it is useful to simulate alternative systems (as shown in Fig. 6.1) where a completely relaxed set of graphite layers becomes in contact with the supercritical fluid. Figure 6.3 displays the results of the system shown in Fig. 6.1 after equilibration at the experimental critical temperature, slightly subcritical (0.98 T_c) for the TraPPE model, and at the experimental critical pressure that is slightly supercritical (1.025 P_c) for the TraPPE model. It is observed that the graphene layers start bending and the CO_2 molecules are not, at this point, intercalated between the layers.

As time evolves, depending on the P and T conditions, the graphene layers may be separated and allow the intercalation of the CO_2 molecules between them. For example, at a pressure below the critical point of CO_2 (0.95 $P_c = 7.011$ MPa) the simulations reveal that it is necessary, as a minimum, the experimental critical point temperature T_c in order to observe the CO_2 molecules inside the layers. Also, at the P_c and T_c conditions and higher, the CO_2 is able to compress the graphene layers inducing separation and bonding of individual sheets, creating almost a single layer of graphene.

Figure 6.4 displays images of representative cases. The first row (Fig. 6.4a) corresponds to the P and T of the experimental CO_2 critical point. After the first 15 ps, there is clear evidence of bending and some separation of the graphene layers.

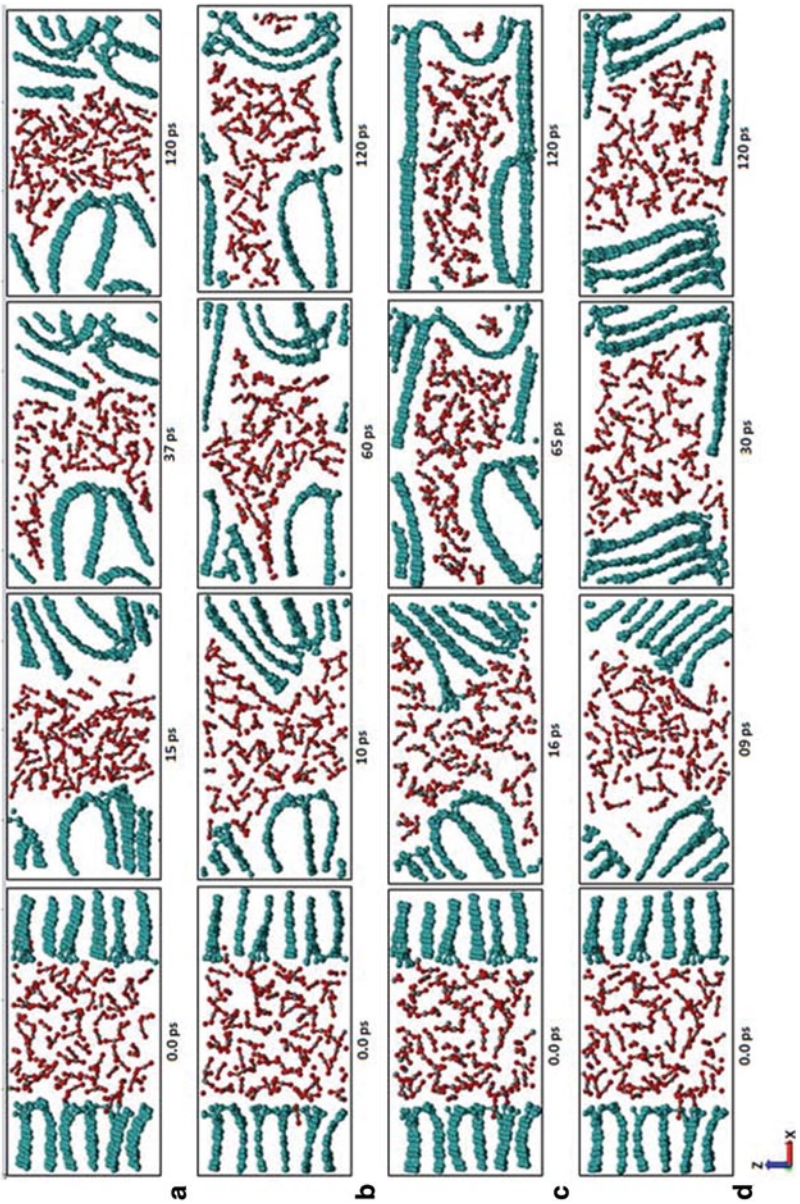


Fig. 6.4 Representative sequences of snapshots from NPT simulations at different conditions and simulation times. **a** Experimental critical point: P = 7.38 MPa, T = 304.25 K, **b** P = 7.52 MPa and T = 295.15 K, **c** P = 7.60 MPa and T = 301.15 K, **d** P = 7.75 MPa and T = 301.15 K. Rotation and twisting of the graphene layers is observed

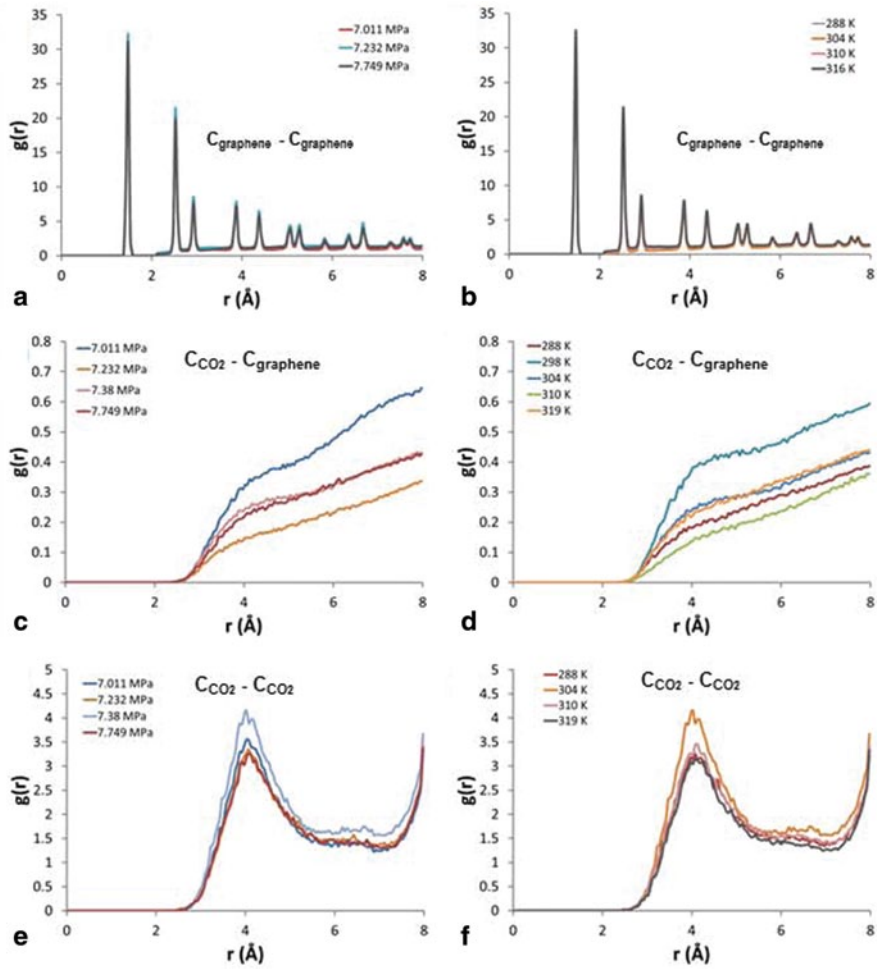


Fig. 6.5 Radial distribution function plots for **a**, **b** C–C in graphene; **c**, **d** C from graphene–C from CO_2 and **e**, **f** C–C in CO_2. **a**, **c** and **e** correspond to systems at 304 K and various values of pressure. **b**, **d** and **f** correspond to systems at 7.38 MPa and various values of temperature

At 37 ps, CO_2 molecules intercalate into the graphite structure causing further restructuring of the layers that is preserved at the last snapshot taken at 120 ps. The 2nd row corresponds to a subcritical temperature and a supercritical pressure. At these conditions, the observed phenomena are qualitatively similar to those in Fig. 6.4a. Further increases in pressure (Fig. 6.4c, d) lead to separation of the graphene layers and formation of longer graphene sheets via bonding of the individual layers.

Figure 6.5 shows radial distribution functions calculated at several P and T conditions. The first row illustrates the average graphite structure evaluated during the entire simulation at the given conditions of T and P. On the *average*, the structure

does not show significant changes; however there are huge changes as evidenced in Fig. 6.4 but they cannot be detected on the property calculated over all the simulation history. The second row in Fig. 6.5 displays the interactions between C of CO_2 and C of graphite. At constant temperature (304 K) the effect of pressure shown in Fig. 6.5c suggests a different behavior between supercritical and subcritical pressures, with higher interactions detected at subcritical pressures. This is in agreement with the observations from Fig. 6.4, where we observed more clustering of CO_2 molecules as the conditions become supercritical. Note that the less interactive system is found at the critical pressure of the TraPPE model (7.2 MPa). Similarly, Fig. 6.5d shows that the less interactive CO_2/graphite system is found at the temperature closest to the critical T of the model (309.1 K).

Less variation is found the CO_2–CO_2 interactions (Fig. 6.5e, f) although slightly enhanced interactions are found at near but subcritical conditions.

The CO_2 self-diffusion coefficients calculated from NPT simulations are shown in Fig. 6.6. Qualitatively, the same trends are found to those described in relation to Fig. 6.2. Although there is no clear trend, it is generally observed, as for the NVT simulations, that the diffusion increases slightly with an increase of the temperature. All diffusion coefficients are in the range of 0.2E-08 to 7.0E-07 m^2/s.

6.4 Conclusions

MD simulations provide new insights into the exfoliation of graphite using supercritical CO_2. The range of interlayer separations for a CO_2 molecule being able to diffuse between graphite interlayers is found to be between 5 and 6 Å. However, at near critical conditions the graphene layers bend and are intercalated by the high pressure/high temperature fluid causing the exfoliation phenomena.

The calculated diffusion coefficients are in the order of 10^{-8} m^2/s, and although not a clear correlation is obtained, certain trend shows increase of the CO_2 mobility as T increases. This behavior suggests that supercritical temperatures may favor much higher fluid motion which may lead to pushing apart the graphene sheets.

In general, the results suggest that the separation of the graphene layers occurs on simulations with a temperature *above* T_c for the systems with subcritical pressures which can be explained by the observed higher mobility exerting exfoliation forces on the system. On the other hand, a temperature *below* T_c is sufficient to achieve graphite exfoliation at supercritical pressures; thus the pressure effect seems to have a larger effect on the phenomena. The separation between layers at the end of the simulations when the CO_2intercalates and exfoliates graphite has a range of approximately 10 to 13 Å.The observations are also supported by the behavior of pair correlation functions which reveal structural features such as reduced CO_2/graphite interactions at supercritical pressures.

Acknowledgements Computer resources from Texas A&M Supercomputing Center and from Brazos Supercomputing Cluster at Texas A&M University are gratefully acknowledged.

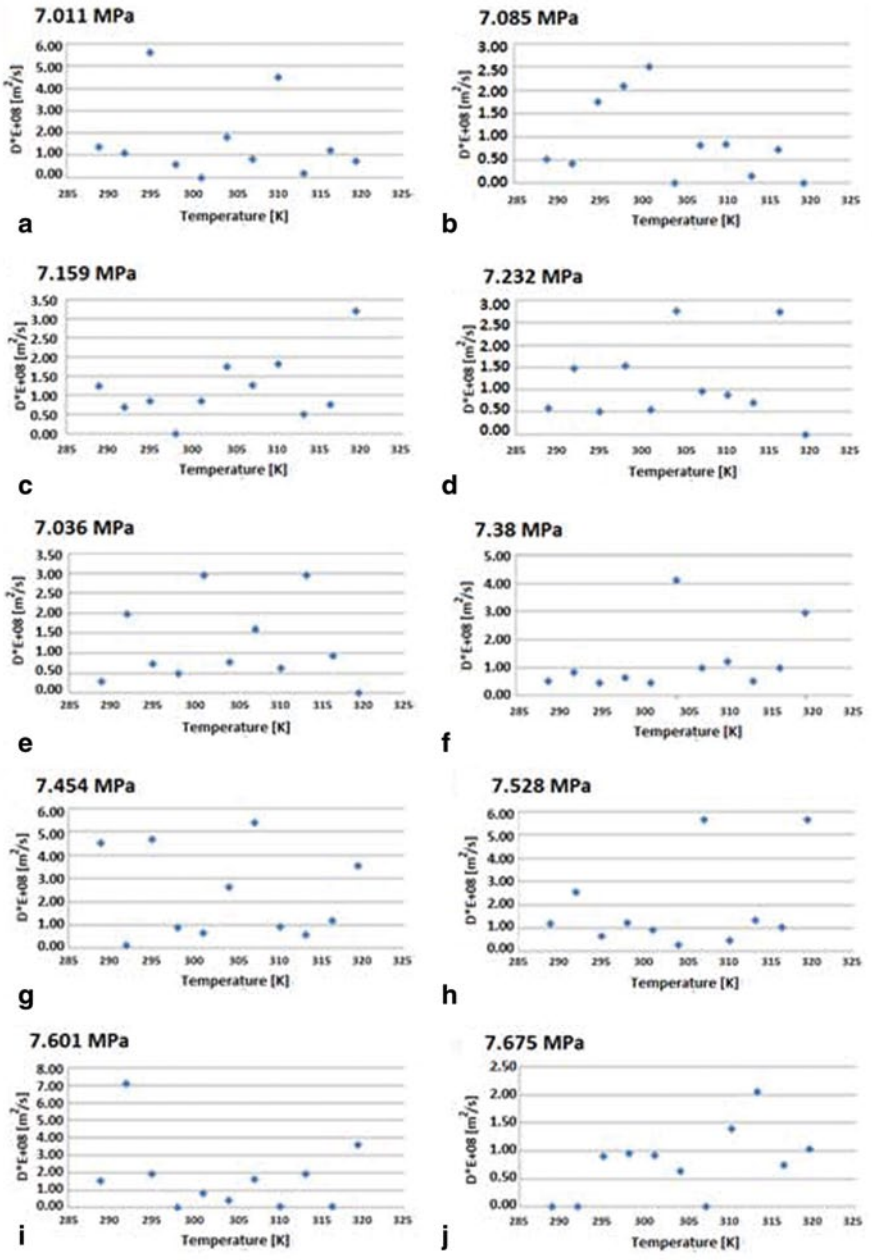


Fig. 6.6 Diffusion coefficient of CO_2 versus temperature for pressures from 0.95 to 1.05 P_c

References

1. Tiwari JN, Tiwari RN, Kim KS (2012) Zero-dimensional, one-dimensional, two-dimensional and three-dimensional nanostructured materials for advanced electrochemical energy devices. Prog Mater Sci 57:724–803
2. Luque A, Marti A, Stanley C (2012) Understanding intermediate-band solar cells. Nat Photonics 6:146–152
3. Ariga K, Ji QM, McShane MJ, Lvov YM, Vinu A, Hill JP (2012) Inorganic nanoarchitectonics for biological applications. Chem Mater 24:728–737
4. Randall CL, Gultepe E, Gracias DH (2012) Self-folding devices and materials for biomedical applications. Trends Biotechnol 30:138–146
5. Mlinar V (2012) Role of theory in the design of semiconducting nanostructures. J Mater Chem 22:1724–1732
6. Iijima S (1991) Helical microtubules of graphitic carbon. Nature 354:56–58
7. Iijima S, Ichihashi T (1993) Single-shell carbon nanotubes of 1-nm diameter. Nature 363:603–605
8. Avouris P, Martel R, Derycke V, Appenzeller J (2002) Carbon nanotube transistors and logic circuits. Physica B 323:6–14
9. Bose S, Kuila T, Mishra AK, Rajasekar R, Kim NH, Lee JH (2012) Carbon-based nanostructured materials and their composites as supercapacitor electrodes. J Mater Chem 22:767–784
10. Bernholc J, Brenner D, Nardelli MB, Meunier V, Roland C (2002) Mechanical and electrical properties of nanotubes. Ann Rev Mater Res 32:347–375
11. Collins PG, Arnold MS, Avouris P: (2001) Engineering carbon nanotubes and nanotube circuits using electrical breakdown. Science 292:706–709
12. Dresselhaus MS, Avouris P (2001) Carbon nanotubes: synthesis, structure, properties and applications. Springer, Berlin
13. Novoselov KS, Geim AK, Morozov SV, Jiang D, Zhang Y, Dubonos SV, Grigorieva IV, Firsov AA (2004) Electric field effect in atomically thin carbon films. Science 306:666–669
14. Novoselov KS, Geim AK, Morozov SV, Jiang D, Katsnelson MI, Grigorieva IV, Dubonos SV, Firsov AA (2005) Two-dimensional gas of massless Dirac fermions in graphene. Nature 438:197–200
15. Novoselov KS, Jiang D, Schedin F, Booth TJ, Khotkevich VV, Morozov SV, Geim AK (2005) Two-dimensional atomic crystals. Proc Natl Acad Sci U S A 102:10451–10453
16. Novoselov KS (2011) Graphene: materials in the flatland. Int J Mod Phys B 25:4081–4106
17. Allen MJ, Tung VC, Kaner RB (2010) Honeycomb carbon: a review of graphene. Chem Rev 110:132–145
18. Cohen-Tanugi D, Grossman JC (2012) Water desalination across nanoporous graphene. Nano Lett 12:3602–3608
19. Xia ZY, Pezzini S, Treossi E, Giambastiani G, Corticelli F, Morandi V, Zanelli A, Bellani V, Palermo V (2013) The exfoliation of graphene in liquids by electrochemical, chemical, and sonication-assisted techniques: a nanoscale study. Adv Funct Mater. doi:10.1002/adfm.201203686
20. Sham AYW, Notley SM (2013) A review of fundamental properties and applications of polymer-graphene hybrid materials. Soft Matter 9:6645–6653
21. Shen H, Zhang LM, Liu M, Zhang ZJ (2012) Biomedical applications of graphene. Theranostics 2:283–294
22. Wattanaprayoon C (2011) Graphite exfoliation by supercritical carbon dioxide extraction. Michigan Technological University. MS Thesis, http://digitalcommons.mtu.edu/etds/8/, 2011
23. Pu NW, Wang CA, Sung Y, Liu YM, Ger MD (2009) Production of few-layer graphene by supercritical CO_2 exfoliation of graphite. Mater Lett 63:1987–1989
24. Li LH, Zheng XL, Wang JJ, Sun Q, Xu Q (2013) Solvent-exfoliated and functionalized graphene with assistance of supercritical carbon dioxide. ACS Sustain Chem Eng 1:144–151
25. Allen MP, Tildesley DJ (1990) Computer simulation of liquids. Oxford University, Oxford

26. Tersoff J (1988) New empirical-approach for the structure and energy of covalent systems. Phys Rev B 37:6991–7000
27. Tersoff J (1989) Modeling solid-state chemistry: interatomic potentials for multicomponent systems. Phys Rev B 39:5566–5568
28. Span R, Wagner W (1996) A new equation of state for carbon dioxide covering the fluid region from the triple-point temperature to 1100 K at pressures up to 800 MPa. J Phys Chem Ref Data 25:1509–1596
29. Potoff JJ, Siepmann JI (2001) Vapor-liquid equilibria of mixtures containing alkanes, carbon dioxide, and nitrogen. Aiche J 47:1676–1682
30. Zhang ZG, Duan ZH (2005) An optimized molecular potential for carbon dioxide. J Chem Phys 122:214507
31. Ewald PP (1921) The calculation of optical and electrostatic grid potential. Ann Phys -Berlin 64:253–287
32. Bojan MJ, Steele WA (1987) Interactions of diatomic molecules with graphite. Langmuir 3:1123–1127
33. Smith W, Forester TR (1996) DL_POLY_2.0: a general-purpose parallel molecular dynamics simulation package. J Mol Graphics 14:136–141
34. Berendsen HJC, Postma JPM, Gunsteren WFv, Nola AD, Haak JR (1984) Molecular dynamics with coupling to an external bath. J Chem Phys 81:3684–3690
35. Andzelm J (2007) Materials studio. Chem World-Uk 4:72–72
36. Mayo SL, Olafson BD, Goddard WA (1990) Dreiding: a generic force field for molecular simulations. J Phys Chem 94:8897–8909
37. Hoover W (1985) Canonical dynamics: equilibrium phase-space distributions. Phys Rev A 31:1695
38. Lim YI, Bhatia SK, Nguyen TX, Nicholson D (2010) Prediction of carbon dioxide permeability in carbon slit pores. J Membr Sci 355:186–199

Chapter 7
Functionalized Graphene and Cobalt Phthalocyanine Based Materials with Potential Use for Electrical Conduction

Gloria I. Cárdenas-Jirón, Paola León-Plata and Jorge M. Seminario

Abstract In this work we investigate at the density functional theory level (B3PW91, B3LYP, M05-2X) the electrical properties of complexes formed by cobalt phthalocyanine (CoPc) and cobalt tetraaminophthalocyanine (CoTAPc) adsorbed on functionalized graphene (FG). As functionalization are studied the carboxylate (18 complexes), epoxide (three complexes), hydroxyl (three complexes) and carboxyl (two complexes) groups. Three models of graphene molecules are used; pristine, defect (Def), and vacancy (Vac), leading to a total of 26 complexes. We studied three main orientations for the interaction graphene-phthalocyanine; parallel, perpendicular and extended. Binding energies show a very large stability for G–COO^--CoTAPc complexes (~ −100 to −150 kcal/mol) in an extended orientation and a little lower for G–O–CoPc and G–OH–CoPc in a parallel orientation (~ −20 to −65 kcal/mol). No adsorption of CoPc occur on G–COOH. HOMO-LUMO Gap (HLG) show higher values for the complexes than the fragment FG when the functionalization COO- is by the edge of graphene; giving account of a favorable adsorption of CoPc (CoTAPc) in agreement with the binding energies. For epoxide and hydroxyl (except for G-Vac) where the functionalization is on the center of G, we found that HLG is shorter in ~0.5 eV with respect to FG (~4 eV). The high HLG values for these complexes suggest that the adsorption of CoPc is completely favorable. Several of these complexes present an electron acceptor species (FG) and an electron donor species (CoPc, CoTAPc). For the stable complexes, we found a higher current conduction for the parallel orientation. Thus, complexes with carboxylate functionalization present a conduction of ~7 μA similar for hydroxyl

G. I. Cárdenas-Jirón (✉)
Laboratorio de Química Teórica, Facultad de Química y Biología,,
Universidad de Santiago de Chile, Casilla 40, Correo 33, Santiago, Chile
e-mail: gloria.cardenas@usach.cl

P. León-Plata · J. M. Seminario
Department of Chemical Engineering, Texas A&M University,
College Station, Texas, USA
e-mail: seminario@tamu.edu

J. M. Seminario
Department of Electrical and Computer Engineering, Texas A&M University,
College Station, Texas, USA
e-mail: seminario@tamu.edu

J. M. Seminario (ed.), *Design and Applications of Nanomaterials for Sensors,*
Challenges and Advances in Computational Chemistry and Physics 16,
DOI 10.1007/978-94-017-8848-9_7, © Springer Science+Business Media Dordrecht 2014

(~7 μA) but some lower than for epoxide (~18 μA). The results have shown that the adsorption of cobalt phthalocyanines on functionalized graphene is feasible; yielding a tunable hybrid material that allows sensing because of the intrinsic electrical properties provided by functionalized G and CoPc.

7.1 Introduction

Pristine graphene (G) is a flat two-dimensional structure [50] of carbon atoms with unique mechanical and electronic properties due to its rigid hexagonal sp^2 rings, allowing a conjugation through their π molecular orbitals, which yield excellent conduction properties, even superior to those of carbon nanotubes [25, 51, 67, 79, 85]. Individual graphene sheets have been characterized by transmission electron microscopy, which revealed that these sheets are not perfectly flat; on the contrary, they show intrinsic microscopic roughening with out-of-plane deformations in the order of 1 nm [48] and can be used in any of the scenarios for molecular electronics [77].

Graphene surfaces may feature alterations, defects (Def), or vacancies (Vac) that affect their electronic properties as it has been showed for a mono-vacancy, a di-vacancy, and a Stone–Wales defects using calculated Raman spectra density functional theory (DFT) with a non-orthogonal tight-binding model [62]; it was found that the Raman intensity can be enhanced up to one order of magnitude by the presence of defects in comparison with a pristine graphene [62], and these spectra can serve as signatures for specific defects.

It has been showed that Stone–Wales (SW) defects yield changes in the electronic properties of graphene and affect the reactivity towards the adsorption of adsorbates [4, 9, 16, 39, 44, 45, 88]. It is also known that the presence of vacancies in graphene nanoribbons modifies the electronic transport properties, affecting the conductance of these nanomaterials [46]. A study on multi-vacancies in carbon nanotubes has also revealed the existence of stability at magic numbers [52]. Graphene based complexes have been explored in energy conversion [38], electrical conduction [18], solubility [90], and composites formation [2, 35].

Graphite oxide (GO) structures have been studied using the technique of ^{13}C and ^{1}H NMR. These studies have proposed a new structural model for GO; epoxide (1,2-ethers) and hydroxyl groups are distributed randomly in oxidized rings and aromatic entities along the basal plane, while the sheets terminate with C–OH and COOH groups [11, 43]. Using atomic force microscopy (AFM) and scanning tunneling microscopy (STM) was observed the presence of wrinkles giving account of non planar regions and a model for the bonding sites of epoxide and hydroxyl functionalization to graphene is proposed [21, 53, 68]. These studies have shown that functionalized graphene is electrically conducting [21, 53, 68].

Carboxylic acid-functionalized graphene nanosheets have been obtained by chemical reduction of graphite oxide and used to build together amine-functionalized graphene nanosheets thin films of graphene via layer-by-layer assembly through electrostatic interactions, which can have applications such as transparent electrodes and highly sensitive biosensors [55]. Other studies report carboxylic

acid-functionalized graphene as biosensors for simultaneous determination of adenine and guanine in DNA [36].

The mechanism of chemical functionalization of pristine, vacancy, and SW defect graphene models through COOH groups has also been studied using density functional theory [3], whereby the attachment of functional groups is stronger in graphene with SW defects and vacancies as justified by its larger binding energy than pristine graphene. Chemical functionalization of graphene oxide with porphyrin TPP–NH^2 (5-4(aminophenyl)-10,15,20-triphenylporphyrin) has been reported and confirmed using FTIR, UV-vis absorption, and TEM studies, indicating that these molecules are covalently connected through one amide bond [89]. Thus, multifunctional materials at nanometer-scale can take advantage of porphyrin as it improves the solubility of graphene in organic solvents in addition to its optoelectronic and catalytic properties.

Some works have been reported for the adsorption of phthalocyanines on graphene; reduced graphene oxide (RGO) composites containing tetrasulfonate salt of copper phthalocyanine (TSCuPc), which have been fabricated and could be used as optoelectronics devices. These composites have higher photoconductivity and photoresponsivity than RGO films because the presence of donor/acceptor materials and large donor/acceptor (D/A) interfaces for charge generation [47]. Iron phthalocyanine molecules have been observed by scanning tunneling microscopy (STM) to be self-assembled on a monolayer graphene, demonstrating that the latter can act as a template for the fabrication of unique nano-architectures with interesting properties [17]. Graphene oxide covalently functionalized with zinc tri(p-tert-butylphenoxyl)aminophthalocyanine was synthesized by an amidation reaction and confirmed the amide bond between GO and the zinc substituted phthalocyanine by X-ray photoelectron and FTIR [93].

We have previously shown from a theoretical point of view that the adsorption of nickel and cobalt phthalocyanine on functionalized graphene form a stable complex where an oxygen based functionalization is favored thermodynamically. [13, 20] The metallophthalocyanines (MPc`s) adsorbed on graphite are used for the development of electrodes in where the MPc`s act as mediators in electrochemical processes of charge transfer, being useful for the detection of a diversity of organic molecules.[12–15, 19, 54].

In this work we investigated the covalent adsorption of cobalt phthalocyanine on graphene functionalized with carboxylate, epoxide, hydroxyl and carboxyl. The electric conduction between the fragments given by the functionalized graphene and CoPc was also studied with the aim to investigate if this type of complexes could be considered as potential conductor materials.

7.2 Computational and Theoretical Aspects

We used three kind of graphene layers containing 19 hexagonal cells; pristine (G), with one Stone–Wales defect [84] (G-Def) and with one vacancy (G-Vac) (Fig. 7.1). A total of 13 graphene layers containing the functionalization were built and then

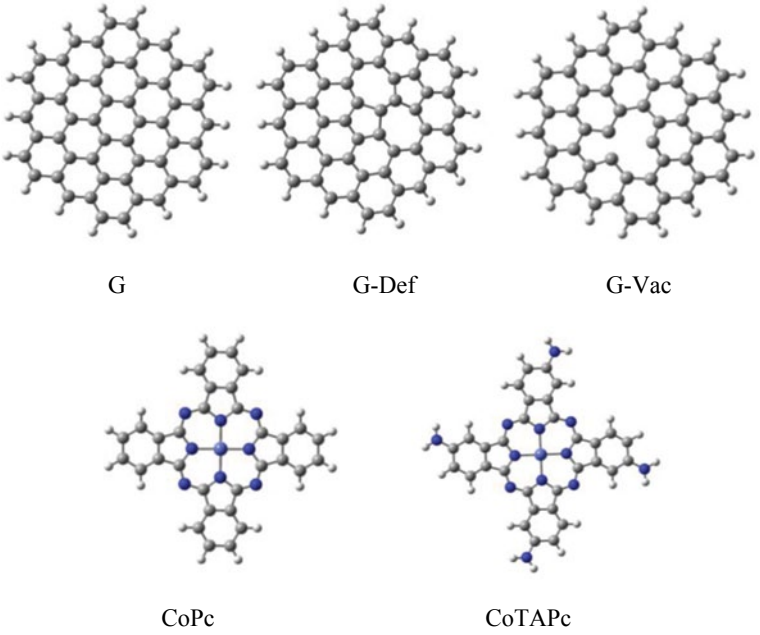
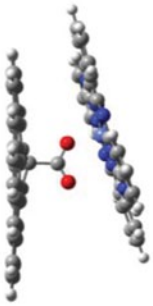


Fig. 7.1 Graphene structural models (*G*, *Def*, and *Vac*) and cobalt phthalocyanines (*CoPc* and *CoTAPc*)

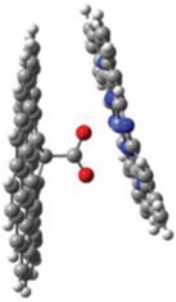
used to form the complex functionalized graphene (FG)-CoPc giving place to 26 molecular complexes.

For the functionalization with carboxylate anion ($-CO2^{-}$), two types of bonding with graphene were considered, on basal plane and at the edges giving place to 18 complexes. This choice was taken into account to investigate the interaction with CoPc through cobalt (**1–12**) and through ligand (**13–18**), as can be seen in Fig. 7.2. We also analyzed the substituent effect on CoPc, thus four amine groups were added in the beta position of the benzenic rings (CoTAPc) (Fig. 7.1). Complexes **1–6** are functionalized in the basal plane of graphene, while in **7–12** the functionalization is located at the edge of the graphene (LAT). In **13–18** complexes, the covalent bond between CoTAPc and graphene is by the amine group forming an amide bond. In the complexes **1–18** the molecular geometry was optimized considering the frozen functionalized graphene but previously optimized and using for the whole complex the density functional theory. It was used the B3LYP exchange correlation hybrid functional [7, 8, 42, 49] and the quasi-relativistic pseudopotential LANL2DZ [32, 33, 87] for the cobalt atom and the basis set 6-31G [34] for C, N, H and O. The optimization on each complex and fragment is performed with the program Gaussian 03 [28].

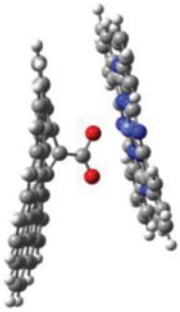
According to the larger electrical conduction of complexes bonded by the basal plane of graphene (**1–6**) calculated by us in relation to the interaction by the edge, we studied other functionalizations following this kind of interaction graphene-CoPc. Thus complexes with functionalization of the type epoxide (**19–21**), hydroxyl (**22–24**) and carboxyl (**25–26**) were studied. As illustration we show in Fig. 7.3



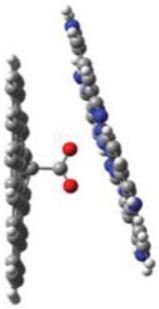
1: G-CO2^{-}-CoPc



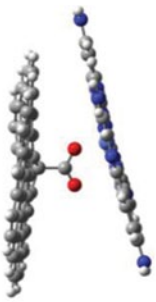
2: G-Def-CO2^{-}-CoPc



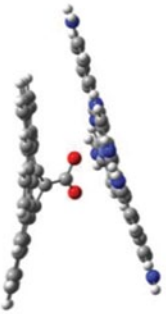
3: G-Vac-CO2^{-}-CoPc



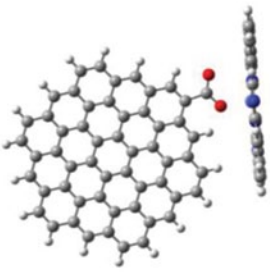
4: G-CO2^{-}-CoTAPc



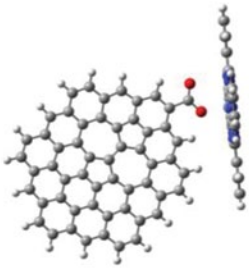
5: G-Def-CO2^{-}-CoTAPc



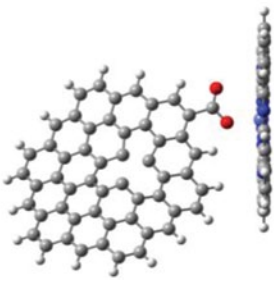
6: G-Vac-CO2^{-}-CoTAPc



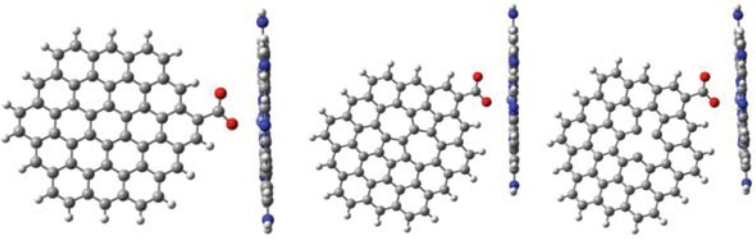
7: G-CO2^{-}-LAT-CoPc



8: G-Def-CO2^{-}-LAT-CoPc



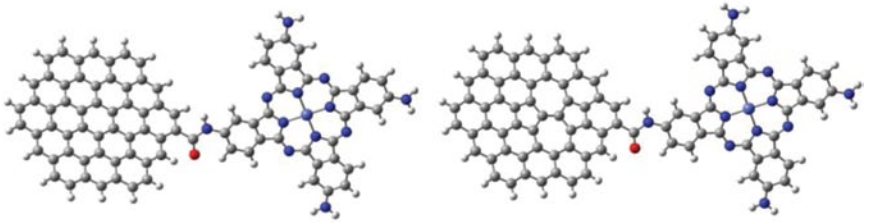
9: G-Vac-CO2^{-}-LAT-CoPc



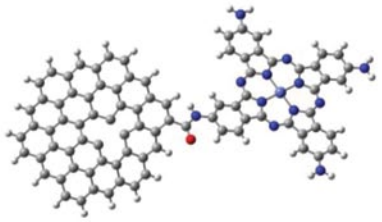
10: G-CO_2^--LAT-CoTAPc 11: G-Def-CO_2^--LAT-CoTAPc 12: G-Vac-CO_2^--LAT-CoTAPc



13: G-CO-CoTAPc 14: G-Def-CO-CoTAPc 15: G-Vac-CO-CoTAPc



16: G-CO-LAT-CoTAPc **17**: G-Def-CO-LAT-CoTAPc



18: G-Vac-CO-LAT-CoTAPc

Fig. 7.2 Optimized molecular structures for the complexes obtained at the level of calculation B3LYP/LANL2DZ/6-31G

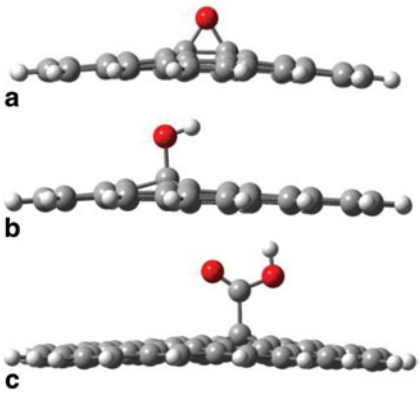


Fig. 7.3 Graphene pristine model with functionalization: **a** epoxide, **b** hydroxyl and **c** carboxyl

these functionalizations for graphene pristine model. All these complexes were fully optimized at the density functional theory with the functional M05-2X [82, 92], and the basis set 6-31G(d) (all lighter atoms)/LANL2DZ (Co). All the calculations were carried out with the package Gaussian09 [29].

To determine the adsorption of the phthalocyanine on functionalized graphene, we calculated the adiabatic binding energy from the substraction between the total energy of the complex and the total energy of the isolated fragments, functionalized graphene and cobalt phthalocyanine. The latter being previously optimized at the same level of calculation. Cobalt atom is in oxidation state (II) in both structures, CoPc and CoTAPc, and then the spin multiplicity used for these compounds is 2. Complexes **1–12** are calculated with a total charge (Q) of −1; **1–6** as singlet and **7–12** as doublet. For **13–18** we use Q = 0; **13–15** as singlet and **16–18** as doublet. In the case of complexes **19–21** we used Q = 0 and doublet, and for complexes **22–26** we calculated them with Q = 0 and singlet.

We model an electric circuit placing two gold atoms at each side of the conjugated structures (augmented complexes) used as interface to electrodes, which a voltage difference is applied to the complexes. Gold contacts are placed at the same distance and in the proximity of the same atom for complexes of equal conformation. Figure 7.4 shows as illustration the four types of conformations for the complex structures of graphene and phthalocyanine (**1–18**): two cobalt-centered (a) parallel and (b) perpendicular, and two ligand-centered (c) perpendicular and (d) extended. The numerical bolded label of molecules extended with gold atoms appears primed. Thus, complex **1'** shows graphene functionalized with $CO2^{-}$ at its center, and cobalt phthalocyanine in parallel conformation and linked through the cobalt. However, in **7'** the conformation of graphene with cobalt phthalocyanine is nearly perpendicular and $–CO2^{-}$ graphene functionalization is at the edge of the graphene. For complexes **13'** and **16'** the graphene is functionalized with CO at the center and edge of graphene, respectively and it is linked to phthalocyanine through the amine group localized at phthalocyanine ligand boundary; thus the phthalocyanine in **13'** is perpendicular and in **16'** both conjugates have an extended conformation. In all cases the electrodes are exactly of the same nature in order to have a consistent comparison among all complexes.

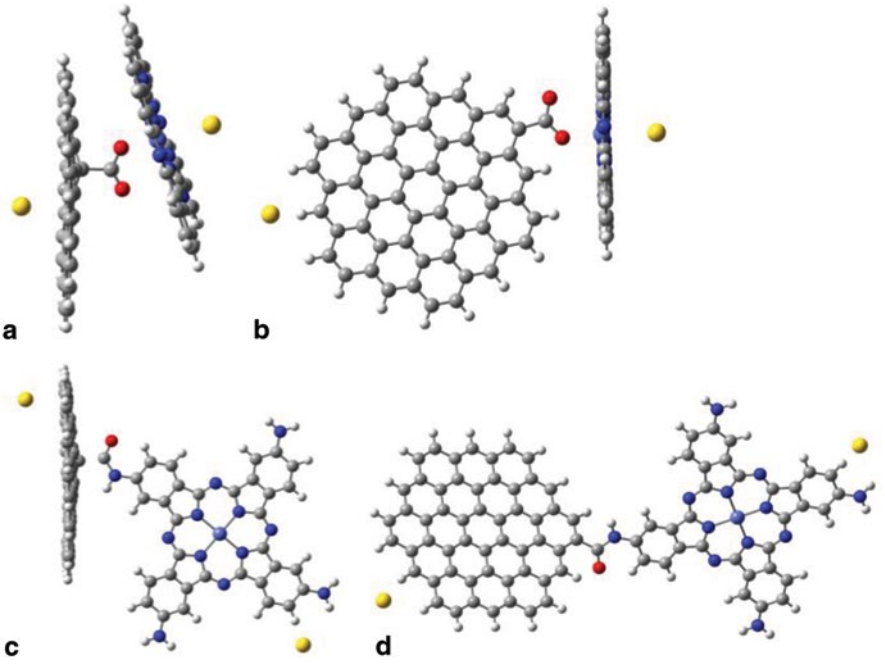


Fig. 7.4 G and CoPc (CoTAPc) complexes attached to Au terminals. **a 1'**: G–CO2^{-}–CoPc–Au_2, **b 7'**: G–CO2–LAT–CoPc–Au_2, **c 13'**: G–CO–CoTAPc–Au_2, **d 16'**: G–CO–LAT–CoTAPc–Au_2. Color code: carbon (*gray*), hydrogen (*white*), nitrogen (*blue*), oxygen (*red*), cobalt (*steel blue*) and gold (*yellow*)

DFT calculations are carried out to the augmented complexes including an external electric dipole field that yields a bias voltage (V) between the gold contacts using the program Gaussian 09 [29]. For the external voltage biased structures, we use the hybrid functional B3PW91, which uses a combination of Becke3 (B3) [8] exchange functional, Hartree–Fock (HF) exchange and Perdew–Wang (PW91) [10, 56–59] correlation functional. The quasi-relativistic pseudopotential and basis sets LANL2DZ [32, 33, 87] is used for Au and Co atoms, and the 6-31G(d) [60, 61] basis set for C, N, O and H atoms. The use of the LANL2DZ has been successfully been used in the past for other transition metals [5, 23, 70, 72, 78].

The density of states (DOS) of the bulk contacts is calculated with the program Crystal -06 [26, 65] which uses DFT with periodic boundary conditions. The continuum DOS is combined with the Hamiltonian and overlap matrices of the augmented complexes calculated with the Gaussian 09 [29] at each bias voltage. The Green's function procedure encoded in the program GENIP [23] is used to calculate the current-voltage characteristics of the complexes, in addition to the DOS and transfer functions of the junctions (complexes plus electrodes). GENIP uses the discrete (augmented molecule) and the continuous (bulk contacts) in a Green's function technique to determine the electron transport through single molecules [6, 63, 66, 76] and several nanojunctions [22, 37, 64]; for details see Refs. [71, 73, 81], and references therein.

The procedure is summarized as follows; the Green's function for the problem can be obtained from

$$H_{KS}(V)\psi(V) = E(V)S(V)\psi(V) \tag{7.1}$$

where the Hamiltonian $H_{KS}(V)$ and overlap matrices $S(V)$ are calculated at each applied voltage V. The Hamiltonian can be partitioned into the electrodes (1 and 2) and the molecule (M),

$$H_{KS}(V) = \begin{bmatrix} H_{11}(V) & H_{1M}(V) & H_{12}(V) \\ H_{M1}(V) & H_{MM}(V) & H_{M2}(V) \\ H_{21}(V) & H_{2M}(V) & H_{22}(V) \end{bmatrix} \tag{7.2}$$

Thus, the Green's function for the junction becomes

$$G(E,V) = \frac{1}{E(V)S(V) - H_{KS}(V)}$$

where H_{ij} (for $i \neq j$) refer to submatrices representing the coupling between electrodes and the molecule. The Green's function for the standalone molecule, G_M, is obtained from the full Green function $G(E, V)$ of the molecular junction [23], using the H and S matrices taken from the augmented molecule, as a function of the energy E of the crossing electron at each applied voltage,

$$G(E,V) = \begin{bmatrix} g_1^{-1} & -\tau_1 & 0 \\ -\tau_1^{+} & ES_{MM}(V) - H_{MM}(V) & -\tau_2^{+} \\ 0 & -\tau_2 & g_2^{-1} \end{bmatrix} = \begin{bmatrix} G_1 & G_{1M} & G_{12} \\ G_{M1} & G_M & G_{2M} \\ G_{21} & G_{M2} & G_2 \end{bmatrix} \tag{7.3}$$

where $\tau_i = (ES_{iM} - H_{iM})$, and S_{MM} is the overlap submatrix and H_{MM} is the Hamiltonian of the standalone molecule. The complex green function g_i, for the contact i is defined as

$$g_i(E) = -\pi\sqrt{-1}\begin{bmatrix} g_i^1 & \cdots & 0 \\ \vdots & \ddots & \vdots \\ 0 & \cdots & g_i^{ni} \end{bmatrix}$$

where the diagonal corresponds to the contribution from s, p and d character of the electrodes DOS obtained using DFT with PBC. From Eq. 7.3, we get

$$G_M(E,V) = ES_{MM}(E,V) - H_{MM}(E,V) - \Sigma_1(E,V) - \Sigma_2(E,V)^{-1} \tag{7.4}$$

where the self energy terms for electrodes 1 and 2 are

$$\sum_i (E,V) = (ES_{Mi} - H_{Mi}) g_i (ES_{iM} H_{iM})$$

Here we are able to combine the continous and discrete wavefunction in the same formalism [69]. The transmission probability, T, and the total density of states, D, of the molecular junction are calculated as follows [37, 66, 80]:

$$T(E,V) = Trace(\Gamma_1(E,V) G_M(E,V) \Gamma_2(E,V) G_M^+(E,V)) \tag{7.5}$$

$$D(E,V) = Trace(i\left[G_M(E,V) - G_M^+(E,V)\right] S(V)) \tag{7.6}$$

where $\Gamma_i = \sqrt{-1}(\Sigma_i(E,V)) - \Sigma_i^+(E,V) \quad (i,j = 1,2)$ describes the coupling between the contacts and the molecule, $S(V)$ is the overlap matrix at each applied voltage, G_M is the retarded Green function for the standalone molecule and G_M^+ is its adjoint.

Therefore the current is obtained from:

$$I \approx \frac{2e}{h} \int_{E_f + V_1}^{E_f + V_2} T(E,V) dE \tag{7.7}$$

where e is the charge of the electron, h is Planck's constant and E_f is the Fermi level of the molecular junction. Calculations for several kind of systems have been performed in the past [24, 71, 74–76]. The combined DFT-Green function formalism had been used by other groups to study the electron transport through organic molecules between gold electrodes, such as DNA [83, 86], porphyrins [41, 91], molecular wires [1], molecular diodes and switches [27, 30] and CNTs [40].

We also investigated the electric conduction in complexes **19–26** following the same procedure used for **1–18**, but in this case the functional M05-2X instead of B3PW91 was considered that allow a description of the electronic correlation to a medium-range. As illustration, gold contacts for the complexes **19–26** containing the graphene pristine are shown in Fig. 7.5.

7.3 Results and Discussion

7.3.1 Carboxylate Functionalization

Binding Energy Firstly we investigated the adsorption of cobalt phthalocyanine on the functionalized graphene (FG) by means of the calculation of the binding energy with the aim to determine the stability of the complex. The binding energy is obtained from $E_{bind} = E_{complex} - (E_{CoPc} + E_{FG})$ and the results calculated with the functional B3PW91 are presented in Table 7.1. For comparison the B3LYP results are also included in the table. Both functionals have the same percentage of Hartree Fock exact exchange (20%) but differ in the correlation functional, PW91 and LYP

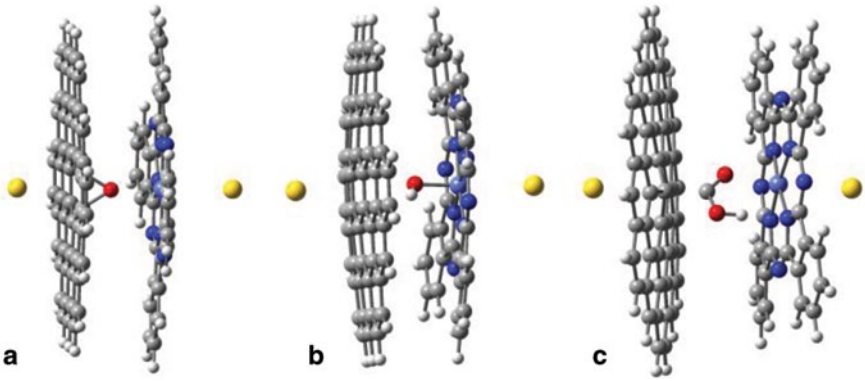


Fig. 7.5 Molecular view of the complexes attached to Au terminals containing graphene pristine and the functionalization: **a** epoxide, **b** hydroxyl, **c** carboxyl. Color code: carbon (*gray*), hydrogen (*white*), nitrogen (*blue*), oxygen (*red*), cobalt (steel *blue*) and gold (*yellow*)

for B3PW91 and B3LYP respectively. The structural conformations of the complexes are very different and consequently their binding energies too. In overall we can see that both functionals predict more or less the same trend with some differences.

The parallel conformations (**1–6**) present a low or non stability with B3PW91 but B3LYP gives a stability of −5 to −15 kcal/mol. The perpendicular conformations (**7–12**) achieve more negative binding energies up to −25 kcal/mol giving account of an interaction more favorable. This could be explained by the distance Co–O in **7–12** whose values ~2.15 Å indicate the formation of a covalent bond that leads to a stronger interaction than van der Waals formed in the parallel conformation (**1–6**). For complexes with ligand-centered attachment, **13–18**, B3PW91 and B3LYP suggest higher stability for **16–18** (~−100 to −150 kcal/mol), it can be understood because of the lower electronic repulsion between graphene and phthalocyanine in its extended structure. B3PW91 functional foretells that complexes **13–15** would not be formed because of the positive values in binding energy, and B3LYP foretells it for **13**. An explanation to that is due to the perpendicular conformation for CoPc with respect to FG in **13–15** that could provoke a repulsion between the two π atomic orbitals of the oxygen atom of CO and the π cloud of graphene. The theoretical results for **16–18** confirm the experimental trend in the sense that structures **16–18** have been synthesized for graphene oxide linked to porphyrin through an amide bond CO–NH [33] that could explain the higher stability that these complexes have with respect to the others studied in this work.

In conclusion we can say that the adsorption of CoPc (CoTAPc) on carboxylate functionalized graphene occurs, with some exceptions. For interaction centered on cobalt (with CO_2^-) (**1–12**) a covalent bond Co–O of ~1.9–2.2 Å is formed and for interaction centered on ligand (with CO) (**13–18**) the covalent bond formed correspond to C(CO)–N(NH) with values of ~1.3 Å.

Frontier Molecular Orbitals In relation to the electronic stability given by the HOMO-LUMO frontier molecular orbitals, we found that these orbitals in com-

Table 7.1 Binding (E_{bind}) energies, electrical dipole moment (μ), HOMO, LUMO, and HOMO-LUMO Gap energies of all the complexes at the B3PW91/6-31G(d)/LANL2DZ level of theory. For comparison E_{bind} calculated with B3LYP is also included

Complex	E_{bind} B3PW91 (kcal/mol)	E_{bind} B3LYP (kcal/mol)	μ (D)	HOMO (eV)	LUMO (eV)	HLG (eV)
Interaction centered on Cobalt						
1: G–CO2$^-$–CoPc	14.06	−8.97	1.92	−1.61	−0.60	1.00
2: G-Def–CO2$^-$–CoPc	13.21	−14.87	4.09	−1.82	−0.86	0.96
3: G-Vac–CO2$^-$–CoPc	13.19	−11.51	4.47	−1.70	−0.78	0.91
4: G-CO2$^-$–CoTAPc	−5.36	1.92	4.27	−1.35	−0.31	1.03
5: G-Def–CO2$^-$–CoTAPc	−7.65	−9.26	6.29	−1.56	−0.55	1.01
6: G-Vac–CO2$^-$–CoTAPc	−8.02	−5.23	6.60	−1.44	−0.49	0.96
7: G–CO2$^-$–LAT–CoPc	−1.28	−25.51	9.22	−2.70	−0.52	2.18
8: G-Def–CO2$^-$–LAT–CoPc	−0.64	−25.89	8.82	−2.73	−0.94	1.79
9: G-Vac–CO2$^-$–LAT–CoPc	−1.50	−26.38	9.86	−2.68	−1.28	1.40
10: G-CO2$^-$–LAT–CoTAPc	−19.80	−18.27	7.21	−2.09	−0.42	1.67
11: G-Def–CO2$^-$–LAT–CoTAPc	−19.86	−17.05	6.89	−2.10	−0.83	1.27
12: G-Vac–CO2$^-$–LAT–CoTAPc	−19.75	−16.09	7.91	−2.07	−1.17	0.89
Interaction centered on ligand						
13: G–CO–CoTAPc	25.24	6.30	3.65	−4.01	−3.74	0.27
14: G-Def–CO–CoTAPc	13.48	−2.45	6.23	−4.27	−3.98	0.30
15: G-Vac–CO–CoTAPc	7.42	−9.42	2.18	−4.31	−3.84	0.48
16: G-CO–LAT–CoTAPc	−107.54	−156.99	4.49	−4.05	−2.37	1.67
17: G-Def–CO–LAT–CoTAPc	−135.89	−157.33	5.07	−4.49	−2.78	1.70
18: G-Vac–CO–LAT–CoTAPc	−135.87	−151.08	4.81	−4.47	−3.12	1.35
G			0.00	−5.09	−2.27	2.82
G–CO2$^-$			8.13	−1.51	0.16	1.67
G_Def–CO2$^-$			8.44	−1.84	0.04	1.88
G_Vac–CO2$^-$			7.66	−1.92	0.13	2.05
G−CO2$^-$–LAT			23.51	−1.90	−0.31	1.59
G_Def–CO2$^-$–LAT			23.78	−1.93	−0.72	1.21
G_Vac–CO2$^-$–Lat			23.87	−1.89	−1.06	0.83
G–CO			2.28	−4.72	−2.94	1.78
G-Def–CO			1.51	−4.86	−3.60	1.26
G-Vac–CO			1.64	−4.70	−3.80	0.90
G–CO–LAT			6.17	−7.67	−6.18	1.49
G-Def–CO–LAT			5.69	−7.49	−6.17	1.32
G-Vac–CO–LAT			5.63	−7.68	−6.17	1.51

plexes **13–18** are lower in energy than in **1–12** (see Table 7.1). However the HOMO-LUMO gap (HLG) is larger mainly for perpendicular orientation (**7–12**) in the cobalt centered interaction and for extended orientation in the ligand centered interaction (**16–18**). To simplify the analysis we show in Fig. 7.6 the values of HLG of the complexes compared to their fragments. In comparison with graphene pristine (2.82 eV), all the complexes (**1–18**) present a shorter HLG as a consequence of the extension of the conjugation or increasing of π electrons when the cobalt

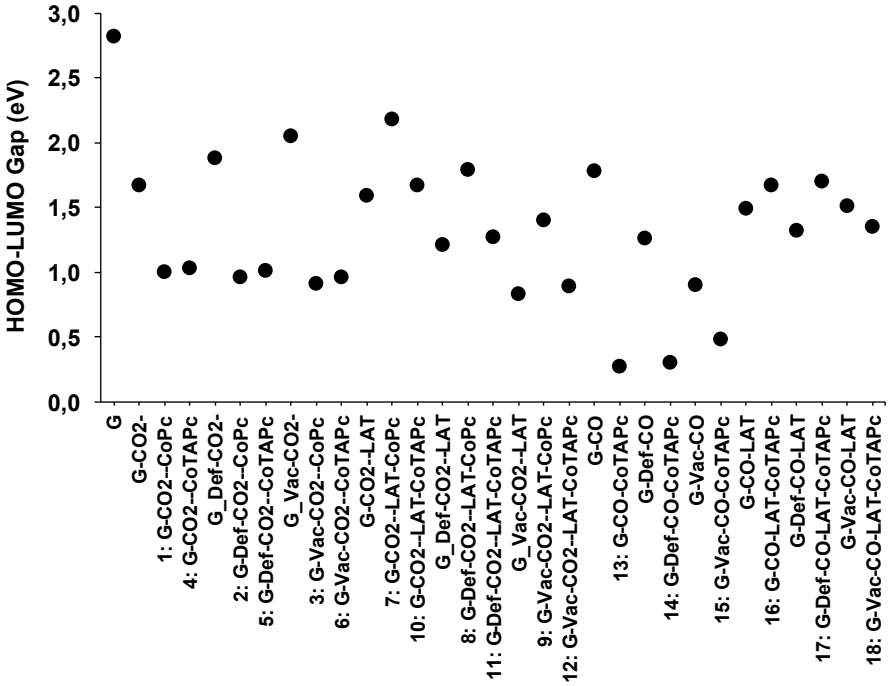


Fig. 7.6 HOMO-LUMO Gap (HLG) of complexes and fragments calculated at the B3PW91/6-31G(d)/LANL2DZ level of theory

phthalocyanine (CoPc, CoTAPc) interacts with graphene. From the point of view of the reactivity, this means that all the complexes are more reactive than graphene pristine that is understood due to the large amount of π electrons belonging to each structure. The π electrons are of higher energy than σ electrons and therefore they are more available to be excited to higher energy levels.

In relation to the fragments of graphene, the adsorption of phthalocyanine produces a different effect and it depends of the orientation type. In the case of the complexes with a parallel orientation (**1–6**), the effect of CoPc or CoTAPc is the decreasing of the HLG. The perturbation between graphene and the ligand phthalocyanine clearly is produced because both are located face to face. A covalent bond Co–O of ~1.90 Å is formed by the attraction donor (O)-acceptor (Co) of both atoms. A similar result occurs with the complexes with perpendicular orientation where graphene interacts with CoTAPc by the ligand (**13–15**) through the functionalization CO, the HLG values decrease with respect to the corresponding graphene fragment. It is important to note that in the complexes **1–6** and **13–15** the functionalization is located in the center of the graphene.

For other complexes the effect of the phthalocyanine is an increase of the HLG with respect to the graphene fragment. It is the case of **7–9** where the covalent interaction between both fragments occur by one oxygen atom of the $–CO2^{–}$ group and

the cobalt atom with a distance Co–O of ~2.16 Å. The interaction is by a perpendicular orientation and centered on cobalt atom. The functionalization $–CO2^-$ is placed in the edge of the graphene. Similar structures are **10–12** but in this case the donor ability of the amine substituents in CoPc leads to a delocalization of the electronic density toward the phthalocyanine core. Thus the lower HLG of **10–12** with respect to **7–9** could be explained in terms of a slight electronic repulsion between the electronic density of the macrocycle and the π orbitals of the oxygen atom of $CO2^-$. In spite of that, all the complexes **7–9** and **10–12** present a higher HLG than the corresponding functionalized graphene meaning that CoPc or CoTAPc stabilize the graphene models. Complexes **16** and **17** also present higher HLG than the respective graphene fragments where the functionalization CO is by the edge of graphene.

In summary, we found that complexes where the functionalization is located on the center of graphene lead to lower HLG than FG and therefore would be more reactive than the latter. By the contrary, when the functionalization is by the edge of graphene the complexes present a higher HLG than FG doing the complexes less reactive than the latter.

On the other hand, HOMO and LUMO surfaces are shown to be dependent on the conformation of the conjugated structures (Fig. 7.7). Parallel orientations (**1–6**) show high participation of graphene in both molecular orbitals with a contribution of cobalt atom in the phthalocyanine. Perpendicular orientations (**7–12**) show that their HOMOs are localized on the phthalocyanine ligand (no metal) and the LUMO on the graphene, suggesting that in these complexes, CoPc (CoTAPc) is an electron donor species and the graphene is an electron withdrawing one. This suggests a charge transfer from HOMO to LUMO and therefore a shifting of electronic density from phthalocyanine to graphene. Similar behavior has been found for composites of copper tetrasulfonate phthalocyanine and graphene oxide [17]. This feature of graphene to increase its electronic charge induced by other molecule, makes it a potential resistance-based sensor.

Complexes **13–15** show similar HOMO and LUMO, which are mainly localized on the graphene and cobalt with a minor contribution in the phthalocyanine ligand. No meaningful changes are seen between both molecular orbitals for **13–14**, but for **15**, a higher contribution in the LUMO of phthalocyanine ligand (in the C–N of the G–CoTAPc linking) is observed.

Meanwhile **16–18** show a similar behavior than **7–12**; their HOMOs are localized in phthalocyanine ligand, with a contribution from the cobalt to the HOMO in **16**; and the LUMOs are on the graphene; therefore, complexes **16–18** might show electron transfer from phthalocyanine HOMO to graphene LUMO, thus, similarly to **7–12**, they could be used as charge-transfer sensors. For these complexes (**7–12**, **16–18**), although their LUMO are on the graphene, it is clear for the complexes with G-Vac (**9**, **12**, **18**) that their LUMO's are mostly localized in the vacancy rather than delocalized over the graphene, suggesting a reduced electron transfer. However, the orientation of phthalocyanine with respect to graphene could affect the amount of charge transferred.

After the analysis of the frontier molecular orbitals, and considering they are in both conjugates, we can understand why the HLG of **1–6** is smaller than the HLG

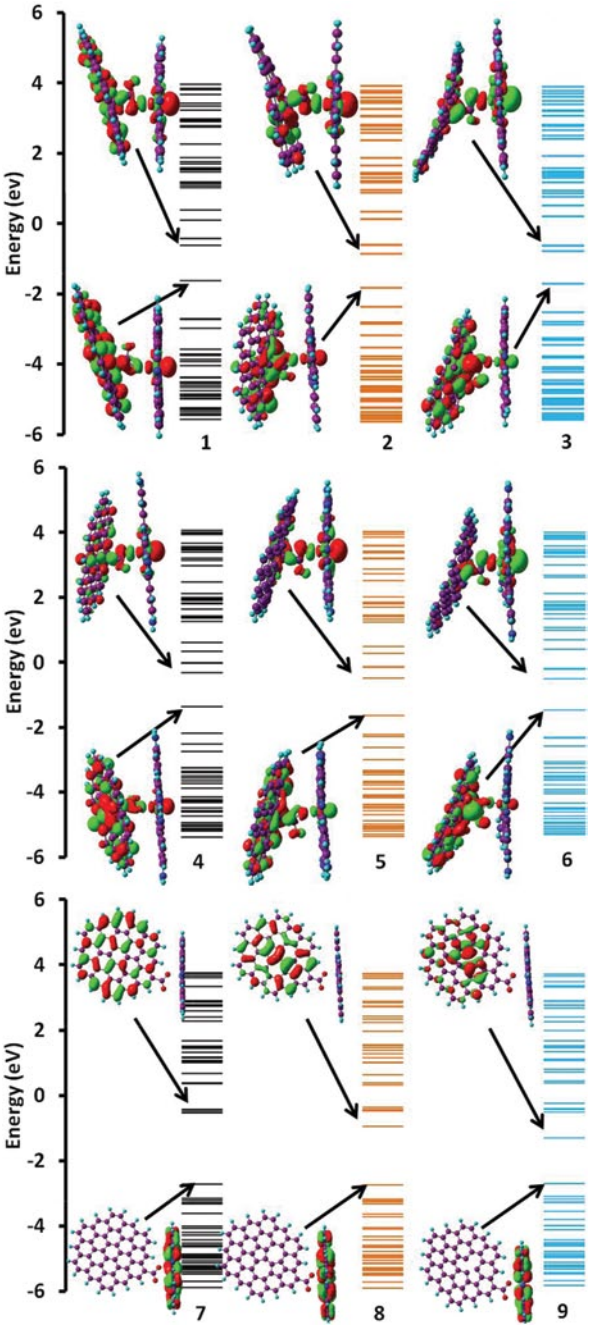


Fig. 7.7 Molecular orbitals of the complexes calculated at the B3PW91/6-31G(d)/LANL2DZ level of theory. G (*black*), G-Def (*orange*), G-Vac (*light blue*). Isosurfaces of the LUMO (*top*) and HOMO (*bottom*) are also included

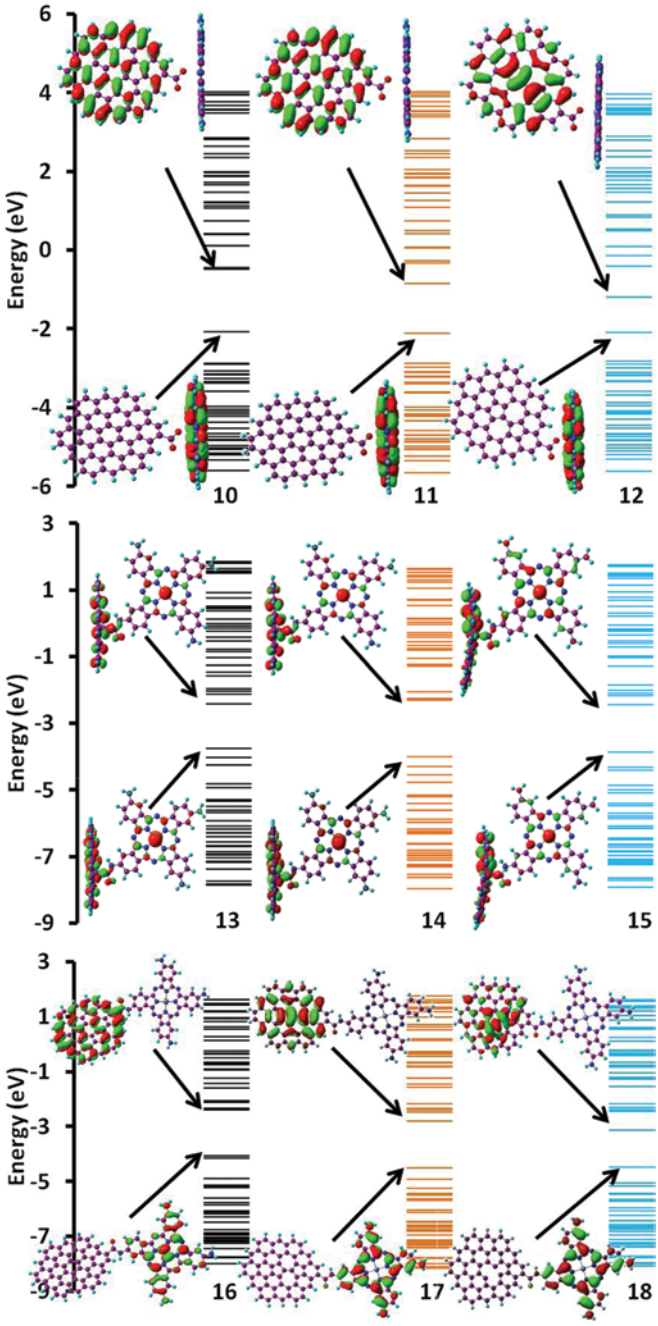


Fig. 7.7 (continued)

of **7–12**, when both have –$CO2^{-}$ functionalization; this is because the conjugated structures in **1–6** are facing in parallel orientation favoring charge transfer between the π clouds.

Current-Voltage Analysis of the complexes obtained through DFT-Green's function calculations are showed in Fig. 7.8; the results are shown by complex conformations and phthalocyanine model, and the influence of each graphene model (G, G-Def, G-Vac) is compared. For all complexes, we applied positive bias in a way that current from phthalocyanine to graphene is induced, CoPc (CoTAPc) → G; the electric current is calculated at −1 V (negative bias), 0 V and +1 V (positive bias).

For parallel orientations, cobalt-centered complexes (G–$CO2^{-}$ center functionalization) (**1–6**), the standard current (define for positive charges) is shifted in both directions, but higher in the direction of CoPc (CoTAPc) → G for complexes with pristine graphene (**1,4**) and G-Def (**2,5**); while in the opposite direction, G → CoPc (CoTAPc), for complexes with G-Vac (**3,6**). Complexes with pristine graphene (**1,4**) show higher current than those with G-Def (**2,5**) and G-Vac (**3,6**), despite that **1** and **4** have larger HLGs. For **1** and **4** the effect of the amine groups (NH_2) is large as substituent in the phthalocyanine ligand, because it causes a decrease in the electric current, for instance, the currents in **1** are −3.88 and +7.40 μA and for **4** are −2.85 and +4.71 μA for voltages different from zero, in which HLG for **1** is 0.03 eV smaller than the gap in **4**.

For perpendicular orientation cobalt-centered complexes (G–$CO2^{-}$ edge functionalization) (**7–12**), the conduction decreases remarkably with respect to the complexes with parallel orientation (**1–6**), due to the arrangement of the conjugated structures, G and CoPc (CoTAPc), where the communication is just through a linking bond, and thus the charge transferred is lower. Though there is conduction in both directions, the current is slightly higher from G → CoPc (CoTAPc); which is in agreement with their frontier orbitals, because the HOMO is in CoPc (CoTAPc) and the LUMO in G; this shows an easy way for the electrons to be carried from CoPc (CoTAPc) to G. However, for this orientation at a bias of higher currents, the complexes with G, G-Def, and G-Vac show similar values of transferred current. Also, as it takes place in **1** and **4**, we found **7** (−0.03 nA) showing slightly higher current than **10** (−0.02 nA), at ~1 V; despite the HLG of **7** (2.18 eV) is larger; the same trend is observed between those with defect and vacancy; complexes with CoPc feature higher current.

In the case of CO functionalized complexes, **13–18**, we notice a difference in the electric conduction for perpendicular and extended orientations. For **13–15** the currents are shifted in the direction CoTAPc → G and remarkably the highest conduction is observed for the complex with G-Vac **15** (+0.1 μA at 1 V). This can be due to its HOMO having more contribution in G–CO bonding and also because the LUMO has more contribution in the attachment region G–CoTAPc (C–N bond) than the LUMOs of **13** and **14**. The conduction increases for complex **15** despite it has larger HLG than pristine graphene **13**.

We notice that the complexes functionalized with CO, **13–15**, show higher currents than complexes functionalized with –$CO2^{-}$ (**10–12**, even **7–9**) when both

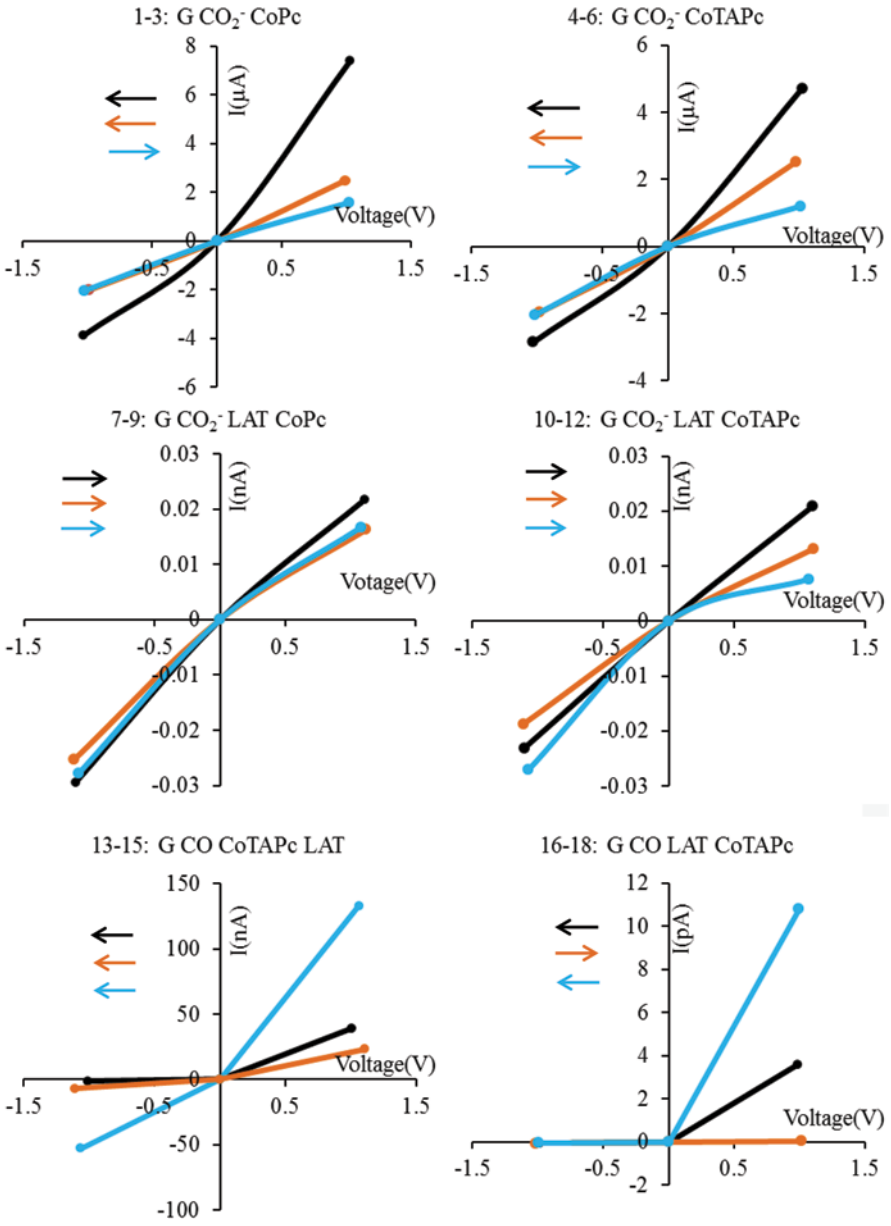


Fig. 7.8 Current-voltage characteristics of complexes G–CoPc (CoTAPc). The arrows indicates the preferred current direction. According to conjugates positions in Fig. 7.2, at positive (direct) bias the current is from CoPc (CoTaPc) to G (→). Color curves relates to graphene models in complexes: G (*black*), G-Def (*orange*), G-Vac (*light blue*); however their points are interconnected to help the eye

conformations have G–CoTAPc attachment and perpendicular orientation. Complexes **10–12** have perpendicular orientation of graphene and the linking is through (Co–O), while **13–15** have perpendicular orientation of phthalocyanine (CoTAPc), and the linking is through (C–N), being the latter linking better for electronic transfer, in addition to the fact that these complexes (**13–15**) show smaller HLG.

The extended orientation of complexes **16–18** is not planar and that factor can affect the conduction, which is lower (~0.01 nA) than **13–15**, but again the higher conduction takes place in the complex with G-Vac (**18**). A characteristic of complexes **13–18**, but **17**, is that the conduction is not symmetric in both directions, resembling a diode behavior, and it is larger for the direction CoTAPc → G; the complex **17** has the smallest current (and HLG larger than **16**), and it is in the order of 0.01 pA at both positive and negative bias.

In summary, we found that the complexes that present a larger current conduction (**1–6**) correspond to the structures where the electric field, applied through the electrodes given by the gold atoms, is able to perturbate the phthalocyanine and graphene. Given the parallel orientation between them a significative conduction is achieved.

7.3.2 Epoxide, Hydroxyl and Carboxyl Functionalization

Binding Energy The absorption of CoPc was also investigated on graphene with other functionalizations (complexes **19–26**). Considering the functionalizations used for the graphene oxide at the experimental level with success such as epoxide, hydroxyl and carboxyl, and the larger current conduction for the parallel orientation with the interaction centered on the cobalt (**1–6**); we built complexes with these characteristics. The optimized molecular structures of the complexes **19–26** are shown in Fig. 7.9.

We calculated the binding energy between functionalized graphene and CoPc and the results are shown in Table 7.2. We found that epoxide leads to stable complexes (**19–21**) with negative E_{bind} values given by a strong covalent interaction Co–O (~2.2 Å). This functionalization is of higher stability between these studied in this section. Complexes **22** and **23** show that hydroxyl is a good functionalization for the adsorption of CoPc but only in conformation pristine and with defect, respectively. In both cases the OH group is bonded to cobalt atom with distance Co–O of ~1.6 Å. This is a good example when the remotion of OH from graphene is required. Our stability results are in agreement with experimental results such as NMR, [43, 11] AFM, [21, 68] and STM [53] where it is suggested that epoxide and hydroxyl groups are localized in the basal plane of G. Besides, our DFT calculations for G-OH are consistent with those reported using DFT pseudopotential plane-wave methods, [31] in the sense that the adsorption of hydroxyl groups on sites of G with defects and vacancies is stronger than on pristine sites, [31] suggesting that these sites cause the retention of the functional group in the G.

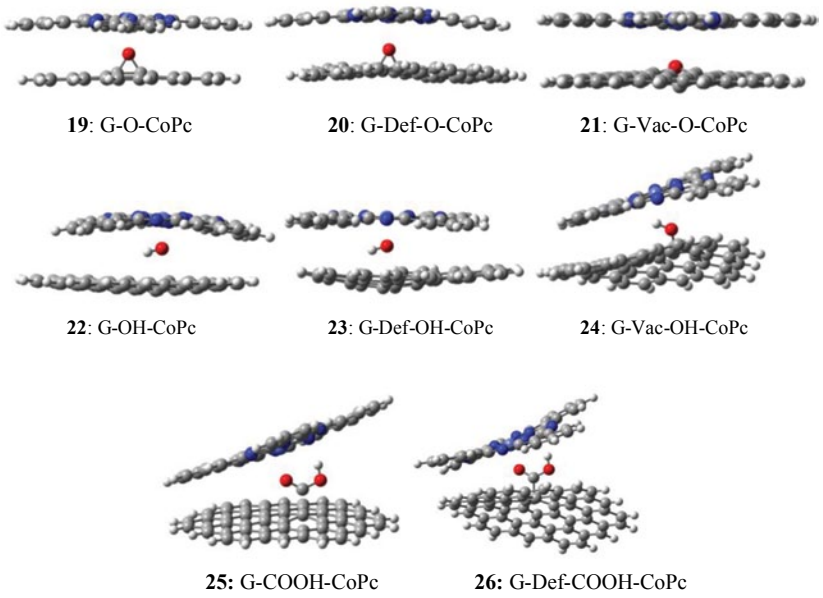


Fig. 7.9 Optimized molecular structures for the complexes obtained at the level of calculation M05-2X/6-31G(d)/LANL2DZ

Table 7.2 Binding (E_{bind}) energies, electrical dipole moment (μ), HOMO, LUMO, and HOMO-LUMO Gap energies of all the complexes at the M05-2X/6-31G(d)/LANL2DZ level of theory

Complex	E_{bind} (kcal/mol)	μ (D)	HOMO (eV)	LUMO (eV)	HLG (eV)
19: G–O–CoPc	−43.26	3.57	−5.29	−1.83	3.46
20: G-Def–O–CoPc	−43.57	2.67	−5.34	−1.84	3.50
21: G-Vac–O–CoPc	−65.52	1.40	−5.42	−2.22	3.19
22: G–OH–CoPc	−32.05	0.92	−5.58	−2.05	3.53
23: G-Def–OH–CoPc	−19.10	2.09	−5.56	−2.09	3.47
24: G-Vac–OH–CoPc	15.94	11.18	−4.99	−3.38	1.61
25: G–COOH–CoPc	24.02	4.99	−4.97	−2.94	2.03
26: G-Def–COOH–CoPc	27.04	2.09	−5.16	−3.10	2.06
G	–		−6.00	−1.55	4.46
G-Def	–		−5.80	−2.01	3.80
G-Vac	–		−5.89	−1.68	4.21
CoPc	–		−5.76	−1.69	4.08
G–O			−5.97	−1.78	4.19
G-Def–O			−5.89	−1.81	4.08
G-Vac–O			−5.32	−2.40	2.92
G–OH			−5.47	−1.50	3.98
G-Def–OH			−5.76	−1.65	4.11
G-Vac–OH			−5.38	−1.44	3.95
G–COOH			−5.26	−1.47	3.79
G-Def–COOH			−5.80	−1.64	4.16

The vacancy in graphene in **24** produces a flattening of OH avoiding a favorable interaction with CoPc stated in the positive value of E_{bind}. Some similar occurs with graphene–COOH, the interaction with CoPc is unfavorable, as can be seen for complexes **25–26**. Although two strong interactions are produced (rCo–O(COOH) ~ 2.2 Å and N(pirrol)–H(COOH) ~ 1.9 Å), the phthalocyanine ligand loss its planarity and provokes an approaching of ~3 Å to G–COOH (G-Def–COOH) in one edge but of ~ 7 Å in the other edge. Therefore, it is not possible the adsorption of CoPc to these functionalized graphenes. It is important to note that complexes **25** and **26** had difficulties to achieve the convergence in the calculation of the geometry optimization. Even the calculation of the complex G-Vac–COOH–CoPc had serious convergence problems to be obtained. It is the reason why the latter is not included in the set of complexes.

In summary, the adsorption of CoPc is possible on graphene functionalized with epoxide better than hydroxyl. In a previous work we investigated the adsorption of nickel phthalocyanine and nickel tetrasulphophthalocyanine on glassy carbon through an oxo or and hydroxo bridge [20]. We also concluded, as in the present work, that the oxo binding is favored in the adsorption of the phthalocyanines denoted by a lower binding energy, in agreement with the experimental data, [20] and a larger charge transfer is produced than with hydroxo binding.

Frontier Molecular Orbitals As was discussed previously with the carboxylate functionalization on graphene, we included in Table 7.2 the frontier molecular orbitals HOMO, LUMO and the gap between them. In overall we found that the modification of graphene pristine with defect or vacancy produces a stabilization in HOMO and LUMO. It is observed a relation between the binding energy and the HLG values, complexes with negative E_{bind} (**19–23**) present a larger HLG than those having positive E_{bind} (**24–26**) giving account of the instability of the latter. Taking as reference the graphene pristine, all the complexes **19–26** present an HOMO of higher energy but LUMO is stabilized to lower energy. Figure 7.10 shows a comparison of HLG between the complexes **19–26** and the fragments corresponding to the functionalized graphene.

In relation to the functionalized graphene, we found that the adsorption of CoPc generates a decreasing in HLG (at exception of **21**) but its value follow being numerically significant (~3.5 eV). Graphene with epoxide, hydroxyl and carboxyl have a HLG close to 4.0 eV. A decreasing in HLG implies a higher reactivity that is understood in terms of the parallel orientation that have the complexes. Although the number of π electrons increases in the complexes, the constituent structures (CoPc and FG) are only linked by a covalent bond between the functionalization and the cobalt atom. Van der Waals interaction through the π clouds produce a weak communication between CoPc and FG.

It is interesting to note the agreement between E_{bind} and HLG, the complexes not formed by the positive value of E_{bind} (**24–26**) give account of a HLG of ~ 2.0 eV that is much less than in **19–23**.

On the other hand, the molecular orbital surfaces (Fig. 7.11) show in all cases a degeneration as in the occupied MOs as in virtual MOs, that is a characteristic also

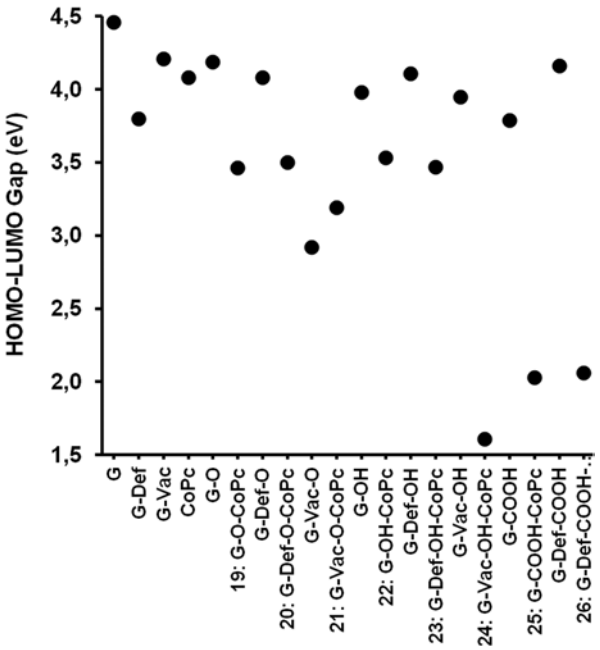


Fig. 7.10 HOMO-LUMO Gap (HLG) of complexes and fragments calculated at the M05-2X/6-31G(d)/LAN-L2DZ level of theory

found for the complexes **1–18**. It could be attributed to the extended conjugation of the π electrons. Clearly can be observed that **24** is different in the region HOMO-LUMO with respect to the other complexes of the same series (OH functionalization in graphene). A very shorter HLG is obtained for **24** (1.6 eV) as result of the unfavorable interaction between G-Vac–OH and CoPc. Some similar occurs for **25** and **26**, a very short HLG and a little degeneration with respect to **19–23**.

At difference of complexes **1–6** with parallel orientation, it can be seen that the epoxide functionalization generates donor-acceptor species (**19–21**) where the donor species (HOMO) corresponds to CoPc and the acceptor one (LUMO) is for the graphene-epoxide. Similar result is obtained for **22** and **24** with hydroxyl and was also found for complexes **7–12** and **16–18**. However **23** do not show a preference in its donor molecular orbital HOMO because is located in both graphene-def-hydroxyl and CoPc. Complexes **25** and **26** present a very different behavior, both HOMO and LUMO are located in the cobalt atom, part of graphene and CO (COOH).

In summary, stable donor acceptor complexes with epoxide (**19–21**) and hydroxyl (**22**) functionalization are attractive because could be used as current sensors. From that point of view **25** and **26** are not attractive as sensors because they do not present a change in their frontier molecular orbitals.

Current-Voltage Results obtained with the DFT-Green's function procedure GENIP calculations for the complexes **19–26** are showed in Fig. 7.12; a same figure is used to compare the effect of the graphene model (G, G-Def, G-Vac). For all complexes, we applied positive bias in a way that current from phthalocyanine to

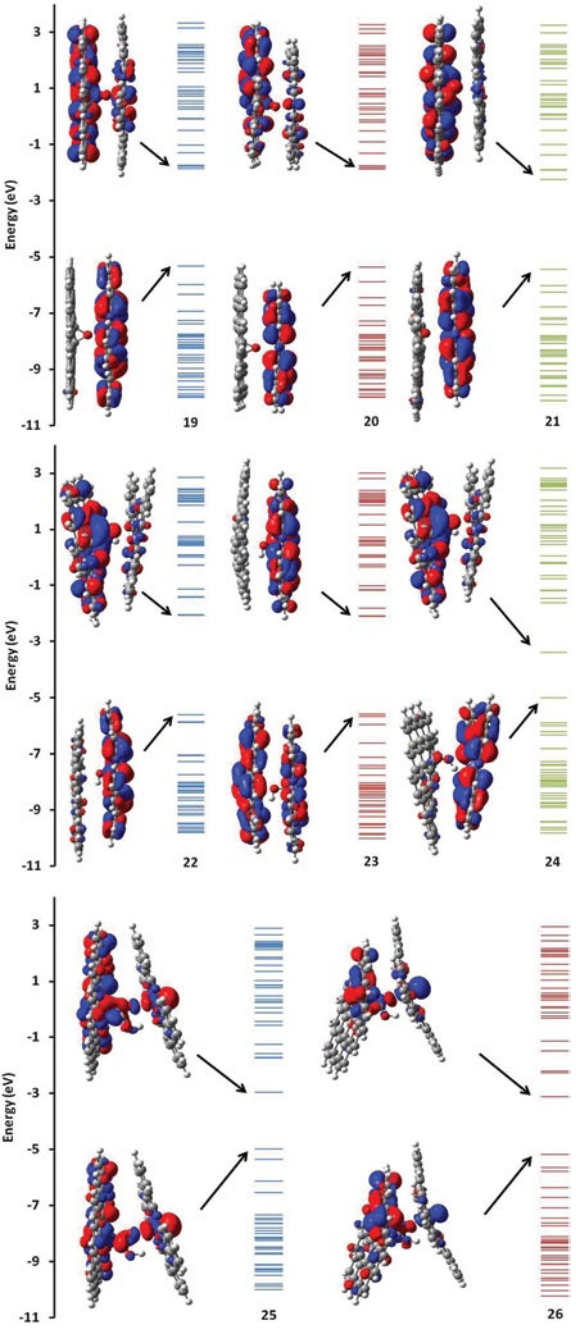


Fig. 7.11 Molecular orbitals of the complexes calculated at the M05-2X/6-31G(d)/LANL2DZ level of theory. G (*blue*), G-Def (*brown*), G-Vac (*green*). Isosurfaces of the LUMO (*top*) and HOMO (*bottom*) are also included

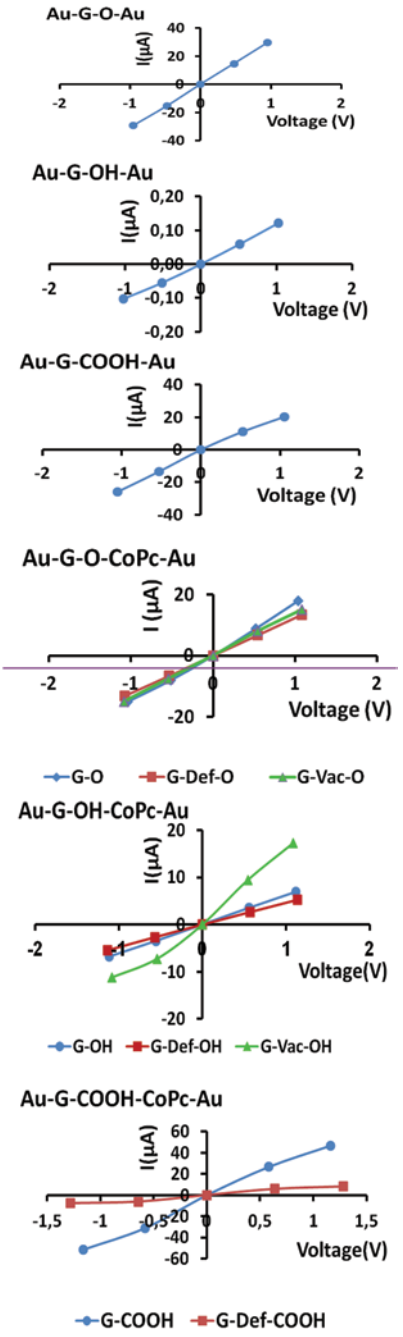


Fig. 7.12 Current-voltage characteristics for the G-functionalization-CoPc complexes. According to conjugates positions in Fig. 7.5, at positive (direct) bias the current is from CoPc to G (→). Color curves relates to graphene models in complexes: G (*blue*), G-Def (*brown*), G-Vac (*green*); however their points are interconnected to help the eye

graphene is induced, CoPc → G; the electric current is calculated at −1 V (negative bias), 0 V and +1 V (positive bias). The two gold contacts simulating to the electrodes are at a distance of ~9–10 Å for the complexes and ~6–7 Å for the graphene fragments with the aim to produce an efective current. As comparison, we also calculated the current of the graphene pristine functionalized with epoxide, hydroxyl and carboxyl (Fig. 7.2).

The graphenes yield nearly symmetric currents in both directions given by the similar values obtained for positive and negative bias. From Fig. 7.12, it is clear that epoxide and carboxyl favor the current transmission in the graphene with values from 30 and 20 μA at 1 V bias, respectively. By the contrary graphene-hydroxyl yield a small current of ~0.12 μA (at 1 V) that could be explained by the presence of H in the OH group. This one by its characteristic of electroacceptor atom prevent the electron transport that is verified by the atomic charge. The value of the Mulliken charge of H in G–OH is 0.43 and in G–COOH is 0.49.

The comparison of the fragments with the corresponding complexes shows that in the case of G–O (~30 μA) the adsorption of CoPc (**19**) decreases the current at positive bias (~18 μA). However, in G–OH (~0.1 μA) is increased to ~7 μA for the complex **22** and in G–COOH (~ 20 μA) is increased to ~ 49 μA for the complex **25**.

For the complexes shown to be stable by the calculation of the binding energy (**19–23**), we found similar current for different graphene models (pristine, defect, vacancy) but this is slightly higher for those with graphene pristine (**19,22**). It is interesting to note that the best complex with functionalization $CO2^{-}$ corresponding to complex **1** has a current of ~7 μA that is similar to **22** (~7 μA) with hydroxyl but much less that **19** (~18 μA). The high value found for G–COOH–CoPc in both directions (CoPc -> G and G -> CoPc) could be attributed to the distorsion of the phthalocyanine that provokes a larger approaching of the fragments in some regions.

In summary, the adsorption of CoPc on functionalized graphene oxide (epoxide, hydroxyl, carboxyle) generates structures able to yield a current conduction in stable complexes. Using a hydroxyl functionalization the conduction is improved with the adsorption of CoPc (~7 μA) and significant with the epoxide functionalization (~13–18 μA). Defect and vacancy in graphene produces a lower current conduction than pristine. The magnitude of current obtained (~7 to 18 mA) could be useful for instance in the cases of interfaces for catalysis where currents in the order hundreds of nanoampers approaching to microamperes are desired.

7.4 Conclusions

We have presented a theoretical study at the density functional theory level (B3PW91, B3LYP, M05-2X with basis set 6-31G(d)/LANL2DZ (Co)) where investigated the ability that cobalt phthalocyanines adsorbed on functionalized graphene can yield current conduction. We use three graphene models (pristine, defect, vacancy), four functionalizations (carboxylate, epoxide, hydroxyl, carboxyle) and

two cobalt phthalocyanines (unsubtituted and tetraaminosubstituted) generating 26 complexes functionalized graphene-cobalt phthalocyanine. The adsorption given by the binding energy calculation is achieved for an extended orientation of the complex with carboxylate and for a parallel orientation of the complex with epoxide and hydroxyl. No adsorption was found for carboxyl. HOMO-LUMO Gap values confirm a less reactivity (high stability) for complexes with functionalization $–COO^-$ in the edge of graphene and for complexes with epoxide and hydroxyl than the corresponding fragments. Finally, we show that several of these complexes with $–COO^-$, $–O^-$ and –OH in a parallel orientation can conduct the electrical current that goes from ~7 to 18 μA at a bias voltage of 1 V.

Acknowledgement GICJ thanks the financial support from CONICYT-CHILE through Projects FONDECYT N°1090700 N°1131002 and DICYT-USACH from Project Apoyo Complementario by computational time provided. JMS acknowledges the high-performance computing support provided by the Texas A&M Supercomputer Facility and the Texas Advanced Computing Center as well as the financial support from the U.S. Defense Threat Reduction Agency (DTRA) through the U.S. Army Research Office (ARO), project no. W91NF-06-1-0231; and ARO/MURI project no. W911NF-11-1-0024.

References

1. Aghaie H, Gholami MR, Monajjemi M, Ganji MD (2008) Electron transport phenomenon simulation through the carborane nano-molecular wire. Physica E Low Dimens Syst Nanostruct 40(9):2965–2972. doi:http://dx.doi.org/10.1016/j.physe.2008.02.014
2. Akhavan O (2011) Photocatalytic reduction of graphene oxides hybridized by ZnO nanoparticles in ethanol. Carbon 49(1):11–18. doi: 10.1016/j.carbon.2010.08.030
3. Al-Aqtash N, Vasiliev I (2009) Ab initio study of carboxylated graphene. J Phys Chem C 113(30):12970–12975. doi:10.1021/jp902280f
4. An W, Wu X, Yang JL, Zeng XC (2007) Adsorption and surface reactivity on single-walled boron nitride nanotubes containing Stone–Wales defects. J Phys Chem C 111(38):14105–14112. doi:10.1021/jp072443w
5. Balbuena PB, Altomare D, Agapito L, Seminario JM (2003) Theoretical analysis of oxygen adsorption on pt-based clusters alloyed with Co, Ni, or Cr embedded in a pt matrix. J Phys Chem B 107(49):13671–13680. doi:10.1021/jp035729j
6. Bautista EJ, Yan L, Seminario JM (2007) Ab initio analysis of electron transport in oligoglycines. J Phys Chem C 111 (39):14552–14559
7. Becke AD (1988) Density-functional exchange-energy approximation with correct asymptotic behavior. Phys Rev A 38(6):3098–3100
8. Becke AD (1993) Density-functional thermochemistry. III. The role of exact exchange. J Chem Phys 98(7):5648–5652
9. Boukhvalov DW, Katsnelson MI (2008) Chemical functionalization of graphene with defects. Nano Lett 8(12):4373–4379. doi:10.1021/nl802234n
10. Burke K, Perdew JP, Wang Y (1998) In: Dobson JF, Vignale G, Das MP (eds) Electronic density functional theory: recent progress and new directions. Plenum, New York
11. Cai W, Piner RD, Stadermann FJ, Park S, Shaibat MA, Ishii Y, Yang D, Velamakanni A, An SJ, Stoller M, An J, Chen D, Ruoff RS (2008) Synthesis and Solid-State NMR Structural Characterization of 13 C-Labeled Graphite Oxide. Science 321(5897):1815–1817. doi:10.1126/science.1162369

12. Cárdenas-Jirón GI, Berríos C (2008) Theoretical evidence of the Ni (III) participation in the chlorophenol oxidation on tetrasulphonated nickel phthalocyanine. Int J Quantum Chem 108 (13):2586–2594. doi:10.1002/qua.21732
13. Cárdenas-Jirón GI, Caro CA, Venegas-Yazigi D, Zagal JH (2002) Theoretical study of the interaction energy profile of cobalt phthalocyanine and 2-mercaptoethanol. Effect of the graphite on the global reactivity. J Mol Struct 580 (1–3):193–200. doi:http://dx.doi.org/10.1016/S0166-1280(01)00613-3
14. Cárdenas-Jirón GI, Gonzalez C, Benavides J (2012) Nitric Oxide Oxidation Mediated by Substituted Nickel Phthalocyanines: A Theoretical Viewpoint. J Phys Chem C 116 (32):16979–16984. doi:10.1021/jp3025232
15. Cárdenas-Jirón GI, Paredes-García V, Venegas-Yazigi D, Zagal JH, Páez M, Costamagna J (2006) Theoretical Modeling of the Oxidation of Hydrazine by Iron(II) Phthalocyanine in the Gas Phase. Influence of the Metal Character. J Phys Chem A 110 (42):11870–11875. doi:10.1021/jp060647r
16. Carlsson JM, Scheffler M (2006) Structural, electronic, and chemical properties of nanoporous carbon. Phys Rev Lett 96(4):046806
17. Chunder A, Pal T, Khondaker SI, Zhai L (2010) Reduced graphene oxide/copper phthalocyanine composite and its optoelectrical properties. J Phys Chem C 114(35):15129–15135. doi:10.1021/jp104587n
18. Compton OC, Dikin DA, Putz KW, Brinson LC, Nguyen ST (2010) Electrically conductive "Alkylated" graphene paper via chemical reduction of amine-functionalized graphene oxide paper. Adv Mater 22(8):892–896. doi:10.1002/adma.200902069
19. Cortés-Arriagada D, Cárdenas-Jirón GI (2011) A through-space charge transfer mechanism for explaining the oxidation of 2-chlorophenol on a tetrasulphonated nickel (III) phthalocyanine. Comput Theor Chem 963 (1):161–167. doi:http://dx.doi.org/10.1016/j.comptc.2010.10.015
20. Cortez L, Berríos C, Yáñez M, Cárdenas-Jirón GI (2009) Theoretical study of the binding nature of glassy carbon with nickel(II) phthalocyanine complexes. Chem Phys 365(3):164–169. doi:10.1016/j.chemphys.2009.10.016
21. Cote LJ, Kim F, Huang J (2008) Langmuir–Blodgett assembly of graphite oxide single layers. J Am Chem Soc 131(3):1043–1049. doi:10.1021/ja806262m
22. Cristancho D, Seminario JM (2010) Polypeptides in alpha-helix conformation perform as diodes. J Chem Phys 132(6). 065102. doi:10.1063/1.3310387
23. Derosa PA, Seminario JM (2001) Electron transport through single molecules: scattering treatment using density functional and green function theories. J Phys Chem B 105 (2):471–481
24. Derosa PA, Guda S, Seminario JM (2003) A programmable molecular diode driven by charge-induced conformational changes. J Am Chem Soc 125(47):14240–14241. doi:10.1021/ja035071n
25. Dikin DA, Stankovich S, Zimney EJ, Piner RD, Dommett GHB, Evmenenko G, Nguyen ST, Ruoff RS (2007) Preparation and characterization of graphene oxide-based paper. Nature 448:457–460
26. Dovesi R, Saunders VR, Roetti R, Orlando R, Zicovich-Wilson CM, Pascale F, Civalleri B, Doll K, Harrison NM, D'Arco P, Llunell M (2006) CRYSTAL06 User's Manual. University of Torino, Torino
27. El-Hendawy MM, El-Nahas AM, Awad MK (2011) The effect of constitutional and conformational isomerization on the electrical properties of diblock molecular diode. Org Electron 12(6):1080–1092. doi:http://dx.doi.org/10.1016/j.orgel.2011.03.022
28. Frisch MJ, Trucks GW, Schlegel HB, Scuseria GE, Robb MA, Cheeseman JR, Montgomery JA, Vreven JT, Kudin KN, Burant JC, Millam JM, Iyengar SS, Tomasi J, Barone V, Mennucci B, Cossi M, Scalmani G, Rega N, Petersson GA, Nakatsuji H, Hada M, Ehara M, Toyota K, Fukuda R, Hasegawa J, Ishida M, Nakajima T, Honda Y, Kitao O, Nakai H, Klene M, Li X, Knox JE, Hratchian HP, Cross JB, Bakken V, Adamo C, Jaramillo J, Gomperts R, Stratmann RE, Yazyev O, Austin AJ, Cammi R, Pomelli C, Ochterski JW, Ayala PY, Morokuma K, Voth GA, Salvador P, Dannenberg JJ, Zakrzewski VG, Dapprich S, Daniels AD, Strain MC, Farkas

O, Malick DK, Rabuck AD, Raghavachari K, Foresman JB, Ortiz JV, Cui Q, Baboul AG, Clifford S, Cioslowski J, Stefanov BB, Liu G, Liashenko A, Piskorz P, Komaromi I, Martin RL, Fox DJ, Keith T, Al-Laham MA, Peng CY, Nanayakkara A, Challacombe M, Gill PMW, Johnson B, Chen W, Wong MW, Gonzalez C, Pople JA (2007) Gaussian 03, Revision E.01

29. Frisch MJ, Trucks GW, Schlegel HB, Scuseria GE, Robb MA, Cheeseman JR, Scalmani G, Barone V, Mennucci B, Petersson GA, Nakatsuji H, Caricato M, Li X, Hratchian HP, Izmaylov AF, Bloino J, Zheng G, Sonnenberg JL, Hada M, Ehara M, Toyota K, Fukuda R, Hasegawa J, Ishida M, Nakajima T, Honda Y, Kitao O, Nakai H, Vreven T, Montgomery JA, Peralta JE, Ogliaro F, Bearpark M, Heyd JJ, Brothers E, Kudin KN, Staroverov VN, Kobayashi R, Normand J, Raghavachari K, Rendell A, Burant JC, Iyengar SS, Tomasi J, Cossi M, Rega N, Millam NJ, Klene M, Knox JE, Cross JB, Bakken V, Adamo C, Jaramillo J, Gomperts R, Stratmann RE, Yazyev O, Austin AJ, Cammi R, Pomelli C, Ochterski JW, Martin RL, Morokuma K, Zakrzewski VG, Voth GA, Salvador P, Dannenberg JJ, Dapprich S, Daniels AD, Farkas Ö, Foresman JB, Ortiz JV, Cioslowski J, Fox DJ (2009) Gaussian 09, Revision A.02
30. Ganji MD, Nourozi F (2008) Density functional non-equilibrium Green's function (DFT-NEGF) study of the smallest nano-molecular switch. Phys E Low-Dimensional Sys Nanostruct 40(7):2606–2613. doi:http://dx.doi.org/10.1016/j.physe.2007.09.123
31. Ghaderi N, Peressi M (2010) First-Principle Study of Hydroxyl Functional Groups on Pristine, Defected Graphene, and Graphene Epoxide. J Phys Chem C 114 (49):21625–21630. doi:10.1021/jp108688m
32. Hay PJ, Wadt WR (1985) Ab initio effective core potentials for molecular calculations—potentials for K to Au including the outermost core orbitals. J Chem Phys 82:299–310
33. Hay PJ, Wadt WR (1985) Ab initio effective core potentials for molecular calculations—potentials for the transition-metal atoms Sc to Hg. J Chem Phys 82:270–283
34. Hehre WJ, Ditchfield R, Pople JA (1972) Self-consistent molecular orbital methods. XII. Further extensions of Gaussian-type basis sets for use in molecular orbital studies of organic molecules. J Chem Phys 56(5):2257–2261
35. Hu Y, Shen J, Li N, Shi M, Ma H, Yan B, Wang W, Huang W, Ye M (2010) Amino-functionalization of graphene sheets and the fabrication of their nanocomposites. Polym Composite 31(12):1987–1994. doi:10.1002/pc.20984
36. Huang K-J, Niu D-J, Sun J-Y, Han C-H, Wu Z-W, Li Y-L, Xiong X-Q (2011) Novel electrochemical sensor based on functionalized graphene for simultaneous determination of adenine and guanine in DNA. Colloid Surf, B 82(2):543–549. doi:10.1016/j.colsurfb.2010.10.014
37. Jauregui LA, Salazar-Salinas K, Seminario JM (2009) Transverse electronic transport in double-stranded DNA nucleotides. J Phys Chem B 113(18):6230–6239
38. Kamat PV (2011) Graphene-based nanoassemblies for energy conversion. J Phys Chem Lett 2(3):242–251. doi:10.1021/jz101639v
39. Kang J, Bang J, Ryu B, Chang KJ (2008) Effect of atomic-scale defects on the low-energy electronic structure of graphene: perturbation theory and local-density-functional calculations. Phys Rev B 77(11):115453
40. Kang Y-J, Kim Y-H, Chang KJ (2009) Electrical transport properties of nanoscale devices based on carbon nanotubes. Curr Appl Phys 9(1 Suppl):S7–S11. doi:http://dx.doi.org/10.1016/j.cap.2008.08.028
41. Kondo H, Kino H, Nara J, Ohno T (2008) Transport properties of iron–porphyrin molecule sandwiched between Au surfaces. Appl Surface Sci 254(23):7985–7988. doi:http://dx.doi.org/10.1016/j.apsusc.2008.04.077
42. Lee C, Yang W, Parr RG (1988) Development of the Colle–Salvetti correlation-energy formula into a functional of the electron density. Phys Rev B 37(2):785–789
43. Lerf A, He H, Forster M, Klinowski J (1998) Structure of graphite oxide revisited†. J Phys Chem B 102(23):4477–4482. doi:10.1021/jp9731821
44. Li Y, Zhou Z, Golberg D, Bando Y, Schleyer PvR, Chen Z (2008) Stone–Wales defects in single-walled boron nitride nanotubes: formation energies, electronic structures, and reactivity. J Phys Chem C 112(5):1365–1370. doi:10.1021/jp077115a

45. Ma J, Alf A, Michaelides A, Wang E (2009) Stone–Wales defects in graphene and other planar sp^2 -bonded materials. Phys Rev B 80(3):033407
46. Ma KL, Yan XH, Xiao Y, Chen YP (2010) Electronic transport properties of metallic graphene nanoribbons with two vacancies. Solid State Commun 150(29–30):1308–1312. doi:10.1016/j.ssc.2010.05.011
47. Mao J, Zhang H, Jiang Y, Pan Y, Gao M, Xiao W, Gao HJ (2009) Tunability of supramolecular kagome lattices of magnetic phthalocyanines using graphene-based MoireÌ patterns as templates. J Am Chem Soc 131(40):14136–14137. doi:10.1021/ja904907z
48. Meyer JC, Geim AK, Katsnelson MI, Novoselov KS, Booth TJ, Roth S (2007) The structure of suspended graphene sheets. Nature 446(7131):60–63. doi:http://www.nature.com/nature/journal/v446/n7131/suppinfo/nature05545_S1.html
49. Miehlich B, Savin A, Stoll H, Preuss H (1989) Results obtained with the correlation-energy density functionals of Becke and Lee, Yang and Parr. Chem Phys Lett 157:200–206
50. Novoselov KS, Geim AK, Morozov SV, Jiang D, Zhang Y, Dubonos SV, Grigorieva IV, Firsov AA (2004) Electric field effect in atomically thin carbon films. Science 306:666–669
51. Novoselov KS, Geim AK, Morozov SV, Jiang D, Katsnelson MI, Grigorieva IV, Dubonos SV, Firsov AA (2005) Two-dimensional gas of massless Dirac fermions in graphene. Nature 438:197–200
52. Padilha JE, Amorim RG, Rocha AR, da Silva AJR, Fazzio A (2011) Energetics and stability of vacancies in carbon nanotubes. Solid State Commun 151(6):482–486. doi:10.1016/j.ssc.2010.12.031
53. Pandey D, Reifenberger R, Piner R (2008) Scanning probe microscopy study of exfoliated oxidized graphene sheets. Surface Sci 602(9):1607–1613. doi:10.1016/j.susc.2008.02.025
54. Paredes-García V, Cárdenas-Jirón GI, Venegas-Yazigi D, Zagal JH, Páez M, Costamagna J (2005) Through-Space and Through-Bond Mixed Charge Transfer Mechanisms on the Hydrazine Oxidation by Cobalt(II) Phthalocyanine in the Gas Phase. J Phys Chem A 109 (6):1196–1204. doi:10.1021/jp045223g
55. Park JS, Cho SM, Kim W-J, Park J, Yoo PJ (2011) Fabrication of graphene thin films based on layer-by-layer self-assembly of functionalized graphene nanosheets. ACS Appl Mater Interface 3(2):360–368. doi:10.1021/am100977p
56. Perdew JP (1991) Unified theory of exchange and correlation beyond the local density approximation. In: Ziesche P, Eschrig H (eds) Electronic structure of solids. Akademie Verlag, Berlin, pp 11–20
57. Perdew JP, Chevary JA, Vosko SH, Jackson KA, Pederson MR, Singh DJ, Fiolhais C (1992) Atoms, molecules, solids, and surfaces: applications of the generalized gradient approximation for exchange and correlation. Phys Rev B 46(11):6671–6687
58. Perdew JP, Chevary JA, Vosko SH, Jackson KA, Pederson MR, Singh DJ, Fiolhais C (1993) Atoms, molecules, solids, and surfaces—applications of the generalized gradient approximation for exchange and correlation (vol 46, p 6671, 1992). Phys Rev B 48(7):4978–4978
59. Perdew JP, Burke K, Wang Y (1996) Generalized gradient approximation for the exchange-correlation hole of a many-electron system. Phys Rev B 54(23):16533–16539
60. Petersson GA, Al-Laham MA (1991) A complete basis set model chemistry. II. Open-shell systems and the total energies of the first-row atoms. J Chem Phys 94(9):6081–6090
61. Petersson GA, Bennett A, Tensfeldt TG, Al-Laham MA, Shirley WA, Mantzaris J (1988) A complete basis set model chemistry. I. The total energies of closed-shell atoms and hydrides of the first-row elements. J Chem Phys 89(4):2193–2218
62. Popov VN, Henrard L, Lambin P (2009) Resonant Raman spectra of graphene with point defects. Carbon 47(10):2448–2455. doi:http://dx.doi.org/10.1016/j.carbon.2009.04.043
63. Rangel NL, Seminario JM (2010) Single molecule detection using graphene electrodes. J Phys B: At Mol Opt Phys 43(11):115101
64. Rangel NL, Seminario JM (2010) Vibronics and plasmonics based graphene sensors. J Chem Phys 132(12):125102–125104. doi:10.1063/1.3364863
65. Roetti C (1996) The CRYSTAL code. In: Pisani C (ed) Quantum-mechanical ab-initio calculation of the properties of crystalline materials, vol 67. Springer-Verlag, Berlin, pp 125–137

66. Salazar-Salinas K, Jauregui LA, Kubli-Garfias C, Seminario JM (2009) Molecular biosensor based on a coordinated iron complex. J Chem Phys 130:105101–105101-105109
67. Schedin F, Geim AK, Morozov SV, Hill EW, Blake P, Katsnelson MI, Novoselov KS (2007) Detection of individual gas molecules adsorbed on graphene. Nat Mater 6(9):652–655. doi:http://www.nature.com/nmat/journal/v6/n9/suppinfo/nmat1967_S1.html
68. Schniepp HC, Li J-L, McAllister MJ, Sai H, Herrera-Alonso M, Adamson DH, Prud'homme RK, Car R, Saville DA, Aksay IA (2006) Functionalized single graphene sheets derived from splitting graphite oxide. J Phys Chem B 110(17):8535–8539. doi:10.1021/jp060936f
69. Seminario JM, Sanders FC (1990) Application of Z-dependent perturbation theory to autoionizing states of heliumlike atoms: Feshbach projection method. Phys Rev A 42(5):2562–2572
70. Seminario JM, Tour JM (1997) Systematic study of the lowest energy states of Aun (n = 1–4) using DFT. Int J Quantum Chem 65(5):749–758. doi:10.1002/(sici)1097-461×(1997)65:5<749::aid-qua41>3.0.co;2-t
71. Seminario JM, Yan L (2005) Ab initio analysis of electron currents in thioalkanes. Int J Quantum Chem 102:711–723
72. Seminario JM, Zacarías AG, Castro M (1997) Systematic study of the lowest energy states of Pd, Pd2, and Pd3. Int J Quantum Chem 61(3):515–523. doi:10.1002/(sici)1097-461×(1997)61:3<515::aid-qua19>3.0.co;2-7
73. Seminario JM, Cordova LE, Derosa PA (2003) An ab initio approach to the calculation of current-voltage characteristics of programmable molecular devices. Proc IEEE 91(11):1958–1975
74. Seminario JM, De La Cruz C, Derosa PA, Yan L (2004) Nanometer-size conducting and insulating molecular devices. J Phys Chem B 108(46):17879–17885. doi:10.1021/jp046554w
75. Seminario JM, Derosa PA, Cordova LE, Bozard BH (2004) A molecular device operating at terahertz frequencies: theoretical simulations. IEEE Trans Nanotechnol 3(1):215–218. doi:10.1109/tnano.2004.824012
76. Seminario JM, Araujo RA, Yan L (2004) Negative differential resistance in metallic and semiconducting clusters. J Phys Chem B 108(22):6915–6918. doi:10.1021/jp0377811
77. Seminario JM, Yan L, Ma Y (2005) Scenarios for Molecular-Level Signal Processing. Proc IEEE 93(10):1753–1764. doi:10.1109/jproc.2005.853541
78. Seminario JM, Agapito LA, Yan L, Balbuena PB (2005) Density functional theory study of adsorption of OOH on Pt-based bimetallic clusters alloyed with Cr, Co, and Ni. Chem Phys Lett 410(4–6):275–281. doi:http://dx.doi.org/10.1016/j.cplett.2005.05.077
79. Soldano C, Mahmood A, Dujardin E (2010) Production, properties and potential of graphene. Carbon 48(8):2127–2150. doi:10.1016/j.carbon.2010.01.058
80. Sotelo JC, Seminario JM (2007) Biatomic substrates for bulk-molecule interfaces: The PtCo-oxygen interface. J Chem Phys 127(24):244706 (244713 pp)
81. Sotelo JC, Yan L, Wang M, Seminario JM (2007) Field induced conformational changes in bimetallic oligoaniline junctions. Phys Rev A 75(2):022511
82. Staroverov VN, Scuseria GE, Tao J, Perdew JP (2003) Comparative assessment of a new nonempirical density functional: Molecules and hydrogen-bonded complexes. J Chem Phys 119 (23):12129–12137
83. Staykov A, Tsuji Y, Yoshizawa K (2011) Conductance through Short DNA Molecules. J Phys Chem C 115(8):3481–3490. doi:10.1021/jp110803a
84. Stone AJ, Wales DJ (1986) Theoretical studies of icosahedral C60 and some related species. Chem Phys Lett 128(5–6):501–503. doi:10.1016/0009-2614(86)80661-3
85. Subrahmanyam KS, Vivekchand SRC, Govindaraj A, Rao CNR (2008) A study of graphenes prepared by different methods: characterization, properties and solubilization. J Mater Chem 18(13):1517–1523
86. Tsukamoto T, Ishikawa Y, Sengoku Y, Kurita N (2009) A combined DFT/Green's function study on electrical conductivity through DNA duplex between Au electrodes. Chem Phys Lett 474(4–6):362–365. doi:http://dx.doi.org/10.1016/j.cplett.2009.04.071

87. Wadt WR, Hay PJ (1985) Ab initio effective core potentials for molecular calculations—potentials for main group elements Na to Bi. J Chem Phys 82:284–298
88. Wei D, Liu Y, Wang Y, Zhang H, Huang L, Yu G (2009) Synthesis of N-Doped Graphene by chemical vapor deposition and its electrical properties. Nano Lett 9(5):1752–1758. doi:10.1021/nl803279t
89. Xu Y, Liu Z, Zhang X, Wang Y, Tian J, Huang Y, Ma Y, Zhang X, Chen Y (2009) A Graphene hybrid material covalently functionalized with porphyrin: synthesis and optical limiting property. Adv Mater 21(12):1275–1279. doi:10.1002/adma.200801617
90. Yang H, Shan C, Li F, Han D, Zhang Q, Niu L (2009) Covalent functionalization of polydisperse chemically-converted graphene sheets with amine-terminated ionic liquid. Chem Commun (26):3880–3882
91. Yanov I, Kholod Y, Leszczynski J, Palacios JJ (2007) Electron transport properties of the porphyrin molecule located between gold electrodes. Chem Phys Lett 445(4–6):238–242. doi:http://dx.doi.org/10.1016/j.cplett.2007.07.084
92. Zhao Y, Truhlar DG (2007) Density Functionals for Noncovalent Interaction Energies of Biological Importance. J Chem Theory Comput 3:289–300
93. Zhu J, Li Y, Chen Y, Wang J, Zhang B, Zhang J, Blau WJ (2011) Graphene oxide covalently functionalized with zinc phthalocyanine for broadband optical limiting. Carbon 49(6):1900–1905. doi:10.1016/j.carbon.2011.01.014

Chapter 8
Computational Nanochemistry Report of the Molecular Structure, Properties and Chemical Reactivity of Pheophorbide A

Daniel Glossman-Mitnik

Abstract The M06 family of density functionals has been assessed for the calculation of the molecular structure and properties of the Pheophorbide A molecule. Besides the determination of the molecular structures, the UV–Vis spectra has been computed using TD-DFT in the presence of a solvent and the results compared con the experimental data available. The chemical reactivity descriptors have been calculated through Conceptual DFT. The active sites for nucleophilic and electrophilic attacks have been chosen by relating them to the Fukui function indices. A comparison between the descriptors calculated through vertical energy values and those arising from the Koopmans' theorem approximation have been performed in order to check for the validity of the last procedure.

8.1 Introduction

Photodynamic therapy (PDT) combines the topical or systemic administration of a photosensitizer with the selective illumination of the target lesion with visible light, which results in localized oxidative photodamage and subsequent cell death [1]. The basic principle is the combination of a photosensitizing drug capable of absorbing within the body's therapeutic window, a light source (e.g. laser) of appropriate wavelength and molecular oxygen. PDT is becoming a potential alternative to the antimicrobial agent in the inactivation of many microbial infections. For these reasons, in the last decades the interest in proposing new photosensitizers for PDT is rapidly growing and different generations of new synthesized molecules have been proposed [2].

D. Glossman-Mitnik (✉)
Departamento de Simulación Computacional y Modelado Molecular, Laboratorio Virtual NANOCOSMOS, Centro de Investigación en Materiales Avanzados—CIMAV, Miguel de Cervantes 120—Complejo Industrial Chihuahua, 31109 Chihuahua, Mexico
e-mail: daniel.glossman@cimav.edu.mx

J. M. Seminario (ed.), *Design and Applications of Nanomaterials for Sensors,*
Challenges and Advances in Computational Chemistry and Physics 16,
DOI 10.1007/978-94-017-8848-9_8, © Springer Science+Business Media Dordrecht 2014

Pheophorbide A (C35H36N4O5: mol. wt. 592.68; IUPAC Name (3 S, 4 S)-9-Ethenyl-14-ethyl -21-(methoxycarbonyl)-4,8,13,18-tetramethyl-20-oxo-3-phorbine propanoic acid) is the product of the Pheophorbide A breakdown. It is widely used as a photosensitizer, specially for nanodevices related to photodynamic therapy. Thus, the aim of this work is to do a comparative study of the performance of the M06 family of density functionals for the description of the molecular structure, infrared (IR) and absorption (UV–Vis) spectra and chemical reactivity of Pheophorbide A.

The knowledge of the reactivity on a molecule is an essential concept; it is of a crucial interest because it allows to understand interactions that are operating during a reaction mechanism. In particular electrostatic interactions have been successfully explained by the use of the molecular electrostatic potential [3, 4].

On the other hand, there is no a unique tool to quantify and rationalize covalent interactions, however since 2005 a descriptor of local reactivity whose name is simply dual descriptor [5, 6], has allowed to rationalize reaction mechanisms in terms of overlapping nucleophilic regions with electrophilic regions in order to get a maximum stabilization thus leading to final products or intermediates; all those favorable nucleophilic–electrophilic interactions have been explained as a manifestation of the Principle of Maximum Hardness [7] in addition, chemical reactions have been understood in terms of the The Hard and Soft Acids and Bases Principle [8–11], principle that has been used even with the aim of replacing the use of the Molecular Orbital Theory to understand the whole Chemistry [12]. In fact the present work is a good chance to test the capability of the most recent reactivity descriptors coming from the Conceptual DFT [13–16], therefore the framework of this conceptual theory will be presented in the next section.

8.2 Theory and Computational Details

At a local level, electronic density is the first local reactivity descriptor to be used when electrostatic interactions are predominant between molecules; within the framework of Conceptual DFT it is defined as follows:

$$\rho(\mathbf{r}) = \left[\frac{\delta E}{\delta v(\mathbf{r})}\right]_N \tag{8.1}$$

But when chemical reactions are governed by interactions mainly of covalent nature, in such a case a second order LRD called Fukui function [15] is used instead of electronic density. Fukui function is defined in terms of the derivative of $\rho(\mathbf{r})$ with respect to N; through a Maxwell relation, the same descriptor is interpreted as the variation of μ with respect to $v(\mathbf{r})$ [15]:

$$f(\mathbf{r}) = \left(\frac{\partial \rho(\mathbf{r})}{\partial N}\right)_{v(\mathbf{r})} = \left[\frac{\delta \mu}{\delta v(\mathbf{r})}\right]_N \tag{8.2}$$

The function $f(\mathbf{r})$ reflects the ability of a molecular site to accept or donate electrons. High values of $f(\mathbf{r})$ are related to a high reactivity at point $\mathbf{r}$ [15].

Since the number of electrons N is a discrete variable [17], right and left derivatives of $\rho(\mathbf{r})$ with respect to N have emerged. By applying a finite difference approximation to Eq. (8.2), two definitions of Fukui functions depending on total electronic densities are obtained:

$$f^{+}(\mathbf{r}) = \left(\frac{\partial \rho(\mathbf{r})}{\partial N}\right)^{+}_{\upsilon(\mathbf{r})} = \rho_{N+1}(\mathbf{r}) - \rho_{N}(\mathbf{r}) \tag{8.3}$$

$$f^{-}(\mathbf{r}) = \left(\frac{\partial \rho(\mathbf{r})}{\partial N}\right)^{-}_{\upsilon(\mathbf{r})} = \rho_{N}(\mathbf{r}) - \rho_{N-1}(\mathbf{r}) \tag{8.4}$$

where $\rho_{N+1}(\mathbf{r})$, $\rho_{N}(\mathbf{r})$ and $\rho_{N-1}(\mathbf{r})$ are the electronic densities at point $\mathbf{r}$ for the system with $N+1$, N and $N-1$ electrons, respectively. The first one, $f^{+}(\mathbf{r})$, has been associated to reactivity for a nucleophilic attack so that it measures the intramolecular reactivity at the site $\mathbf{r}$ toward a nucleophilic reagent. The second one, $f^{-}(\mathbf{r})$, has been associated to reactivity for an electrophilic attack so that this function measures the intramolecular reactivity at the site $\mathbf{r}$ toward an electrophilic reagent [18].

The densities of frontier molecular orbitals (FMOs), $\rho_{\mathrm{L}}(\mathbf{r})$ (LUMO density) and $\rho_{\mathrm{H}}(\mathbf{r})$ (HOMO density), come to the picture since it has been shown [18, 19] that when the frozen orbital approximation (FOA) is used there is a direct relation between $f^{+/-}(\mathbf{r})$ and the density of the appropriate FMO thus avoiding calculations of the system with $N+1$ and $N-1$ electrons:

$$f^{+}(\mathbf{r}) \simeq \rho_{\mathrm{L}}(\mathbf{r}), \tag{8.5}$$

$$f^{-}(\mathbf{r}) \simeq \rho_{\mathrm{H}}(\mathbf{r}). \tag{8.6}$$

On the other hand, the use of Eqs. (8.5) and (8.6) instead of Eqs. (8.3) and (8.4) allows one to diminish the computational effort without loosing the qualitative picture of the local reactivity, but this approach should be always checked by comparison of these two couples of working equations because the first level of approximation based on total electronic densities will always be more accurate that the second level of approximation based on densities of FMOs.

Condensation to atoms is achieved through integration within the k^{th}–atomic domain Ω_k [20, 21]:

$$f_K^{+/-} = \int_{\Omega k} f^{+/-}(\mathbf{r}) d\mathbf{r}. \tag{8.7}$$

$f_K^{+/-}$ is now an atomic index that is used to characterize the electrophilic/nucleophilic power of atom *k*.

Even much better, Morell et al. [6, 10, 12, 22–25] have proposed a local reactivity descriptor (LRD) which is called the dual descriptor (DD) $f^{(2)}(\mathbf{r}) \equiv \Delta f(\mathbf{r})$. In spite of having been discovered several years ago, a solid physical interpretation was not provided in such a moment. [26]. They used the notation $\Delta f(\mathbf{r})$, but currently it has been replaced by the modern notation $f^{(2)}(\mathbf{r})$ in order to highlight that this is a Fukui function of second order. Its physical meaning is to reveal nucleophilic and electrophilic sites on a molecular system at the same time. Mathematically it is defined in terms of the derivative of the Fukui function, $f(\mathbf{r})$(15), with respect to the number of electrons, *N*. Through a Maxwell relation, this LRD may be interpreted as the variation of η (the molecular hardness which measures the resistance to charge transfer [27]) with respect to $\upsilon(\mathbf{r})$, the external potential. The definition of $f^{(2)}(\mathbf{r})$ is shown as indicated by Morell et al. [6, 10]:

$$f^{(2)}(\mathbf{r}) = \left(\frac{\partial f(\mathbf{r})}{\partial N}\right)_{\upsilon(\mathbf{r})} = \left[\frac{\delta\eta}{\delta\upsilon(r)}\right]_N . \tag{8.8}$$

As mentioned above, DD allows one to obtain simultaneously the preferably sites for nucleophilic attacks ($f^{(2)}(\mathbf{r}) > 0$) and the preferably sites for electrophilic attacks ($f^{(2)}(\mathbf{r}) < 0$) into the system at point **r**. DD has demonstrated to be a robust tool to predict specific sites of nucleophilic and electrophilic attacks in a much more efficient way than the Fukui function by itself because dual descriptor is able to distinguish those sites of true nucleophilic and electrophilic behavior, in consequence some works have been published with the aim of remarking the powerfulness of $f^{(2)}(\mathbf{r})$ and all those LRDs depending on DD [6, 10, 12, 22–25].

The general working equation to obtain DD is given by the difference between nucleophilic and electrophilic Fukui function [12]. A well-known first level of approximation implies the use of finite difference method where to the sum of electronic densities of the system with one more electron and one less electron is subtracted by the double of the total electronic density of the original system. Since this level of approximation implies a time-demanding computing, a second level of approximation has been used for some years where the densities of FMOs provide an easier-to-compute working equation:

$$f^{(2)}(\mathbf{r}) = f^{+}(\mathbf{r}) - f^{-}(\mathbf{r}) \simeq \rho_{\mathrm{L}}(\mathbf{r}) - \rho_{\mathrm{H}}(\mathbf{r}),$$

where densities of LUMO and HOMO are represented by $\rho_{\mathrm{L}}(\mathbf{r})$ and $\rho_{\mathrm{H}}(\mathbf{r})$, respectively.

Molecular symmetry can influence upon the local reactivity, and on the other hand has been demonstrated that the Fukui function must conserve the symmetry [28]. In addition, as the degeneration that may arise in frontier molecular orbitals is related with the molecular symmetry, within the framework of the second level

of approximation, this phenomenon has been taken into account thus providing a mathematical expression to be applied on closed-shell molecular systems [29].

Hence, when an interaction between two species is well described through the use of this LRD, it is said the reaction is controlled by frontier molecular orbitals (or frontier-controlled) under the assumption that remaining molecular orbitals do not participate during the reaction.

The dual descriptor can also be condensed through an appropriate integration within the k^{th}–atomic domain Ω_k:

$$\int_{\Omega k} f^{(2)}(\mathbf{r}) d\mathbf{r} = f_k^{(2)}. \tag{8.9}$$

When $f_k^{(2)} > 0$ the process is driven by a nucleophilic attack on atom k and then that atom acts an electrophilic species; conversely, when $f_k^{(2)} < 0$ the process is driven by an electrophilic attack over atom k and therefore atom k acts as a nucleophilic species.

8.3 Results and Discussion

All computational studies were performed with the Gaussian 09 [30] series of programs with density functional methods as implemented in the computational package. The equilibrium geometries of the molecules were determined by means of the gradient technique. The force constants and vibrational frequencies were determined by computing analytical frequencies on the stationary points obtained after the optimization to check if there were true minima. The basis set used in these work was MIDIY, which is the same basis set as MIDI! with a polarization function added to the hydrogen atoms. The MIDI! basis is a small double-zeta basis with polarization functions on N–F, Si–Cl, Br, and I [31–36].

8.3.1 Molecular Structures

For the calculation of the molecular structure and properties of the studied system, we have chosen the hybrid meta-GGA density functionals M06, M06L, M06-2X and M06HF [37], which consistently provide satisfactory results for several structural and thermodynamic properties. Solvation energies were computed by the Integral Equation Formalism–Polarizable Continuum Model (IEF-PCM) [38], including the UAKS model and ethanol as a solvent.

The molecular structure of pheophorbide a was pre-optimized by starting with the readily available PDB structure, and finding the most stable conformer by means of the Conformers module of Materials Studio through a random sampling

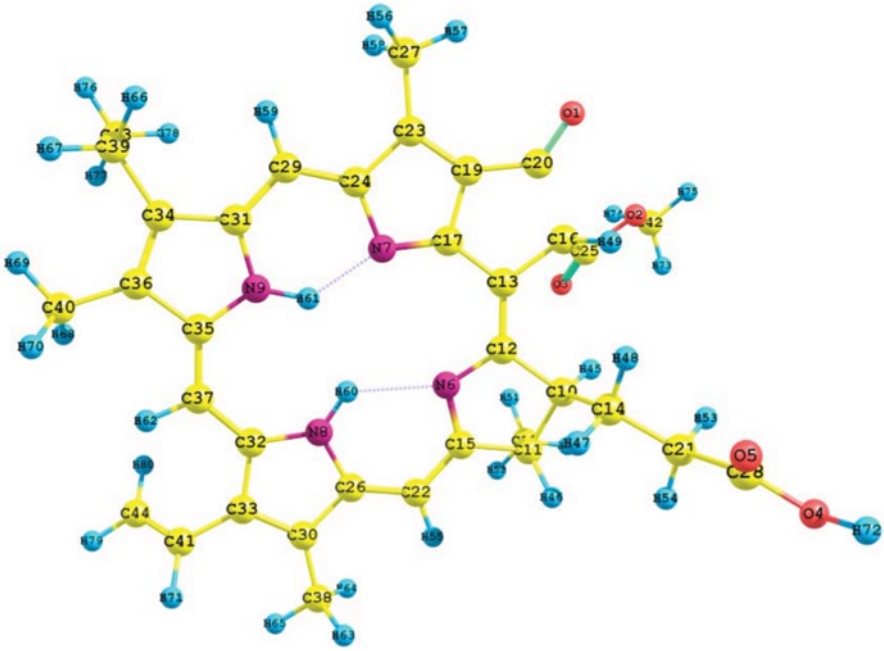


Fig. 8.1 Optimized molecular structure of the pheophorbide a molecule calculated with the M06 density functional and the MIDIY basis set

with molecular mechanics techniques and a consideration of all the torsional angles. The structure of the resulting conformer was then optimized with the M06, M06L, M06-2X and M06-HF density functionals in conjunction with the MIDIY basis set. The optimized molecular structure of the pheophorbide a molecule calculated with the four density functionals are shown in Figs. 8.1, 8.2, 8.3, and 8.4, while the bond distances (in Å) and the bond angles (in degrees) calculated with the M06, M06L, M06-2X and M06-HF functionals in conjunction with the MIDIY basis set are presented in Tables 8.1, 8.2, 8.3, 8.4, 8.5, 8.6, 8.7, and 8.8, respectively. It is not the objective of this study to analyze in detail the results predicted by the different functionals for the optimized structure of the Pheophorbide A molecule. However, a comparison of the results by superimposing structures reveals that there are not important differences between them. This not surprising because modern density functionals are able to predict molecular structures with a good degree of accuracy and using low-cost basis sets.

8.3.2 IR and UV–Vis Spectra

The calculation of the ultraviolet (UV–Vis) spectra of the studied system has been performed by solving the time-dependent DFT (TD-DFT) equations according to

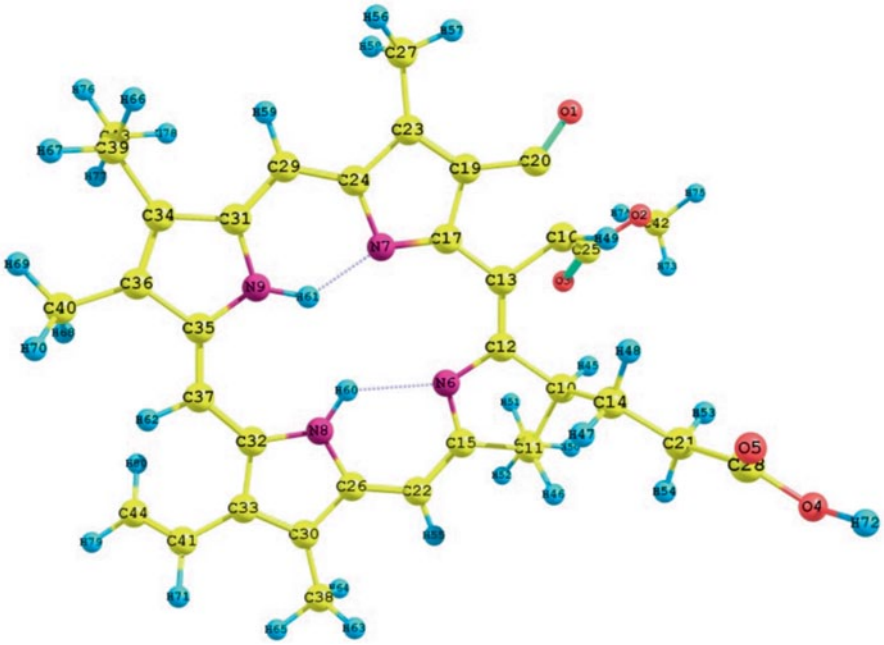


Fig. 8.2 Optimized molecular structure of the pheophorbide a molecule calculated with the M06L density functional and the MIDIY basis set

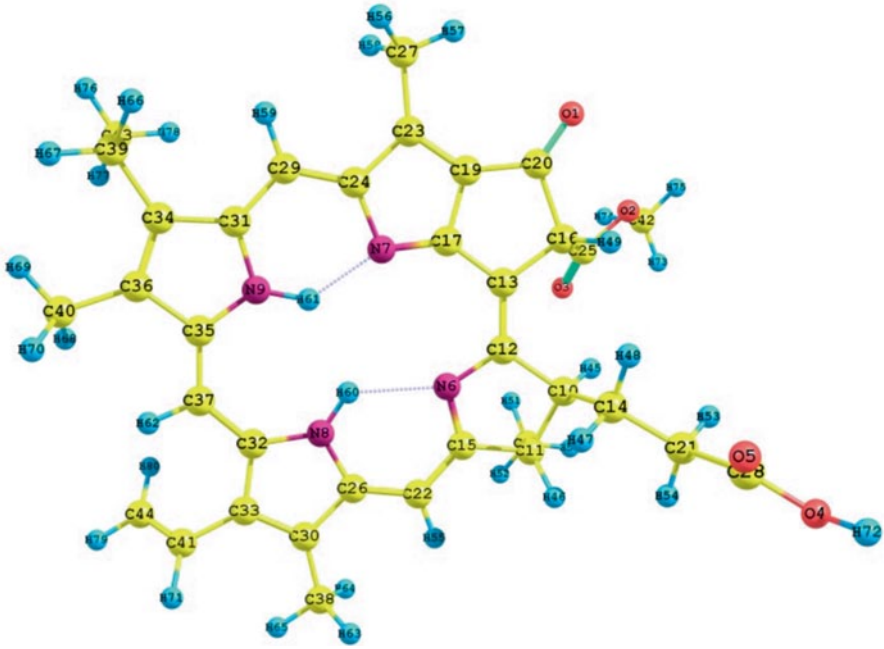


Fig. 8.3 Optimized molecular structure of the pheophorbide a molecule calculated with the M06-2X density functional and the MIDIY basis set

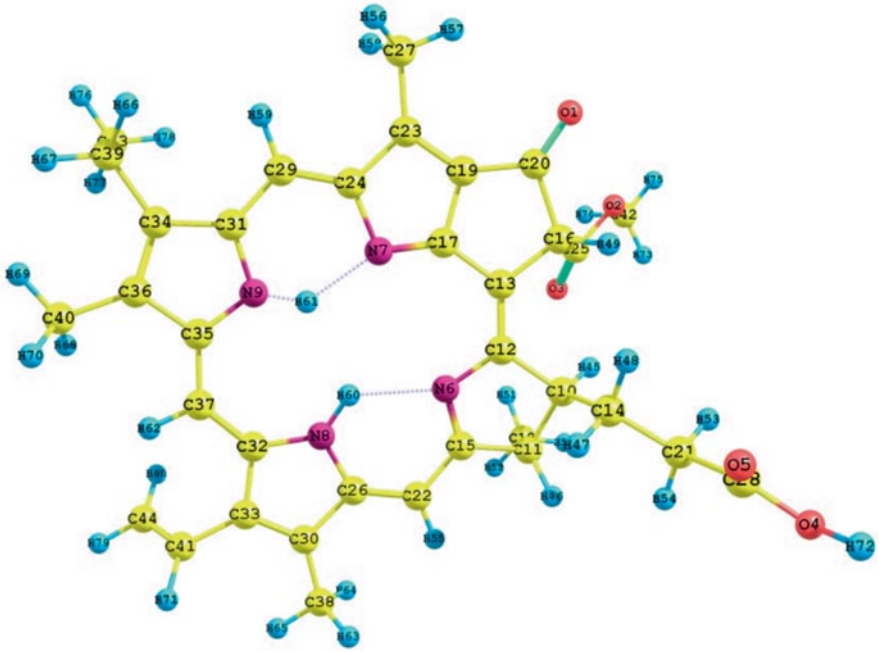


Fig. 8.4 Optimized molecular structure of the pheophorbide a molecule calculated with the M06-HF density functional and the MIDIY basis set

the method implemented in Gaussian 09 [33, 39–41]. The equations have been solved for 10 excited states.

The infrared (IR) and ultraviolet (UV–Vis) spectra were calculated using the Swizard program [42, 43] and visualized with Gabedit [44]. In all cases the displayed spectra show the calculated frequencies and absorption or emission wavelengths.

The situation is quite different for the prediction of the IR and UV–Vis spectra (in comparison with molecular structures) and this could be adscribed to the different functional form of the density functionals. The infrared spectra of the phephorbide a molecule calculated with the M06, M06L, M06-2X and M06-HF density functionals and the MIDIY basis sets are shown in Figs. 8.5, 8.6, 8.7, and 8.8. Indeed, we should note that none of the IR spectra display a frequency value below zero or imaginary, and this means that the structures predicted by all the functionals are a minimum on the potential energy surface. It is well known that calculated Hartree-Fock (HF) IR spectra must be scaled to account for the effects of anharmonicity and correlation. With modern density functionals that explicitly include correlation, this scaling factor is close to 1 and this can be an indication of the goodness of a given functional. For the results presented here, it is remarkable that the M06 and the local M06L predict so well the IR spectrum of pheophorbide a in comparison with experimental measures [45]. Notwithstanding, these results should be taken with care because the experimental spectrum has been taken from

Table 8.1 Optimized bond distances (in Å) of the pheophorbide a molecule calculated with the M06 density functional and the MIDIY basis set

Bond	Distance	Bond	Distance	Bond	Distance	Bond	Distance
R(1–20)	1.211	R(11–18)	1.539	R(23–24)	1.458	R(38–64)	1.102
R(2–25)	1.354	R(11–46)	1.100	R(23–27)	1.486	R(38–65)	1.098
R(2–42)	1.440	R(12–13)	1.371	R(24–29)	1.387	R(39–43)	1.542
R(3–25)	1.214	R(13–16)	1.515	R(26–30)	1.429	R(39–66)	1.101
R(4–28)	1.360	R(13–17)	1.410	R(27–56)	1.103	R(39–67)	1.101
R(4–72)	0.968	R(14–21)	1.526	R(27–57)	1.099	R(40–68)	1.103
R(5–28)	1.210	R(14–47)	1.102	R(27–58)	1.103	R(40–69)	1.099
R(6–12)	1.360	R(14–48)	1.101	R(29–31)	1.395	R(40–70)	1.102
R(6–15)	1.343	R(15–22)	1.388	R(29–59)	1.091	R(41–44)	1.336
R(7–17)	1.333	R(16–25)	1.516	R(30–33)	1.375	R(41–71)	1.095
R(7–24)	1.396	R(16–49)	1.101	R(30–38)	1.489	R(42–73)	1.099
R(8–26)	1.376	R(17–19)	1.438	R(31–34)	1.429	R(42–74)	1.099
R(8–32)	1.383	R(18–50)	1.101	R(32–33)	1.449	R(42–75)	1.095
R(8–60)	1.023	R(18–51)	1.102	R(32–37)	1.382	R(43–76)	1.100
R(9–31)	1.375	R(18–52)	1.101	R(33–41)	1.455	R(43–77)	1.101
R(9–35)	1.367	R(19–20)	1.448	R(34–36)	1.377	R(43–78)	1.101
R(9–61)	1.036	R(19–23)	1.362	R(34–39)	1.492	R(44–79)	1.091
R(10–11)	1.544	R(21–28)	1.512	R(35–36)	1.437	R(44–80)	1.092
R(10–12)	1.525	R(21–53)	1.103	R(35–37)	1.393	R(6–60)	2.044
R(10–14)	1.538	R(21–54)	1.102	R(36–40)	1.491	R(7–61)	1.777
R(10–45)	1.099	R(22–26)	1.389	R(37–62)	1.090		
R(11–15)	1.522	R(22–55)	1.091	R(38–63)	1.103		

the solid, while the present calculations have been done in the presence of ethanol simulated through a polarized continuum method. It should be noticed that a recent work on the estimation of scaling factors for a large number of density functionals have shown that functionals with low percentages of HF exchange tend to predict more accurate frequencies [46].

The visible part of the electronic absorption spectrum is one of the more fascinating features of chlorophyll and chlorophyll-derived molecules [47]. For this reason, there is a great interest in the study of photosynthetic materials for their application in organic solar cells and photodynamic therapy. First, we can refer to a theoretical study of the excited states of chlorophyll a and pheophytin a using a combination of density functional theory and the multireference configuration interaction method (DFT/MRCI) [48].

In a second place, there has been several interesting experimental and theoretical studies on photosynthetic materials: (i) chlorophyll a derivatives with various hydrocarbon ester groups for efficient dye-sensitized solar cells [49]; (ii) natural chlorophyll-related porphyrins and chlorins for dye-sensitized solar cells [50] and (iii) to a significant enhancement in the power-conversion efficiency of chlorophyll co-sensitized solar cells by mimicking the principles of natural photosynthetic light-harvesting complexes. Indeed, this is a very enlightment work but in this study we only want to compare our results with the available experimental data for the absorption spectrum of pheophorbide a in ethanol [45]. There is also a recent DFT

Table 8.2 Optimized bond angles (in degrees) of the pheophorbide a molecule calculated with the M06 density functional and the MIDIY basis set

Bond	Angle	Bond	Angle	Bond	Angle	Bond	Angle
A(1–20–19)	130.9	A(35–9–61)	133.7	A(25–16–49)	107.9	A(32–37–35)	131.2
A(25–2–42)	112.9	A(9–35–36)	106.9	A(17–19–20)	111.4	A(32–37–62)	114.0
A(2–25–3)	124.2	A(9–35–37)	127.3	A(17–19–23)	107.9	A(33–41–44)	126.4
A(2–25–16)	109.3	A(9–61–7)	134.9	A(50–18–51)	107.8	A(33–41–71)	115.5
A(2–42–73)	110.9	A(11–10–12)	100.9	A(50–18–52)	108.6	A(36–34–39)	127.9
A(2–42–74)	110.8	A(11–10–14)	112.3	A(51–18–52)	108.8	A(34–36–35)	108.0
A(2–42–75)	105.5	A(11–10–45)	111.4	A(20–19–23)	140.7	A(34–36–40)	127.7
A(3–25–16)	126.4	A(10–11–15)	101.1	A(19–23–24)	104.2	A(34–39–43)	111.4
A(28–4–72)	104.6	A(10–11–18)	110.3	A(19–23–27)	127.3	A(34–39–66)	110.0
A(4–28–5)	123.2	A(10–11–46)	113.1	A(28–21–53)	107.9	A(34–39–67)	110.2
A(4–28–21)	110.9	A(12–10–14)	109.8	A(28–21–54)	108.0	A(36–35–37)	125.8
A(5–28–21)	125.9	A(12–10–45)	111.2	A(53–21–54)	105.4	A(35–36–40)	124.3
A(12–6–15)	108.4	A(10–12–13)	125.3	A(26–22–55)	116.9	A(35–37–62)	114.8
A(6–12–10)	111.9	A(14–10–45)	110.8	A(22–26–30)	127.8	A(36–40–68)	111.8
A(6–12–13)	122.7	A(10–14–21)	112.3	A(24–23–27)	128.4	A(36–40–69)	111.4
A(12–6–60)	149.9	A(10–14–47)	109.5	A(23–24–29)	126.7	A(36–40–70)	111.9
A(6–15–11)	112.7	A(10–14–48)	110.4	A(23–27–56)	111.9	A(63–38–64)	106.9
A(6–15–22)	123.4	A(15–11–18)	109.7	A(23–27–57)	108.9	A(63–38–65)	107.8
A(15–6–60)	101.7	A(15–11–46)	111.6	A(23–27–58)	112.0	A(64–38–65)	107.2
A(17–7–24)	104.8	A(11–15–22)	123.8	A(24–29–31)	123.2	A(43–39–66)	109.6
A(7–17–13)	136.9	A(18–11–46)	110.6	A(24–29–59)	118.7	A(43–39–67)	109.6
A(7–17–19)	111.9	A(11–18–50)	110.6	A(26–30–33)	107.9	A(39–43–76)	111.4
A(17–7–61)	152.9	A(11–18–51)	109.5	A(26–30–38)	124.2	A(39–43–77)	110.5
A(7–24–23)	111.2	A(11–18–52)	111.6	A(56–27–57)	108.4	A(39–43–78)	110.4
A(7–24–29)	122.1	A(12–13–16)	125.2	A(56–27–58)	107.0	A(66–39–67)	105.8
A(24–7–61)	102.3	A(12–13–17)	126.3	A(57–27–58)	108.5	A(68–40–69)	107.1
A(26–8–32)	110.5	A(16–13–17)	108.5	A(31–29–59)	118.1	A(68–40–70)	106.9
A(26–8–60)	118.0	A(13–16–25)	113.3	A(29–31–34)	131.1	A(69–40–70)	107.4
A(8–26–22)	124.8	A(13–16–49)	115.1	A(33–30–38)	127.9	A(44–41–71)	118.2
A(8–26–30)	107.4	A(13–17–19)	111.1	A(30–33–32)	108.2	A(41–44–79)	121.0
A(32–8–60)	131.5	A(21–14–47)	110.2	A(30–33–41)	125.6	A(41–44–80)	122.2
A(8–32–33)	106.1	A(21–14–48)	108.6	A(30–38–63)	111.7	A(73–42–74)	108.4
A(8–32–37)	128.8	A(14–21–28)	111.7	A(30–38–64)	111.4	A(73–42–75)	110.7
A(8–60–6)	126.9	A(14–21–53)	111.0	A(30–38–65)	111.6	A(74–42–75)	110.6
A(31–9–35)	110.3	A(14–21–54)	112.5	A(31–34–36)	107.5	A(76–43–77)	108.3
A(31–9–61)	116.0	A(47–14–48)	105.5	A(31–34–39)	124.6	A(76–43–78)	108.5
A(9–31–29)	121.6	A(15–22–26)	125.1	A(33–32–37)	125.1	A(77–43–78)	107.6
A(9–31–34)	107.3	A(15–22–55)	118.0	A(32–33–41)	126.3	A(79–44–80)	116.7

benchmark calculation on the performance of density functional based methods in the description of some biological systems [51].

The absorption or UV–Vis spectra of the pheophorbide a molecule calculated with the M06, M06L, M06-2X and M06-HF density functionals and the MIDIY basis sets are presented in Figs. 8.9, 8.10, 8.11, and 8.12, respectively. The experimental absorption spectrum of pheophorbide a in ethanol has been reported [45] and displays the characteristics bands at 410 and 667 nm. All the calculated spectra have

Table 8.3 Optimized bond distances (in Å) of the pheophorbide a molecule calculated with the M06L density functional and the MIDIY basis set

Bond	Distance	Bond	Distance	Bond	Distance	Bond	Distance
R(1–20)	1.222	R(11–18)	1.546	R(23–24)	1.463	R(38–64)	1.102
R(2-25)	1.368	R(11-46)	1.099	R(23-27)	1.491	R(38-65)	1.097
R(2–42)	1.454	R(12–13)	1.382	R(24–29)	1.399	R(39–43)	1.550
R(3–25)	1.225	R(13–16)	1.520	R(26–30)	1.432	R(39–66)	1.100
R(4–28)	1.373	R(13–17)	1.414	R(27–56)	1.102	R(39–67)	1.100
R(4–72)	0.966	R(14–21)	1.532	R(27–57)	1.097	R(40–68)	1.102
R(5–28)	1.220	R(14–47)	1.100	R(27–58)	1.101	R(40–69)	1.098
R(6–12)	1.365	R(14–48)	1.099	R(29–31)	1.398	R(40–70)	1.101
R(6–15)	1.355	R(15–22)	1.393	R(29–59)	1.090	R(41–44)	1.346
R(7–17)	1.345	R(16–25)	1.516	R(30–33)	1.389	R(41–71)	1.094
R(7–24)	1.402	R(16–49)	1.099	R(30–38)	1.493	R(42–73)	1.098
R(8–26)	1.385	R(17–19)	1.444	R(31–34)	1.437	R(42–74)	1.097
R(8–32)	1.389	R(18–50)	1.099	R(32–33)	1.454	R(42–75)	1.094
R(8–60)	1.023	R(18–51)	1.100	R(32–37)	1.392	R(43–76)	1.099
R(9–31)	1.384	R(18–52)	1.099	R(33–41)	1.453	R(43–77)	1.099
R(9–35)	1.375	R(19–20)	1.450	R(34–36)	1.383	R(43–78)	1.099
R(9–61)	1.036	R(19–23)	1.374	R(34–39)	1.497	R(44–79)	1.089
R(10-11)	1.552	R(21-28)	1.517	R(35-36)	1.446	R(44-80)	1.090
R(10-12)	1.530	R(21-53)	1.101	R(35-37)	1.397	R(6-60)	2.058
R(10-14)	1.545	R(21-54)	1.101	R(36-40)	1.494	R(7-61)	1.778
R(10–45)	1.097	R(22–26)	1.399	R(37–62)	1.088		
R(11–15)	1.529	R(22–55)	1.090	R(38–63)	1.101		

the same shape and it is the same as for the experimental absorption spectrum. However, there is a shift in each one of the spectrum that can be related to the amount of HF exchange that it is included for every density functional considered in this study. The functional form of the M06, M06-2X and M06-HF functionals is the same, with the only difference given by the aforementioned amount of HF exchange. It is evident from the results in Figs. 8.9, 8.10, 8.11, and 8.12, that a larger amount of HF exchange included leads to larger shifts of the peaks when comparing with the experimental spectrum. Notwithstanding, only the M06L density functional results are able to reproduce the experimental spectrum although with a large shift for the band belonging to the maximum wavelength (587 nm). The results for the orbital transition assignments for each one of the calculations are given in Tables 8.9, 8.10, 8.11, and 8.12.

8.3.3 Dipole Moments and Polarizabilities

The molecular dipole moment is perhaps the simplest experimental measure of charge distribution in a molecule. The accuracy of the overall distribution of electrons in a molecule is hard to quantify, since it involves all the multipoles. The polarizability α contributes to the understanding of the response of the system when the external field is changed, while the number of electrons N is kept

Table 8.4 Optimized bond angles (in degrees) of the pheophorbide a molecule calculated with the M06L density functional and the MIDIY basis set

Bond	Angle	Bond	Angle	Bond	Angle	Bond	Angle
A(1–20–19)	131.5	A(35–9–61)	133.6	A(25–16–49)	108.2	A(32–37–35)	131.4
A(25–2–42)	112.1	A(9–35–36)	106.8	A(17–19–20)	111.6	A(32–37–62)	114.0
A(2–25–3)	124.1	A(9–35–37)	127.6	A(17–19–23)	107.7	A(33–41–44)	127.5
A(2–25–16)	109.1	A(9–61–7)	135.0	A(50–18–51)	107.9	A(33–41–71)	114.8
A(2–42–73)	110.5	A(11–10–12)	101.4	A(50–18–52)	108.5	A(36–34–39)	127.7
A(2–42–74)	110.5	A(11–10–14)	112.0	A(51–18–52)	108.5	A(34–36–35)	108.1
A(2–42–75)	105.1	A(11–10–45)	111.4	A(20–19–23)	140.7	A(34–36–40)	127.7
A(3–25–16)	126.8	A(10–11–15)	101.3	A(19–23–24)	104.2	A(34–39–43)	111.9
A(28–4–72)	104.5	A(10–11–18)	110.7	A(19–23–27)	127.8	A(34–39–66)	110.0
A(4–28–5)	123.2	A(10–11–46)	112.5	A(28–21–53)	108.2	A(34–39–67)	110.0
A(4–28–21)	110.8	A(12–10–14)	110.4	A(28–21–54)	108.2	A(36–35–37)	125.6
A(5–28–21)	125.9	A(12–10–45)	110.8	A(53–21–54)	105.1	A(35–36–40)	124.2
A(12–6–15)	108.3	A(10–12–13)	124.9	A(26–22–55)	116.5	A(35–37–62)	114.6
A(6–12–10)	112.4	A(14–10–45)	110.5	A(22–26–30)	128.0	A(36–40–68)	111.9
A(6–12–13)	122.8	A(10–14–21)	111.7	A(24–23–27)	128.0	A(36–40–69)	111.2
A(12–6–60)	149.7	A(10–14–47)	109.8	A(23–24–29)	126.8	A(36–40–70)	112.0
A(6–15–11)	112.8	A(10–14–48)	110.6	A(23–27–56)	111.9	A(63–38–64)	106.9
A(6–15–22)	123.0	A(15–11–18)	110.2	A(23–27–57)	109.5	A(63–38–65)	107.7
A(15–6–60)	101.9	A(15–11–46)	111.5	A(23–27–58)	111.9	A(64–38–65)	107.0
A(17–7–24)	104.5	A(11–15–22)	124.1	A(24–29–31)	123.1	A(43–39–66)	109.4
A(7–17–13)	136.5	A(18–11–46)	110.2	A(24–29–59)	118.8	A(43–39–67)	109.4
A(7–17–19)	112.1	A(11–18–50)	110.5	A(26–30–33)	107.9	A(39–43–76)	111.2
A(17–7–61)	152.9	A(11–18–51)	109.8	A(26–30–38)	124.3	A(39–43–77)	110.6
A(7–24–23)	111.5	A(11–18–52)	111.6	A(56–27–57)	108.3	A(39–43–78)	110.6
A(7–24–29)	121.7	A(12–13–16)	124.7	A(56–27–58)	106.7	A(66–39–67)	106.0
A(24–7–61)	102.6	A(12–13–17)	126.9	A(57–27–58)	108.3	A(68–40–69)	107.2
A(26–8–32)	110.5	A(16–13–17)	108.4	A(31–29–59)	118.1	A(68–40–70)	106.8
A(26–8–60)	118.2	A(13–16–25)	113.9	A(29–31–34)	131.1	A(69–40–70)	107.5
A(8–26–22)	124.6	A(13–16–49)	114.8	A(33–30–38)	127.8	A(44–41–71)	117.7
A(8–26–30)	107.4	A(13–17–19)	111.4	A(30–33–32)	108.0	A(41–44–79)	120.8
A(32–8–60)	131.2	A(21–14–47)	110.0	A(30–33–41)	125.1	A(41–44–80)	122.5
A(8–32–33)	106.2	A(21–14–48)	108.9	A(30–38–63)	111.6	A(73–42–74)	108.5
A(8–32–37)	128.6	A(14–21–28)	111.8	A(30–38–64)	111.8	A(73–42–75)	111.0
A(8–60–6)	126.8	A(14–21–53)	111.1	A(30–38–65)	111.5	A(74–42–75)	111.1
A(31–9–35)	110.3	(14–21–54)	112.1	A(31–34–36)	107.5	A(76–43–77)	108.3
A(31–9–61)	116.0	A(47–14–48)	105.7	A(31–34–39)	124.7	A(76–43–78)	108.4
A(9–31–29)	121.5	A(15–22–26)	125.4	A(33–32–37)	125.2	A(77–43–78)	107.6
A(9–31–34)	107.3	A(15–22–55)	118.0	A(32–33–41)	126.9	A(79–44–80)	116.6

fixed. The polarizability is calculated as the average of the polarizability tensor $<\alpha>=\frac{1}{3}(\alpha_{xx}+\alpha_{yy}+\alpha_{zz})$.

The molecular dipole moments μ (in Debye) and global polarizabilities α (in Bohr3) of the Pheophorbide A molecule calculated with the M06, M06L, M06-2X and M06-HF density functionals and the MIDIY basis set are shown in Table 8.13.

Table 8.5 Optimized bond distances (in Å) of the pheophorbide a molecule calculated with the M06-2X density functional and the MIDIY basis set

Bond	Distance	Bond	Distance	Bond	Distance	Bond	Distance
R(1–20)	1.215	R(11–18)	1.550	R(22–55)	1.088	R(38–63)	1.100
R(2–25)	1.355	R(11–46)	1.097	R(23–24)	1.468	R(38–64)	1.101
R(2–42)	1.450	R(12–13)	1.369	R(23–27)	1.499	R(38–65)	1.097
R(3–25)	1.218	R(13–16)	1.525	R(24–29)	1.386	R(39–43)	1.555
R(4–28)	1.364	R(13–17)	1.422	R(26–30)	1.445	R(39–66)	1.099
R(4–72)	0.973	R(14–21)	1.537	R(27–56)	1.101	R(39–67)	1.099
R(5–28)	1.213	R(14–47)	1.099	R(27–57)	1.097	R(40–68)	1.101
R(6–12)	1.372	R(14–48)	1.099	R(27–58)	1.100	R(40–69)	1.097
R(6–15)	1.340	R(15–22)	1.400	R(29–31)	1.404	R(40–70)	1.100
R(7–17)	1.331	R(16–20)	1.601	R(29–59)	1.089	R(41–44)	1.339
R(7–24)	1.406	R(16–25)	1.525	R(30–33)	1.371	R(41–71)	1.092
R(8–26)	1.380	R(16–49)	1.100	R(30–38)	1.501	R(42–73)	1.097
R(8–32)	1.391	R(17–19)	1.450	R(31–34)	1.432	R(42–74)	1.096
R(8–60)	1.027	R(18–50)	1.099	R(32–33)	1.462	R(42–75)	1.093
R(9–31)	1.380	R(18–51)	1.100	R(32–37)	1.381	R(43–76)	1.098
R(9–35)	1.369	R(18–52)	1.099	R(33–41)	1.469	R(43–77)	1.098
R(9–61)	1.043	R(19–20)	1.463	R(34–36)	1.384	R(43–78)	1.099
R(10–11)	1.552	R(19–23)	1.363	R(34–39)	1.503	R(44–79)	1.089
R(10–12)	1.533	R(21–28)	1.520	R(35–36)	1.440	R(44–80)	1.090
R(10–14)	1.548	R(21–53)	1.100	R(35–37)	1.405	R(6–60)	2.040
R(10–45)	1.096	R(21–54)	1.100	R(36–40)	1.504	R(7–61)	1.767
R(11–15)	1.532	R(22–26)	1.390	R(37–62)	1.088		

8.3.4 HOMO and LUMO Orbitals

The Highest-Occuppied Molecular Orbital (HOMO) and Lowest-Occuppied Molecular Orbital (LUMO) were extracted from the calculations and visualized using the Chemcraft Program—Revision 1.6 [52].

The HOMO and LUMO orbitals of the pheophorbide a molecule calculated with the M06, M06L, M06-2X and M06-HF density functionals and the MIDIY basis set are shown in Fig. 8.13.

8.3.5 Chemical Reactivity

Within the conceptual framework of DFT [15, 27], the chemical potential μ, which measures the escaping tendency of electron from equilibrium, is defined as:

$$\mu = \left(\frac{\partial E}{\partial N}\right)_{\upsilon(\vec{r})} = -\chi \tag{8.10}$$

Table 8.6 Optimized bond angles (in degrees) of the pheophorbide a molecule calculated with the M06-2X density functional and the MIDIY basis set

Bond	Angle	Bond	Angle	Bond	Angle	Bond	Angle
A(1–20–16)	124.8	A(9–35–36)	107.1	A(16–20–19)	104.5	A(32–37–62)	114.4
A(1–20–19)	130.7	A(9–35–37)	127.4	A(25–16–49)	107.5	A(33–41–44)	125.3
A(25–2–42)	112.5	A(9–61–7)	134.8	A(17–19–20)	111.0	A(33–41–71)	115.8
A(2–25–3)	123.8	A(11–10–12)	101.0	A(17–19–23)	107.9	A(36–34–39)	127.9
A(2–25–16)	110.1	A(11–10–14)	112.1	A(50–18–51)	108.2	A(34–36–35)	107.9
A(2–42–73)	110.3	A(11–10–45)	111.6	A(50–18–52)	108.7	A(34–36–40)	127.8
A(2–42–74)	110.3	A(10–11–15)	101.1	A(51–18–52)	109.0	A(34–39–43)	111.4
A(2–42–75)	105.3	A(10–11–18)	110.6	A(20–19–23)	141.1	A(34–39–66)	109.9
A(3–25–16)	126.1	A(10–11–46)	113.0	A(19–23–24)	104.2	A(34–39–67)	110.0
A(28–4–72)	105.1	A(12–10–14)	109.6	A(19–23–27)	127.8	A(36–35–37)	125.5
A(4–28–5)	123.2	A(12–10–45)	111.0	A(28–21–53)	108.1	A(35–36–40)	124.3
A(4–28–21)	111.6	A(10–12–13)	125.3	A(28–21–54)	107.9	A(35–37–62)	114.8
A(5–28–21)	125.3	A(14–10–45)	111.1	A(53–21–54)	106.1	A(36–40–68)	111.4
A(12–6–15)	108.5	A(10–14–21)	111.9	A(26–22–55)	117.2	A(36–40–69)	110.9
A(6–12–10)	111.9	A(10–14–47)	109.6	A(22–26–30)	127.3	A(36–40–70)	111.7
A(6–12–13)	122.8	A(10–14–48)	110.4	A(24–23–27)	128.0	A(63–38–64)	107.4
A(12–6–60)	148.8	A(15–11–18)	109.8	A(23–24–29)	126.8	A(63–38–65)	108.2
A(6–15–11)	113.1	A(15–11–46)	111.4	A(23–27–56)	111.4	A(64–38–65)	107.6
A(6–15–22)	123.1	A(11–15–22)	123.6	A(23–27–57)	108.8	A(43–39–66)	109.5
A(15–6–60)	102.7	A(18–11–46)	110.5	A(23–27–58)	111.6	A(43–39–67)	109.6
A(17–7–24)	104.8	A(11–18–50)	110.2	A(24–29–31)	122.9	A(39–43–76)	111.0
A(7–17–13)	137.0	A(11–18–51)	109.3	A(24–29–59)	119.0	A(39–43–77)	110.3
A(7–17–19)	112.1	A(11–18–52)	111.4	A(26–30–33)	107.9	A(39–43–78)	110.2
A(17–7–61)	152.7	A(12–13–16)	124.9	A(26–30–38)	124.0	A(66–39–67)	106.3
A(7–24–23)	111.1	A(12–13–17)	126.7	A(56–27–57)	108.6	A(68–40–69)	107.5
A(7–24–29)	122.2	A(16–13–17)	108.4	A(56–27–58)	107.5	A(68–40–70)	107.4
A(24–7–61)	102.5	A(13–16–20)	105.2	A(57–27–58)	108.8	A(69–40–70)	107.7
A(26–8–32)	110.4	A(13–16–25)	112.9	A(31–29–59)	118.2	A(44–41–71)	118.9
A(26–8–60)	118.4	A(13–16–49)	115.0	A(29–31–34)	131.0	A(41–44–79)	121.1
A(8–26–22)	125.4	A(13–17–19)	111.0	A(33–30–38)	128.1	A(41–44–80)	121.8
A(8–26–30)	107.4	A(21–14–47)	109.9	A(30–33–32)	108.4	A(73–42–74)	108.8
A(32–8–60)	131.2	A(21–14–48)	108.8	A(30–33–41)	126.0	A(73–42–75)	111.1
A(8–32–33)	106.0	A(14–21–28)	111.0	A(30–38–63)	111.3	A(74–42–75)	111.1
A(8–32–37)	129.3	A(14–21–53)	111.3	A(30–38–64)	111.1	A(76–43–77)	108.7
A(8–60–6)	126.0	A(14–21–54)	112.3	A(30–38–65)	111.0	A(76–43–78)	108.7
A(31–9–35)	110.1	A(47–14–48)	106.0	A(31–34–36)	107.3	A(77–43–78)	107.9
A(31–9–61)	116.2	A(15–22–26)	124.3	A(31–34–39)	124.7	A(79–44–80)	117.0
A(9–31–29)	121.4	A(15–22–55)	118.4	A(33–32–37)	124.7		
A(9–31–34)	107.5	A(20–16–25)	109.1	A(32–33–41)	125.7		

where χ is the electronegativity.

The global hardness η can be seen as the resistance to charge transfer:

$$\eta = \frac{1}{2}\left(\frac{\partial^2 E}{\partial N^2}\right)_{\upsilon(\vec{r})} \tag{8.11}$$

Table 8.7 Optimized bond distances (in Å) of the pheophorbide a molecule calculated with the M06-HF density functional and the MIDIY basis set

Bond	Distance	Bond	Distance	Bond	Distance	Bond	Distance
R(1–20)	1.206	R(11–46)	1.092	R(23–24)	1.469	R(38–64)	1.096
R(2–25)	1.345	R(12–13)	1.344	R(23–27)	1.509	R(38–65)	1.093
R(2–42)	1.452	R(13–16)	1.527	R(24–29)	1.370	R(39–43)	1.562
R(3–25)	1.210	R(13–17)	1.445	R(26–30)	1.468	R(39–66)	1.094
R(4–28)	1.361	R(14–21)	1.542	R(27–56)	1.095	R(39–67)	1.094
R(4–72)	0.977	R(14–47)	1.094	R(27–57)	1.093	R(40–68)	1.096
R(5–28)	1.203	R(14–48)	1.093	R(27–58)	1.095	R(40–69)	1.093
R(6–12)	1.394	R(15–22)	1.419	R(29–31)	1.413	R(40–70)	1.096
R(6–15)	1.313	R(16–20)	1.586	R(29–59)	1.085	R(41–44)	1.332
R(7–17)	1.308	R(16–25)	1.530	R(30–33)	1.349	R(41–71)	1.087
R(7–24)	1.417	R(16–49)	1.096	R(30–38)	1.507	R(42–73)	1.091
R(8–26)	1.373	R(17–19)	1.453	R(31–34)	1.417	R(42–74)	1.093
R(8–32)	1.393	R(18–50)	1.094	R(32–33)	1.482	R(42–75)	1.089
R(8–60)	1.031	R(18–51)	1.096	R(32–37)	1.358	R(43–76)	1.093
R(9–31)	1.376	R(18–52)	1.094	R(33–41)	1.480	R(43–77)	1.094
R(9–35)	1.355	R(19–20)	1.469	R(34–36)	1.390	R(43–78)	1.095
R(10–11)	1.551	R(19–23)	1.354	R(34–39)	1.509	R(44–79)	1.084
R(10–12)	1.533	R(21–28)	1.523	R(35–36)	1.424	R(44–80)	1.086
R(10–14)	1.552	R(21–53)	1.096	R(35–37)	1.426	R(6–60)	1.987
R(10–45)	1.090	R(21–54)	1.094	R(36–40)	1.513	R(7–61)	1.751
R(11–15)	1.532	R(22–26)	1.370	R(37–62)	1.084	R(9–61)	1.049
R(11–18)	1.557	R(22–55)	1.082	R(38–63)	1.096		

Using a finite difference approximation and Koopmans' theorem [33–36], the above expressions can be written as:

$$\mu \approx \frac{1}{2}(I + A) \approx \frac{1}{2}(\epsilon_L + \epsilon_H) \tag{8.12}$$

$$\eta \approx \frac{1}{2}(I - A) \approx \frac{1}{2}(\epsilon_L - \epsilon_H) \tag{8.13}$$

where ε_H and ε_L are the energies of the highest occupied and the lowest unoccupied molecular orbitals, HOMO and LUMO, respectively. However, within the context of density functional theory, the above inequalities are justified in light of the work of Perdew and Levy [53], where they commented on the significance of the highest occupied Kohn–Sham eigenvalue, and proved the ionization potential theorems for the exact Kohn–Sham density functional theory of a many-electron system. In addition the use of the energies of frontier molecular orbitals as an approximation to obtain I and A is supported by the Janak's Theorem [54]. In particular, The negative of Hartree–Fock and Kohn–Sham HOMO orbital has been found to define upper

Table 8.8 Optimized bond angles (in degrees) of the pheophorbide a molecule calculated with the M06-HF density functional and the MIDIY basis set

Bond	Angle	Bond	Angle	Bond	Angle	Bond	Angle
A(1–20–16)	124.9	A(9–35–37)	127.1	A(25–16–49)	107.5	A(33–41–44)	124.0
A(1–20–19)	130.0	A(35–9–61)	133.8	A(17–19–20)	110.8	A(33–41–71)	116.2
A(25–2–42)	113.1	A(11–10–12)	100.7	A(17–19–23)	108.1	A(36–34–39)	127.6
A(2–25–3)	123.4	A(11–10–14)	111.9	A(50–18–51)	108.6	A(34–36–35)	107.6
A(2–25–16)	111.3	A(11–10–45)	112.1	A(50–18–52)	109.1	A(34–36–40)	127.8
A(2–42–73)	109.9	A(10–11–15)	100.9	A(51–18–52)	109.6	A(34–39–43)	110.6
A(2–42–74)	109.8	A(10–11–18)	110.6	A(20–19–23)	141.1	A(34–39–66)	110.0
A(2–42–75)	105.2	A(10–11–46)	113.5	A(19–23–24)	104.1	A(34–39–67)	109.9
A(3–25–16)	125.3	A(12–10–14)	109.1	A(19–23–27)	127.5	A(36–35–37)	125.2
A(28–4–72)	106.1	A(12–10–45)	110.9	A(28–21–53)	107.9	A(35–36–40)	124.6
A(4–28–5)	122.8	A(10–12–13)	125.9	A(28–21–54)	107.4	A(35–37–62)	114.8
A(4–28–21)	112.2	A(14–10–45)	111.6	A(53–21–54)	107.0	A(36–40–68)	111.0
A(5–28–21)	125.0	A(10–14–21)	111.7	A(26–22–55)	118.7	A(36–40–69)	110.5
A(12–6–15)	108.5	A(10–14–47)	109.3	A(22–26–30)	127.0	A(36–40–70)	111.3
A(6–12–10)	110.8	A(10–14–48)	110.3	A(24–23–27)	128.4	A(63–38–64)	108.2
A(6–12–13)	123.2	A(15–11–18)	109.2	A(23–24–29)	127.5	A(63–38–65)	108.9
A(12–6–60)	148.0	A(15–11–46)	111.3	A(23–27–56)	111.0	A(64–38–65)	108.3
A(6–15–11)	113.7	A(11–15–22)	122.6	A(23–27–57)	107.9	A(43–39–66)	109.6
A(6–15–22)	123.7	A(18–11–46)	110.9	A(23–27–58)	110.9	A(43–39–67)	109.8
A(15–6–60)	103.4	A(11–18–50)	109.8	A(24–29–31)	123.1	A(39–43–76)	110.8
A(17–7–24)	105.2	A(11–18–51)	108.7	A(24–29–59)	118.9	A(39–43–77)	109.8
A(7–17–13)	137.4	A(11–18–52)	111.0	A(26–30–33)	107.9	A(39–43–78)	109.6
A(7–17–19)	112.2	A(12–13–16)	125.2	A(26–30–38)	123.6	A(66–39–67)	106.8
A(17–7–61)	152.4	A(12–13–17)	126.8	A(56–27–57)	109.3	A(68–40–69)	107.7
A(7–24–23)	110.3	A(16–13–17)	108.0	A(56–27–58)	108.4	A(68–40–70)	108.2
A(7–24–29)	122.2	A(13–16–20)	105.5	A(57–27–58)	109.2	A(69–40–70)	108.0
A(24–7–61)	102.4	A(13–16–25)	111.6	A(31–29–59)	117.9	A(44–41–71)	119.8
A(26–8–32)	110.7	A(13–16–49)	115.3	A(29–31–34)	131.3	A(41–44–79)	121.2
A(26–8–60)	118.1	A(13–17–19)	110.4	A(33–30–38)	128.5	A(41–44–80)	121.6
A(8–26–22)	125.8	A(21–14–47)	110.0	A(30–33–32)	108.7	A(73–42–74)	109.3
A(8–26–30)	107.2	A(21–14–48)	108.7	A(30–33–41)	126.9	A(73–42–75)	111.4
A(32–8–60)	131.2	A(14–21–28)	110.2	A(30–38–63)	110.6	(74–42–75)	111.1
A(8–32–33)	105.5	A(14–21–53)	111.4	A(30–38–64)	110.5	A(76–43–77)	109.2
A(8–32–37)	130.9	A(14–21–54)	112.6	A(30–38–65)	110.3	A(76–43–78)	109.1
A(8–60–6)	126.5	A(47–14–48)	106.7	A(31–34–36)	107.1	A(77–43–78)	108.3
A(31–9–35)	109.9	A(15–22–26)	122.5	A(31–34–39)	125.2	A(79–44–80)	117.2
A(9–31–29)	121.0	A(15–22–55)	118.8	A(33–32–37)	123.6	A(7–61–9)	135.1
A(9–31–34)	107.7	A(20–16–25)	109.4	A(32–33–41)	124.3		
A(31–9–61)	116.2	A(20–16–49)	107.4	A(32–37–35)	130.5		
A(9–35–36)	107.7	A(16–20–19)	105.1	A(32–37–62)	114.7		

and lower limits, respectively, for the experimental values of the first ionization potential [55] thus validating the use of energies of Kohn–Sham frontier molecular orbitals to calculate reactivity descriptors coming from Conceptual DFT.

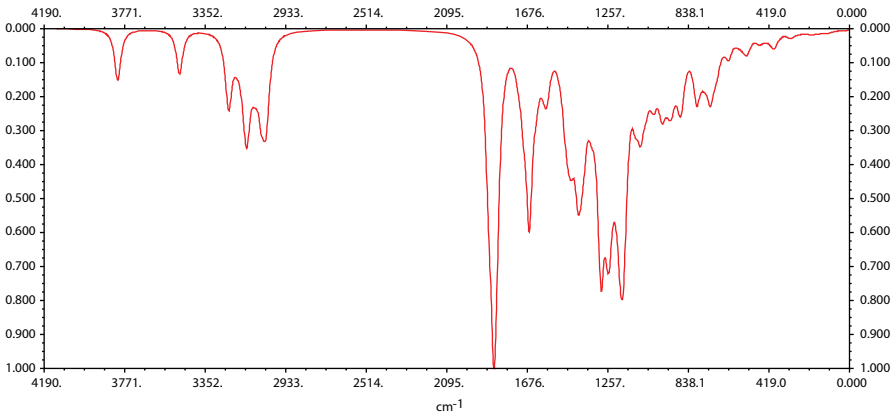


Fig. 8.5 Infrared spectrum of the pheophorbide a molecule calculated with the M06 density functional and the MIDIY basis set



Fig. 8.6 Infrared spectrum of the pheophorbide a molecule calculated with the M06L density functional and the MIDIY basis set

The electrophilicity index ω represents the stabilization energy of the systems when it gets saturated by electrons coming from the surrounding:

$$\omega = \frac{\mu^2}{2\eta} \approx \frac{(I+A)^2}{2(I-A)} \approx \frac{(\epsilon_L + \epsilon_H)^2}{2(\epsilon_L - \epsilon_H)} \tag{8.14}$$

The validity of the Koopmans' theorem within the DFT approximation is controversial. However, it has been shown [55] that although the KS orbitals may differ in shape and energy from the HF orbitals, the combination of them produces Conceptual DFT reactivity descriptors that correlate quite well with the reactivity descrip-

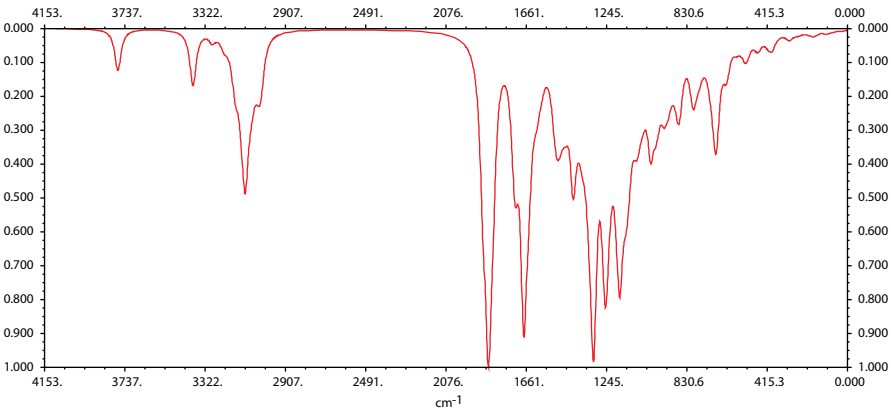


Fig. 8.7 Infrared spectrum of the pheophorbide a molecule calculated with the M06-2X density functional and the MIDIY basis set

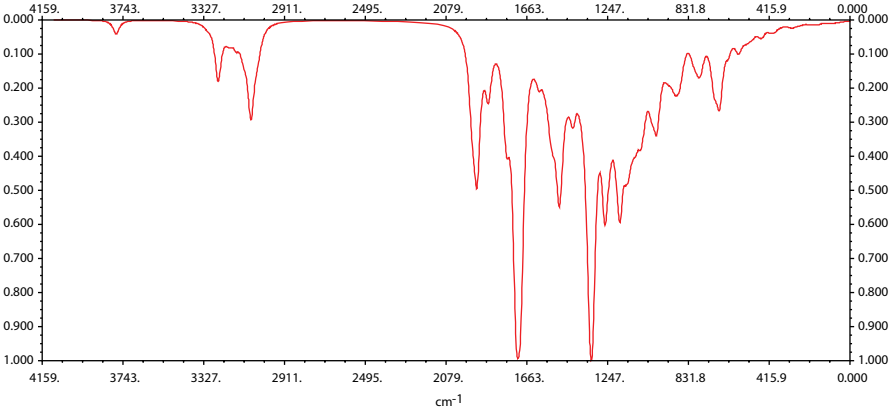


Fig. 8.8 Infrared spectrum of the pheophorbide a molecule calculated with the M06-HF density functional and the MIDIY basis set

tors obtained through Hartree–Fock calculations. Thus, it is worth to calculate the electronegativity, global hardness and global electrophilicity for the studied systems using both approximations in order to verify the quality of the procedures.

The HOMO and LUMO orbital energies (in eV), ionization potentials I and electron affinities A (in eV), and global electronegativity χ, total hardness η, and global electrophilicity ω of the pheophorbide a molecule calculated with the M06, M06L, M06-2X and M06-HF density functionals and the MIDIY basis set are presented in Table 8.14. The upper part of the table shows the results derived assuming the validity of Koopmans' theorem and the lower part shows the results derived from the calculated vertical I and A.

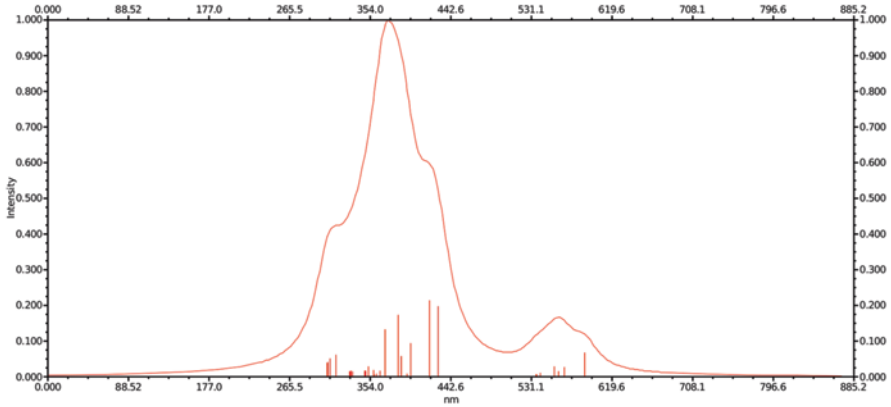


Fig. 8.9 Absorption spectrum of the pheophorbide a molecule calculated with the M06 density functional and the MIDIY basis set

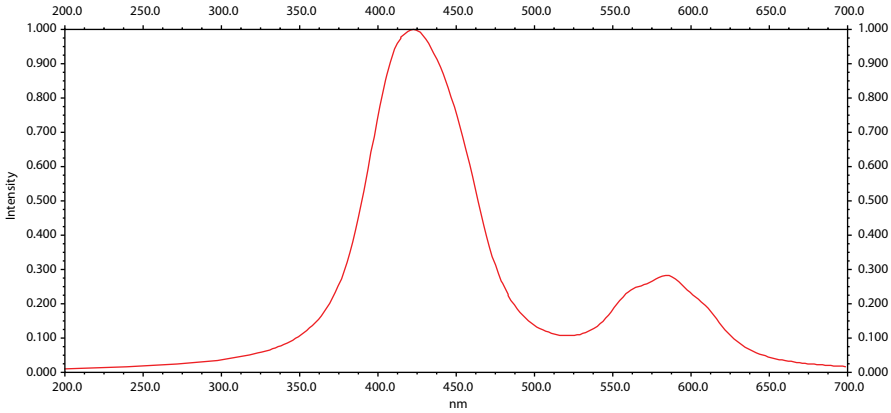


Fig. 8.10 Absorption spectrum of the pheophorbide a molecule calculated with the M06L density Functional and the MIDIY basis set

The condensed Fukui functions can also be employed to determine the reactivity of each atom in the molecule. The corresponding condensed functions are given by $f_k = q_k(N+1) - q_k(N)$ (for nucleophilic attack), where q_k is the gross charge of atom k in the molecule.

It is possible to evaluate condensed Fukui functions from single-points calculations directly, without resorting to additional calculations involving the systems with $N-1$ and $N+1$ electrons:

$$f_k^{+} = \sum_{a \in k} \left[{c_{ai}}^2 + c_{ai} \sum_{b \neq a} c_{bi} S_{ab} \right] \quad \text{(where i = LUMO)} \tag{8.15}$$

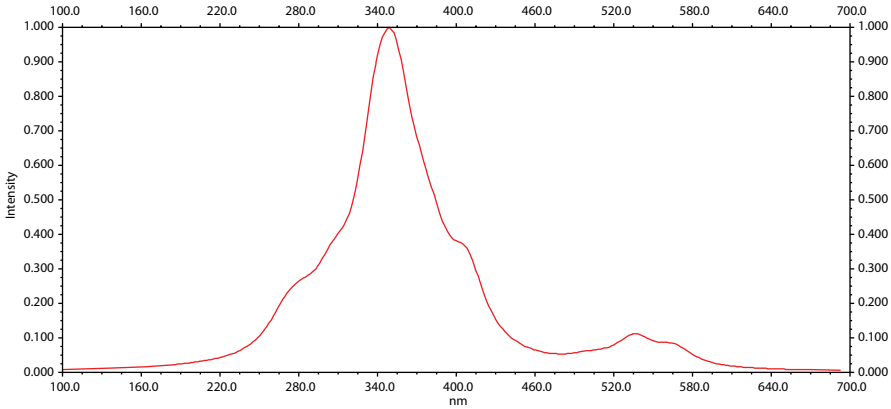


Fig. 8.11 Absorption spectrum of the pheophorbide a molecule calculated with the M06-2X density functional and the MIDIY basis set

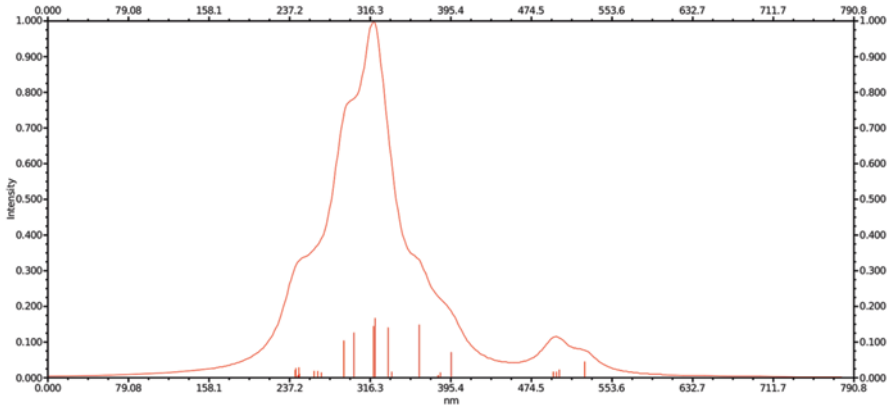


Fig. 8.12 Absorption spectrum of the pheophorbide a molecule calculated with the M06-HF density functional and the MIDIY basis set

and

$$f_k^- = \sum_{a \in k} \left[c_{ai}^{\,2} + c_{ai} \sum_{b \neq a} c_{bi} S_{ab} \right] \quad \text{(where i = HOMO)} \tag{8.16}$$

with c_{ai} being the LCAO coefficients and S_{ab} the overlap matrix. The condensed Fukui functions are normalized, thus $\sum_k f_k = 1$.

The condensed Fukui functions have been calculated using the AOMix molecular analysis program [43, 56] starting from single-point energy calculations. We have presented, discussed and successfully applied the described procedure in our previous studies on different molecular systems [57–60].

Table 8.9 Transition assignments for the TD-DFT calculation of the UV–Vis Spectrum of pheophorbide a with the M06 density functional and the MIDIY basis set

#	nm	(f)	Assignments
1	561.1	0.1049	H−0→L+0(+59%) H−1→L+0(17%) H−1→L+1(+17%) H−0→L+1(+6%)
2	536.9	0.0518	H−1→L+0(+56%) H−0→L+1(19%) H−0→L+0(+19%)
3	394.7	0.0091	H−3→L+0(+84%) H−3→L+2(6%)
4	388.7	0.3925	H−0→L+1(+56%) H−1→L+0(+15%) H−1→L+2(7%) H−4→L+0(+7%) H−2→L+0(+6%)
5	370.7	0.8881	H−1→L+1(+68%) H−0→L+0(19%)
6	359.2	0.0484	H−2→L+0(84%) H−4→L+0(+6%)
7	349.0	0.1199	H−4→L+0(+58%) H−6→L+0(+18%)
8	348.4	0.0934	H−6→L+0(+67%) H−4→L+0(14%)
9	332.1	0.1054	H−5→L+0(+85%) H−4→L+0(10%)
10	307.5	0.2538	H−0→L+2(49%) H−1→L+2(+18%) H−2→L+1(+12%)

The condensed dual descriptor has been defined as $f^{(2)}(\mathbf{r}) = f_k^+ - f_k^-$ [61, 62].

From the interpretation given to the Fukui function, one can note that the sign of the dual descriptor is very important to characterize the reactivity of a site within a molecule toward a nucleophilic or an electrophilic attack. That is, if $f^{(2)}(\mathbf{r}) > 0$, then the site is favored for a nucleophilic attack, whereas if $f^{(2)}(\mathbf{r}) < 0$, then the site may be favored for an electrophilic attack [61–63].

The electrophilic f^+ and nucleophilic f^+ condensed Fukui functions and $f^{(2)}(\mathbf{r})$ over the atoms of the pheophorbide a molecule calculated with the M06, M06L, M06-2X and M06-HF density functionals and the MIDIY basis set are shown in Table 8.15. The actual values have been multiplied by 100 for an easier comparison.

The electron donating (ω^-) and electron accepting (ω^+) powers have been defined as [64]:

$$\omega^- = \frac{(3I + A)^2}{16(I - A)} \tag{8.17}$$

Table 8.10 Transition assignments for the TD-DFT calculation of the UV–Vis spectrum of pheophorbide a with the M06L density functional and the MIDIY basis set

#	nm	(f)	Assignments
1	586.8	0.0690	H−0→L+0(+71%) H−1→L+1(21%) H−1→L+0(+6%)
2	559.8	0.0786	H−1→L+0(+69%) H−0→L+1(+22%) H−0→L+0(6%)
3	479.6	0.0004	H−2→L+0(+100%)
4	437.1	0.0069	H−3→L+0(+96%)
5	427.8	0.2428	H−0→L+1(+57%) H−1→L+0(12%) H−0→L+2(+9%) H−1→L+2(+9%) H−4→L+0(6%)
6	414.7	0.0987	H−5→L+0(+56%) H−4→L+0(18%) H−1→L+1(13%)
7	412.8	0.0342	H−4→L+0(+56%) H−5→L+0(+34%)
8	405.1	0.2088	H −6→L+0(+45%) H −1→L+1(+24%) H−4→L+0(8%) H−0→L+0(+7%) H−7→L+0(+6%)
9	395.0	0.0289	H−7→L+0(+90%)
10	391.9	0.0054	H−2→L+1(+97%)

and

$$\omega^{+} = \frac{(I+3A)^2}{16(I-A)} \tag{8.18}$$

It follows that a larger ω^{+} value corresponds to a better capability of accepting charge, whereas a smaller value of ω^{-} value of a system makes it a better electron donor. In order to compare ω^{+} with $-\omega^{-}$, the following definition of net electrophilicity has been proposed [65]:

$$\Delta\omega^{\pm} = \omega^{+} - (-\omega^{-}) = \omega^{+} + \omega^{-} \tag{8.19}$$

that is, the electron accepting power relative to the electron donating power.

The electrodonating (ω^{-}) and electroaccepting (ω^{+}) powers and net electrophilicity $\Delta\omega^{\pm}$ of the pheophorbide a molecule calculated with the M06, M06L, M06-2X and M06-HF density functionals and the MIDIY basis sets are presented in Table 8.16. The upper part of the table shows the results derived assuming the validity of

Table 8.11 Transition assignments for the TD-DFT calculation of the UV–Vis spectrum of pheophorbide a with the M06-2X density functional and the MIDIY basis set

#	nm	(f)	Assignments
1	534.9	0.1404	H−0→L+0(+72%) H−1→L+1(+18%) H−1→L+0(6%)
2	496.4	0.0185	H−1→L+0(+59%) H−0→L+1(30%) H−0→L+0(+7%)
3	353.0	0.9712	H−0→L+1(+62%) H−1→L+0(+31%)
4	338.8	1.0008	H−1→L+1(+74%) H−0→L+0(18%)
5	332.0	0.0403	H−5→L+0(+40%) H−5→L+2(24%) H−7→L+2(9%) H−7→L+0(+7%)
6	304.4	0.2097	H−2→L+0(32%) H−3→L+0(+26%) H−4→L+0(25%)
7	300.4	0.0231	H−2→L+0(42%) H−3→L+0(37%) H−3→L+1(6%) H−2→L+1(6%)
8	284.1	0.0315	H−7→L+0(+41%) H−5→L+0(20%) H−4→L+0(+13%)
9	281.9	0.1030	H−4→L+0(47%) H−3→L+0(16%) H−7→L+0(+12%) H−2→L+0(+6%) H−5→L+0(6%)
10	269.0	0.1255	H−0→L+2(+68%) H−1→L+2(23%)

Koopmans' theorem and the lower part shows the results derived from the calculated vertical I and A.

The results from Table 8.16 clearly indicate that pheophorbide a is an electrodonating molecule, with the same result predicted by all the four density functionals considered in this study. However, only the results obtained through the calculations with the M06 and M06L density functionals are in fairly agreement between those from vertical calculations of I and A and those coming from the assumption of the validity of the Koopmans' theorem in DFT.

Table 8.12 Transition assignments for the TD-DFT calculation of the UV–Vis spectrum of pheophorbide a with the M06-HF density functional and the MIDIY basis set

#	nm	(f)	Assignments
1	496.2	0.1631	H−0→L+0(+76%) H−1→L+1(+17%)
2	383.3	0.0675	H−0→L+1(+55%) H−1→L+0(35%)
3	335.9	0.0049	H−8→L+2(33%) H−8→L+0(17%) H−7→L+2(+6%)
4	320.0	1.3536	H−1→L+0(+52%) H−0→L+1(+27%) H−1→L+1(+15%)
5	290.8	0.9934	H−1→L+1(+59%) H−0→L+0(13%) H−0→L+1(12%) H−1→L+0(6%)
6	261.8	0.1819	H−2→L+0(+43%) H−4→L+0(+30%) H−3→L+0(+5%)
7	245.9	0.0721	H−4→L+0(+35%) H−2→L+0(35%) H−3→L+1(13%)
8	243.3	0.2110	H−3→L+0(42%) H−4→L+1(+19%) H−3→L+1(12%)
9	237.9	0.0156	H−7→L+1(+24%) H−7→L+0(+13%) H−8→L+1(+8%) H−10→L+1(+7%)
10	234.1	0.0011	H−10→L+0(+30%) H−7→L+0(26%) H−7→L+1(+15%) H−10→L+1(6%)

8.4 Conclusions

From the whole of the results presented in this contribution it has been clearly demonstrated that the sites of interaction of the pheophorbide a molecule can be predicted by using DFT-based reactivity descriptors such as the hardness, softness, and electrophilicity, as well as Fukui function calculations. These descriptors were used in the characterization and successfully description of the preferred reactive sites and provide a firm explanation for the reactivity of the pheophorbide a molecule.

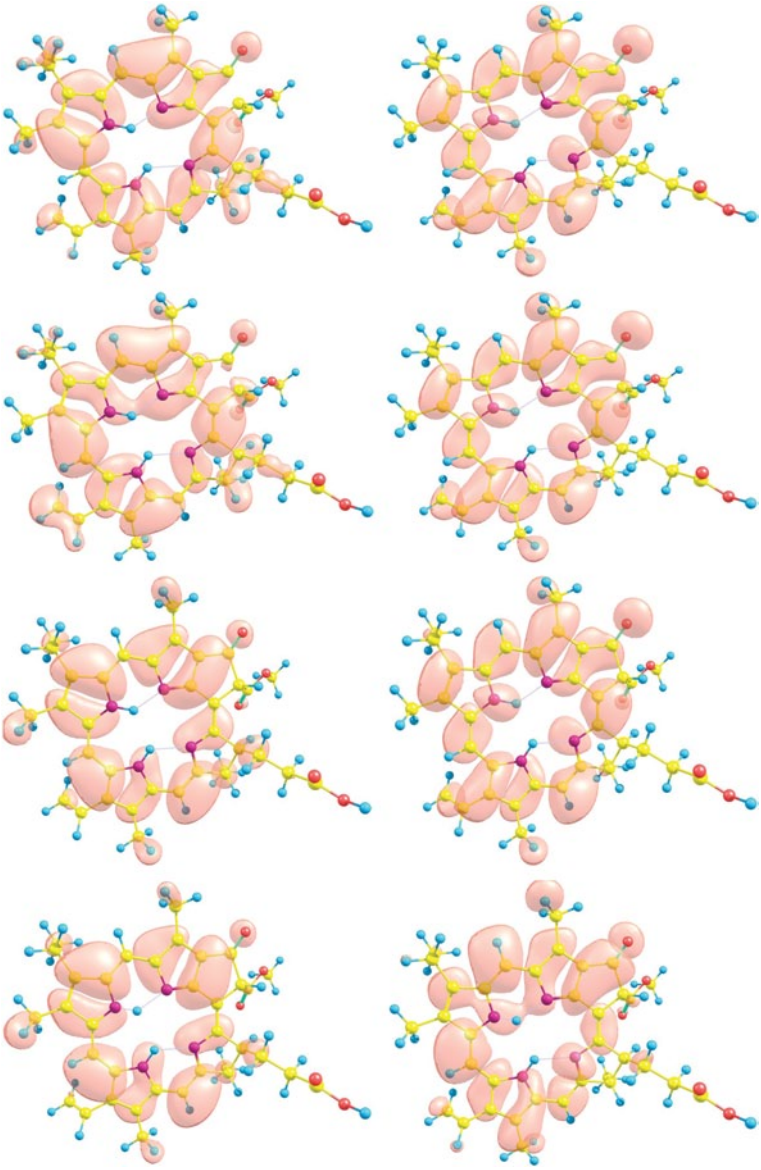


Fig. 8.13 HOMO and LUMO orbitals of the pheophorbide a molecule calculated with the M06, M06L, M06-2X and M06-HF density functionals and the MIDIY basis set

Table 8.13 Molecular dipole moments μ (in Debye) and global polarizabilities α (in Bohr3) of pheophorbide a calculated with the M06, M06L, M06-2X and M06-HF density functionals and the MIDIY basis set

Property	M06	M06L	M06-2X	M06-HF
μ	4.2243	4.3253	4.4436	4.4608
α	527.54	545.18	518.08	492.65

Table 8.14 HOMO and LUMO orbital energies (in eV), ionization potentials I and electron affinities A (in eV), and global electronegativity χ, total hardness η, and global electrophilicity ω of pheophorbide a calculated with the M06, M06L, M06-2X and M06-HF density functionals and the MIDIY basis set. The upper part of the table shows the results derived assuming the validity of Koopmans' theorem and the lower part shows the results derived from the calculated vertical I and A

Property	M06	M06L	M06-2X	M06-HF
HOMO	5.257	4.692	5.889	7.026
LUMO	2.395	2.925	1.829	0.654
χ	3.8260	3.8085	3.8589	3.8403
η	1.4314	0.8832	2.0303	3.1861
ω	5.1133	8.2114	3.6672	2.3144
I	6.808	6.245	6.376	6.456
A	0.808	1.391	1.345	1.205
χ	3.8080	3.8178	3.8606	3.8307
η	3.0003	2.4272	2.5157	2.6257
ω	2.4166	3.0026	2.9622	2.7944

These results could be of interest for the application of the pheophorbide a molecule in the fields of Dye Sensitized Solar Cells (DSSC), Artificial Photosynthesis, and Photodynamic Therapy.

The M06 family of density functionals (M06, M06L, M06-2X and M06-HF) used in the present work leads to the same qualitatively and quantitatively similar description of the chemistry and reactivity of the pheophorbide a molecule, yielding reasonable results. However, for the case of the M06 and M06L functionals, the agreement between the results obtained through energy calculations and those the assume the validity of the Koopmans' theorem is fairly good.

Table 8.15 Electrophilic f^+ and nucleophilic f^- condensed Fukui functions and $f^{(2)}(\mathbf{r})$ over the atoms of the Pheophorbide A molecule calculated with the M06, M06L, M06-2X and M06-HF density functionals and the MIDIY basis set. The actual values have been multiplied by 100 for an easier comparison. Hydrogen atoms are not shown

	M06			M06L			M06-2X			M06-HF		
Atom	f^+	f^-	$f^{(2)}(\mathbf{r})$	f^+	f^-	$f^{(2)}(\mathbf{r})$	f^+	f^-	$f^{(2)}(\mathbf{r})$	f^+	f^-	$f^{(2)}(\mathbf{r})$
1O	3.56	0.94	2.62	4.43	0.55	3.88	3.12	0.91	2.21	3.00	0.72	2.28
2O	0.02	0.01	0.01	0.02	0.05	−0.03	0.01	0.01	0.00	0.01	0.01	0.00
3O	0.15	0.18	−0.03	0.21	0.12	0.09	0.10	0.10	0.00	0.10	0.04	0.06
4O	0.00	0.01	−0.01	0.00	0.01	−0.01	0.00	0.00	0.00	0.00	0.00	0.00
5O	0.00	0.01	−0.01	0.00	0.01	−0.01	0.00	0.00	0.00	0.00	0.00	0.00
6N	8.57	0.28	8.29	9.12	2.90	6.22	7.65	1.12	6.53	8.71	1.91	6.80
7N	0.26	2.31	−2.05	0.49	2.52	−1.53	0.06	0.21	−0.15	0.16	1.50	−1.34
8N	0.09	0.44	−0.35	0.08	0.39	−0.31	0.11	1.66	−1.55	0.34	3.84	−3.50
9N	4.46	0.39	4.07	4.09	2.47	1.62	4.82	0.20	4.62	5.04	0.41	4.63
10C	0.03	0.27	−0.24	0.02	0.26	−0.24	0.03	0.17	−0.14	0.03	0.10	−0.07
11C	0.05	0.29	−0.16	0.04	0.26	−0.22	0.04	0.19	−0.15	0.04	0.11	−0.07
12C	1.63	9.66	−8.03	1.61	8.83	−7.18	1.57	6.94	−5.37	2.65	3.33	−0.68
13C	6.89	2.70	4.19	7.67	1.25	6.42	5.33	0.09	5.24	0.92	0.12	0.80
14C	0.05	0.64	−0.59	0.05	0.59	−0.54	0.04	0.44	−0.40	0.07	0.22	−0.15
15C	0.68	8.74	−8.06	0.74	7.15	−6.41	0.59	6.39	−5.80	−0.01	2.56	−2.55
16C	0.01	0.01	0.00	0.00	0.11	−0.11	0.01	0.02	−0.01	0.14	0.04	0.10
17C	2.78	6.32	−3.54	2.37	2.84	−0.47	3.26	7.09	−3.73	4.98	5.57	−0.59
18C	0.03	0.61	−0.58	0.04	0.58	−0.54	0.02	0.40	−0.38	0.01	0.17	−0.16
19C	4.58	2.23	2.35	4.48	0.73	3.75	4.70	2.69	2.01	4.81	2.80	2.01
20C	2.56	0.15	2.41	3.04	0.07	2.97	2.19	0.13	2.16	2.19	0.06	2.13
21C	0.04	0.14	−0.10	0.05	0.15	−0.10	0.04	0.10	−0.06	0.06	0.04	0.02
22C	8.84	2.18	6.66	8.82	0.28	8.54	8.70	6.39	2.41	9.15	6.22	2.93
23C	8.94	3.25	5.69	9.74	1.83	7.91	8.72	3.20	5.52	11.48	2.00	9.48
24C	4.68	9.27	−4.59	4.16	3.99	0.17	4.84	10.76	−5.92	4.10	10.77	−6.67
25C	0.08	0.02	0.06	0.07	0.24	−0.17	0.08	0.02	0.06	0.10	0.05	0.05
26C	3.31	6.31	−3.00	3.11	7.36	−3.25	3.44	3.32	0.12	1.66	0.55	1.11

Table 8.15 (continued)

	M06			M06L			M06-2X			M06-HF		
Atom	f^{+}	f^{-}	$f^{(2)}(\mathbf{r})$	f^{+}	f^{-}	$f^{(2)}(\mathbf{r})$	f^{+}	f^{-}	$f^{(2)}(\mathbf{r})$	f^{+}	f^{-}	$f^{(2)}(\mathbf{r})$
27C	0.03	0.14	−0.11	0.05	0.10	−0.05	0.02	0.10	−0.08	0.01	0.06	−0.05
28C	0.00	0.01	−0.01	0.00	0.01	−0.01	0.00	0.01	−0.01	0.00	0.00	0.00
29C	5.88	1.92	2.96	8.52	5.35	3.17	7.44	0.07	7.37	16.82	0.03	16.79
30C	6.36	3.42	2.94	6.39	0.97	5.42	6.49	4.41	2.08	4.83	3.89	0.94
31C	2.08	7.79	−5.71	1.72	1.86	−0.14	1.96	11.75	−9.79	0.48	15.21	−14.73
32C	4.57	8.88	−4.31	3.98	4.58	−1.60	5.44	9.57	−4.13	6.16	8.66	−2.70
33C	4.44	1.85	2.59	4.18	3.80	1.38	4.53	0.43	4.10	2.52	0.03	2.49
34C	0.79	3.32	−2.53	0.67	3.18	−2.51	1.21	2.56	−1.35	2.28	4.21	−1.93
35C	1.81	9.72	−7.91	1.48	6.30	−4.82	2.55	9.86	−7.31	5.72	10.21	−4.49
36C	1.02	2.30	−1.28	0.86	0.22	0.64	0.86	4.45	−3.61	0.02	7.03	−7.01
37C	6.28	0.00	6.28	5.66	3.38	2.28	6.25	1.72	4.53	5.88	3.09	2.79
38C	0.02	0.08	−0.06	0.02	0.05	−0.03	0.02	0.06	−0.04	0.02	0.03	−0.01
39C	0.01	0.05	−0.04	0.01	0.03	−0.02	0.01	0.05	−0.04	0.00	0.06	−0.06
40C	0.01	0.08	−0.07	0.01	0.03	−0.02	0.02	0.09	−0.07	0.02	0.09	−0.07
41C	0.15	0.02	0.13	0.21	0.15	0.06	0.10	−0.01	0.11	0.03	0.03	0.00
42C	0.00	0.00	0.00	0.00	0.01	−0.01	0.00	0.01	−0.01	0.01	0.01	0.00
43C	0.05	0.21	−0.16	0.04	0.21	−0.17	0.07	0.16	−0.09	0.15	0.22	−0.07
44C	1.75	0.75	1.00	2.44	2.09	0.35	1.34	0.19	1.05	0.48	0.05	0.43

Table 8.16 Electrodonating (ω^-) and electroaccepting (ω^+) powers and net electrophilicity $\Delta\omega^{\pm}$ of pheophorbide a calculated with the M06, M06L, M06-2X and M06-HF density functionals and the MIDIY basis set. The upper part of the table shows the results derived assuming the validity of Koopmans' theorem and the lower part shows the results derived from the calculated vertical I and A

Property	M06	M06L	M06-2X	M06-HF
ω^-	7.2052	10.2257	5.8503	4.6328
ω^+	3.3792	6.4175	1.9915	0.7926
$\Delta\omega^{\pm}$	10.5844	16.6432	7.8418	5.4254
ω^-	4.6955	5.2147	4.6521	5.0379
ω^+	0.8876	1.3970	1.3464	1.2072
$\Delta\omega^{\pm}$	5.5831	6.6117	5.9985	6.2451

Acknowledgements This work has been partially supported by CIMAV, SC and Consejo Nacional de Ciencia y Tecnología (CONACYT, Mexico). DGM is a researcher of CONACYT and CIMAV

References

1. Calzavara-Pintón P, Venturini M, Sala R (2005) J Photochem Photobiol B 78:1
2. Quartarolo A, Russo N, Sicilia E, Adamo C (2012) In: Nyokong T, Ahsen V (ed) Photosensitizers in medicine, environment, and security. Springer Science+Bussiness Media B.V., Dordrecht, The Netherlands
3. Politzer P, Murray J (2002) Theor Chem Acc 108:134
4. Murray J, Politzer P (2011) WIREs Comput Mol Sci 1:153
5. Morell C, Grand A, Toro-Labbé A (2005) J Phys Chem A 109(1):205
6. Morell C, Grand A, Toro-Labbé A (2006) Chem Phys Lett 425(4–6):342
7. Pearson R (1993) Accounts Chem Res 26:250
8. Pearson R (1963) J Am Chem Soc 85:3533
9. Pearson R (1987) J Chem Educ 64:561
10. Gázquez J (1997) J Phys Chem A 101:4657
11. Ayers P, Parr R, Pearson R (2006) J Chem Phys 124:194107
12. Cárdenas C, Rabi N, Ayers P, Morell C, Jaramillo P, Fuentealba P, (2009) J Phys Chem A 113:8660
13. Chermette H (1998) Coordin Chem Rev 178180:699
14. Chermette H, (1999) J Comput Chem 20:129
15. Geerlings P, De Proft F, Langenaeker W (2003) Chem Rev 103:1793
16. Zevatskii Y, Samoilov D (2007) Russ J Org Chem 43:483
17. Ayers P (2008) J Math Chem 43:285
18. Parr R, Yang W (1984) J Am Chem Soc 106:4049
19. Yang W, Parr RG, Pucci R (1984) J Chem Phys 81(6):2862
20. Fuentealba P, Pérez P, Contreras R (2000) J Chem Phys 113:2544
21. Bulat F, Chamorro E, P. Fuentealba, Toro-Labbé A (2004) J Phys Chem A 108:342
22. Toro-Labbé A (ed) (2007) Theoretical Aspects of Chemical Reactivity, vol. 19. Elsevier Science, Amsterdam
23. Ayers P, Morell C, De Proft F, Geerlings P (2007) Chem—A Eur J 13(29):8240
24. Morell C, Ayers P, Grand A, Gutiérrez-Oliva S, Toro-Labbé A (2008) Phys Chem—Chem Phys 10:7239
25. Morell C, Hocquet A, Grand A, Jamart-Grégoire B (2008) J Mol Struct: Theochem 849:46
26. Fuentealba P, Parr RG (1991) J Chem Phys 94(8):5559

27. Parr RG, Yang W (1989) Density functional theory of atoms and molecules. Oxford University Press, New York
28. Flores-Moreno R, (2010) Chem Theory Comput 6(1):48
29. Martínez J (2009) Chem Phys Lett 478:310
30. Frisch MJ, Trucks GW, Schlegel HB, Scuseria GE, Robb MA, Cheeseman JR, Scalmani G, Barone V, Mennucci B, Petersson GA, Nakatsuji H, Caricato M, Li X, Hratchian HP, Izmaylov AF, Bloino J, Zheng G, Sonnenberg JL, Hada M, Ehara M, Toyota K, Fukuda R, Hasegawa J, Ishida M, Nakajima T, Honda Y, Kitao O, Nakai H, Vreven T, Montgomery Jr JA, Peralta JE, Ogliaro F, Bearpark M, Heyd JJ, Brothers E, Kudin KN, Staroverov VN, Kobayashi R, Normand J, Raghavachari K, Rendell A, Burant JC, Iyengar SS, Tomasi J, Cossi M, Rega N, Millam JM, Klene M, Knox JE, Cross JB, Bakken V, Adamo C, Jaramillo J, Gomperts R, Stratmann RE, Yazyev O, Austin AJ, Cammi R, Pomelli C, Ochterski JW, Martin RL, Morokuma K, Zakrzewski VG, Voth GA, Salvador P, Dannenberg JJ, Dapprich S, Daniels AD, Farkas A, Foresman JB, Ortiz JV, Cioslowski J, Fox DJ (2009) Gaussian 09 revision A.1. Gaussian Inc., Wallingford
31. Huzinaga S, Andzelm J, Klobulowski M, Radzio-Audselm E, Sakai Y, Tatewaki H, (1984) Gaussian basis sets for molecular calculations. Elsevier, Amsterdam
32. Easton R, Giesen D, Welch A, Cramer C, Truhlar D (1996) Theor Chem Acc 93:281
33. Lewars E (2003) Computational chemistry—Introduction to the theory and applications of molecular and quantum mechanics. Kluwer Academic, Dordrecht
34. Young DC (2001) Computational chemistry—a practical guide for applying techniques to real-world problems. Wiley, New York
35. Jensen F (2007) Introduction to computational chemistry, 2nd edn. Wiley, Chichester
36. Cramer CJ (2004) Essentials of computational chemistry—theories and models, 2nd edn. Wiley, England
37. Zhao Y, Truhlar DG (1999) Acc Chem Res 41(2):157
38. Tomasi J, Mennucci B, Cancès E (1999) J Mol Struct: Thoechem 464(1–3):211
39. Stratmann R, Scuseria G, Frisch M (1998) J Chem Phys 109(19):8218
40. Bauernschmitt R, Ahlrichs R, (1996) Chem Phys Lett 256(4–5):454
41. Casida ME, Jamorski C, Casida KC, Salahub DR (1998) J Chem Phys 108(11):4439
42. Gorelsky S (2010) Swizard Program Revision 4.6. http://www.sgchem.net/. University of Ottawa, Ottawa. Accessed 2014
43. Gorelsky S, Lever A (2001) J Organomet Chem 635(1–2):187
44. Allouche A (2011) J Comput Chem 32(1):174. http://dx.doi.org/10.1002/jcc.21600
45. Hackbart S, Horneffer V, Viehe A, Hillenkamp F, Roder B (2001) Chem Phys 269:339
46. Alecu I, Zheng J, Zhao Y, Truhlar D, (2010) J Chem Theory Comput 6:2872
47. Sundholm D (1999) Chem Phys Lett 302:480
48. Parusel AB, Grimme S (2000) J Phys Chem B 104:5395
49. Wang XF, Tamiaki H, Wang L, Tamai N, Kitao O, Zhou H, Sasaki S (2010) Langmuir 26(9):6320
50. Wang XF, Kitao O (2012) Molecules 17(4):4484
51. Alberto M, Marino T, Russo N, Sicilia E, Toscano M (2012) Phys Chem Chem Phys 14:14943
52. Zhurko G, Zhurko D (2012) In: GA Zhurko (ed) Chemcraft Program Revision 1.6. http://www.chemcraft.com/. United States. Accessed 2014
53. Perdew J, Burke K, Ersernhof M (1997) Phys Rev Lett 78:1396
54. Janak J (1978) Phys Rev B 18:7165
55. Zevallos J, Toro-Labbé A (2003) J Chil Chem Soc 48:39
56. Gorelsky S (2011) AOMix Program for Molecular Orbital Analysis—Version 6.5. http://www.sg-chem.net/. University of Ottawa, Ottawa. Accessed 2014
57. Ruiz-Anchondo T, Glossman-Mitnik D (2009) J Mol Str: Theochem 913(1–3):215
58. Glossman-Mitnik D (2009) Int J Photoenergy vol. 2009. Article ID 806714, 8 pages
59. Glossman-Mitnik D (2009) J Mol Str: Theochem 911(1–3):105
60. Ruiz-Anchondo T, Flores-Holguín N, Glossman-Mitnik D (2010) Molecules 15(7):4490
61. Morell C, Grand A, Toro-Labbé A (2005) J Phys Chem A 109(1):205

62. Morell C, Grand A, Toro-Labbé A (2006) Chem Phys Lett 425(4–6):342
63. Gázquez JL (2009) In Chattaraj PK Chemical reactivity theory: a density functional view, Chap. 2. CRC—Taylor & Francis Group, Boca Raton, pp 7–21
64. Gázquez JL, Cedillo A, Vela A (2007) J Phys Chem A 111(10):1966
65. Chattaraj PK, Chakraborty A, Giri S (2009) J Phys Chem A 113(37):10068

Chapter 9
The Local Ionization Energy as a Guide to Site Reactivities on Graphenes

Jane S. Murray, Zenaida Peralta-Inga Shields and Peter Politzer

Abstract The average local ionization energy $\bar{I}(\mathbf{r})$ has the very important practical advantage that its minimum values on molecular surfaces, the $\bar{I}_{S,min}$, can generally identify the most reactive sites in a system in a *single* calculation, that encompasses all possible sites. The $\bar{I}_{S,min}$ can also, in many instances, rank these sites. Our analyses have shown interaction energies for hydrogenation at interior carbons of defect-containing model graphenes correlate with the $\bar{I}_{S,min}$ at these sites. Furthermore, we are able to show a relationship between the magnitude of the lowest interior $\bar{I}_{S,min}$ within each member of a series of pristine and defect-containing graphene models and the corresponding hydrogenation energies. A limitation of $\bar{I}(\mathbf{r})$ that must be recognized is that it corresponds to the system *prior* to interaction, and cannot reflect factors that may accompany or follow it. Such factors may reinforce or oppose the predictions from the $\bar{I}_{S,min}$. Considerable experience has shown, however, that the $\bar{I}_{S,min}$ can generally identify satisfactorily at least the most reactive sites—and can often rank the next ones as well.

9.1 Graphene

During the past 30 years, there has been a veritable revolution in the area of nanomaterials, much of it focusing upon different forms of carbon. An important milestone was the observation [1] and subsequent production [2] of fullerene, C_{60}. This stimulated a great deal of research activity; see, e.g., Kadish and Ruoff [3]. Fullerenes can be viewed as a special case of carbon nanotubes, the formulation of which soon followed [4]. What is often overlooked is that both fullerene and carbon nanotubes can be said to have been anticipated by earlier work. This is discussed by Hargittai [5] for the former and Harris for the latter [6].

P. Politzer (✉) · J. S. Murray · Z. P.-I. Shields
CleveTheoComp, 1951 W. 26th Street, Suite 409, Cleveland, OH 44113, USA
e-mail: ppolitze@uno.edu

J. S. Murray · P. Politzer
Department of Chemistry, University of New Orleans, New Orleans, LA 70148, USA

J. M. Seminario (ed.), *Design and Applications of Nanomaterials for Sensors,*
Challenges and Advances in Computational Chemistry and Physics 16,
DOI 10.1007/978-94-017-8848-9_9, © Springer Science+Business Media Dordrecht 2014

Carbon nanotubes have been found to have remarkable structural, mechanical, optical and electronic properties, which have aroused a huge amount of interest [6–10]. Related structures, such as carbon nanohorns, were shown to be possible and other elements could be incorporated into nanotubes—boron, nitrogen, aluminum, silicon, etc. Noncarbon nanotubes, e.g. boron/nitrogen, have also been prepared.

The newest carbon material to be creating excitement is graphene, which is really just a special case of graphite, a form of carbon that has long been known. Graphite has a layered structure, consisting of two-dimensional sheets of fused unsaturated six-membered carbon rings [11]. The carbons are linked by strong covalent bonds within the layers, with delocalized π electrons giving these some double bond character; the C–C distances are 1.415 Å, slightly longer than the typical value for aromatic C–C bonds, 1.397 Å [12]. In contrast, there are only weakly attractive interactions between the layers, which have a separation of 3.35 Å [11], approximately twice the van der Waals radius of carbon, 1.70 Å [13].

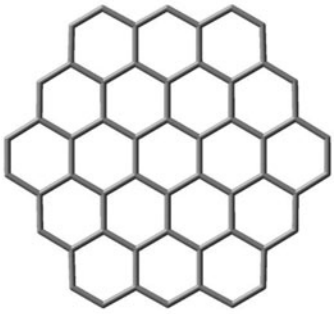
A single one of the two-dimensional one-atom-thick sheets that comprise graphite is known as graphene (**1**). (The framework shown in **1** should be viewed as continuing indefinitely in two dimensions). Graphene can alternatively be viewed as an "unrolled" carbon nanotube. Until a few years ago, graphene was simply a hypothetical concept, but then it was actually obtained by exploiting the weak interlayer attractions in graphite; it proved possible to essentially "peel off" one of these layers [14–16].

While graphene has an obvious structural relationship to carbon nanotubes, it lacks their curvatures and the associated properties, as well as the possible chiralities of nanotubes. Graphene is a zero-band-gap semiconductor with zero-rest-mass conduction electrons [15–17]. Its potential applications include electrodes and high-frequency transistors [18–20], data storage devices [21], sensors and pollutant traps [22–25]. Functions such as sensing and pollutant trapping can take advantage of the very large surface/volume ratio of graphene. Overviews of graphene preparation, characterization and properties have been given by Dinadayalane and Leszczynski [10] and by Flynn [16]. It has now been demonstrated that single-atom-thick boron/nitrogen sheets can also be prepared [26].

There is much interest in the possibilities of modifying graphene, for instance by introducing non-carbon atoms ("doping") [27, 28], by incorporating structural defects [29–31], or by chemical functionalization [32–43]. Such modifications may make it possible to tailor, or "tune," the properties of graphene to maximize its effectiveness for specific applications. This could involve, for example, the designed development of a band gap, or changes in electrical conductivity to improve sensing capabilities. Functionalization—which can include hydrogenation, fluorination, hydroxylation, oxidation, alkylation, etc.—should be feasible, given the unsaturated carbon rings that constitute graphene.

In a nonfunctionalized sheet of graphene that has no structural defects, all interior sites are essentially equivalent. (This is not true of sites near the edges of the sheet, as shall be seen). However even the interior sites become nonequivalent if there is any perturbation of the two-dimensional framework—such as the incorporation

of a foreign atom, any degree of chemical functionalization, or the introduction of a structural defect. An example of the latter is the Stones-Wales defect [44, 45], wherein four fused hexagonal rings (as in **1**) are replaced by two fused heptagonal rings that are in turn fused to two pentagonal (**2**). (The surrounding hexagonal rings in **2** should be viewed as continuing indefinitely in two dimensions).



1



2

Any one of these sorts of perturbations will eliminate the equivalence of the interior sites of the graphene; one consequence is that they may then have different chemical reactivities. For planned functionalization of graphene, it is clearly very important to know the relative reactivities of various sites, i.e. how these are affected by a particular perturbation of the graphene framework. The most direct approach is of course to compute the interaction energy at each nonequivalent site. To be reasonably realistic, however, a rather large model system is required, which is likely to have a sizable number of nonequivalent sites. Computing the interaction energy separately at each of these could be extremely demanding in terms of time and resources.

We have shown that an alternative procedure can be quite effective for determining relative site reactivities, doing so much more rapidly and requiring less in the way of computational resources. This procedure involves calculating the average local ionization energies, $\bar{I}(\mathbf{r})$, at the various sites. $\bar{I}(\mathbf{r})$ is a measure of the ease of removing an electron from a point **r** in a system [46, 47]. It can therefore indicate the relative availabilities of the electrons at all points of interest, and hence their relative reactivities toward both electrophiles and free radicals. *The key advantage of* $\bar{I}(\mathbf{r})$ *is that a single calculation suffices to rank all of the possible sites in a system.*

Such use of $\bar{I}(\mathbf{r})$ has been demonstrated in several studies of both functionalized and defect-containing model carbon nanotubes and model graphenes. In this chapter we shall discuss this work, focusing particularly upon the model graphenes, and assess both the strengths and the limitations of $\bar{I}(\mathbf{r})$ for such applications—which can of course be extended to any large (or small) system.

9.2 Average Local Ionization Energy

Chemical reactivity is a local, site-specific property. If it is desired to identify and rank the sites in a system that are most reactive toward electrophiles and/or free radicals, then there is a need for a means of determining how energetic and readily available are the electrons at the various possible sites. What is required is an ionization energy that focuses upon the specific point in space rather than a particular orbital, i.e. an average *local* ionization energy, $\bar{I}(\mathbf{r})$.

The formulation of $\bar{I}(\mathbf{r})$ proposed by Sjoberg et al. is given by Eq. (9.1) [46]:

$$\bar{I}(\mathbf{r}) = \frac{\sum_i \rho_i(\mathbf{r}) \left| \varepsilon_i \right|}{\rho(\mathbf{r})} \tag{9.1}$$

In Eq. (9.1), $\rho_i(\mathbf{r})$ is the electronic density of orbital *i,* having energy ε_i, and $\rho(\mathbf{r})$ is the total electronic density. The summation is over all occupied orbitals.

Equation (9.1) can be derived within the context of Hartree-Fock theory, in terms of which the ionization energy I_i of an electron in an orbital φ_i is,

$$I_i = \left| \varepsilon_i \right| \tag{9.2}$$

Equation (9.2) is valid if it is assumed that the occupied orbitals of the system are not affected by the loss of an electron from φ_i. This is a major assumption. Some support comes from Koopmans' theorem, which assures the stability of φ_i itself [48, 49], and Eq. (9.2) also benefits from a fortuitous partial cancellation of errors. This is discussed, and the validity of Eq. (9.2) is assessed, in a recent review [47].

If Eq. (9.2) is accepted, then the $\bar{I}(\mathbf{r})$ formula, Eq. (9.1), follows by noting that the average orbital energy at a point **r** is [50, 51],

$$\bar{\varepsilon}(\mathbf{r}) = \frac{\sum_i \rho_i(\mathbf{r}) \varepsilon_i}{\rho(\mathbf{r})} \tag{9.3}$$

Equation (9.1) results by combining Eqs. (9.2) and (9.3).

While $\bar{I}(\mathbf{r})$ was introduced as a guide to chemical reactivity, as shall be discussed, it is interesting to note that the expression on the right side of Eq. (9.3) appears in both Hartree-Fock [52] and Kohn-Sham density functional [53] formalisms relating to local kinetic energy density $t(\mathbf{r})$, which has been used to define local temperature $T(\mathbf{r})$ [53]. Ayers et al. [54] and Bulat et al. [55] have demonstrated an explicit link, within Kohn-Sham theory, between $\bar{I}(\mathbf{r})$ and $T(\mathbf{r})$, as well as $V(\mathbf{r})$, the electrostatic potential due to the electrons and nuclei of the system.

$\bar{I}(\mathbf{r})$ has further been related to atomic shell structure, electronegativity and local polarizability/hardness. These aspects of $\bar{I}(\mathbf{r})$ are reviewed elsewhere [47]. (With respect to $\bar{I}(\mathbf{r})$ and electronegativity, however, a more recent analysis is given by

Politzer et al. [56].) Ayers and Nagy have in fact shown that $\bar{I}(\mathbf{r})$ is an alternative to the electronic density as a fundamental descriptor of Coulombic systems [57].

When $\bar{I}(\mathbf{r})$ is used to analyze and predict molecular reactive behavior, it is typically computed on the "surface" of the molecule, since this is what an approaching reactant encounters. The surface is usually taken to be the 0.001 au (electrons/bohr^3) contour of the molecule's electronic density $\rho(\mathbf{r})$, as suggested by Bader et al. [58], and $\bar{I}(\mathbf{r})$ on this surface is labeled $\bar{I}_S(\mathbf{r})$. Its qualitative features would be the same for other outer contours of $\rho(\mathbf{r})$ [46, 59, 60]. What is of primary interest are the magnitudes and locations of the lowest values of $\bar{I}_S(\mathbf{r})$, the local minima $\bar{I}_{S,min}$. These indicate the sites of the least strongly-held, most reactive electrons, which should be the sites most susceptible to electrophilic or free radical attack.

While $\bar{I}(\mathbf{r})$ was formulated within the framework of Hartree-Fock theory, its application to molecular reactivity can as well be in terms of Kohn-Sham density functional theory. The Kohn-Sham $\bar{I}_{S,min}$ have different magnitudes than do the Hartree-Fock, but the trends tend to be similar [47, 59], and this is what is important for determining the relative reactivities of different sites.

The effectiveness of $\bar{I}_{S,min}$ in identifying and ranking sites that are vulnerable to electrophilic attack has been well documented. For example, they correctly predict the *ortho*-/*para*- or *meta*-directing tendencies of benzene substituents, as well as their activation or deactivation of the ring [46, 59, 61, 62]. $\bar{I}_{S,min}$ have been shown to correlate well with substituent constants (such as the Hammett and the Taft), proton affinities and basicities [61].

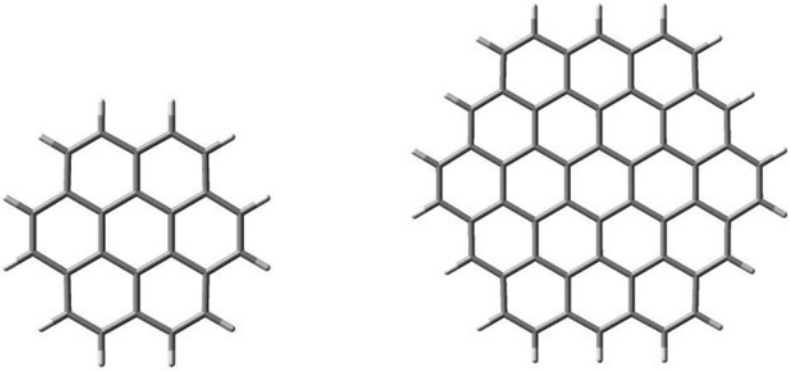
$\bar{I}_{S,min}$ are not limited to atomic sites. They are associated, for instance, with localized buildups of electronic charge in bond regions. Thus, as shall be seen, they can serve as indicators of double bond character. They also reveal radical sites and strained C–C bonds. All of this is summarized in detail in a recent review [47].

$\bar{I}_S(\mathbf{r})$ has been used extensively to study carbon nanotubes, as well as their analogues containing boron and nitrogen atoms [8, 63, 64]. Some of this work will be discussed later in this chapter. However we would like to draw attention to one particularly interesting feature: the ability of (n,0) carbon nanotubes to transmit electronic perturbations [63–67]. [Tubes of the type (n,0) have alternate C–C bonds parallel to their axes as one traces a path from one end of the tube to the other, and are also called "zigzag" tubes.] Even a small perturbation at one end of the tube (e.g. a structural asymmetry) propagates electronically throughout its length and results in striking gradations in both $\bar{I}_S(\mathbf{r})$ and also in the electrostatic potential $V_S(\mathbf{r})$ on the tube surface.

We will conclude this introduction to $\bar{I}(\mathbf{r})$ by briefly examining what are, overall, the relative roles of $\bar{I}_S(\mathbf{r})$ and $V_S(\mathbf{r})$ with respect to molecular reactivity. While they sometimes yield similar insights, as in the above example of (n,0) carbon nanotubes, this should not be generally assumed. For instance, $V_S(\mathbf{r})$ does not correctly predict the directing tendencies of substituents on benzene [47, 62]. We view the roles of $V_S(\mathbf{r})$ and $\bar{I}_S(\mathbf{r})$ as being essentially complementary [62, 64, 68], $V_S(\mathbf{r})$ being more appropriate for noncovalent interactions and $\bar{I}_S(\mathbf{r})$ for covalent ones.

9.3 Pristine and Defect-Containing Model Graphene Systems

Various polycyclic aromatic hydrocarbons have been used as models for pristine graphene; a common one is coronene ($C_{24}H_{12}$, **3**) [40, 64, 69–71]. The six central carbons are viewed as representing the carbons in an infinite sheet of graphene. Another, larger model is an extended version of coronene, $C_{54}H_{18}$ (**4**) [71], having twenty-four interior carbons, six in the central ring and eighteen in the six nearest-neighbor rings. The structural features of **3** and **4** have been discussed elsewhere [71], but we want to emphasize the differences between the interior C–C bond lengths (the ones linking only interior carbons) and the peripheral C(H)–C(H):



3 **4**

The six interior C–C bond lengths in **3** are 1.425 Å, computed at the B3LYP/6-311G(d,p) level. The twenty-four in **4** range from 1. 417 to 1.427 Å. These closely bracket the experimental 1.420 Å of graphene [72]. In contrast, the peripheral C(H)–C(H) bonds in **3** and **4** are significantly shorter, 1.369 and 1.360 Å, respectively [71]. This suggests considerable double bond character in the C(H)–C(H) bonds, since typical C=C distances are about 1.32 Å [12].

What happens structurally to graphene-like frameworks when defects are present, such as some of the hexagonal rings being replaced by pentagonal ones or by pentagonal/heptagonal combinations? Some examples are in models **5**–**8**. (Note that **8** is simply an expanded version of **7**.) Structure **5** ($C_{32}H_{14}$) contains the Stone-Wales defect [44, 45], which was shown earlier in **2**; two fused heptagonal rings are fused to two pentagonal, replacing four hexagonal rings. The presence of the Stone-Wales defect in **5** does *not* result in any degree of nonplanarity. However **6**–**8** are nonplanar [73]. Structure **6** (corannulene, $C_{20}H_{10}$) is simply a pentagonal ring fused to five hexagonal ones [74–76]; it has a bowl-like shape and is often called a "bucky bowl" since it can be viewed as being a portion of fullerene (C_{60}) [77]. Structures **7** ($C_{26}H_{12}$) and **8** ($C_{42}H_{16}$) contain the inverse-Stone-Thrower-Wales defect [78–80]:

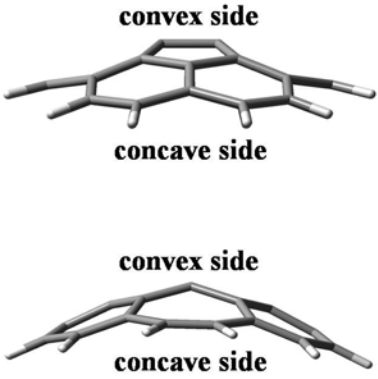
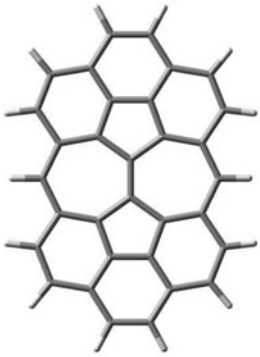
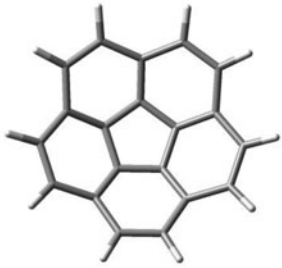


Fig. 9.1 Two side-views of defect-containing structure **7**, showing nonplanarity and indicating convex and concave sides. In the *upper* view, the bond fusing the two pentagons is at the *top*; in *lower* view, one of the carbons of this bond is at the *top* and one of the heptagons is in the center

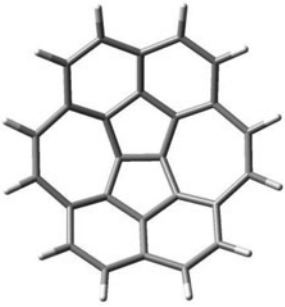
two fused pentagons are fused to two heptagons [10]. **7** and **8** each protrude from the plane around the bond between the two fused pentagons; see Fig. 9.1.



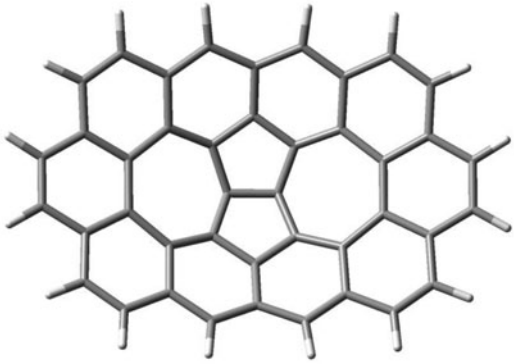
5



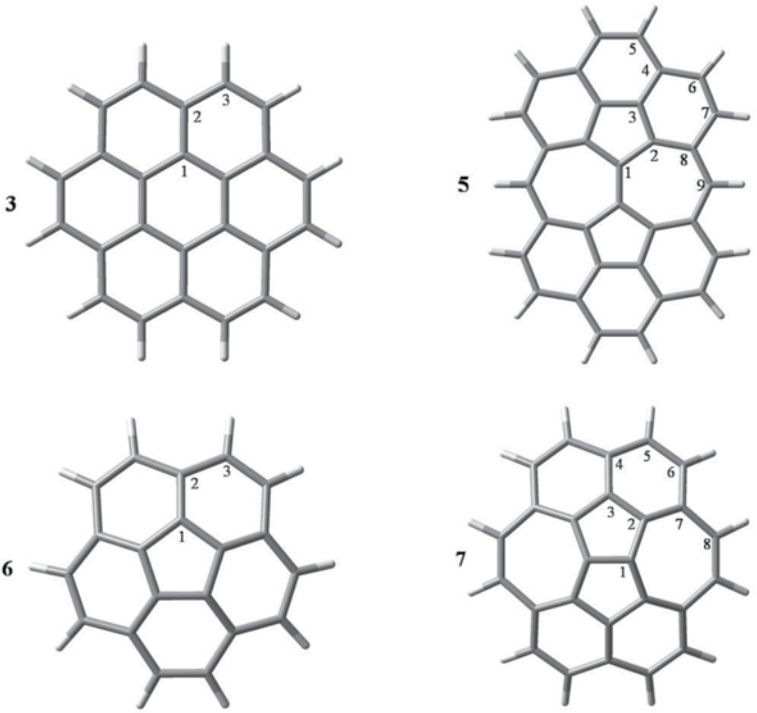
6



7



8



3		5		6		7	
Bond	Length (Å)	Bond	Length (Å)	Bond	Length (Å)	Bond	Length (Å)
C_1-C_1	1.425	C_1-C_1	1.359	C_1-C_1	1.414	C_1-C_1	1.389
C_1-C_2	1.419	C_1-C_2	1.450	C_1-C_2	1.383	C_1-C_2	1.428
C_2-C_3	1.422	C_2-C_3	1.396	C_2-C_3	1.445	C_2-C_3	1.419
C_3-C_3	1.371	C_3-C_3	1.410	C_3-C_3	1.388	C_3-C_4	1.394
		C_3-C_4	1.394			C_4-C_5	1.430
		C_4-C_5	1.420			C_5-C_6	1.389
		C_5-C_5	1.402			C_6-C_7	1.437
		C_4-C_6	1.439			C_7-C_8	1.460
		C_6-C_7	1.377			C_8-C_8	1.375
		C_7-C_8	1.456			C_2-C_7	1.389
		C_8-C_9	1.413				
		C_2-C_8	1.416				

Table 9.1 Calculated C–C bond lengths in pristine and defect-containing graphene models **3**, **5**, **6** and **7**. (Data for **3**, **6** and **7** are taken from reference 73; those for **5** are from present work.) Computational level: B3PW91/6-31G*

In Table 9.1 are the computed C–C bond lengths in **3**, which is defect-free, and in **5**–**7**, which contain defects. These bond lengths were obtained with the B3PW91/6-31G(d) procedure; this accounts for the slight difference in the C(H)–C(H) value for **3** from that given earlier, which came from B3LYP/6-311G(d,p) calculations [71]. The struc-

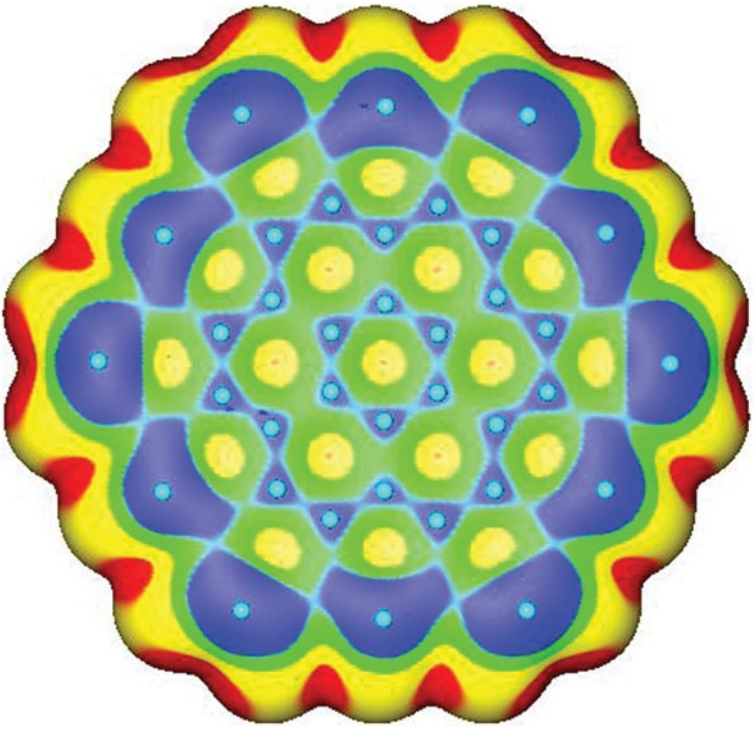


Fig. 9.2 Average local ionization energy $\bar{I}_S(\mathbf{r})$ on the 0.001 au surface of $C_{54}H_{18}$ (**4**), computed at the B3LYP/6-311G(d,p) level. Color ranges, in eV, are: *blue*, less than 10.1; *green*, between 10.1 and 11.0; *yellow*, between 11.0 and 12.0; *red*, more positive than 12.0. The locations of $\bar{I}_{S,min}$ with magnitudes less than 10.1 are indicated by *light blue* circles. The larger is the blue area around the circle, the lower is the $\bar{I}_{S,min}$ value

tures with the larger defects, **5** and **7**, have numerous nonequivalent C–C bonds, and their lengths range as high as 1.460 Å. The C(H)–C(H) bonds along the peripheries of **5**–**7** again tend to be relatively short, as are some of the interior C–C bonds. Among the latter, the shortest are the C_1–C_1 in **5**, which fuses two heptagons, and the C_1–C_1 in **7**, that fuses two pentagons; their lengths are 1.359 and 1.389 Å, respectively.

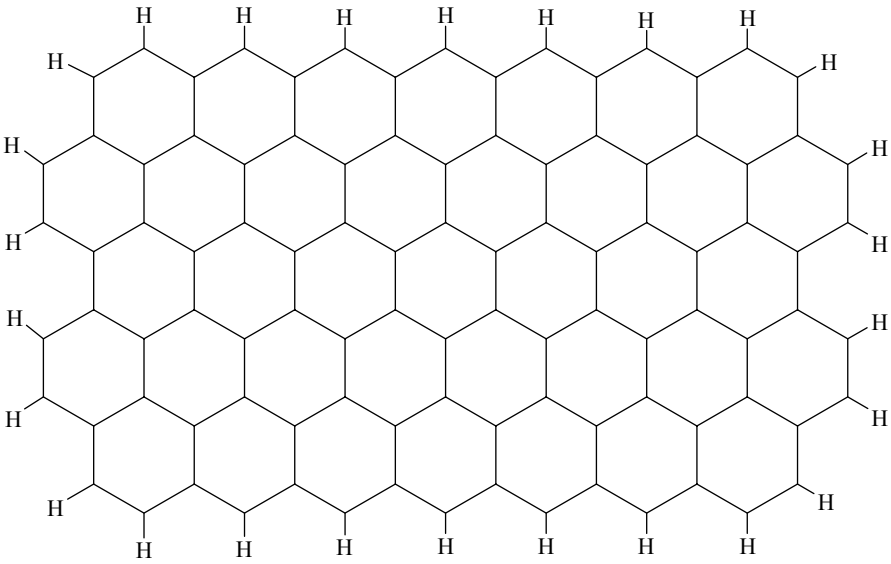
9.4 Reactive Sites and Initial Interactions on Pristine and Defect-Containing Model Graphene Systems

9.4.1 Locations of $\bar{I}_{S,min}$

Our approach for identifying the sites for initial interactions on graphene models is straightforward: we evaluate and plot the average local ionization energies $\bar{I}_S(\mathbf{r})$ on the 0.001 au surfaces of these systems, focusing upon their local minima, the $\bar{I}_{S,min}$.

As an example, Fig. 9.2 shows $\bar{I}_S(\mathbf{r})$ on the surface of the larger graphene model, **4**. The lowest $\bar{I}_{S,min}$, indicating the sites most reactive toward electrophiles and free radicals, are around the periphery of the system: above the centers of the C(H)–C(H) bonds ($\bar{I}_{S,min} = 8.85eV$) and above the C(H) carbons between the C(H)–C(H) bonds ($\bar{I}_{S,min} = 8.99eV$).

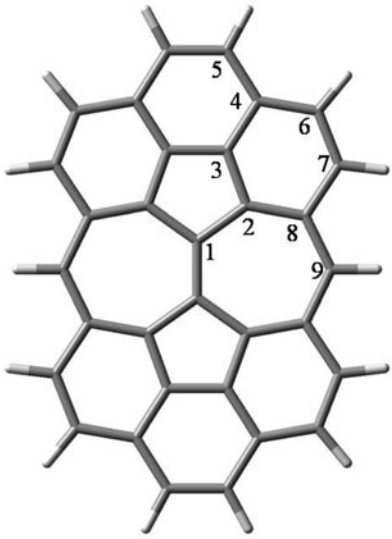
It has been shown earlier that polycyclic aromatic hydrocarbons have $\bar{I}_{S,min}$ above some peripheral C(H)–C(H) bonds and C(H) atoms [47, 71, 81, 82], and considerable experimental work, cited in these references, shows that these $\bar{I}_{S,min}$ are indicative of partial double bond and radical characters, respectively. The result is enhanced reactivities at these sites. Figure 9.2 indicates that this should be the case for graphene sheets as well, and this is supported by a recent study by Sharma et al. [83], who showed spectroscopically that the edges of a graphene sheet are at least twice as reactive as the interior toward a 4-nitrobenzene diazonium salt. As they point out, this can be quite significant for applications involving graphene ribbons. It should be noted that when graphene is modeled by a rectangular sheet (a graphene ribbon), such as **9**, two edges will have only the C(H)–C(H) sites and the other two only the C(H). Furthermore, a model system like **3** completely lacks the C(H).



9

It is gratifying that the carbons that we have designated as "interior" ones in the pristine models **3** and **4** (six in **3** and twenty-four in **4**) do all have $\bar{I}_{S,min}$ that are nearly uniform in magnitude, falling in a narrow range of 9.8–10.0 eV (Fig. 9.2). This supports the validity of using these carbons to represent those in the extended

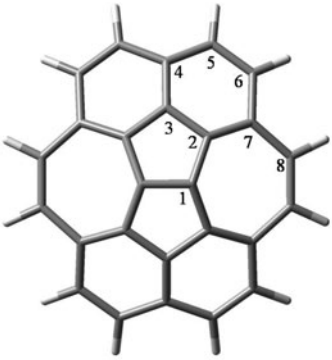
sheet of graphene. Our present interest is in the interior carbons of graphene systems, but since these are essentially equivalent for the defect-free, we will focus upon defect-containing ones.



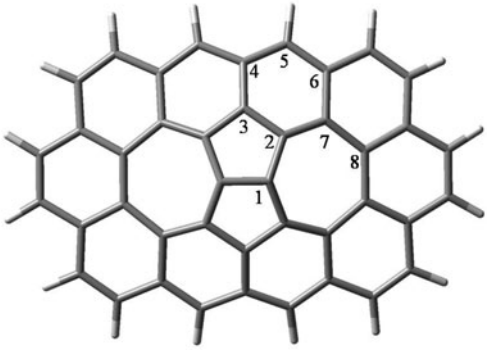
5

Where are the most reactive interior carbons in the planar Stone-Wales defect model **5**? Figure 9.3 answers this question; the lowest $\bar{I}_{S,min}$ are above the four equivalent C_2 positions at the junctions of five-, six- and seven-membered rings. These $\bar{I}_{S,min}$ have values of 9.46 eV. It is noteworthy that the lowest interior $\bar{I}_{S,min}$ on a (5,5) carbon nanotube model with a Stone-Wales defect were found to be at the analogous positions, the four carbons that are parts of five-, six- and seven-membered rings [84]. The only other interior $\bar{I}_{S,min}$ in **5** is over the C_1–C_1 bond fusing the two heptagons (10.16 eV), which is consistent with the shorter length of this bond (Table 9.1) and the inference of some double bond character. The interior carbon C_3 lacks an $\bar{I}_S(\mathbf{r})$ minimum (Fig. 9.3).

Proceeding to the nonplanar defect-containing models **6**–**8**, an important point to keep in mind is that nonplanar systems have two types of surfaces, the convex and the concave, as can be seen for **7** in Fig. 9.1. What we have found previously is that the $\bar{I}_{S,min}$ on the convex sides of these systems are lower in magnitude than those on the concave sides [73]. For **6**, the lowest interior $\bar{I}_{S,min}$ are on the convex side of the five equivalent interior carbons, with values of 9.24 eV; on the concave side, these carbons have no $\bar{I}_S(\mathbf{r})$ minima.



7



8

In Fig. 9.4 is the $\bar{I}_S(\mathbf{r})$ for inverse-Stone-Thrower-Wales defect model **7**. For both **7** and **8**, the lowest $\bar{I}_{S,min}$ are on the convex side carbons that fuse the two pentagons (the two C_1 carbons), 8.08 eV on **7** and 8.14 eV on **8**. The only other interior convex side $\bar{I}_{S,min}$ in **7** and the next lowest ones in **8** are at the two equivalent C_3 sites, 9.13 eV in **7** and 9.11 eV in **8**. Structure **8** also has interior convex side $\bar{I}_{S,min}$ with larger values at C_7 (9.68 eV) and C_8 (9.74 eV).

On the concave sides of structures **7** and **8**, there are no $\bar{I}_{S,min}$ at the C_1 carbons, but there are $\bar{I}_{S,min}$ at the interior C_2 and C_3 positions. Their magnitudes are 10.21 and 10.09 eV for **7** and 9.99 eV and 9.85 eV for **8**. Structure **8** also has $\bar{I}_{S,min}$ at the concave side C_8 positions, with values of 9.87 eV. Thus the concave side interior $\bar{I}_{S,min}$ in **7** and **8** are all higher than those on the convex side and are similar to the $\bar{I}_{S,min}$ of the interior carbons of pristine models **3** and **4** [71, 73].

A point of interest is that attempted hydrogenation at one of the concave side C_1 carbons of structures **6** and **7** (which lack $\bar{I}_{S,min}$) resulted in the structures inverting so that the hydrogens were positioned on the convex side of each [73]. It is anticipated that similar behavior would be found for **8**.

9.4.2 *Relationships of $\bar{I}_{S,min}$ and Interaction Energies*

Is there any relationship, within a particular system, between the the magnitudes of the $\bar{I}_{S,min}$ and interaction energies ΔE at these sites? This is one of the key issues in the work that is being discussed. In earlier studies, we have indeed observed a general correlation between interaction energies at sites within a given system and the magnitudes of the $\bar{I}_{S,min}$ at these sites. These studies included pristine graphene models **3** and **4** [71], a Stone-Wales defect-containing (5,5) nanotube model [84], a chlorinated pristine (5,5) nanotube model [85], and the inverse Stone-Thrower-Wales defect models **7** and **8** [73]. Overall, the ΔE become more negative—indicat-

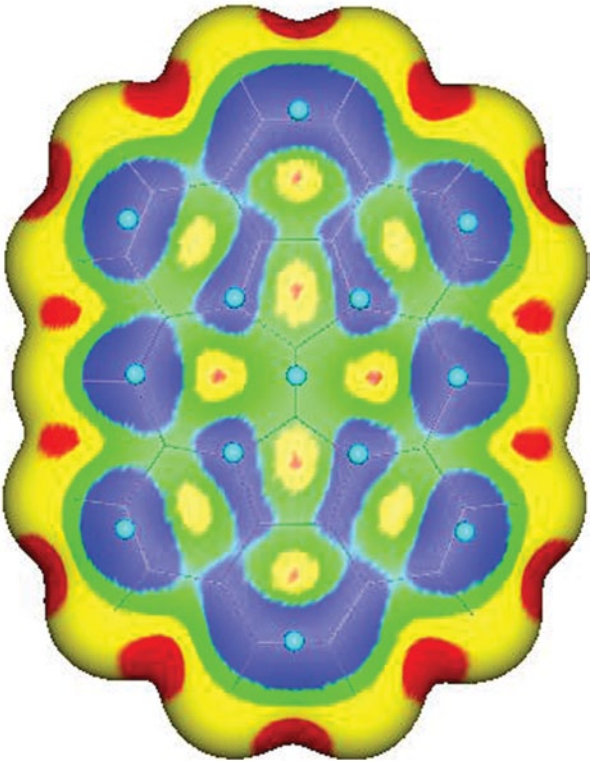


Fig. 9.3 Average local ionization energy $\bar{I}_S(\mathbf{r})$ on the 0.001 au surface of $C_{32}H_{14}$ (**5**), computed at the B3PW91/6-31G(d) level. Color ranges, in eV, are: *blue*, less than 10.1; *green*, between 10.1 and 11.0; *yellow*, between 11.0 and 12.0; *red*, more positive than 12.0. The locations of $\bar{I}_{S,min}$ with magnitudes less than 10.1 are indicated by *light blue* circles. The larger is the *blue* area around the circle, the lower is the $\bar{I}_{S,min}$ value

ing stronger binding—as the $\bar{I}_{S,min}$ decrease. We have also found that carbons lacking $\bar{I}_{S,min}$ are less favorable sites for interaction, and in some cases simply did not interact at all (computationally) [73, 84, 85]. In the discussion to follow, we shall focus specifically upon monohydrogenation, although we have also investigated fluorination [71, 84] and chlorination [85].

For defect-containing graphene models with more than one type of interior carbon, such as **5**, **7** and **8**, the hydrogenation energy at the site of the lowest interior $\bar{I}_{S,min}$ is more negative than at any other interior site [73]. For **5**, for example, the computed energy of hydrogenation at C_2 ($\bar{I}_{S,min} = 9.46$ eV) is −38.5 kcal/mol, while hydrogenation at interior site C_1 ($\bar{I}_{S,min} = 10.16$ eV) failed. Hydrogenation at the third interior site, C_3, did occur even though there is no $\bar{I}_{S,min}$, but the interaction is weaker ($\Delta E = -24.7$ kcal/mol) than at C_2.

Looking now at the group of models **3** and **5**–**8**, is there any relationship between the interaction energy at the site C* of the lowest $\bar{I}_{S,min}$ within each system and the magnitude of that $\bar{I}_{S,min}$? We see in Table 9.2 that there is a definite tendency for the energy of hydrogenation to become more negative as the $\bar{I}_{S,min}$ at that site decreases. This is shown in Fig. 9.5, which has a correlation coefficient R of 0.922.

Since $\bar{I}_S(\mathbf{r})$ data pertain to systems prior to interaction, our $\bar{I}_{S,min}$ cannot account for any effects that accompany or follow the interaction, such as additional strain or

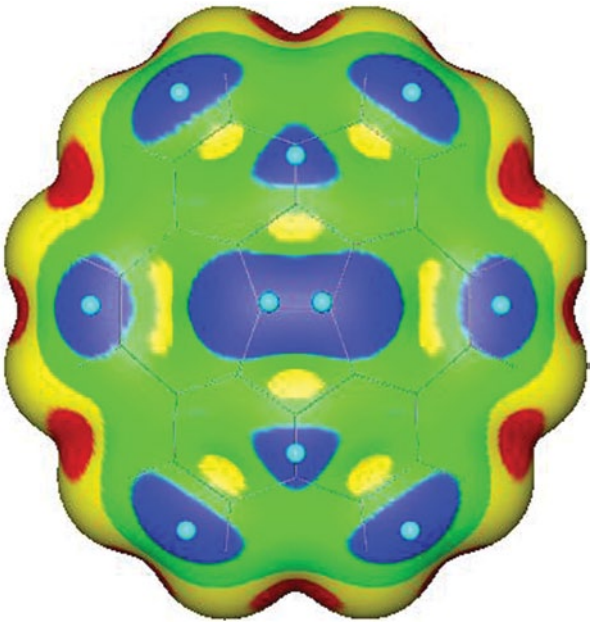


Fig. 9.4 Average local ionization energy $\bar{I}_S(\mathbf{r})$ on the convex side of the 0.001 au surface of $C_{26}H_{12}$ (**7**), computed at the B3PW91/6-31G(d) level. Color ranges, in eV, are: *blue*, less than 9.6; *green*, between 9.6 and 11.0; *yellow*, between 11.0 and 12.0; *red*, more positive than 12.0. The locations of $\bar{I}_{S,min}$ with magnitudes less than 9.6 are indicated by *light blue* circles. The larger is the *blue* area around the circle, the lower is the $\bar{I}_{S,min}$ value

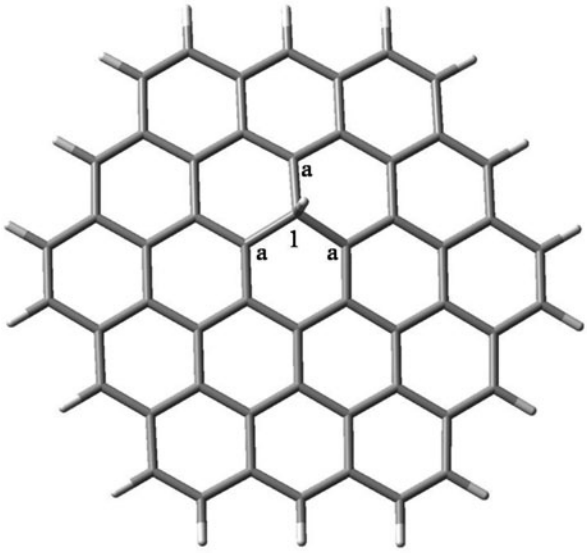
stabilization, interatomic repulsion, etc. [71, 73, 85]. One such effect of which we are aware is that the interaction distorts the geometry around the site C*. If the model was originally planar, the interaction results in a bulge at C*; if the model was already non-planar, the protrusion (as in Fig. 9.1) becomes greater. This can be seen from the sum of the C–C*–C bond angles before and after interaction that are given in Table 9.2. The importance that such effects can have is demonstrated very strikingly by expanding the relationship between ΔE and $\bar{I}_{S,min}$ for the models in Table 9.2 to include the sums of the C–C*–C angles before and after hydrogenation as variables in addition to $\bar{I}_{S,min}$. This takes into account the changes in geometry at the site due to the interaction. The average absolute deviation of the predicted and computed ΔE is now just 0.4 kcal/mol!

Finally, we point out that the trends in the values of the $\bar{I}_{S,min}$ are the same whether computed on surfaces defined by the 0.001 au contour of the electronic density or surfaces closer to the nuclei of the molecules, such as the 0.003 au and 0.005 au. This is shown in Table 9.3 for the lowest interior $\bar{I}_{S,min}$ on each of the models **3** and **5**–**8**.

9.5 Reactive Sites on Monohydrogenated Model Graphene Systems

What happens to $\bar{I}_S(\mathbf{r})$ when one of the interior carbons of **3**–**8** bears a hydrogen atom? This has been examined for **3** and **4** by Bulat et al. [71] and by Murray et al. for **6**–**8** [73]. Here we will summarize the highlights of their studies, along with our current results for **5**.

For planar models such as **3**–**5** it is most informative to look at $\bar{I}_S(\mathbf{r})$ on the side of the system that does not bear the initial hydrogen, because its presence obscures the nearby sites, at least on the 0.001 au molecular surface [71]. For example, Fig. 9.6 shows the $\bar{I}_S(\mathbf{r})$ of **4**, with one hydrogen bonded to it. This corresponds to structure **4-H** (see below); the hydrogen is at position C_1. On the sides without the hydrogens (in models **3-H**—**5-H**), the lowest values of $\bar{I}_S(\mathbf{r})$ are observed to be on the three carbons adjacent to the site of hydrogenation, indicating that these three carbons (labeled "a") have the most reactive electrons. See Fig. 9.6, lower plot, for **4-H**. These $\bar{I}_{S,min}$ are not visible in the upper plot of Fig. 9.6, which shows the side of **4-H** with the hydrogen.



4-H

The three most reactive sites in **4-H**, the "a" carbons, are *ortho* to C_1. It is noteworthy that the positions *meta* to C_1 on each of the three rings that share C_1 have no $\bar{I}_{S,min}$, while the carbons in the *para* positions have $\bar{I}_{S,min}$ similar to those of the interior carbons of pristine **4** [71].

This brings up a point to keep in mind when considering a graphene model. In coronene hydrogenated at a carbon C_1 in the central ring, designated **3-H**, two of the three adjacent carbons are interior and one is exterior, whereas in **4-H**, all three carbons adjacent to any central ring carbon are interior ones. **4** is accordingly preferable to **3** for modeling defect-free graphene interactions, if one wants to probe beyond the first hydrogenation. Similarly if the hydrogen in **5-H** is at C_2 (or C_3), then

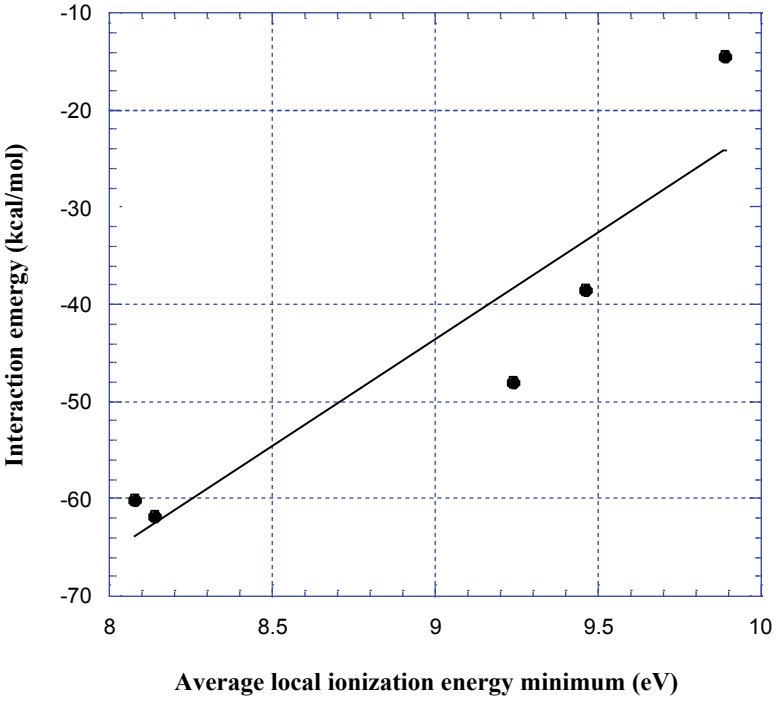


Fig. 9.5 Plot of interaction energy of hydrogenation at the site of the lowest interior $\bar{I}_{S,min}$ *vs.* computed $\bar{I}_{S,min}$ at these sites for the graphene model systems listed in Table 9.2. Correlation coefficient is 0.922

Table 9.2. Minimum average local ionization energy $\bar{I}_{S,min}$ at an interior carbon on 0.001 au surface of each of the systems **3** and **5**–**8**, and interaction energy ΔE at 0 K for hydrogenation at that site. Also included are the sums of the C–C*–C bond angles (where C* is the site of hydrogenation) before and after the interaction.[a] For the nonplanar models **6**–**8**, the $\bar{I}_{S,min}$ correspond to the convex sides

Model graphene	$\bar{I}_{S,min}$ (eV)	ΔE (kcal/mol)	∑ C–C*–C without H (degrees)	∑ C–C*–C with H (degrees)
3	9.89	−14.46	360.0	343.3
5	9.46[b]	−38.53[b]	360.0[b]	337.8[b]
6	9.24	−47.95	354.0	326.5
7	8.08	−60.06	346.0	317.3
8	8.14	−61.74	347.6	319.5

[a] The values in this table, except for those related to **5**, have been taken from reference 73. Computational level: B3PW91/6-31G*

[b] Present work

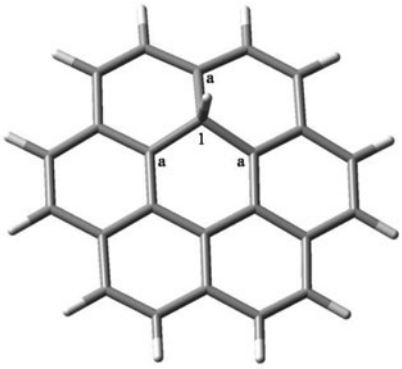
Table 9.3 Minimum average local ionization energy $\bar{I}_{S,min}$ at an interior carbon on 0.001 au, 0.003 au and 0.005 au surfaces of each of the systems **3** and **5**–**8**. For the nonplanar models **6**–**8**, the $\bar{I}_{S,min}$ correspond to the convex sides. In parentheses are the distances in Å from the carbon nucleus to the respective surfaces

Model graphene	$\bar{I}_{S,min}$ (0.001 au)	$\bar{I}_{S,min}$ (0.003 au)	$\bar{I}_{S,min}$ (0.005 au)
3	9.89 (1.97)	10.23 (1.68)	10.42 (1.55)
5[b]	9.46 (1.98)	9.79 (1.70)	9.98 (1.56)
6	9.24 (1.94)	9.57 (1.66)	9.73 (1.52)
7	8.08 (2.00)	8.44 (1.69)	8.63 (1.55)
8	8.14 (2.04)	8.52 (1.70)	8.71 (1.55)

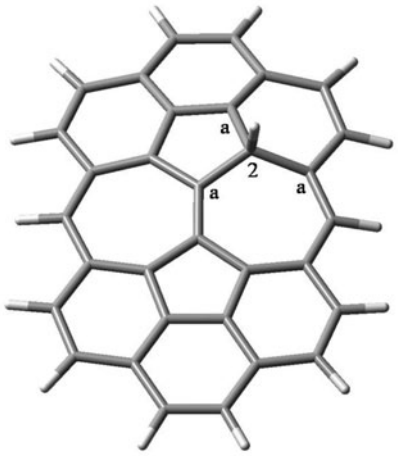
[a] The values in this table, except for **5**, have been taken from reference 73. Computational level: B3PW91/6-31G*

[b] Present work

one of the adjacent sites is an exterior carbon. Accordingly an extended model with additional hexagonal rings would be preferable to **5** for modeling a Stone-Wales defect system, if one plans to study second or further hydrogenation.



3-H



5-H

For the nonplanar models **6**–**8**, the $\bar{I}_S(\mathbf{r})$ of the monohydrogenated systems (**6-H**, **7-H** and **8-H**) can actually be viewed on the sides bearing the hydrogens, which are the convex sides, since the presence of the curvature allows one to see the carbons adjacent to the hydrogenated site [73]. The lowest interior $\bar{I}_{S,min}$ of **6-H**—**8-H** are again on adjacent carbons, the two adjacent ones in **6-H** and the adjacent C_1 in **7-H**

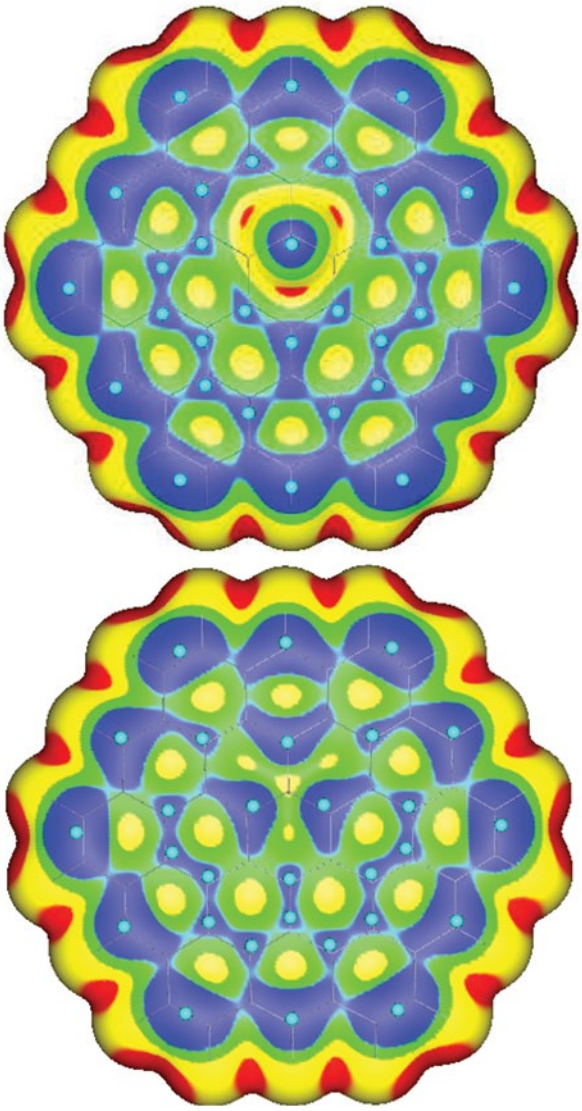


Fig. 9.6 Average local ionization energy $\bar{I}_S(\mathbf{r})$ on the 0.001 au surface of $C_{54}H_{19}$ (**4-H**), computed at the B3LYP/6-311G (d,p) level. The *top* view shows the side with an added hydrogen; the bottom shows the side without the hydrogen. Color ranges, in eV, are: *blue*, less than 10.1; *green*, between 10.1 and 11.0; *yellow*, between 11.0 and 12.0; *red*, more positive than 12.0. The locations of $\bar{I}_{S,min}$ with magnitudes less than 10.1 are indicated by *light blue* circles

and **8-H** [73]. For most of the monohydrogenated systems, the $\bar{I}_{S,min}$ at the forementioned adjacent interior sites (predicted to be the most reactive) are lower than the corresponding sites before hydrogenation.

9.6 Summary

The average local ionization energy $\bar{I}(\mathbf{r})$ has the very important practical advantage that its minimum values on molecular surfaces, the $\bar{I}_{S,min}$, can generally identify the most reactive sites in a system in a *single* calculation, that encompasses all possible sites. The $\bar{I}_{S,min}$ can also, in many instances, rank these sites. Furthermore using $\bar{I}(\mathbf{r})$ does not involve the undesirable feature of evaluating a small difference between large numbers, as does the interaction energy—another approach to the same objectives.

When plotted on pristine graphene models we find the interior carbons to all have $\bar{I}_{S,min}$ of similar magnitudes. However on defect-containing models, some of the interior carbons have $\bar{I}_{S,min}$ and others do not. Our analyses have shown interaction energies for hydrogenation at interior carbons of defect-containing model graphenes correlate with the $\bar{I}_{S,min}$ at these sites. Furthermore, we are able to show a relationship between the magnitude of the lowest interior $\bar{I}_{S,min}$ within each member of a series of pristine and defect-containing graphene models and the corresponding hydrogenation energies.

A limitation of $\bar{I}(\mathbf{r})$ that must be recognized is that it corresponds to the system *prior* to interaction, and cannot reflect factors that may accompany or follow it. Such factors may reinforce or oppose the predictions from the $\bar{I}_{S,min}$. Sometimes they can be anticipated and taken into account, as was shown in this chapter for the geometry changes resulting from hydrogentation. Considerable experience has shown, however, that the $\bar{I}_{S,min}$ can generally identify satisfactorily at least the most reactive sites—and can often rank the next ones as well.

References

1. Kroto HW, Heath JR, O'Brien SC, Curl RF, Smalley RE (1985) Nature 318:162–163
2. Krätschmer W, Lamb LD, Fostiropoulos K, Huffman DR (1990) Nature 347:354–358
3. Kadish KM, Ruoff RS (eds) (1996) Fullerenes: recent advances in the physics and chemistry of fullerenes and related materials. Electrochemical Society, Pennington
4. Iijima S (1991) Nature 354:56–58
5. Hargittai I (2010) Struct Chem 21:1151–1154
6. Harris PJF (1999) Carbon nanotubes and related structures. Cambridge University Press, Cambridge
7. Dresselhaus MS, Dresselhaus G, Avouris P (2001) Carbon nanotubes: synthesis, structure, properties and applications. Springer, Berlin
8. Politzer P, Murray JS, Lane P, Concha MC (2006) In: Balandin AA, Wang KL (eds) Handbook of semiconductor nanostructures and nanodevices, vol 2. American Scientific Publishers, Stevenson Ranch, Chap 7, pp 215–240
9. Dinadayalane TC, Leszczynski J (2006) In: Balbuena PB, Seminario JM (eds) Nanomaterials: design and simulation. Elsevier, Amsterdam, pp 167–199
10. Dinadayalane TC, Leszczynski J (2010) Struct Chem 21:1155–1169
11. Cotton FA, Wilkinson G (1980) Advanced inorganic chemistry, 4th ed. Wiley-Interscience, New York (Sect. 11-1)
12. Lide DR (ed) (1997) Handbook of chemistry and physics, 78th ed. CRC Press, Boca Raton

13. Bondi A (1964) J Phys Chem 68:441–451
14. Novoselov KS, Geim AK, Morozov SV, Jiang D, Zhang Y, Dubonos SW, Grigorieva IV, Firsov AA (2004) Science 306:666–669
15. Katsnelson MI (2007) Mater Today 10:20–27
16. Flynn GW (2011) J Chem Phys 135:50901(1–8).
17. Novoselov KS, Geim AK, Morozov SV, Jiang D, Katsnelson MI, Grigorieva IV, Dubonos SV, Firsov AA (2005) Nature 438:197–200
18. Bolotin KI, Sikes KJ, Hone J, Stormer HL, Kim P (2008) Phys Rev Lett 101:96802–96804
19. Castro Neto AH, Guinea F, Peres NMR, Novoselov KS, Geim AK (2009) Rev Mod Phys 81:109–162
20. Bae S, Kim H, Lee Y, Xu X, Park J-S, Zheng Y, Balakrishnan J, Lei T, Kim HR, Song Y II et al (2010) Nat Nanotech 5:574–578
21. Serrano J, Bosak A, Arenal R, Krisch M, Watanabe K, Taniguchi T, Kanda H, Rubio A, Wirtz L (2007) Phys Rev Lett 98:95503–95504
22. Kang HS (2005) J Am Chem Soc 127:9839–9843
23. Schedin F, Geim AK, Morozov SV, Hill EW, Blake P, Katsnelson MI, Novoselov KS (2007) Nature Mater 6:652–655
24. Rangel NL, Seminario JM (2010) J Chem Phys 132:125102(1–4)
25. Yavari F, Koratkar N (2012) J Phys Chem Lett 3:1746–1753
26. Meyer JC, Chuvilin A, Algara-Siller G, Biskupek J, Kaiser U (2009) Nano Lett 9:2683–2689
27. Cabria I, López MJ, Alonso JA (2005) J Chem Phys 123:204721(1–9)
28. Denis PA (2011) Comput Theor Chem 974:21–25
29. nanotechweb.org, http://nanotechweb.org/cws/article/tech/39191.
30. Oubal M, Picaud S, Rayez M-T, Rayez J-C (2012) Comput Theor Chem 990:159–166
31. Chigo Ahota EC, Escobedo-Morales A, Salazar Villanueva MS, Vázquez-Cuchillo O, Rubio Rosas ER (2013) J Mol Model 19:839–846
32. Dikin DA, Stankovich S, Zimney EJ, Piner RD, Dommett GHB, Evmenenko G, Nguyen ST, Ruoff RS (2007) Nature 448:457–460
33. Luo Z, Yu T, Kim K, Ni Z, You Y, Lim S, Shen Z (2009) ACS Nano 3:1781–1788
34. Dai J, Yuan J, Giannozzi P (2009) Appl Phys Lett 95:232105(1–3)
35. Johnson JJ, Behnam A, Pearton JJ, Ural A (2010) Adv Mater 22:4877–4880
36. Burgess JS, Baldwin JW, Robinson JT, Bulat FA, Houston BH (2011) In: Nelson DJ, Brammer CN (eds) Fluorine-related nanoscience with energy applications, vol 1064. ACS Symposium Series, pp 11–30
37. Burgess JS, Matis BR, Robinson JT, Bulat FA, Perkins FK, Houston BH, Baldwin JW (2011) Carbon 49:4420–4426
38. Casolo S, Lovvik OM, Martinazzo R, Tantardini GF (2009) J Chem Phys 130:54704(1–10)
39. Denis PA, Iribarne F (2009) J Mol Struct (Theochem) 907:93–103
40. Teillet-Billy D, Rougeau N, Ivanovskaya VV, Sidis V (2010) Int J Quantum Chem 110:2231–2236
41. Ghosh A, Rao KV, Voggu R, George SJ (2010) Chem Phys Lett 488:198–201
42. Nava Contreras C, Hernandez Cocoletzi H, Chigo Anota E (2011) J Mol Model 17:2093–2097
43. Šljivančanin Ž, Balog R, Hornekaer L (2012) Chem Phys Lett 541:70–74
44. Stone AJ, Wales DJ (1986) Chem Phys Lett 128:501
45. Crespi VH, Benedick LX, Cohen ML, Louie SG (1996) Phys Rev B 53:R13303
46. Sjoberg P, Brinck T, Murray JS, Politzer P (1990) Can J Chem 68:1440–1443
47. Politzer P, Murray JS, Bulat FA (2010) J Mol Model 16:1731–1742
48. Koopmans TA (1934) Physica 1:104–113
49. Nesbet RK (1965) Adv Chem Phys 9:321–363
50. Nagy Á, Parr RG, Liu S (1996) Phys Rev A 53:3117–3121
51. Gál T, Nagy Á (1997) Mol Phys 91:873–880
52. Ghosh SK, Balbás LC (1985) J Chem Phys 83:5778–5783
53. Ghosh SK, Berkowitz M, Parr RG (1984) Proc Natl Acad Sci USA 81:8028–8031

54. Ayers PW, Parr RG, Nagy Á (2002) Int J Quantum Chem 90:309–326
55. Bulat FA, Levy M, Politzer P (2009) J Phys Chem A 113:1384–1389
56. Politzer P, Shields ZP-I, Bulat FA, Murray JS (2011) J Chem Theor Comput 7:377–384
57. Ayers PW, Nagy Á (2007) J Chem Phys 126:144108(1–6)
58. Bader RFW, Carroll MT, Cheeseman JR, Chang C (1987) J Am Chem Soc 109:7968–7979
59. Politzer P, Abu-Awwad F, Murray JS (1998) Int J Quantum Chem 69:607–613
60. Bulat FA, Toro-Labbé A, Brinck T, Murray JS, Politzer P (2010) J Mol Model 16:1679–1691
61. Murray JS, Brinck T, Politzer P (1992) J Mol Struct (Theochem) 255:271–281
62. Politzer P, Murray JS, Concha MC (2002) Int J Quantum Chem 88:19–27
63. Politzer P, Murray JS, Lane P, Concha MC (2006) In: Sokalski WA (ed) Molecular materials with specific interactions: modeling & design. Springer, London, Chap 5
64. Politzer P, Bulat FA, Burgess J, Baldwin JW, Murray JS (2013) In: Sukumar N (ed) A matter of density. Wiley, Hoboken, Chap 9
65. Politzer P, Murray JS, Lane P, Concha MC, Jin P, Peralta-Inga Z (2005) J Mol Model 11:258–264
66. Politzer P, Murray JS, Concha MC (2007) In: Seminario JM (ed) Molecular and nano electronics: analysis, design and simulation. Elsevier, Amsterdam
67. Xiao D, Bulat FA, Yang W, Beratan D (2008) Nano Lett 8:2814–2818
68. Murray JS, Politzer P (2011) WIREs Comp Mol Sci 1:153–163
69. Hernández Rosas JJ, Ramirez GRE, Escobedo-Morales A, Chigo Anota E (2011) J Mol Model 17:1133–1139
70. Wang Y, Qian HJ, Morokuma K, Irle S (2012) J Phys Chem A 116:7154–7160
71. Bulat FA, Burgess JS, Matis BR, Baldwin JW, Macaveiu L, Murray JS, Politzer P (2012) J Phys Chem A 116:8644–8652
72. Baskin Y, Meyer I (1955) Phys Rev 100:544
73. Murray JS, Shields ZP-I, Lane P, Macaveiu L, Bulat FA (2013) J Mol Model 19:2825–2833
74. Barth WE, Lawton RG (1966) J Am Chem Soc 88:380–381
75. Hedberg L, Hedberg K, Cheng P-C, Scott LT (2000) J Phys Chem A 104:7689–7694
76. Slayden SW, Liebman JF (2001) Chem Rev 101:1541–1566
77. Scott LT, Bronstein HF, Preda DV, Ansems RBM, Bratchen MS, Hagen S (1999) Pure Appl Chem 71:209–219
78. Lusk MT, Carr DC (2008) Phys Rev Lett 100:1–4
79. Lusk MT, Carr DC (2009) Phys Rev Lett 47:2226–2232
80. Lusk MT, Wu DT, Carr DC (2010) Phys Rev B 81:1–9
81. Murray JS, Abu-Awwad F, Politzer P (2000) J Mol Struct (Theochem) 501–502:241–250
82. Peralta Z, Murray JS, Grice ME, Boyd S, O'Connor CJ, Politzer P (2001) J Mol Struct (Theochem) 549:147–158
83. Sharma R, Baik JH, Perera CJ, Strano MS (2010) Nano Lett 10:398–405
84. Dinadayalane TC, Murray JS, Concha MC, Politzer P (2010) J Chem Theory Comp 6:1351–1357
85. Saha S, Dinadayalane TC, Murray JS, Leszczynska D, Leszczynski J (2012) J Phys Chem C 116:22399–22410

Chapter 10
Moiré Patterns Observed in Bi Layer Graphene Irradiated with High Energetic Protons

D. H. Galvan, A. Posada Amarillas, S. Mejía, C. Wing and M. José-Yacamán

Abstract Customarily, it is likely that irradiated graphene yield indication of perturbations induced by irradiation. High Resolution Transmission Electron Microscopy (HRTEM) analysis has been performed on proton irradiated graphene. The analysis indicates the existence of Moiré patterns produced by the rotations induced by the irradiation in between planes. The rotations measured fluctuate between 3 and 5 degrees respectively. These rotations may influence the electronic properties of the material under investigation. In order to explain the observed rotations in between planes, theoretical analysis were performed under the scheme of extended Hückel tight-binding method. Average total energy of the system was careful analyzed throughout the experiment composed of two graphene layers with two carbon vacancies and then the replaced carbons were intercalated in between the two layers. The results obtained indicate that the system remain semi metallic. Moreover, the theoretical results yielded that the 3 degree rotation is favored, although the 5 degree rotation is not discarded. Furthermore, energy bands as well as total and projected DOS were performed in order to provide more information about the electronic changes induced by the rotations applied to the system.

D. H. Galvan (✉)
Centro de Nanociencias y Nanotecnología—Universidad Nacional Autónoma de México,
Apartado Postal 2681, CP 22800 Ensenada, BC, México
e-mail: donald@cnyn.unam.mx

P. O. 439036, 92143, San Ysidro, CA, USA

A. P. Amarillas
Departamento de Investigación en Física, Universidad de Sonora,
Apartado Postal 5-088, CP 83190 Hermosillo, SON, México

S. Mejía
Facultad de Ciencias Físico-Matemáticas, Universidad Autónoma de Nuevo León,
CP 66451 San Nicolas de los Garza, NL, México

D. H. Galvan · M. José-Yacamán
Department of Chemical Engineering and International Center for Nanotechnology
& Advanced Materials, University of Texas at Austin, Austin, TX 78712, USA

C. Wing
Instituto Nacional de Energía Nuclear, Ocoyoacac, Estado de México, México

J. M. Seminario (ed.), *Design and Applications of Nanomaterials for Sensors,*
Challenges and Advances in Computational Chemistry and Physics 16,
DOI 10.1007/978-94-017-8848-9_10, © Springer Science+Business Media Dordrecht 2014

10.1 Introduction

The study of radiation damage was extensively studied in the past because the interest in fission reactors. Recently, a renewed interest in radiation damage studies has been driven by the need to expand new sources of energy and avoid environmental effects of hydrocarbons. Indeed, the development of advanced nuclear reactors is linked to the development of materials capable to operate under higher irradiation fluxes [1, 4, 5, 9, 16, 26].

Graphene is the name given to a monolayer of carbon atoms packed in a two dimensional honeycomb lattice. This system shows a peculiar effect, reminiscent of a Relativistic Quantum Hall effect [20], which trigger the scientific curiosity for the fundamental physics behind its behavior. Graphene showed unusual properties derived from its reduced dimensionality as well as its small size, which yielded an enormous potential to be used in ultra fast electronic transistors and switches.

Graphene shows a very high conductivity and an unusual Hall Effect.

In order to form a single hexagonal sheet of graphene, it could be built by means of two intercalated networks A and B, added to the interaction with the conduction electrons (electrons or holes) of each atom, create a new *quasi-particle* with special characteristics that they carry charge but without mass. These characteristics permit the *quasi* particle to travel inside the lattice, with a velocity of the order of 300 times less than the velocity of light and at the same times, without dispersion.

In this work we undertake the study of graphite in the form of HOPG (Highly Oriented Pyrolytic Graphite) subject to a highly energetic proton beam. It has been shown before [3, 7, 10], that irradiation of HOPG using a high flux electron beam, produces breaking of the basal plane, disordering and even some tilt in the sample. In this case the main radiation damage is produced by the electron beam. In the present case, we used a proton beam of 5 MeV and a total dose of 2.4×10^8 Gy. The samples are then studied by Scanning Transmission Electron Microscopy (STEM) methods, which have minimum additional radiation. In particular we used bright field images in the STEM mode.

We found that as result of the irradiation, the graphene layers on the surface are rotated along an axis perpendicular to the graphite basal plane. Moreover, a rotation of about three degrees is often observed. We calculated energy bands and density of states of the rotated layer, and found some changes of the electronic properties of graphene.

10.2 Experimental Methods

Gold nanoparticles passivated with 1-dodecanethiol were synthesized by the Brust method reported elsewhere [8, 13]. Three milligrams of the passivated gold particles were mixed with 100 mg of graphite in 0.5 mol of toluene and then mounted over a brass sample holder. The solvent was allowed to evaporate until a dry pellet of the sample was formed.

Samples were irradiated in an EN Tandem Van de Graaff accelerator, with a proton beam of 5 MeV. The beam was oriented along the basal plane of the sample, and total dose of 2.4×10^8 Gy. was used. Afterwards, samples were cleaved using a scotch tape until an electron transparent film was obtained [19, 20]. Optical methods were used to verify the sample thickness. Then the sample was placed on a lacey carbon copper grid for transmission electron microscopy (TEM) analysis. The samples were analyzed using a JEOL 2010 F and Tecnai microscopes equipped with a Schottky-type field emission gun, ultra-high resolution pole piece (Cs = 0.5 mm), and an Scanning-Transmission (STEM) unit with a high angle annular dark field detector (HAADF) operating at 200 kV. A Gatan CCD camera was used for image acquisition. Images were obtained either, using an annular aperture in the STEM mode or in the HRTEM using the optimum focus condition. HRTEM simulated images were obtained using multi slice calculations.

10.3 Theoretical Calculations

The calculations were carried out by means of the tight-binding method [27] within the Extended Hückel [14] framework using YAeHMOP computer package [12, 18]. It is good to stress that the Extended Hückel method is a semi empirical approach for solving Schrödinger equation for a system of electrons, based on the variational theorem. In this approach, explicit electron correlation is not considered except for the intrinsic contributions included in the parameter set which were obtained from S. Alvarez et al. [2] or from the most accurate *ab initio* calculations. The calculations were performed in the supercomputer Altix 350 using the input files accordingly to each specific case.

These calculations were performed on a system selected as a repeated cluster originated from a super cell. The super cell was generated from an infinite single sheet of carbon atoms, as depicted in Fig. 10.1a, which aroused from crystalline graphite using the following primitive vectors: a = 2.456 Å, c = 6.696 Å, space group 186 [15].

To prepare our theoretical *sample*, an infinite hexagonal honeycomb arrangement of carbon atoms were considered as depicted in Fig. 10.1a. To make the calculations simpler, a graphite single sheet made of 40 carbon atoms as depicted in Fig. 10.1b were considered and in which 2 carbon atoms (3 and 13) were removed, as it would be a likely case of the effect of the proton irradiated beam on the sheet of carbon atoms. Moreover, these two carbon atoms were located at a distance of 1.67 Å from the top layer and intercalated in between the second sheet, following a duplication of the second sheet and constructed of 40 carbon atoms in the AA configuration in order to create the 2 L-graphene. The former configuration was made with the purpose of simulating a *real* scenario if 2L-graphene were subjected to proton irradiation.

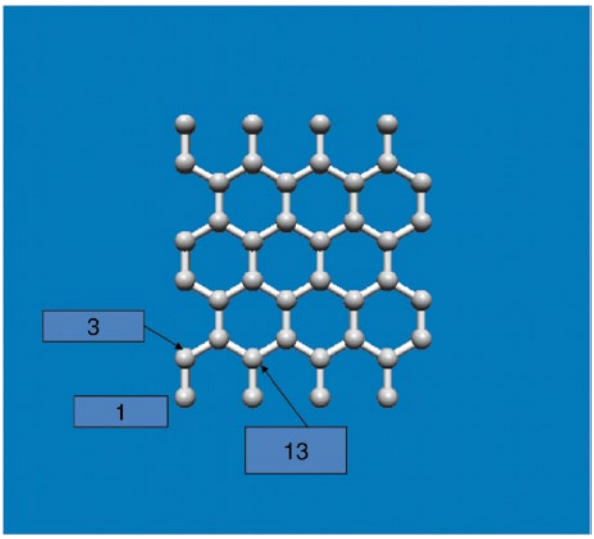


Fig. 10.1 **a** Band structure calculations for graphene 2-L, with two carbon vacancies intercalated in between layers. **b** Band structure calculations for graphene 2-L, with vacancies and intercalated. One of the layers (surface) has been rotated by three degrees

10.4 Results and Discussion

The samples of proton irradiated graphene were observed using TEM. A typical image is observed in Fig. 10.2a. A disordered structure can be observed. The structure can be revealed using micro diffraction. The nano diffraction mode of the microscope was used to obtain the patterns of different regions; a typical pattern is shown in Fig. 10.2b. As it is possible to see, the pattern is formed by two rotated hexagonal arrays of spots. The most common average angle was 3 degrees. In a few cases a larger rotation of ~ 5 degrees was observed.

Several groups [17, 21, 24, 25, 29] have reported that by using Scanning Tunneling Microscopy on carbon samples superlattices which they related to be Moiré patterns. On the other hand Rong et al. [24, 25] reported that by STM a hexagonal superlattice which show that it could be related to be a Moiré produced by the rotation of the top most plane with respect to the other layer. The rotation reported was 2.1. Furthermore, Xhie et al. [29] reported anomalous super lattices on (HOPG) using STM. They attributed that the periodic features reported may be caused to Moiré patterns due to rotations of one plane of the crystal with respect to the underlying graphite single crystal. The reported angle of rotation in between planes was of the order of 3.5.

Figure 10.1a shows a simulated image of the disordered layer. A very well defined Moiré pattern is observed. The micro diffraction image of two layers rotated by 3 degrees is shown in Fig. 10.1b. A very good agreement with the experiment is obtained. HAADF-STEM images to estimate the thickness of the disordered layers was used. Indeed the intensity of this type of images depends on the mass-thickness of the sample, and is mainly due to thermal Diffuse Scattering. The intensity has an approximate dependence of the atomic number $\sim Z^{1.7}$ [22]. Regions near the edge of the sample consisted in few layers of graphene was estimated.

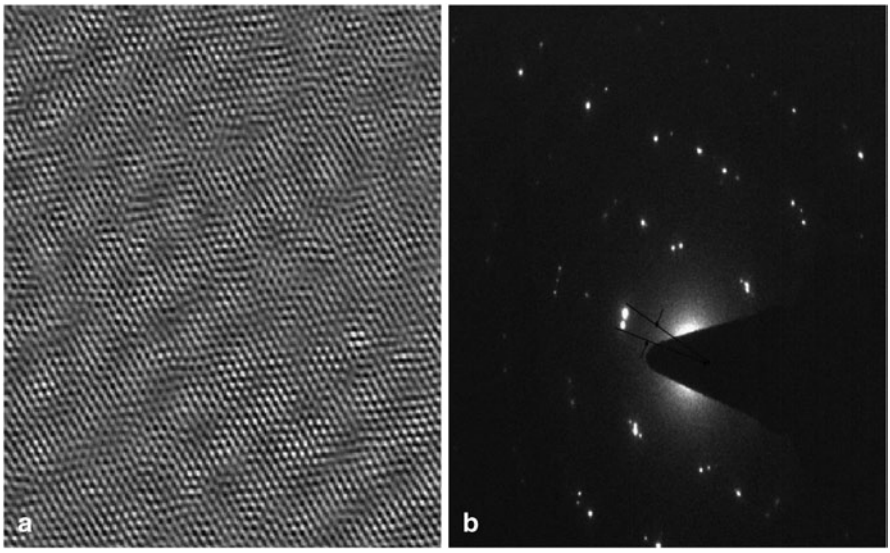


Fig. 10.2 **a** HRTEM micrograph for HOPG samples. **b** Diffraction patterns for the same material

In order to explain the results, we considered that the main damage produced by the protons is due to knock-on atom displacements [4]. A threshold energy of about 15–20 eV was estimated by Banhart et al. [4]. As a result of the high energy irradiation vacancies and interstitials will be formed. The mobility of the vacancies is low enough as to prevent rapid recombination.

In order to explain the diffraction patterns in 2-L rotated graphene with two carbon vacancies and intercalated in between layers (from now, this structure will be called as graphene 2-L), it proceed in the following way: Considering the average total energy of the system without rotation and after the rotation was applied, and taking into consideration that one of the layers is maintained fixed while the other layer is rotated by the appropriate amount around atom 1, see Fig. 10.3b. It is assumed that the interstitials are located between the layers and located 1.64 Å from the top layer, rather than in the graphene plane.

Band structure calculations for 2-L unrotated graphene, 2-L graphene with applied rotatations by 3 and 5 , were calculated using 51 k-points for each case, and sampling the First Brillouin zone (FBZ) as depicted in Fig. 10.4a, b.

Atomic parameters for carbon atom used through the calculations were obtained from Alvarez et al. [2] and provided in Table 10.1. Experimental lattice parameters instead of optimized values were used searching for a best matching of our theoretical results with the available experimental information

The inset in Fig. 10.4 depicts the Wigner-Seitz cell for a hexagonal configuration used in the calculations. The Fermi level is indicated by a horizontal dotted line separating the valence band (VB) from the conduction band (CB) respectively. Energy in eV *vs* k-values (in the reciprocal space) were plotted for each case, ranging from Γ (0 0 0) to M (1/2 0 0) to K (1/3 1/3 0) of $(4/\sqrt{3})^*$ (π/a).

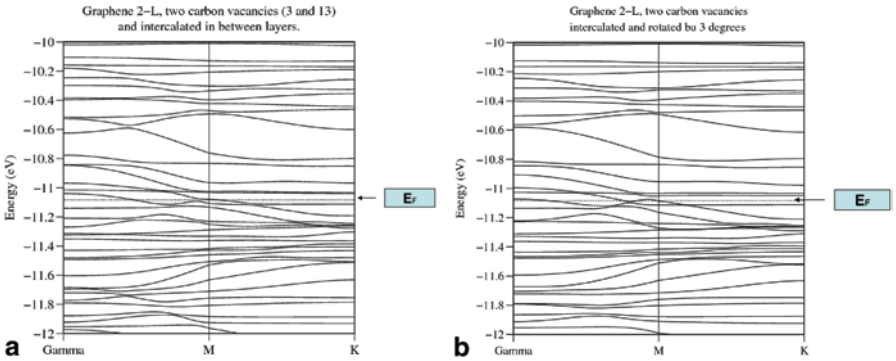


Fig. 10.3 A cell made out of 40 carbon atoms per layer was constructed

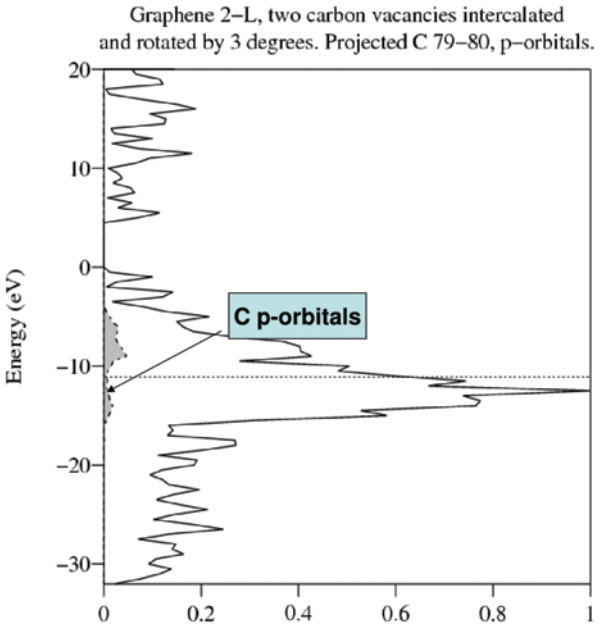


Fig. 10.4 Total and projected DOS for graphene 2-L, with vacancies and intercalated. The surface had been rotated by 3 degrees. Projected C 79–80 p-orbitals

Table 10.2 provides information about the structure, Fermi energy location and average total energy (eV). First, notice that for graphene 2-L unrotated, the average total energy is −5600.6454 eV and looking at Fig. 10.4a, the system has a semi metallic behavior due that two degenerate bands overlap at the E_f. Secondly, Fig. 10.4b provides the energy bands when one of the layers (the one that we shall call *surface* which contains the two carbon vacancies) had been rotated by 3 degrees, the system behaves as a semi metal, also with three bands overlapping at the Fermi energy and with an average total energy of −5600.9678 eV, similar to the unrotated case, which indicates that the rotation applied was not severe enough as to maintain the

Table 10.1 Atomic parameters used in the extended Hückel tight-binding calculations, H_{ii} (eV) and ς (Valence orbital ionization potential and exponent of Slater type orbitals). Each exponent is followed by a weighting coefficient in parentheses. A modified Wolfsberg-Helmholtz formula was used to calculate H_{ij} [28]

Atom	Orbital	H_{ii}	ς_{i1}	C_1	ς_{i2}	C_2
C	2s	−21.4	1.62			
	2p	−11.40	1.62	0.0000	0.0000	0.0000

Table 10.2 Structure, Fermi energy (eV) and Total average energy (eV) for the structures analyzed

Structure	Fermi energy (eV)	Total average enegy (eV)	Behavior
Graphene 2-L nonrotated	E_f=−11.2834	−5622.2462	Semi metallic
Graphene 2-L with vacancies and intercalated	E_f=−11.0834	−5600.6454	Semi metallic
Graphene 2-L with vacancies, intercalated and rotated by 3°	E_f=−11.1004	−5600.9678	Semi metallic
Graphene 2-L with vacancies, intercalated and rotated by 5°	E_f=−11.1587	−5601.9677	Semi metallic

system in a similar space group as the original one, favoring these rotated states. Furthermore, in the case when the applied rotation to the surface was 5 degrees, the system still is in the semi metallic state, but the total energy is of the order of −5601.9677 eV, different to the unrotated and 3 degrees rotation applied. This indicates that the rotation applied was severe enough as to break the original space group producing states which are less likely favored.

Total and projected density of states (PDOS) for graphene 2-L with two carbon vacancies (3 and 13) intercalated, when C 1 to 8 p-orbitals (for brevity) had been projected and depicted in Fig. 10.5a, it is necessary to point out that, it has been shown only the projection regarding to those atoms. Solid line represents total DOS (density of states), while the hatched dotted lines are the selected projected DOS for each orbital of the selected atoms. Horizontal dotted line indicates the Fermi level. Furthermore, concentration on those orbitals from the atoms which contributes most to the total DOS in the vicinity of E_f was considered because they manifest their electronic behavior preferentially around that area. Notice that the main contribution to the total DOS comes from carbon π-contributions. It is necessary to stress that if all contributions from all the 78 carbon atoms were added, it will reproduce the total DOS (solid line). On the other hand Fig. 10.5b yield information regarding graphene 2-L with two carbon vacancies (3 and 13) intercalated and then rotated (the surface layer) by 3^0 rotation, when C 1 to 8 π-contributions (for brevity) had been projected notice small differences, when compared to the

unrotated case, could be detected in the total DOS, but the overall contribution from the π-contributions are almost the same. These small differences could be attributed to the strain induced by rotation of one of the layers.

Moreover, Fig. 10.5c yielded information regarding carbon 79 and 80 (two carbon atoms displaced from the original location and intercalated in between the two layers). Notice that the π-contributions are negligible contributions to the total DOS at the Fermi level.

Due that the effect of rotation in between planes of graphene was considered, the effect is similar to the nanotubes subjected to distortion as reported by Rochefort et al. [23] they reported the effect of structural distortions of armchair carbon nanotubes on their electronic properties. One of the effects produced is to open of band gaps at some symmetric point of the FBZ, especially at the K point of the reciprocal space. The observed band gap was due to the asymmetric compression and dilation of the C-C bonds along NT. Moreover, they also reported that whenever they plot band gap *vs* twisting angle a maximum band gap of 0.6 eV occurred at 15 degrees

10.5 Conclusions

By comparing experimental results with quantum chemical calculations at the semi empirical level, it has been possible to explain that the disordered structures observed in proton irradiated graphene are due to rotation in the graphene honeycomb network. The calculations shown that the rotation of 3 degrees is favored producing a semi metallic behavior of the material in agreement to experimental results.

References

1. Ajayan PM, Ebbesen T (1997) Nanometric-size tubes of carbon. Rep Prog Phys 60(10):1025–1062
2. Alvarez S (March 1993) Tables of parameters for extended Hückel calculations. Universitat de Barcelona
3. Banhart F (1997) The transformation of graphitic onions to diamond under electron irradiation. J Appl Phys 81(8):3440–3445
4. Banhart F (1999) Irradiation effects in carbon nanostructures. Rep Prog Phys 62(8):1181–1221
5. Banhart F, Füller T, Redlich Ph, Ajayan PM (1997) The formation, annealing and self-compression of carbon onions under electron irradiation. Chem Phys Lett 269(3–4):349–355
6. Berger C, Song Z, Li T, Li X, Ogbazghi AY, Feng R, Dai Z, Marchenov AN, Conrad EH, First PN, de Heer WA (2004) Ultrathin epitaxial graphite: 2D electron gas properties and a route toward graphene-based nanoelectronics. J Phys Chem B 108(52):19912–19916
7. Berger C, Song Z, Li X, Wu X, Brown N, Naud C, Mayou D, Li T, Hass J, Marchenkov AN, Conrad EH, First PN, de Heer WA (2006) Electronic confinement and coherence in patterned epitaxial graphene. Science 312:1191–1196
8. Brust M, Walker M, Bethell D, Schiffrin DJ, Whyman R (1994) Synthesis of thiol-derivatised gold-nanoparticles, in a two-phase liquid-liquid system. J Chem Soc Chem Commun 801–802

9. Burden PA, Hutchison JL (1996) Real-time observation of fullerene generation in a modified electron microscope. J Cryst Growth 158(1–2):185–188
10. Burden PA, Hutchison JL (1997) An investigation of the electron irradiation of graphite in a helium atmosphere using a modified electron microscope. Carbon 35(4):567–578
11. Geim AK, Novoselov KS (2007) The rise of graphene. Nat Mater 6:183–191
12. Glassey WV, Papoian GA, Hoffmann R (1999) The energy partition within one-electron formalism: a Hamiltonian population of study surface-CO interaction in the c(2 × 2)-CO/Ni (100) chemisorption system. J Chem Phys 111(3)893–910
13. Gutierrez-Wing C, Santiago P, Ascencio JA, Camacho A, José-Yacamán M (2000) Self-assembling of gold nanoparticles in one, two and three dimensions. Appl Phys A, Mater Sci Process 71(3):237–243
14. Hoffmann R (1963) An extended Huckel theory. I. Hydrocarbons. J Chem Phys 39(6):1397–1412
15. Hoffmann U, Wilm DZ (1936) The crystal structure of graphite. Elektrochem 42:42
16. Koike J, Pedraza DF (1994) Dimensional changes in highly oriented pyrolytic graphite due to electron irradiation. J Mater Res 9(7):1899–1907
17. Kuwara M, Clarke DR, Smith DA (1990) Anomalous superperiodicity in scanning tunneling microscope images of graphite. Appl Phys Lett 56(24):2396–2398
18. Landrum GA The YAeHMOP package is freely available on www at: http://overlap.chem.Cornell.edu:8080/yaehmop.html. F orbitals are included in the calculations as version 3.0x, using W. V. Glassey's routine
19. Novoselov KS, Geim AK, Morozov SV, Jiang D, Zhang Y, Dubonos SV, Grigorieva IV, Firsov AA (2004) Electric field effect in atomically thin carbon films. Science 306:666–669
20. Novoselov KS, McCann E, Morozov SV, Fal'ko FI, Katsnelson MI, Zeitler U, Jiang D, Schedine F, Geim AK (2006) Unconventional quantum Hall effect and Berry's phase of 2_{π} in bilayered graphene. Nat Phys 2(3):177–180
21. Osing J, Shvets IV (1998) Bulk defects in graphite observed with a scanning tunneling microscope. Surf Sci 417(1):145–150
22. Peng Y, Nellist PD, Pennycook SJ (2004) HAADF-STEM imaging with sub-angstrom probes: a full Bloch wave analysis. J Electron Microsc 53(3):257–266
23. Rochefort A, Avouris P, Lesage F, Salahub DR (1991) Electrical and mechanical properties of distorted carbon nanotubes. Phys Rev B 60:13824–13830
24. Rong ZY (1994) Extended modifications of electronic structures caused by defects: scanning tunneling microscopy of graphite. Phys Rev B 50:1839–1843
25. Rong ZY, Kuiper P (1993) Electronic effects in scanning tunneling microscopy: Moiré pattern on a graphite surface. Phys Rev B 48:17427–17431
26. Thrower PA, Mayer RM (1978) Point defects and self-diffusion in graphene. Phys Status Solidi a 47(1):11–37
27. Whangbo MH, Hoffmann R (1978) The band structure of tetracyanoplatinate chain. J Am Chem Soc 100(19):6093–6098
28. Wolfsberg MW, Helmholtz L (1952) The spectra and electronic structure of the tetrahedral ions MnO_4^-, CrO_4^-, and ClO_4^-. Chem Phys 20(5):837–843
29. Xhie J, Sattler K, Ge M, Venkateswaran N (1993) Phys Rev B 47:15835–15841

Chapter 11
Theoretical Study of bi Layer Graphene used as Gas Detector

Diana Barraza-Jimenez, M. A. Flores-Hidalgo and D. H. Galvan

Abstract A theoretical study was performed in a bilayer graphene when a CO molecule was located over one sheet. The geometry was relaxed using Density Functional Theory with B97-D functional and 6-31G (d) basis set, both implemented in the Gaussian 09 computer package. In contrast to the infinite graphene sheet which is a zero-gap semiconductor. When irradiated with C^+ ions, the energy gap changes to 1.618 eV. While when the CO molecule is located above the circumcoronene, the HOMO-LUMO gap changes to 1.612 eV, an indication that the molecule had been adsorbed.

11.1 Introduction

It is generally accepted that for a detection method to be successful, it is mandatory to detect at least, one atom or molecule. The main reason for some detectors for not being able to achieve that level of sensitivity, is fluctuation due to thermal motions of charge and defects [3], which produces intrinsic noise exceeding the signal that is requested.

Solid state gas sensors are known for the high sensitivity that they operate [11]. Recently, a brand new gas detectors have been produced using carbon nanotubes and semiconductor nanowires [9, 2], which claim exceptional sensitivity detecting toxic gases in concentrations as low as 1 part in a billion.

D. H. Galvan (✉)
Centro de Nanociencias y Nanotecnología, Universidad Nacional Autónoma de México,
Apartado Postal 2681, C. P. 22800 Ensenada, BC, México
e-mail: donald@cnyn.unam.mx

P. O. 439036, San Ysidro, CA 92143, USA

D. Barraza-Jimenez
Centro de Investigación en Alimentación y Desarrollo, A. C. Unidad Delicias,
Av. 4ª Sur 3820, Fracc. Vencedores del Desierto, Cd. 33089 Delicias, Chih, México

M. A. Flores-Hidalgo
División de Estudios de Posgrado, Facultad de Ingeniería Mecánica y Eléctrica,
Universidad Autónoma de Nuevo León, Pedro de Alba s/n, Ciudad Universitaria,
C.P. 66451, San Nicolás de los Garza, N.L., Mexico

J. M. Seminario (ed.), *Design and Applications of Nanomaterials for Sensors,*
Challenges and Advances in Computational Chemistry and Physics 16,
DOI 10.1007/978-94-017-8848-9_11, © Springer Science+Business Media Dordrecht 2014

Graphene [5] a two dimensional (2D) sheet of carbon atoms in a honeycomb arrangement had attracted a huge scientific interest mainly due to the outstanding transport properties, chemical and mechanical stability and to the scalability of graphene devices to nano-dimensions. Thanks to charge carrier oneness, graphene-based electrical sensors have the potential to revolutionize sensor technology. Moreover, the operational principle of mono or bilayer graphene devices is based on changes in the electrical conductivity, σ, due to gas molecules adsorbed on graphene's surface which acts as donors or acceptors [7].

11.2 Molecular Model of Bi Layer Graphene Sheet

In order to thoughtfully understand the experimental results, one needs to have a profound knowledge of the molecule's behavior of graphene surface.

This work is based in molecular simulation of graphitic/graphenic islands, which can provide a suitable molecular model of graphene islands.

In order to simulate a graphene single sheet, a suggested model of Campagnini et al [1]. was used. The model consists of considering a circumcoronene which is a planar polycyclic Aromatic hydrocarbon (PAH) with D_{6h} symmetry.

Bi layer graphene geometry was relaxed using Density Functional Theory (DFT) [6] with B97-D functional [6] and 6-31G(d) basis set both as implemented in the series of programs Gaussian 09 [4].

Frequency and energy values were calculated for the graphene sheet in the ground state. All the calculations were performed in a singlet state because stability presented the same state.

11.3 Results and Discussion

In order to simulate bi layer graphene as we explained before, each graphene single sheet is formed by a circumcoronene of 19 Benzene rings, as depicted in Fig. 11.1, following the C^+ ion irradiation by 500 keV in order to isolate graphitic domains in nanometer range as suggested by Campagnini et al. [1]

Molecules were obtained from PubChem data. [8] The separation distance between the selected molecule carbon monoxide in this case, and the graphene bilayer was 2.0 Å. Once the molecule is placed over the graphene sheet, geometry optimization using the same theoretical level (with the same functional B97-D and the same basis set 6-31G (d) as used in to treat circumcoronene in prior calculations) was performed. Subsequently, the next calculation was to obtain the frequencies, using the same functional and basis set as previously described, in order to corroborate the stationary points (non-existence of imaginary frequencies).

To optimize the graphene molecule, we used the central hexagon of a circumcoronene and the atoms were located in the C–C bridge bond sites.

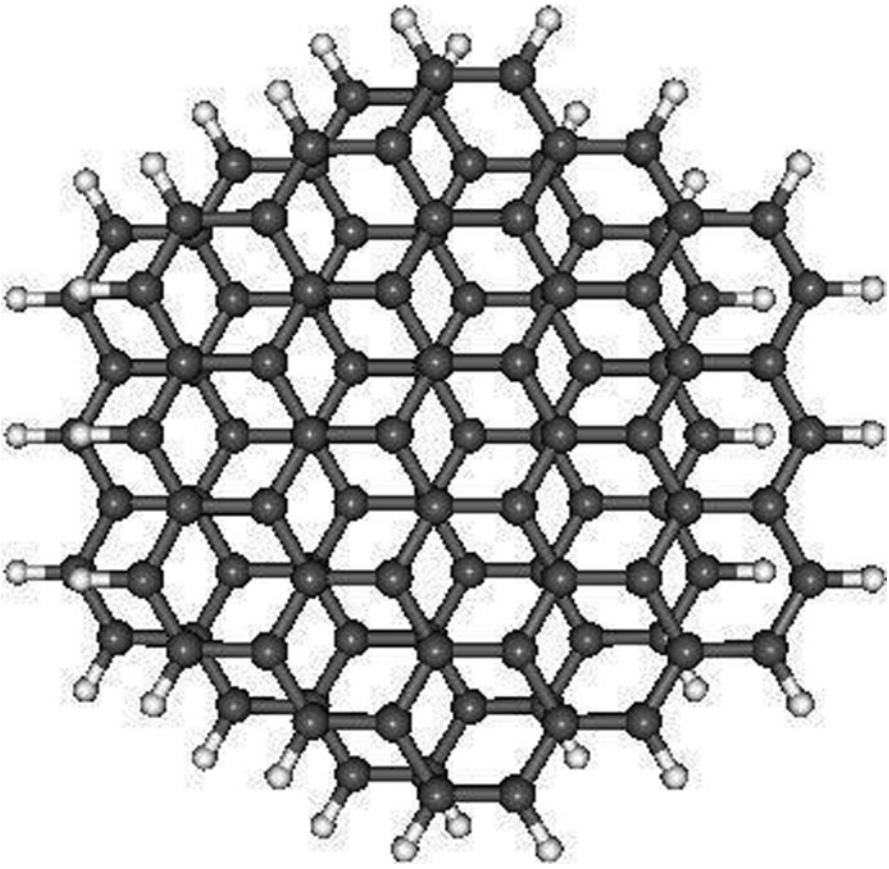


Fig. 11.1 Molecular model for bilayer graphene. Each layer is a circumcoronene of 19 Benzenerings

Finally, the neutral energy is calculated, and from such calculations, the frontier orbitals HOMO and LUMO were obtained.

Table 11.1 provides the C–C, interlayer and CO-graphene distances for each configuration like graphene before, graphene after and CO-graphene optimized structures. C–C distance is 1.40 Å, while for the interlayer distance is 3.35 Å for graphene before optimization. In addition, for graphene after optimization, C–C distance is 1.42 Å and 3.23 Å for the interlayer distance. Notice a small difference due to the optimized method used. See Figs. 11.2 and 11.4 respectively. Furthermore, when the CO molecule is located over the graphene layer, the C–C distance and the interlayer distance remain to be 1.42 and 3.23 Å respectively, while the CO-graphene yields to be 3.42 Å.

Figures 11.3 and 11.5 yield information about structure and Frontier orbital analysis for Graphene optimized and CO-Graphene optimized structures. Such information is provided in Table 11.2. For Graphene optimized struc-

Table 11.1 Structure, C–C distance (Å), interlayer distance (Å), CO-graphene distance (Å) for the analyzed structures

Structure	C–C distance (Å)	Interlayer distance (Å)	CO-graphene distance (Å)
Graphene before optimization	1.40	3.35	
Graphene after optimization	1.42	3.23	
CO-Graphene optimized	1.42	3.23	3.42

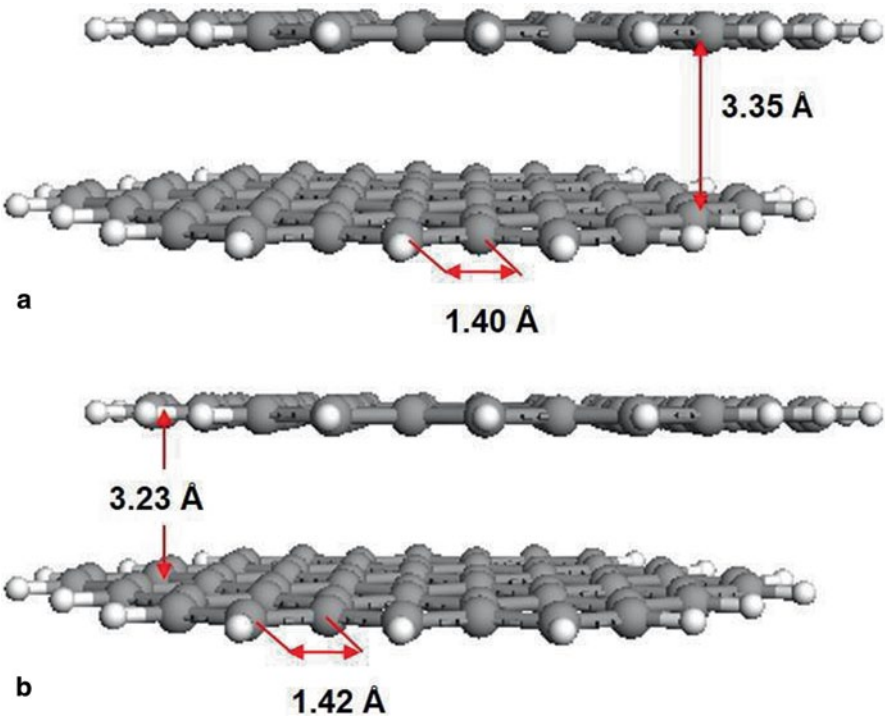


Fig. 11.2 **a** Graphene before optimization. **b** Graphene after optimization

ture, the HOMO is located at −4.099429 eV, while for the LUMO is located at −2.4912501 eV, with a reported HOMO-LUMO Gap of 1.618 eV. Afterwards, when the CO molecule is located over the graphene sheet and performing the optimization to such structure, the HOMO is located at −4.104055 eV and the LUMO is located at −2.4912501 eV, while the HOMO-LUMO Gap slightly changes to 1.612 eV. The small change observed could be attributed to the CO molecule adsorbed to the graphene surface.

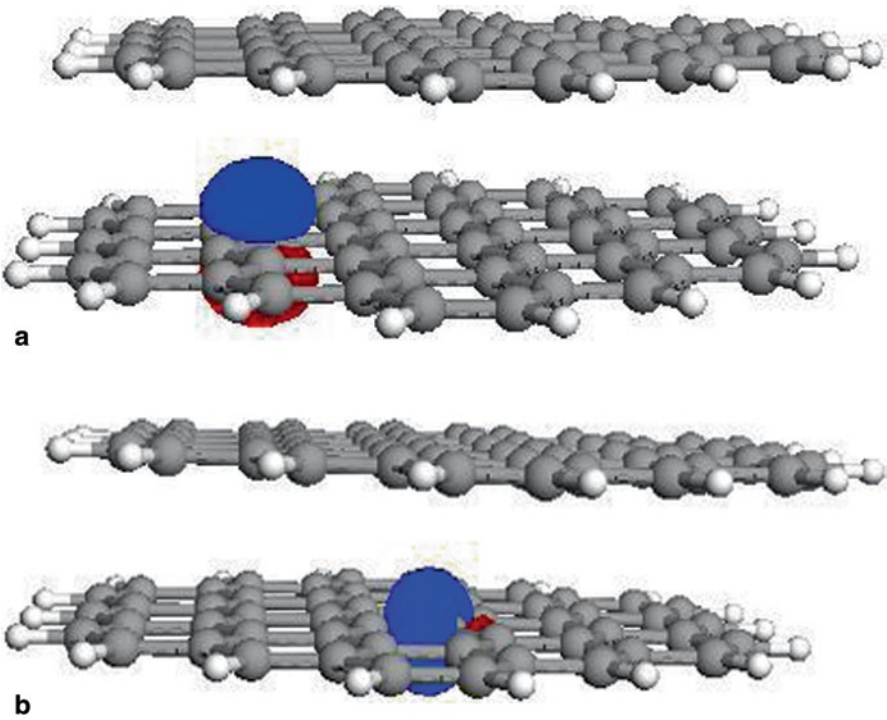


Fig. 11.3 **a** Graphene frontier orbitals HOMO. **b** Graphene frontier orbitals LUMO

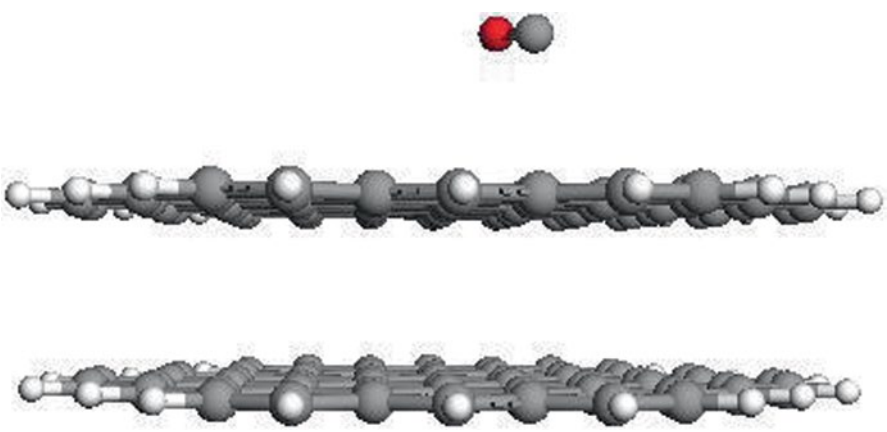


Fig. 11.4 CO-Graphene optimized structure

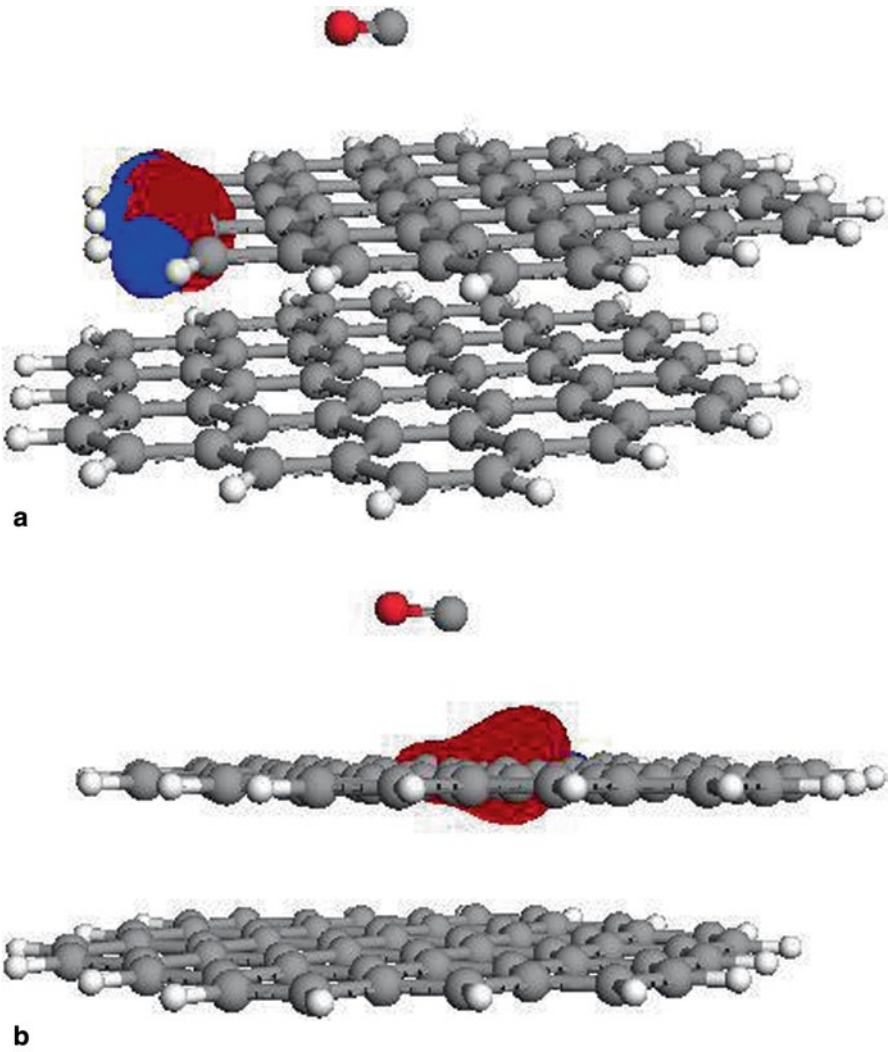


Fig. 11.5 **a** CO-Graphene frontier orbitals HOMO. **b** CO-Graphene frontier Orbitals LUMO

Table 11.2 Structure, HOMO (eV), LUMO (eV), HOMO—LUMO Gap (eV) for the analyzed structures

Structure	HOMO (eV)	LUMO (eV)	HOMO—LUMO Gap (eV)
Graphene after optimization	−4.099429	−2.4912501	1.618
CO-Graphene optimized	−4.104055	−2.4912501	1.612

11.4 Conclusions

In contrast with the infinite graphene sheet which has been reported to be a zero-gap semiconductor, this electronic behavior changes when the graphene sheet is irradiated. Our molecular model yields a gap of 1.618 eV for the HOMO-LUMO GAP. For our analyzed case of CO-Graphene, the gap is reduced to 1.612 eV, which yields indication that the CO molecule was adsorbed on the surface. The trend observed in the adsorption energy is in agreement with the trend reported by other authors like Leenaert et al. [10] except that our reported values are bigger.

References

1. Campagnini G, Forte G, Giannazzo F, Raineri V, La Magna A, Deretzis I (2011) Ion beam induced defects in graphene: Raman spectroscopy and DFT calculations. J Mol Struct 993: 506–509
2. Collins PG, Bradley K, Ishigami M, Zettl A (2000) Extreme oxygen sensitivity of electronic properties of carbon nanotubes. Science 287:1801–1804
3. Dutta P, Horn PM (1981) Low frequency fluctuations in solids: 1/f noise. R Mod Phys 53: 497–516
4. Frisch MJ, Trucks GW, Schlegel HB, Scuseria GE, Bob MA, Cheesman JR, Scalamani G, Barone V, Mennucci B, Petersson GA, Nakatsuji H, Caricato M, Li X, Hratchian HP, Izmaylov AF, Bloino J, Zheng G, Sonnenberg JL, Hada M, Ehara M, Toyota K, Fukuda R, Hasegawa J, Ishida M, Nakajima T, Hondo Y, Kitao O, Nakai H, Vreven T, Montgomery JA Jr, Peralta JE, Ogliaro F, Bearpark M, Heyd JJ, Brothers E, Kudin KN, Staroverov VN, Kobayashi R, Normand J, Raghavachari K, Rendell A, Burant JC, Iyengar SS, Tomasi J, Cossi M, Rega N, Millam NJ, Klene M, Knox JE, Cross JB, Bakken V, Adamo C, Jaramillo J, Gomperts R, Stratmann RE, Yazyev O, Austin AJ, Cammi R, Pomelli C, Ochterski JW, Martin RL, Morokuma K, Zakrzewski VG, Voth GA, Salvador P, Danneberg JJ, Dapprich S, Daniels AD, Farkas Ö, Foresman JB, Ortiz JV, Cioslowski J, Fox DJ (2009) Gaussian 09, Revision A. 1. Gaussian Inc., Wallingford, CT
5. Geim AK, Novoselov KS (1964) The rise of graphene. Nat Mater 6:183–191
6. Grimme S (2006) Semiempirical GGA-type density functional constructed with a large-range dispersion correction. J Comput Chem 27(15):1787–1799
7. Hohenberg P, Kohn W (1964) Inhomogeneous electron gas. Phys Rev 136:B864–B871
8. http://pubchem.ncbi.nlm.nih.gov/. Accessed 10 Mar 2011
9. Kong J, Franklin NR, Zhou C, Chapline MG, Peng S, Cho K, Doi H (2000) Nanotube molecular wires as chemical sensors. Science 287:622–625
10. Leenaerts O, Partoens B, Peters FM (2008) Adsorption of H_2O, NH_3, CO, NO_2 and NO on graphene: a first-principle study. Phys Rev B 77:125416
11. Moseley PT (1997) Solid state gas sensors. Meas Sci Technol 8:223–237

Index

A
Aptamer
  based sensors, 62
    with graphene and CNT substrates, 66
  biosensor
    aptasensor, 62
    electrochemical, 63, 64
    optical, design of, 62
    with graphene-based FET structure, 67*f*
  molecule beacons, 63
  thrombine binding aptamer, 90
Average local ionization energies, 251, 257

B
Biosensor *see under* Aptamer

C
Carbon nanotubes (CNTs), 65, 86, 100, 186, 249, 253, 259, 278, 281
  based gas sensor, 103–118
  CNTFET, 107, 108*f*
  heat dissipation by, 102
  MWCNT, 88
  peptides binding to, 87–89
  SWNT, 33, 34*f*, 35*f*, 36*t*, 42*t*, 66, 104
  thermal transport in, 118–130
  unrolled, 250
Catalyst, 77, 138, 140, 143, 146
  types of
    biological, 141, 142, 158–165
    chemical, 140, 141, 146–157
Chemical reactivity, 252
  of pheophorbide A, 218, 229–239
Chemical sensors, 66
Cobalt phthalocyanine, 187, 188f, 191, 194, 209, 210
Conceptual DFT, 218, 232, 233

D
Density functional theory (DFT), 33, 88, 105, 123, 143, 146, 158, 161, 166, 186–188, 191, 225, 231, 253, 282
  calculations, 3, 8, 11, 13, 24, 39, 88, 163, 166, 192, 203
Density of states (DOS), 9, 23*f*, 47*f*, 133, 192, 194, 272
  PDOS, 277
  VDOS, 124, 125*f*
Deoxyribonucleic acid (DNA), 32, 33, 53, 54*f*, 55, 56, 62, 64, 79–82, 90, 91*f*, 187, 194

E
Electrical conduction, 186, 188
Energy bands, 272, 276
Enzyme, 63, 69, 79, 141–144, 158, 159, 161–164, 166

F
Field-effect
  CNTFET, 107
  FET, 65, 66, 69
  GEFT, 65
Fuel cell, 139, 166
  applications, types of catalysts for
    biological catalysts, 141, 142
    chemical catalysts, 140, 141
  PEM, 138

Note: Page numbers followed by "*f*", "*t*" indicate figures and tables respectively

J. M. Seminario (ed.), *Design and Applications of Nanomaterials for Sensors,*
Challenges and Advances in Computational Chemistry and Physics 16,
DOI 10.1007/978-94-017-8848-9, © Springer Science+Business Media Dordrecht 2014

Fuel oxidation, 141, 142, 158, 165
Functionalized graphene *see under* Graphene

G
Graphene, 249–251, 272, 277*t*, 284, 285*f*
and graphene based FET structure, 64–66
fabrication, 187
functionalized graphene (FG), 173, 186, 187, 191, 194, 198, 203, 205, 209, 210
models, 187, 198, 202*f*, 208*f*, 209, 256*f*, 257, 260, 261, 267
peptides binding to, 86, 87
structural models, 188*f*
Green function, 8, 9, 24, 193, 194

H
Hydrogenation energies, 267

I
Ionization potentials and electron affinities, 32–33, 37*f*, 38*f*, 57, 234, 242*t*

M
Modeling, 120, 121, 142, 143, 263, 265
biological catalysts, challenges in, 158–165
chemical catalysts, challenges in, 146–157
Molecular simulations, 282
Molecular structure, 11, 221
of complexes, 190*f*, 204*f*,
of pheophorbide, 222*f*–224*f*

N
Nanodevice, 61, 74, 83, 218
for DNA cleaving, 80–82
Nanosensor, 2, 24, 61
SERS, 82
design considerations, 89–92
Nanowires (NWs), 62, 70, 76, 77*f*, 83, 84, 85*f*, 86, 281

P
Peptides
CNT binding, 87–89
graphene binding, 86, 87
Pheophorbide A, 218, 225, 226*t*–232*t*, 237*t*–240*t*, 242*t*, 243*t*, 245*t*
absorption spectrum of, 235*f*, 236*f*
chemical reactivity of, 218, 229–239
HOMO and LUMO orbitals of, 241*f*
infrared spectrum of, 233*f*, 234*f*
molecular structure of, 222*f*–224*f*
Piezoelectric effect, 70
Platinum, 85, 138, 142, 147–151, 166 *see also* Catalyst
Plutonium, 1, 2, 11–13, 15, 18, 23, 24
Pristine and defect-containing graphene model, 254–257
C–C bond lengths in, 256*t*
reactive sites and initial interactions on, 257–262

Q
Quantum dots (QDs), 62
biological applications of, 78–80
core shell, 75
on semiconductor surfaces, 76–78
Quantum transport processes, 103, 105

R
Redox chemistry, 32, 37, 43, 57
Ribonucleic acid (RNA), 62, 63, 81, 82
Rotated diffraction patterns, 275*f*

S
Self-diffusion, 180
Site reactivities, 251
Supercritical fluids, 172

T
Thermal properties of nanotubes, 103
Tight-bind, 105, 186, 273, 277*t*
Transistor, 70, 101, 108*f*, 250, 272
CNTFET, 107
FET, 65, 66, 69
GEFT, 65

U
Uranium, 1, 2, 11, 18, 23